AG ARD

ADVISORY GROUP FOR AEROSPACE RESEARCH & DEVELOPMENT

7 RUE ANCELLE

AGARD LECTURE SERIES No.121

High Angle-of-Attack Aerodynamics

DTIC
ELECTE
MAY 3 1983

H

NORTH ATLANTIC TREATY ORGANIZATION

DISTRIBUTION AND AVAILABILITY
ON BACK COVER

83 05 02 123

AGARD-LS-121

NORTH ATLANTIC TREATY ORGANIZATION

ADVISORY GROUP FOR AEROSPACE RESEARCH AND DEVELOPMENT

(ORGANISATION DU TRAITE DE L'ATLANTIQUE NORD)

AGARD/VKI Lecture Series No.121

HIGH ANGLE-OF-ATTACK AERODYNAMICS

THE MISSION OF AGARD

The mission of AGARD is to bring together the leading personalities of the NATO nations in the fields of science and technology relating to aerospace for the following purposes:

— Exchanging of scientific and technical information;

— Continuously stimulating advances in the aerospace sciences relevant to strengthening the common defence posture;

— Improving the co-operation among member nations in aerospace research and development;

— Providing scientific and technical advice and assistance to the North Atlantic Military Committee in the field of aerospace research and development;

— Rendering scientific and technical assistance, as requested, to other NATO bodies and to member nations in connection with research and development problems in the aerospace field;

— Providing assistance to member nations for the purpose of increasing their scientific and technical potential;

— Recommending effective ways for the member nations to use their research and development capabilities for the common benefit of the NATO community.

The highest authority within AGARD is the National Delegates Board consisting of officially appointed senior representatives from each member nation. The mission of AGARD is carried out through the Panels which are composed of experts appointed by the National Delegates, the Consultant and Exchange Programme and the Aerospace Applications Studies Programme. The results of AGARD work are reported to the member nations and the NATO Authorities through the AGARD series of publications of which this is one.

Participation in AGARD activities is by invitation only and is normally limited to citizens of the NATO nations.

ii

FOREWORD

In 1978, an AGARD Fluid Dynamics Panel Symposium was organized in Sandefjord.
Norway on the subject "High Angle-of-Attack Aerodynamics", the corresponding publication
was AGARD Conference Proceedings No.247. The aim of the symposium was "to bring
together those working on fundamental fluid mechanics aspects of flight at high incidence
and those concerned with the aerodynamic design of flight vehicles . . .". Due to the rapid
increase of interest in this subject since 1978, the AGARD Fluid Dynamics Panel decided
to organize a Lecture Series bearing the same title and having essentially the same aim;
however, as a Lecture Series, the meeting will have the flavor of a tutorial.

Two formats have been chosen for the Lecture Series. The DFVLR in Göttingen.
Germany and NASA Langley in the United States will each host a two-day version featuring
seven lecturers whose presentations are included in this volume. A one-week version will be
hosted and co-sponsored by the von Kármán Institute for Fluid Dynamics in Rhode-Saint-
Genèse. Belgium.

The Lecture Series begins with a review of three-dimensional flows on simple
components including separation and reattachment. Particular emphasis is placed on the
vortical flows which characterize the high-alpha regime. Vortex breakdown, vortex control.
and the effect of compressibility on these three-dimensional flows as well as the present and
future capabilities of computational techniques are discussed. These fundamental lectures
are supplemented by a description of the techniques currently employed by combat aircraft
and missile design groups. Finally, the important field of unsteady aerodynamics and its
implications for the high-alpha case is reviewed.

These lectures should be of interest to fundamental aerodynamicists who have been
attracted by the fluid mechanics of vortices and three dimensional geometries as well as to
design engineers from establishments concerned either with combat aircraft or maneuvering
missiles.

I take this opportunity to thank the lecturers for preparing a very interesting set of
notes and their organizations for supporting this activity.

J.F.WENDT
Lecture Series Director

iii

LIST OF SPEAKERS

Lecture Series Director: Professor J.F.Wendt
von Kármán Institute for Fluid Dynamics
Chaussée de Waterloo, 72
1640 Rhode-Saint-Genèse
Belgium

SPEAKERS

Mr G.Gregoriou
Messerschmitt Bölkow-Blohm GmbH
Postfach 801149
8000 München 80
Germany

Dr B.Hunt
British Aircraft Corporation
Military Aircraft Division
Warton Aerodrome
Preston PR4 1AX
Lancashire
UK

Dr K.Orlik-Rückemann
Unsteady Aerodynamics Laboratory
National Research Council
Montreal Road
Building M-10
Ottawa, Ontario K1A OR6
Canada

Mr L.Vigevano*
von Kármán Institute for Fluid Dynamics
Chaussée de Waterloo, 72
1640 Rhode-Saint-Genèse
Belgium

Dr J.R.Deane*
British Aerospace
Dynamics Group
Bristol Division, P.O.B. 5
Filton, Bristol BS12 7QW
UK

Dr D.J.Peake
NASA Ames Research Center
Mail Stop 227-8
Moffett Field
California 94035
USA

Mr A.Skow
Northrop Corporation
Mail Stop 3815/85
1 Northrop Avenue
Hawthorne
California 90250
USA

Mr H.Werlé
ONERA
29, Avenue de la Division Leclerc
92320 Châtillon
France

Dr W.Wedekind*
Dept. B.F.
Dornier GmbH
Postfach 1420
799 Friedrichshafen 1
Germany

Dr E.Wedemeyer*
DFVLR
Bunsenstrasse, 10
3400 Göttingen
Germany

---

* VKI presentation only.

iv

CONTENTS

---

* Additional papers presented only at the VKI

THREE-DIMENSIONAL SEPARATION AND REATTACHMENT

David J. Peake and Murray Tobak
Ames Research Center, NASA
Moffett Field, California 94305, U.S.A.

SUMMARY

One of the common ingredients of the inviscid-viscous interacting flow fields about bodies at angle of attack is the predilection of the boundary layers growing around the body to detach from the leeward surface along swept separation lines to form coiled vortex motions. In all cases of three-dimensional flow separation and reattachment, the assumption of continuous vector fields of skin-friction lines and external flow streamlines, coupled with simple laws of topology, provides a flow grammar whose elemental constituents are the singular points: the nodes, spiral nodes (foci), and saddles. The phenomenon of three-dimensional separation may be construed as either a local or a global event, depending on whether the skin-friction line that becomes a line of separation originates at a node or a saddle point. Adopting these notions enables us to create sequences of plausible flow structures, to deduce mean flow characteristics, to expose flow mechanisms, and to aid theory and experiment where lack of resolution in wind-tunnel observations or in the results from numerical computations causes imprecision in diagnosis.

1. INTRODUCTION

The separation of three-dimensional (3-D) turbulent boundary layers from the lee of flight vehicles at high angles of attack results in dominant, large-scale, coiled vortex motions that pass along the body in the general direction of the free stream. Such complex and highly interactive flow fields remain an area of fluid mechanics and aerodynamics that is still beyond the reach of definitive theory or numerical computation. If the aerodynamic design of a lifting vehicle with flow separation is to be successful over the full range of flight conditions, the vehicle must be controllable at all times and possess no unpleasant changes in force and moment characteristics. To achieve these aims, the primary lines of separation should remain symmetrically placed and preferably fixed on the body and give rise to symmetric vortices to eliminate the development of potentially uncontrollable side forces and yawing moments. In fact, flow separation in three dimensions is of vital significance to the entire spectrum of aerodynamic design, for the skin-friction-line pattern containing swept lines of attachment, separation, and reattachment, in association with a limited number of singular points, constitutes the skeleton structure around which the elements of the entire flow field can be assembled (Ref. 1).

The obtainment of these skin-friction lines (that is, the loci of the local skin-friction vectors) has usually been attempted with oil-streak techniques on the surfaces of wind-tunnel models (Refs. 2-4), where it has been customarily considered that a necessary condition for the occurrence of flow separation is the convergence of oil-streak lines toward a particular line. Whether this is also a sufficient condition is a matter of current debate. Of the many attempts to make sense of these oil-flow patterns, few of the contending arguments have lent themselves to a precise mathematical formulation. Here, we wish to draw attention to the hypothesis supplied by Legendre (Ref. 5) as being one that provides a mathematical framework of considerable depth. The ensuing discussion follows closely that given already by Tobak and Peake (Ref. 6).

2. LIMITING STREAMLINES AND SKIN-FRICTION LINES

Legendre (Ref. 5) proposed that a pattern of streamlines immediately adjacent to the surface (in his notation, "wall streamlines," but more conventionally termed "limiting streamlines") be viewed as trajectories having properties consistent with those of a continuous vector field, the principal one being that through any regular (nonsingular) point there passes one and only one trajectory. On the basis of this postulate, it follows that the elementary singular points of the field, namely the nodes, spiral nodes (foci), and saddles (see Fig. 1) can be categorized mathematically. Hence, the types of singular points, their number, and the rules governing the relations between them, can be said to characterize the pattern. Flow separation in this view has been defined by the convergence of wall streamlines toward a particular wall streamline that originates from a singular point of particular type, the saddle point. This view of flow separation is not universally accepted, however, and situations exist in which a more nuanced description of flow separation appears to be required.

Addressing himself specifically to viscous flows, Lighthill (Ref. 7) tied the postulate of a continuous vector field to the pattern of skin-friction lines rather than to the limiting streamlines just above the surface. Parallel with Legendre's definition, the convergence of skin-friction lines toward a particular skin-friction line originating from a saddle point was defined as the necessary condition for flow separation. [Note that in the above, the separation line is the asymptote of the adjacent skin-friction lines and not the envelope, as Maskell (Ref. 1) had proposed.] More recently, Hunt et al. (Ref. 8) have shown that the notions of elementary singular points and the simple rules that they collectively obey can be extended to the flow above the surface in planes of symmetry, in projections of conical flows (Ref. 9), in crossflow planes, and so on (see also Ref. 10). Further applications and extensions can be found in the various contributions of Legendre (Ref. 11-13), Oswatitsch (Ref. 14), and in the review article by Peake and Tobak (Ref. 4).

The question of an adequate, yet convincing, description of 3-D separated flow arises with especial poignancy when one asks how 3-D separated flow patterns originate and how they succeed one another as the relevant parameters of the problem (e.g., angle of attack, Mach number, and Reynolds number) are varied. In a recent essay (Ref. 6), we suggested that we might answer this question by placing Legendre's hypothesis (utilizing skin-friction lines) within a framework broad enough to include the notions of topological structure and structural stability (see Refs. 15, 16) coupled with arguments from bifurcation theory (see Refs. 17, 18, 19). In the following, we shall try to show that the emergence of a description of 3-D

separated flow about configurations at angle of attack will, in fact, be facilitated by this broader framework. In so doing, we limit our attention to 3-D viscous flows that are steady in the mean.

3. HYPOTHESIS

The postulate that the skin-friction lines on the surface of the body are the trajectories of a continuous vector field can be interpreted mathematically as follows. Let (ξ, η, ζ) be general curvilinear coordinates with (ξ, η) set as orthogonal axes in the surface and ζ normal to them. Let the length parameters be $h_1(\xi,\eta)$ and $h_2(\xi,\eta)$. Except at singular points, it follows from the adherence condition that very close to the surface, the components of the velocity vector (u_1, u_2) parallel to the surface must grow from zero linearly with ζ. Hence, a particle on a streamline near the surface will have velocity components

$$h_1(\xi,\eta) \frac{d\xi}{dt} = \zeta \frac{\partial u_1}{\partial \zeta}(\xi,\eta,0) = -\zeta\omega_2(\xi,\eta) = \zeta P(\xi,\eta) \Biggr\}$$

and
$$\qquad\qquad (1)$$

$$h_2(\xi,\eta) \frac{d\eta}{dt} = \zeta \frac{\partial u_2}{\partial \zeta}(\xi,\eta,0) = \zeta\omega_1(\xi,\eta) = \zeta Q(\xi,\eta) \Biggr\}$$

where (ω_1, ω_2) are the local orthogonal components of the surface vorticity vector. (Note that the surface vortex lines that exist everywhere at right angles to the skin-friction lines are also trajectories of a continuous vector field.) The specification of a steady flow allows (u_1, u_2) to be independent of time. With ζ treated as a parameter and P and Q functions only of the coordinates, Eq. (1) is composed of a pair of autonomous ordinary differential equations. Their form places them in the same category as the equations studied by Poincaré (Refs. 20 and 21; an English translation of his complete works is given in Ref. 22) in his classical investigation of the curves defined by ordinary differential equations. Letting

$$\tau_{w_1} = \mu \frac{\partial u_1}{\partial \zeta}(\xi,\eta,0) \Biggr\}$$

$$\qquad\qquad (2)$$

$$\tau_{w_1} = \mu \frac{\partial u_2}{\partial \zeta}(\xi,\eta,0) \Biggr\}$$

be components of the skin-friction parallel to ξ and η, respectively, we have for the equation governing the trajectories of the surface shear-stress vector, from Eqs. (1),

$$\frac{h_1 d\xi}{\tau_{w_1}} = \frac{h_2 d\eta}{\tau_{w_2}} \qquad\qquad (3)$$

Alternatively, for the trajectories of the surface vorticity vector, the governing equation is

$$\frac{h_1 d\xi}{\omega_1} = \frac{h_2 d\eta}{\omega_2} \qquad\qquad (4)$$

4. SINGULAR POINTS

Singular points in the pattern of skin-friction lines occur at isolated points on the surface where the skin-friction (τ_{w_1}, τ_{w_2}) in Eq. (3) or, alternatively, the surface vorticity (ω_1, ω_2) in Eq. (4), becomes identically zero. Singular points are classifiable into two main types: nodes and saddle points. Nodes may be further subdivided into two subclasses: nodal points and spiral nodes (often called foci of attachment or separation).

A nodal point (Fig. 1a) is the point common to an infinite number of skin-friction lines. At the point, all of the skin-friction lines except one (labeled AA in Fig. 1a) are tangential to a single line BB. At a nodal point of attachment, all of the skin-friction lines are directed outward away from the node. At a nodal point of separation, all of the skin-friction lines are directed inward toward the node. In the presence of axisymmetry, the node degenerates into a "star-like" or "source-like" form.

A spiral node or focus (Fig. 1b) differs from a nodal point in Fig. 1a in that it has no common tangent line. An infinite number of skin-friction lines spiral around the singular point, either away from it (at attachment) or into it (at separation). Spiral nodes of attachment occur generally in the presence of rotation, either of the flow or of the surface, and will not be included in this study. In the exceptional case, the trajectories of the spiral node form closed paths around the singular point. The spiral node is then called a center.

At a saddle point (Fig. 1c), there are only two particular lines, CC and DD, that pass through the singular point. The directions on either side of the singular point are inward on one particular line and outward on the other particular line. The remainder of the skin-friction lines take directions consistent with the direction of the adjacent particular lines. As can be determined from Fig. 1c, the particular lines act as barriers in the field of skin-friction lines, making one set of skin-friction lines inaccessible to an adjacent set.

For each of the patterns in Figs. 1a-1c, the surface vortex lines form a system of curves orthogonal at every point to the system of skin-friction lines. Of all the possible patterns of skin-friction lines

on the surface of a body, only those are admissible whose singular points obey a simple topological rule: the number of nodes (including spiral nodes if present) must exceed the number of saddle points by two (see Refs. 7, 21, 23).

5. TOPOGRAPHY OF SKIN-FRICTION LINES

The singular points, acting either in isolation or in combination, fulfill certain characteristic functions that largely determine the distribution of skin-friction lines on the surface. The nodal point of attachment is typically a stagnation point on a forward-facing surface, such as the nose of a body, where the external flow from far upstream attaches itself to the surface. The nodal point of attachment thereby acts as a source of skin-friction lines that emerge from the point and spread out over the surface. Conversely, the nodal point of separation is typically a point on a rearward-facing surface; it acts as a sink where the skin-friction lines that have circumscribed the body surface may vanish.

The saddle point acts typically to separate the skin-friction lines issuing from or entering into adjacent nodes; for example, adjacent nodal points of attachment. An example of this function is illustrated in Fig 2a (Ref. 7) and in the skin-friction-line pattern on the cockpit windows of a Space Shuttle model (Fig. 2b, courtesy of L. Seegmiller, Ames Research Center). Skin-friction lines emerging from the nodal points of attachment are prevented from crossing by the presence of a particular skin-friction line emerging from the saddle point. Lighthill (Ref. 7) called this particular line a line of separation, and identified the existence of a saddle point from which the particular line emerges as the necessary condition for flow separation. As the patterns in Fig. 2 illustrate, skin-friction lines from either side tend to converge on the particular line issuing from the saddle point. However, the convergence of skin-friction lines on either side of a particular line occurs in situations in which a saddle point can neither be seen nor can be rationally argued to exist. It can happen, for example, that a skin-friction line, one of the infinite set of lines emanating from a nodal point of attachment, may become a line toward which others of the set converge.

In the following, we shall attempt to construct an appropriate physical description of flow separation by utilizing the notions already advanced and by appealing to the theory of structural stability and bifurcation. Adopting a terminology that is suggested by the theoretical framework, we say that a skin-friction line emerging from a saddle point is a global line of separation and leads to global flow separation. In the alternative case, in which the skin-friction line on which other lines converge does not originate from a saddle point, we shall identify the line as being a local line of separation, leading to local separation. (When no modifier is used, what is said will apply to either case.)

The notion of local separation may be clarified by taking the example of the flow over a smooth slender body of revolution that is inclined at a small angle of attack to a uniform oncoming stream. A streamline in the oncoming flow attaches itself to the nose at the stagnation point and nodal singular point of attachment. This is the source of the continuous pattern of skin-friction lines that emerge from this point and envelop the body, all of which disappear into a nodal point of separation at the rear. Because of favorable pressure gradient in the circumferential direction, all the way from the windward ray to the leeward ray, the skin-friction lines emanating from the nodal point of attachment sweep around the sides of the body and converge on either side of the particular skin-friction line running along the leeward ray. This particular leeward skin-friction line, beginning at the node of attachment and finishing at the node of separation, is hence a local separation line. It follows that a body of revolution experiences flow separation at all angles of attack other than zero.

The converse of the line of separation is the line of attachment, from which adjacent skin-friction lines diverge. Two lines of attachment are illustrated in Fig. 2a, emanating from each of the nodal points of attachment.

The limiting streamlines, that is, the ones that pass very close to the surface, leave the proximity of the surface very rapidly in the vicinity of a separation line. A simple argument due to Lighthill (Ref. 7) illustrates the flow mechanism. Referring to Eq. (3), let us align (ξ, n) with the external streamline coordinates so that τ_{w_1} and τ_{w_2} are the streamwise and crossflow skin-friction components respectively. If n is the distance between two adjacent limiting streamlines (see Fig. 3) and h is the height of a rectangular streamtube (being assumed small so that the local resultant velocity vectors are coplanar and form a linear profile), then the mass flux through the streamtube is

$$\dot{m} = \rho h n \bar{u}$$

where ρ is the density and $\bar{u}$ the mean velocity of the cross section. But the resultant skin friction at the wall is the resultant of τ_{w_1} and τ_{w_2} or

$$\tau_w = \mu \frac{\bar{u}}{h/2}$$

so that

$$\bar{u} = \frac{\tau_w h}{2\mu}$$

Hence,

$$\dot{m} = \frac{h^2 n \tau_w}{2\nu} = \text{constant}$$

yielding

$$h = C\left(\frac{\nu}{n\tau_w}\right)^{\frac{1}{2}} \; ; \; \nu = \frac{\mu}{\rho}$$

Thus, as the line of separation is approached, h, the height of the limiting streamline above the surface, increases rapidly. There are two reasons for this increase in h: first, whether the line of separation is global or local, the distance n between adjacent limiting streamlines falls rapidly as the limiting streamlines converge toward the line of separation; second, the resultant skin-friction τ_w drops toward a minimum as the line of separation is approached and, in the case of the global line of separation, actually approaches zero as the saddle point is approached.

Limiting streamlines rising on either side of the line of separation are prevented from crossing by the presence of a stream surface stemming from the line of separation itself. The existence of such a stream surface is characteristic of flow separation; how it originates determines whether the separation is of global or local form. In the former case, the presence of a saddle point as the origin of the global line of separation provides a mechanism for the creation of a new stream surface that originates at the wall. Emanating from a saddle point and terminating at nodal points of separation (either nodes or spiral nodes), the global line of separation traces a smooth curve on the wall which forms the base of the stream surface, the streamlines of which have all entered the fluid through the saddle point. We shall call this new stream surface a dividing surface. The dividing surface extends the function of the global line of separation into the flow, acting as a barrier separating the set of limiting streamlines that have arisen from the surface on one side of the global line of separation from the set arisen from the other side. On its passage downstream, the dividing surface rolls up to form the familiar coiled sheet around a central vortical core. Because it has a well-defined core, we use the popular terminology, calling the flow in the vicinity of the coiled-up dividing surface a vortex.

Now we consider the origin of the stream surface characteristic of local flow separation. We note that if a skin-friction line emanating from a nodal point of attachment ultimately becomes a local line of separation, then there will be a point on the line beyond which each of the orthogonal surface vortex lines crossing the line is shaped concave facing downstream. At this point, the skin-friction along the line has become locally minimum. A surface, starting at this point and stemming from the skin-friction line downstream of the point, can be constructed that will be the locus of a set of limiting streamlines originating from far upstream; this surface may also roll up on its development downstream.

This section concludes with a discussion of the remaining type of singular point, the spiral node (also called focus). The spiral node invariably appears on the surface in company with a saddle point. Together they allow a particular form of global flow separation. One leg of the (global) line of separation emanating from the saddle point winds into the spiral node to form the continuous curve on the surface from which the dividing surface stems. The spiral node on the wall extends into the fluid as a concentrated vortex filament, while the dividing surface rolls up with the same sense of rotation as the vortex filament. When the dividing surface extends downstream, it quickly draws the vortex filament into its core. In effect, then, the extension into the fluid of the spiral node on the wall serves as the vortical core about which the dividing surface coils. This flow behavior was first hypothesized by Legendre (Ref. 11), who also noted (Ref. 12) that an experimental confirmation existed in the results of earlier experiments carried out by Werlé (Ref. 24). Figure 4a shows Legendre's original sketch of the skin-friction lines; Fig. 4b is a photograph illustrating the experimental confirmation. The dividing surface that coils around the extension of the spiral node (Fig. 4c) will be termed here a "horn-type dividing surface." On the other hand, it can happen that the dividing surface to which the spiral node is connected does not extend downstream. In this case the vortex filament emanating from the spiral node remains distinct and is seen as a separate entity on crossflow planes downstream of its origin on the surface.

6. CHARACTER OF DIVIDING SURFACES

We have seen how the combination of a spiral node and a saddle point in the pattern of skin-friction lines allows a particular form of global flow separation characterized by a horn-type dividing surface. The nodal points of attachment and separation may also combine with saddle points to allow additional forms of global flow separation, again characterized by their particular dividing surfaces. The characteristic dividing surface formed from the combination of a nodal point of attachment and a saddle point is illustrated in Fig. 5a. This form of dividing surface typically occurs in the flow before an obstacle (see Fig. 34 in Peake and Tobak, Ref. 4), or near the nose of a blunt body at a very high angle of attack (see Fig. 81 in Peake and Tobak, Ref. 4). In the example illustrated in Fig. 5, it will be noted that the dividing surface admits of a point in the external flow at which the fluid velocity is identically zero. This is a three-dimensional singular point, which in Fig. 5a acts as the origin of the streamline running through the vortical core of the rolled up dividing surface.

The characteristic dividing surface formed from the combination of a nodal point of separation and a saddle point is illustrated in Fig. 5b, again a form of global separation. This form of dividing surface often occurs in nominally two-dimensional separated flows such as in the separated flow behind a backward-facing step (see Fig. 24 in Tobak and Peake, Ref. 25) and the separated flow at a cylinder-flare junction (both two and three dimensional; compare Figs. 47 and 48 in Peake and Tobak, Ref. 4). We note in both Figs. 5a and 5b that the streamlines on the dividing surface have all entered the fluid through the saddle point in the pattern of skin-friction lines.

Finally, in Fig. 5c the form of dividing surface materializing at a typical local separation is sketched. Here the eruption of the fluid from the surface, and hence the commencement of the dividing surface, occurs not from a nodal point of separation nor from a saddle point of separation, but from a regular (nonsingular) point on the surface where the surface vortex lines crossing a particular skin-friction line change curvature from concave facing upstream to concave facing downstream. At this point the skin-friction lines adjacent to the one particular skin-friction line begin to converge rapidly toward this particular line, the local separation line. The departure of the fluid from the vicinity of the surface again results in a tight coiling of the dividing surface and the adjacent external flow streamlines.

7. TOPOLOGY OF STREAMLINES IN TWO-DIMENSIONAL SECTIONS OF THREE-DIMENSIONAL FLOWS

Results reported by Smith (Refs. 9, 26), Perry and Fairlie (Ref. 10), and Hunt et al. (Ref. 8), have made it clear that the rules governing the behavior of skin-friction lines may be adapted and extended to yield similar rules governing the behavior of the flow field itself. This is possible when we construct two-dimensional sections of the three-dimensional flow, for example, crossflow planes and streamwise planes of symmetry, which are especially useful for flows around bodies at angle of attack. In particular, Hunt et al. (Ref. 8) have noted that if

$$\underline{v} = [u(x,y,z_0), \; v(x,y,z_0), \; w(x,y,z_0)]$$

is the mean velocity vector, whose u,v components are measured in a plane $z = z_0 = $ constant, above a surface situated at $y = Y(x;z_0)$ (see Fig. 6), then the mean streamlines in the plane are the solutions of

$$\frac{dx}{u} = \frac{dy}{v} \tag{5}$$

which are a direct counterpart of Eq. (3) for skin-friction lines on the surface. For a streamwise plane of symmetry $w(x,y,z_0) = 0$, then the streamlines defined by Eq. (5) are identifiable with particle path lines in the plane when the flow is steady, or with instantaneous streamlines when the flow is unsteady. Note, however, that if an arbitrary, two-dimensional section of the flow is chosen, Eq. (5) will not nec-essarily represent the projections of the three-dimensional streamlines on to that plane $z = z_0$.

In any case, since $[u(x,y), \; v(x,y)]$ is a continuous vector field $\underline{V}(x,y)$, with only a finite number of singular points in the interior of the flow at which $\underline{V} = 0$, it follows that nodes and saddles can be defined in the plane just as they were for skin friction lines on the surface. Nodes and saddles within the flow, excluding the boundary $y = Y(x;z_0)$, are labeled N and S, respectively, and are shown in their typical form in Fig. 6. The only new feature of the analysis that is required is the treatment of singu-lar points on the boundary, $y = Y(x,z_0)$. Since, for a viscous flow, $\underline{V}$ is zero everywhere on the boundary, the boundary is itself a singular line in the plane $z = z_0$. Singular points on the line occur where the component of the surface vorticity vector normal to the plane $z = z_0$ is zero. Thus, for example, it is ensured that a singular point will occur on the boundary wherever it passes through a singular point in the pattern of skin-friction lines, since the surface vorticity is identically zero there. As introduced by Hunt et al. (Ref. 8), singular points on the boundary are defined as half-nodes N' and half-saddles S' (Fig. 6). With this simple amendment to the types of singular points allowable, all of the previous notions and descriptions relevant to the analysis of skin-friction lines carry over to the analysis of the flow within the plane.

In a parallel vein, Hunt et al. (Ref. 8) have recognized that just as the singular points in the pat-tern of skin-friction lines on the surface obey a topological rule, so must the singular points in any of the sectional views of three-dimensional flows obey topological rules. Although a very general rule applying to general bodies can be derived (Ref. 8), we list here only those special rules that will be useful in subsequent studies of the flow past wings and bodies at angle of attack. In the five topological rules listed below, we assume that the body is simply connected and immersed in a flow that is uniform far upstream.

1. Skin-friction lines on a three-dimensional body (Refs. 7, 23):

$$\sum_N - \sum_S = 2 \tag{6}$$

2. Skin-friction lines on a three-dimensional body B connected simply (without gaps) to a plane wall P that either extends to infinity both upstream and downstream or is the surface of a torus:

$$\left(\sum_N - \sum_S\right)_{P+B} = 0 \tag{7}$$

3. Streamlines on a two-dimensional plane cutting a three-dimensional body:

$$\left(\sum_N + \frac{1}{2}\sum_{N'}\right) - \left(\sum_S + \frac{1}{2}\sum_{S'}\right) = -1 \tag{8}$$

4. Streamlines on a vertical plane cutting a surface that extends to infinity both upstream and downstream:

$$\left(\sum_N + \frac{1}{2}\sum_{N'}\right) - \left(\sum_S + \frac{1}{2}\sum_{S'}\right) = 0 \tag{9}$$

5. Streamlines on the projection onto a spherical surface of a conical flow past a three-dimensional body (Ref. 9):

$$\left(\sum_N + \frac{1}{2}\sum_{N'}\right) - \left(\sum_S + \frac{1}{2}\sum_{S'}\right) = 0 \tag{10}$$

8. TOPOLOGICAL STRUCTURE AND STRUCTURAL STABILITY

How, then, do 3-D separated flow patterns originate and how do they succeed one another as the relevant parameters (e.g., angle of attack, Reynolds number, and Mach number) are varied? Our approach to dealing with this question will be offered in physical terms, although our definitions should be compatible with whatever set of partial differential equations is assumed to govern the fluid motion. Specifically, we shall apply definitions of topological structure and structural stability to the properties of skin-friction-line patterns, since in so doing, we shall be able to utilize experimental oil-streak patterns directly.

A pattern of skin-friction lines on a given part of the body surface is a map (called a "phase portrait" by Andronov et al., Ref. 16) of the surface shear-stress vector. Two maps have the same topological structure if the paths in the first map are preserved in the second. This may be visualized by imagining a map of skin-friction lines on a deformable sheet of rubber. Disallowing folding or tearing of the sheet, every deformation is a path-preserving mapping. A topological property is then defined as any characteristic of the map that stays invariant under all deformations. The number and types of singular points and the existence of paths connecting the singular points are examples of topological properties. The set of all topological properties of the map describes the topological structure.

Let us also define the structural stability of a map relative to a parameter α; for instance, α may be the angle of attack. The map is said to be structurally stable at a given value of α if the map resulting from a very small change in α has the same topological structure as the initial one. Structurally stable maps of the surface shear-stress vector then have two properties in common: first, the singular points in the map are all elementary singular points (i.e., simple nodes or saddles); and second, there are no saddle-point-to-saddle-point connections in the map.

In speaking of the stability of the viscous/inviscid flow external to the surface, we shall find it necessary to distinguish between structural stability and asymptotic stability of the flow. The definition of structural stability follows from that introduced in reference to the map of the surface shear-stress vector. An external flow is called structurally stable relative to α if a small change in that parameter does not alter the topological structure (e.g., the number and types of 3-D singular points) of the external 3-D velocity vector field. Asymptotic stability is defined as follows: Suppose that the fluid motions evolve according to time-dependent equations of the general form

$$u_t = G(u,\alpha) \tag{11}$$

where α again is a parameter. Solutions of $G(u,\alpha) = 0$ represent steady mean flow of the kind we have been considering. A mean flow u_0 is an asymptotically stable flow if small perturbations from it (at fixed α) decay to zero as time $t \to \infty$. When the parameter α is varied, one mean flow may persist (in the mathematical sense, that it remains a valid solution of $G(u,\alpha) = 0$) but become unstable to small disturbances as α crosses a critical value. At such a transition point, a new mean flow may bifurcate from the known flow. A characteristic property of the bifurcation flow (such as, e.g., a transverse velocity component) that was zero in the known flow takes on increasing values as the parameter increases beyond the critical point. Finally, we shall find it convenient to distinguish between local and global characteristics of the instabilities. We shall call an instability global if it permanently alters the topological structure of either the external 3-D velocity vector field or the map of the surface shear-stress vector. We shall call an instability local if it does not result in an alteration of the topological structure of either vector field.

This distinction between local and global events suggests why we distinguish between local and global lines of separation in the pattern of skin-friction lines. If an (asymptotic) instability in the flow field does not alter the topological structure of the map of surface skin-friction lines, then the convergence of skin-friction lines on to one (or several) particular skin-friction line(s) can only be a local event. Accordingly, we label the particular lines local lines of separation, and these will usually all stem from a node of attachment (the stagnation point) on a forward facing part of the body. If, on the other hand, an instability (asymptotic or structural) of the flow field does change the topological structure of the skin-friction-line map, thus resulting in the emergence of a saddle point in this pattern, then this is construed as a global event insofar as the skin-friction-line map is concerned. Accordingly, we label the particular skin-friction line emanating from the saddle point a global line of separation.

9. BIFURCATION

The bifurcation phenomenon alluded to in the discussion of Eq. (11) is conveniently displayed on a bifurcation diagram, two examples of which are shown in Fig. 7. Flows that bifurcate from the known flow are represented by the ordinate ψ, which may be any quantity that characterizes the bifurcation flow alone. Stable flows are indicated by solid lines, unstable flows by dashed lines. Thus, over the range of α where the known flow is stable, ψ is zero, and the stable known flow is represented along the abscissa by a solid line. The known flow becomes unstable for all values of α larger than α_c, as the dashed line along the abscissa indicates. New mean flows bifurcate from $\alpha = \alpha_c$ either supercritically or subcritically.

At a supercritical bifurcation (Fig. 7a), as the parameter α is increased just beyond the critical point α_c, the bifurcation flow that replaces the unstable known flow can differ only infinitesimally from it. The bifurcation flow breaks the symmetry of the known flow, adopting a form of lesser symmetry in which dissipative structures arise to absorb just the amount of excess available energy that the more symmetrical known flow no longer was able to absorb. Because the bifurcation flow initially departs only infinitesimally from the unstable known flow, the structural stability of the surface shear-stress initially is unaffected. However, as α continues to increase beyond α_c the bifurcation flow departs significantly from the unstable known flow and begins to affect the structural stability of the surface shear stress. Ultimately a value of α is reached at which the surface shear stress becomes structurally unstable, evidenced either by one of the elementary singular points of its map becoming a singular point of

(odd) multiple order or by the appearance of a new singular point of (even) multiple order. An additional infinitesimal increase in the parameter α results in the splitting of the singular point of multiple order into an equal number of elementary singular points. Thus there emerges a new structurally stable map of the surface shear-stress vector and a new external flow from which additional flows ultimately will bifurcate with further increases of the parameter.

At a subcritical bifurcation (Fig. 7b), when the parameter is increased just beyond the critical point α_c, there are no adjacent bifurcation flows that differ only infinitesimally from the unstable known flow. Here, there must be a finite jump to a new branch of flows that may represent a radical change in the topological structure of the external flow and perhaps in the map of the surface shear-stress vector as well. Further, with ψ on the new branch, when α is decreased just below α_c, the flow does not return to the original stable known flow. Only when α is decreased far enough below α_c to pass α_0 (Fig. 7b) is the stable known flow recovered. Thus, subcritical bifurcation always implies that the bifurcation flows will exhibit hysteresis effects.

This completes a framework of terms and notions that should suffice to describe how the structural forms of three-dimensional separated flows originate and succeed each other. The following section is devoted to illustrations of the use of this framework in two examples involving supercritical and sub-critical bifurcations.

10. SUPERCRITICAL AND SUBCRITICAL BIFURCATIONS

10.1 Blunt Body of Revolution at Angle of Attack

Let us first consider how a separated flow may originate on a slender round-nosed body of revolution, as one of the main parameters of the problem, angle of attack, is increased from zero in increments. We adopt this example to illustrate a sequence of events in which supercritical bifurcation is the agent leading to the formation of large-scale dissipative structures.

At zero angle of attack (Fig. 8a) the flow is everywhere attached. All skin-friction lines originate at the nodal point of attachment at the nose and, for a sufficiently smooth slender body, disappear into a nodal point of separation at the tail. The relevant topological rule, Eq. (6), is satisfied in the simplest possible way ($N \approx 2$, $S = 0$).

At a very small angle of attack (Fig. 8b) the topological structure of the pattern of skin-friction lines remains unaltered. All skin-friction lines again originate at a nodal point of attachment and dis-appear into a nodal point of separation. However, the favorable circumferential pressure gradient drives the skin-friction lines leeward where they tend to converge on the skin-friction line running along the leeward ray. Emanating from a node rather than a saddle point and being a line onto which other skin-friction lines converge, this particular line qualifies as a local line of separation according to our definition. The flow in the vicinity of the local line of separation provides a rather innocuous form of local flow separation, typical of the flows leaving surfaces near the symmetry planes of wakes.

As the angle of attack is increased further, a critical angle α_c is reached just beyond which the external flow becomes locally unstable. Coming into play here is the well-known susceptibility of inflexional boundary-layer velocity profiles to instability (Refs. 27-29). The inflexional profiles develop on crossflow planes that are slightly inclined from the plane normal to the external inviscid flow direction. Called a crossflow instability, the event is often a precursor of boundary-layer transi-tion, typically occurring at Reynolds numbers just entering the transitional range (Refs. 30, 31). Referring to the bifurcation diagrams of Fig. 7 and identifying the parameter α with angle of attack, we find that the instability occurs at the critical point α_c where a supercritical bifurcation (Fig. 7a) leads to a new stable mean flow.

Within the local space influenced by the instability, the new mean flow contains an array of dissi-pative structures. The structures, illustrated schematically in Fig. 8c, are initially of very small scale, with spacing of the order of the boundary-layer thickness. Because they resemble an array of streamwise vortices having axes slightly skewed from the direction of the external flow, the structures will be called vortical structures. The representation of the structures on a crossflow plane in Fig. 8c is intended to be merely schematic; nevertheless, the sketch satisfies the topological rule for stream-lines in a crossflow plane, Eq. (8). As illustrated in the side view of Fig. 8c, the array of vortical structures is reflected in the pattern of skin-friction lines by the appearance of a corresponding array of alternating lines of attachment and (local) separation. Because the bifurcation is supercritical, however, the vortical structures initially are of infinitesimal strength and cannot affect the topologi-cal structure of the pattern of skin-friction lines. Therefore, once again, these are local lines of separation, each of which leads to a locally separated flow that is initially of very small scale.

At Reynolds numbers typical of those at which boundary-layer transition occurs, the production of longitudinal vortices within the rapidly skewing three-dimensional boundary layer appears on not only blunt body shapes but on pointed configurations also. Figure 9a, for instance, shows evidence of struc-tures on the surface of a hemisphere cylinder at an angle of attack of 19°; the striations are formed by the scouring effect of the longitudinal vortices on the sublimation material. Fig. 9b shows evidence of the longitudinal vortices on a circular cone at an angle of attack of 5° as evidenced in an oil-flow pattern (see also Figs. 180-182 in Peake and Tobak, Ref. 4).

Although the vortical structures are initially all very small, they are not of equal strength, being immersed in a nonuniform crossflow. Viewed in a crossflow plane, the strength of the structures increases from zero starting from the windward ray, reaches a maximum near halfway around, and diminishes toward zero on the leeward ray. Recalling that the parameter ψ in Fig. 7 was supposed to characterize the bifurcation flow, we find it convenient to let ψ designate the maximum crossflow velocity induced by the largest of the vortical structures. Thus, with further increase in angle of attack, ψ increases accord-ingly, as Fig. 7a indicates. Physically, ψ increases because the dominant vortical structure captures the greater part of the oncoming flow feeding the structures, thereby growing while the nearby structures

structures diminish and are drawn into the orbit of the dominant structure. Thus, as the angle of attack increases, the number of vortical structures near the dominant structure diminishes while the dominant structure grows rapidly. Meanwhile, with the increase in angle of attack, the flow in a region closer to the nose becomes subject to the crossflow instability and develops an array of small vortical structures similar to those that had developed farther downstream at a lower angle of attack. The situation is illustrated on Fig. 8d. We believe that this description is a true representation of the type of flow that Wang (Refs. 32, 33) has characterized as an "open separation." We note that although the dominant vortical structure now appears to represent a full-fledged case of flow separation, the surface shear-stress vector has remained structurally stable so that, in our terms, this is still a case of a local flow separation.

With further increase in the angle of attack, the crossflow instability in the region upstream of the dominant vortical structure prepares the way for the forward movement of the structure and its associated local line of separation. Eventually an angle of attack is reached at which the influence of the vortical structures is great enough to alter the structural stability of the surface shear-stress vector in the immediate vicinity of the nose. A new (unstable) singular point of second order appears at the origin of each of the local lines of separation. With a slight further increase in angle of attack, the unstable singular point splits into a pair of elementary singular points — a spiral node of separation and a saddle point. This combination produces the horn-type dividing surface described earlier (Fig. 4) and illustrated again in Fig. 8c (see Figs. 11 and 12 in Werlé, Ref. 34). We now have a global form of flow separation. A new stable mean flow has emerged from which additional flows ultimately will bifurcate with further increase of the angle of attack.

10.2 Asymmetric Vortex Breakdown on Slender Wing

In contrast to supercritical bifurcations, which are normally benign events, beginning as they must with the appearance of only infinitesimal dissipative structures, subcritical bifurcations may be drastic events, involving sudden and dramatic changes in flow structure. Although we are only beginning to appreciate the role of bifurcations in the study of separated flows, we can anticipate that sudden large-scale events, such as those involved in aircraft buffet and stall, will be describable in terms of sub-critical bifurcations. Here we cite one example where it is already evident that a fluid dynamical phenomenon involving a subcritical bifurcation can significantly influence the aircraft's dynamical behavior. This is the case of asymmetric vortex breakdown which occurs with slender swept wings at high angles of attack.

We leave aside the vexing question of the mechanisms underlying vortex breakdown itself (see Ref. 35), as well as its topological structure, to focus on events subsequent to the breakdown of the wing's primary vortices. Lowson (Ref. 36) noted that when a slender delta wing was slowly pitched to a sufficiently large angle of attack with sideslip angle held fixed at zero, the breakdown of the pair of leading-edge vortices, which at lower angles had occurred symmetrically (i.e., side by side), became asymmetric, with the position of one vortex breakdown moving closer to the wing apex than the other. Which of the two possible asymmetric patterns was observed after any single pitch-up was probabilistic. Once established, however, the relative positions of the two vortex breakdowns would persist over the wing, even as the angle of attack was reduced to values at which the breakdowns had occurred initially downstream of the wing trailing edge. After identifying terms, we show that these observations are perfectly compatible with our previous description of a subcritical bifurcation (Fig. 7b).

Let us denote by Δc the difference between the chordwise positions of the left-hand and right-hand vortex breakdowns and let Δc be positive when the left-hand breakdown position is the closer of the two to the wing apex. Referring now to the subcritical bifurcation diagram in Fig. 7b, we identify the bifurcation parameter ψ with Δc and the parameter α with angle of attack. We see that, in accordance with observations, there is a range of α, $\alpha < \alpha_c$, in which the vortex breakdown positions can coexist side by side, a stable state represented by $|\Delta c| = 0$. At the critical angle of attack α_c, the breakdowns can no longer sustain themselves side by side, so that for $\alpha > \alpha_c$ the previously defined stable state $|\Delta c| = 0$ is no longer stable. Immediately beyond $\alpha = \alpha_c$ there are no adjacent bifurcation flows, and $|\Delta c|$ must jump to a distant branch of stable flows; this represents the sudden shift forward of one of the vortex breakdown positions. Further, with $|\Delta c|$ on the new branch, as the angle of attack is reduced $|\Delta c|$ does not return to zero at α_c but only after α has passed a smaller value α_0. All of this is in accordance with observations (Ref. 36). At any angle of attack at which $|\Delta c|$ can be nonzero under symmetric boundary conditions, the variation of Δc with sideslip or roll angle must necessarily be hysteretic. This also has been demonstrated experimentally (Ref. 32). Further, since Δc must be directly proportional to the rolling moment, the consequent hysteretic behavior of the rolling moment with sideslip or roll angle makes the aircraft susceptible to the dynamical phenomenon of wing-rock (Ref. 38).

11. CONCLUSION

Holding strictly to the notion that patterns of skin-friction lines and external streamlines above bodies at angle of attack reflect the properties of continuous vector fields enables us to characterize the patterns on the surface and on particular projections of the flow (the crossflow plane, for example) by a restricted number of singular points (nodes, saddle points, and spiral nodes). It is useful to consider the restricted number of singular points, and the topological rules that they obey, as components of an organizing principle: a flow grammar whose finite number of elements can be combined in myriad ways to describe, understand, and connect the properties common to all steady, three-dimensional, viscous, separated flows. Introducing a distinction between local and global properties of the flow resolves an ambiguity in the proper definition of a three-dimensional separated flow. Adopting the notions of topological structure, structural stability and bifurcation gives us a framework in which to describe how three-dimensional separated flows originate on bodies and how they succeed each other as the relevant parameters of the problem, for example, angle of attack, are varied.

12. REFERENCES

1. Maskell, E. C., "Flow Separation in Three Dimensions." RAE Aero Rept. 2565, 1955.

2. Maltby, R. L., "Flow Visualization in Wind Tunnels Using Indicators." AGARDograph No. 70, 1962.

3. Meyer, R. F., "A Note on a Technique of Surface Flow Visualization." Nat. Res. Coun. of Canada Aero. Rept. LR-457, 1966.

4. Peake, D. J., and Tobak, M., Three-Dimensional Interactions and Vortical Flows with Emphasis on High Speeds. AGARDograph No. 252, 1980.

5. Legendre, R., "Séparation de l'écoulement laminaire tridimensionnel." Rech. Aero., No. 54, 1956, pp. 3-8.

6. Tobak, M., and Peake, D. J., Topology of Three-Dimensional Separated Flow. Ann. Rev. Fluid Mechanics, Vol. 14, 1982, pp. 61-85.

7. Lighthill, M. J., "Attachment and Separation in Three-Dimensional Flow." In Laminar Boundary Layers, Chap. II, Sec. 2.6, ed. L. Rosenhead, Oxford Univ. Press, 1963, pp. 72-82.

8. Hunt, J.C.R., Abell, C. J., Peterka, J. A., and Woo, H., "Kinematical Studies of the Flows Around Free or Surface Mounted Obstacles: Applying Topology to Flow Visualization." J. Fluid Mech., Vol. 86, Pt. 1, 1978, pp. 179-200.

9. Smith, J.H.B., "Remarks on the Structure of Conical Flow." RAE TR 69119, 1969.

10. Perry, A. E., and Fairlie, B. D., "Critical Points in Flow Patterns." In Advances in Geophysics, Vol. 18B, Academic Press, New York, 1974, pp. 299-315.

11. Legendre, R., "Lignes de courant d'un écoulement continu." Rech. Aérosp., No. 105, 1965, pp. 3-9.

12. Legendre, R., "La condition de Joukowski en écoulement tridimensionnel." Rech. Aérosp., No. 5, 1972, pp. 24-48.

13. Legendre, R., "Lignes de courant d'un écoulement permanent: décollement et séparation." Rech. Aérosp., No. 1977-6, pp. 372-455.

14. Oswatitsch, K., "The Conditions for the Separation of Boundary Layers." In Contributions to the Development of Gasdynamics, eds. W. Schneider and M. Platzer, Braunschweig/Wiesbaden, Vieweg, 1980, pp. 6-18.

15. Andronov, A. A., Leontovich, E. A., Gordon, I. I., and Maier, A. G., "Theory of Bifurcations of Dynamic Systems on a Plane." NASA TT F-556, 1971.

16. Andronov, A. A., Leontovich, E. A., Gordon, I. I., and Maier, A. G., Qualitative Theory of Second-Order Dynamic Systems. Wiley, New York, 1973.

17. Joseph, D. D., Stability of Fluid Motions, I. Springer, Berlin, 1976.

18. Benjamin, T. B., "Bifurcation Phenomena in Steady Flows of a Viscous Fluid. I. Theory. II. Experiments." Proc. R. Soc. London Ser. A, Vol. 359, 1978, pp. 1-43.

19. Sattinger, D. H., "Bifurcation and Symmetry Breaking in Applied Mathematics." Bull. (New Ser.) Am. Math. Soc., Vol. 3, 1980, pp. 770-819.

20. Poincaré, H., "Sur les propriétés des fonctions définies par des équations aux differences partielles." In Oeuvres Complètes. Tome 1. 1879, p. CVI.

21. Poincaré, H., "Les courbes définies par une équation differéntielle." Journal de Mathématiques 3 to 7, 1881, p. 375 (see also Oeuvres Complètes, Tome 1).

22. Poincaré, H., Oeuvres de Henri Poincaré. Tome I. Gauthier-Villars, Paris, 1928.

23. Davey, A., "Boundary-Layer Flow at a Saddle Point of Attachment." J. Fluid Mech., Vol. 10, 1961, pp. 593-610.

24. Werlé, H., "Separation on Axisymmetrical Bodies at Low Speed." Rech. Aérosp., No. 90, 1962, pp. 3-14.

25. Tobak, M., and Peake, D. J., "Topology of Two-Dimensional and Three-Dimensional Separated Flows." AIAA Paper 79-1480, 1979.

26. Smith, J.H.B., "A Review of Separation in Steady, Three-Dimensional Flow." AGARD CP-168, 1975.

27. Gregory, N., Stuart, J. T., and Walker, W. S., "On the Stability of Three-Dimensional Boundary Layers with Application to the Flow Due to a Rotating Disc." Philos. Trans. R. Soc. London Ser. A, Vol. 248, 1955, pp. 155-199.

28. Stuart, J. T., "Hydrodynamic Stability." In Laminar Boundary Layers, Chap. IX, ed. L. Rosenhead, Oxford Univ. Press, 1963, pp. 492-579.

29. Tobak, M., "On Local Inflexional Instability in Boundary-Layer Flows." Z. Angew. Math. Phys., Vol. 24, 1973, pp. 330-354.

30. McDevitt, J. B., and Mellenthin, J. A., "Upwash Patterns on Ablating and Nonablating Cones at Hypersonic Speeds." NASA TN D-5346, 1969.

31. Adams, J. C., Jr., "Three-Dimensional Laminar Boundary-Layer Analysis of Upwash Patterns and Entrained Vortex Formation on Sharp Cones at Angle of Attack." AEDC-TR-71-215, 1971.

32. Wang, K. C., "Boundary Layer over a Blunt Body at High Incidence with an Open Type of Separation." Proc. R. Soc. London Ser. A, Vol. 340, 1974, pp. 33-35.

33. Wang, K. C., "Separation of Three-Dimensional Flow." In Reviews in Viscous Flow, Proc. Lockheed-Georgia Co. Symp. LG 77ER0044, 1976, pp. 341-414.

34. Werlé, H., "Tourbillons de corps fuselés aux incidences élevées." L'Aèro. L'Astro., No. 79, 1979, p. 6.

35. Hall, M. G., "Vortex Breakdown." Ann. Rev. Fluid Mech., Vol. 4, 1972, pp. 195-218.

36. Lowson, M. V., "Some Experiments with Vortex Breakdown." J. R. Aero. Soc., Vol. 68, 1964, pp. 343-346.

37. Elle, B. J., "An Investigation at Low Speed of the Flow Near the Apex of Thin Delta Wings with Sharp Leading Edges. British ARC 19780 R & M 3176, 1961.

38. Schiff, L. B., Tobak, M., and Malcolm, G. N., "Mathematical Modeling of the Aerodynamics of High-Angle-of-Attack Maneuvers." AIAA Paper 80-1583-CP, 1980.

(a) Node.

(b) Spiral node

(c) Saddle.
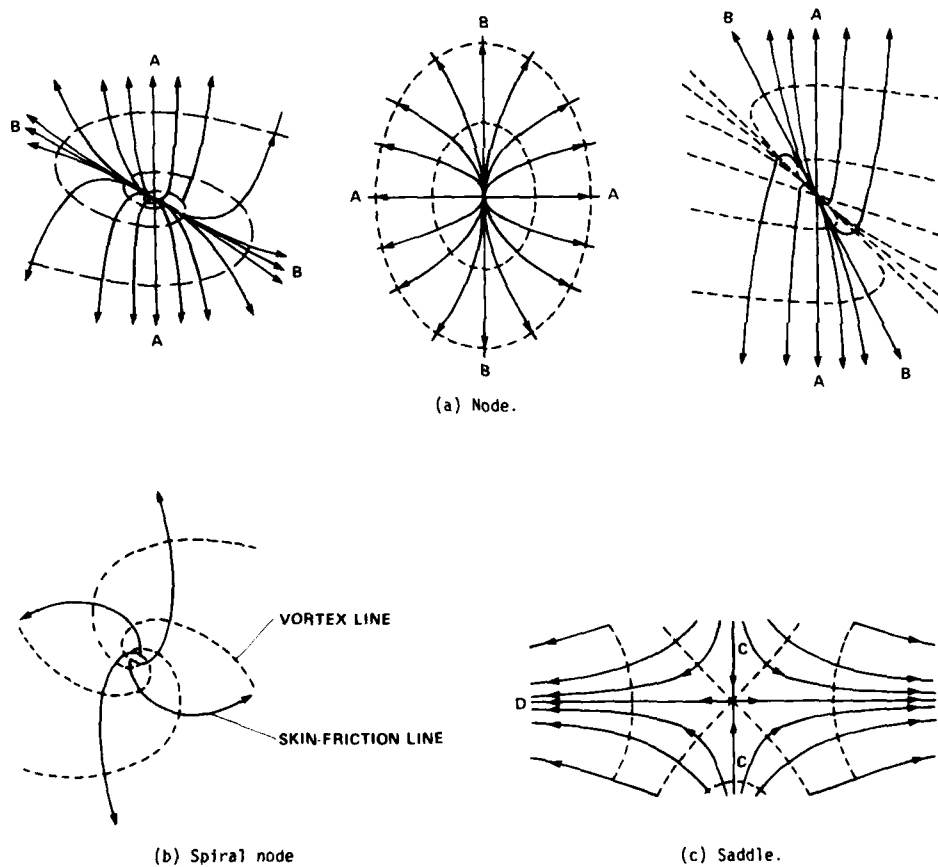
Figure 1. Singular points.
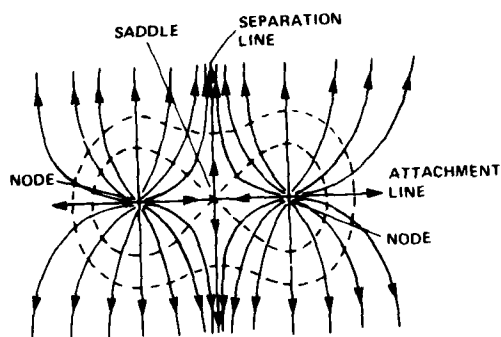
(a) Lighthill (Ref. 7).
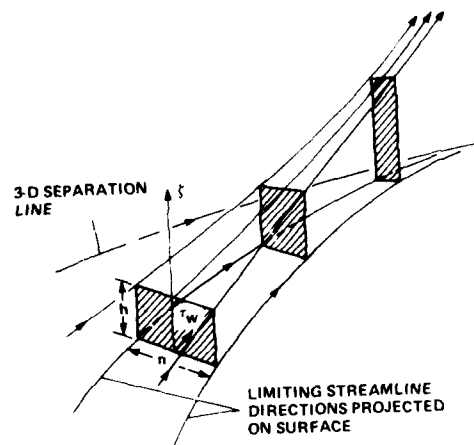
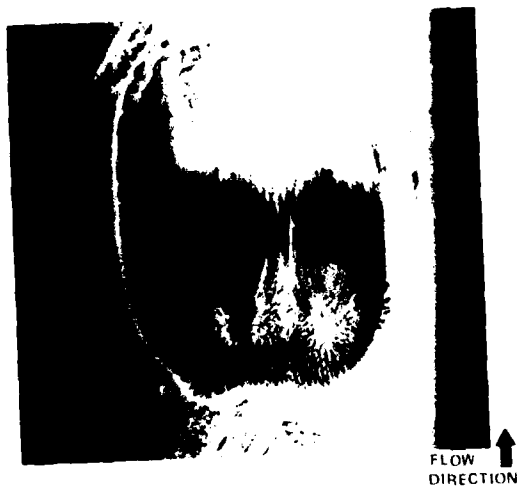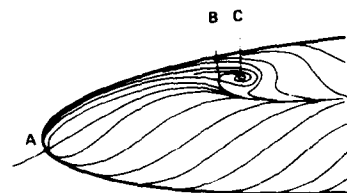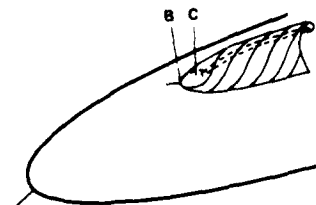Figure 3. Limiting streamlines near 3-D separation line.

(b) Plan view of shuttle model windshield, $M_\infty = 7.4$, $R_{L_\infty} \propto 3.4 \times 10^6$, vehicle length, $L = 1.3$ ft; $\alpha = 15°$ (courtesy L. Seegmiller, Ames Research Center).

Figure 2. Example of adjacent nodes and saddle point.

(a) Original sketch of skin-friction lines by Legendre (Ref. 11).
A — Nodal attachment point
B — Saddle point
C — Spiral node separation

(b) Experiment of Werlé (Ref. 24).

(c) Extension of spiral node, Legendre (Ref. 11).

Figure 4. Spiral node of separation.

N_s, NODAL POINT OF SEPARATION

3D SINGULAR POINT

N_a, NODAL POINT OF ATTACHMENT

VERTICAL PLANE

(b) Global dividing surface formed from nodal point of separation and saddle point.

NO SINGULAR POINT ON SURFACE

VORTEX LINE ON SURFACE

(a) Global dividing surface formed from nodal point of attachment and saddle point.

PARTICULAR SKIN-FRICTION LINE TOWARDS WHICH ADJACENT SKIN-FRICTION LINES CONVERGE. ALL SKIN-FRICTION LINES EMERGE FROM NODE OF ATTACHMENT UPSTREAM

(c) Local dividing surface.

Figure 5. Global and local dividing surfaces.

PLANE $z = z_0$

SEPARATION   ATTACHMENT
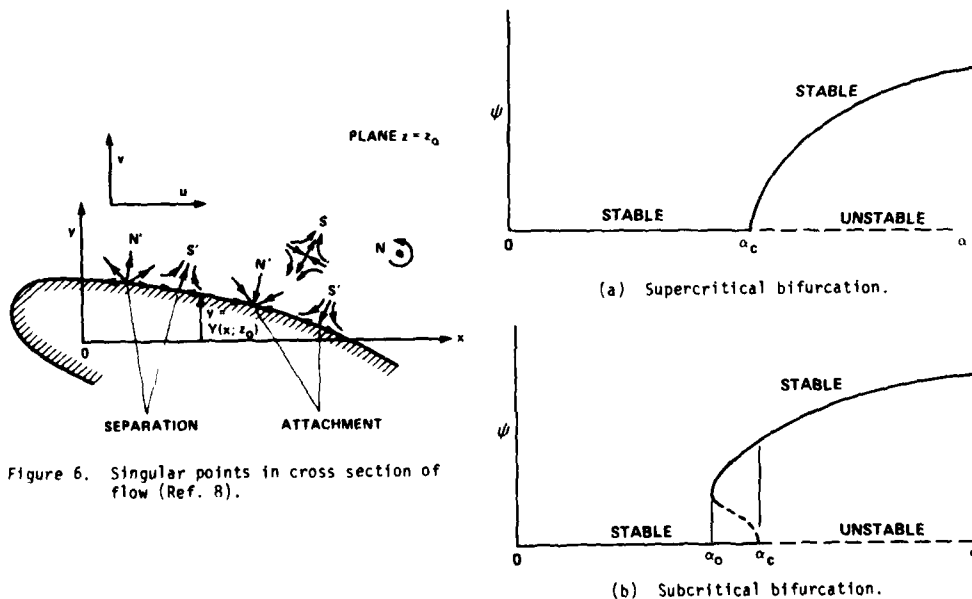
Figure 6. Singular points in cross section of flow (Ref. 8).

ψ

STABLE

STABLE   UNSTABLE

α_c

(a) Supercritical bifurcation.

ψ

STABLE

STABLE   UNSTABLE

α_0 α_c

(b) Subcritical bifurcation.

Figure 7. Examples of bifurcation.
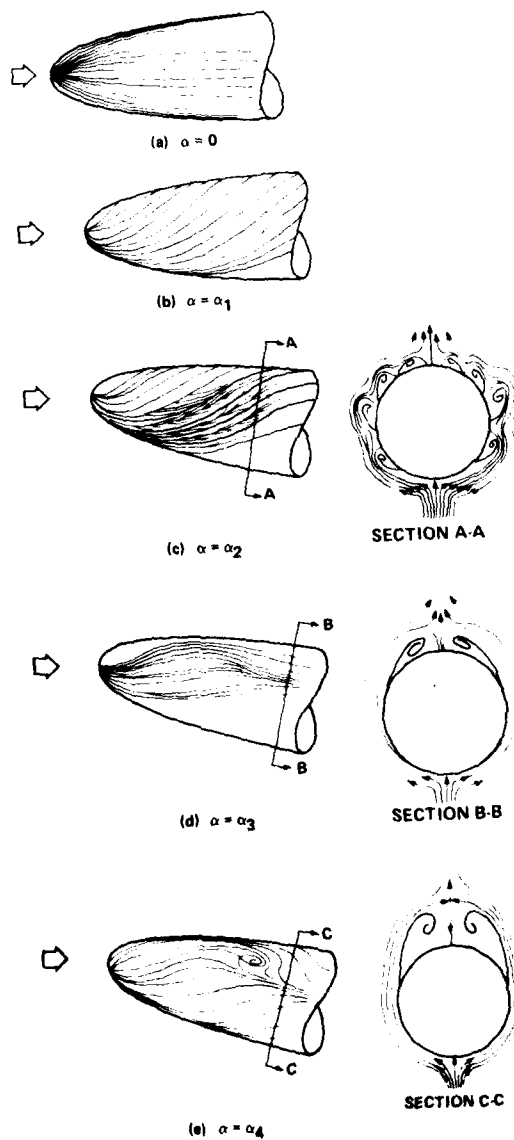
Figure 8. Sequence of flows leading to global three-dimensional flow separation on round-nose body of revolution as angle of attack is increased.

FLOW

STRIATIONS IN
SUBLIMATION MATERIAL

(a) Sublimation material on hemisphere-cylinder at α = 19°, M_∞ = 1.2,
R_{L_∞} = 4.9 × 10^6, L = 7.5D, D = 2.6 in.

(b) Oil-film study on a 10° semi-angle cone at α = 5°, M_∞ = 7.4,
R_{L_∞} = 3 × 10^6, T_T = 1050°K (Ref. 30).

Figure 9. Evidence of streamwise vortices on blunt and sharp configurations
at angle of attack.

THREE-DIMENSIONAL FLOWS ABOUT SIMPLE COMPONENTS AT
ANGLE OF ATTACK

David J. Peake and Murray Tobak
Ames Research Center, Moffett Field, California 94035

SUMMARY

The structures of three-dimensional separated flows about some chosen aerodynamic components at angle of attack are synthesized, holding strictly to the notion that streamlines in the external flow (viscous plus inviscid) and skin-friction lines on the body surface may be considered as trajectories having properties consistent with those of continuous vector fields. Singular points in the fields are of limited number and are classified as simple nodes and saddles. Analogous flow structures at high angles of attack about blunt and pointed bodies, straight and swept wings, etc., are discussed, highlighting the formation of spiral nodes (foci) in the pattern of the skin-friction lines. How local and global three-dimensional separation lines originate and form is addressed, and the characteristics of both symmetric and asymmetric leeward wakes are described.

1. INTRODUCTION

Invoking our previously introduced notions (Ref. 1) of topological structure, structural stability, and local and global lines of separation, we shall attempt to demonstrate how these assist us in deducing the complex patterns of skin-friction lines and external-flow streamlines about simple aerodynamic components at angle of attack. The components may be considered typical of those used in aeronautical applications. They include blunt and pointed bodies, and straight, swept, and slender wings. Initially, however, we shall take the case of a simple hemisphere-cylinder, immersed in a Mach 1.2 free stream at constant Reynolds number (R_l = 4.9 × 10⁶), and increase the angle of attack α in stages in the range 0° < α < 32.5°. We shall see that the types of singular points with their accompanying characteristic developments of local and global separation zones, and the progressive changes in the patterns as the angle of attack increases, will form a useful foundation for understanding the flow fields about the other flow components discussed in subsequent sections.

2. HEMISPHERE-CYLINDER

Oil-flow patterns indicative of the development of the skin-friction lines on the hemisphere-cylinder are illustrated in Figs. la to li as angle of attack is increased progressively from axisymmetric conditions (α = 0°) to α = 32.5°. Figure 2 portrays the conceptual patterns of singular points associated with the skin-friction lines (and streamline projections in some chosen crossflow planes) that have been synthesized from the oil-flow patterns in Fig. 1 and laser vapor-screen crossflow visualization shown in Figs. 3 and 4. To assist the reader, Fig. 3 shows the experimental setup of the expanded laser beam (see Ref. 2) that cuts the body at x/D = 6.5 perpendicular to its axis. Flow is from right to left, so that the photographs in both Figs. 3 and 4 display views looking toward the back of the body on the starboard side.

Figures la and 2a portray the axisymmetric skin-friction line pattern about the hemisphere-cylinder at M_∞ = 1.2. All skin-friction lines originate at the nodal singular point of attachment at the nose (the stagnation point) and stop at a singular line of separation around the body just downstream of the junction between the hemisphere and the cylinder. The stream surface departing from the separation line reattaches at the singular line of attachment situated a short distance farther downstream, to form a closed separation bubble. A parallel pattern of skin-friction lines emerges from the reattachment line in both the upstream and downstream directions. Under the present experimental conditions, the wedges in the oil-flow pattern on the cylinder (see Fig. la) indicate that the axisymmetric separation and reattachment are laminar, with transition to turbulence occurring downstream shortly thereafter. The downstream-directed skin-friction lines, for a sufficiently smooth and slender afterbody, will disappear into a nodal point of separation at the tail, satisfying the relevant topological rule for a closed-body surface that the sum of the nodes on the surface must always exceed the number of saddle points by two. Here, of course, we have only the nodes of attachment and separation and no saddle points. Figure 3 illustrates the axisymmetric boundary-layer growth in the vapor screen at x/D = 6.5, with the bounding shock wave surrounding the body cross section.

When the angle of attack is increased to a small value, say 1°, we expect to find the pattern of skin-friction lines drawn conceptually in Fig. 2b. The slightest departure from axisymmetry causes the skin-friction line pattern to pass through a structural instability: the axisymmetric singular separation and reattachment lines disappear and are replaced by saddle and nodal points of attachment on the windward ray, and nodal and saddle points of separation on the leeward ray. There is a characteristic dividing surface in the flow that is anchored on the leeward ray and that emanates from the nodal point of separation, N_S. We note that streamlines on this dividing surface in the meridian plane have all entered the fluid through the saddle point of separation, S_1, in the pattern of skin-friction lines along the leeward ray. At this small angle of attack, the dividing surface will grow very slowly with progression downstream as the adjacent boundary layers converge very slowly toward the leeward ray. The existence of this dividing surface stemming from a combination of nodal and saddle points of separation on the leeward ray will be clearly evident as a dark line in the leeward meridian plane in the vapor-screen photographs at elevated angles of attack. In fact, it is through our description of the dividing surface that we are able to explain the presence of this obvious feature of the vapor-screen photographs (see Fig. 4).

When the angle of attack is increased to 3.5° (Figs. 1b and 2c) the pattern of skin-friction lines undergoes another structural change. The lines of separation emanating from the saddle point on the windward ray terminate in spiral nodes just short of the leeward ray. The simultaneous appearance of a pair of saddle points on either side of the nodal point of separation on the leeward ray maintains the differential between nodes and saddles required by the topological rule. Figure 5b of the previous lecture illustrates the form of the dividing surfaces that typically emanate into the external flow from this combination of surface-flow topology.

Increasing the angle of attack to 5° (Figs. 1c and 2d) provides us with a topology at the front of the body that is similar to that at 3.5°, but toward the end of the body the skin-friction lines, all emanating from the nodal point of attachment on the windward ray, show indications of converging toward primary separation zones that will produce primary vortices. The enhanced thickening of the viscous flow along the leeward is shown in Fig. 4a. At 6.5° (Fig. 1d), we have, in addition, certain evidence of the phenomenon of instability in the crossflow velocity profiles just downstream of the hemispherical cap. There are fine striations in the oil-flow pattern superimposed over the regular pattern of skin-friction lines, lending credence to the proposal that the laminar boundary layer has undergone a supercritical bifurcation (such as that described in the previous lecture), resulting in the appearance of an array of small-scale vortices within the boundary layer.

Continuing to increase the angle of attack toward 10° (Figs. 1e, 2e, 4b) causes the singular points on the windward ray to come together and to eventually disappear. Meanwhile, additional singular points appear on the leeward. At the precise angle(s) of attack at which the singular points disappear and appear, we pass through new structural instabilities in the skin-friction line pattern. We also detect another particular line in the skin-friction line pattern, situated between the primary separation line and the leeward ray, toward which adjacent boundary-layer material is also converging — the so-called secondary separation line. The stream surface from this line coils up as a secondary vortex that is of opposite rotation to and is tucked beneath the primary vortex. Now with the disappearance of the windward saddle and nodal points of attachment, the entire pattern of skin-friction lines on the body surface all stem from the nodal point of attachment at the nose. Thus, referring to Fig. 2e, in our classification according to the mathematical notions of topological structure and structural stability, the primary separation lines are local ones and the secondary separation lines stemming from the leeward saddle points, S4 and S5, are global separations. Note now, however, that the eruptions from the spiral nodes will key the roll-up of the secondary vortices, so that the single dividing surface growing from the leeward ray appears as a thin shadow with no evidence of the "mushroom" or "T-shape" that we proposed at α = 3.5° (see Fig. 4b). The single dividing surface will continue to grow until the primary vortices induce a downward component of flow velocity along the leeward meridian. Thereafter, the height of this leeward dividing surface will diminish.

As angle of attack increases still further to 15° (Figs. 1f, 2e, 4c) the character of the flow remains the same, but the streaks near the nose cap caused by the crossflow instability are even more noticeable. Close to α = 19°, however (Figs. 1g, 2f, 4d), the skin-friction line pattern entertains two additional structural instabilities, whereupon we now see evidence of two additional pairs of spiral nodes that have formed very close to the join-line between the hemispherical cap and the cylinder. Figure 2f illustrates the substantial increase in the overall number of singular points in order to incorporate these two additional pairs of spiral nodes. The intricacies in the patterns are especially interesting; they have been studied previously by Hsieh (Ref. 3) and Hsieh and Wang (Ref. 4), and more recently by Hsieh (Ref. 5) in an attempt to refine the computational scheme proposed for the flow field by Pulliam and Steger (Ref. 6). In those papers, details of how the spiral nodes combine with other singular points in the pattern of skin-friction lines on the leeward foreparts of the body have been especially elusive. The description advanced herein from our own experimental results updates that offered by Peake and Tobak (Ref. 7) and by Tobak and Peake (Ref. 8) from oil-flow pictures kindly supplied by T. Hsieh. As we have seen, recognizing the existence of a nodal point of separation on the leeward ray accounts for an essential feature of the flow structure. Nevertheless, the downward induction effect of the primary vortices along the leeward ray is particularly significant, so much so that the single dividing surface along the leeward ray has reduced substantially in extent by the time the given laser vapor-screen crossflow image is reached along the body (Fig. 4d). As we see in the range 0° < α < 19°, there is no evidence that the eruptions from the spiral nodes appear in the crossflow plane, unlike the flow fields viewed by Jorgensen (Ref. 9) about tapered blunt-nosed bodies.

The characteristic dividing surface in the external flow formed from the combination of an adjacent saddle point and a spiral node (see also Fig. 4 in the preceding paper) has been termed a "horn-type" dividing surface by Legendre (Ref. 10). The patterns in Figs. 2b to 2f are drawn on the assumption that there is no mechanism available to alter the already existent nodal and saddle singular points of separation on the leeward ray — this extends to higher angles of attack also — and that these may then be coupled to the spiral nodes via additional singular points. The summation of nodes and saddles on the surface must always differ by two; this rule is obeyed if we take the simplest conjectural case that all skin-friction lines disappear into a node of separation at the tail. Any elaboration of this one node of separation into an appropriate array of singular points to cap off the separation lines obviously can be introduced as required.

Our next pictures of the skin-friction line pattern at α = 27.5° (Figs. 1h and 2g) show the development of spiral nodes close to the commencement of the primary and secondary separation lines. Structural instabilities have again occurred in the skin-friction line patterns, and now we see that both primary and secondary separations are of the global type, each starting at a saddle point.

The final photographs in Fig. 1i at α = 32.5° evidence additional considerable complexity. It appears that relatively strong shock waves in the leeward crossflow are causing a significant predisposition of the primary separation line to split into a series of saddle points and spiral nodes along its initial length. Ripples in the skin-friction-line pattern to the leeward of the primary separation line are further indicative of shocks in the leeward crossflow. Moreover, we detect additional spiral nodes forming on the hemisphere cap itself.

Thus, in the sequence of changing α from 0° to 32.5° for the hemisphere-cylinder in transonic flow, where the shock-wave/boundary-layer interactions are evidently very complex, we have conjectured at least six separate structural instabilities in the skin-friction-line map to herald new topological structures in the surface pattern and in the external viscous/inviscid flow field. In addition, we have been able to discern on the basis of experimental evidence that these changes were accompanied by at least one asymptotic instability of the external flow, leading to a bifurcation flow. This was when the evidence suggested that the crossflow instability mechanism had led to the appearance of an array of streamwise vortices in the boundary layer (see Fig. 9 in the previous paper). We note that the concept of bifurcation — one flow replacing another flow that has become unstable — is principally a theoretical one; it is exceedingly difficult in practice to confirm that there is a flow other than the one observed that could exist in the absence of perturbations. It may be necessary to await the further development of theory based on the equations governing these flows before we can deduce the specific role played by bifurcations in determining the observed sequence of topological structures. We have also seen the particular developments of local and global lines of 3-D separation. Let us now look at some additional examples in which the formation of spiral nodes on other configurations substantially influences the flow-field structure.

3. RECTANGULAR WING: ASPECT RATIO 0.25

For the hemisphere-cylinder, the existence of a two-dimensional separation bubble at $\alpha = 0°$ allowed us to deduce easily how the singular separation and reattachment skin-friction lines were transformed into singular points as a result of the three-dimensional effects introduced by a small angle of attack. We saw that the favorable transverse pressure gradient from windward to leeward created conditions for the appearance of a nodal point of separation on the leeward ray. We can follow this approach to some extent with the rectangular wing as well by focusing our attention on the flow near the leeward centerline of the wing. In contrast with the previous flow, near the leading edge the transverse pressure gradient is favorable from leeward to windward and, as a consequence, we shall detect a saddle point of separation on the wing centerline. As an example of this behavior, Wickens' 1966 investigation of a low-aspect-ratio rectangular wing (Ref. 11) is such a case.

The oil-flow patterns taken by Wickens were on the leeward surface of a low-aspect-ratio (0.25) rectangular wing at an angle of attack of 20° (Fig. 5). This investigation was carried out in a low-speed wind tunnel, and we assume that the flow was laminar, at least on the forepart of the wing. Figure 6a is a deduction from Fig. 5 of the corresponding pattern of skin-friction lines; it represents the 3-D end-product of what had been, at very much lower angles of attack, a nominally two-dimensional separation bubble on the wing topside close to the leading edge. We see in Fig. 6a four spiral nodes, one nodal point of attachment, and five saddle points on the leeward surface, and that the windward surface must contain one nodal point of attachment (the stagnation point). Each of the five saddle points on the leeward surface separates the flows from adjacent pairs of nodes, a necessity in the buildup of the skin-friction-line topology (Ref. 12). Springing from the saddle points are dividing surfaces, the forms of which we attempt to portray in Fig. 6b. On each side of the centerline, we suppose that the primary separation consists of the dividing surface, which runs into the spiral node nearest the edge of the wing, taking the form of the "horn-type" dividing surface described previously by Legendre (Ref. 10).

Particularly noteworthy is the other spiral-node/saddle-point combination nearer the centerline of the wing. We see from Wickens' pressure measurements at $\alpha = 20°$ in Fig. 6d that there is a favorable pressure gradient from the wing centerline outboard toward the tip, supporting the argument for a saddle point on the topside wing centerline and a direction toward the tip of the local skin-friction lines. Note that in the case of the hemisphere-cylinder, the direction of the skin-friction lines around the forepart of the body was toward the leeward ray, and, that in contrast, we saw the emergence of a nodal point of separation there. Farther outboard in the present example (but inboard of the tip region) the combined effect of the spanwise and chordwise pressure gradients is to turn downstream the dividing surface originating at the centerline saddle point, and to wind it up into a spiral node. Emanating from the node into the flow is an isolated vortex filament which passes downstream, perhaps very close to the surface.

4. RECTANGULAR WING: ASPECT RATIO 3.5

We now extend the aspect ratio of the rectangular wing to 3.5 and examine the results of Winkelmann and Barlow (Ref. 13). Figure 7 shows one particular example (at $\alpha = 23°$) of many low-speed flows investigated by these authors. Figure 7a illustrates the surface oil-flow picture of the wing topside with some slight "run-down" of the oil toward the trailing edge, a result of stopping the wind tunnel. Nevertheless the essential features of the skin-friction-line pattern can be read from Fig. 7a; they are shown in Fig. 7b. The skin-friction-line trajectories that were evident in the Wickens flow in Fig. 6 appear in analogous form very close to the leading edge of the present example. Downstream of the flow reattachment at the node N_a on the centerline; however, we find another saddle point of separation, the separation line from which terminates in a pair of large spiral nodes covering an extensive area of the wing. The wing-tip line of separation shown in Fig. 6a in the Wickens flow is now situated inboard in the Winkelmann flow, and winds up into the large spiral node. By our definition, all separation lines starting from saddle points of separation are global separation lines. Notice now, however, that the separation line at the wing tip, providing the wing-tip vortex, originates from the attachment node on the underside centerline and is hence, again by definition, a local line of separation. This local line of separation terminates in another spiral node close to the trailing-edge tip.

We should comment that the external viscous/inviscid flow away from the wing surface is usually quite unsteady for angles of attack of the order of 23°, which is past the point of maximum lift coefficient. The oil pattern is essentially responsive to only very low frequencies and thus provides a time-mean of the instantaneous skin-friction-line pattern. The view of the external flow along the centerline of the wing must be construed similarly.

5. HIGH-ASPECT-RATIO SWEPT WING OF TRANSPORT AIRCRAFT

The next example we wish to comment on is a high-aspect-ratio swept wing immersed in a high subsonic speed environment close to the angle of attack at which buffet onset occurs (Fig. 8). A substantial pressure rise through a relatively strong swept shock wave on the wing topside dominates the flow-field development over almost the entire semispan, causing a swept 3-D separation line (see Fig. 8a). Toward the root, the single shock-wave structure would appear to split into the well-known lambda form, with a fairly strong forward leg and a weak aft-shock. Close to the shock-wave triple point, we detect a large spiral node in the pattern of skin-friction lines in conjunction with a saddle point of separation and a nodal point of separation.

An examination of the oil-flow picture in Fig. 8a and the conceptual skin-friction-line pattern in Fig. 8b for this swept-wing example demonstrates the close analogy with the combination of singular points (node of separation/saddle point/spiral node of separation) that exists on the top of the hemisphere in Fig. 1.

6. SLENDER DELTA WING

About the simplest of all cases of 3-D separation is the flow field about a slender delta wing at angle of attack (Figs. 9, 10). It is well known that the characteristic feature of this flow is the appearance of free-shear layers that coil tightly around dividing surfaces of separation springing from the leading edges. Figures 9 and 10 show, respectively, typical patterns of limiting streamlines and skin-friction lines on the top surface of a delta wing with a 15° semiapex angle, at $M_\infty = 0$ (Fig. 9) and 1.95 (Fig. 10). We see at $\alpha = 25°$ for this wing the existence of primary and secondary separation lines at both Mach numbers, giving rise to primary, secondary, and possibly tertiary vortices. Beneath the cores of the primary vortices, the wing experiences peak suction pressures. However, the origin of the dividing surfaces and their detailed behavior in the vicinity of the apex remains conjectural. On the theoretical side, the difficulty is associated with the presence of sharp edges which violate ideas about analyticity; on the experimental side, the difficulty is associated simply with insufficient powers of visual or instrumental resolution.

Theoreticians have attacked the problem by focusing on a small region of the apex and magnifying the scale to a degree such that the edges there appear to be rounded enough to dispose of the question of analyticity. Then it is reasonable to assume that just as for smooth round-nosed bodies, the flow in the vicinity of the apex must be describable within the framework of rules governing the behavior of singular points. The assumption is not sufficiently exclusive to enable the determination of a unique flow pattern but only a number of physically plausible ones. For example, if we restrict ourselves to the low-angle-of-attack case in which a primary separation line exists, we may have only a simple node of attachment on the apex resulting in local lines of separation on the wing. Presuming the sequential flow development around the apex to follow the case of a blunt-body flow already discussed in the previous paper, then as the angle of attack is raised at sufficiently high Reynolds number, we will expect the apex flow to bifurcate from a uniform attached flow to a flow with tiny streamwise vortices immersed within the boundary layer which will subsequently coalesce to form the primary separation. That such streamwise vortices, resulting from, in this case, instability of the crossflow velocity profiles near the leading edge, can exist on a slender wing is evident in Fig. 11, for example. At higher angles of attack, it is reasonable that the array of singular points proposed by Legendre (Ref. 16) or Lighthill (Ref. 12) (see Fig. 12) may also be candidate topologies on the apex. Note that when effects of the base become dominant as angle of attack becomes very large, substantial spiral nodes may form on the rear surface of the delta wing (see Fig. 13). Whether the leading-edge shape of the slender wing is straight, of ogival form, or of ogee form, qualitatively (i.e., from the topological standpoint) the skin-friction line patterns and the external flow streamlines are virtually identical for the three forms.

We now wish to demonstrate the benefit of combining a slender-wing type flow with that about a small-aspect-ratio swept-back wing under transonic conditions where, utilizing our topological notions, we are able to deduce the flow-field structure from some experimental results, the oil-flow picture from which is not totally definite.

7. LOW-ASPECT-RATIO SWEPT WING OF FIGHTER AIRCRAFT

The large leading-edge extension or strake offers the advantage that induced lift provided by the vortices from the sharp edges can be used to extend the combat-maneuvering capabilities of a fighter aircraft, particularly in transonic flow. Improvements in lift boundary and reductions in rolling moment unsteadiness and root-mean-square wing-root bending moments can be realized as a result of the drastic alteration of the wing-root flow caused by addition of the strake (see Figs. 14a to 14d). Küchemann (Ref. 18) has suggested that the strake vortex avoids the necessity for the formation of the usual forward branch of the wing-shock pattern by providing a "soft" boundary for the flow turning inboard over the leading edge, instead of the "stiff" boundary given by the fuselage side.

Figure 14a illustrates some experimental measurements reported by Moss (Ref. 19) of contours of constant pitot pressure and vorticity behind a straked wing at angle of attack. Figure 14b shows a sketch (Moss, Ref. 19) of the oil-flow pattern on the top wing surface at a slightly lower angle of attack than that at which the contours were taken, but, nevertheless, where the same overall qualitative flow features hold. These experimental observations, taken together, allow us to synthesize patterns of skin-friction lines (Fig. 14c) and external flow streamlines (Fig. 14d) that although still conjectural, offer a rational description of the complex separation phenomena.

Clearly, the effect of the strake is to split the wing flow field into two regions, each with a dominant vortical structure, of the same rotational sense. The strake modifies the wing-root flow to one of a slender-wing-type flow, with both primary and secondary vortices. Further outboard, the termination of the separation line beneath the strong shock wave near the leading edge is considered to be at a spiral

node N_1 on the wing surface, of counter-rotating direction to the larger spiral node N_2, shown in Moss' sketch (Fig. 14b). These spiral nodes produce a T-shaped pattern of vortical structures in the crossflow which are clearly evident in the wake traverse plane showing vorticity contours (Fig. 14a) downstream of the trailing edge. (Note the wing downwash field has moved the rotational flow from these spiral nodes below the level of the trailing edge in Fig. 14a.) At the junction of the wing trailing edge with the fuselage, we may infer the likelihood of another spiral node (see Fig. 14d of Peake and Tobak, Ref. 7). The respective topological rules for the surface skin-friction line pattern on Fig. 14c and for the cross-flow plot in Fig. 14d are satisfied, as shown on the illustrations. Again we should be cognizant of the spiral-node/saddle-point formations in both the pattern of skin-friction lines and in the crossflow pattern, in direct analogy with those formations witnessed on the hemisphere-cylinder at angle of attack.

8.   CIRCULAR CONE

Next to the flow about a lifting slender delta wing, the flow about a slender cone at angle of attack is the simplest 3-D flow field that may be envisaged. The cone, moreover, is a common forebody shape used in the design of supersonic flight vehicles. If viscosity is neglected, the flow field about the cone in a supersonic free stream has the unique property that no changes in flow quantities occur along rays (i.e., in direction r) emanating from the cone apex. The stream surfaces projected on to concentric spheres centered at the apex (called conical flow streamlines) are then similar. In practice, experimenters have demonstrated that many features of the viscous/inviscid interacting flow field — such as bow shock-wave locations, circumferential pressure distributions, normal force coefficients, circumferential positions of separation lines, and surface shear-stress directions — are conical or nearly so. The growth of a laminar viscous layer cannot be conical, because it develops according to $r^{0.5}$. In a fully turbulent flow, the exponent of r is nearer unity, implying a flow field very close to conical conditions.

When the Reynolds number is sufficiently high so that transition occurs in proximity to the apex, the near-conical nature of the experimentally measured flow demonstrates a virtual absence of length effects in the streamwise direction: the flow is dominated completely by the circumferential pressure field (Refs. 20-23). Thus, the characteristics of these flow fields can be determined through measurement or by computation at essentially one streamwise station. In fully turbulent and fully laminar subsonic free-stream flow, even though base and thickness effects become measurable, the circumferential pressure gradients still dominate, to the extent that virtual conicity of the separation lines and shear-stress directions is still maintained. Then, because the effects of axial pressure gradients are subsidiary to those of circumferential pressure gradients on most other slender pointed forebody shapes, we may use the cone as a suitable model to obtain a basic understanding of forebody flows.

9.   SYMMETRIC THREE-DIMENSIONAL SEPARATED FLOWS ON THE LEEWARD OF CONES

About the cone, the three-dimensional separation zone may be precipitated at circumferential angles ϕ of 120° or greater (measured from the windward ray), depending on relative incidence (angle of attack α divided by cone semi-nose angle θ_c), Mach number, and Reynolds number (see Fig. 63 in Peake and Tobak, Ref. 7). Provided that the viscous flow is either all laminar or completely turbulent from the apex, the windward boundary layers separate from primary separation lines that are along conical rays, rolling up into well-organized vortex structures situated close to the leeward meridian. The new leeward boundary layers grow outboard on each side of the leeward meridian by the induced swirling motion of the primary vortices. At sufficiently high angles of attack, they also separate from additional conical separation lines to form small secondary vortices that are tucked beneath and are of opposite rotation to the primary vortices. Whether, for a sharp apex, the separation lines (which are particular skin-friction lines) emanate from either the nodal point of attachment at the apex, or from saddle points very close to the nose in the continuous pattern of skin-friction lines, has not been resolved (see Sec. 6). Nevertheless, sequences of plausible skin-friction line patterns with saddle singular points in the vicinity of the nose as angle of attack is increased may be drawn (see, e.g., Peake and Tobak, Ref. 7).

The structure of the symmetric separated flow about a slender cone at angle of attack with both primary and secondary vortices on the leeward has been well established in experiments (e.g., Rainbird, Refs. 20, 21) and computations (e.g., McRae et al., Ref. 24) and is illustrated in Fig. 15. This drawing shows a conical flow projection with the zero velocity points (i.e., singular points in this projection) that govern the pattern of the conical-flow streamlines. Note that the topology law for the conical flow projection is satisfied (see Eq. (10) in our previous paper). The shear layers departing from the surface at the three-dimensional separation lines are depicted by their dividing surfaces starting at half-saddle points, S', and coiling into vortices, the nodal foci N. The remaining half-saddle points S' denote attachments to the surface in this projection. Above the primary vortices in the plane of the leeward meridian is an enclosing saddle point S and a node N. This node is the point in the conical flow projection where most of the conical streamlines in the external flow "disappear." In the three-dimensional flow, of course, all flow at such singular points is concentrated along a conical ray.

Figure 15 presents the conceptual model of the flow field that has been investigated in flight and in the wind tunnel. The experiments (Ref. 23) proceeded under subsonic and supersonic free-stream conditions (M_∞ = 0.6, 1.5, and 1.8) and at an angle of attack of 11° (relative incidence of 2.2). The same sharp 5° semi-angle cone and instrumentation were used both in flight and in the wind tunnel (see Fig. 16). Numerical computations were run for the Mach number 1.5 and 1.8 conditions, with a code utilizing the conically symmetric Navier-Stokes equations (Ref. 24). Details of the cone surface conditions beneath the turbulent viscous flow are presented at Reynolds numbers of typically 4×10^6 for the wind-tunnel measurements and 10×10^6 for the flight measurements; they are compared with computations. These Reynolds numbers are based on free-stream conditions and on a 30-in. (76.2 cm) axial length to the first measuring station on the cone surface.

9.1 Mean Static Pressures at the Cone Surface

Figures 17 and 18 illustrate circumferential static pressure distributions on the cone surface at the test Mach numbers of 1.8 and 1.5. The pressures are shown for the station 30 in. (76.2 cm) from the cone apex, with the outputs from four orifices at 90° intervals around the surface plotted in the same figure (Fig. 17). In addition, measurements are also provided at x = 31, 33, and 35 in. (78.7, 83.8, and 88.9 cm) (Fig. 18). The pressure distributions displayed virtual symmetry about the meridian plane, so that only measurements made on one side of the cone are presented.

The respective flight and wind-tunnel Mach-1.8 results at station 30 are shown in Figs. 17a and 17b. The results are plotted as surface mean pressure coefficients versus circumferential angle ϕ, where the windward generator is recognized at ϕ = 0°. The experimental results are plotted with symbols, and the computed results are plotted with a continuous line. The flight and wind-tunnel data are in reasonable agreement in both trend and magnitude. The high quality of the flight data is especially noteworthy: the static pressure outputs at station 30 are virtually superimposed. However, some discrepancies appear near the windward ray and toward the leeward ray in the zone where the primary and secondary separations exist ($\pm 140°$ < ϕ $\leq$ $180°$). Note the suction peak close to ϕ = $\pm 165°$, which signifies the presence of the primary vortex core above the surface.

The computation duplicates the trends in the measurements, especially on the windward side. On the leeward, however, the numerical results provide a more positive level of pressure, although the suction peaks beneath the vortex cores are close to the experimental locations.

Figure 18 portrays the flight circumferential pressure distributions at Mach 1.5 along the cone at four axial stations, x = 30, 31, 33, and 35 in. (76.2, 78.7, 83.8 and 88.9 cm) from the apex. The pressures along the cone are virtually invariant, confirming the near absence of length effects at supersonic Mach numbers.

Thus, from Figs. 17 and 18 it may be deduced that up to the flank position on the cone, the boundary layer develops from the windward ray and undergoes acceleration in a very favorable pressure gradient. Once past ϕ = 100°, the viscous flow encounters a stiff adverse pressure gradient, departing from the surface at the primary separation line, ϕ_{S_1}. The thin boundary layer that then develops from the leeward attachment line does so in the region of favorable pressure gradient from ϕ = 180° to about 165°. Subsequently, the flow separates at ϕ_{S_2}. The experimental primary and secondary separation line positions marked in Figs. 17 and 18 are given from the pressure distributions obtained with the obstacle blocks described below. These measurements of $\phi_{S_1} \approx 142°$ and $\phi_{S_2} \approx 157.5°$ are demonstrated to be in close agreement at both supersonic Mach numbers; the computations, on the other hand, predict values of ϕ_{S_1} and ϕ_{S_2} that are marginally displaced toward the windward side.

9.2 Obstacle Block Pressures and Separation Line Position

To determine separation-line positions where use of an oil indicator on the surface is inappropriate, obstacle blocks (Refs. 25-27) may be used. These are small machined cuboids that are attached to the cone surface abutting static pressure orifices, as shown in Fig. 19. The performance of the block is analogous to that of a surface pitot tube, the signature from which is sufficiently sensitive to yield either a large increase in amplitude through a transition zone (Ref. 28) or well-defined troughs at three-dimensional separation lines (Ref. 24).

Figure 19a indicates block-pressure coefficients $CPB = (p_b - p_{local})/q_\infty$ obtained at the four pressure orifices at station 30 for the Mach 1.8 flight case. These results compared very closely with the wind-tunnel results (see Fig. 19b). The pronounced troughs in the values of CPB close to ϕ = 140° and 160° denote the primary and secondary separation line positions where the skin friction has a minimum but finite value. (Only at the singular points at which the separation line begins and ends is the magnitude of the local skin friction equal to zero in a three-dimensional viscous flow.) Note the elevated values of CPB toward the attachment lines where the boundary layers are thin: at the windward ray, leeward ray, and between the separation lines. In the wind-tunnel tests, the block outputs at stations 30 and 30B were calibrated directly against Preston tubes at stations 30A and 30C with the cone at 0° angle of attack. The Preston-tube calibration for compressible flow developed in Bradshaw and Unsworth (Ref. 29)(with slight modifications[1]) was used to give skin-friction magnitudes. Figure 19b indicates the corresponding skin-friction levels obtained from the blocks at high and low point values of CPB at α = 11°. Results analogous to those at Mach 1.8 were obtained at Mach 1.5 and 0.6. The measured and predicted primary and secondary separation line positions are shown in Figs. 17a and 17b.

Some details of the external mean flow field are captured in the Mach 1.8 computed pitot contours shown in Fig. 20. Here, the height above the surface H is a fraction of the local radius of the cross section. The dividing surface from the primary separation line location ϕ_{S_1} is shown as a chain-dot line; the locus of the inflexional zero velocity point in the crossflow velocity profiles (in the conical projection) is indicated as a dashed line. There is close qualitative agreement between this computed result and previously published measurements in the external flow (Rainbird, Refs. 20, 21; Peake et al., Ref. 30). It shows the extensive domain of the primary vortex close to the leeward ray, with the vortical core immediately above the circumferential angle ϕ = 166°, exactly where the calculated suction peak appeared in the Mach 1.8 static pressure distribution in Fig. 17.

9.3 Surface Shear-Stress Directions

The computed limiting streamline angles relative to conical rays can be compared with the experimental surface shear-stress directions obtained by oil-dot surface flow visualization in the wind tunnel. To provide a complete map of the wall shear-stress directions, precisely cut tracing paper was placed on the

---

[1]Private communication from P. Bradshaw.

cone surface, and oil dots were applied around the circumference at given axial stations prior to a tunnel run. After the run, the paper was carefully unwrapped from the cone and photographed to give a flat projection. Figure 21 presents a section of one of these photographs taken for a Mach-1.8 run at 12.5° angle of attack in the wind tunnel. This angle is higher than the 11° test condition presented thus far; the skin-friction line map, however, is qualitatively identical at both angles of attack. The limiting flow at the base of the three-dimensional boundary layer sweeps around the cone from the windward ray, and then turns to approach asymptotically the primary separation line in the region of circumferential adverse pressure gradient (Fig. 17b). The leeward boundary layer grows outboard from the leeward meridian (a line from which the adjacent skin-friction lines diverge) to approach asymptotically the secondary separation line. As Fig. 21 shows distinctly, there is another reattachment line between the primary and secondary separation lines (see also Fig. 15).

The computed limiting streamline angles are drawn in Fig. 21 for a Navier-Stokes calculation equivalent to the experimental conditions. The computed separation lines are shown as solid lines and reattachment lines by dashed lines. The lines are repeated at the base of the cone for clarity. The agreement between the computational results and the experiment is good.

9.4 Fluctuating Pressure Measurements on the Cone Surface

Microphone and Kulite pressure signatures were obtained at $\alpha = 11°$ in flight and in the wind tunnel at the station 34 in. (86.4 cm) from the apex as the cone was rolled about its axis. All microphone and Kulite data provided the same qualitative trends in a given test, but absolute levels did vary slightly, perhaps as a result of minute differences in flushness of the installation of the sensors in the cone surface.

Measurements from one microphone obtained at Mach 1.5 in the wind tunnel are shown in Fig. 22 as root-mean-square values of the surface pressure fluctuation <p>, normalized by the free-stream mean dynamic pressure q_∞. The characteristic feature of these measurements is the progressive reduction in signal amplitude as the primary separation line ϕS_1 is approached, with a similarly low level at the secondary separation line ϕS_2. This feature was found at all Mach numbers and was witnessed in an earlier investigation (see Peake et al., Ref. 31). The signal amplitude climbs again toward the leeward attachment line to a level close to that on the windward ray attachment line. Not understood, however, is the reason for the changing amplitudes in the attached flow around the flank of the core. Note that the fluctuation level on the windward ray at $\alpha = 11°$ is close to that measured at $\alpha = 0°$, and to the free-stream fluctuating static pressure in the empty tunnel. The flight measurements yielded signal levels typically one order less than in the wind tunnel, with much less relative distinction between those levels at the separation and attachment lines.

Figure 23 shows sample wind-tunnel power-spectral density results indicating a reduced energy level at primary separation relative to the windward and attachment-line boundary layers. When, on the other hand, the root-mean-square pressure output is normalized by the local value of skin friction, characteristic peaks (again see Peake et al., Ref. 31) are demonstrated at the primary and secondary separatics lines, as we see in Fig. 24. In other words, as separation is approached, the local skin-friction decreases at a faster rate than does the root-mean-square pressure fluctuation. We see that the "roller coaster" region around the flank in Fig. 22 does not translate into a similarly obvious region in Fig. 24; rather, there is a relatively smooth enhancement of $(<p>/\tau_w)$ in the ϕ range $40° <\phi> 120°$. Note that there is a noticeable peak in the wind-tunnel spectral outputs in Fig. 23 at 1.6 kHz. This appears to be a harmonic of the fan rotational speed, rather than a characteristic feature of the flow-separation phenomena or a discrete tone from the slots in the tunnel working section, since the same peak was also observed on the $\alpha = 0°$ runs, with and without the slots sealed. Finally, the value of measuring the fluctuating pressure at the surface of the cone has been that it provides a qualitative guide as to how the eddy viscosity distribution should be tailored in the computation (Ref. 23). It appears that the eddy viscosity should rise and fall in sympathy with the absolute fluctuating pressure signal.

10. SEPARATED FLOW ABOUT LONG SLENDER BODIES

The body of a typical missile or rocket consists of a low-drag nose shape attached to a circular cylindrical afterbody. The afterbody is about 10 body diameters in length and has stabilizing fins or a flare mounted close to the base end. Such long bodies are very prone to flow separation once they depart from a zero angle of attack flight condition. To oversimplify the picture, we may regard the long cylinder as a cone of essentially zero included angle and so for any small angle of attack, the relative incidence is very large and separation is inevitable somewhere down the body. The typical separated flow regimes encountered on the leeward with increasing angle of attack are (1) a symmetrical vortex wake about the meridian plane; (2) a relatively steady asymmetric vortex wake; and (3) an unsteady diffuse vortex wake. These regimes are illustrated (Figs. 25a-25c) in side elevation in the water-tunnel experiments of Fiechter (Ref. 32) for a tangent-ogive cylinder up to angles of attack of about 60°.

10.1 Steady Symmetric Separations

On very long pointed or blunt-nosed slender configurations, separation first occurs symmetrically with a pair of vortices trailing back along the body. Figure 26 illustrates such body separations in side elevation on a blunted cone-cylinder-flare model at a low relative incidence in a Mach 4 airstream. The separations and vortex wake are recognizable in the photograph at about 1-2 body diameters behind the cone-cylinder junction and proceed downstream on the lee of the body in a well-ordered and structured fashion (see Fig. 25a). These symmetric vortices are virtually identical in form in the crossflow plane at corresponding relative incidences, provided the crossflow is subsonic. By way of example, Fig. 27a shows the crossflow about an ogive-cylinder at 20° angle of attack at $M_\infty \sim 0$, made visible with dye and aluminum particles in a water-tunnel study by Werlé (Ref. 33). The close analogy between this low-speed case and a Mach-2 wind-tunnel result for another ogive-cylinder at 26° angle of attack (Ref. 34) is revealed in Fig. 27b. The figure shows a composite of laser vapor-screen photographs for various crossflow planes along the body, assembled in an isometric view. Both primary and secondary vortices are observable.

Careful measurements of the crossflow velocity vectors and contours of constant pitot-pressure deficit in low-speed symmetrical flow were made by Grosche (Ref. 35), as shown in Figs. 28a and 28b. The pitot contours display evidence of both the primary and secondary separations that were seen on the cone in Fig. 20. Note in Fig. 28c that when a wing is added to the body at the same angle of attack, there is a substantial shift in the position of the body vortices as a result of the larger induced effects of the controlled flow separations at the edges of the swept wing.

Some painstaking experiments on missile configurations at angle of attack were made by Boersen (Ref. 36) to elucidate the fine details of the skin-friction line patterns. Figure 29 shows some of his results. Figure 29a displays the local primary separation line in turbulent flow along a $\theta_c = 20°$ blunted cone-cylinder (without flare or fins) at a low relative incidence of 0.6, $R_{L_\infty} \sim 10 \times 10^6$, and at Mach 2.3. The flow is symmetrical about the meridian plane but notice (on the unwrapped surface of the cylinder) in Fig. 29b, the gradual convergence of the skin-friction lines emanating from the clearly defined windward attachment line zone, followed by the very abrupt turning into the local primary separation line S_1. The induced downflow between the primary vortices (Fig. 27a) causes a rapid divergence along the leeward generator A_1, toward the apparent beginning of local secondary separation region S_2. Naturally, if we maintain our hypothesis of demanding patterns of continuous skin-friction lines associated with a limited number of singular points, the attachment and local separation lines that are very evident in these elegant flow visualization studies of Boersen (Ref. 36) must emanate from the attachment node on the surface at the nose. Only when the local circumferential pressure gradients become sufficiently adverse do we see the rapid turning of skin-friction lines to form asymptotes to the particular skin-friction lines that are the local primary and secondary separation lines.

Changing the forebody to a $\theta_c = 20°$ sharp cone (see Fig. 30a) at the same relative incidence of 0.6 (Ref. 36) produces no substantial change to either the flow symmetry or to the commencement of the 3-D separated region, but a tertiary and even a fourth separation line are now observed on the downstream part of the cylinder. (Again, we assume these to be local separation lines). Circumferential pressure distributions at the axial stations identified in Fig. 30a are plotted in Fig. 30b, where increasing Reynolds number is demonstrated to typically enhance the magnitude of the suction pressures, particularly those beneath the primary vortices. Note that the windward generator is on the right-hand side of the figure, and circumferential angle increases toward the left, the reverse notation to that used, for example, for the cone in Fig. 18. At station 1, the circumferential pressures are still dominated by the apparent attached viscous flow leaving the pointed conical forebody and no observable separation has developed just downstream of the cone-cylinder juction, even though the circumferential pressure gradient is adverse between $120° < \phi < 180°$. Except near the cone-cylinder junction, the axial pressure gradients are negligible. Beyond the minimum pressure point at stations 2 - 5, however, close to $\phi \sim 90°$, the circumferential adverse pressure gradient has steepened sufficiently to provoke primary separation near the flank. At station 3, the pressure distribution is reminiscent of the cone flow in Fig. 18, with the primary and secondary separations present (compare also the oil flows in Figs. 21 and 30c). At subsequent stations downstream along the cylindrical afterbody, further very sharp changes in the curvature of the pressure distributions are detected, consistent with possible embedded shock waves at positions c and d in Fig. 30c, and the associated development of additional local separation lines at positions e and g. A tentative sketch of the crossflow is provided in Fig. 30c, which differs in some respects from that proposed by Boersen (Ref. 36).

These body separations have an important effect on the vehicle's static and dynamic stability. At small relative incidences, where the separation is essentially steady and symmetrical with respect to the angle-of-attack plane, the ensuing body vortices produce a nonlinear contribution to the overall normal force and pitching moment. If the fin system is not symmetrically orientated with respect to the angle-of-attack plane, however, a cross-coupling side force, yawing moment, and rolling moment can arise, even at small angles of attack.

Flows such as these were studied extensively in the 1950's, particularly at NASA, by Jernell (Ref. 37) (cone cylinders and ogive cylinders, $0° < \alpha < 180°$) and by Jorgensen and Nelson (Refs. 38, 39) (cylinders with assorted nose shapes and bodies of elliptical cross section). A summary of these latter experiments and force predictions from crossflow methods is given by Jorgensen (Ref. 40). A good understanding, in an overall sense, has been obtained on the development of both forces and moments. An estimate, in incompressible flow, of the overall forces and moments acting on a slender body of revolution without fins was offered by Küchemann (Ref. 41), summarizing an analysis done 20 years earlier. Vortex sheets, as plane vertical surfaces, were assumed to exist all along the cylinder and the vorticity vector in the sheet was assumed to lie in a direction halfway between the direction of the free stream and the body axis. Results of typical calculations utilizing this very simple symmetric model are shown (Fig. 31) to be in quite reasonable agreement with experimental results.

To demonstrate the effects of nose shape, a series of tests at high Reynolds number was reported by Peake et al. (Ref. 42) who summarized the experiments of Atraghji (Refs. 43, 44) on the characteristics of a family of 16 pointed conical and tangent-ogives attached to cylindrical aterbodies (see Fig. 32). Each nose could be fitted to a cylindrical afterbody length of either 6 or 12 body diameters, but there were no stabilizing fins attached. Forces and circumferential pressures were measured, and the oil dots applied to the surface of the models yielded the patterns of skin-friction lines. At low angles of attack (typically up to $\alpha \sim 3°$) where there was attached flow, the slope of the normal force/angle-of-attack plot, C_{N_α} increased with Mach number and semi-nose angle, θ_c (see Fig. 33). The effect of overall slenderness ratio L/D was less clear, although at $M_\infty = 0.5$ the trend was established of an increasing C_{N_α} with L/D. Calculations using slender body theory (Ref. 45), the USAF "Datcom" data sheets (Ref. 46), and the method due to Öhman (Ref. 47) were also performed. As a general rule, the theories appear to underpredict C_{N_α} at a given semi-nose angle and slenderness ratio.

In the range of angle of attack (characteristically, $\alpha = 3°$ to $11°$) for the series of nose shapes tested, three-dimensional leeward flow separation is symmetric. The induced suction pressures from the rolled-up shear layers generate a large nonlinear normal force component, but no side force. With the normal force represented by a quadratic in α:

$$C_N = K + b_1\alpha + d_1\alpha^2$$

where K only removes the experimental uncertainty in the true measurement, Fig. 34 illustrates the increase in coefficients b_1 and d_1 with both Mach number and slenderness ratio, with a significant variation in d_1 at a given Mach number and slenderness ratio attributable to the semi-nose angle, θ_c. The more slender ogives listed in Fig. 32 (07, 09, and 011) would appear to generate a larger nonlinear lift throughout the Mach number range and for both afterbody lengths.

Rational calculations of the symmetrical separated flow field about long slender bodies at angle of attack are few. Development of a "Navier-Stokes" computational technique similar to that used by Pulliam and Steger (Ref. 6) to determine the separated flow about a long blunt body at moderate angle of attack (see discussion of the hemisphere-cylinder, Sec. 2) should be encouraged, to attain finer resolution of the flow-field details in the vortex wake and on the surface.

10.2 Asymmetrical Separations

At relative incidences of long slender bodies higher than those just discussed, say for values typically more than 2, separations and body vortices become asymmetric but still relatively steady in space. The result is that large side forces, yawing moments, and rolling moments are developed, especially on fin-stabilized vehicles.

The onset of asymmetry and the initial direction of the side force are responsive to small changes in geometry at the nose, Reynolds number, Mach number, and perturbution level of the free stream up to angles of attack where conditions in the leeward crossflow become transonic. In addition, the maximum overall side forces are particularly sensitive to the roll orientation of the body. As speed increases further, the significant side forces disappear (Ref. 42). The asymmetries occur in laminar, transitional, and turbulent flows. Nevertheless, the implication from recent tests by Lamont (Refs. 48, 49) with tangent-ogive cylinders at angle of attack (at Reynolds numbers encompassing laminar, transitional, and turbulent boundary-layer separation) is that the vortex wake is less structured in the transition domain, leading to reduced side and normal forces at a given subsonic Mach number. In the fully laminar or turbulent regions, on the other hand, where the organization of the flow field is well defined, the respective magnitudes of the side force are larger and are closely matched — see Fig. 35, in which the results for maximum side force versus Reynolds number are plotted for a missile with a 2-D ogival nose and a 5.5-D body (Lamont, Ref. 48).

There appear to be two candidate mechanisms that cause the development of asymmetry in the leeward vortex wake, and hence produce side force. The first, which appears to operate in both the laminar and fully turbulent separation regimes, may be related to the stability of the velocity profiles in the vicinity of the saddle singular point that exists in crossflow planes above the projections of the body vortices. The second may be a result of the occurrence of asymmetric transition leading to an effective asymmetric mean flow at given body cross sections. Although the second mechanism is operable only within the transition zone, the former mechanism plays a role in both laminar and fully turbulent flow (see Ref. 48, 49). It will be discussed further in the subsequent paper by Skow and Peake in this lecture series. Typical asymmetrical circumferential pressure distributions are shown in Figs. 36 and 37 for laminar, turbulent, and transitional body flows for the 2-D ogival nose, 5.5-D length afterbody of Lamont (Ref. 48).

In turbulent flow, certainly, it would appear that at forebody relative incidences where asymmetry of the vortex wake commences, we are always dealing not only with separation of the primary boundary layers that develop on each side from the windward generator, but with secondary separations of the leeward boundary layer in addition. The onset of asymmetry would seem to be characterized initially by a rapid, local movement circumferentially of one (or both) secondary separation lines followed, as angle of attack is increased further, by circumferential movement of the primary separation lines (Refs. 42, 50). The asymmetric skin-friction line pattern on the conical surface development shown in Fig. 38 illustrates this latter flow situation, with "wobbly" primary and secondary separation line traces existing all along the cone (Ref. 51). There, the free-stream Mach number is 2.94 and the relative incidence is 4.5. At lower free-stream Mach numbers, however, the asymmetric separation lines have been found to be conical (Ref. 30).

The asymmetric vortex wake usually develops from asymmetric separation line positions on the body, but the latter does not appear to be a necessary condition for the former to occur. An appraisal by Keener and Chapman (Ref. 52)) of some earlier, low-subsonic speed tests of Shanks (Ref. 53), in which forces and moments were measured on very slender, flat-plate, delta wings (sweep angles of 70° to 84°) at angle of attack, indicates that even though the separation lines were fixed at the sharp leading edges, asymmetry in the leading-edge vortices, as determined by the onset of significant rolling moment, occurred when the angle of attack was about 3 to 4 times the wing semi-nose angle. This angle of attack for asymmetry is splendidly illustrated on the vapor-screen pictures (Fig. 39) about another very slender delta wing immersed in a Mach 2.8 flow (Ref. 54). Nonetheless, the sharp edges have a beneficial effect in delaying the onset of asymmetry to higher relative incidences than those obtained with smooth pointed forebodies or forebody-clinder configurations (Refs. 42, 55, 56).

Because the development of the turbulent flow structures in the three-dimensional swept separation zones and in the tightly coiled free-shear layers is virtually unexplored, the modeling of the leeward flow asymmetries poses severe problems. Recourse has been made, for rough predictions of the flows about missile shapes, to inviscid flow approximations of the leeward region, utilizing arrays of line vortices (see the review by Nielsen, Ref. 57), of nonlinearities in missile behavior at high angles of attack). Alternatively, the impulsively started flow analogy proposed many years ago by Allen and Perkins (Ref. 58) has frequently been applied (Ref. 59). In this hypothesis, the development of the crossflow with distance along an inclined body of revolution is likened to the growth with time of the two-dimensional flow past the corresponding circular cylinder impulsively started from rest. Useful engineering formulae have certainly resulted utilizing the analogy. Nevertheless, given the complexities of the three-dimensional boundary-layer growth, separation, and vortex development about slender bodies at angle of attack, it is

intriguing that the impulsive-flow analogy can provide more than just qualitative details of the flow. If we restrict ourselves to invoking the impulsive-flow analogy to provide only the overall flow structure, the topologies of the 2-D unsteady and the 3-D steady cases appear virtually analogous (Ref. 60). If we demand stricter correspondence between the two, there are issues for debate. For instance, the growth of the unsteady 2-D vortex differs essentially from that of the steady 3-D vortex in space. Küchemann and Weber (Ref. 61) point out that in three dimensions, fluid entering the core of the vortex can be discharged axially, whereas in two dimensions no such escape is available. Thus, the 2-D core must expand continuously outward with time to accommodate all of the fluid entering the vortex. Küchemann and Weber show further that there is only one case in inviscid flow in which the two kinds of vortices are formally identical: where the steady three-dimensional flow is conical (so that slenderness assumptions can be invoked); and where the unsteady flow is permitted to grow linearly with time. Hence, if the development of the real viscous wake (in 2-D with time, and in 3-D with distance along the body) can be represented by these respective but special inviscid approximations to vortex growth, then the impulsive-flow analogy should be a suitable artifice under conditions of high Reynolds number.

For the missile at sufficiently high angle of attack, the asymmetric leeward flow is coupled with asymmetries in primary (and secondary) separation line positions. An example is shown in Fig. 40 where the asymmetric primary separation line positions on the port and starboard of a 5.8° cone-cylinder and a 13.9° ogive-cylinder, at Mach 0.6 and at identical angles of attack (18°), are plotted. The boundary layers are turbulent. This figure demonstrates the important influence of nose shape on the asymmetry of the flow. We detect that on the very slender conical nose, at its relative incidence of just over 3, there is substantial flow asymmetry all along the body (solid lines in Fig. 40). In contrast, because the less slender ogival nose is at a relative incidence of about only 1.3, the commencement of separation there shows only slight asymmetry, with less difference in separation line positions from side to side (dashed lines in Fig. 40).

Figure 41 illustrates the magnitude of the mean side-force coefficient C_Y with respect to the normal-force coefficient C_N, as model angle of attack is increased, for the selection of nose shapes shown in Fig. 32 with the 12-D afterbody length. Unsteady fluctuations in side-force coefficient, with peak-to-peak amplitudes as high as ± 0.3 at $\alpha = 25°$ were measured, superimposed upon the mean C_Y levels. For angles of attack up to about 27°, increasing either the semi-nose angle or the Mach number reduced the amplitude of the side force. In fact, at $M_\infty = 2$ when $\theta_C > 10°$, and for all configurations at $M_\infty = 3.5$, no measureable side force was obtained. Figure 42 presents the critical angle for flow asymmetry (judged by the side force exceeding, say 5% of the normal force) plotted against the semi-nose angle θ_C. As before, we confirm that the onset of flow asymmetry is delayed by increasing θ_C and Mach number. But the effect of the longer afterbody is to provoke asymmetry at a lower angle of attack.

Keener et al. (Ref. 56) attempted to draw some tentative boundaries based on angle of attack and fineness ratio between the various flow regimes that appear on the leeward of ogive-cylinder bodies in subsonic flow. Figure 43 illustrates these zones at Mach 0.6 for nominally turbulent viscous flows. We observe that three angle-of-attack boundaries are plotted as functions of overall fineness ratio, thus separating the angle of attack range of 0° to 90° into the three regions of different vortex formations that were introduced in Fig. 25. Recall that the regions are (1) regions of symmetrical steady vortices, typically up to angles of attack of about 1.5 times the semi-nose angle in subsonic flow; (2) regions of quasi-steady asymmetric vortex flows; and (3) at very high angles of attack, a "two-dimensional unsteady wake-like" flow. In Fig. 42, we detected in the high Reynolds number data of Peake et al. (Ref. 42) that the angle of attack at which the onset of asymmetric side-force development occurred was particularly sensitive to semi-nose angle, and less dependent on afterbody length. The data in Fig. 52 have been plotted again in Fig. 43. Along a given vertical bar representing fixed nose and afterbody fineness ratios, we see again the dependency of onset angle on semi-nose angle. The higher Reynolds number data of Peake et al. (Ref. 42) indicate the onset of asymmetry at lower angles of attack than the data presented by Keener et al (Ref. 56).

11. SHARP AND BLUNT CONES OF EQUILATERAL TRIANGULAR CROSS SECTION WITH ROUNDED CORNERS

There is a renewal of interest in fuselages of cross-sectional shape other than circular (see Hasel and Kouyoumjian, Ref. 64) to investigate whether flat-sided configurations (which can be more volume productive for housing avionics) may also provide improved aerodynamic performance, lateral stability characteristics, fuselage load distributions etc., at high angles of attack. A recent investigation at Ames Research Center by Clarkson et al. (Ref. 65) has concentrated on forebody shapes of rounded triangular and square cross section. From the extensive body of experimental results collected therein, we shall select for comment only a small sample dealing with the flows about sharp and blunt cones of triangular cross section at a particular angle of attack and Reynolds number. We shall see that the flow structures have many of the same topological features as those observed previously on sharp and blunt-nose bodies of circular cross section, under similar flow conditions.

Details of the sharp and blunt-nose triangular cone models are given in Fig. 44. Circumferential rings of orifices for surface pressure measurements were located at three axial stations as indicated in the figure. Tests were carried out in the Ames 12-ft wind tunnel at low speeds. The models were placed in the wind tunnel at angle of attack and at zero roll angle, the latter orientation being defined as occurring when a flat side of the model was directly windward.

Figure 45 present the results of oil-flow visualization experiments for the two models under essentially identical flow conditions (angle of attack = 45°, Reynolds number based on base height = 1.1×10^6 and 1.2×10^6 for the blunt- and sharp-nose triangular cone, respectively). Figure 46 presents the corresponding circumferential surface pressure distribution at the three axial locations indicated in Fig. 44.

Surface oil-flow patterns on the blunt-nose model (Fig. 45a) show evidence of primary and secondary lines of separation occurring on each flank of the body just after the flow has turned the corner of the blunt windward face. The primary separation is global, originating at a saddle point, and the secondary separation, occurring farther downstream, is local. There is an intricate flow on the leeward face of the

blunt nose, giving evidence of a pair of spiral nodes on either side of the plane of symmetry. Flow patterns here bear a resemblance to those over the nose of the hemisphere-cylinder at angle of attack (see in particular Figs. 1g-1i), in either case being the result of a series of abrupt local changes in both streamwise and circumferential pressure distributions. It will be noted that the surface flow pattern appears to be symmetric with respect to the angle of attack plane. This is borne out by the results of the circumferential surface pressure measurements (Fig. 46a), which are virtually identical on the port and starboard sides at all three stations.

Surface oil-flow patterns for the sharp-nose model (Fig. 45b) again show evidence of primary and secondary lines of separation. Here, however, it is probable that the primary and secondary lines of separation are local, both originating from the nodal point of attachment at the nose. Furthermore, the presence of a sharp nose eliminates the appearance of the intricate pattern of spiral nodes that was observed on the leeward face of the nose with the blunt-nose model. It is, however, the very marked asymmetry in the location of the secondary lines of separation in the oil-flow pattern for the sharp-nose model (Fig. 45b) that is the principal distinction between the patterns for the two models. This asymmetry is accompanied (see Fig. 46b) by a similarly marked asymmetry in the surface pressure distributions on the port and starboard sides at all three stations. There is reason to believe that just as for slender sharp-nose bodies of circular cross section (see discussion in connection with Fig. 37), the occurrence of this asymmetry, reflected first by the rapid circumferential movement of the secondary lines of separation, is associated with the onset of boundary-layer transition. Thus, just as for bodies of circular cross-section, it appears that for bodies of triangular cross-section, blunting the nose helps delay both the onset of flow asymmetry and boundary-layer transition.

12. SUPERSONIC INLET INTERACTING WITH FLOWS ON ADJACENT SURFACES

The half-cone or quarter-cone inlet mounted adjacent to a fuselage sidewall and wing/fuselage intersection may cause a substantial problem of swept shock wave/turbulent boundary-layer interaction, particularly at off-design conditions. The intake is usually raised from the fuselage surface to permit both bleeding and diversion of the oncoming viscous flows (Ref. 66).

Figure 47 shows an oil-flow pattern taken by Culley (Refs. 67, 68) about a θ_c = 25° half-cone intake at Mach 1.6 and at a Reynolds number of 6×10^6, based on the wetted run to the intake capture face of 2 in. (5 cm) diameter. The inlet was operating at design shock cone position and at maximum mass flow (with some spillage, as seen on the Schlieren photograph). Even though auxiliary ram (bleed) intakes were located in the plane of the cowl lip to ingest the turbulent fuselage boundary layer, there was clearly a substantial diversion of the fuselage boundary layer upstream of the bleed ducts. The fuselage flow was three-dimensionally separated by intersection with the intake pressure field, the separation line coinciding approximately with the projection of the cone shock on the fuselage wall. Thus it would appear that the most deficient portion of the fuselage boundary layer is spilled as vortices into the airplane flow field.

As an initial step in predicting this flow field, a calculation of the partial cone flow itself about the same θ = 25° half-cone at Mach 1.6 was performed (Peake et al., Ref. 69) but without a reflection plane. The pressure field that would be impressed upon the fuselage is approximately that existing between the shock wave and the half-cone, as shown in Fig. 48. The maximum overall pressure ratio between the shock and the cone is greater than 1.5, so that, as we saw earlier, 3-D separation would be expected.

Culley (Refs. 68, 70) also showed that with a quarter axisymmetric intake model, the use of a splitter plate to isolate the airframe boundary layer from the adverse influence of the intake could involve a multishock viscous compression and 3-D separation of the fuselage boundary layer upstream of the splitter plate (Fig. 49) that was not influenced by variations in the intake mass flow.

Other serious swept-shock/boundary-layer interaction problems in propulsion layouts may be encountered beneath supersonic wing planforms when designers attempt to take advantage of "favorable interference" effects (Refs. 71, 72) from compressions about engine nacelles and boundary-layer diverters.

Figure 50a shows the oil-dot flow pattern on the undersurface of a lifting 70° delta wing at C_L = 0.08 in a free-stream flow of M_∞ = 2.75 at a Reynolds number, based on the maximum wing chord, of 24×10^6 (Ref. 73). The four-nacelle arrangement is typical, in position and scale, of a supersonic transport layout. The two uppermost intakes were operating at design mass flow with cone shock on lip. One will note a small region of three-dimensional separation caused by the wedge-shaped pylons (diverters) and cowl pressure field in Fig. 50b, where the propulsion nacelles have been removed to facilitate inspection of the oil flow. The lower pair of intakes was throttled internally to about 70% design mass flow, forcing the throat normal shock outside of the cowl lip. The result of operating subcritically is to cause a massive three-dimensional separation of the starboard under-wing boundary layer and high local heat-transfer rates in the reattachment regions downstream of the separation. Figure 50c exhibits a postulated pattern of singular points and skin-friction lines in the region where the adjacent separation lines interfere with each other. The interference appears to result in the formation of a nodal point of separation interspersed between the two saddle points immediately ahead of each wedge-shaped diverter. A sketch of the streamlines in the streamwise plane of symmetry passing through the node of separation is also given in Fig. 50c. The accompanying changes in normal force are shown in Fig. 51. At a cruise lift coefficient of 0.08, occurring at an angle of attack of about 3° for this symmetrical wing, there is a 20% increase in lift from the throttling of the four intakes to 70% of the design mass flow; the corresponding increase in drag for subcritical operation is illustrated in Fig. 52. At off-design Mach numbers, the shock/boundary-layer interactions and resulting 3-D separations may be even more severe in their effects on drag.

13. CONCLUDING REMARKS

We have described the structure of 3-D separated flows about various types of aerodynamic components immersed in both low-speed and high-speed flows and encompassing the viscous flow regimes from laminar to turbulent. Typical components displayed have been slender shapes such as the cone (with circular and triangular cross sections), hemisphere-cylinder, and delta wing, a number of rectangular and swept wings of low and high aspect ratio, and supersonic inlets.

By holding strictly to the notions of continuous vector fields of skin-friction lines and external streamlines in association with a restricted number of singular points (nodes, saddles, and spiral nodes) on the surface and in particular projections of the flow (the crossflow plane, for example) we have a language to classify rationally and unambiguously the 3-D separated flow field about any useful aerodynamic configuration. Sequences of structures of ascending elaboration of nodes, saddles, and spiral nodes can be assembled which are then available to guide experiments when observation is imprecise, or to check the veracity of numerical calculations. We have shown, moreover, that in cross-sectional projections of diverse 3-D separated flows, the mechanisms become familiar, occurring repeatedly from flow to flow. As an approach to design, we may postulate sequences, starting with the simplest number of singular points on the surface and in the flow, for a vehicle at low angle of attack, and increasing in complexity as angle of attack becomes large. The philosophy of design, especially at high angles of attack when the leeward vortical flows have a tendency to become asymmetric, must be one of controlling the locations of the 3-D separations on the vehicle, such as at sharp edges, or by active control from blowing, for example. The design aims, in summary, are that we require steady boundary conditions to provide steady flows, and symmetric boundary conditions to yield symmetric flows. We further demand that as flow regimes change with increasing angle of attack there should be no discontinuous jumps to give uncontrollable forces and moments.

This collection of diverse 3-D separated flows has demonstrated that when a 3-D boundary layer detaches from the surface it will, almost without exception, leave along a swept separation line, rolling up in the process into a well-organized nominally steady vortical motion. The underlying mechanism appears to be independent of both Reynolds number and Mach number, although under laminar conditions the flow features are normally more exaggerated. Hence, the overall details of many flows of practical interest can be determined in a water-tunnel facility in which aircraft and missile designers can make changes to configurations quickly and very cheaply. Some airplane and missile companies are currently doing this.

We deem it useful to end this review by specifying the issues that have been raised, from both experiments and calculations, in the study of singular points. First, there is the question of scale effects. Many large-scale flow phenomena involve a small-scale organized substructure (e.g., arrays of longitudinal vortices on the scale of the thickness of the transitional boundary layer or vortex-shedding on the scale of a shear-layer thickness). In some cases, all or a part of this organized substructure is capable of determining the outcome of the evolution of the large-scale structure; in other cases, it is not. Is it possible, then, to formulate a principle that will distinguish between the vital and the unimportant organized substructures? Can one devise an averaging technique that will preserve the essential structures and smear out the remaining ones? A clarification of these queries should also shed light on similar problems involved in turbulence modeling. The utilization of meshes in finite difference calculations obviously provides a process of averaging, but more work is needed to understand the ramifications of altering mesh intervals, especially insofar as they affect the representation of vital organized substructures. Moreover, we need to incorporate an adequate treatment of the essential singular points in numerical calculation schemes, either by refining the mesh size about the singular points or by including some analytical representation of the flow about the singular points within the numerical scheme.

Second, the rules underlying the placement, number, and types of singular points in terms of the governing flow parameters and body geometry need elaboration. This is particularly true in the nose region where the nature of the origins of lines of separation becomes obscure.

Third, the mechanisms by which stationary flow structures change their topology from one level of complexity to the next (i.e., as they pass through structural instabilities and bifurcations) need to be exposed. For example, studies are needed to provide the links between structural instabilities and bifurcations and the large-scale structural changes in the flow that are characteristic of buffet, stall, and vortex breakdown.

Finally, although we have demonstrated a satisfactory understanding in general of the structures of 3-D separated flows, we are only able to compute them about a limited number of simple aerodynamic components. Numerical techniques invoking either inviscid approximations to model the coiling shear layers, or approximate forms of the Navier-Stokes equations, have been successful and should be encouraged further. But the physics of the turbulence in 3-D separated flow regimes has not yet been investigated to any great extent, and an appeal to well-planned experiments with nonintrusive instrumentation must be made in this regard. To restrict the avenues of possible research, and as a suitable starting point, it might be useful to concentrate on measuring the fluctuating flow quantities in the vicinity of the singular points to determine if there is any identifiable, and perhaps universal, turbulence field associated with each type of singular point.

14.   REFERENCES

1.   Tobak, M., and Peake, D. J., "Topology of Three-Dimensional Separated Flows." Ann. Rev. Fluid Mech. vol. 14, 1982, pp. 61-85.

2.   Peake, D. J., and Owen, F. K., "Control of Forebody Three-Dimensional Flow Separations." AGARD CP-262, May 1979.

3.   Hsieh, T., "An Investigation of Separated Flows About a Hemisphere-Cylinder at Incidence in the Mach Number Range from 0.6 to 1.5." AIAA Paper 77-179, Jan. 1977.

4.   Hsieh, T., and Wang, K. C., "Concentrated Vortex on the Nose of an Inclined Body of Revolution." AIAA J., vol. 14, no. 5, 1976, pp. 698-700.

5.   Hsieh, T., "Calculating Viscous, Sonic Flow Over Hemisphere-Cylinder at 19-Degree Incidence: The Capturing of Nose Vortices." AIAA Paper 81-0189, 1981.

6.   Pulliam, T. H., and Steger, J. L., "On Implicit Finite-Difference Simulations of Three-Dimensional Flow." AIAA Paper 78-10, Jan. 1978.

7.   Peake, D. J., and Tobak, M., "Three-Dimensional Interactions and Vortical Flows with Emphasis on High Speeds." AGARDograph 252, July 1980.

8.   Tobak, M., and Peake, D. J., "Topological Structures of Three-Dimensional Separated Flow." AIAA Paper 81-1260, June 1981.

9.   Jorgensen, L. H., "Prediction of Aerodynamic Characteristics for Slender Bodies Alone and with Lifting Surfaces to High Angles of Attack." AGARD CP-247, Oct. 1978.

10.   Legendre, R., "Séparation de l'Écoulement Laminaire Tridimensionnel." La Recherche Aeronautique no. 54, Nov.-Dec. 1956, pp. 3-8.

11.   Wickens, R. H., "The Vortex Wake and Aerodynamic Load Distribution of Slender Rectangular Plates (The Effects of a 20-Degree Bend at Mid-Chord)." National Research Council of Canada Aero Report LR-458, July 1966.

12.   Lighthill, M. J., "Attachment and Separation in Three-Dimensional Flow." Laminar Boundary Layers, Sec. II 2.6, L. Rosenhead, ed., Oxford U. Press, 1963, pp. 72-82.

13.   Winkelmann, A. E., and Barlow, J. B., "Flowfield Model for a Rectangular Planform Wing Beyond Stall." AIAA J., vol. 18, no. 8, 1980, pp. 1006-1008.

14.   Monnerie, B., and Werlé, H., "Étude de l'Écoulement Supersonique et Hypersonique autour d'une Aile Élancée en Incidence." AGARD CP-30, May 1968.

15.   Maltby, R. L., "Flow Visualization in Wind Tunnels Using Indicators." AGARDograph 70, Apr. 1962.

16.   Legendre, R, "La Condition de Joukowski en Écoulement Tridimensionnel. Rech. Aérosp., no. 5, 1972.

17.   Legendre, R., "Lignes de Courant d'un Écoulement Continu," Rech. Aérosp. no. 105, 1965, pp. 3-9.

18.   Küchemann, D., "On the Possibility of Designing Wings that Combine Vortex Flows with Classical Aerofoil Flows." Unpublished RAE Tech. Memorandum, 1971.

19.   Moss, G. F., "Some UK Research Studies of the Use of Wing-Body Strakes on Combat Aircraft Configurations at High Angles of Attack." AGARD CP-247, Oct. 1978.

20.   Rainbird, W. J., "The External Flow Field About Yawed Circular Cones." AGARD CP-30, May 1968.

21.   Rainbird, W. J., "Turbulent Boundary-Layer Growth and Separation on a Yawed 12-1/2° Cone at Mach Numbers 1.8 and 4.25." AIAA J., vol. 6, no. 12, Dec. 1968, pp. 2410-2416.

22.   Nebbeling, C., and Bannink, W. J., "Experimental Investigation of the Supersonic Flow Field About a Slender Cone at High Incidences." Rept. LR-233, Delft Univ. Technology, Dept. of Aerosp. Eng., The Netherlands, Nov. 1976.

23.   Peake, D. J., Fisher, D. F., McRae, D. S., "Flight Experiments with a Slender Cone at Angle of Attack." AIAA Paper 81-0337, Jan. 1981.

24.   McRae, D. S., Peake, D. J., and Fisher, D. F., "A Computational and Experimental Study of High Reynolds Number Viscous/Inviscid Interaction About a Cone at High Angle of Attack." AIAA Paper 80-1422, July 1980.

25.   Nituch, M. J., "The Use of Congruent Obstacle Blocks for the Indirect Measurement of Turbulent Skin Friction on Smooth Surfaces." Thesis, Carleton U., Ottawa, Aug. 1972.

26.   Peake, D. J., "Three-Dimensional Swept Shock/Turbulent Boundary Layer Separations with Control by Air Injection." Ph.D. Thesis, Carleton U., Ottawa, 1975; also National Research Council of Canada Aero. Report LR-592, July 1976.

27.   Elfstrom, G. M., "Indirect Measurement of Turbulent Skin-Friction. DME/NAE Quarterly Bulletin, no. 1, National Research Council of Canada, 1979, pp. 21-51.

28. Dougherty, N. S., and Fisher, D. F., "Boundary-Layer Transition on a 10-Degree Cone: Wind-Tunnel/ Flight Data Correlation." AIAA Paper 80-0154, Jan. 1980.

29. Bradshaw, P., and Unsworth, K., "A Note on Preston Tube Calibrations in Compressible Flow." IC-Aero-73-07, Imperial College of Science and Technology, London, England, Sept. 1973.

30. Peake, D. J., Owen, F. K., and Johnson, D. A., "Control of Forebody Vortex Orientation to Alleviate Side Forces," AIAA Paper 80-0183, Jan. 1980.

31. Peake, D. J., Owen, F. K., and Higuchi, H., "Symmetrical and Asymmetrical Separations About a Yawed Cone." AGARD CP-247, Oct. 1978.

32. Fiechter, M., "Uber Wirbelsysteme an schlanken Rotationskorpern und ihren.Einfluss auf die aero- dynamischen Beiwerte." Deutsch-Franzosisches Forschungs-Institut Saint-Louis," Report 10/66, 1966.

33. Werlé, H., "La Tunnel Hydrodynamique au Service de la Recherche Aérospatiale." ONERA Publication No. 156, 1974.

34. O'Hare, J., and Jones, J., "Flow Visualization Photography of a Yawed Tangent Ogive Cylinder at Mach 2." AEDC-TR-73-45, 1973.

35. Grosche, F. R., "Wind Tunnel Investigation of the Vortex System Near an Inclined Body of Revolution with and without Wings." AGARD CP-71, Sept. 1970.

36. Boersen, S., "Reynolds Number Effects on Pressure and Normal Force Distributions Along a Conically Pointed Circular Cylinder at Mach Number of 2.3." NLR TR 75124U, Sept. 1975.

37. Jernell, L. S., "Aerodynamic Characteristics of Bodies of Revolution at Mach Numbers from 1.50 to 2.86 and Angles of Attack to 180°." NASA TM X-1658, 1968.

38. Jorgensen, L. H., and Nelson, E. R., "Experimental Aerodynamic Characteristics for a Cylindrical Body of Revolution with Various Noses at Angles of Attack from 0° to 58° and Mach Numbers from 0.6 to 2.0." NASA TM X-3128, 1974.

39. Jorgensen, L. H., and Nelson, E. R., "Experimental Aerodynamic Characteristics for Bodies of Elliptical Cross-Section at Angles of Attack from 0° to 58° and Mach Numbers from 0.6 to 2.0." NASA TM X-3129, 1975.

40. Jorgensen, L. H., "Prediction of Static Aerodynamic Characteristics for Slender Bodies Alone and with Lifting Surfaces to Very High Angles of Attack." NASA TR R-474, 1977.

41. Küchemann, D., "The Aerodynamic Design of Aircraft — An Introduction. Part 3." RAE Tech. Memo. Aero 1535, Aug. 1973; also Pergamon Press, 1978.

42. Peake, D. J., Rainbird, W. J., and Atraghji, E. G., "Three-Dimensional Separations on Aircraft and Missiles." AIAA J., vol. 10, no. 5, May 1972, pp. 567-580.

43. Atraghji, E. G., "The Influence of Mach Number, Reynolds Number, Semi-Nose Angle and Roll Rate on the Development of the Forces and Moments Over a Series of Long Slender Bodies of Revolution at Incidence." National Research Council of Canada, NAE 5 x 5/0020, Mar. 1967.

44. Atraghji, E. G., "Pressure Distribution Over a Family of Inclined Long Slender Bodies of Revolution at M_∞ = 0.5, 2.0 and 3.5." National Research Council of Canada, NAE 4 x 5/0029, Aug. 1968.

45. Ward, G. N., "Linearised Theory of High Speed Flow," Chap. 9. Cambridge U. Press, England, 1955.

46. Hoak, D. E., "Body Lift in the Non-Linear Angle-of-Attack Range." Sec. 4.2.12, USAF Stability and Control Datcom, Flight Control Div., Air Force Flight Dynamics Lab., Wright-Patterson Air Force Base, Ohio, Oct. 1960 (revised, Nov. 1965).

47. Ohman, L. H., "A Surface Flow Solution and Stability Derivatives for Bodies of Revolution in Complex Supersonic Flow." Parts I and II, National Research Council of Canada Aero. Reports LR-419, 519, Nov. and Dec. 1964.

48. Lamont, P. J., "Pressure Measurements on an Ogive-Cylinder at High Angles of Attack with Laminar, Transition or Turbulent Separation." AIAA Paper 80-1556-CP, Aug. 1980.

49. Lamont, P. J., "The Complex Asymmetric Flow Over a 3.5D Ogive Nose and Cylindrical Afterbody at High Angles of Attack." AIAA Paper 82-0053, Jan. 1982.

50. Rainbird, W. J., Crabbe, R. S., Peake, D. J., and Meyer, R. F., "Some Examples of Separation in Three-Dimensional Flows." CASI J., vol. 12, no. 10, Dec. 1966, pp. 409-423.

51. Bannink, W. J., and Nebbeling, C., "Measurements of the Supersonic Flow Field Past a Slender Cone at High Angles of Attack." AGARD CP-247, Oct. 1978.

52. Keener, E. R., and Chapman, G. T., "Similarity in Vortex Asymmetries Over Slender Bodies and Wings." AIAA J., vol. 15, no. 9, Sept. 1977, pp. 1370-1372.

53. Shanks, R. E., "Low Subsonic Measurements of Static and Dynamic Stability Derivatives of Six Flat Plate Wings Having Leading-Edge Sweep Angles of 70° to 84°." NASA TN D-1822, 1963.

54. Fellows, K. A., and Carter, E. C., "Results and Analysis of Pressure Measurements on Two Isolated Slender Wings and Slender Wing-Body Combinations at Supersonic Speeds. Vol. 1, Analysis." ARA Report 12, Nov. 1969.

55. Keener, E. R., and Chapman, G. T., "Onset of Aerodynamic Side Forces at Zero Sideslip on Symmetric Forebodies at High Angles of Attack." AIAA Paper 74-770, Aug. 1974.

56. Keener, E. R., Chapman, G. T., and Kruse, R. L., "Effects of Mach Number and Afterbody Length on Onset of Asymmetric Forces on Bodies at Zero Sideslip and High Angles of Attack." AIAA Paper 76-66, Jan. 1976.

57. Nielsen, J. N., "Non-Linearities in Missile Aerodynamics." AIAA Paper 78-20, Jan. 1978.

58. Allen, H. J., and Perkins, E. W., "A Study of Effects of Viscosity on Flow Over Slender Inclined Bodies of Revolution." NACA Report 1048, 1951.

59. Deffenbaugh, F. D., and Koerner, W. G., "Asymmetric Vortex Wake Development on Missiles at High Angles of Attack." J. Spacecraft & Rockets, vol. 14, no. 3, Mar. 1977, pp. 155-162.

60. Tobak, M., and Peake, D. J., "Topology of Two-Dimensional and Three-Dimensional Separated Flows." AIAA Paper 79-1480, July 1979.

61. Küchemann, D., and Weber, J., "Vortex Motions." ZAMM, vol. 7, no. 8, 1965, pp. 457-474.

62. Tinling, B. E., and Allen, C. Q., "An Investigation of the Normal Force and Vortex-Wake Characteristics of an Ogive-Cylinder-Body at Subsonic Speeds." NASA TN D-1297, 1962.

63. Thomson, K. D., and Morrison, D. F., "The Spacing Position and Strength of Vortices in the Wake of Slender Cylindrical Bodies at Large Incidences." J. Fluid Mech., vol. 50, pt. 4, 1971, pp. 751-783.

64. Hasel, L. E., and Kouyoumjian, W. L., "Investigation of Static Pressures and Boundary-Layer Characteristics on the Forward Parts of Nine Fuselages of Various Cross-Sectional Shapes at M_∞ = 2.01." NACA RM-L56I13, Jan. 1957.

65. Clarkson, M. H., Malcolm, G. N., and Brittain, V. A., "Aerodynamic Characteristics of Bodies with Non-Circular Cross Sections at High Angles of Attack." To appear as AIAA Paper 82-0056, 1982.

66. Faro, I.D.V., "Supersonic Inlets." AGARDograph 102, May 1965, pp. 121-123.

67. Culley, M., "A Side-Mounted Supersonic Intake and the Problem of Three-Dimensional Boundary-Layer Separation." ARL ME 137, Australia, June 1972.

68. Culley, M., "Viscous Interaction in Integrated Supersonic Intakes." First International Symposium on Air Breathing Engines, Marseilles, France, June 1972.

69. Peake, D. J., Jones, D. J., and Rainbird, W. J., "The Half-Cone Flow and its Significance to Side-Mounted Intakes." AGARD CP-71, Sept. 1970.

70. Culley, M., "A Brief Examination of the Flow External to an F-111 Intake at Mach 1.6." ARL/ME 357, Australia, July 1975.

71. Swan, W. C., "A Discussion of Selected Aerodynamic Problems on Integration of Propulsion Systems with the Airframe of Transport Aircraft." AGARDograph 103, Pt. 1, Oct. 1965, pp. 23-68.

72. Sigalla, A., and Hallstaff, T. H., "Aerodynamics of Powerplant Installation on Supersonic Aircraft." J. Aircraft, vol. 4, no. 4, July-Aug. 1967, pp. 273-277.

73. Peake, D. J., and Rainbird, W. J., "The Drag Resulting from Three-Dimensional Separations Caused by Boundary-Layer Diverters and Nacelles in Subsonic and Supersonic Flow." AGARD CP-124, Apr. 1973.

2-16

SIDE VIEW

$M_\infty = 1.2$

PLAN VIEW

(a) $\iota = 0°$.

SIDE VIEW

$M_\infty = 1.2$

PLAN VIEW

(b) $\iota = 3.5°$.

SIDE VIEW

$M_\infty = 1.2$

PLAN VIEW

(c) $\iota = 5.0°$.
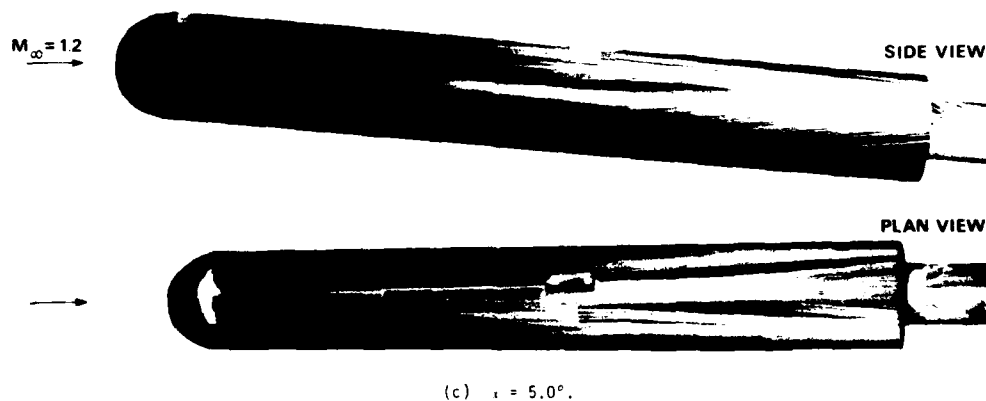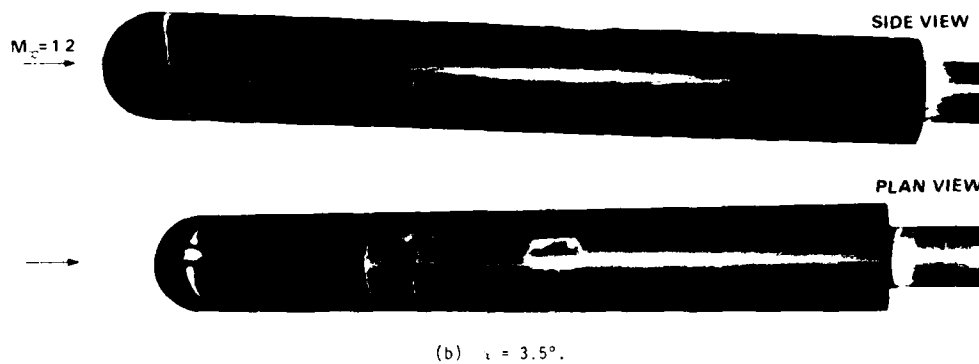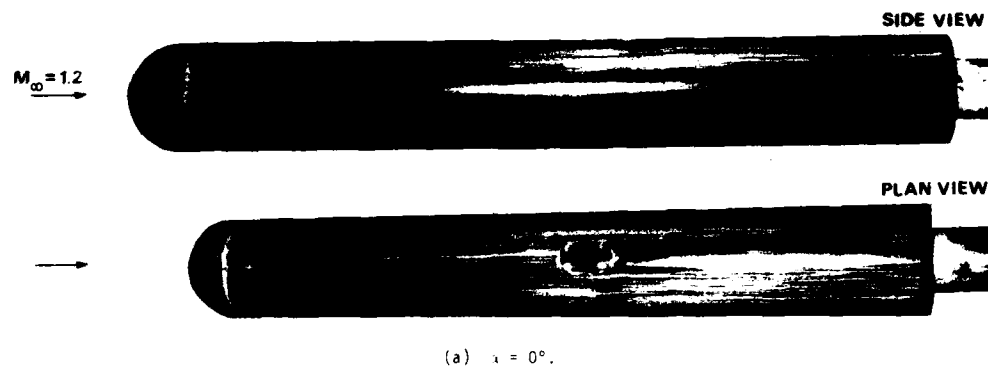
Fig. 1. Oil-streak patterns about a hemisphere-cylinder at angle of attack at $M_\infty = 1.2$, $R_{L_\iota} = 4.9 \times 10^6$, L = 7.5D, D = 2.6 in.

$M_\infty = 1.2$

SIDE VIEW

PLAN VIEW

(d) $\alpha = 6.5°$.

$M_\infty = 1.2$

SIDE VIEW

PLAN VIEW

(e) $\alpha = 10.0°$.

$M_\infty = 1.2$

SIDE VIEW

PLAN VIEW

(f) $\alpha = 15°$.

Fig. 1. Continued.

$M_\infty = 1.2$

SIDE VIEW

PLAN VIEW

(g) $\alpha = 19.0°$.

$M_\infty = 1.2$

SIDE VIEW

PLAN VIEW

(h) $\alpha = 27.5°$.

Fig. 1. Continued.

$M_\infty = 1.2$

SIDE VIEW

PLAN VIEW

(i) $\iota = 32.5°$.

Fig. 1. Concluded.

$\Rightarrow N_a$

(SINGULAR) LINE
OF SEPARATION

(SINGULAR) LINE
OF ATTACHMENT

(a) $\iota = 0°$.
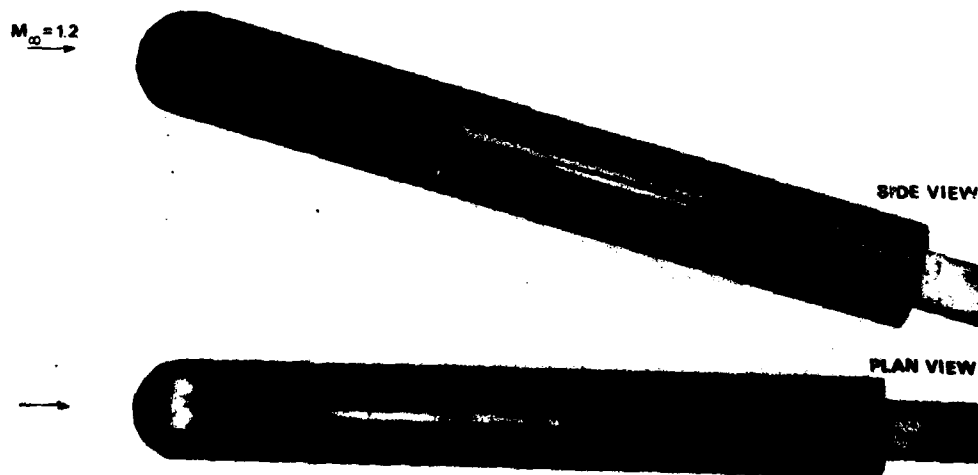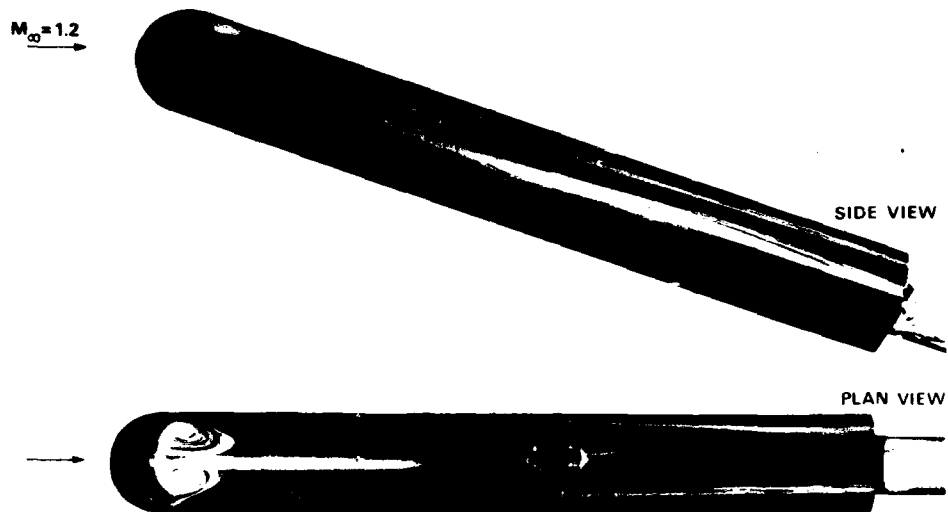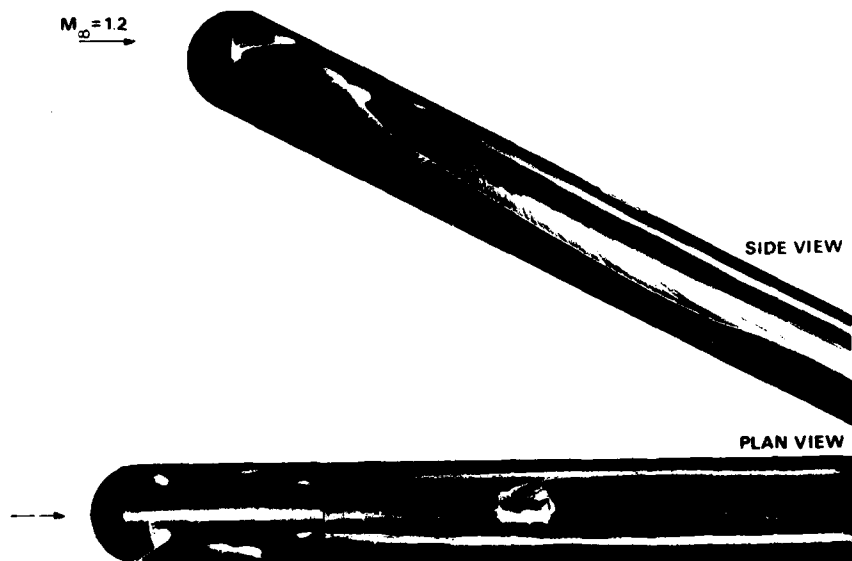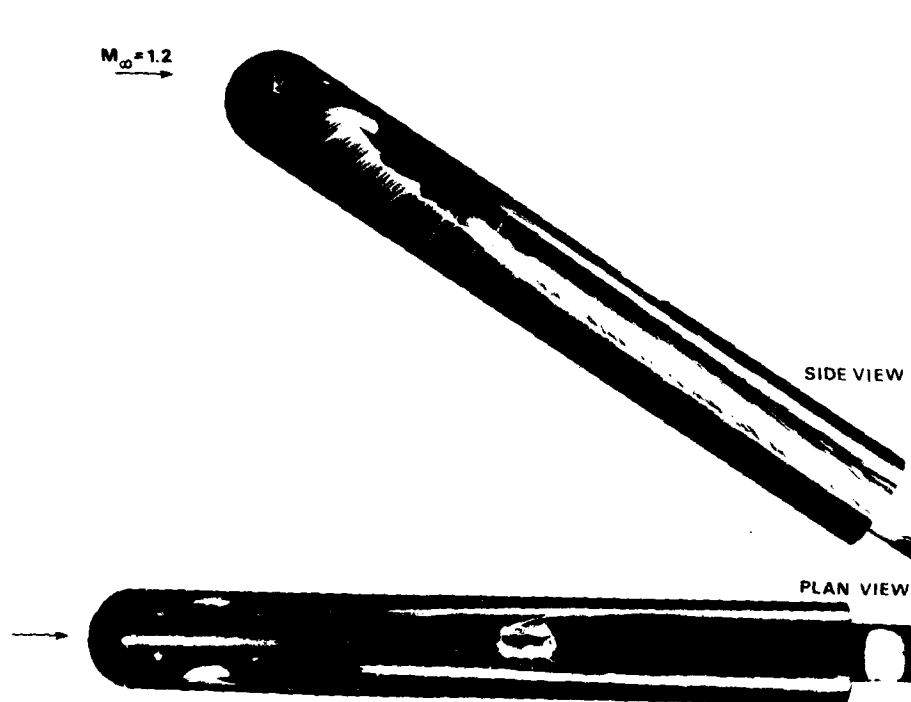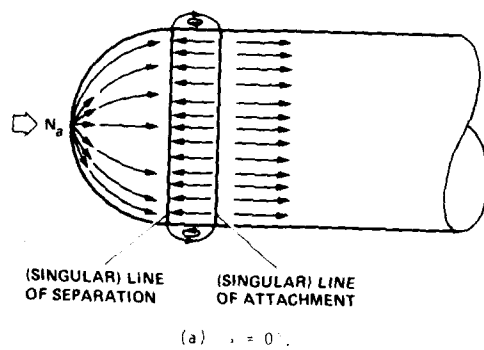
Fig. 2. Conceptual sketches of skin-friction line patterns about a hemisphere-
cylinder at angle of attack (drawn from Fig. 1).

APPEARS ON VAPOR SCREEN
AS DARK LINE, EVIDENCE OF
VORTICAL FLOW ON DIVIDING
SURFACE FROM N_s, S

LEEWARD SINGULAR POINTS
SPREAD AS α INCREASES

A DIVIDING SURFACE

N_s S

N_a

S_a N_a

A

WINDWARD SINGULAR POINTS
APPROACH EACH OTHER AS
α INCREASES

SIDE VIEW

SECTION A-A

N_s S

TOP VIEW

(b) α = 1°.

DIVIDING SURFACE

N_s S

S N

N_a

$S_a N_a$

SIDE VIEW

S N

N_s S

S N

TOP VIEW

(c) α = 3.5°.

Fig. 2. Continued.

PRIMARY LINE OF SEPARATION

DIVIDING SURFACE

SECTION B-B

(d) $\alpha = 5.0°$.

SECONDARY

PRIMARY

(PRIMARY OUT OF N_a. SECONDARY FROM SADDLE POINT)

(e) $\alpha = 10.0°,\ 15.0°$.

Fig. 2. Continued.

SECONDARY
PRIMARY

SECTION D-D
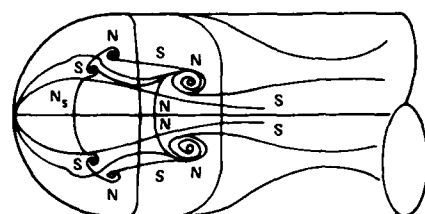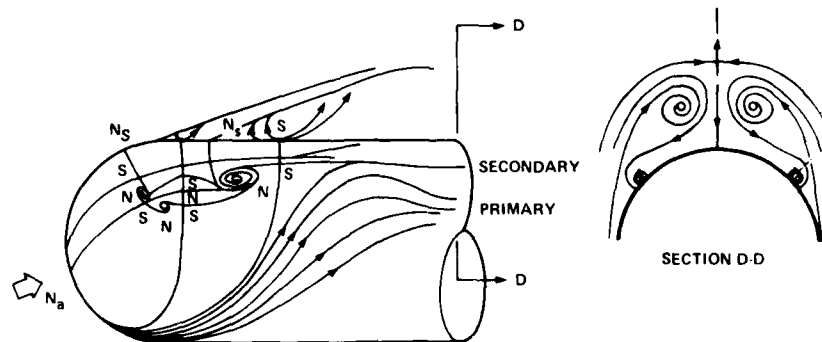
(PRIMARY OUT OF N_c, SECONDARY FROM SECOND OF A PAIR OF SPIRAL NODES)

(f) $\alpha = 19.0°$.
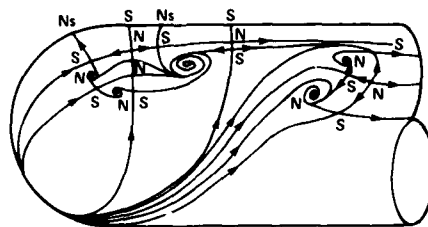
(g) $\alpha = 27.5°$.

Fig. 2. Concluded.
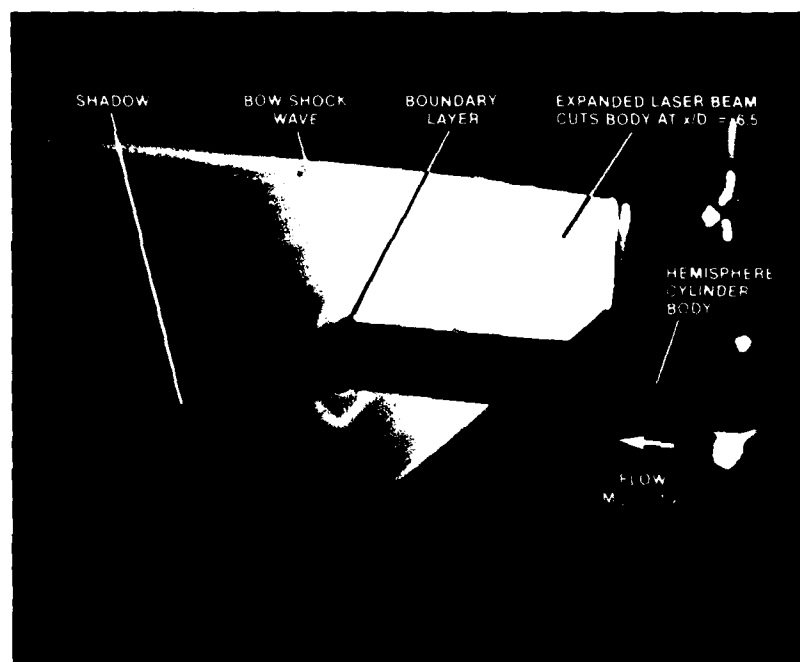
Fig. 3. Axisymmetric crossflow vapor screen at x/D = 6.5 along hemisphere-cylinder at M_∞ = 1.2, R_L = 4.9 × 10^6, L = 7.5D, D = 2.6 in.

(a) α = 5°.

FLOW

(b) α = 10°.

(c) α = 15°.

(d) α = 19°.

VIEW TOWARDS RIGHT-HAND SIDE OF BODY LOOKING DOWNSTREAM
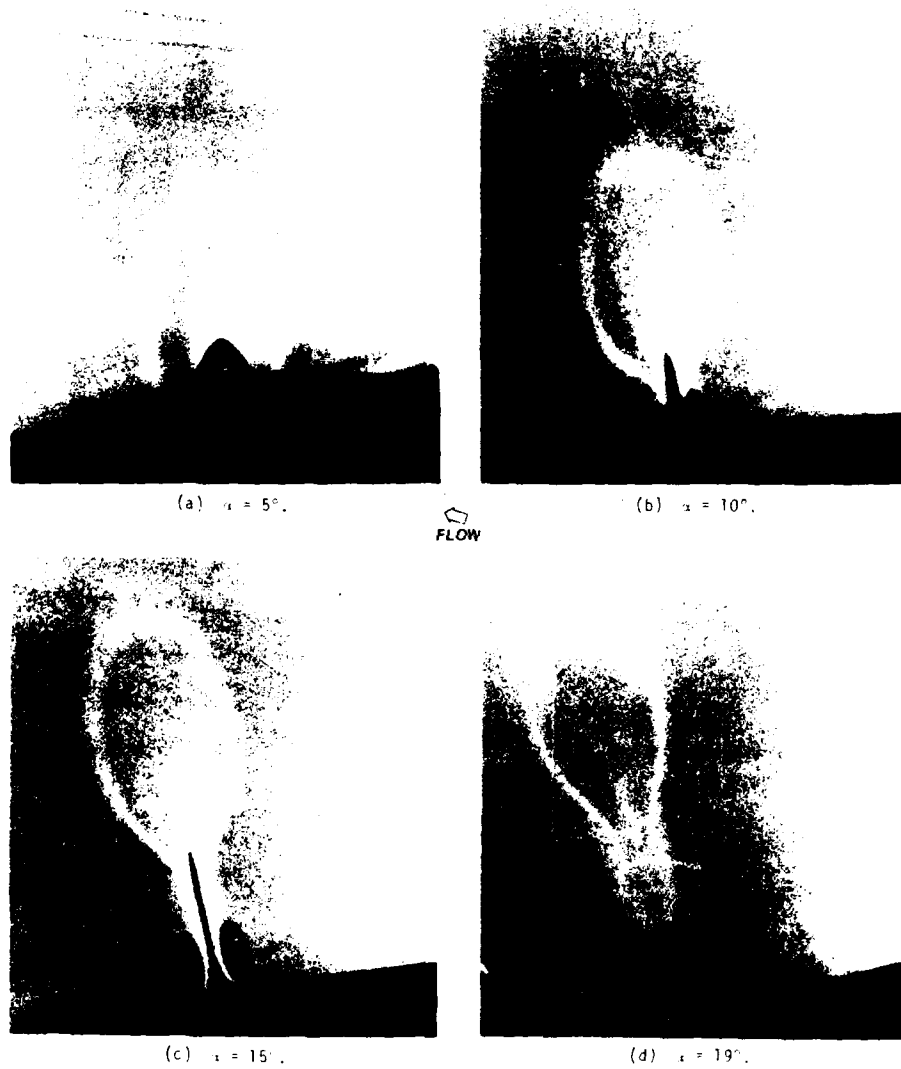
Fig. 4. Crossflow vapor screens at x/D = 6.5 along hemisphere-cylinder at
M_∞ = 1.2, R_{L_∞} = 4.9 × 10^6, L = 7.5D, D = 2.6 in.
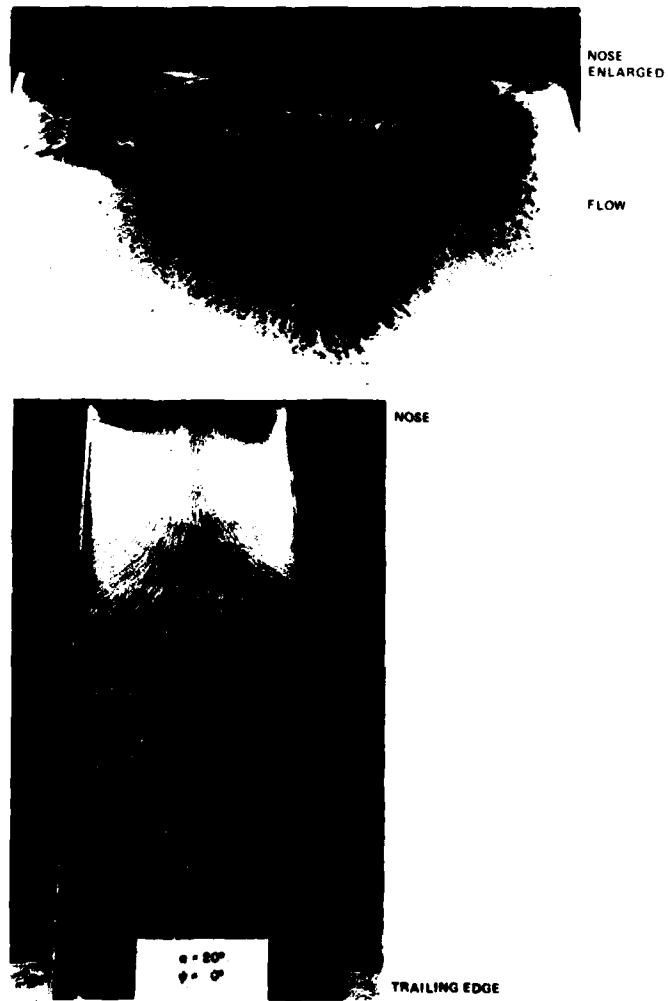
Fig. 5. Oil-flow pattern on slender, rectangular wing at ι = 20° (Ref. 11).
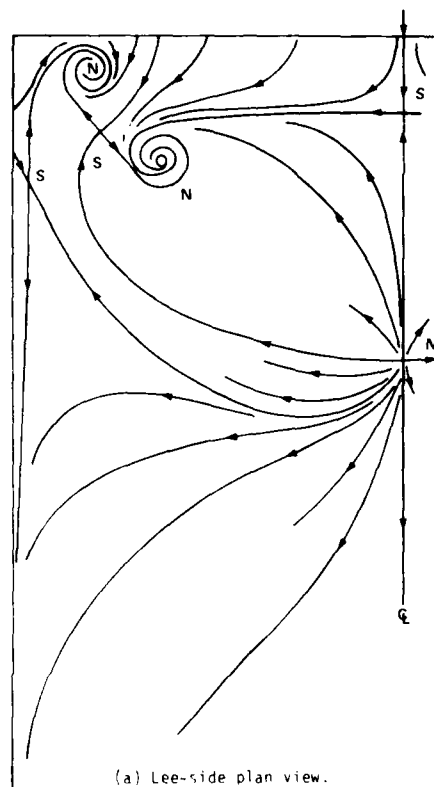
(a) Lee-side plan view.

(b) Perspective.

CORE LIFTING OFF SURFACE

CORE "PARALLEL" TO SURFACE

CORE OF PRIMARY SEPARATION
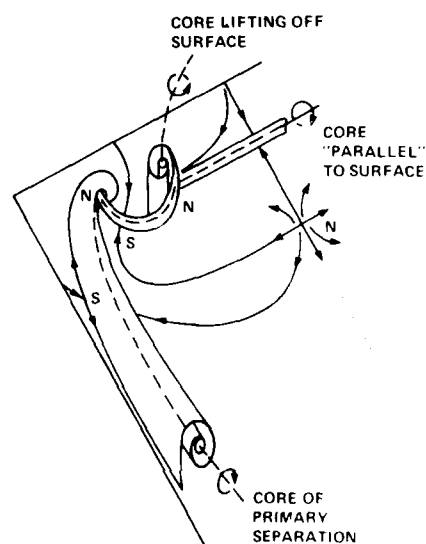
(c) Trailing-edge region.

NOTE: THERE WILL BE 1 NODE OF ATTACHMENT ON UNDERSIDE ₵

CHORDWISE POSITION OF SPANWISE PRESSURE DISTRIBUTION

	x/c = 0.014
○	0.041
◇	0.083
△	0.166
✕	0.248
+	0.417
●	0.584
■	0.750
▲	0.917

C_P

POSITION ON SEMISPAN
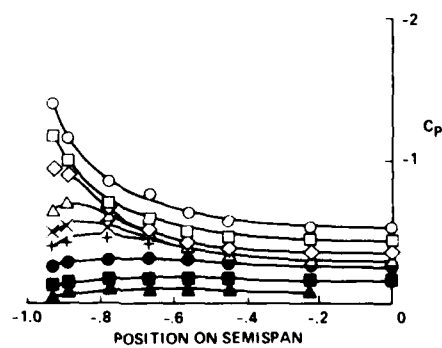
(d) Spanwise pressure distributions on topside.

Fig. 6. Interpretation of skin-friction lines and pressures on slender, rectangular wing, aspect ratio 0.25, at $\imath$ = 20° in low-speed flow (Ref. 11).

$\downarrow U_\infty$
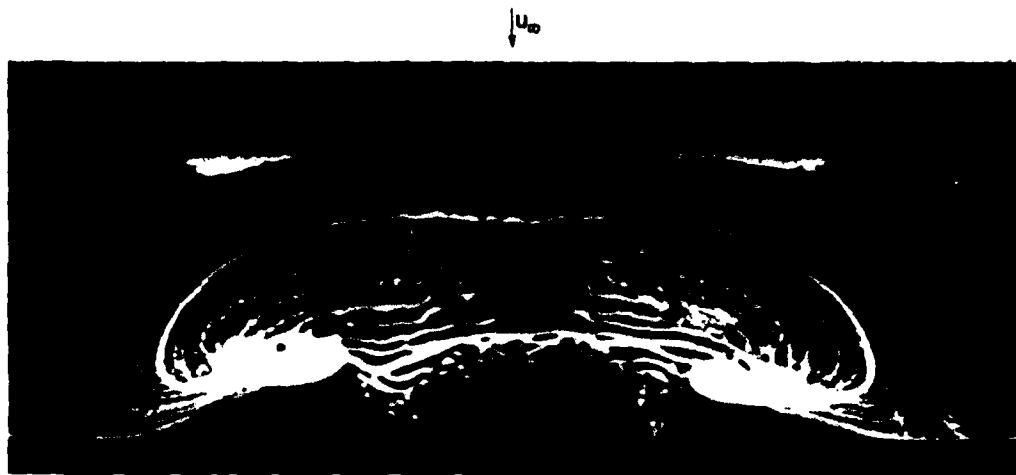
(a) Oil flow on Clark Y airfoil: c = 3.5 in., s = 12.25 in., R_c = 2.5 × 10^5.

A

A

SECTION AA
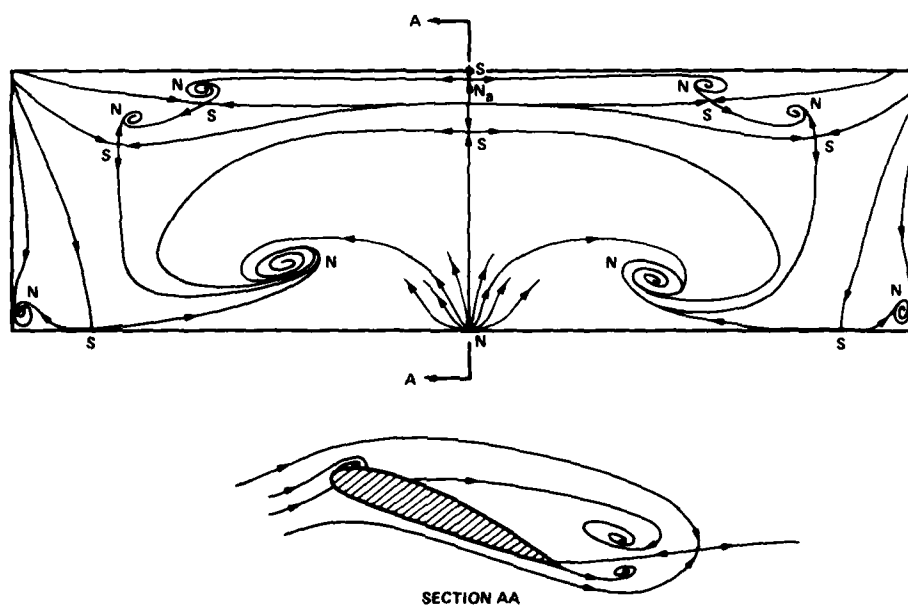
(b) Conjectured pattern of skin-friction lines.

Fig. 7. Rectangular wing, aspect ratio 3.5, at α = 20° in low-speed flow (Ref. 13).

(a) OIL FLOW: MEAN CHORD $\bar{c}$ = 10.1 in. AT 37.5% OF SEMISPAN

N_a = NODE OF ATTACHMENT
N_s = NODE OF SEPARATION
N = SPIRAL NODE OF SEPARATION

(b) CONCEPTUAL SKIN-FRICTION LINE PATTERN
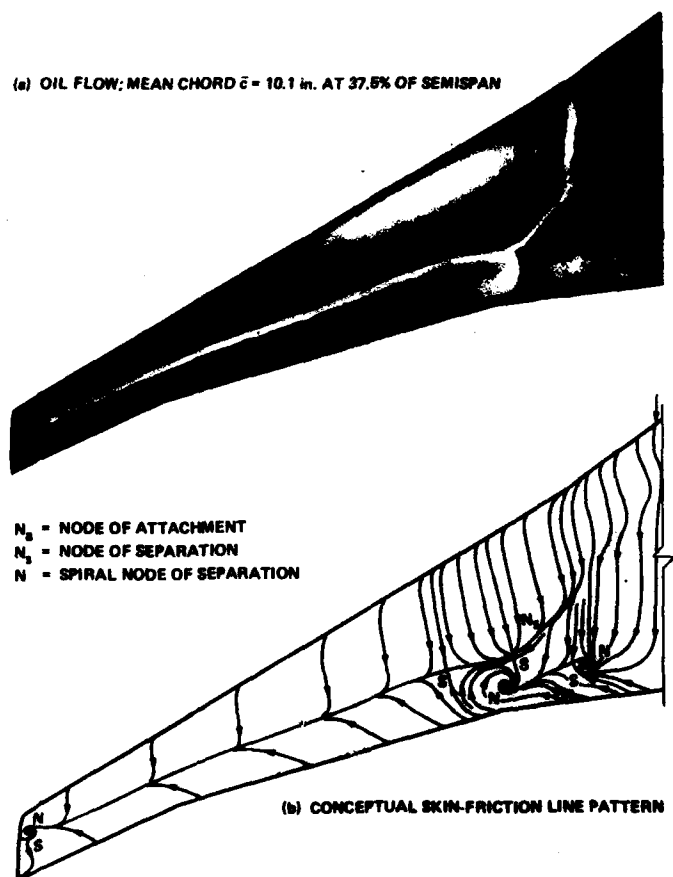
Fig. 8. Early transport swept-wing design close to buffet onset conditions:
M_∞ = 0.82, $R_{\bar{c}}$ = 2.5 × 10^6.

$M_\infty = 0$

$\alpha = 25$

CORE OF
PRIMARY VORTEX

(a) Side elevation.

PRIMARY
SEPARATION LINE

SECONDARY
SEPARATION LINE

ATTACHMENT
LINE

CORE OF
PRIMARY VORTEX

(b) Plan view.

CORE OF
PRIMARY VORTEX

(c) Cross flow.
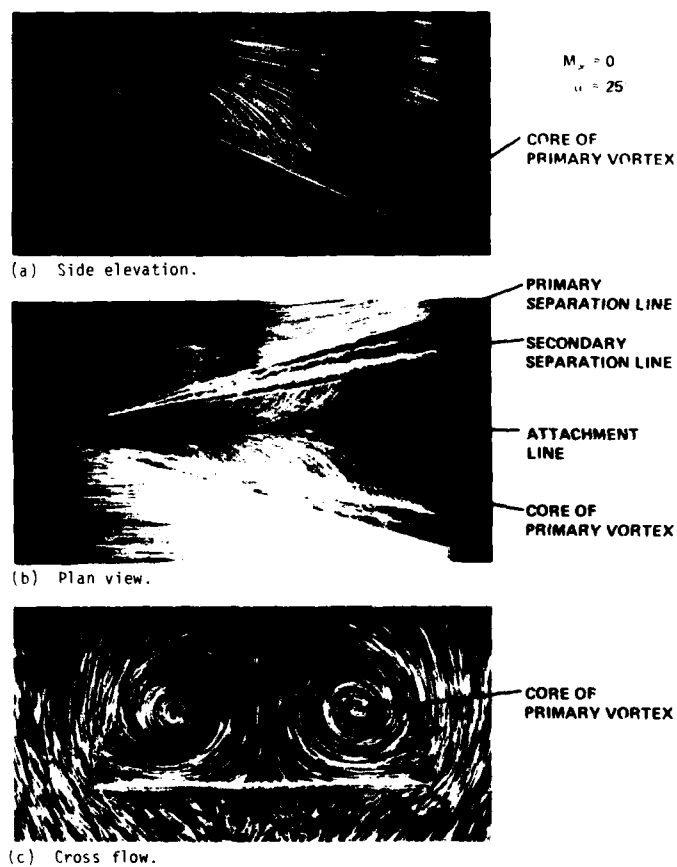
Fig. 9. Very low-speed 75° delta wing flow of Monnerie and Werlè (Ref. 14).

(a) Schlieren

PRIMARY VORTEX
WEAK SHOCK

PRIMARY SEPARATION
LINE ALONG EDGE

TERTIARY
SEPARATION LINE

SECONDARY
SEPARATION LINE

ATTACHMENT LINE

(b) Lee-side pattern of skin-friction lines.

b IS LOCAL SEMI-SPAN
OF WING

$M_\infty = 1.95$
$\alpha = 25°$
$\alpha_N = 61°$
$M_N = 0.94$

$p_i'/p_i =$

1.0
0.65
0.6
0.5
0.4
0.3
0.2
0.1
0.05
0.2
0.1

Z/b

PRIMARY VORTEX

SECONDARY VORTEX

CENTER-LINE
SHOCK

0.5 0.4 0.05

Y/b
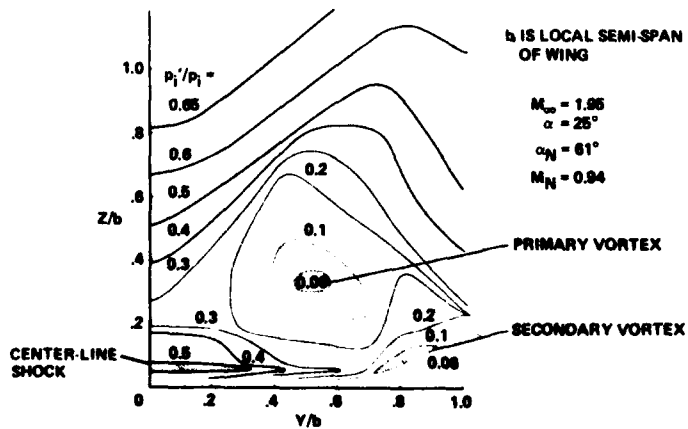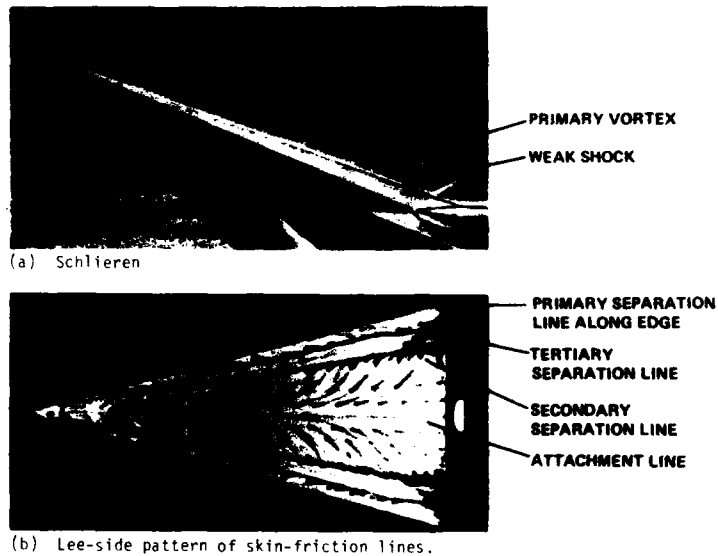
(c) Contours of constant pitot pressure.

Fig. 10. Seventy-five-degree delta wing flow of Monnerie and Werle (Ref. 14)
with subsonic leading edges.
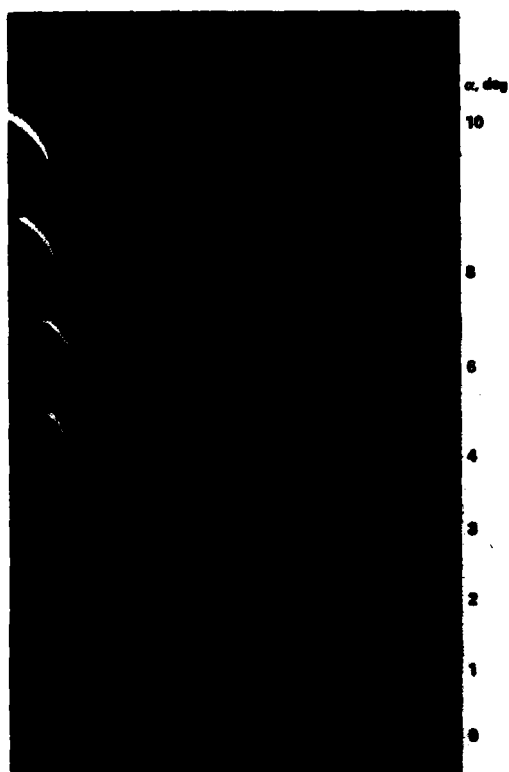
Fig. 11. Vapor-screen photographs of flow behind cambered delta wing at $M_\infty = 1.88$ (Maltby, Ref. 15).

LIGHTHILL 1963

FOCUS, N
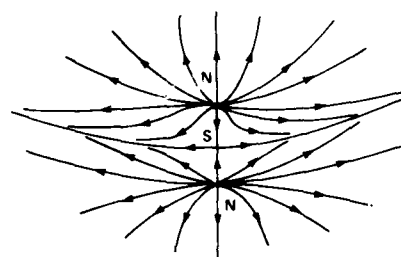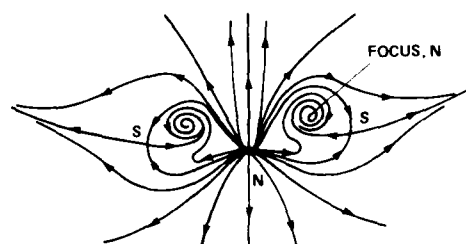
LEGENDRE 1972

Fig. 12. Postulated patterns of skin-friction lines at rounded apex of delta wing.

IN WATER TUNNEL (WERLÉ 1974)

ATTACHMENT NODE

SADDLE POINT

FOCUS

SKIN-FRICTION LINES

ROLL-UP OF DIVIDING SURFACE
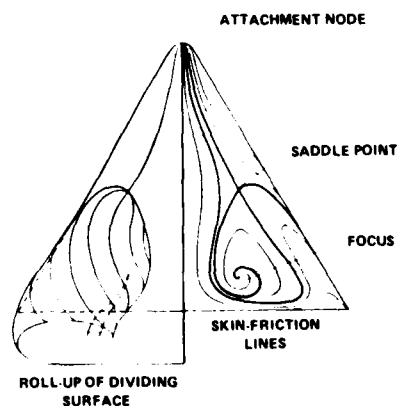
POSTULATED PATTERNS OF LEGENDRE 1965

Fig. 13. Laminar flow on slender delta wing at high angle of attack (Legendre, Ref. 17).

$\alpha = 14°$

PITOT PRESSURE

$$\frac{H - H_\infty}{\frac{1}{2}\rho U_\infty^2}$$

RAE MODEL 494

Z(mm)

200

TRAVERSE PLANE

100

0   200   300   400   900

$\alpha = 14$ STREAMWISE VORTICITY

$$\frac{\xi\ell}{U_\infty}$$

(+)

(−)

Z(mm)

200

100

0

AIRCRAFT $\mathcal{C}$ AT $_Y = 0$

(a)

-100

0   200   300   400   500   600   700   800   900

Y, mm
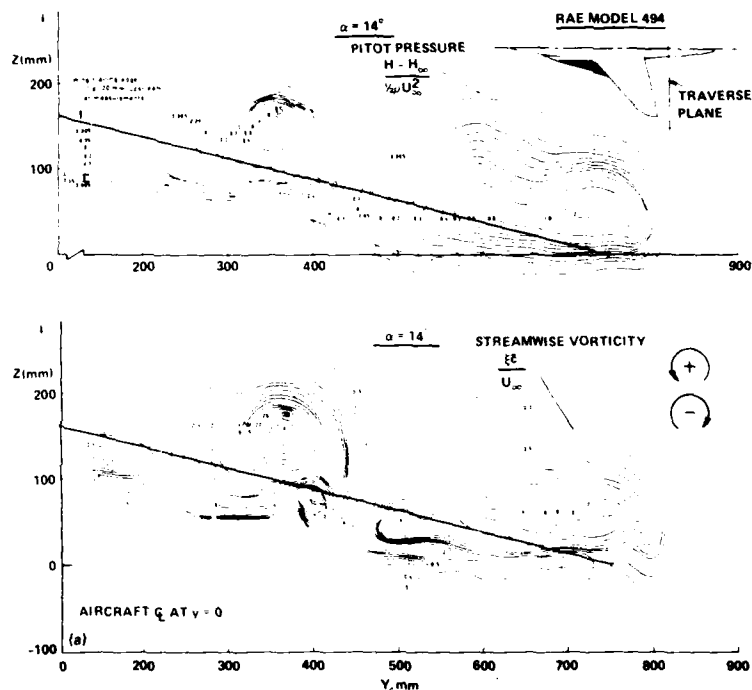
(a)   Contours of constant pitot pressure and vorticity.

NOTE: TOPOLOGY LAW IS $\Sigma_N - \Sigma_S = 2$
ASSUMING NODES OF ATTACHMENT AND SEPARATION
AT THE NOSE AND TAIL, FOR BOTH L.H. AND
R. H. SIDES, $\Sigma_N = 2 \times 8 + 2$ = 18
$\Sigma_S = 2 \times 8$ 16 $\Sigma = 2$

M_∞

FLOW LEAVES SURFACE

T.E. SEPARATION

STRONG SHOCK WAVES

M_∞

S

N_A

N_1

S

N_A

S

S

N_S S   S N_2 N_S
N_S N_S
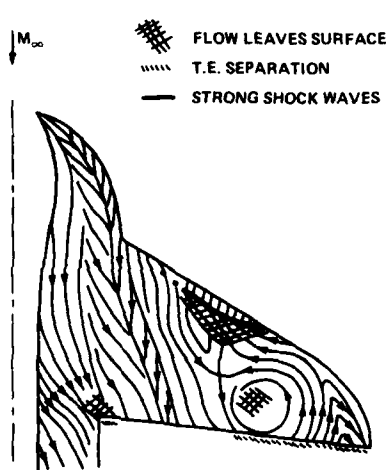
(b)   Sketch of oil flow by Moss 1978
$M_\infty = 0.9$, $\alpha = 8.3°$.
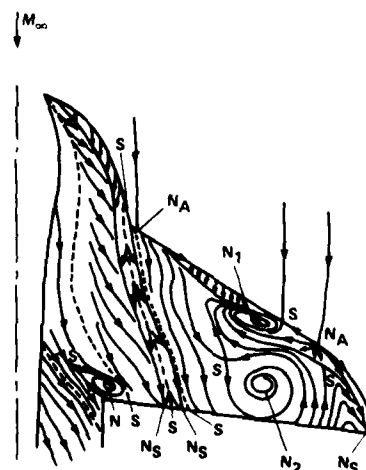
(c)   Our interpretation of skin-friction
lines.

Fig. 14.   Low-aspect-ratio straked wing of fighter aircraft
at angle of attack (Ref. 19).

NOTE: TOPOLOGY LAW IS $\Sigma_N - (\Sigma_S + \frac{1}{2}\Sigma_{S'}) = -1$ FOR
STREAMLINES IN A 2-D PLANE CUTTING A 3-D BODY
HERE, FOR L.H. AND R.H. SIDES, $\Sigma_N = 2 \times 5 = 10$
$\Sigma_S = (2 \times 2) + 1 = 5$ $\Sigma = -1$
$\Sigma_{S'} = (2 \times 7) + 2 = 16$

NODE

ENCLOSING
SADDLE POINT

FROM SPIRAL
NODES ON WING
SURFACE

WING TIP
VORTEX

STRAKE
VORTEX

SECONDARY
SEPARATION LINES

PRIMARY
SEPARATION
LINES

SECONDARY
SEPARATION

FROM SPIRAL
NODE IN CORNER

ATTACHMENT
LINE
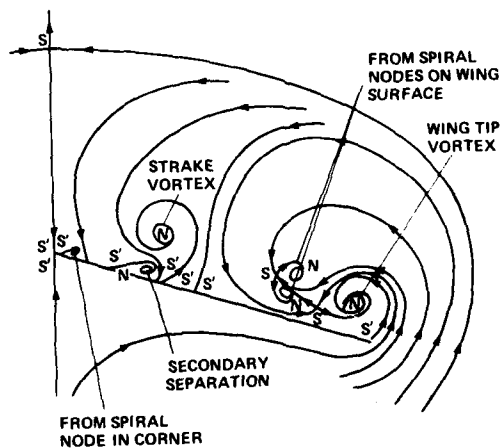
(d) Conjectured external streamlines in plane
close to wing trailing edge (starboard
side only).

Fig. 14. Concluded.
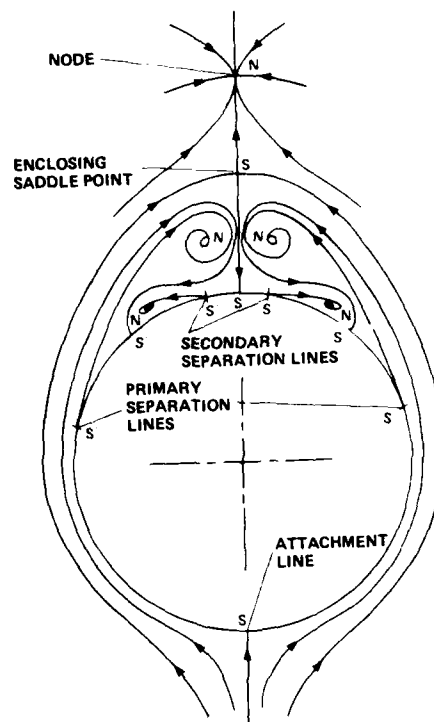
TOPOLOGY LAW FOR CONICAL FLOW PROJECTION IS:
$\Sigma_N - (\Sigma_S + \frac{1}{2}\Sigma_{S'}) = 0$. HERE, $\Sigma_N = 5$, $\Sigma_S = 1$, $\Sigma_{S'} = 8$; $\Sigma = 0$

Fig. 15. Flat projection of three-dimensional
stream surfaces intersecting sphere centered on
cone vertex with both primary and secondary
separation. There are five nodes and spiral
nodes (Σ_N), one saddle, and eight half-saddles.

OBSTACLE BLOCKS SITUATED ADJACENT TO
STATIC PRESSURE ORIFICES

MOVIE
CAMERA

ROLL
GEAR

TRANSITION STRIP
(0.014 in. diam GLASS BEADS)

STING SUPPORT

TUFTS

COMBINED PITOT-STATIC/FLOW
DIRECTION PROBE

MICROPHONES AND KULITE
PRESSURE TRANSDUCERS

Fig. 16. Five-degree semiapex angle cone.
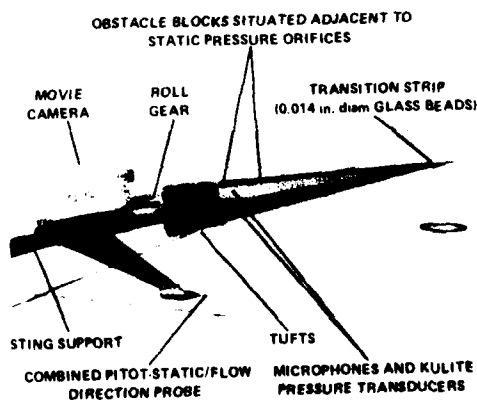
(a) Flight results.

(b) Wind-tunnel results.
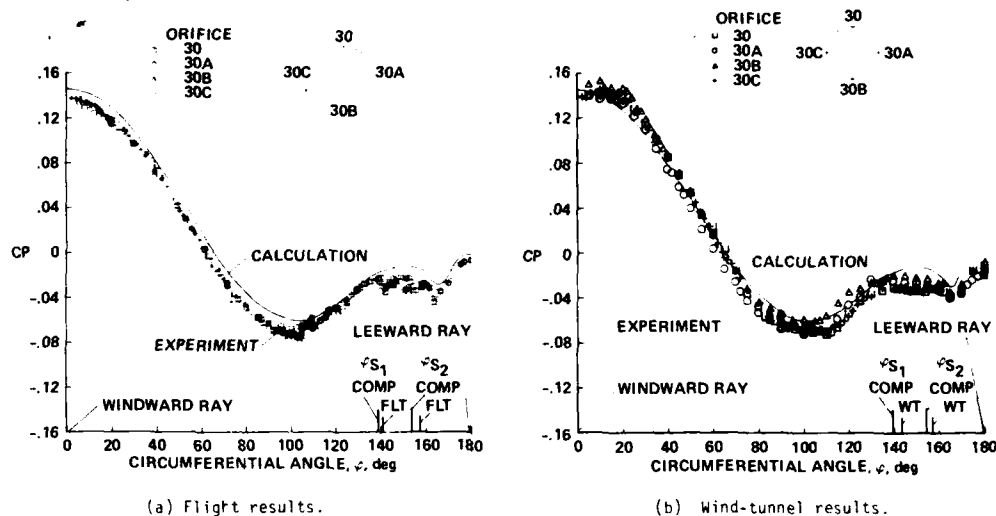
Fig. 17. Five-degree semiapex angle cone flight and wind-tunnel results for Mach 1.8.
Circumferential mean pressure distributions at one axial station, x = 30 in., ι = 11°.
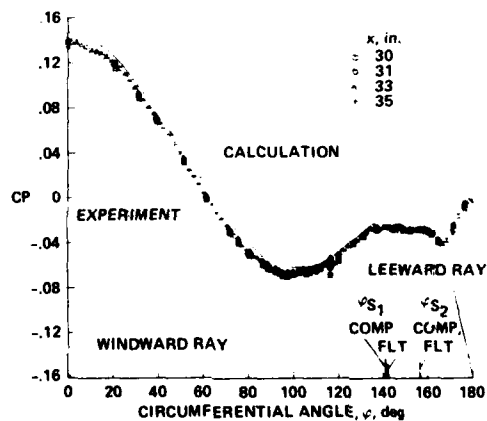
Fig. 18. Five-degree semiapex angle cone flight results at Mach 1.5.
Circumferential mean pressure distributions at several axial stations,
x = 30 to 35 in., ι = 11°.

(a) Flight results

(b) Wind-tunnel results
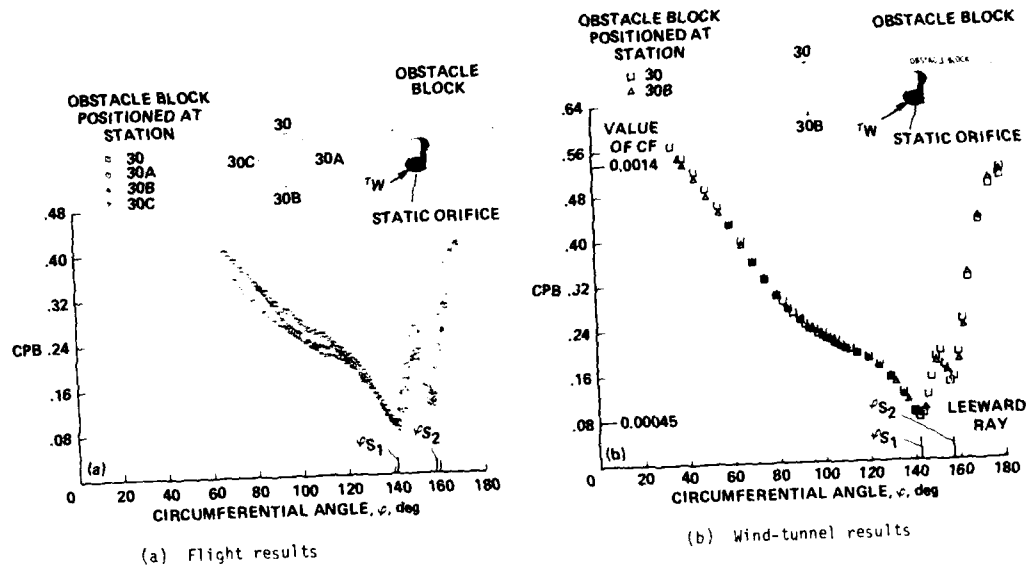
Fig 19. Five-degree semiapex angle cone flight and wind-tunnel
skin-friction results at Mach 1.8, x = 30 in., α = 11°.

PITOT CONTOURS, p_p/p_{TOT_∞}

DIVIDING STREAMLINE
LOCUS OF ZERO VELOCITIES IN BOUNDARY
LAYER PROFILES IN CONICAL-FLOW
PROJECTION

ϕ_{S_1} PRIMARY SEPARATION LINE

ϕ_{S_2} SECONDARY SEPARATION LINE
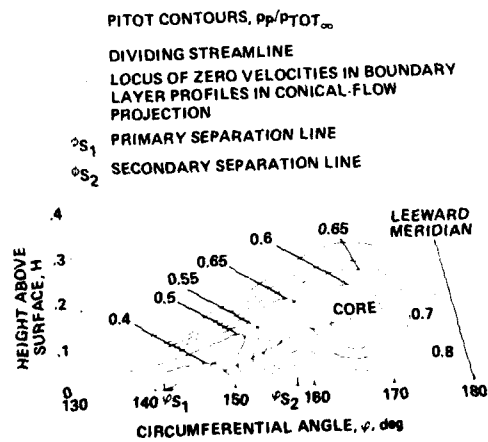
Fig. 20. Computed contours of constant pitot
pressure on leeward of 5° semiapex angle cone,
$M_\infty = 1.8$, α = 11°, $R_{x_\infty} = 9.8 \times 10^6$.
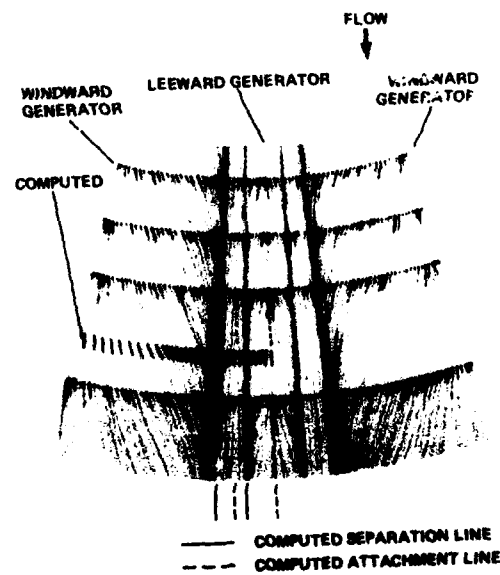
Fig. 21. Unwrapped pattern of experimental
skin-friction lines on 5° semiapex angle
cone, compared with computed limiting
streamline directions at Mach 1.8, α = 12.5°.

013

012

011

$\dfrac{p}{q_\infty}$

.010

009

.008

NOTE
SUPPRESSED ZERO

₵ PROBE IN
EMPTY TUNNEL

WINDWARD RAY
AT α = 0

$^{\checkmark}S_1$ $^{\checkmark}S_2$

0   20   40   60   80   100   120   140   160   180
CIRCUMFERENTIAL ANGLE, φ, deg
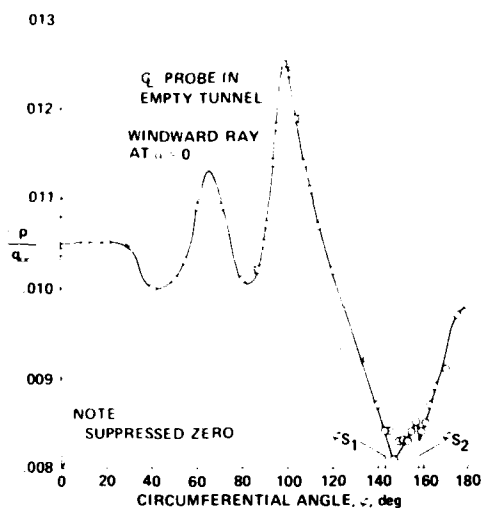
Fig. 22. Wind-tunnel measurements on 5° semi-
apex angle cone of root-mean-square microphone
output at one axial station, x = 34 in., α = 11°,
M_∞ = 1.5, RN = 2.9 × 10⁶/ft.

—— 0°, WINDWARD
– – – 151°, $^{\checkmark}S_1$
— — 180°, LEEWARD

-20

+ 140 dB, 1 kHz
CALIBRATION
(0.029 psi rms)

+ 130 dB, 1 kHz
CALIBRATION
(0.009 psi rms)

-40

POWER SPECTRAL DENSITY, dB

-60

FAN

-80

.1   1   10   20
LOG FREQUENCY, kHz
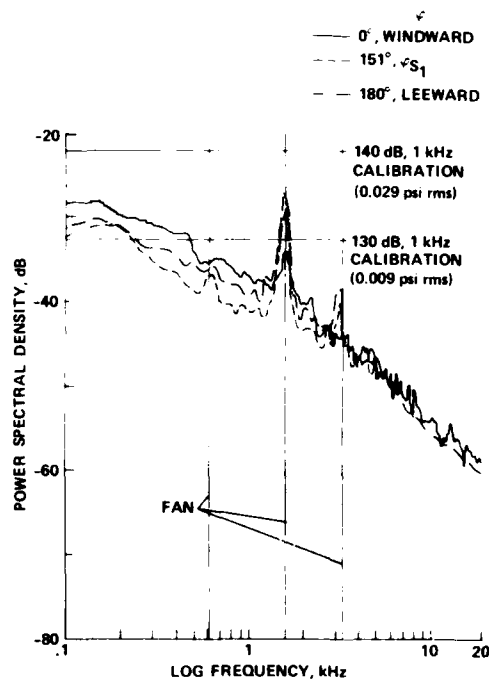
Fig. 23. Mach 1.5 wind-tunnel results of selected
spectra from microphone at x = 34 in. in surface
of 5° semiapex angle cone. RN = 2.9 × 10⁶/ft.,
α = 11°.

$\dfrac{p}{\tau_W}$

$^{\checkmark}S_1$ $^{\checkmark}S_2$

0   20   40   60   80   100   120   140   160   180
CIRCUMFERENTIAL ANGLE, φ, deg
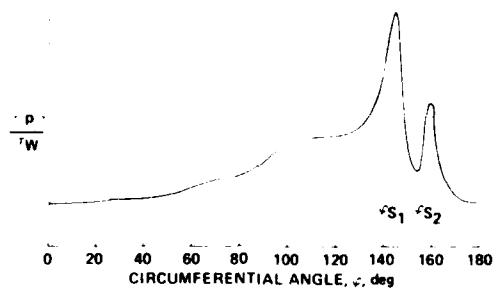
Fig. 24. Mach 1.5 wind-tunnel results of root-mean-square pressure
fluctuation at x = 34 in. along surface of 5° semiapex angle cone,
normalized by local wall shear-stress, α = 11°, RN = 2.9 × 10⁶/ft.

(a) $\alpha \sim 25°$, symmetric.

STARBOARD

PORT

STARBOARD

PORT
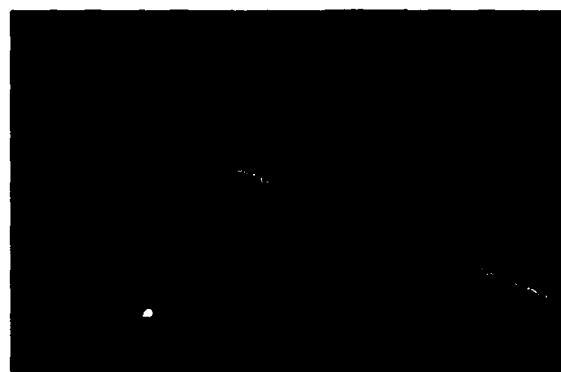
(b) $\alpha \sim 48°$, asymmetric and relatively steady.
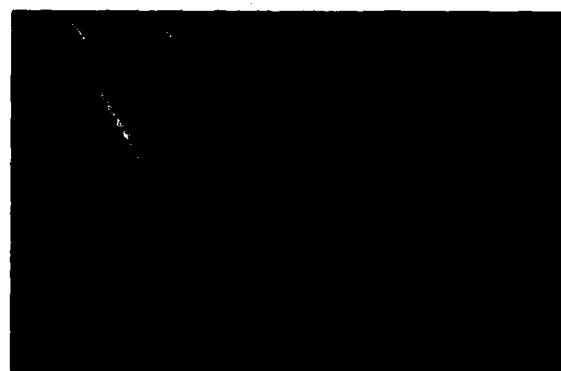
(c) $\alpha \sim 60°$, asymmetric and unsteady.

Fig. 25. Lee vortex wake about 18° semiapex angle tangent-ogive-cylinder at angle of attack in water tunnel (Fiechter, Ref. 32).
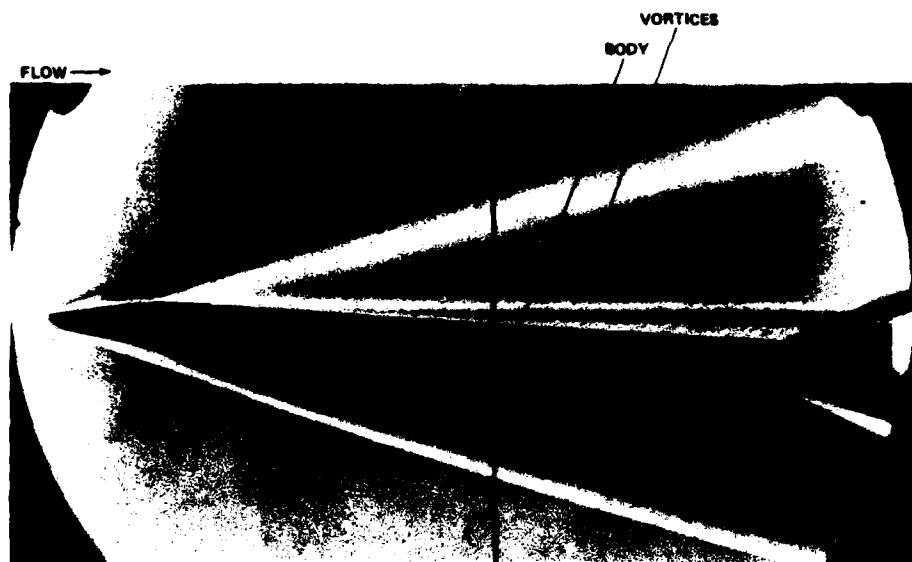
Fig. 26. Body separations on 10° semiapex angle blunted cone-cylinder-flare at $M_\infty = 4$, and $\alpha = 5°$.

(a) Symmetric cross flow, water tunnel, $M_\infty \sim 0$, $\alpha = 20°$ (Werlé 1974).

(b) Laser vapor screen, oil flow and Schlieren flow visualization, $M_\infty = 2$, $\alpha = 26°$ (O'Hare and Jones, 1973).
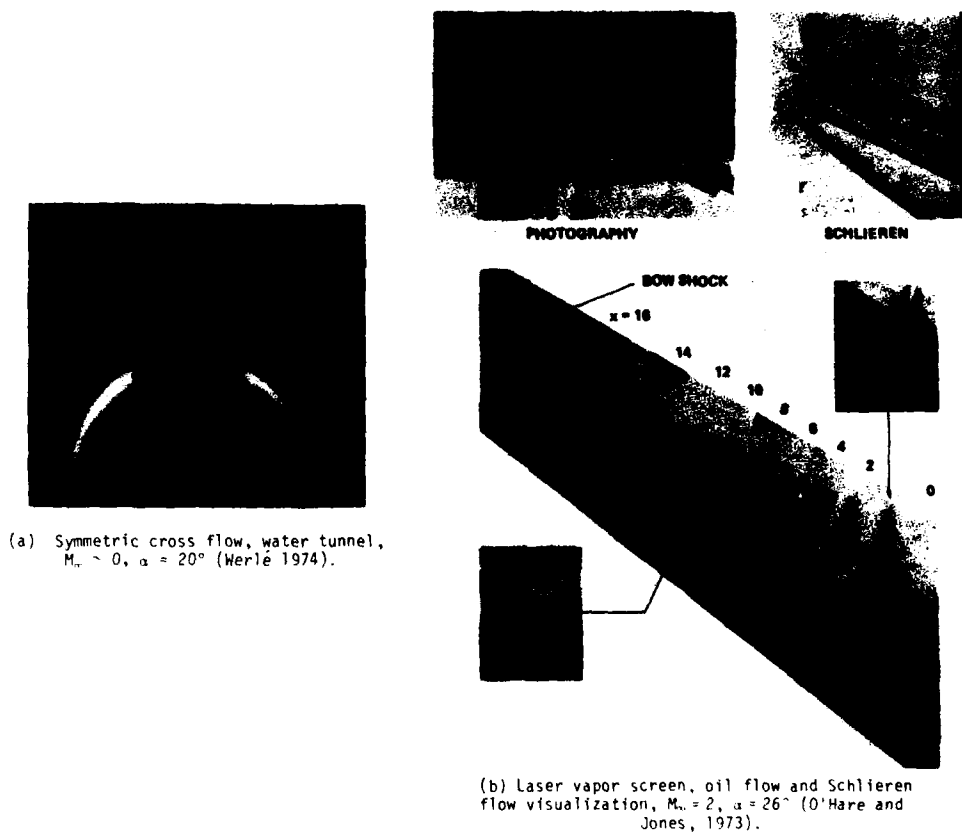
Fig. 27. Views of the symmetric vortex wake in the crossflow plane about tangent-ogive cylinders at angle of attack.
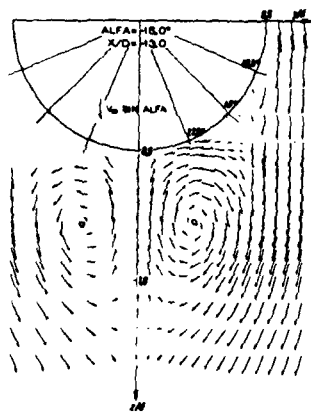
(a) Cross flow velocities
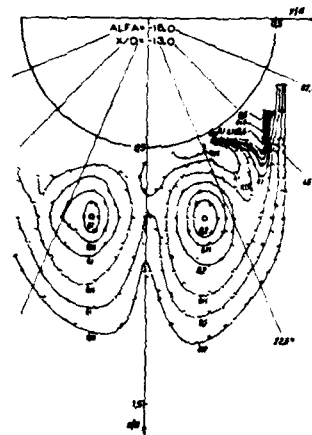
(b) Isobars of total pressure loss
$(p_{t_\infty} - p_t)/q_\infty$ = const
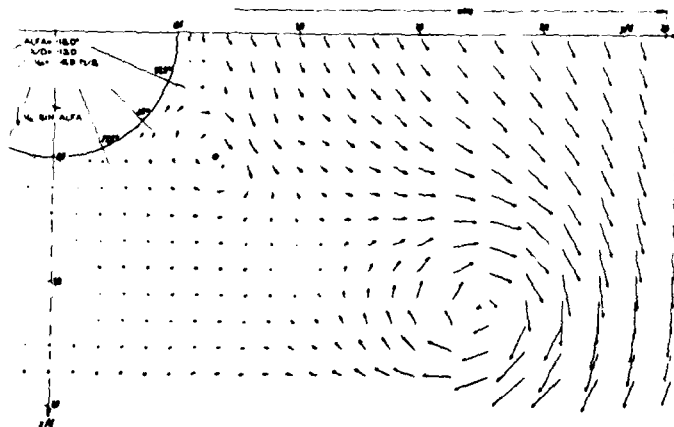
(c) Cross flow velocities at the plane X/D = 13; angle of
attack α = -15°; with delta wing

Fig. 28. Body vortices about 19° semiapex angle tangent-ogive
cylinder in low-speed turbulent flow at α = -15°
(Grosche, Ref. 35).

(a) Side elevation, $R_{L_\infty} \sim 10 \times 10^6$, $R_D = 1.3 \times 10^6$
length $l = 38.2$ cm (15 in); $D = 5.0$ cm (1.97 in.).

(b) Unwrapped surface of clindrical afterbody,
$R_{L_\infty} \sim 10 \times 10^6$, $R_D = 1.3 \times 10^6$.

Fig. 29. Surface oil-flow patterns on 20° semiapex angle blunted cone-cylinder
at $\alpha = 12°$, $M_\infty = 2.4$, with turbulent boundary layers (Boersen, Ref. 36).
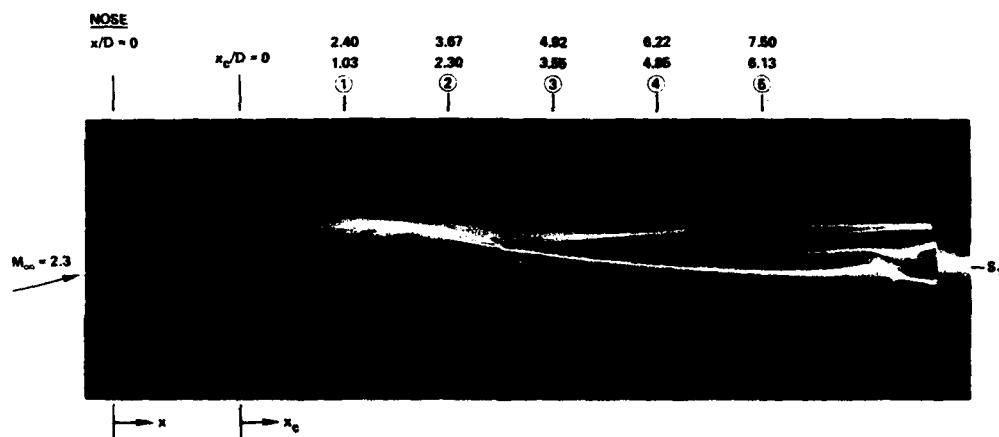
(a) Side elevation, $R_{L_\infty} \sim 32 \times 10^6$ $(R_D = 4 \times 10^6)$
length, $L = 40$ cm (15.75 in.); $D = 5.0$ cm (1.97 in.)

Fig. 30. Surface oil-flow patterns and circumferential pressures on 20° semiapex
angle pointed cone-cylinder at $\alpha = 12°$, $M_\infty = 2.3$, with turbulent boundary
layers (Boersen, Ref. 36).
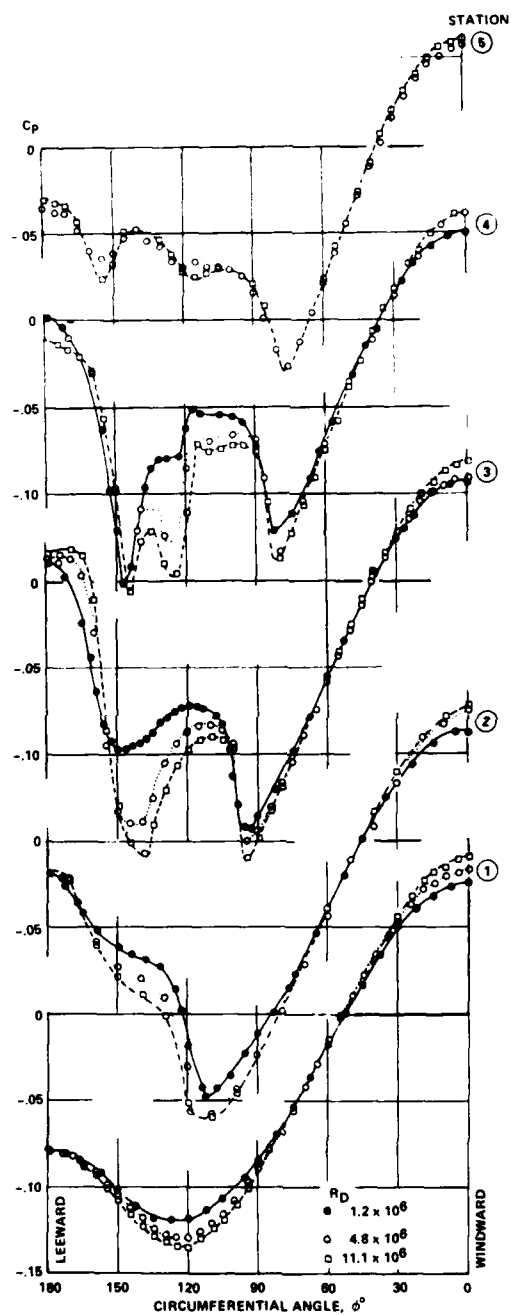
(b) Circumferential pressure distributions on afterbody of cone-cylinder

Fig. 30. Continued.

FLOW

$R_D = 1.6 \times 10^6$

— STATION ③

— $x_c/D = 4$

— STATION ④

CROSSFLOW

ⓐⓕⓑ PROMINENT ATTACHMENT LINES

ⓒⓖⓔⓓ SEPARATION LINES

LEEWARD GENERATOR

WINDWARD GENERATOR

ⓑ ⓓⓔⓕⓖ ⓒ ⓐ

STATION 4
● $R_D = 1.2 \times 10^6$
◻ $R_D = 11.1 \times 10^6$
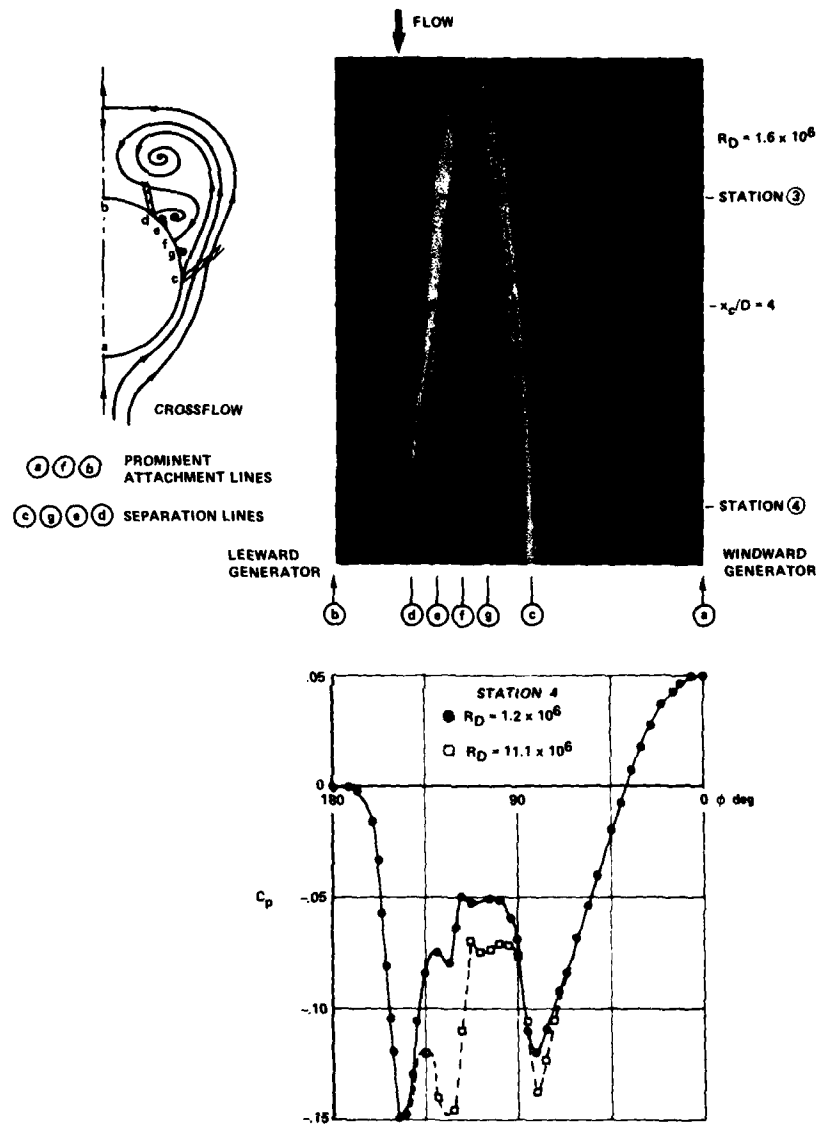
(c) Oil flow and surface pressures on downstream part of afterbody

Fig. 30. Concluded.

BODY I, L/D = 21

BODY II, L/D = 13

BODY I

—— CALCULATION
○ △ EXPERIMENT

C_L

BODY II

LINEAR THEORY

ANGLE OF ATTACK, α, deg
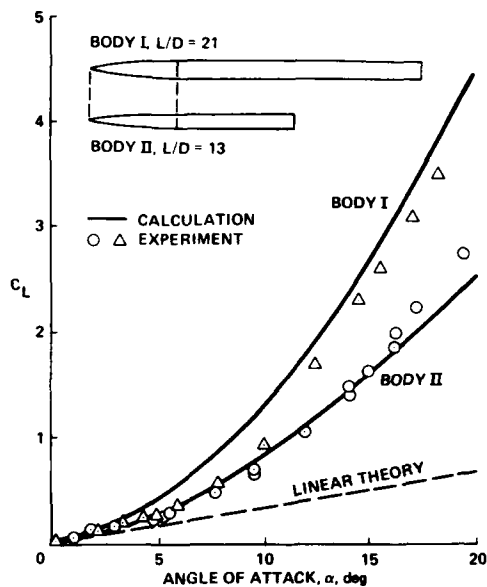
Fig. 31. Overall lift of two bodies of revolution (see Küchemann, Ref. 41).

CONFIGURATION	SEMI-APEX ANGLE θ_c	NOSE LENGTH $\frac{L_N}{D}$	AFTERBODY LENGTH $\frac{L - L_N}{D}$	m
C5 - 12D	5° 43'	5	12	1
O7 - 12D	7° 36'	5	12	4/3
O9 - 12D	9° 28'	5	12	5/3
O11 - 12D	11° 19'	5	12	2
C9 - 12D	9° 28'	3	12	1
O12 - 12D	12° 31'	3	12	4/3
O15 - 12D	15° 31'	3	12	5/3
O18 - 12D	18° 26'	3	12	2
C5 - 6D	5° 43'	5	6	1
O7 - 6D	7° 36'	5	6	4/3
O9 - 6D	9° 28'	5	6	5/3
O11 - 6D	11° 19'	5	6	2
C9 - 6D	9° 28'	3	6	1
O12 - 6D	12° 31'	3	6	4/3
O15 - 6D	15° 31'	3	6	5/3
O18 - 6D	18° 26'	3	6	2

C = CONE, O = OGIVE
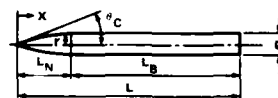
NOSE CONTOUR: $\frac{r}{D} = \frac{1}{2}\left[1 - (1 - \frac{x}{L_N})^m\right]$

Fig. 32. Details of long, pointed slender bodies tested at NAE, Canada (Peake et al., Ref. 42).

OPEN SYMBOLS ARE CALCULATIONS ACCORDING TO ÖHMAN 1964
CLOSED SYMBOLS ARE EXPERIMENT OF PEAKE et al., 1972

L/D	
◆	17
●	15
▲	11
■	9

C_{N_α}

$M_\infty = 3.5$

WITH B/L CORRECTION

C_{N_α}

$M_\infty = 2.0$

SLENDER BODY THEORY (WARD 1955)

C_{N_α}

DATCOM METHOD (HOAK 1965)

$M_\infty = 0.5$

θ_c, deg

Fig. 33. Low angle-of-attack performance of long, pointed slender bodies in terms of normal force slope versus semi-nose angle at $M_\infty = 0.5$, 2.0, and 3.5, at $R_D = 1 \times 10^6$ to 4×10^6 (Peake et al., Ref. 42).

○ C5   + C9
□ O7   ✕ O12
△ O9   ⅄ O15   SEE FIG. 32
▽ O11   ⅄ O18

NON-LINEAR, $C_N = K + b_1\alpha + d_1\alpha^2$, ($\alpha$ rad.)

$\frac{(L - L_N)}{D}$

12

d_1

6

LINEAR C_N, FOR $\frac{(L - L_N)}{D}$ = 6 AND 12

b_1

MACH NUMBER, M_∞

Fig. 34. Linear and nonlinear lift on long, pointed slender bodies at $R_D = 1 \cdot 10^6$ to $4 \cdot 10^6$ (Peake et al., Ref. 42).
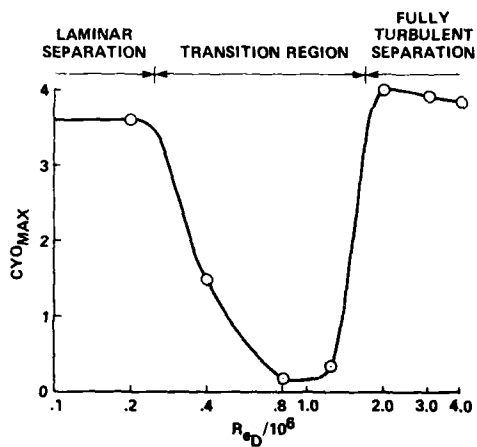
Fig. 35. Effect of Reynolds number on maximum
side force at α = 55° on ogive/cylinder (2D/
13D in length), M_∞ = 0.3 (Lamont, Ref. 48).
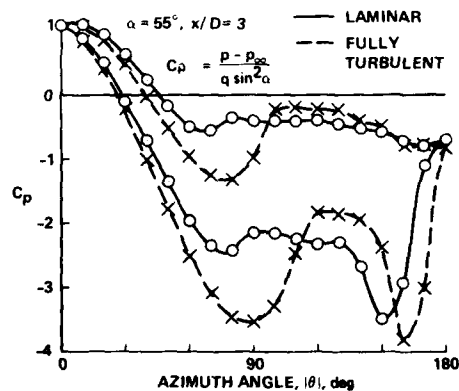
Fig. 36. Typical asymmetric pressure distri-
butions for laminar and turbulent flow at
α = 55° on ogive/cylinder (2D/13D in
length, M_∞ = 0.3 (Lamont, Ref. 48).
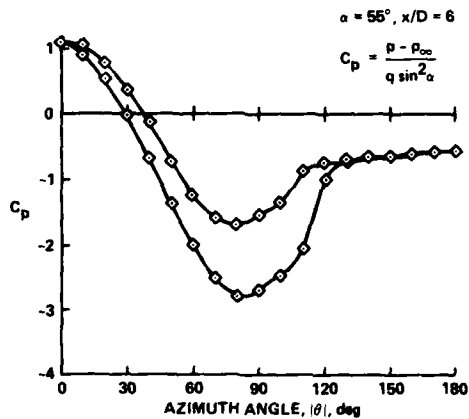
Fig. 37. Asymmetric pressure distributions in transitional flow
at α = 55° on ogive/cylinder (2D/13D in length),
M_∞ = 0.3 (Lamont, Ref. 48).

SCHLIEREN PHOTO

$M_\infty = 2.94$

ASYMMETRIC
VORTEX WAKE

CONE   BOW SHOCK WAVE

WINDWARD GENERATOR, $\phi = 0°$

LEEWARD
GENERATOR,
$\phi = 180°$

OIL FLOW

WINDWARD GENERATOR, $\phi = 0°$

$\alpha = 34°$; $\bar\alpha = 4.53$; ASYMMETRY BEGAN AT $\bar\alpha \sim 3.7$
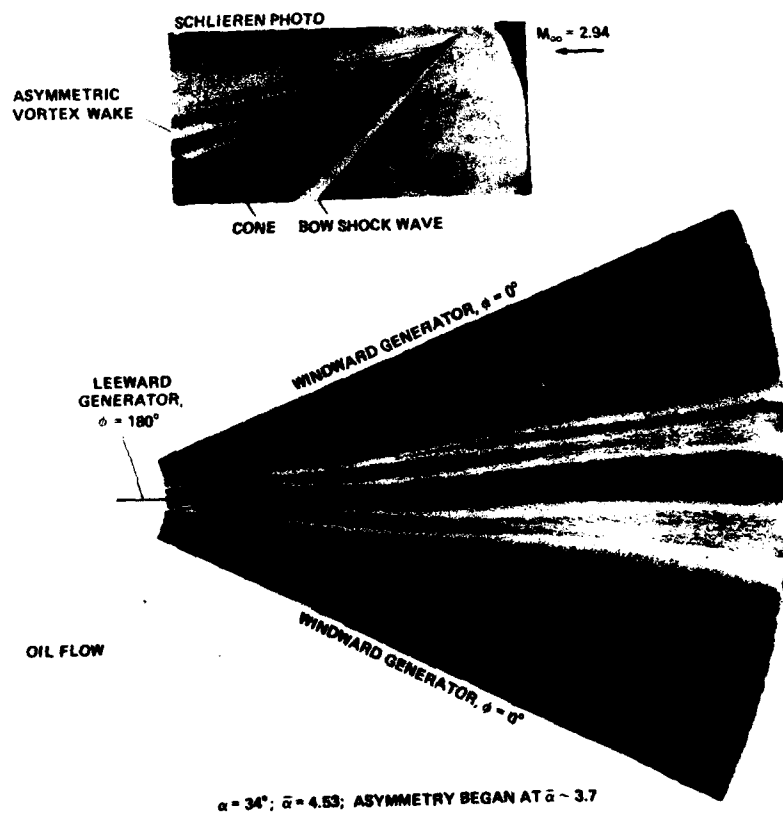
Fig. 38. Asymmetric oil-flow pattern on unwrapped surface, and Schlieren
photograph of a 7.5° semiapex angle cone at $M_\infty = 2.94$, turbulent,
$R_{L_\infty} = 7 \times 10^6$ (Bannink and Nebbeling, Ref. 51).
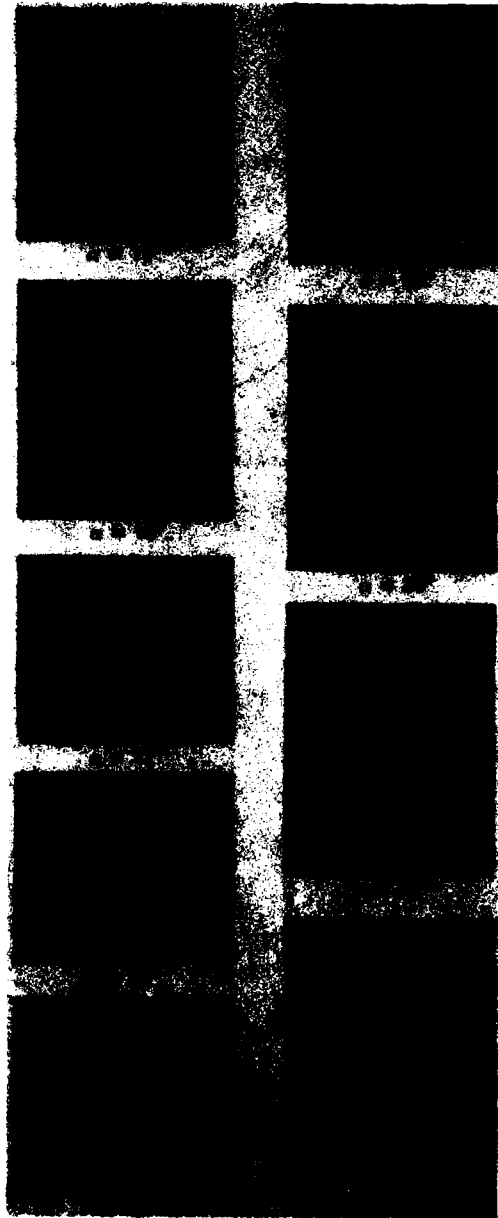
Fig. 39. Asymmetric flow over slender delta wing at angle of attack at M_∞ = 2.8 (Fellows and Carter, Ref. 54).
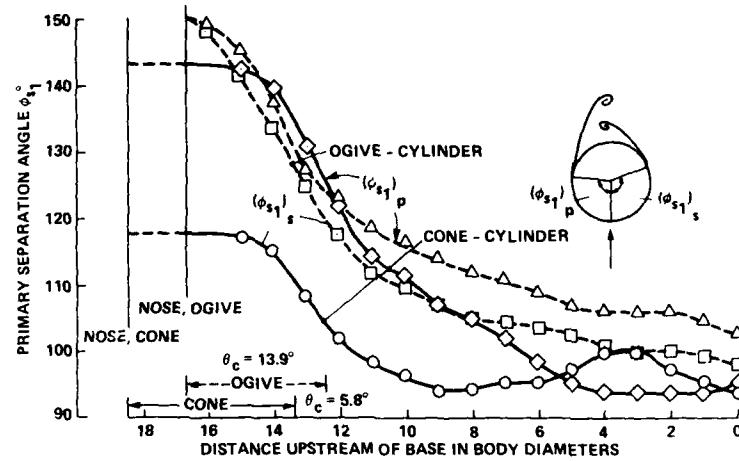
Fig. 40. Asymmetric primary separation on cone and ogive-
cylinders, $\alpha = 18°$, $M_\infty = 0.6$, $R_{L_\infty} = 3.5 \times 10^7$
(Rainbird et al., Ref. 50).
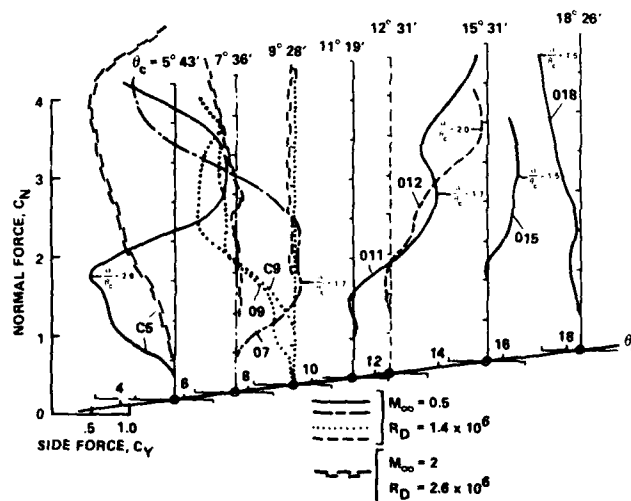
Fig. 41. Influence of semiapex angle of nose, θ_c, on side-force/
normal-force polar for afterbody length of 12D at $R_D = 1 \cdot 10^6$
to $4 \cdot 10^6$ (Peake et al., Ref. 42).
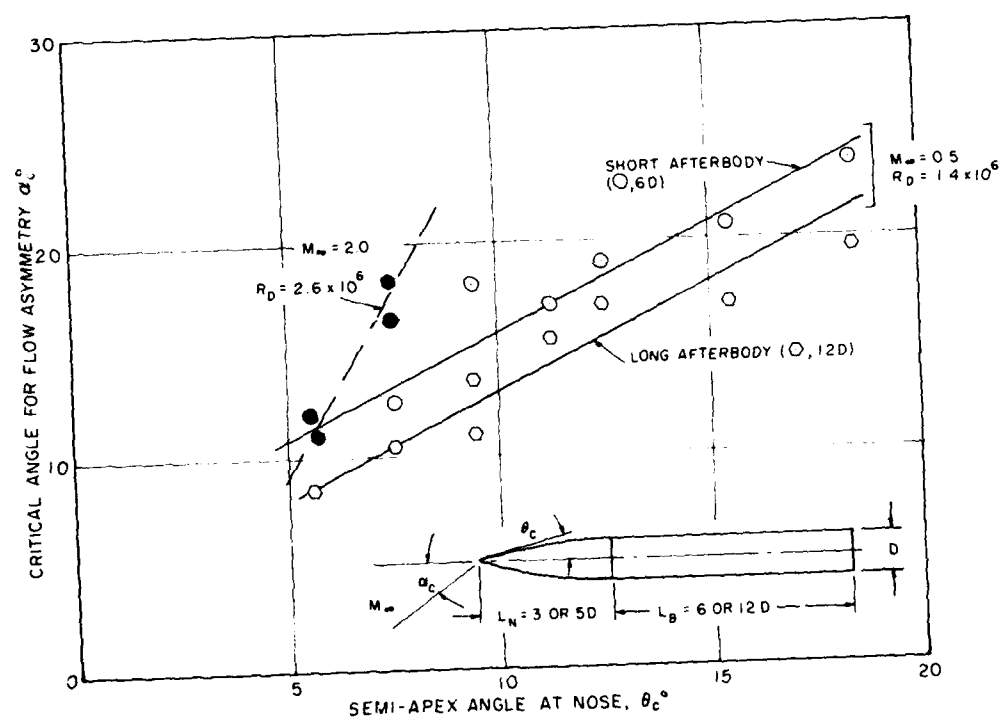
Fig. 42. Critical angle of attack for onset of flow asymmetry (Peake et al., Ref. 42).

FINENESS RATIO

L_N/D = FOREBODY

$(L - L_N)/D$ = AFTERBODY
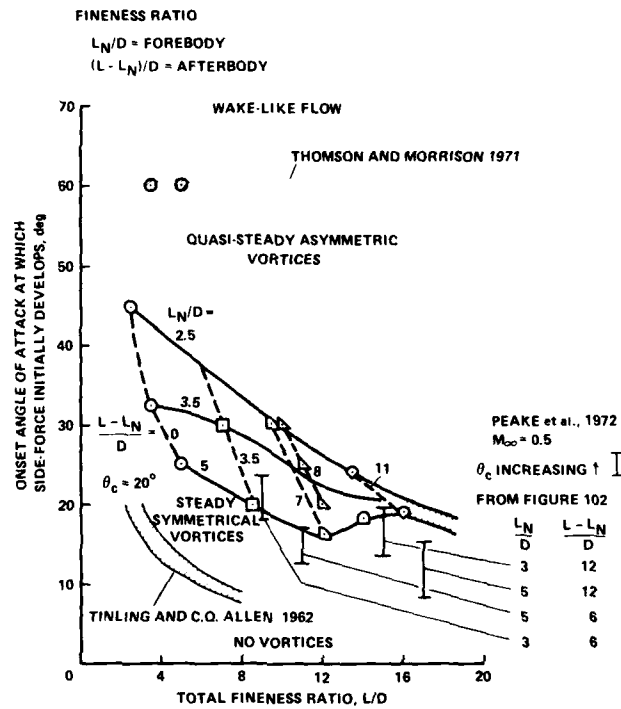
Fig. 43. Boundaries for various types of leeward flow separation about tangent-ogive/
cylinders at $M_\infty = 0.6$ (Keener et al., Ref. 56; Tinling and Allen, Ref. 62;
Thomson and Morrison, Ref. 63).
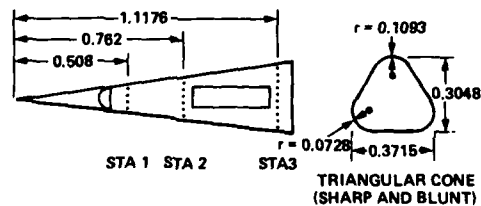
ALL DIMENSIONS IN METERS

Fig. 44. Blunt and sharp-nose triangular cone models.
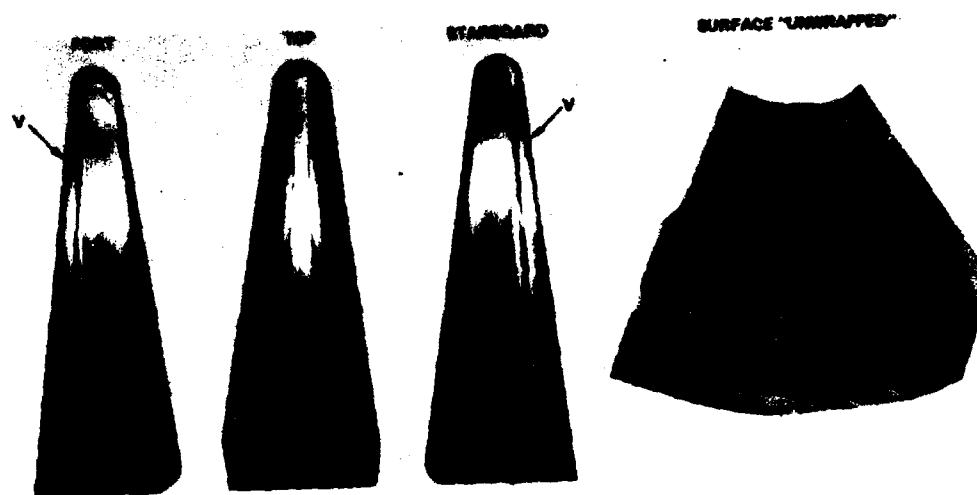
(a) Blunt-nose cone, $\sigma = 45°$, $Re_h = 1.1 \times 10^6$.
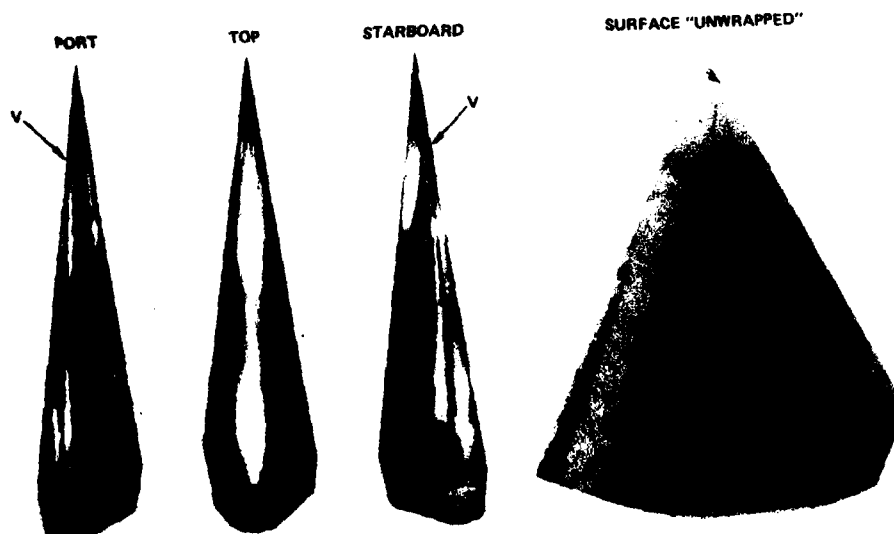
(b) Sharp-nose cone, $\sigma = 45°$, $Re_h = 1.2 \times 10^6$.

Fig. 45. Surface oil-flow patterns on blunt and sharp-nose triangular cones.
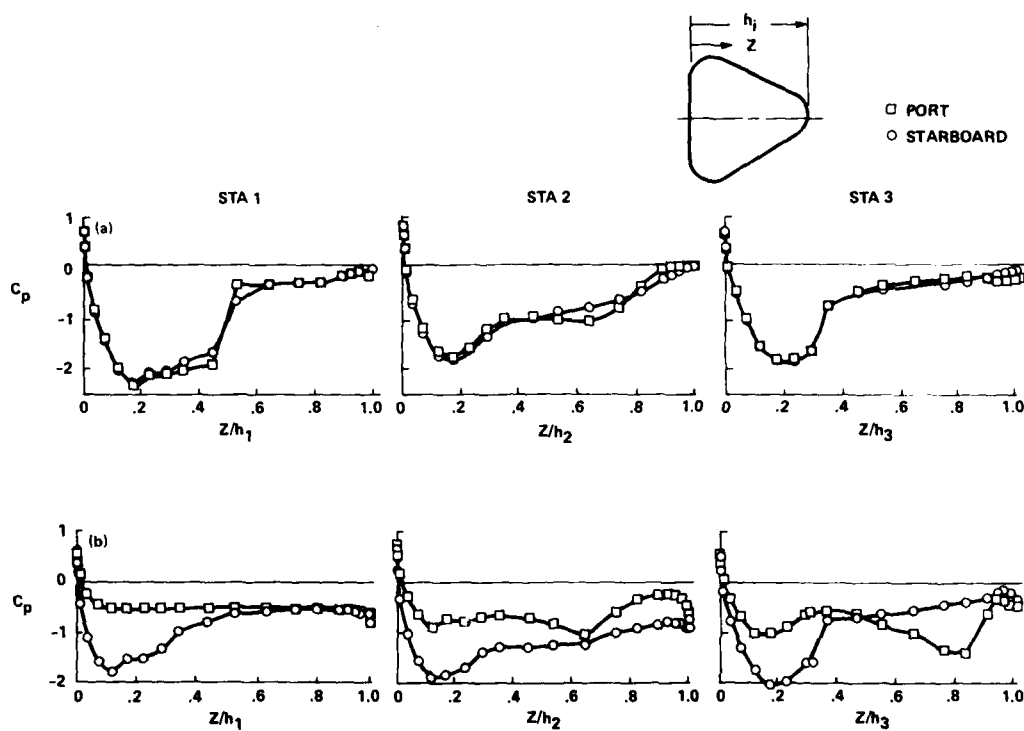
Fig. 46.   Pressure distributions on blunt and sharp-nose triangular cones.
(a)   Blunt-nose cone, $\sigma = 45°$, $R_{e_h} = 1.1 \times 10^6$.
(b)   Sharp-nose cone, $\sigma = 45°$, $R_{e_h} = 1.2 \times 10^6$.

SCHLIEREN

CONE
SHOCK

D

OIL PATTERN

$R_D \sim 1 \times 10^6$ BASED ON INTAKE DIMENSION D
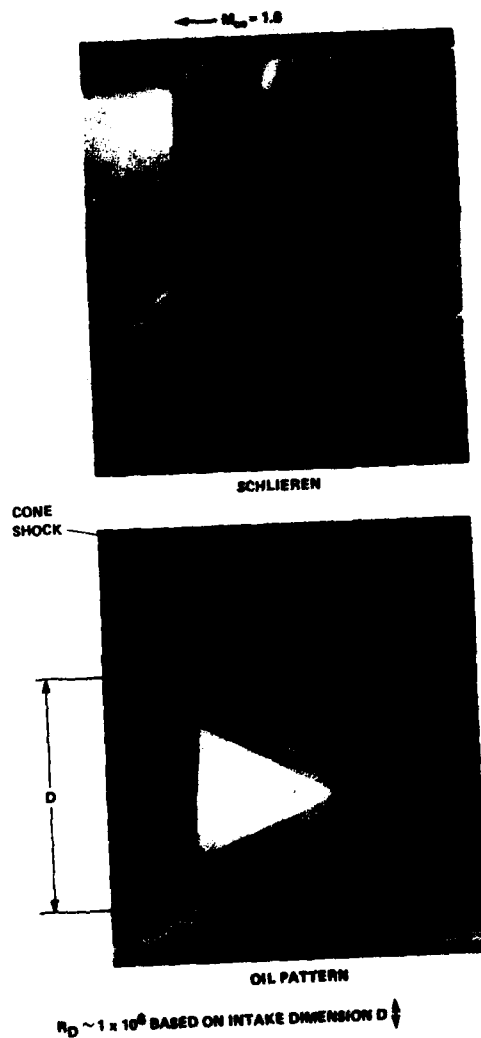
Fig. 47. Oil-flow pattern due to swept-shock-induced 3-D separation about half cone intake $M_\infty = 1.6$ (Culley, Refs. 67, 68).

$M_\infty = 1.6$

R

R_b

P

$\bar{P}$

θ_s

θ

θ_b

R_s

SHOCK

SEMI-CONE

$M_\infty = 1.6$

$\dfrac{p\,\text{WALL}}{P_\infty}$

1.8

$\bar{P}$

1.6

← FLOW

1.4

1.2

1.0

0   .2   .4   .6   .8   1.0

DISTANCE BETWEEN HALF-CONE
AND SHOCK WAVE,

$\dfrac{R - R_b}{R_s - R_b} = \dfrac{\tan\theta - \tan\theta_b}{\tan\theta_s - \tan\theta_b}$

CONE SURFACE
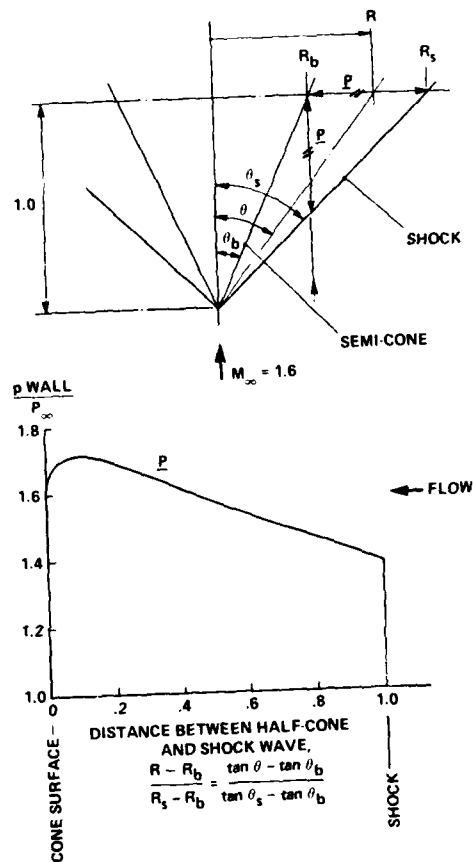
SHOCK

Fig. 48. Calculated pressure field between shock wave and Fourier half-cone at $M_\infty = 1.6$ (Peake, et al., Ref. 69).

2-54

$M_\infty = 1.6$
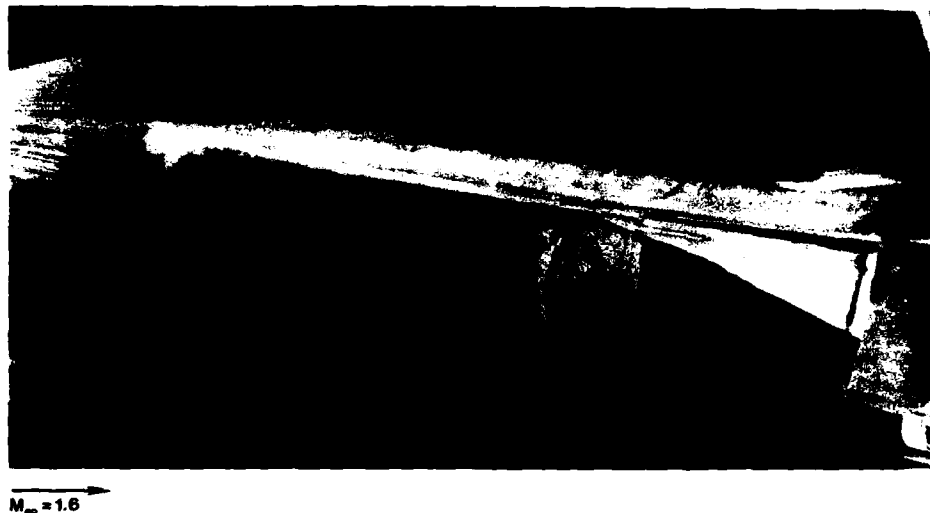
Fig. 49. Side view of 3-D separation of fuselage boundary layer induced by boundary-layer splitter-plate quarter-cone inlet; model angle of attack = 4.5°, M_∞ = 1.6 (Culley, Refs. 68, 70).

UPPERMOST NACELLES OPERATING AT
DESIGN MASS FLOW

LOWER NACELLES THROTTLED TO 70% OF
DESIGN MASS FLOW

$M_\infty = 2.75$
$RL_\infty = 24 \times 10^6$
$C_L = 0.08$
$\alpha = 3°$
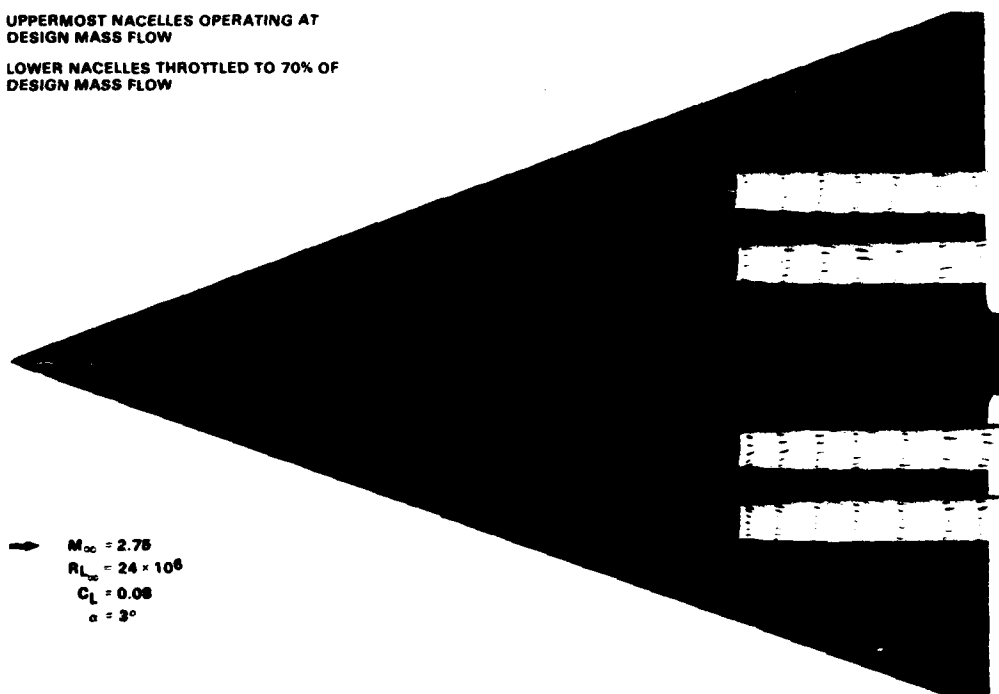
(a) Nacelles on.

Fig. 50. Oil-dot flow visualization on lower surface of 70° delta wing showing swept-back turbulent boundary-layer interactions associated with propulsion nacelles (Peake and Rainbird, Ref. 73).

(b) Nacelles removed.

N_A = NODAL POINT OF REATTACHMENT
N_S = NODAL POINT OF SEPARATION
S = SADDLE POINT OF SEPARATION

Fig. 50. Concluded.

PLAN VIEW

SECTION ALONG x-x
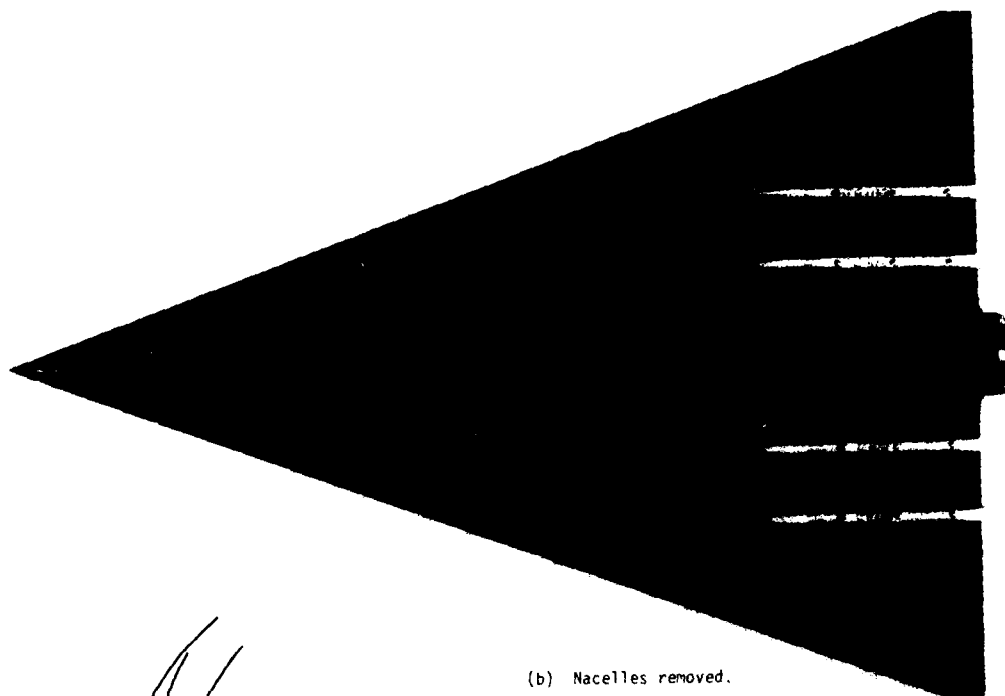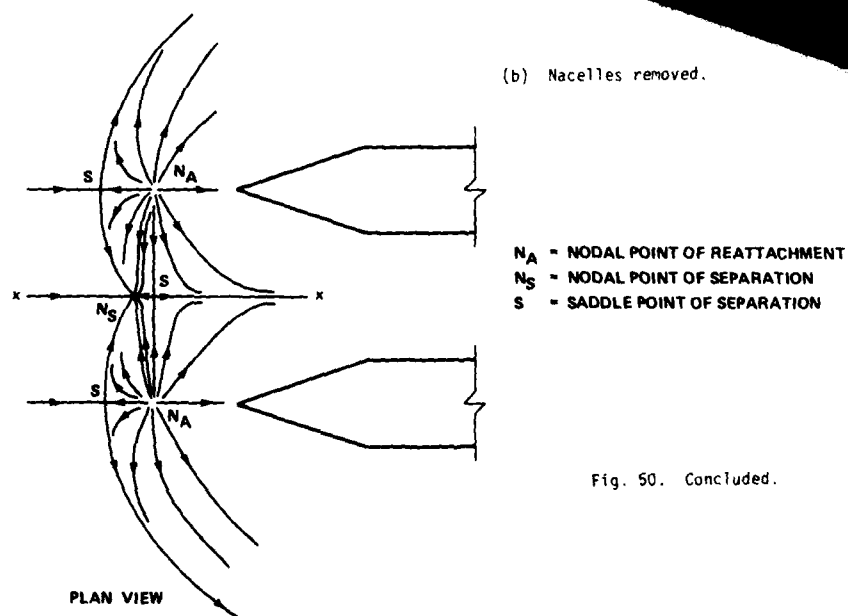
(c) Postulated patterns of skin-friction lines and external flow streamlines.
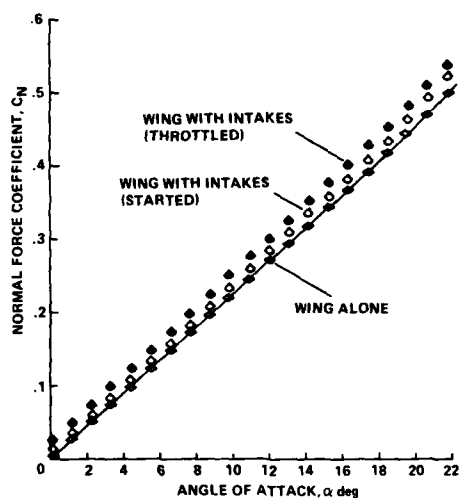
Fig. 51. "Favorable interference" effect on lift of 70° delta wing
at $M_\infty = 2.75$, $R_{L_\infty} = 24 \times 10^6$ (Peake and Rainbird (Ref. 73).
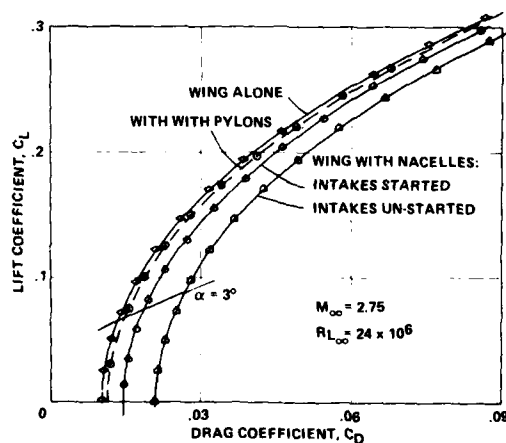
Fig. 52. Lift-drag polars: 70° delta wing with four nacelles supported on
pylons at design Mach number, $M_\infty = 2.75$ (Peake and Rainbird, Ref. 73).

FLOW VISUALIZATION TECHNIQUES FOR THE STUDY OF HIGH INCIDENCE AERODYNAMICS

by H. Werlé

OFFICE NATIONAL D'ETUDES ET DE RECHERCHES AEROSPATIALES
29 Avenue de la Division Leclerc, 92320 CHATILLON (France)

SUMMARY

This paper* is a review of the principal methods of visualizing flows using solid, liquid or gas tracers, in water tunnels and wind tunnels, especially in the experimental facilities at ONERA.

Such visualizations bring to light the physical flow patterns with all their parietal singularities as well as the evolution of these patterns as a function of their principal parameters : incidence, yaw-angle, Reynolds number, etc. These visualizations also reveal in particular the separation phenomena which characterize high angles of attack; in addition, they define with precision all vortical, transitional and unsteady aspects.

Some examples** of results obtained for profiles, swept-back wings, slender bodies, inlets, complete aircraft, etc. show the great variety of topics which are covered by these methods.

1. INTRODUCTION

The whole history of fluid mechanics, especially that of aerodynamics in the aerospace field, has been marked by the development of visualization techniques ; indeed, seeing a phenomenon is usually being able to analyse it, often to explain it, and sometimes it is a first step toward the solution of theoretical or experimental problems.

Undoubtedly visualization, which made a start in 1883 with the first experiments by Reynolds, contributed to the progress in the study of flows around models, first at usual angles of attack, that is in optimal conditions corresponding to stable flows with limited separated zones.

But visualization becomes obviously still more necessary now that aerodynamics ventures into the difficult realm of high angles of attack where the flow displays large separated zones, organized or not, of steady or unsteady character.

Thus are brought to light the problems of stability and control raised by these large angles of attack which are now often imposed by present day flying conditions :

— manoeuvrability of combat aircraft in tight turns,

— flight safety of transport aircraft during their trajectory at low altitude aimed at reducing their nuisance,

— control of missiles at launch in the presence of strong cross wind, and inanoeuvring conditions.

Whereas flow visualization in flight is exceptional, it is quite currently practiced in the wind tunnel, whose main purpose however remains measurements, especially that of aerodynamic forces and pressures.

On the other hand, visualization in water, generally more precise and easier to implement, is developed especially in water tunnels, often designed for this kind of test.

It is not possible here to present a complete survey of such a vast subject, so the present paper will be limited to visualization methods involving solid, liquid or gas tracers, and will start with a description of the main types of existing water tunnels.

The paper will then examine a series of visualizations concerning the aerodynamics of high angles of attack, obtained with simple models (profiles, wings, isolated fuselages, etc...) or more elaborate models (wing-fuselage assemblies, complete aircraft).

2. EXPERIMENTAL TECHNIQUES

2.1 — Water tunnels

There exist a broad variety of hydraulic set-ups used for flow visualizations, differing essentially by the arrangement of their test section and their operating principle.

The three following main types can be distinguished :

(i) Vertical, open circuit tunnels, usually operating by draining under the effect of gravity, such as those of ONERA (Fig. 1) [1] ;

(ii) Tunnels with vertical or horizontal test section, operating in close circuit with a pomp or fan driven by a motor. They are the most common, and we shall mention first those of NAE [2] (Ottawa); Avradcom [3] (U.S. Army / Ames) and Northrop Corp. [4] (Hawthorne) (Fig. 2abc).

(iii) Canals with free surface, usually without water circulation, in which the model is towed by a trolley, such as that of DFVLR [6] (Göttingen) (Fig 2 dd').

The best known tunnels are listed in the following table with their main characteristics, and the mean Reynolds number Values obtained during flow visualizations

Establishment (country)	Type of tunnel (test section)	Max. velocity (Reynolds Nr).	Observations
ONERA Châtillon FRANCE	Vertical TH1 0.22 x 0.22 m TH2 0.45 x 0.45 m TH3 0.80 x 0.80 m	0.25 m/s $(0.5.10^5)$ 1.50 m/s $(6.5.10^5)$ 0.065 m/s $(0.5.10^5)$	voir Fig. 1 a, Fig. 3, etc...
NAE Ottawa CANADA	horizontal 0.25 x 0.33 m	3 m/s $(6.5.10^5)$	voir Fig. 2 a
NASA Ames Moffett Field USA	horizontal 0.20 x 0.30 m	6 m/s (2.10^6)	pressurisable voir Fig. 2 c et 13 aa'
NORTHROP Hawthorne USA	vertical 0.40 x 0.61 m	0.076 m/s (3.10^4)	voir Fig. 2 b et 16 c
ARL Melbourne AUSTRALIE	horizontal 0.25 x 0.25 m	0.76 m/s (10^4)	voir Fig. 6 efg
INSTITUT AEROTECHNIQUE Saint Cyr FRANCE	horizontal 0.45 x 0.45 m	1.20 m/s (10^5)	voir Fig. 13 g-k
BRIT. AERO. DYN. GROUP Warton ENGLAND	horizontal 0.45 x 0.45 m	3 m/s (3.10^4)	voir Fig. 16 e
MBB Ottobrun ALLEMAGNE	vertical 0.34 x 0.34 m	1.4 m/s $(0.6.10^6)$	voir Fig. 11 de,[6]
ISL Saint Louis FRANCE	vertical 0.25 x 0.25 m	0.20 m/s (10^4)	voir Fig. 10 a
NPL Teddington ENGLAND	horizontal 0.25 x 0.33 m	2.4 m/s (5.10^4)	
OCEANICS INC. Plainview USA	horizontal 0.50 x 0.50 m	2.4 m/s (5.10^4)	
VKI Rhode Saint Genèse BELGIUM	0.15 x 0.15 m	0.21 m/s (4.10^4)	
DFVLR Göttingen FRG	tow tank 1.10 x 0.90 m	5 m/s (5.10^6)	voir Fig. 2 dd' et 10 c
MATRA Velizy FRANCE	tow tank 1.0 x 1,0 m	1.8 m/s (10^6)	
University Kyushu JAPAN	tow tank 0.5 x 0.5 m	0.30 cm/s $(1.5.10^5)$	
LOCKHEED Marietta USA	horizontal 0.33 x 0.25 m	0.25 m/s $(0.5.10^5)$	voir Fig. 13 b

| DOUGLAS Aircraft Huntington BEACH USA | tow tank 0.60 x 0.35 m | 2.45 m/s (0.8.10⁶) |

DOUGLAS Aircraft   tow tank
Huntington   0.60 x 0.35 m   2.45 m/s (0.8.10⁴)
BEACH USA

BERTIN   veine horizontale
Plaisir   0.40 x 0.40 m   5 m/s (10⁴)
FRANCE

2.2 — Visualization methods

The methods using tracers for visualization in air or in water are many, and of different natures. The interested reader may consult the various review papers [7-11] which described the state of the art. Only the most commonly used processes will be recalled here.

It should be noted that these methods, based on the use of elements in suspension within the fluid, are in some cases [12] limited by the discrepancies between the trajectories of the particles and of the fluid elements they represent. This concerns mainly particles not having the same density and viscosity as the fluid ; as they have different diameters they are subjected to averaging effects ; they are also affected by centrifugal forces and gravity effects, these particularly trombersome in horizontal test sections.

Let us recall that if the trajectories and emission lines of correct tracers coincide with the streamlines of a steady flow, at least in laminar regime, this is no more true for an unsteady flow or in turbulent regime ; however, as will be seen later, these tracers may, provided that some precautions are taken, give a correct picture of the instantaneous or averaged flow with the separations occurring at high angles of attack.

There are the main tracers used in water :

2.2.1 — Solid tracers

They are usually introduced by a probe upstream of the model :

— aluminum grains [13],
— polystyrol balls of spherical shape and of a density close to that of water (Fig 13 g-k) [14],
— glass balls, perspex powder, etc... see [11].

2.2.2 — Liquid tracers

They are emitted from the models or from ramps upstream :

— diluted milk (mixture of milk, alcohol, and dye whose density and viscosity are the same as those of water) used in the ONERA tunnels up to 1979 (Fig. 17) [15],

— diluted rhodorsil (stable whith mixture replacing milk), used since 1979,

— fluorescent dyes [16],

— ink, commercial dye, solution of carbon tetrachloride and benzine, potassium permanganate, etc... see [11].

2.2.3 — Gas tracers

For generalities on the use of bubbles, see Ref. [17].

— air bubbles obtained by means of an emulsifying agent introduced during the tank filling (ONERA process) (Fig. 3) [15].

— air bubbles injected from ramps or emission holes on the model surface or forming naturally in the test conditions, for instance under the effect of cavitation [18].

— hydrogen bubbles obtained by electrolysis, a method created by Geller [19] and widely used [20-22] (Fig. 6 b-g).

2.2.4 — Other methods

— textile tufts fixed on the model surface (Fig. 13 g-k) ;

— floating matter (aluminum grains, hostaflon powder or other hight tracers spread on the fill surface), the use of which is generally limited to two-dimensional flows.

— dyes or oils covering the model, or chemical methods limited to surface flows.

2.3 — Methods used in wind tunnels

These methods [23] have been the subject of recent surveys [24], particularly that of T. Mueller [25] who, at the Notre - Dame University, utilizes specific facilities adapted to visualization by smoke (wind tunnels with great contraction coefficient and low turbulence rate, smoke emission ramps, etc...).

2.3.1 — Smoke techniques

The smoke, usually white, is obtained by means of generators or smoke wire from titanium tetrachloride (J.K. Harvey, Fig. 6 a), kerosene (Mueller [26], Fig. 4 abc), oil vapor or water condensed by liquid nitrogen [27,57] (Fig. 5h and 10 fgh).

2.3.2 − Liquid surface flow techniques

− Continuous emission of couloured liquids at the model surface ; this process is used in the ONERA wind tunnels and makes it possible to operate at various Mach numbers, pitch and yaw angle without stopping the wind tunnel [28] (Fig. 7 ab and Fig. 16 g) ; viscous coatings (Fig. 7 cde), plastic paints (Fig. 5 b, 9 j), thermoluminescent points, oils (Fig. 17 d), liquid crystals or sublimation of acenaphtène [28], all processes requiring the setting of the coating before each test.

2.3.3 − Tuft techniques

Tiny wool or nylon tufts glued on the model (Fig. 16 i) or fixed on a grid (Fig. 12 d) [29]. This process has even been successfully applied to the case of a propeller in flight (fluorescent minitufts of Dr Crowder [30] (Fig. 15 ab), requiring sparks of UV light of a five milliseconds duration).

2.3.4 − Helium bubbles

These soap bubbles filled with helium and "floating" within the air constitute privileged tracers, but require a cylindrical generator upstream (Sage Action BFS 1035) [31-32] adapted to the wind tunnel velocity ; these bubbles provide visualizations as detailed as those obtained in the water tunnel (Fig. 11 fg).

2.3.5 − Other methods

A particularly original method, that of Dr Crowder, of Boeing [33], expresses as bright spots of various colours a stagnation pressure probing in a crosswise plane behind the model and thus reveals without tracers the vortex wake of a wing with flaps (Fig. 16 h).

3. EXAMPLES OF RESULTS

The limited scope of this paper allows only a brief survey of the many instances in which visualization has brought a valuable contribution to the study of high angles of attack. The examples presented here, classified according to the type of flow or phenomenon under study, are illustrated by 15 figures (3 through 17).

3.1 − Two-dimensional air intakes and wing sections

The laminar flow along a flat plate with sharp leading edge separates under the effect of incidence ; this separation, starting at the loading edge is at first, localized then develops rapidly from upstream to downstream.

It is also the case for an air intake with parallel duct, functioning with a flow-rate coefficient ϵ close to 1 : indeed, at $\alpha \approx 20°$, we can see an internal separated bubble fixed at the lower lip, and this separation expands to the whole duct at $\alpha = 40°$. In this example, air bubbles reveal the shape of the mean flow (Fig. 3 ab), while dye emitted as a sheet reveals the formation of vortex - like rollers at the separation boundaries, a phenomenon which triggers transition from laminar turbulant within the air intake (Fig. 3 a'b') [34].

On a thin flat plat at 20° incidence (Fig. 3 c), this favourable "canal effect" does not exist, and the separated zone involves the whole upper surface and closes only behind the trailing edge. A spanwise jet [35] emitted near the leading edge in this separated zone reduces this separation to a small bubble, even at very high angle of attack (Fig. 3 de).

On a wing section with rounded leading edge, the upper surface separation remains free, and is consequently more sensitive to Reynolds number effects ; however at high angles of attack this parameter does not entail any structural modification of the separated zone (Fig. 3 hi).

Let us notice here that the parietal coloured filets emitted in the separated zone reveal the direction and the character of the reverse flow (Fig. 3 g), while the dye sheet emitted at the leading edge of the same profile at low angle of attack visualizes the natural transition of the upper surface boundary layer (Fig. 3 f) [36].

The visualizations by smoke filets realized by T. Mueller (Fig. 4 abc) [37] confirm the results on wing sections obtained in water :

− generalized separation for $\alpha = 14 - 15°$ (Fig. 4 aa'),

− thin separation bubble with turbulent reattachment, then separation at the rear for $\alpha = 10 - 12°$ (Fig. 4 bb'),

− more extended separation bubble when the Reynolds number is reduced (compare Fig. 4 b and 4 c).

The method of enlarged leading edge used at ONERA [38] makes it possible to obtain more detailed pictures of this phenomenon :

− separation bubble ensuring transition (Fig. 4 c'c''),

− generalized separation (Fig. 4 d),

− reattachment under the effect of lateral blowing (Fig. 4 e) ,

− reattachment obtained by a slotted leading edge (natural blowing) : (Fig. 4 f).

3.2 − Thin delta wings

A classical example of aerodynamic study at high angle of attack is that of the vortex - like separation forming on the upper surface of a thin delta wing with a large enough sweep angle (known as a "Slender Wing"). This regime ensures a complement of lift, increasing with angle of attack, but limited by the onset of the vortex breakdown phenomena.

Visualizations obtained in the water tunnel revealed the organization and structure of the vortices issued from the wing apex, and resulting from the "scroll" rolling-up [39 - 40] of the sheet separating along the sharp leading edge on either side of the wing (Fig. 5 acd). They make it possible to ascertain the physical scheme of the flow (Fig. 5 g) [41].

This research has been extended to the breakdown phenomenon [42] which disorganizes these vortices at high angles of attack (Fig. 5 efh).

Wind tunnel visualizations (S3-Ch ONERA) by smoke illuminated by a thin, plane laser beam (Fig. 5 h) confirmed the spiral structure of the broken down vortex core.

These visualizations also showed the displacement of the breakdown point as a function of various parameters, for example, angle of attack (Fig. 5 i). Through intermittent dye emissions, it has been possible to determine the velocity evolution along the vortex axis down to the breakdown point and for various angles of attack (Fig. 5 j).

Lastly, experiments showed that the organization and structure of these vortices remain the same in supersonic flow (Fig. 5 b) [43].

In order to bring to light the scroll vortex sheet, and only this sheet, we had to call upon water tunnel : Fig. 6 b shows a visualization by hydrogen bubbles, obtained by electrolysis by means of a cathode installed on the wing leading edge. This picture of the sheet is quite similar to that obtained by smoke in a wind tunnel by J.K. Harvey (Fig. 6 a). This sheet can be seen as a cross section by means of a plane of light. Thus, Dr D. Thomson [44] showed the evolution of this sheet as a function of abscissa, angle of attack and sweep angle (Fig. 5 efg). In the same manner, the trace obtained in the ONERA water tunnel, in a plane at mid-chord or at the trailing edge of a delta wing, has been compared with results of a numerical calculation representing the sheet by a pattern of concentrated vortices (Fig. 6 cd) [45].

3.3 – Thick wings

A first example is that of an untapered wing with large sweep angle ($\varphi_{LE} \approx 60°$) having an "ONERA-D" symmetrical profile (relative thickness $e/c = 0.105$), whose three-dimensional flow systematically studied by ONERA up to transonic velocities [46].

The various visualizations of figure 7 show the evolution with Mach number of the wall flow on the upper surface of the model at 24° angle of attack.

We can clearly see the position of the shock waves in transonic flow (Fig. 7 ab), and especially the zones directly swept by the main and secondary vortices (Fig. 7 c).

Coloured emissions in the water tunnel (Fig. 7 f) provide a spatial visualization of the upper surface vortex structure, which fits that provided by a calculation of emission lines based on a panel method (Fig. 7 g) [47].

A finer analysis of the flow has been carried out by means of probings and visualizations [48], in particular in the apex zone of a half wing fixed on a plate. It is around this apex (Fig. 7 de and Fig. 17 abc) that the origin of these vortices is located at high angles of attack, and we can see separations of the boundary layer formed on the plate.

A second example of thick swept wing is again that of a complete delta wing [49]: on the upper surface of this wing ($\varphi = 60°$), parietal coloured emissions reveal the singularities characterizing the flow at medium angles of attack (Fig. 8 cc' and diagram 8 d), then at high angle of attack (Fig. 8 ab). In both cases, we observe on the front part of the upper surface the development of a crosswise sheared stream layer, i.e. characterized by a shift towards the leading edge of the streamlines becoming parietal. When this layer separates, it constitutes the sheet which rolls up to form the upper surface vortex. Even at 20° angle of attack, the vortex origin is still at some distance from the apex, while their breakdown occurs already upstream of the trailing edge. Thus, the main vortices remain separated, as at 10° angle of attack, by a non-vortex median zone, on this 60° - sweep wing.

An example of separation with a quite different structure is that concerning the upper surface of a trapezoidal wing with low sweep : whereas, at low Reynolds number, upper surface separations appear even at low angle of attack and develop more rapidly when α increases, these visualizations reveal the shape of the wall streamlines which we shall eventually find again at high angles of attack in tests at high Reynolds number (Fig. 16 g) [50].

On a model with rounded leading edge, separation generally appears near the trailing edge at low angle of attack (Fig. 8 e), and eventually expands over the whole upper surface at high angle of attack (Fig. 8 fg) [51]. On a model with sharp leading edge, a three-dimensional bubble forms first on the leading edge (Fig. 8 h), and suddenly covers the whole upper surface when α increases (Fig. 8 ij).

3.4 – Slender bodies

The fundamental study, started above with isolated wings, has been pursued with another class of basic models, that of slender bodies whose behaviour at high angles of attack is of direct interest to aircraft fuselages or missiles.

A first series of visualizations concerns axisymmetrical nose cones (Fig. 9) and makes it possible to distinguish, as for wings, different types of separations [52 - 53] :

– on a relatively blunt nose (Fig. 9 ab), the upper surface separation results from the junction between the median bubble, which affects the nose at low angle of attack, and the vortex- like separation developing on either side of the model ;

– on a streamlined nose with rounded tip (Fig. 9 cde, diagram 9 f) we find again, as on a thick delta wing at medium incidence, two separated zones with, between them, a corridor of clean flow ;

– on a streamlined nose with sharp tip (Fig. 9 g), an organized vortex structure develops up to the neighbourhood of the apex, and eventually to the apex itself at very high angles of attack (Fig. 10 b) ;

– on a nose with contoured shape without curvature discontinuity or important variation (conical ogive with rounded nose connected by a clothoid), we observe the junction at the nose of the two main vortices which then form the two branches of a horseshoe vortex (Fig. 9 hi).

These vortex phenomena remain at high velocities : indeed, even in hypersonic flow (Fig. 9 j), we may observe on a visualization by viscous coating, the surface flow induced by the vortices formed in the separated zone on the upper surface of

the model at 20° incidence [43].

The following examples, presented together on Fig. 10, concern long cylindrical fuselages and missile models :

Assymetrical vortices appear on a cylindrical fuselage at high angle of attack : M. Fiecher [54] gave one of the first visualizations of this phenomenon in 1966 (Fig. 10 a).

This configuration of steady separation sets between 35° and 60° angle of attack on smooth bodies (Fig. 10 cdeh) [55-56], which induces parasitic lateral forces on the model.

Near the nose (Fig. 10 b), this vortex structure retains its symmetry at first, as it normally does all along the model at lower incidence (Fig. 16 ef) [57 · 58]. At angles of attack above 60°, the separated structure becomes unsteady, with formation of alternate vortices, of Bénard-Karman type.

An efficient stabilization means for avoiding the onset of lateral forces consists in adding, on either side of the body of revolution, thin "strakes" of small aspect ratio (Fig. 10 gij). Then, the separation is fixed along the sharp edge of the strakes and ensures, at zero sideslip , the formation of symmetrical and stable vortices which should provide to the model a complement of vortex lift already seen on aspect ratio wings [40, 59].

In case of sideslip (Fig. 10 kl), the flow is no more symmetrical and the strake vortices separate laterally from the fuselage, crossing the plane of symmetry of the model. For a critical sideslip angle, one of the vortices may then find on its trajectory the vertical fin of the missile and then be the cause of detrimental interaction effects [60].

3.5 — Model configurations giving rise to interaction effects

In many cases, such interactions may occur between vortex separations originated from the front part, and the rear parts of more complex configurations, particularly at high angles of attack.

It is the case of fuselage vortices which, according to the model incidence and the vertical location of the horizontal tail unit, may reduce its pitch efficiency (Fig. 11 ab).

A few examples concern the foreplanes in front of the main wing, often called "canards" : In the first case (Fig. 11 c), it is a small "canard" located behind the cockpit of a Concorde model and whose efficiency is ensured by the location and negative dihedral adapted to approach and landing angles of attack. Their purpose would be to make easier the longitudinal trim of a slender wing [40, 55].

In a second example, this swept - back canard surface is closer to the main slender wing, (Fig. 11 de) [61]; the vortices from this close coupled canard are then picked up by those of the wing, which thus "recuperates" their energy to avoid a premature vortex breakdown on the main wing at large angles of attack.

A third formula consists of a canard surface located directly above the apex of the main wing. Its action is similar, but it also produces a favourable "canal" effect which, in particular, brings back the breakdown phenomenon of the wing vortex (Fig. 11 fg and 17 def) [32 , 62].

A last example concerns a forward - swept wing, a new formula of the type recently studied for the USAF [63]. This wing takes advantage of a well structured vortex regime, locked to the forward wing tip in spite of a relatively small leading edge sweep angle (φ_{LE} = - 39°). See Fig. 11 h.

The canard surface plays a vital role for such a configuration : i.e. it generates a vortex wake acting on the separated flow at the wing root) (Fig. 11 i).

Highly swept strakes are usually located in front of low sweep wings, forming sometimes a double-delta wing [40] (Fig. 16 ci and 17 g). The favourable effect of this strong vortex sheet from the strake extends in these conditions over part of the main wing that follows it. At high angles of attack (Fig. 17 h), the vortex breaks down and a spanwise blowing is then necessary (Fig. 17 i) to recover an organized vortex structure on the model [62].

3.6 — Aircraft models

With a view to carrying out a study of the flow as exhaustive as possible, many tests involve complete models (sideslip effects) with realistic wings (e.g. equipped with their flaps) and more or less motorized (simulation of air intakes and engine jets).

Thus, in the case of a delta wing combat aircraft, the separation is limited to the wing at moderate angles of attack (Fig. 12 a), with well structured vortices (Fig. 12 d), then with increased incidence these vortices tend to get disorganized downstream (Fig. 16 a) and this phenomenon [60], confirmed in flight (Fig. 16 b), travels upstream up to a complete disorganization over the wing (Fig. 12 bb') with asymmetric vortices along the fuselage (Fig. 16 c) : we must then use a jet of sufficient intensity, emitted along the vortex axis (Fig. 12 cc'), for re-establishing an organized vortex flow over the wing-fuselage assembly [64-66].

Lastly, on some aircraft configurations, we may detect the effects due to the functioning of the air intake, often close to the wing apex where the upper surface vortices originate ; it is the same with engine jet effects on wing vortices (Fig. 12 eff') [67].

Finally, even at low incidence, the highly deflected flaps of the wing of a transport aircraft are in the conditions of high angle of attack ; they give rise to a whole series of vortices (Fig. 12 g) of which an exact image can be found in stagnation pressure probings concerning the wake and picked up in the transverse plane by means of the Dr Crowder's process (Fig. 16 h) [33].

3.7 — Tests in unsteady conditions

Around a profile actuated by a motion of harmonic oscillations in pitch (Fig. 13 a-f) or of flapping with cyclic modulation of angle of attack (Fig. 13 g-k), the various types of tracers used (air bubbles, hydrogen bubbles emitted by a cathode

either fixed upstream or placed on the profile, polystyrol beads, or tufts glued on the model) reveal the vortex sheddings occuring at each cycle when the circulation around the profile varies [68]. It is known that such an oscillation motion simulates the cycling pitch variation of a helicopter blade [69-71]. The time lag and the typical vortex character of the dynamic stall at high angles of attack explain the favourable hysteresis effect on the maximum mean lift observed in unsteady regime on the retreating blade of a helicopter rotor.

Similar phenomena characterize the three-dimensional flow around a delta wing aircraft model (Fig. 14 i-p). The cyclic variations of vortex intensity observed make it possible to better interpret the measurements performed in dynamic conditions during similar wind tunnel tests.

Another class of unsteady flows is that concerning models in uniform rotation : at low angle of attack (Fig. 14 a-d), this rotation simulates a roll manoeuvre, and at high incidence (Fig. 14 e-h) a flat spin. In both cases, vortex phenomena develop on the side of the descending half wing and vanish on the opposite side [72].

On model in uniform rotation, visualizations may also provide useful information on surface flow : it is the case with fluorescent mini-tufts (Dr Crowder's process) glued on aircraft propellers in flight and which reveal not only the parietal streamlines on the blades and hub (Fig. 15 a) but also the trace of the shock near the wing tip at transonic regime (Fig. 15 b). Wall emissions of smoke (Fig. 15 c), of dye (Fig. 15 d) and even of air bubbles (Fig. 15 d') also bring to light the structure of the flow transition along a cylinder rotating as a whole [73] or in part [36].

A last example in unsteady regime concerns tip vortices ; these are the vortices forming at the tip of a three bladed of tilt rigid rotor-placed at an angle of attack of-45° and rotating in an uniform flow [74]: the dye emitted at the blade tip reveals the cycloidal shape of the vortices (Fig. 15 e). It is the vortex developing at the free tip of a rectangular wing of small aspect ratio placed at 30° angle of attack in a fluid started in uniform translation from rest (Fig. 15 fg) [75]: this vortex is visualized by means of emission lines, which can be compared with those obtained by calculation (Fig. 15 h) which also implies a start of the fluid motion from rest [76].

4. CONCLUSION

In both steady and unsteady regimes, the various tracers used in water tunnel and in wind tunnel bring to light the phenomena characterizing the aerodynamics of models at high angles of attack [77] :

— on wings, separations expand from the leading or the trailing edge and their structure becomes vortex - like and organized on highly swept wings, but with a limitation due to vortex breakdown ;

— on slender bodies the vortices, symmetrical at first, become asymmetrical, then unsteady with increasing angle of attack ;

— on complete models of missiles and aircraft comprizing combinations of these various basic elements, the coexistence of these various phenomena does not fail to produce many interaction effects, whether favourable or not.

In these conditions, it has been possible to check the usefulness of various devices or processes aiming at reducing the drawbacks and re-establishing an organized flow, such as slats, canard surfaces, strakes, spanwise blowing, etc.

REFERENCES

[1] ONERA Activities 1981 and film 1037 (1981).

[2] DOBRODZICKI G.A., Flow Visualization in the NAE Water Tunnel. NRC, NAE LR-557 (Febr. 1972).

[3] OLSEN J. and LIU H.T., The Construction and Operation of a Water Tunnel in Application to Flow Visualization Studies of an Oscillating Airfoil, Flow Res. Rep. n° 13-CR 114 696 (May 1973).

[4] ERICKSON G.E., Water Tunnel Flow Visualization : insight into Complex Three-Dimensional Flow Fields. AIAA Paper n° 79-1530 (July 1979).

[5] BIPPES H. and COLAK-ANTIC P., Der Wasserschleppkanal der DFVRL. ZFW 21 (1973), p. 113-120.

[6] STIEB R. and GROSS V., The Water Tunnel - a Helpful Simulation Facility for the Aircraft Industry (MBB). ICIASF Congress (Sept. 1981).

[7] BALINT E. (1953) Aircr. Eng. 25 : 161-67.

[8] CLUTTER D., SMITH A., BRAZIER J. (1959) Douglas Aircr. Co. Rep. n° ES 29075.

[9] HOYT J. (1962) Appl. Mech. Rev. 15 : 419-25.

[10] WUEST W. (1963) Aerodyn. Versuchsanst. Forsch. Rep. n° 63-03 (Göttingen).

[11] MACAGNO E. (1969) IIHR Rep. n° 114. Des Moines : Univ. Iowa.

[12] FAURE J. (1963). La Houille Blanche 18 n° 3 : 298-306.

[13] BOUROT J. (1949). Ministère de l'Air, PST Paris n° 426.

[14] WERLÉ H. (1952), Rech. Aero. n° 26 : 13-18.

[15] WERLÉ H. (1974), ONERA Publication n° 156.

[16] CAMPBELL D.R. (1973), ARL Rep. 73-005.

[17] BIRKHOFF G., CAYWOOD T. (1949), J. Appl. Phys. 20 : 646-59.

[18] BEAUFRERE J. (1962), Mémoires et Travaux de la SHF Suppl. 1, La Houille Blanche.

[19] GELLER E. (1954), J. Aeronaut. Sci. 22 : 869-70.

[20] SCHRAUB F., KLINE S., HENRY J., RUNSTADLER P., LITTEL A. (1964), Stanford Univ. Rep. MD-12.

[21] MATTINGLY G.E. (1966), The Hydrogen Bubble Flow Visualization Technique DTMB Rep. 2146.

[22] THOMPSON D.H. (1973), ARL Aero Note 338 (Melbourne).

[23] MALTBY R.L. (1962), Flow Visualization in Wind Tunnels Using Indicators AGARDograph 70.

[24] MERZKIRCH W. (1974), Flow Visualization - Academic Press Inc. New-York.

[25] MUELLER T.J. (1981), Flow Visualization by Direct Injection Short Course of Fluid Mechan. Measur., Univ. Minnesota.

[26] MUELLER T.J. (1978), Smoke Visualization of Subsonic and Supersonic Flows - Univ. Notre-Dame, Rep. UNDAS TN-3412-1.

[27] BISPLINGHOFF R.L., COFFIN J.B. and HALDEMAN C.W., Water Fog Generation System for Subsonic Flow Visualization. AIAA Journal, Vol. 14, n° 8 (1976).

[28] WERLÉ H., LAVERRE J. et SOULIER Ch., (1977), Techniques de Visualisations d'Ecoulements pariétaux. ONERA-TP 1977-86.

[29] BIRD J.D., (1952), Visualization of Flow Fields by Use of a Tuft Grid Technique. Journ. Aeron. Sci., 19, p. 481-485.

[30] CROWDER J.P. (1980), Fluorescent MiniTufts for Non Intrusive Surface Flow Visualization. Int. Symp. Bochum-Ruhr. Univ., p. 612-616.

[31] HALE R.W., TAN P. and ORDWAY D.E., Experimental Investigation of Several Neutrally-Buoyant Bubble Generators for Aerodynamic Flow Visualization. Nav. Res. Review, p. 19-24 (June 1971).

[32] HALE R.W., TAN P., STOWELL R.C. and ORDWAY D.E., Sage Action, Inc. Rep. SAI-RR 7107 (Dec. 1971).

[33] CROWDER J.P., Quick and Easy Flow Field Surveys. Astronautics and Aeronautics (Oct. 1980), p. 38.

[34] ONERA Activities 1976, p. 36-38 and Film 848 (1980).

[35] WERLÉ H. et GALLON M., Contrôle d'Écoulements par Jet Transversal. L'Aéron. et l'Astron. n° 34 (1972-2) et Film ONERA n° 849 (1971).

[36] WERLÉ H., Transition et Décollement : Visualisations au Tunnel Hydrodynamique de l'ONERA. Rech. Aerosp. 1980-5, p. 331-345.

[37] MUELLER T.J. and BATILL S.M., Experimental Studies of the Laminar Separation Bubble on a Two-Dimensional Airfoil at Low Reynolds Numbers. AIAA 80-1440 (July 1980).

[38] WERLÉ H., Sur l'Écoulement au Bord d'Attaque d'un Profil Portant. Rech. Aerosp. 1973-4, p. 197-218 et Film ONERA 745 (1974).

[39] ROY M., Caractères de l'Écoulement Autour d'une Aile en Flèche Accentuée. CR. Ac. Sc. t. 234 (1952), p. 2501-2503. and LEGENDRE R., Ecoulement au Voisinage de la Pointe Avant d'une Aile à Forte Flèche aux Incidences Moyennes. Rech. Aeron. n° 30 et 31 (1952)(1953).

[40] POISSON-QUINTON Ph., Slender Wings for Civil and Military Aircraft. 20th Israël Annual Conf. on Aviat. and Astro. Israël Journ. of Techn. Vol. 16 (1978). ONERA TP 1979-123.

[41] WERLÉ H., Etude Physique des Phénomènes Tourbillonnaires au Tunnel Hydrodynamique ATMA (session 1961), n° 1311 et Film ONERA 802 (1975).

[42] WERLÉ H., Sur l'Éclatement des Tourbillons ONERA. Note Techn. 175 (1971).

[43] MONNERIE B. and WERLÉ H., Étude de l'Écoulement Supersonique et Hypersonique autour d'une Aile Élancée. AGARD CP n° 30 (1968), p. 23-1 à 23-19.
CERESUELA R., KRETZSCHMAR G., REHBACH C., Étude Théorique et Expérimentale de l'Écoulement Hypersonique autour d'un Corps Émoussé en Incidence. AGARD CP 30 (1968), p. 22-1 à 22-14.

[44] THOMPSON D.H., A Water Tunnel Study of Vortex Breakdown over Wings with Highly Swept Leading Edges . ARL Aero. n° 356 (1975).

[45] REHBACH C., Étude Numérique de Nappes Tourbillonnaires Issues d'une Ligne de Décollement près du Bord d'Attaque. Rech. Aerosp. 1973-6.

[46] SCHMITT V. et MANIE F., Écoulements Subsoniques et Transsoniques sur une Aile à Flèche Variable. Rech. Aerosp. 1979-4, p. 219-237.

[47] REHBACH C., Calcul Numérique d'Écoulements Tridimensionnels Instationnaires avec Nappes Tourbillonnaires. Rech. Aerosp. 1977-5, p. 289-298 et Film ONERA 921 (1979).

[48] MIRANDE J., SCHMITT V. et WERLÉ H., Système Tourbillonnaire Présent à l'Extrados d'une Aile en Flèche à Grande Incidence. AGARD CP n° 247 (1978), mémoire n° 12.

[49] WERLÉ H., Structures des Décollements sur les Ailes en Flèche. Rech. Aérosp. n° 1980-2, p. 85-108.

[50] MONNERIE B. et CHARPIN F., Essais de Tremblement d'une Aile en Flèche en Transsonique. L'Aéron. et l'Astron. n° 50 (1975-1), p. 3-16., and
LEGENDRE R., Types de Décollements de l'Écoulement Transsonique autour d'une Aile en Flèche. L'Aéron. et l'Astron. n° 75, 1979-2.

[51] WERLÉ H., Écoulements Décollés. Étude Phénoménologique à Partir de Visualisations Hydrodynamiques. AGARD CP 168 (1975), mémoire n° 39, p. 1-14 et Film ONERA 817 (1975).

[52] WERLÉ H., Le Décollement sur les Corps de Révolution à Basse Vitesse. Rech. Aéron. n° 90 (1962). and
LEGENDRE R., Lignes de Courant d'un Écoulement Continu. Rech. Aérosp. n° 105 (1965), p. 3-9.

[53] PEAKE D.J. and TOBAK M., Three-Dimensional Interactions and Vortical Flows with Emphasis on High Speeds. AGARD AG-252 (1980).

[54] FIECHTER M., Über Wirbelsysteme an Schlanken Rotationskörpern und Ihren Einfluss auf die Aerodynamischen Beiwerte. Institut Franco-Allemand de St Louis. Rapport 10/66.

[55] WERLÉ H., Tourbillons de Corps Fuselés aux Incidences Élevées. L'Aéron. et l'Astron. 1979-6, p. 3-22. et Film ONERA 977 (1980).

[56] BIPPES H., Visualization of Flow Separation and Separated Flows with the Aid of Hydrogen Bubbles. Int. Symp. Bochum (Sept. 1980), Ruhr-Univ., p. 225-230.

[57] PHILBERT M., BEAUPOIL R. et FALENI J.P., Application d'un Dispositif d'Éclairage Laminaire à la Visualisation des Écoulements Aérodynamiques en Soufflerie par Émission de Fumée. Rech. Aérosp. 1979-3, p. 173-179.

[58] DEANE J.R., Experimental Investigations into the Interaction between Body Vortices and Wing Panels on a Missile Configuration at Low Speed. AIAA Paper 80-0032.

[59] ERLICH E. et DE SIEVERS A., Sur la Portance des Ailes de très Faible Allongement en Subsonique. Rech. Aérosp. 121 (1967).

[60] POISSON-QUINTON Ph., From Wind-Tunnel to Flight, the Role of the Laboratory in Aerospace Design. J. Aircr., June 1968. ONERA TP 575 (1968) and Film ONERA 551 (1967). and
POISSON-QUINTON Ph. and WERLÉ H., Water Tunnel Visualization Vortex Flow. Astron. and Aeron. (May 1967), p.64-66.

[61] SACHER P., Abgelöste Strömung am Flügel Kleiner Streckung. MBB Rep./FE 122/S/PUB/31. DGLR 80-069.

[62] STAUDACHER W., LASCHKA B., POISSON-QUINTON Ph. and LEDY J., Effect of Spanwise Blowing in the Angle of Attack Regime $\alpha \approx 0°$ to 90°. ICAS, Lisbon, Sept. 1978. ONERA TP 1978-80.

[63] Forward-Swept Wing Potential Studied Aviation Week and Space Technology (January 29, 1979), p. 126-127.

[64] ERICKSON G.E., Vortex Flow Correlation. Northrop AFWAL-TR 80-3143 (January 1981).

[65] MOORE W.A., SKOW A.M. and LORINCZ D.J., Enhanced Departure/Spin Recovery of Flighter Aircraft through Control of the Forebody Vortex Orientation. AIAA 80-0173.

[66] WERLÉ H., Application of Hydrodynamic Visualization to the Study of Low Speed Flow around a Delta Wing Aircraft. Int. Symp. Flow Visualization Tokyo (Oct. 1977). and Film ONERA 888 (1977).

[67] WERLÉ H. et FIANT Cl. Visualisation Hydrodynamique de l'Écoulement à basse Vitesse autour d'une Maquette d'Avion du Type "CONCORDE". Rech. Aérosp. 102 (1964), p. 3-19.

[68] WERLÉ H. et GALLON M., Écoulement Plan autour d'un Modèle Animé d'un Mouvement Périodique. ONERA Note Technique n° 239 (1974).

[69] McCROSKEY W. et PHILIPPE J.J., Écoulement Visqueux Instationnaire sur Profils Oscillants. AIAA Paper n° 74-182 (Jan. 1974).

[70] McAlister K.W. and CARR L.W., Water Tunnel Visualizations of Dynamic Stall. Journ. of Fluids Engineering, Vol. 101, n° 3 (Sept. 1979).

[71] MEHTA, UNMEEL B., Dynamic Stall of an Oscillating Airfoil. AGARD CP 227, Paper 23 (1977).

[72] WERLÉ H., Visualisation Hydrodynamique d'Écoulements Instationnaires. ONERA Note Technique n° 180 (1971).

3-10

General view of the hydrodynamic visualization laboratory at ONERA Châtillon centre.
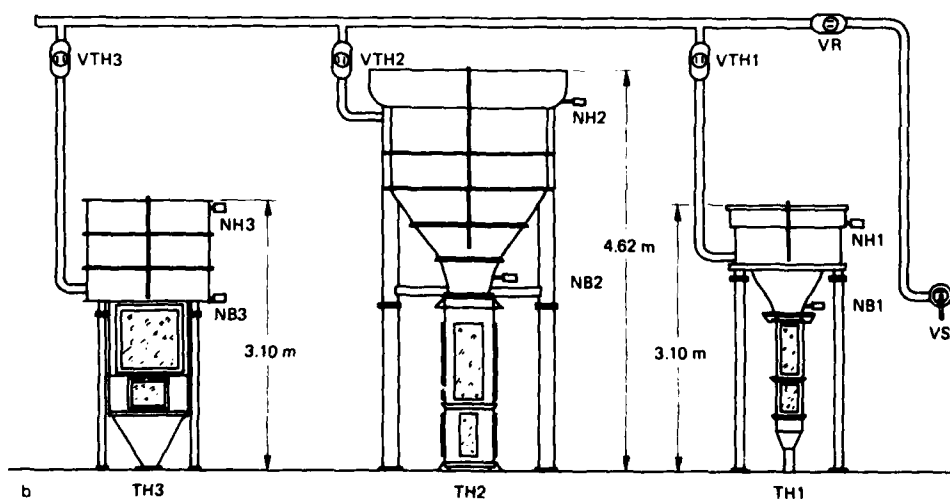
Schematics of the ONERA water tunnels facility.

FIG. 1 – THE ONERA WATER TUNNELS.

Tunnels		Test section L (m)	Maximal speed (m/s)	Typical Re number
TH1		0.22 x 0.22	0.25	0.5.10⁵
TH2	normal duct	0.45 x 0.45	0.25	10⁵
	fast duct		1.50	6.5.10⁵
TH3		0.80 x 0.80	0.065	0.5.10⁵
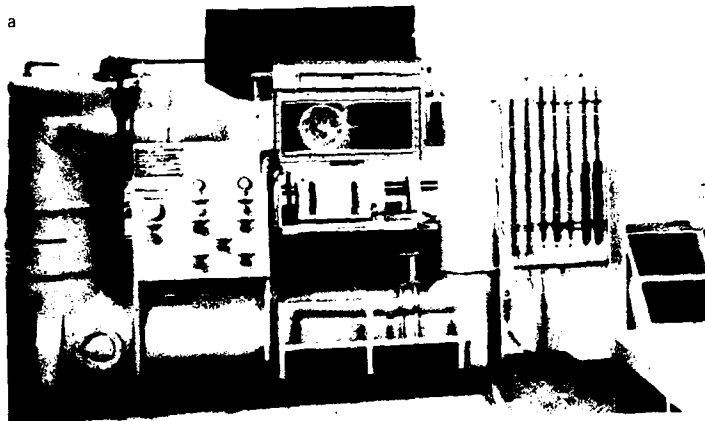
FIG. 2 - OTHER TYPICAL WATER TUNNELS

a

NAE water tunnel (Ottawa)

b

Schematics of the Northrop water tunnel (Hawthorne).

WATER LEVEL

REMOTELY CONTROLLED DYE PROBE

HOISTING CABLES

1.83

DIRECTION OF FLOW

4.72

HONEYCOMB FLOW STRAIGHTENERS AND FOAM

TEST SECTION 0.41 x 0.61 x 1.83

CORRUGATED PIPE SECTION

Ø 305 PIPE

VALVE

PUMP

PERFORATED PLATE

PERFORATED PLATE

c
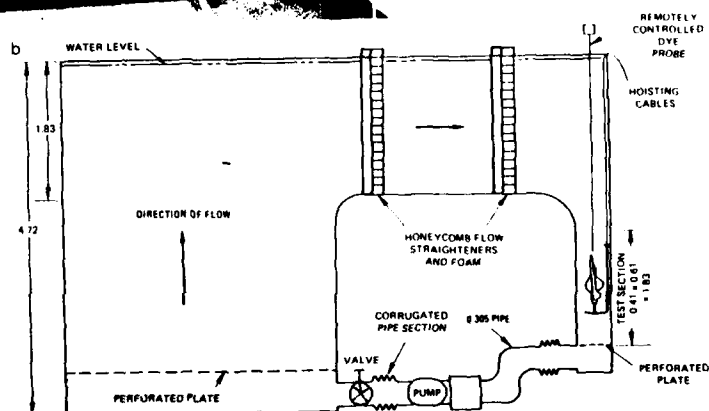
Aeromechanics (Avradcom) water tunnel (Moffet field)

1 Honeycomb
2 Pressure controls
3 Camera support post
4 Propeller section
5 Tunnel drive motor
6 Test section

DFVRL tow water tank (Göttingen)

3-12
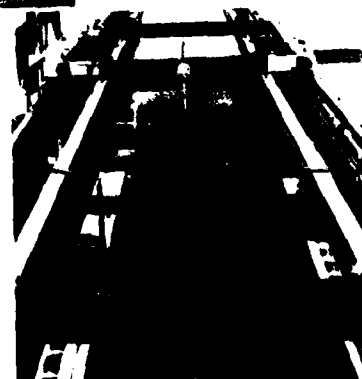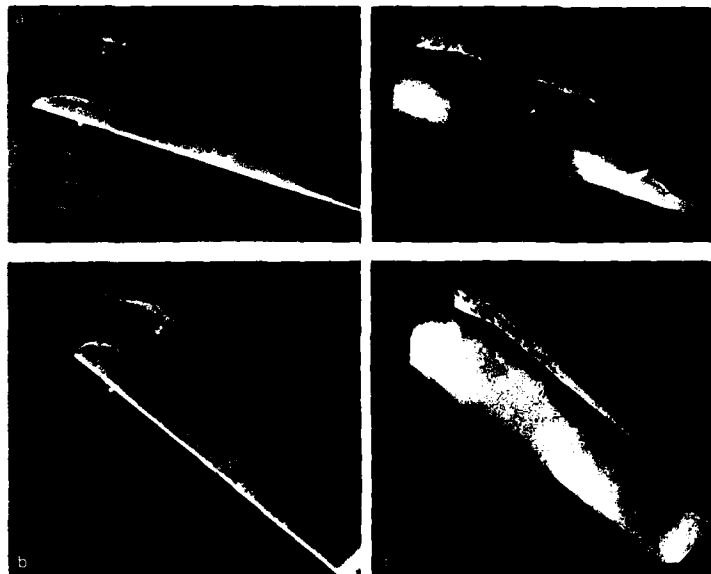
FIG. 3 — TWO-DIMENSIONAL
VISUALIZATIONS.
(ONERA WATER TUNNEL)

Two-dimensional air intake
($\epsilon > 1.0$ · height = 40 mm · $Re_H > 0.4.10^4$)

aa' $\alpha = 20°$

Visualization by air bubbles
(a, b, c, d, e, h, i).

Visualization by dye emissions
(a' b' f g).

bb' $\alpha = 40°$

Thin plate (c = 100 m · $Re_c > 10^4$)

Profile NACA 0012 (c = 200 mm).

f $\alpha = 5$
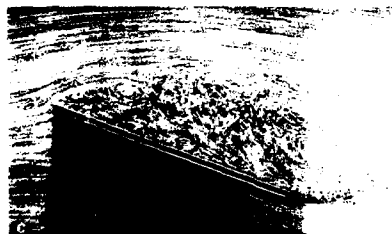
c $\alpha = 20°$ without blowing

g $\alpha = 20°$
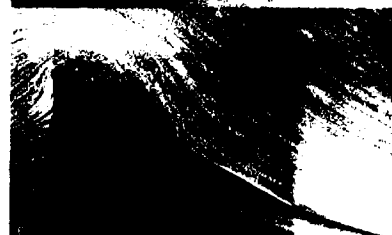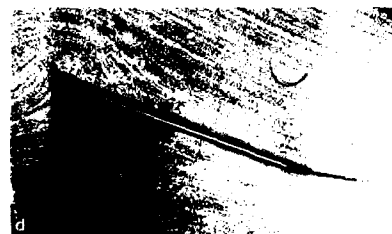
d $\alpha = 20°$
e $\alpha = 40°$ } with spanwise jet

h $\alpha = 20°$

i $\alpha = 20°$
($Re_c > 10^4$
c = 60 mm).

FIG. 4 – TWO-DIMENSIONAL
VISUALIZATIONS.

a $\alpha = 14^\circ$ $Re_c \simeq 4.10^4$
    NACA 66_3 . 0.18
a' $\alpha = 15^\circ$ $Re_c > 10^4$
    NACA 64 A 015

b $\alpha = 12^\circ$ $Re_c \simeq 1.3.10^5$
    NACA 66_3 0.18
b' $\alpha = 10^\circ$ $Re_c \sim 6.10^4$
    NACA 64 A 015

c $\alpha = 12^\circ$ $Re_c \simeq 4.10^4$
    NACA 66_3 . 0.18
c' c'' bubble type separation

a b c   Smoke visualization in wind tunnel
        (Prof. T. Mueller, Notre-Dame University)

a' b' c' } air bubbles visualization in water tunnel
d e f   } ONERA.

c' c'' d e f   enlarged leading edge method.

d   generalized separation
e   reattachment by tangential blowing
f   natural blowing through L.E. slat.

3-14

FIG. 5 – THIN DELTA WING.

a. Flow around the apex (dye emissions).
α = 20°

b. Surface flow   c. Flow over   d. Cross section   e. Flow over the   f. Cross section at the
with plastic   the upper   at the trailing   upper surface.   trailing edge.
paint. α = 25°   surface.   edge. α = 15°   α = 30°
                                   Visualization by air bubbles.
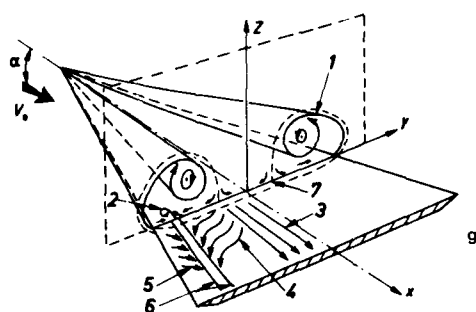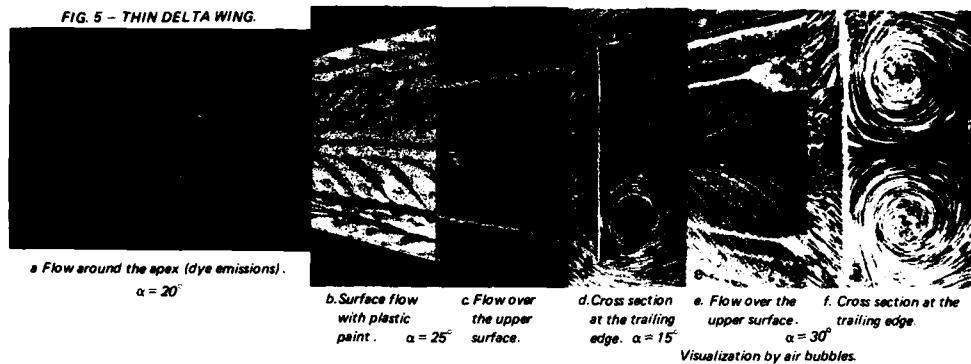
Schematic flow diagram.

1) Scroll vortex sheet forming the main vortex
2) Secondary vortex
3) Central zone without vortex flow
4) Zone induced by the main vortex
5) Zone induced by the secondary vortex
6) Accumulation zone (air bubble or coating)
7) Reattachment line.

h. Section along vortex axis.   α = 20°
Visualization by smoke-lighting by laser plane ; breakdown under
the effect of positive gradient downstream).

a. c - f, i
Water tunnel
TH1 ONERA
$Re_c > 2.10^4$

b
Wind tunnel
S8 Ch. ONERA
$M_0 = 1.95$

h
Wind tunnel
S2L Ch. ONERA
$Re_c = 8.10^5$
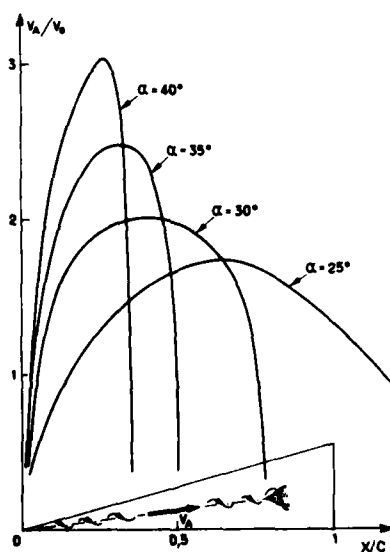
Velocity evolution along vortex axis as a function of angle
of attack.

Influence of angle of attack α on vortex breakdown
from top to bottom : α = 25° α = 30° α = 35° α = 40°

Flow around a thin delta wing ($\varphi_{LE} = 75°$).

FIG. 6 — THIN DELTA WING

a. Side view - visualization by smoke in wind tunnel (J. Harvey)

b. Upper surface flow. $\alpha = 15°$ · $\psi_{LE} = 75°$ · $Re_c < 2.10^4$ water tunnel ONERA.

c. Cross section at mid-chord. } with theoretical
d. Cross section at trailing edge. } points.
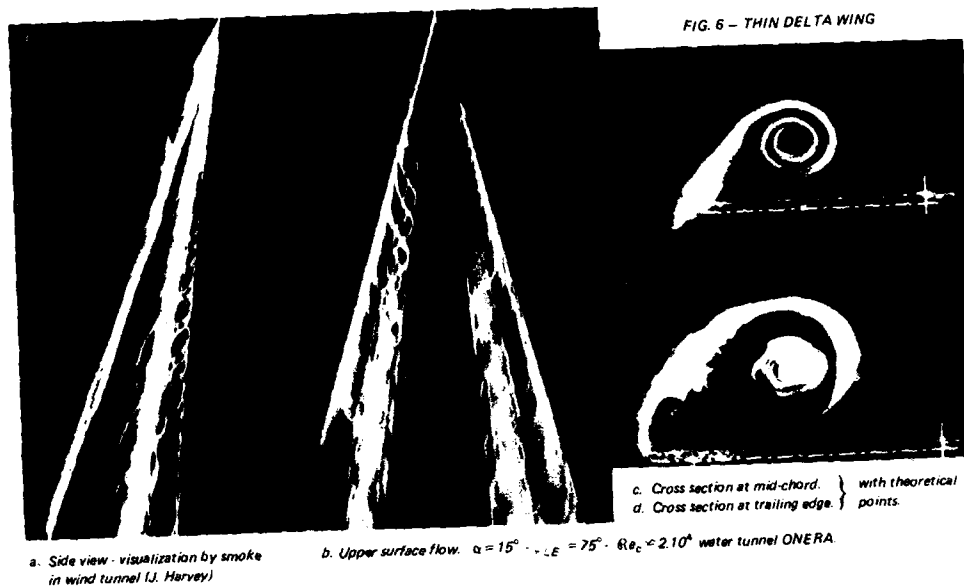
Scroll vortex sheets issued from the sharp leading edges of a thin delta wing

e. $\alpha = 15°$ $\psi_{LE} = 80°$

f. $\alpha = 15°$ $\psi_{LE} = 70°$

g. $\alpha = 24°$ $\psi_{LE} = 70°$ $(Re_c > 10^4)$.
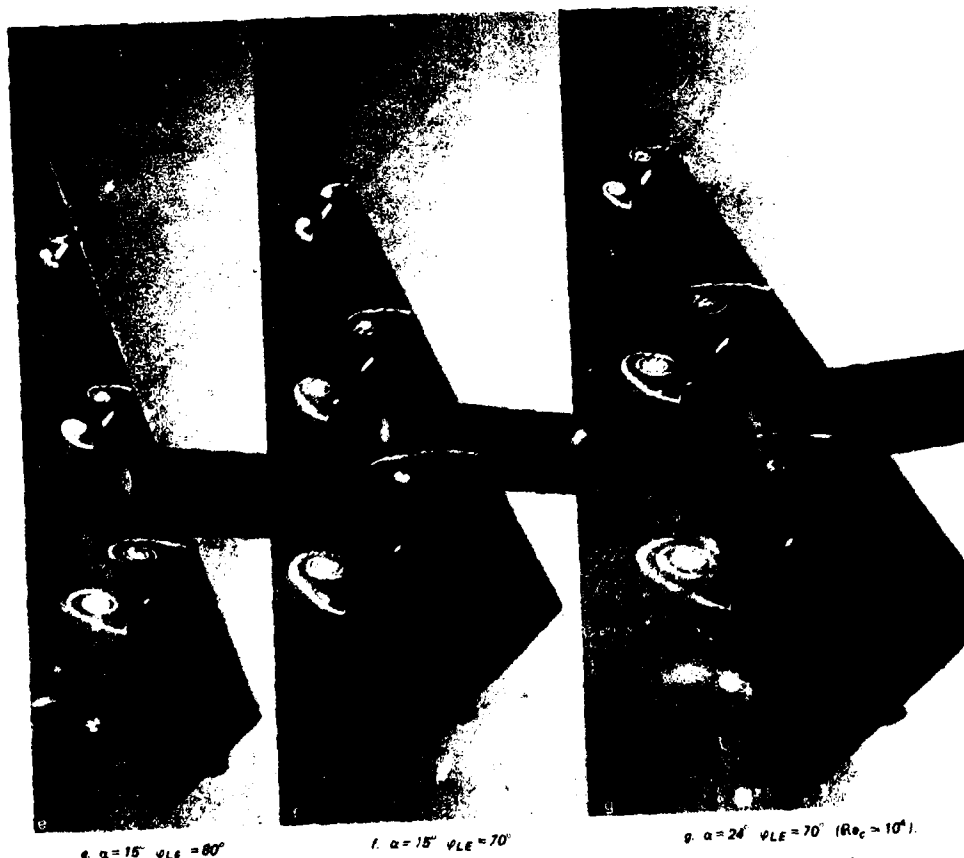
e.f.g   Cross sections at 25 %, 50 % and 75 %. Lighting by laser plane. Water tunnel ARL (Dr. D. Thomson).

b-g   Visualization by hydrogen bubbles (electrolysis).

Mach number $M_0 = 1.2$ ONERA wind tunnel S2 MA. $M_0 = 0.84$

Visualization by wall emissions of dye.

c

d

$M_0 = 0.2$ ONERA wind tunnel F1   ONERA wind tunnel S2 Ch. $M_0 = 0.26$
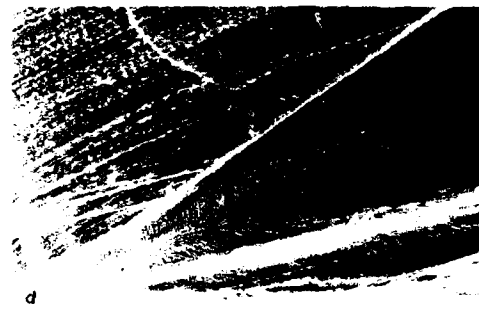
Visualization by viscous coating.   (Detail of apex, lower surface side)

e

$M_0 = 0$ ONERA water tunnel TH1 $(\alpha = 25°)$ ONERA wind tunnel S2 Ch. $M_0 = 0.26$
$(Re_c = 10^4)$ Visualization by dye.   Visualization by viscous coating.   (Detail of apex, upper surface side).

g

Upper surface flow on a rectangular wing $(AR = 2.7)$ with $60°$ sweep at $\alpha = 24°$; ONERA D symmetric profile $(e/c = 10.5\ \%)$.
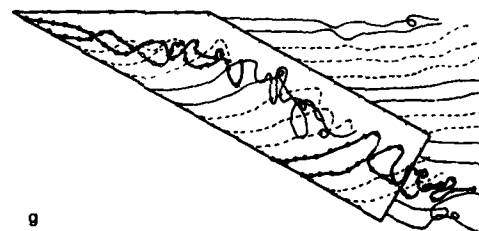
Calculation of the emission lines (singularity method, $\tau = 1.2$) with leading edge separation.

FIG. 7 – SWEPT WINGS WITH THICKNESS.

a. α ≈ 20° ℜe_c ~ 10⁴ view of upper surface.   b. Mid-chord section.

α = 10° ℜe_c > 10⁴   c. View of upper surface.

ONERA TH1 water tunnel.
Visualization by dye emissions
e. α = 2°   ℜe_c ~ 0.6.10⁴
    α = 12° ℜe_c ≈ 1.2.10⁴

f. Intense emissions

g. Parietal emissions.

Model with rounded leading edge.

h. α = 5°   ℜe_c > 1.2.10⁴

i. α = 12° ℜe_c > 1.2.10⁴

j. α = 12° ℜe_c > 0.3.10⁴

Sharp leading edge
(model turned over).
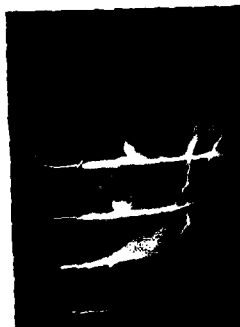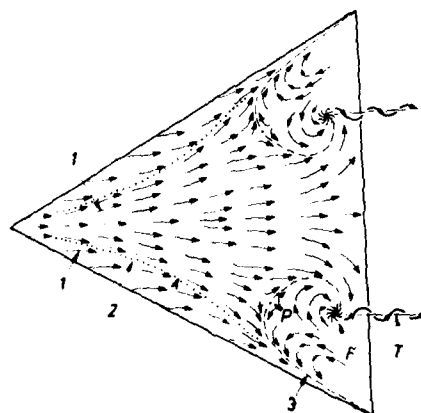
d

Flow schematics :

1. Shape of surface streamlines
2. Boundary of sideslip zone of lines 1
3. Separation line comprizing a partition
   point P and ending at point of spiral
   convergence F, origin of the vortex T.

Delta wing (φ$_{LE}$ = 60°. e/c = 0.10 · c = 100 mm)

Trapezoidal wings (λ = 5 ·profile NACA 0012 · c = 60).

FIG. 8 ~ FLOW ON THE UPPER SURFACE OF THICK WINGS.

3-18

FIG. 9 – OGIVES

ONERA TH1 water tunnel
(dye emissions).

$\alpha = 20°$ $Re_D = 0.6.10^4$
$(D = 60$ mm$)$

Side view.   Ogive with hemispheric nose   View of upper surface

$\alpha = 20°$ $Re_D > 0.6.10^4$
$(D = 60$ mm$)$
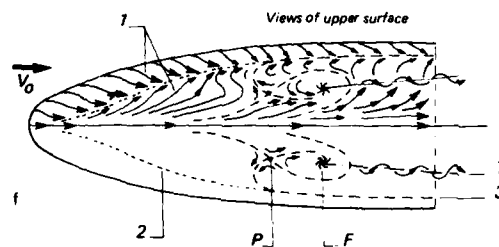
Views of upper surface

Side views.   Streamlined ogive with rounded nose.

Schematics :

1. Shape of surface streamlines
2. Boundary of sideslip zone of lines 1
3. Separation line comprizing a partition
   point P and ending at point of spiral
   convergence F, origin of the vortex T

$\alpha = 40°$ $Re_D > 0.6.10^4$ $(D = 60$ mm$)$.

View of upper surface.   "Gothic" ogive with pointed nose.

Small apex angle cone
with rounded nose.
$\alpha = 40$ $Re_D > 0.8.10^4$
$(D = 80)$.

View of the upper surface.   Cross section at half length (Visualization by air bubbles).
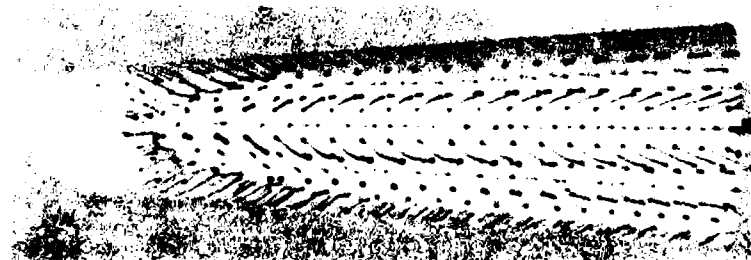
View of upper surface.

$\alpha = 20°$ $M_0 = 10$.

Visualization by viscous coating
ONERA wind tunnel R3 Ch.

FIG 10 — CYLINDRICAL FUSELAGES

a. α = 48°
ISL
water tunnel
(Dr. Fiechter).

b. α = 60°
$Re_c \simeq 0.6.10^4$
ONERA
water tunnel

α = 55°
$Re_c \simeq 10^5$
DFVLR tow
tank
(Dr Bippes,
Dr Hartmann)

Dye emission
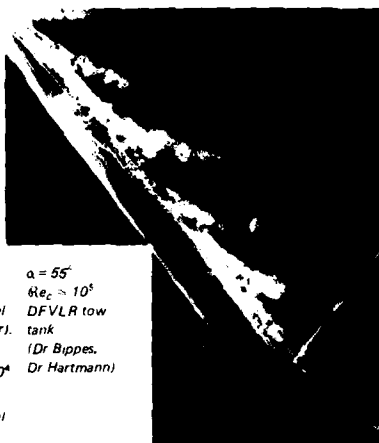
Visualization by hydrogen bubbles.

Visualization by air bubbles
(α = 30 $Re_D \geq 0.2 10^4$)
ONERA water tunnel.

f. Schematic of mounting in test section.
  1. Model
  2. Lighting by laser plane
  3. Smoke emitter
  4. Sighting.

ONERA
wind tunnel
S3 Ch.
(V_0 = 20 m/s)

g. α = 30°
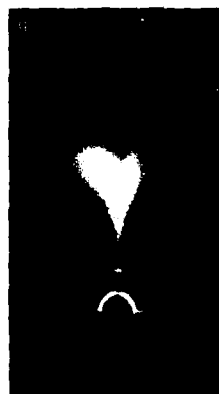
h. α = 50

Visualization by smoke (cross sections).

i. Cylinder with ogive nose, equipped with strakes ("chines") : view of upper surface (α = 20° $Re_D \simeq 1400$), cross section j.

k. Missile with strakes and cruciform tail unit
  α = 18° β = 12° $Re_D \simeq 0.23.10^4$
    k. view of upper surface.
    l. cross section at rear.

3-20

FIG. 11 - INTERACTIONS

Aircraft model with low (a) or high (b)
horizontal tail
α = 25   Re_D > 2000

1 140 scale model of
Concorde with
"moustaches" fixed at
the pointed nose,
deflected downwards
α = 15   Re_D > 2000

ONERA water tunnel

d. Side view
e. Upper surface   α = 30°
MBB water tunnel (P. Sacher).

Delta wing
f. without   g. with
canard
(upper surface)
visualization
with helium
bubbles
Re_c > 0.7.10^6

(Sage Action Inc.
Dr. Hale).

h. Without canard.
i. With canard.
(upper surface)

Forward-swept wing model (φ_LE = -39°   φ_TE = 56°.5   α = 20°   Re_c > 0.9 10^6)

FIG. 12 - COMPLETE AIRCRAFT.

F5-G model with swept wing. $\alpha = 15^\circ$
Visualization by smoke
Northrop wind tunnel
(Dr. G. Erickson).
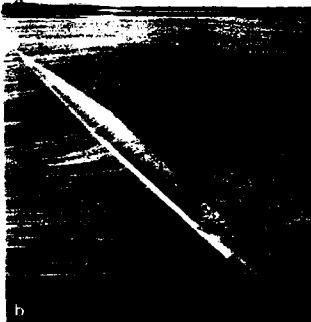
bb'. Without spanwise blowing

c,c'. With spanwise blowing
$(\varphi_{LE} = 60^\circ \quad Re_c \simeq 0.5.10^6)$.

Delta wing aircraft at 45° angle of attack.

Model of arrow wing with swept wing. $\alpha = 14^\circ$
$V_0 = 40$ m/s.
Visualization by tufts
ONERA wind tunnel S1CA.

Photo taken in 1951.

f'. No engine simulation.

1/140-scale model of Concorde with engine simulation.
$\alpha = 12^\circ \quad \beta = 0^\circ$

e. Cross section at trailing trailing edge.

ff'. Section along engine nacelles.

1/250-scale model of Airbus with deflected flaps (no engine simulation)
$\alpha = 0^\circ \quad Re_b = 10^6$
Cross section at trailing edge (visualization by air bubbles).

3-22

a, a', b. Oscillating profile.
Visualization by hydrogen bubbles
Aeromechanics lab water tunnel Moffet Field
(Dr McAlister and Carr)

FIG. 13 – TWO DIMENSIONAL PERIODICAL FLOW

$\alpha = 10° + 10°\ \sin \omega t$
NACA 0012 $c = 100$ mm
$K = 0.25$ $Re_c = 2.10^4$

b. Couloured emissions (closed L.E. view).
Lockheed water tunnel (Marietta) (Dr Whiffen and Cornelius).

c,d,e,f. Oscillating profile
NACA 0012
Visualization by air bubbles, ONERA water tunnel
$\alpha = 12°,5 + 5°\ \sin \omega t$
$c = 60$ mm $k = 0.9$ $Re_c \simeq 0.6.10^4$

g-k. Profile with flapping motion. Karman-Trefftz
$c = 52$ mm $K = 0.125$ St Cyr water tunnel
$e/c = 0.18$ $Re_c \simeq 5.10^4$ $\alpha = 22° + 20°\ \sin \omega t$
Visualization by polystyrol and tufts.

FIG. 14 – UNSTEADY FLOWS.

$N = 0$

$N = 0$

$\alpha = 15^\circ$ $2\pi Nb/V_0 = 0.3$

$2\pi Nb/V_0 = 0.2$

Delta wing aircraft
$(\varphi_{LE} = 60^\circ \cdot c = 69\ mm$ $Re_c = 0.7.10^4)$
$b = 37.5\ mm$

Delta wing
$(\varphi_{LE} = 60^\circ \cdot c = 100\ m)$
$Re_c \simeq 10^4$.

Uniform rotation simulating a horizontal roll (c , d)

Uniform rotation simulating a spin (g, h).

$N = 0$ $\alpha = 60^\circ$ $\pi Nc/V_0 = 0.3$.
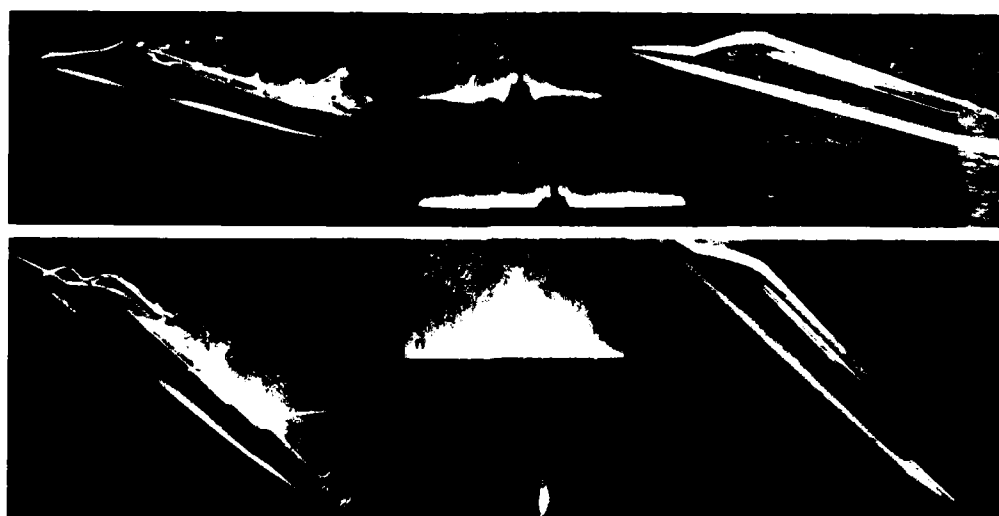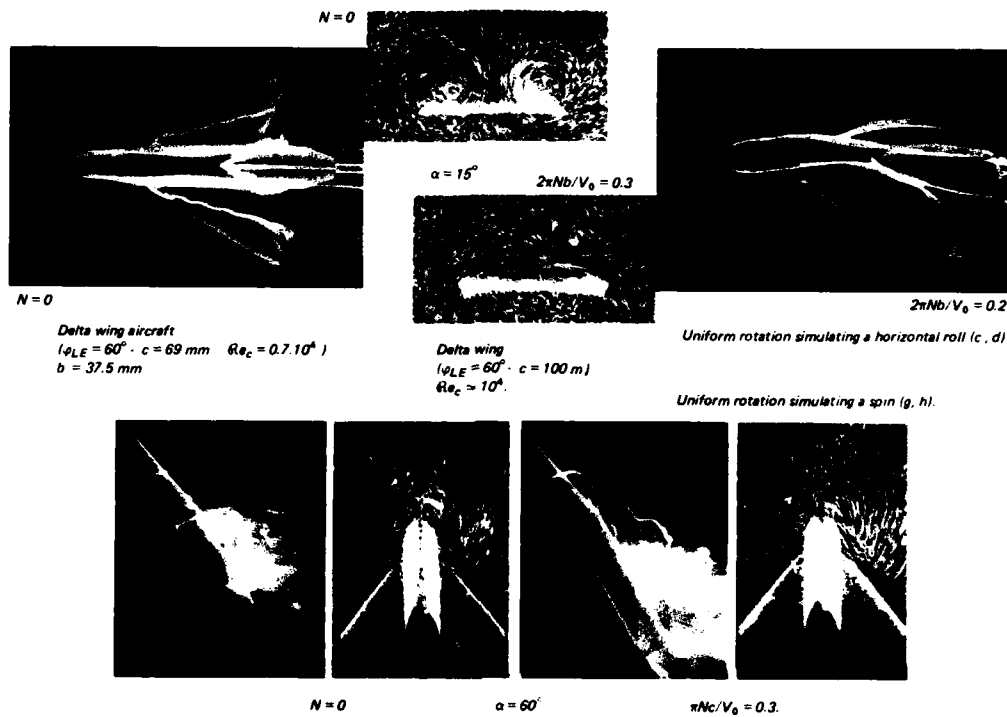
Model with harmonic oscillations in pitch
$\alpha = 30^\circ + 15^\circ \sin \omega t$, $K = 0.27$, $Re_c \simeq 0.7.10^4$

i-l   passage through minimum angle of attack   im ⎫ side views
m-p   passage through maximum angle of attack   ip ⎭

Aircraft model with
double-delta wing

$\varphi_{STRAKE} = 75^\circ$ $\varphi_{LE} = 32^\circ$
ONERA water tunnel.

FIG 15 - UNSTEADY FLOWS.

Fluorescent minitufts on propeller. (Dr. J. Crowder).

Aerostar propeller cruise, 180 kt 20.000 ft.

e. Transition triggered by rotation of a cylinder
$\alpha = 0$ · $V_t = 0.6 V_0$
$Re_L = 10^6$
Visualization by smoke (Prof. T. Mueller, Univ. Notre-Dame).

Machen superstar propeller 240 kt, 25.000 ft.
$M_{tip} = 0.81$.

Transition triggered by rotation of part of a cyl cylinder
$\alpha = 0°$
$Re_L = 10^4$
$V_t \approx 2.2 V_0$ d (visualization by dye emission)
$V_t = 4.4 V_0$ d'' (visualization by air bubbles).
ONERA water tunnel TH1.

Vortices emitted by the blades of a 3-bladed tilt rotor in transition flight.
($\alpha = -45°$ $V_0/V_f = 0.35$ $D = 124$ mm).

FIG. 16 – CAPTIONS →

Douglas F5D experimental aircraft
a. Test at ONERA water tunnel.
b. Flight test (NASA film).
c. Model of F-5F
($\alpha = 40°$ Northrop water tunnel)
d. Model of YF 17
($\alpha = 18°$ Northrop wind tunnel).

Nose-cylinder
e. ($\alpha = 30°$ Werton water tunnel)
f. ($\alpha = 25°$ ONERA water tunnel)
g. M6 wing ($M = 0.84$ $\alpha = 16°$)
ONERA wind tunnel S2 MA
h. Transport aircraft ($\alpha = 3°$)
Boeing wind tunnel.
i. Double delta wing aircraft
($\alpha = 15°$) ONERA wind tunnel S1 MA

Visualization by smoke (b)
Coloured emissions (a, c, e, f, g)
Oil (d). Air bubbles (f). Tufts (i)
and Dr Crowder pressure method (h)

Coloured emission (ONERA water tunnel TH1).

h

f. Start of the flow
g. Permanent regime ($Re_c > 10^4$)
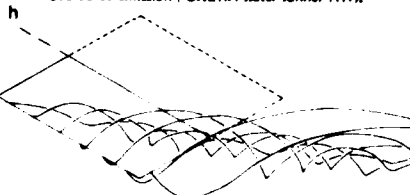
Rolling up of vortex sheets issued from a rectangular wing
($\lambda = 1$ $\alpha = 30°$ $c = 50$ mm)
h. Calculation (Metra)

26
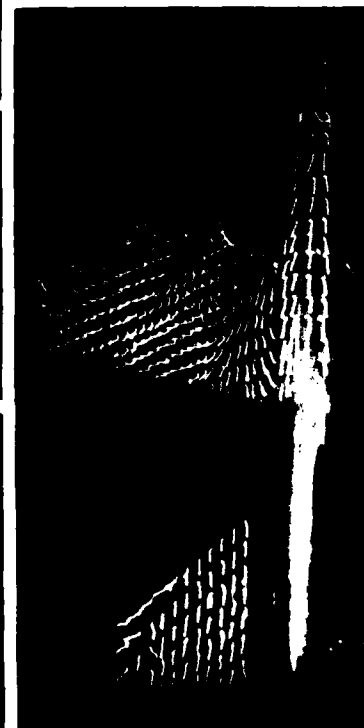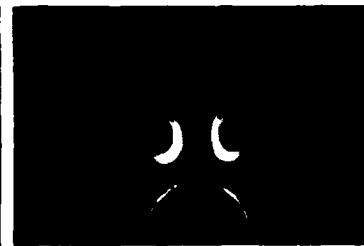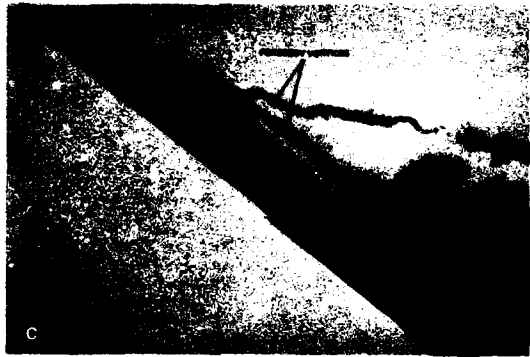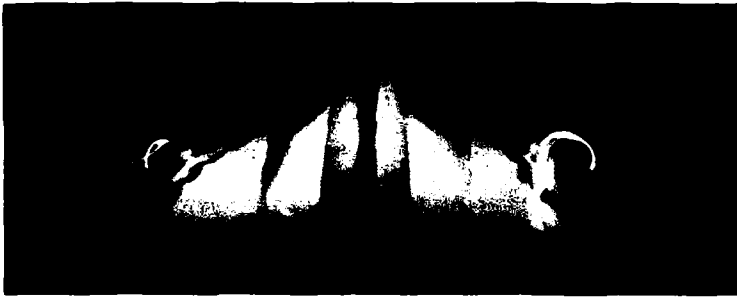
[73] MUELLER T.J., NELSON R.C. and KEGELMAN J.T., Smoke Visualization of Boundary Layer Transition. AIAA Journ. (Dec. 1981).

[74] WERLÉ H. et ARMAND Cl., Mesures et Visualisations Instationnaires sur les Rotors. VIe Colloque AFITAE (1969). ONERA TP 777.

[75] REHBACH C., Calcul Instationnaire des Nappes Tourbillonnaires émises par des Surfaces Portantes Fortement Inclinées. AGARD CP 247 (1978), p. 14-1 à 14-9.

[76] BOSCHIERO M, Communication MATRA : voir Calculs de Structures Tourbillonnaires Tridimensionnelles autour de Missiles. 18è Colloque AAAF, Poitiers (Nov. 1981).

[77] AGARD CP 247 (1978). High Angle of Attack Aerodynamics.

FIG. 17 – CAPTIONS

a   seen from below
b   seen from above   cylindrical sweptback wing ($\varphi = 60°$, angle of attack $\alpha = 20°$)
c   seen sideways $Re_c \simeq 10^4$.

d   test without canard surface ($\alpha = 20°$)
e, f   tests with canard surface ($\alpha = 25°$)   aircraft with low delta wing ($\varphi = 60°$)

g   seen from above ($\alpha = 20°$)
h   seen sideways ($\alpha = 45°$)   without blowing   aircraft with high double-delta wing
i   seen from above ($\alpha = 45°$) with lateral blowing   ($\varphi_{strake} = 75°$, $\varphi_{LE} = 32°$).

Visualization by coloured emissions.
ONERA water tunnel TH1.

METHODES DE VISUALISATION DES ECOULEMENTS POUR L'ETUDE DE L'AERODYNAMIQUE A HAUTE INCIDENCE

par Henri WERLE

Office National d'Etudes et de Recherches Aérospatiales (ONERA)
92320 Châtillon (France)

RESUME

Cet exposé passe en revue les principales méthodes de visualisation à l'aide de traceurs solides, liquides ou gazeux, utilisées en tunnel hydrodynamique et en soufflerie, plus particulièrement dans les installations d'essai de l'ONERA.

De telles visualisations mettent en lumière le schéma physique des écoulements avec toutes ses singularités pariétales, et son évolution en fonction des principaux paramètres : incidence, dérapage, nombre de Reynolds, etc. Elles révèlent notamment les phénomènes de décollement qui caractérisent le domaine des angles d'attaque élevées, en précisant tous les aspects tourbillonnaires, transitionnels et instationnaires.

Quelques exemples (*) de résultats obtenus dans le cas de profils, ailes en flèche, corps fuselés, prises d'air, avions complets, etc... montrent que les procédés adoptés sont en mesure de couvrir un domaine d'applications étendu.

1 - INTRODUCTION -

Toute l'histoire de la mécanique des fluides, et notamment celle de l'aérodynamique du domaine aérospatial, a été marquée par le développement des techniques de visualisation : en effet, voir un phénomène, c'est généralement pouvoir l'analyser, c'est souvent l'expliquer, et c'est parfois faire un pas vers la résolution des problèmes théoriques ou expérimentaux qui en découlent.

Il est indéniable que la visualisation, qui a pris son départ en 1883 avec les premières expériences de Reynolds, a contribué à faire progresser l'étude des écoulements autour des modèles, et tout d'abord aux incidences usuelles, c'est-à-dire dans des conditions optimales correspondant des écoulements stables avec décollements réduits.

Mais cette visualisation devient évidemment encore plus nécessaire à notre époque où l'aérodynamique s'aventure dans le difficile domaine des grands angles d'attaque que caractérisent des écoulements avec décollements étendus, organisés ou non, stationnaires ou instationnaires.

Ainsi sont mis en lumière les problèmes de stabilité et de contrôle que posent ces grands angles d'attaque qui sont désormais souvent imposés par les conditions de vol actuelles :

- manoeuvrabilité des avions de combat effectuant des évolutions serrées,

- sécurité de vol des avions de transport au cours de leurs trajectoires près du sol destinées à réduire leurs nuisances,

- contrôle des engins et missiles durant leur lancement en présence d'un fort vent latéral et leur vol en manoeuvre, etc....

Si la visualisation de l'écoulement en vol reste souvent un fait exceptionnel, elle est plus couramment pratiquée en soufflerie, dont la raison d'être reste cependant les mesures, notamment celle des efforts aérodynamiques et des pressions.

Par contre, la visualisation dans l'eau, généralement plus précise et plus facile à mettre en oeuvre que dans l'air, s'est développée surtout dans des tunnels hydrodynamiques, souvent conçus pour ce type d'essai.

Il n'est pas possible de faire ici un tour d'horizon complet sur un sujet aussi vaste, aussi le présent exposé se limitera aux seules méthodes de visualisation mettant en jeu des traceurs solides, liquides ou gazeux et commencera par une description des principaux types de tunnels hydrodynamiques existants.

La suite de l'exposé est consacrée à l'examen d'une série de visualisations concernant l'aérodynamique des grands angles d'attaque et obtenues aussi bien avec des modèles simples (profils, ailes, fuselages isolés, etc...) qu'avec des maquettes plus élaborées (combinaisons fuselage-ailes, avions complets, etc...).

(*) Des films de visualisations seront présentés au cours des Lecture Series.

2 - TECHNIQUES EXPERIMENTALES -

2.1 - Tunnels hydrodynamiques -

Il existe une grande variété d'installations hydrauliques servant à la visualisation des écoulements et qui diffèrent surtout par la disposition de leur veine d'essai et leur principe de fonctionnement. On peut distinguer les 3 principaux types suivants :

- les tunnels verticaux en circuit ouvert et fonctionnant généralement par vidange sous l'effet de la gravité, comme ceux de l'ONERA (fig.1) [1] ;

- les tunnels à veine verticale ou horizontale et fonctionnant en circuit fermé à l'aide d'une pompe ou d'une hélice actionnée par un moteur. Ce sont les plus nombreux et l'on peut citer d'abord ceux du NAE [2] (Ottawa), du AVRADCOM [3](US Army/Ames) et de NORTHROP [4](Hawthorne) : voir figure 2abc ;

- les bassins à surface libre généralement sans circulation d'eau et dans lequel se déplace la maquette entraînée par un chariot, comme celui de la DFVLR [5](Göttingen) : voir fig. 2dd'.

Les tunnels les plus connus figurent dans le tableau ci-dessous avec leurs caractéristiques principales, et le nombre de Reynolds moyen typique des visualisations.

Etablissement (pays)	Type de tunnel (section veine)	Vitesse max. (Nbre de Reynolds)	Observation
ONERA (Châtillon) FRANCE	Vertical TH1 0,22 x 0,22 m TH2 0,45 x 0,45 m TH3 0,80 x 0,80 m	0,25 m/s $(0,5.10^5)$ 1,50 m/s $(6,5.10^5)$ 0,065 m/s $(0,5.10^5)$	voir fig. 1a, fig.3 etc...
NAE (Ottawa) CANADA	Horizontal 0,25 x 0,33 m	3 m/s $(6.5.10^5)$	voir fig. 2a
NASA Ames Moffett Field USA	Horizontal 0,20 x 0,30 m	6 m/s (2.10^4)	pressurisable voir fig.2c et 13aa'
NORTHROP Hawthorne USA	Vertical 0,4C x 0,61 m	0,076 m/s (3.10^4)	voir fig.2b et 16c
ARL Melbourne AUSTRALIE	Horizontal 0,25 x 0,25 m	0,76 m/s (10^4)	voir fig. 6efg
INSTITUT AEROTECH-NIQUE St CYR FRANCE	Horizontal 0,45 x 0,45 m	1,20 m/s (10^5)	voir fig. 13g-k
BRIT.AERO.DYN.GROUP WARTON ENGLAND	Horizontal 0,45 x 0,45 m	3 m/s (3.10^4)	voir fig. 16e
MBB Ottobrun ALLEMAGNE	Vertical 0,34 x 0,34 m	1,4 m/s $(0,6x10^6)$	voir fig. 11 de,[6]
I.S.L. Saint Louis FRANCE	Vertical 0,25 x 0,25 m	0,20 m/s (10^4)	voir fig. 10a
N.P.L Teddington ENGLAND	Horizontal 0,25 x 0,33 m	2,4 m/s (5.10^4)	
OCEANICS INC. Plainview U.S.A.	Horizontal 0,50 x 0,50 m	12 m/s (8.10^6)	
V.K.I Rhode St Genèse BELGIQUE	0,15 x 0,15 m	0,21 m/s (4.10^4)	
BERTIN Plaisir FRANCE	Veine Horizontale 0,40 x 0,40 m	5 m/s (10^6)	
LOCKHEED Marietta U.S.A.	Horizontal 0,33 x 0,25 m	0,25 m/s $(0,5.10^5)$	voir fig. 13b

DFVLR Göttingen ALLEMAGNE	bassin 1,10 x 0,90 m	5 m/s (5.10^6)	voir fig. 2dd' et 10 c
MATRA Velizy FRANCE	bassin 1,0 x 1,0 m	1,8 m/s (10^6)	
University KYUSHU JAPAN	bassin 0,5 x 0,5 m	0,30 m/s (1,5.10^5)	
DOUGLAS Aircraft Huntington BEACH U.S.A	bassin 0,60 x 0,35 m	2,45 m/s (0,8.10^6)	

2.2 - _Méthodes de visualisation_ -

Les procédés utilisant des traceurs pour la visualisation aussi bien dans l'air que dans l'eau sont aussi fort nombreux et variés. Le lecteur intéressé consultera avec fruit les différentes synthèses [7 - 11] qui à plusieurs reprises ont fait le point de la question. Seuls les procédés les plus utilisés seront évoqués ci-dessous.

On notera ici que ces méthodes, qui mettent en jeu des éléments en suspension dans le fluide, sont dans certains cas [12] limitées par suite des écarts entre les trajectoires de particules et des éléments fluides qu'elles représentent. Ceci concerne surtout les particules n'ayant pas la même densité et viscosité que le fluide et soumises alors du fait de leur diamètre aux effets de moyenne, aux forces centrifuges et à la gravité, ce dernier point étant plus gênant en veine d'essai horizontale.

Il n'est peut être pas inutile de rappeler ici que si les trajectoires et lignes d'émission de traceurs corrects coïncident avec les lignes de courant d'un écoulement stationnaire, tout au moins en régime laminaire, ce n'est plus vrai pour un écoulement instationnaire et en régime turbulent : cependant, comme on le verra ci-dessous, ces traceurs peuvent, moyennant certaines précautions, fournir de même l'allure de l'écoulement instantané ou moyen avec les décollements qui se produisent aux angles d'attaque élevés.

Voici les principaux traceurs utilisés dans l'eau :

2.2.1 - _Traceurs solides_ -

Ils sont généralement introduits par une sonde en amont du modèle :

- paillettes d'aluminium [13];

- perles de polystyrol, sphériques et de densité très voisine de celle de l'eau (fig. 13g-k [14])

- perles de verre, poudre de plexiglas, etc .... voir [11]

2.2.2 - _Traceurs liquides_ -

Ils sont émis à partir des maquettes ou d'une rampe amont :

- lait dilué (mélange de lait, d'alcool, de colorant et d'eau dont la densité et la viscosité sont égales à celle de l'eau), utilisé dans les tunnels ONERA jusqu'en 1979 (fig.17) [15] ;

- rhodorsil dilué (mélange stable et blanc pouvant remplacer le lait) utilisé depuis 1979 ;

- colorants fluorescents [16] ;

- encre, teinture, solution de tétrachlorure de carbone et de benzine, permanganate de potasse, etc..., voir [11].

2.2.3 - _Traceurs gazeux_ -

- généralités concernant l'utilisation des bulles : voir [17] ,

- bulles d'air obtenues à l'aide d'un agent émulsionnant introduit au moment du remplissage du réservoir (procédé ONERA) [15] : voir fig.3 ;

- bulles d'air injectées à partir de rampes ou trous d'émission à la surface des modèles ou se formant naturellement dans les conditions des essais, par exemple sous l'effet de la cavitation [18];

- bulles d'hydrogène obtenues par électrolyse, méthode créée par GELLER [19] et maintes fois reprises [20-22]: fig 6 b-g

2.2.4 - _Autres méthodes_

- brins de textile fixés à la paroi des modèles (fig. 13g-k) ;

- flotteurs (paillettes d'aluminium, poudre d'hostaflon ou autres traceurs légers répandus à la surface libre), dont l'emploi reste généralement limité au courant plan ;

- peintures et huiles recouvrant le modèle ou méthodes chimiques limitées aux écoulements pariétaux.

2.3 - Méthodes utilisées en soufflerie -

Ces méthodes [23] ont fait l'objet de mises à jour récentes [24], parmi lesquelles on note plus particulièrement celle de T.Mueller [25] qui à l'Université de Notre Dame dispose d'installations spécifiques adaptées à la visualisation à l'aide de fumée (souffleries à grand coefficient de contraction et faible taux de turbulence, rampes d'émissions de fumée, etc..):

2.3.1 -"Smoke techniques"-

Ces fumées généralement blanches sont obtenues à l'aide de générateurs ou de "smoke wire" à partir de titanium tetrachloride (J.K HARVEY : fig. 6a), de kérosène (MUELLER [26] : fig. 4 abc), de vapeurs d'huile ou d'eau condensée par de l'azote liquide ([27,57] fig. 5 h et 10fgh).

2.3.2 -"Surface liquide flow techniques"-

- émissions continues de liquides colorés à la surface des maquettes, procédé utilisé dans les souffleries ONERA et permettant d'opérer à différents Mach, incidences et dérapages sans arrêt de la soufflerie [28] (fig. 7ab, fig.16g);

- enduits visqueux (fig. 7cde), peintures plastiques (fig.5b, 9j), peintures thermoluminescentes, huiles (fig.17d), cristaux liquides ou sublimation d'acénaphtène [28], autant de procédés demandant une mise en place préalable de l'enduit avant chaque essai ;

2.3.3 -"Tufts techniques"-

- minuscules brins de laine ou de nylon collés sur le modèle (fig. 16 i) ou fixés sur une grille (fig.12d) [29] ; ce procédé a même été appliqué avec succès au cas d'une hélice en vol("mini tufts"fluorescents du Dr. CROWDER [30]: fig. 15 ab), nécessitant des éclairs de lumière UV de 5 millisecondes)

2.3.4 - Bulles d'hélium -

Ces bulles de savon gonflées d'hélium et flottant dans l'air constituent des traceurs privilégiés, mais nécessitent un générateur cylindrique amont (Sage Action BFS 1035)[31 - 32] adapté à la vitesse de la soufflerie ; ces bulles permettent d'obtenir des visualisations aussi fines que celles effectuées en tunnel hydrodynamique : fig. 11 fg.

2.3.5 - Autres méthodes -

Une méthode particulièrement originale, celle du Dr.CROWDER de BOEING [33], traduit en points lumineux de différentes couleurs un sondage de pression totale effectué dans un plan transversal derrière le modèle et fait apparaître ainsi sans traceurs le sillage tourbillonnaire d'une aile munie de volets de courbure (fig. 16 h).

3 - EXEMPLES DE RESULTATS -

Le cadre limité de cet exposé n'autorise qu'une évocation succincte des nombreux exemples d'études aux incidences élevées auxquels la visualisation a pu apporter une contribution. Ces exemples, classés suivant le type de phénomène ou d'écoulement étudié, sont illustrés par 15 figures (nos 3 à 17).

3.1 - Profils - Prises d'air bidimensionnelles -

L'écoulement laminaire le long d'une paroi plane comportant un bord d'attaque aigu décolle sous l'effet d'une mise en incidence et ce décollement fixé le long de ce bord est d'abord localisé, puis se développe rapidement d'amont en aval.

Il en est ainsi dans le cas d'une prise d'air à canal parallèle fonctionnant avec un coefficient de débit ε voisin de 1 : en effet, à α = 20°, on distingue un bulbe décollé interne fixé à la lèvre inférieure et ce décollement s'étend à l'ensemble du canal à α = 40°. Dans cet exemple, les bulles d'air précisent l'allure de l'écoulement moyen (fig. 3ab), tandis que le colorant émis sous forme de nappe révèle la formation de rouleaux tourbillonnaires à la frontière des décollements, phénomène qui assure la transition laminaire-turbulent à l'intérieur de la prise (fig. 3a'b') [34].

Sur une plaque mince placée à 20° d'incidence (fig. 3c) l'effet"canal"favorable n'existe pas et la zone décollée affecte tout l'extrados et ne se referme qu'en aval du bord de fuite.Un jet transversal [35]émis près du bord d'attaque dans cette zone décollée permet de réduire ce décollement à un petit bulbe, même à incidence très élevée (fig. 3 de).

Sur un profil comportant un bord d'attaque arrondi le décollement d'extrados reste libre et est de ce fait plus sensible aux effets du nombre de Reynolds ; cependant aux incidences élevées,la variation de ce paramètre n'entraîne pas de modification de structure de la zone décollée (fig. 3hi).

Notons ici que les filets colorés pariétaux émis dans la zone décollée précisent la direction et le caractère du courant de retour (fig.3g), tandis que la nappe de colorant émise au bord d'attaque du même profil à faible incidence visualise la transition naturelle de la couche limite d'extrados (fig.3f)[36] .

Les visualisations par filets de fumée réalisées par T.MUELLER [37] (fig.4abc) recoupent les résultats sur les profils obtenus dans l'eau :

- décollement généralisé pour $\propto$ = 14° - 15° (fig. 4 aa'),

- mince bulbe de décollement avec recollement turbulent puis décollement arrière pour $\propto$ = 10° - 12° (fig. 4bb'),

- bulbe décollé plus étendu lorsque diminue le nombre de Reynolds (comparer fig. 4 b et c).

La méthode du bord d'attaque agrandi utilisé à l'ONERA [38] permet d'obtenir des images plus détaillées de ces phénomènes :

- bulbe de décollement assurant la transition (fig. 4c'c"),

- décollement généralisé (fig.4 d),

- recollement sous l'effet d'un soufflage tangentiel (fig.4 e),

- recollement obtenu par un bec à fente (soufflage naturel) : fig.4f.

3.2 - Ailes delta minces -

Une exemple classique d'étude aérodynamique à grande incidence est celui du décollement tourbillonnaire qui se forme sur l'extrados d'une aile delta mince à flèche accentuée. On sait que ce régime assure au modèle un supplément de portance, qui croît avec l'incidence et que limite l'apparition du phénomène d'éclatement des tourbillons.

Les visualisations obtenues au tunnel hydrodynamique ont mis en évidence l'organisation et la structure des tourbillons issus de l'apex et résultant de l'enroulement en "cornet" [39-40] de la nappe qui se détache le long du bord d'attaque aigu de chaque côté de l'aile (fig. 5acd). Elles permettent de dégager le schéma physique de l'écoulement (fig.5g) [41].

Ces recherches ont été étendues au phénomène d'éclatement [42]qui désorganise ces tourbillons aux incidences élevées (fig. 5 efh).

Des visualisations en soufflerie (ONERA S3Ch) par fumée éclairée par un mince faiseau laser plan (fig.5h) ont confirmé la structure spirale du noyau tourbillonnaire éclaté.

Ces visualisations ont en outre précisé le déplacement du point d'éclatement en fonction des paramètres, soit par exemple en fonction de l'incidence (fig.5i). Grâce à des émissions de colorant intermittentes, il a été possible de déterminer l'évolution de la vitesse le long de l'axe du tourbillon jusqu'au point d'éclatement et pour différentes incidences (fig.5j).

Enfin, les expériences ont montré que l'organisation et la structure de ces tourbillons subsistent en supersonique[43] (fig.5b).

Pour mettre en évidence la nappe enroulée en "cornet", et seulement cette nappe, il a fallu faire appel à une visualisation en tunnel hydrodynamique par bulles d'hydrogène, obtenues par électrolyse au moyen d'une cathode disposée au bord d'attaque de l'aile (fig.6b). Cette image de la nappe est tout à fait comparable à celle obtenue par fumée en soufflerie par J.K HARVEY (fig.6a). Cette nappe peut être vue en coupe à l'aide d'un éclairage par plan de lumière. Ainsi le Dr. D.THOMSON [44]a mis en évidence l'évolution de cette nappe en fonction de l'abscisse, de l'incidence et de la flèche de l'aile (fig.5 efg). De même, la trace de la nappe obtenue au tunnel hydrodynamique de l'ONERA, dans un plan situé à la mi-corde et au bord de fuite d'une aile delta a été comparée avec les résultats d'un calcul numérique représentant la nappe par un réseau de tourbillons concentrés (fig. 6cd) [45].

3.3 - Ailes épaisses -

Un 1er exemple est celui de l'aile cylindrique en flèche accentuée (φ_{BA} = 60°) équipée d'un profil symétrique ONERA "D" (épaisseur e/c = 0,105), dont l'écoulement tridimensionnel a fait l'objet à l'ONERA d'une étude systématique allant jusqu'aux vitesses transsoniques [46].

Les différentes visualisations groupées sur la Figure 7 précisent l'évolution en fonction du nombre de Mach, de l'écoulement pariétal sur l'extrados du modèle placé à 24° d'incidence.

On distingue notamment la position des ondes de choc en transsonique (fig. 7ab), et surtout les zones directement balayées par les tourbillons principaux et secondaires (fig. 7c).

Les émissions de colorant au tunnel hydrodynamique (fig.7f) fournissent une visualisation spatiale de la structure tourbillonnaire d'extrados qui rejoint celle fournie par un calcul des lignes d'émission basé sur la méthode des singularités [47](fig. 7g)

Une analyse plus fine de l'écoulement a été effectuée à l'aide de sondages et de visualisations [48], en particulier dans la zone de l'apex de cette demi-aile fixée sur un panneau. C'est au voisinage de l'apex (fig.7 de et fig. 17 abc) que se situe l'origine de ces tourbillons aux incidences élevées et que l'on décèle des décollements de la couche limite qui se forme sur le panneau.

Un deuxième exemple d'aile en flèche épaisse est à nouveau celui de l'aile delta entière [49]. Sur l'extrados de cette aile (φ_{BA} = 60°), des émissions de colorant pariétales révèlent les singularités caractérisant l'écoulement à moyenne incidence (fig. 8cc' et schéma 8d), puis à incidence élevée (fig. 8ab).

Dans les deux cas se développe sur la partie avant de l'extrados une couche de courant cisaillée transversalement, c'est-à-dire caractérisée par une dérapage vers le bord d'attaque des lignes de courant devenant pariétales. Quand cette couche décolle, elle constitue la nappe qui s'enroule pour former le tourbillon d'extrados. Même à 20° d'incidence, l'origine des tourbillons se situe encore à une certaine distance de l'apex tandis que leur éclatement se produit déjà en amont du bord de fuite.

Les tourbillons principaux restent ainsi séparés, comme à 10° d'incidence, par une zone médiane non tourbillonnaire sur cette aile à 60° de flèche.

Un exemple de décollement de structure tout à fait différente est celui qui affecte l'extrados d'une aile trapézoïdale de faible flèche. Même si à faible nombre de Reynolds, les décollements d'extrados apparaissent dès les petites incidences et se développent plus rapidement quand ∝ croît, ces visualisations mettent en évidence la forme des lignes de courant pariétales que l'on finira par retrouver aux incidences élevées lors d'essais effectués à grand nombre de Reynolds (fig. 16 g) [50].

Sur un modèle à bord d'attaque arrondi, le décollement apparaît généralement près du bord de fuite à faible incidence (fig.8e) et finit par s'étendre à la totalité de l'extrados à incidence élevée (fig.8fg) [51].Sur un modèle à bord d'attaque aigu ou moins bien profilé, un bulbe tridimensionnel se forme d'abord au bord d'attaque (fig.8h) et se généralise brutalement à l'extrados quand ∝ croît (fig. 8 ij).

3.4 - Corps fuselés -

L'étude fondamentale commencée ci-dessus avec des voilures isolées a été poursuivie avec une deuxième classe de maquettes de base, celle des corps fuselés dont le comportement aux incidences élevées intéresse directement les lanceurs, missiles et fuselages d'avion.

Une première série de visualisations concerne les ogives de révolution (fig.9) et permet de distinguer comme sur les voilures différents types de décollement [52-53]:

- sur une ogive à nez relativement plat (fig.9ab), le décollement d'extrados résulte d'une jonction entre le bulbe médian qui affecte le nez à faible incidence et le décollement tourbillonnaire qui se développe de chaque côté du modèle ;
- sur une ogive profilée à nez arrondi (fig. 9cde , schéma 9f), on retrouve, comme sur une aile delta épaisse à incidence moyenne, 2 plages décollées séparées par un couloir médian sain ;
- sur une ogive profilée à nez pointu (fig. 9g), une structure tourbillonnaire organisée se développe jusqu'à proximité de l'apex et finit par s'y rattacher aux incidences très élevées (fig. 10b) ;
- sur une ogive à profil courbe et ne comportant pas de discontinuité ou de variation trop importante de courbure (ogive conique à nez arrondi raccordé par une clothoïde), on observe la jonction au sommet du nez des 2 tourbillons principaux qui forment alors les deux branches d'une sorte de tourbillon en fer à cheval (fig.9 hi). Ces phénomènes tourbillonnaires subsistent aux vitesses élevées : en effet, même en hypersonique (fig. 9j), on peut observer sur une visualisation par enduit visqueux la zone balayée par les tourbillons qui se forment dans la zone décollée sur l'extrados du modèle à 20° d'incidence[43].

Les exemples suivants groupés sur la Fig. 10 concernent les fuselages cylindriques longs et les maquettes d'engins.

Un fuselage cylindrique placé à incidence élevée devient le siège de tourbillons assymétriques et c'est à M. FIECHTER [54] que l'on doit l'une des premières visualisations de ce phénomène en 1966 (fig.10a). Cette configuration de décollement stationnaire s'établit entre 35° et 60° d'incidence sur les corps lisses (fig. 10 cdeh) [55 - 56] et se traduit par des forces latérales sur le modèle.

Près de la pointe avant (fig. 10b), cette structure tourbillonnaire conserve d'abord sa symétrie, comme elle l'est normalement tout le long du modèle aux incidences plus faibles [57-58] (fig. 16 ef). Aux incidences supérieures à 60°, la structure décollée devient instationnaire avec formation de tourbillons alternés du type Bénard-Karman.

Un moyen efficace de stabilisation destiné à éviter l'apparition des forces latérales consiste à disposer latéralement de chaque côté du corps de révolution des ailettes minces de faible allongement appelées"nageoires"(fig. 10g, i,j). Le décollement se fixe alors le long du bord aigu des nageoires et assure, à dérapage nul, la formation de tourbillons symétriques et stables, qui doivent assurer au modèle le supplément de portance tourbillonnaire dont bénéficient les ailes de faible allongement [40, 59].

Dans le cas d'un dérapage (fig. 10 kl), l'écoulement cesse d'être symétrique et les tourbillons de nageoires s'éloignent latéralement du fuselage, en franchissant le plan de symétrie du modèle. Pour un angle de dérapage critique, un des deux tourbillons peut donc trouver sur sa trajectoire l'empennage vertical de l'engin et être ainsi à l'origine d'effets d'interaction néfastes [60].

3.5 - Configurations de maquette donnant lieu à des effets d'interaction -

Dans de nombreux cas, de telles interactions peuvent se produire entre les décollements tourbillonnaires se formant à l'avant et les parties arrière de maquettes plus complexes et particulièrement aux incidences élevées.

Il en est ainsi avec les tourbillons de fuselage qui, suivant l'incidence du modèle et la disposition en hauteur de l'empennage horizontal, peuvent réduire l'efficacité de ce dernier (fig. 11 ab).

Quelques exemples mettent en jeu des surfaces auxiliaires du type "canard" à l'avant de la voilure principale d'un avion.

Dans un premier cas (fig.11 c), il s'agit de"moustaches" montées à l'avant d'une maquette de l'avion Concorde et dont l'efficacité est assurée par la position et le dièdre négatif adaptés aux incidences d'approche et d'atterrissage. Leur but est de participer à l'équilibrage longitudinal de l'appareil [40, 55].

Dans un deuxième exemple, ce plan canard en flèche occupe une position plus proche de la voilure principale elle-même en flèche[61](fig. 11 de) : les tourbillons du plan canard sont alors captés par ceux de la voilure principale qui récupèrent ainsi leur énergie: l'éclatement du tourbillon principal peut ainsi être retardé aux grandes incidences.

Une 3ème formule consiste en un plan canard disposé directement au-dessus de l'apex de la voilure principale. Son action est similaire, mais elle produit en outre un effet"canal" favorable qui provoque en particulier le recul du phénomène d'éclatement du tourbillon de voilure (fig. 11 fg et fig. 17 def) [32, 62]

Un dernier exemple met en jeu une voilure à flèche avant, formule nouvelle du type de celle étudiée pour l' USAF (DARPA) [63] . Cette voilure bénéficie d'un régime tourbillonnaire bien structuré et accroché à la pointe avant en dépit d'une flèche de bord d'attaque relativement faible(φ_{BA} =-39°) : voir fig. 11h.

Le plan canard joue le rôle d'un strake dans le cas d'une telle aile, c'est-à-dire engendre un sillage tourbillonnaire qui agit sur la partie moins bien organisée côté emplanture de la voilure principale (fig. 11i).

Les strakes à flèche élevée sont généralement disposés devant des ailes de faible flèche, et parfois constituent le prolongement de ces dernières vers l'avant formant ainsi une voilure en double delta [40] (fig.16 ci et fig. 17 g). L'effet favorable du décollement tourbillonnaire intense du strake se prolonge dans ces conditions sur une partie de l'aile principale qui lui fait suite. Aux incidences élevées (fig. 17 h), le tourbillon éclate et un soufflage transversal est alors nécessaire(fig.17i)pour rétablir une structure tourbillonnaire organisée sur le modèle [62].

3.6 - Maquettes d'avions -

Afin de procéder à une étude de l'écoulement aussi complète que possible, de nombreux essais mettent en jeu des maquettes entières (effet de dérapage) avec des voilures complètes (munies par exemple de leurs volets) et plus ou moins motorisées (simulation des prises d'air et des jets de réacteur).

Ainsi dans le cas d'un avion de combat équipé d'une voilure en delta, le décollement se limite à la voilure aux incidences moyennes (fig. 12 a) avec des tourbillons bien structurés (fig. 12d), puis quand l'incidence augmente ces tourbillons tendent à se désorganiser côté aval (fig. 16 a) et ce phénomène [60], confirmé en vol (fig. 16 b), remonte d'aval en amont jusqu'à désorganisation complète sur l'aile (fig.12bb') et tourbillons assymétriques sur le fuselage (fig. 16c) : il faut alors utiliser un jet d'intensité suffisante émis suivant l'axe du tourbillon (fig. 12cc') pour rétablir un écoulement tourbillonnaire organisé sur l'ensemble fuselage-voilure [64-66].

Enfin, sur certains modèles d'avion,on peut déceler les effets dus au fonctionnement de la prise d'air souvent proche de l'apex de la voilure où se situe l'origine des tourbillons d'extrados ; il en est de même avec les effets des jets de réacteur sur les tourbillons de voilure (fig. 12 eff') [67].

Finalement même à faible incidence, les volets de courbure fortement braqués d'une aile d'avion de transport se trouvent placés dans une situation de grands angles d'attaque ; ils donnent naissance à toute une série de tourbillons (fig. 12g) dont on retrouve l'exacte image dans les sondages de pression totale intéressant le sillage et effectués dans le plan transversal à l'aide du procédé du Dr.CROWDER [33] (fig.16h).

3.7 - Essais en instationnaire -

Autour d'un profil animé d'un mouvement d'oscillations harmoniques en tangage (fig. 13 a-f) ou d'un mouvement de battement avec modulation cyclique de l'incidence (fig. 13 g-k), les différents types de traceurs utilisés (bulles d'air, bulles d'hydrogène émises par une cathode fixe amont ou placée sur le profil, perles de polystyrol ou fils disposés sur le modèle) révèlent les échappements tourbillonnaires qui se produisent à chaque cycle lorsque varie la circulation autour du profil [68] . On sait qu'un tel mouvement d'oscillations en tangage simule la variation cyclique du pas des pales d'un hélicoptère [69 - 71]. Le retard et le caractère tourbillonnaires accentué du décrochement dynamique aux incidences élevées expliquent l'effet d'hystérésis favorable sur la portance moyenne maximale que l'on enregistre en instationnaire sur la pale reculante d'un rotor d'hélicoptère.

Des phénomènes similaires caractérisent l'écoulement tridimensionnel autour d'une maquette d'avion avec voilure en delta (fig. 14 i-p). Les variations cycliques d'intensité des tourbillons observés permettent de mieux interpréter les résultats des mesures effectuées en dynamique au cours d'essais similaires en soufflerie.

Une autre classe d'écoulements instationnaires est celle qui concerne les maquettes animées d'un mouvement de rotation uniforme :

à faible incidence (fig. 14a-d), cette rotation simule un mouvement de tonneau ; à incidence élevée (fig. 14e-h),une vrille "à plat" . Dans les deux cas, les phénomènes tourbillonnaires se développent du côté de la demi-aile descendante et se résorbent du côté opposé [72].

Sur les modèles en mouvement de rotation uniforme, la visualisation peut aussi apporter de précieuses indications sur l'écoulement pariétal : il en est ainsi avec les mini-tufts fluorescents (procédé du Dr CROWDER) collés sur des hélices d'avions en vol et qui révèlent non seulement l'allure des lignes de courant pariétales sur les pales et le moyeu (fig. 15 a), mais aussi la trace du choc près de l'extrémité de la pale en transsonique (fig. 15b) ;

- les émissions pariétales de fumée (fig. 15c), de colorant (fig.15d) et même les bulles d'air (fig.15d')
  mettent aussi en lumière la structure de la transition de l'écoulement le long d'un cylindre dont la
  totalité [73]ou une partie [36] est en rotation.

Un dernier exemple en régime instationnaire concerne les tourbillons marginaux : ce sont les tourbillons qui se forment à l'extrémité des 3 pales d'un rotor rigide placé à une incidence de -45° et en rotation dans un écoulement uniforme [74], le colorant émis en bout de pale révèle l'allure cycloïdale des tourbillons (fig. 15e) ; c'est le tourbillon qui se développe à l'extrémité libre d'une aile rectangulaire de faible allongement placée à 30° d'incidence dans un fluide mis en translation uniforme à partir du repos (fig. 15 fg) [75] : ce tourbillon est visualisé à l'aide de lignes d'émission que l'on peut comparer avec celles obtenues par le calcul (fig. 15 h) qui lui aussi implique une mise en mouvement du fluide à partir du repos [76].

4 - CONCLUSION -

En régime stationnaire comme en régime instationnaire, les différents traceurs utilisés en tunnel hydrodynamique et en soufflerie mettent en lumière les phénomènes caractérisant l'aérodynamique des modèles aux grands angles d'attaque [77]:

- sur les voilures, les décollements se généralisent à partir des bords d'attaque ou de fuite et leur structure devient tourbillonnaire et organisée sur les ailes en flèche accentuée, mais avec la limitation due à l'éclatement des tourbillons ;

- sur les corps fuselés, les tourbillons d'abord symétriques deviennent assymétriques, puis instationnaires quand croît l'incidence ;

- sur les maquettes complètes d'engins et d'avions comportant des combinaisons de ces différents éléments de base, la coexistence de ces différents phénomènes n'est pas sans provoquer de nombreux effets d'interaction, néfastes ou favorables.

Dans ces conditions a pu être vérifiée l'efficacité de différents dispositifs ou procédés destinés à réduire les inconvénients et rétablir un écoulement organisé tels que becs, canards, nageoires, soufflage transversal, etc...

REFERENCES : voir à la fin du texte anglais

MODERN FIGHTER AIRCRAFT DESIGN FOR HIGH-ANGLE-OF-ATTACK MANEUVERING

by

A.M. Skow, Manager, F-5 Aerosciences
G.E. Erickson, Senior Engineer, Aerodynamics Research Department
One Northrop Avenue, Hawthorne, California 90250

CONTENTS

SUMMARY

The design of a fighter aircraft for unrestricted maneuvering to post-stall angles of attack (AOA) can be successfully accomplished if three fundamental areas of design are emphasized:

1. Strict stability criteria for the airframe by careful control of flow breakdown in the leeside of the wing and the fuselage, especially where interactions between the forebody and wings are present

2. Adequate controllability up to α_{max} and down to V_{min} by careful placement and sizing of control surfaces

3. Trouble-free transient operation of the power plant up to α_{max} by careful integration of the propulsion system to preclude engine stall/flameout throughout the flight envelope.

Design methodologies for fighter aircraft that operate at high AOA are discussed. Basic wing design features and the effects of high-lift devices on high-AOA characteristics are presented. Forebody design considerations for high-AOA stability are developed, as are the effects of forebody shape on radar performance. The interaction of the vortex system emanating from the forebody with other vortex systems downstream, such as from a leading-edge extension (LEX) or canard or from a highly swept main wing panel, are shown to be significant.

Control surface placement relative to the wing flowfield and to the vortex flowfield downstream of a highly swept LEX is shown to be important for both stability and controllability. A criterion for high-AOA pitch controllability including the effects of kinematic and inertial coupling is presented.

Inlet design considerations regarding placement relative to the body and wing and the effects of duct geometry on engine compressor face distortion at high AOA are discussed.

1.0 INTRODUCTION

For modern fighter aircraft, flight at high angles of attack (AOA) is an inherent part of both offensive and defensive maneuvering. Even in the early days of air combat, when aircraft had two or more wings and maneuvered at speeds well below 100 knots, the pilots operated their machines to the very edge of their capabilities and to their limits of controllability. The fighter aircraft designer's job in years gone by was relatively straightforward: keep the flow attached. Flow separation meant loss of lift and, usually, loss of control. Pilots today still operate their aircraft at the limits of controllability in serious air combat maneuvering (ACM). The main difference between the fighter aircraft of 1917 and

those of 1982 is that today's designers have significantly extended the speeds at which the maximum maneuver capability is achieved and have significantly increased the AOA to which the aircraft can be controlled.

Typical modern fighter aircraft achieve maximum lift at AOA from approximately 25 to 35 degrees. Aggressive maneuvering can cause pitch overshoots and AOA transients to 60 degrees or more. Assuring adequate controllability of an aircraft flown to AOA as high as 60 degrees is difficult at best, and some designers have been more successful than others.

Since some breakdown of the flow structure around an aircraft operating at a 60 degree AOA is impossible to prevent, the key ingredient allowing some recent aircraft designs to greatly expand the controllable AOA range is the utilization of vortex flows to give some semblance of order to the chaos of separated flow which would otherwise result.

This paper will, therefore, be dominated by discussions of vortex flows around aircraft at high AOA. The wing geometries considered are thin with sharp edges, low-to-moderate aspect ratios, and moderate to high leading edge sweep. The forebodies are slender, appropriate to designs required to operate with low wave drag at supersonic Mach numbers.

2.0 WING DESIGN

Aerodynamic shapes with salient edges often have a fixed line of flow separation at the edge. The flow up to the edge is accelerating, but the flow around it involves retardations that would separate any boundary layer. On thin, sharp-edged wings, the boundary layer on the lower surface cannot negotiate the very large pressure gradients at the leading edge and, consequently, a fixed line of separation exists and a sheet of distributed vorticity is shed at the leading edge. For slender wings, the vortex sheets roll up into the classical leading-edge spiral vortices with concentrated cores, as shown in Figure 1.

Three-dimensional regions of separation exist in many diverse fashions on lifting aerodynamic configurations immersed in flows from subsonic to hypersonic speeds. A common characteristic in all speed regimes (provided the leading edge is subsonic), however, is that the three-dimensional boundary layer detaches from the surface along a swept separation line and, in many cases, rolls up into the vortical motion described above. The scale of the vortical flow relative to the undisturbed boundary layer thickness depends on the configuration, its attitude to the free-stream, and compressibility. Of prime interest is the incompressible flow about slender lifting surfaces at AOA for which the vortex flow is many times greater than the undisturbed boundary-layer thickness, as shown in Figure 2. At high AOA, the flow pattern on slender wings can be dominated by the leading edge separations. The theoretical results presented in Figure 3 (from Reference 1), reveal significant increases in lift above the potential, or attached, flow estimates at high AOA associated with controlled leading-edge separation.
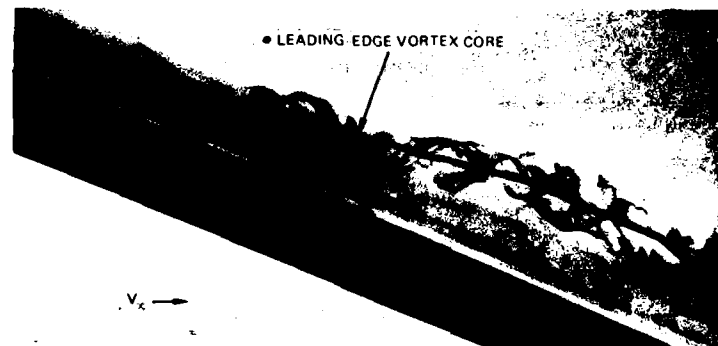
FIGURE 1. LEADING-EDGE VORTEX FLOW ON A SLENDER WING: $a = 20$ DEGREES
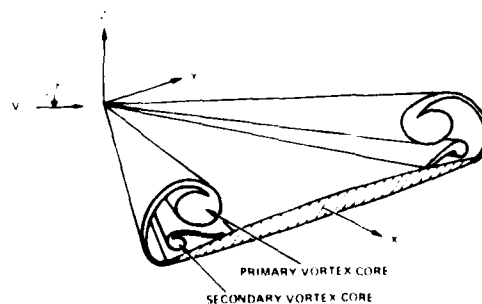
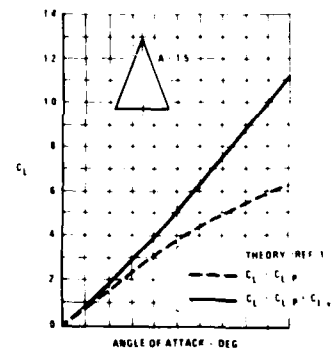FIGURE 2. VORTEX-DOMINATED FLOW ABOUT A
SLENDER WING

FIGURE 3. THEORETICAL LIFT CHARACTERISTICS
ON A SLENDER WING (REFERENCE 1)

Historically, considerable effort has been expended to avoid, or at least minimize, flow separation. Dissipation of the powerful wing-tip vortices on commercial transport aircraft, for example, has become critically important to drag reduction and terminal-area air traffic safety. The application of leading edge vortex-induced lift on commercial and military aircraft became significant as wing aspect ratio decreased. With the advent of commercial supersonic transports (SST), highly maneuverable subsonic transonic fighter aircraft, and the Space Shuttle Orbiter, for example, controlled leading-edge separation was recognized as an important design factor in takeoff, landing, and maneuver performance. Leading edge vortices shed from the thick, rounded-leading-edge, double-delta wing of the Space Shuttle Orbiter are depicted in Figure 4 (from Reference 2). It is evident that thin sections and sharp leading edges are not required for vortex development at high attitudes.

Wing design possibilities featuring vortex flows were suggested by D. Küchemann many years ago (Reference 3). Instead of maintaining a single flow type over a cranked wing (e.g., attached flow) throughout the entire flight range, it was suggested that two flow types be combined. The coexistence of regions of controlled vortex motion and attached flow is the basis of the slender wing and "hybrid" wing designs featured on the Anglo-French Concorde SST and the United States Air Force F-16 and Navy F/A-18 military aircraft. Flow visualization photographs of these configurations are shown in Figures 5 through 7 (References 4 through 6).

FIGURE 4. LEADING-EDGE VORTEX
ON A SPACE SHUTTLE ORBITER
MODEL: a = 20 DEGREES

(a) AND (b) 1/140-SCALE CONCORDE AT 12 DEGREES AOA AND 10-DEGREE SIDESLIP ANGLE (RE - 2 X 10⁴)
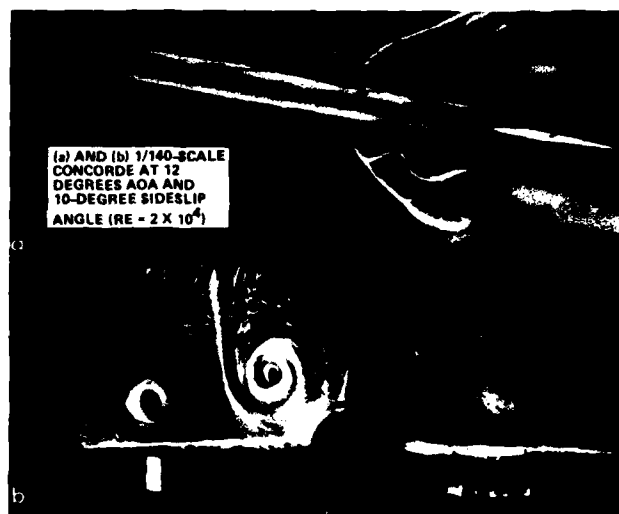
FIGURE 5. VORTEX FLOW DEVELOPMENT ON A CONCORDE SST MODEL
(FROM REFERENCE 4)

LEX VORTEX

VORTEX BREAKDOWN
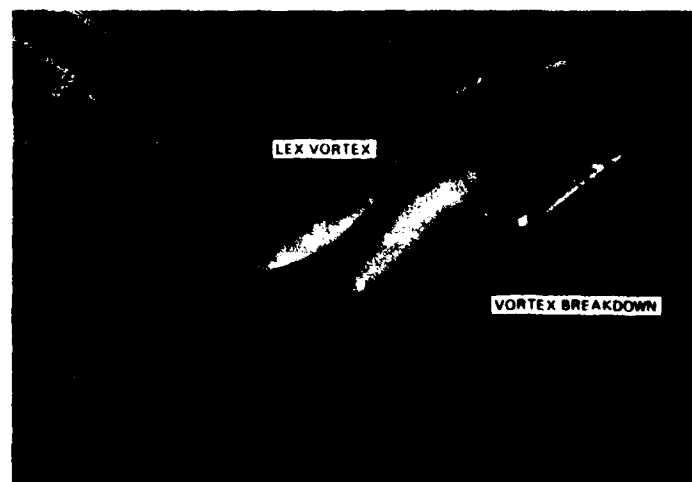
FIGURE 6. LEADING-EDGE EXTENSION (LEX) VORTICES ON THE F-16
(FROM REFERENCE 5)
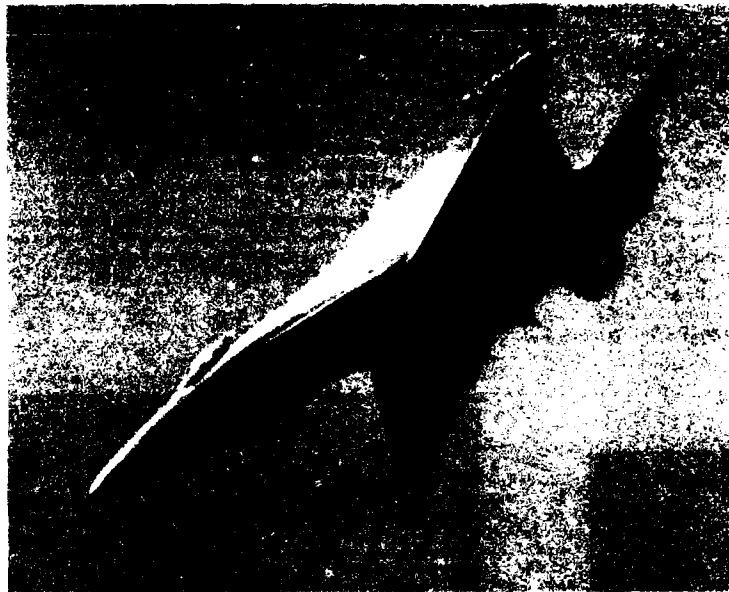
**FIGURE 7. LEADING-EDGE EXTENSION (LEX) VORTICES ON THE F/A-18
(FROM REFERENCE 6)**

First-generation applications of vortex-flow concepts have led to more refined and sophisticated use of these high-energy rotational flows, particularly as they relate to the "cranked" or arrow wings suitable for supersonic cruise fighter aircraft. Concurrent with the large increases in lift on thin, sharp-edged, slender wings at a given AOA are drag increases resulting from a loss of leading-edge suction and, in addition, to the highly nonuniform downwash distribution characteristic of slender wings with vortex flows. Consequently, recent designs (Reference 7) have attempted to "tailor" the wing geometry by suitable twist, camber, and sweep variations. Such designs allow for leading-edge flow separation but tilt the vortex-lift vector forward to provide a thrust component. The "vortex flap" concept (References 8 and 9) is one example of wing design intended to achieve an acceptable compromise between the desired vortex lift and acceptable drag characteristics.

The complexity of the flow about slender wings at high AOA is reflected in the difficulties encountered in developing theoretical models of a leading-edge vortex (Reference 10). Interactions between multiple leading-edge vortices and the inability of the vortex flows to traverse large adverse pressure gradients in the wing flowfield, precipitating vortex "burst," introduce additional complexities. The behavior of leading-edge vortices (vortex trajectory and stability) depends on such parameters as AOA and sideslip; wing sweep; wing leading- and trailing-edge flaps; leading-edge extension (LEX or strake) and canard planform, size, incidence, and dihedral; wing fences and leading-edge discontinuities; and the presence of downstream airframe components such as horizontal and vertical tails.

2.1 Wing Sweep and Angle of Attack Effects on Vortex Core Trajectory

Figure 8 presents the effect of delta wing leading-edge sweep angle on vortex core sweep angle, the latter being measured over the linear region of the core prior to streamwise deflection near the wing trailing edge. An essentially linear relationship exists between the wing sweep and core sweep angles. As far as can be determined in the water tunnel, for the AOA considered (greater than 10 degrees), vortex core sweep for a given wing sweep is relatively insensitive to AOA. The difference between vortex core and wing sweep angles diminishes as wing sweep is increased. Also shown in Figure 8 are experimental results in water and air (from References 11 through 14) obtained at Reynolds numbers from 10^4 to 10^6, which are consistent with the present results.

Variation of vortex core AOA with wing AOA is presented in Figure 9 for a 70-degree delta wing. A linear relationship exists between wing and vortex core AOA, the latter being measured over the region where vortex core height above the wing varies linearly with distance downstream, as shown in Figure 10. For comparison, wind tunnel measurements of vortex core position using a laser anemometer at a Reynolds number of about 10^6 (from Reference 12) are also shown in Figure 9.

2.2 Sideslip Effects on Vortex Core Trajectory

The effect of sideslip on 74-degree delta wing windward and leeward vortex core sweep angles is presented in Figure 10. These water tunnel data indicate that a 5-degree increase in sideslip results in approximately a 1-degree increase and decrease in windward and leeward vortex core sweep angles respectively. Wind tunnel results obtained at a Reynolds number of approximately 3×10^5, based on mean aerodynamic chord and using water vapor (from Reference 15) are also shown in Figure 11, revealing similar trends with sideslip.
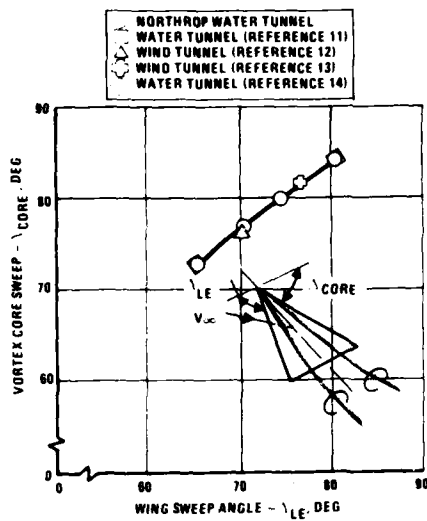
FIGURE 8. EFFECT OF DELTA WING LEADING-
EDGE SWEEP ANGLE ON VORTEX CORE
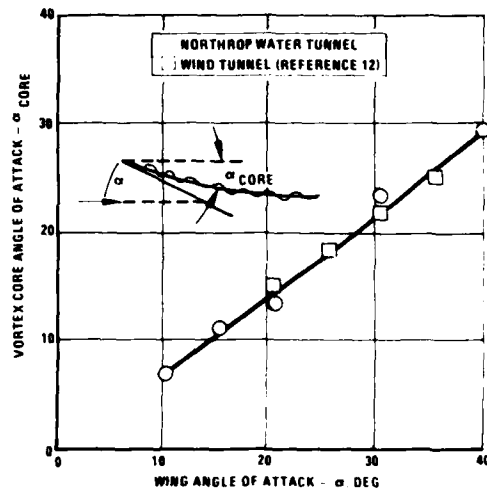SWEEP ANGLE: (σ > 10 DEGREES)

FIGURE 9. EFFECT OF 70-DEGREE DELTA WING AOA
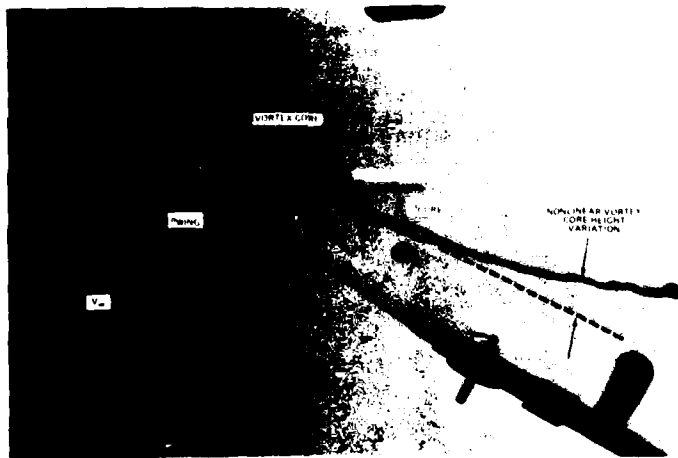ON VORTEX CORE AOA

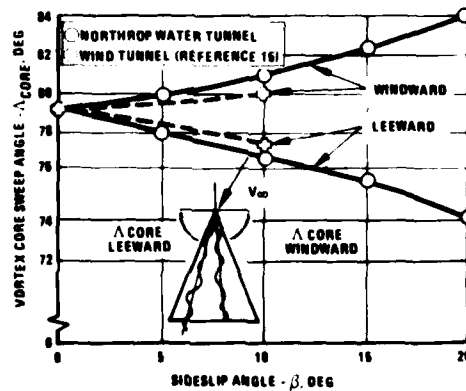FIGURE 10. VORTEX CORE TRAJECTORY ON A SLENDER WING (NORTHROP WATER TUNNEL)

FIGURE 11. EFFECT OF SIDESLIP ON 74-DEGREE DELTA WING
VORTEX CORE SWEEP ANGLES (σ = 20 DEGREES)

In a sideslip condition, the leeward vortex core is displaced outboard and upward over the wing relative to the windward vortex core. This results in an asymmetry in angles between the vortex cores and the wing surface and wing symmetry plane, as shown in Figure 12.

It is interesting to note that at sideslip angles at which the leeward wing leading edge is swept 90 degrees or more, the leading edge is now a "trailing edge" and a discrete vortex is still in evidence. This flow situation, illustrated in Figure 13, is consistent with theoretical flow streamlines presented in Reference 3. A similar vortex motion is observed at the trailing edge of a forward swept wing (Reference 16).

$\alpha = 20^\circ \quad \beta = 0^\circ$

LEEWARD VORTEX CORE

WINDWARD VORTEX CORE

$\alpha = 20^\circ \quad \beta = 15^\circ$
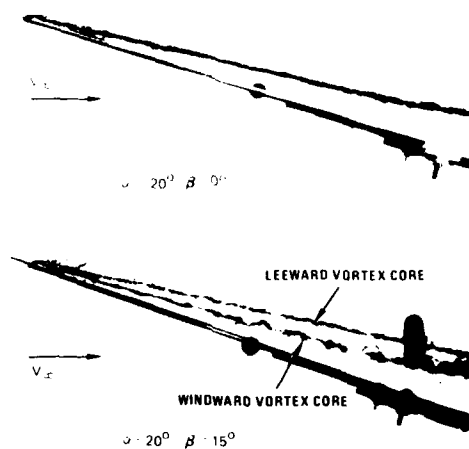
FIGURE 12. EFFECT OF SIDESLIP ON VORTEX CORE
TRAJECTORY: 80-DEGREE DELTA WING

78° DELTA

$\alpha \quad 25^\circ$

$\beta \quad 20^\circ$

VORTEX
CORE

(a) LEEWARD VORTEX CORE TRAJECTORY AT LARGE YAW
ANGLE (NORTHROP WATER TUNNEL)
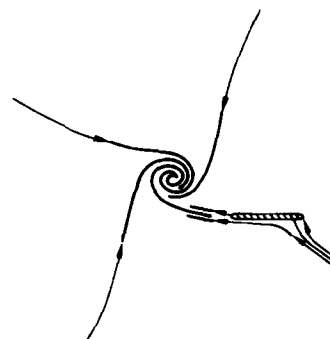
(b) THEORETICAL FLOW STREAMLINES (FROM REFERENCE 3)

FIGURE 13. DELTA WING VORTEX CHARACTERISTICS AT
LARGE YAW ANGLE

2.3 Wing Sweep Effects on Vortex Core Stability

Vortex breakdown is an impressive structural change along the axis of the vortex, and is associ ated with an abrupt axial flow deceleration, expansion of the vortex about a stagnant core, and turbulent flow thereafter. This vortex instability phenomenon, depicted in Figure 14, is influenced by wing sweep, which in turn affects the wing pressure field. The external pressure gradient in the wing potential flow field appears to be a dominant factor in vortex stability at high AOA, although there is as yet no theo retical verification. Because of the strong coupling between the appreciable vortex core axial and swirl velocity components, the core is highly responsive to small perturbations in the external pressure gradient.
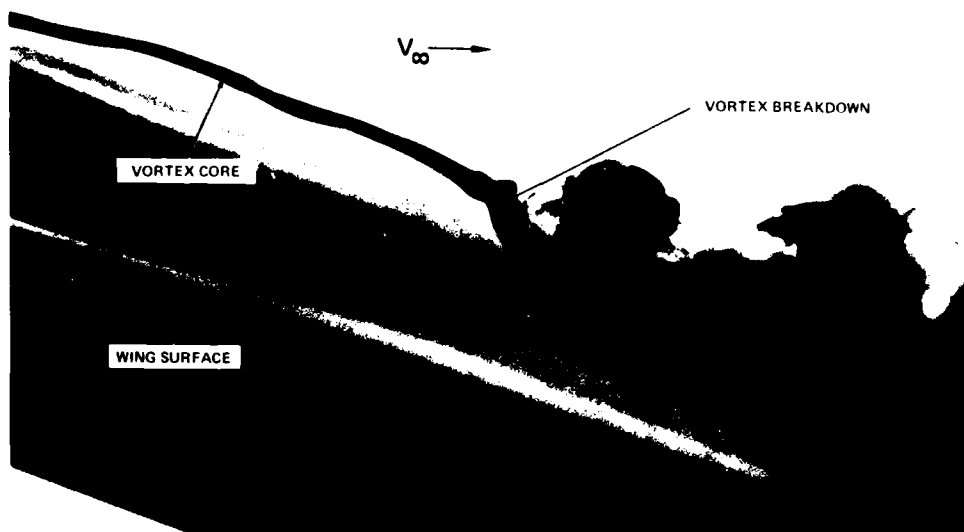
FIGURE 14. LEX VORTEX CORE BREAKDOWN AT 20-DEGREE AOA: CLOSEUP VIEW

Figure 15, which presents data from studies made in the Northrop water tunnel, clearly shows the forward progression of vortex burst point with increased AOA for delta planforms with leading-edge sweep angles ranging from 60 to 80 degrees. Shown in Figure 16 are lift characteristics which indicate that as wing sweep is increased maximum lift tends to coincide with the initial occurrence of vortex burst over the wing surface. The forward progression of core breakdown is more rapid when the burst point is in the region of the wing trailing edge, where external adverse pressure gradients are large, and less rapid as bursting approaches the apex of the wing. Vortex breakdown reaches the trailing edge at a higher AOA as leading-edge sweep angle is increased. This effect is also shown in Figure 17, which presents many burst observations in water and air over a wide range of Reynolds numbers.
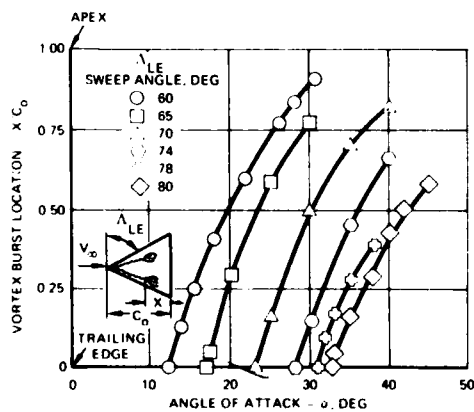
FIGURE 15. WING SWEEP AND AOA EFFECTS ON VORTEX STABILITY
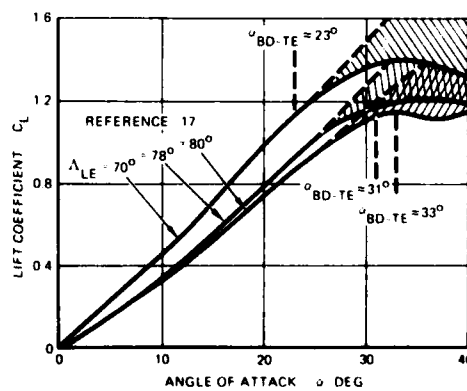
FIGURE 16. NONLINEAR VORTEX - INDUCED LIFT EFFECTS ON DELTA WINGS

Variation of wing sweep with span distance can greatly alter the vortex breakdown characteristics of delta shaped planforms. Figure 18 illustrates the effect of planform contouring on vortex bursting on constant aspect-ratio wings; a high degree of sensitivity is evident. It should be noted, however, that the isolated convex (gothic) planform, which exhibits the poorest vortex burst characteristics, shows a more gradual forward progression of burst location relative to the delta and concave planforms when integrated with a higher-aspect-ratio main wing panel.

	FACILITY	REYNOLDS NUMBER (BASED ON CENTER-LINE CHORD)
NORTHROP	WATER TUNNEL	3.0×10^4
THOMPSON	WATER TUNNEL	9.8×10^3
ERICKSON	WATER TUNNEL	1.0×10^4
POISSON-QUINTON	WIND TUNNEL	1.5×10^6
POISSON-QUINTON	WIND TUNNEL	1.3×10^6
WENTZ & KOHLMAN	WIND TUNNEL	9.0×10^5
HUMMEL & SRINIVASAN	WIND TUNNEL	$1.4 \& 1.7 \times 10^6$
HUMMEL	WIND TUNNEL	2.0×10^6
POISSON-QUINTON	FLIGHT	40.0×10^6
LAMBOURNE & BRYER	WATER TUNNEL	$1.0 \& 3.0 \times 10^4$
CHIGIER	WIND TUNNEL	2.6×10^6
EARNSHAW & LAWFORD	WIND TUNNEL	1.0×10^6
POISSON-QUINTON	WATER TUNNEL	3.0×10^4
LOWSON	WATER TUNNEL	3.0×10^4
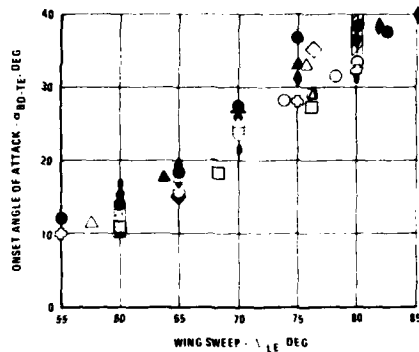
FIGURE 17. EFFECTS OF DELTA WING SWEEP, REYNOLDS NUMBER, AND TEST FACILITY ON VORTEX BREAKDOWN ONSET ANGLE
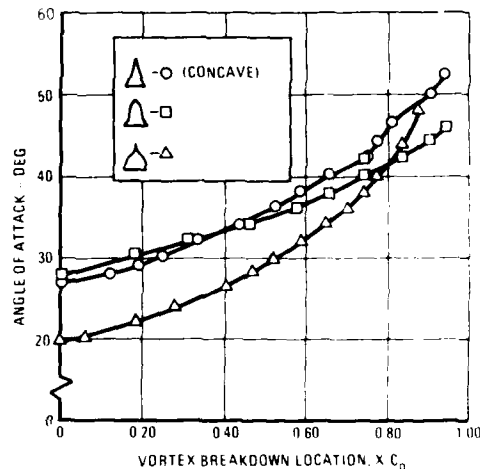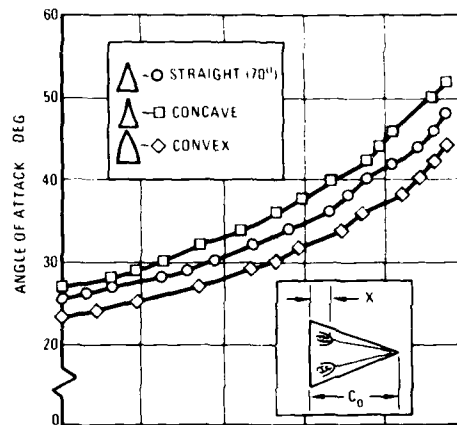
FIGURE 18. EFFECT OF PLANFORM GEOMETRY VARIATIONS ON VORTEX BURST FOR CONSTANT-ASPECT-RATIO WINGS

2.4 Sideslip Effects on Vortex Core Stability

Results depicting the effect of sideslip on leading edge vortex stability are presented in Figure 19 for a 70-degree delta wing. The water tunnel results reveal vortex burst asymmetry due to sideslip, whereby the leeward vortex exhibits greater stability due to the "effective" leading edge sweep increase on the leeward panel. The degree of asymmetry at a given AOA increases with increased sideslip angle.

Vortex burst asymmetry, $\Delta(x/c_0)$, is defined as the difference in burst location over the wing between the windward and leeward sides. Burst location, x, is measured from the wing trailing edge and is normalized by the wing centerline chord, c_0. This parameter correlates with lateral stability trends determined in wind tunnel tests of delta wings (Reference 17) at a Reynolds number of approximately 10^6, as illustrated in Figure 20. Initial reduction in the slope of the lateral stability parameter, C_{l_β}, versus AOA curve corresponds reasonably well with initial vortex breakdown asymmetry. Maximum reduction in lateral stability level occurs at approximately the AOA at which vortex breakdown asymmetry is maximum. Burst position asymmetry is reduced with further increase in AOA, and correspondingly favorable increments in C_{l_β} are observed.
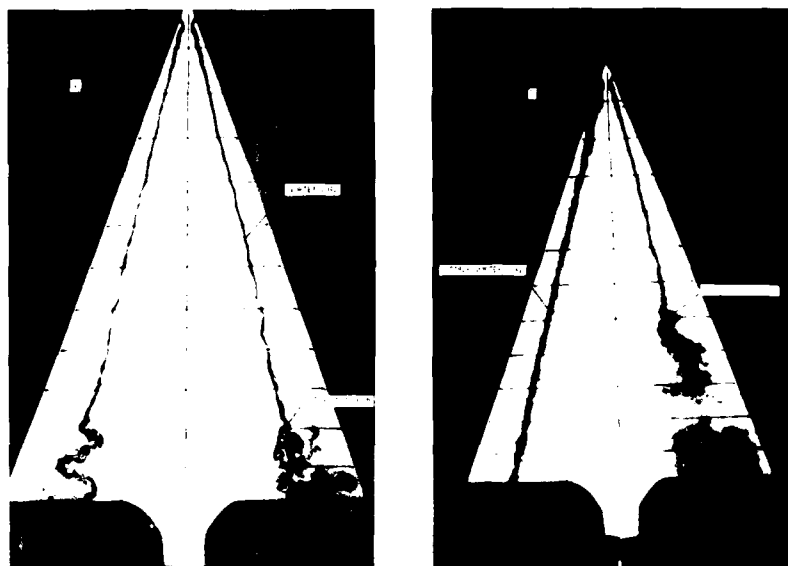
FIGURE 19. EFFECT OF SIDESLIP ON 70-DEGREE DELTA WING VORTEX CORE
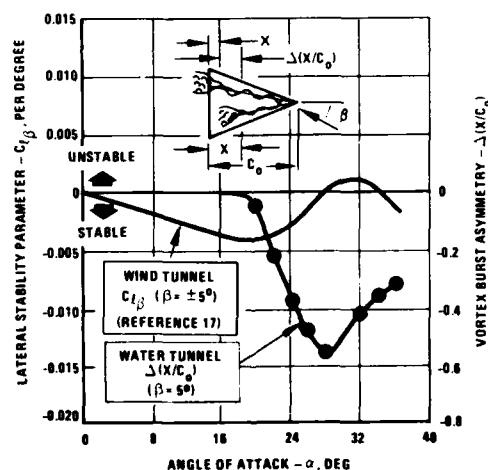STABILITY: $\alpha \approx 25$ DEGREES

FIGURE 20. COMPARISON OF WATER TUNNEL
VORTEX BURST ASYMMETRY AND WIND TUNNEL
LATERAL STABILITY CHARACTERISTICS
(70-DEGREE DELTA WING)

2.5 Leading-Edge Extensions and Canards

Experimental studies and flight tests on a variety of aircraft have shown that significant increases
in maximum lift and reductions in drag at high lift can be obtained by careful generation and control of
concentrated vortices which favorably interact with the flow over a moderate-aspect-ratio main wing
surface. These vortices have been generated by such devices as close-coupled canards and wing LEXs.
These vortex flow-related improvements lead to an increase in maneuvering performance without large
cruise performance penalties. For example, vortex flows developed on canard-wing and LEX-wing geom-
etries have been successfully applied to the Swedish JAKT-VIGGEN, Israeli Kfir C-2, Northrop F-5E/F/G and
YF-17, Air Force/General Dynamics F-16, and Navy/McDonnell Douglas/Northrop F/A-18 fighter configurations.

A favorable flow interaction occurs between a close-coupled canard and main wing panel at high
AOA. The canard downwash reduces the local AOA at wing stations inboard of the canard tip, providing,
in essence, a positive camber effect. Because of canard downwash, the wing leading-edge vortex develop-
ment is of a progressive nature, commencing at wing stations outboard of the canard tip and proceeding
inboard as AOA increases. This spanwise variation of the origin of the wing vortex was observed quite

4-10

clearly in water tunnel flow observations of a scale model of the NASA Rockwell HiMAT configuration (Reference 18). Figure 21 presents a water tunnel photograph of a concentrated wing vortex in the presence of a canard at an AOA of 30 degrees, well beyond the AOA for wing-alone stall.
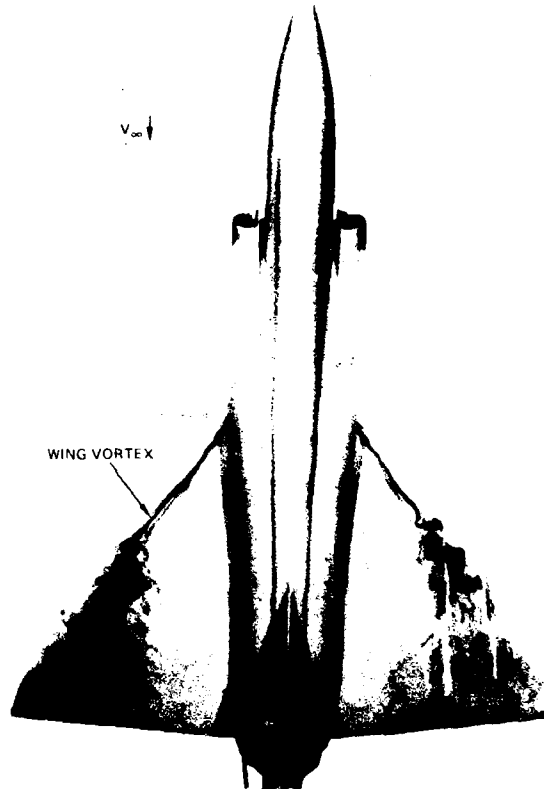

V_∞

WING VORTEX

FIGURE 21. WING VORTEX ON THE SAAB-VIGGEN CANARD-WING AIRCRAFT AT 30-DEGREE AOA (NORTHROP WATER TUNNEL)

A favorable flow interaction also occurs between a highly swept LEX and a higher aspect ratio main wing panel, which delays wing stall to higher AOA. Figure 22 illustrates the induced lift increments that can be generated by LEX vortices. For wing sweep angles generally greater than 40 degrees, this favorable LEX wing flow interaction enables the development of a discrete wing leading edge vortex, the stability of which depends on such factors as LEX planform shape and LEX area. As depicted in Figure 8, a linear relationship exists between wing sweep and vortex core sweep at moderate to high AOA, which provides a means of determining the "effective" increase in wing sweep due to the induced sidewash from the LEX vortex. Figure 23 presents wing vortex core sweep angles determined from water tunnel studies of double delta planforms, general research wing body models, and specific fighter configurations. Results indicate that over a limited AOA range the wing leading edge vortex exhibits a core sweep angle characteristic of a more highly swept planform, as can be seen by comparison with the delta wing alone data in Figure 8.

A qualitative indication of the relative strengths of the LEX and main wing panel vortex flows (for wings of sufficient sweep to develop a discrete vortex) can be gained from water tunnel observations. Studies of slender wings, for example, have revealed increased vortex core axial velocities (observable in the water tunnel by a dye-pulsing technique) and circumferential velocities (qualitative assessment) with increased AOA. Observation of double delta wings reveals distinct and independent forward and aft panel vortices at low AOA, as illustrated in Figure 24, which are indicative of comparable axial and circumferential velocity components. At higher AOA, however, the aft wing vortex is displaced well above the wing and entrained into the dominant forward panel vortex, the latter exhibiting considerably higher axial and swirl velocities. Similar effects are observed on fighter configurations with sufficient wing sweep (around 40 degrees) to allow formation of a concentrated wing leading edge vortex when coupled with a LEX (Figure 25). However, fighter configurations with lower wing sweep (around 30 degrees) do not develop sufficient spanwise flow gradients to enable the formation of a readily apparent wing vortex unless coupled with an unrealistically large LEX or subjected to spanwise blowing for vortex control. As an aside, an alternative concept to a LEX is provided by the Soviet MiG-25 design. This aircraft features long, highly swept, side mounted engine inlets, as shown in Figure 26. Concentrated vortices are developed as a result of flow separation along the sharp edges, as indicated in the figure. This aircraft is, however, not maneuvered at AOAs that would produce these vortex patterns.
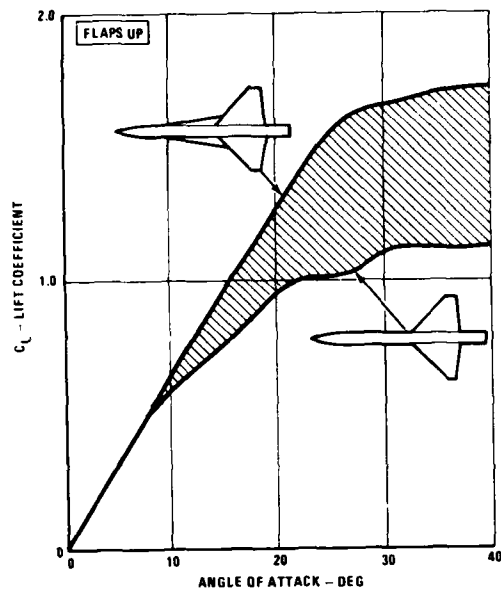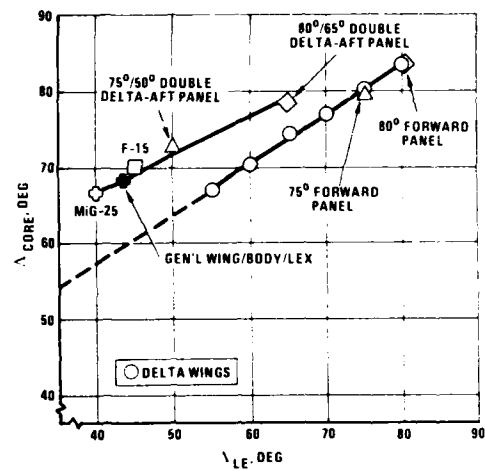
FIGURE 22. EFFECT OF LEADING-EDGE EXTENSION
(LEX) ON LIFT

FIGURE 23. WING PANEL VORTEX CORE SWEEP
ANGLE IN THE PRESENCE OF HIGHLY
SWEPT FORWARD PANEL

(a) α = 8.5 DEGREES
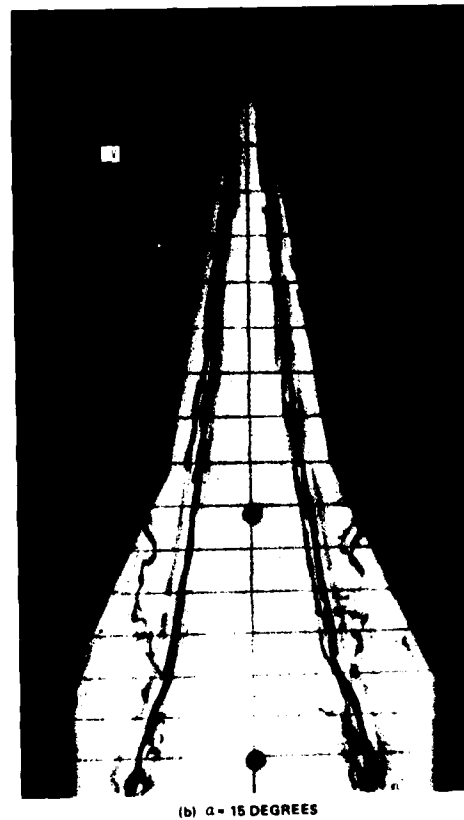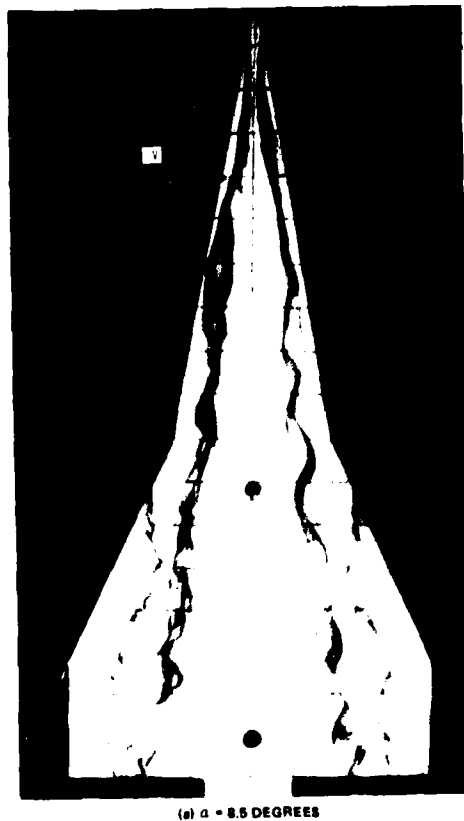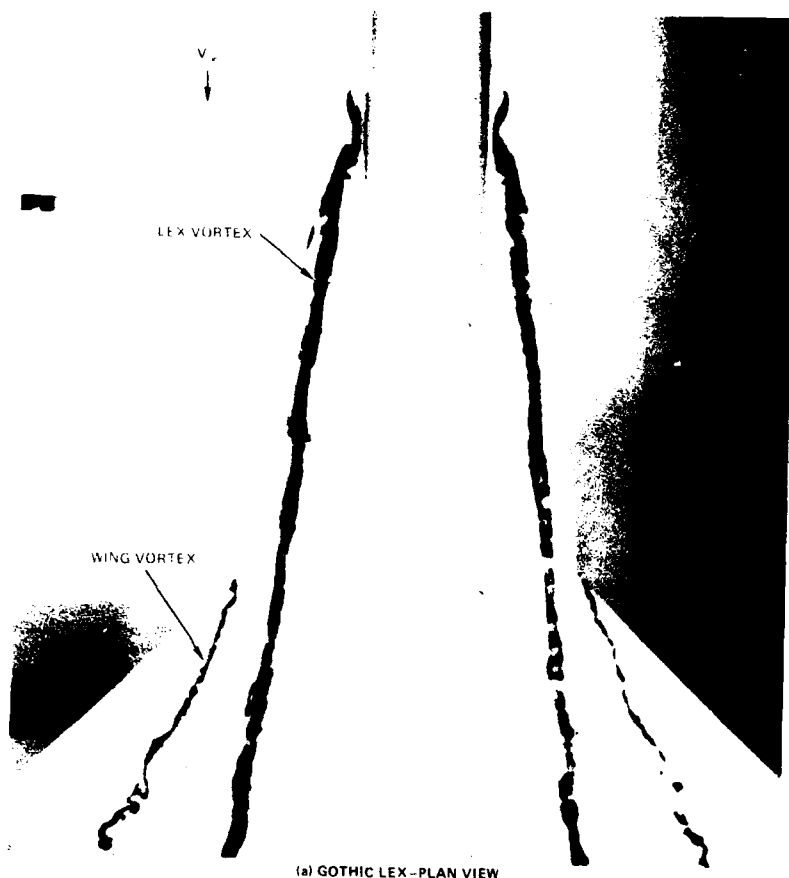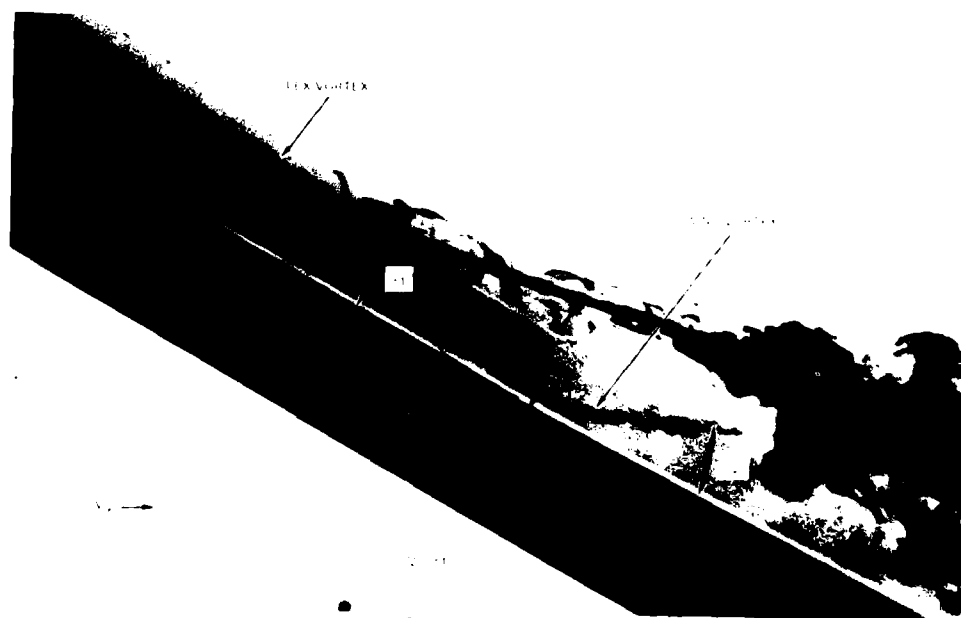
(b) α = 15 DEGREES

FIGURE 24. LEADING-EDGE VORTEX DEVELOPMENT ON A DOUBLE DELTA WING
AT LOW AND HIGH AOA

(a) GOTHIC LEX – PLAN VIEW

(b) GOTHIC LEX – SIDE VIEW

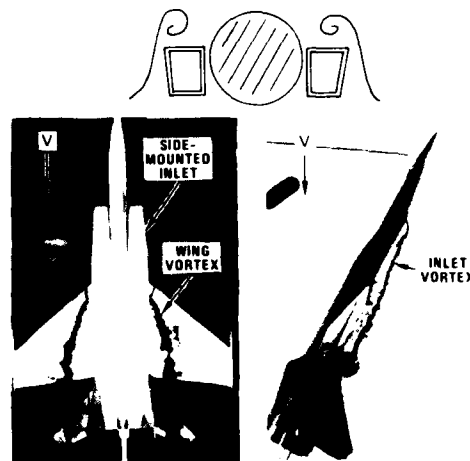FIGURE 25. LEX VORTEX-INDUCED EFFECT ON MAIN WING PANEL (NORTHROP WATER TUNNEL)

**FIGURE 26. VORTEX DEVELOPMENT ON A HIGHLY SWEPT
ENGINE INLET: SOVIET MIG-25**

The flow interactions associated with canard-wing and LEX-wing arrangements differ and, consequently, a brief discussion is warranted. At high AOA mixed regions of potential and vortex flow exist on the main wing panel. In the presence of a canard, the progressive wing vortex development and the persistence of the vortex at high AOA are primarily the result of the canard downwash field. In the presence of a highly swept LEX, a region of attached flow exists at inboard wing stations due to vortex induced downwash. Much of the lift benefits on the wing, however, are derived from the strong LEX vortex-induced upwash and sidewash at wing stations outboard of the LEX-wing junction. In terms of exposed area, a wing LEX appears a somewhat more effective means of lift augmentation relative to a canard of similar size.

The advancement of forward-swept wing (FSW) technology has posed interesting challenges to the effective application of lift enhancement devices such as canards and LEXs. In the case of an aft-swept main wing, such devices are ineffective in delaying the onset of tip stall. Furthermore, the canard and LEX downwash reduces the local lift at inboard wing stations. It is evident, then, that the full lifting capability of the wing is still not utilized at high AOA. Forward-swept wing stall occurs initially at the wing root, as shown in Figure 27, whereas the outboard wing sections maintain attached flow up to very high AOA. Because of the increased positive pressure gradients near the wing root, a LEX is ineffective due to the inability of the vortex to traverse this adverse flowfield (LEX vortex breakdown is discussed below). Furthermore, the LEX vortex-induced upwash and sidewash are opposite to that desired on an FSW. A close coupled canard, however, is an appealing concept when integrated with an FSW. The canard downwash at inboard wing sections, together with the outboard attached flow characteristic of an FSW, offers the possibility of maintaining attached flow on the wing over a large portion of the flight regime.

The generation of vortex induced lift results in an extension of the maneuvering AOA range of the aircraft, which in turn requires that longitudinal- and lateral directional stability and control be maintained in this extended AOA range. Several factors can limit the maneuver performance improvement that can be obtained with a LEX wing combination. Such factors as an abrupt loss of longitudinal or directional stability at high AOA or a loss of lateral stability at high sideslip angles can limit maneuver performance. For wing geometries that develop large amounts of vortex lift, the cause of these problems in flight mechanics can often be attributed in large part to the same fluid mechanics phenomenon; a breakdown of the LEX vortex system. This breakdown limits the maximum lift and can occur in a symmetric or asymmetric manner, depending on the sideslip angle. Asymmetric LEX vortex breakdown on an advanced fighter model is depicted in the flow visualization photograph in Figure 28.

In a sideslip condition, LEX vortex breakdown becomes asymmetric due to an effective increase in the sweep angles of the leeward LEX and wing and a reduction in the windward LEX and wing sweep angles. This is shown schematically in Figure 29 for a fighter configuration. Asymmetric vortex bursting over the wing panels appears to be a strong contributor to the highly nonlinear lateral-directional stability characteristics observed at high AOA in wind tunnel tests of fighter configurations (Reference 19). The asymmetric vortex burst promotes changes in the flowfield at the vertical tails and causes differences in vortex lift between windward and leeward wing panels. If this flow asymmetry is sufficiently strong, a reduction, or loss, of lateral and directional stability can occur. The violent nature of asymmetric vortex bursting has been observed in low-speed wind tunnel tests (Reference 20), where a sting-mounted model oscillated about the body axis. In addition, vortex bursting has been detected by fighter pilots by a sudden increase in noise level outside the cockpit. Examples of the effects of asymmetric LEX vortex bursting are depicted in Figures 30 to 32. Data shown in Figures 31 and 32 indicate significant differences in windward and leeward LEX vortex burst positions at high AOA and corresponding unstable variations of rolling moment with AOA respectively. Examples of directional sensitivity associated with vortex behavior on fighter aircraft with small and large LEXs is provided in Figures 33 and 34. Although the development of powerful vortices is desirable in terms of maximum lift, the LEX vortices can be a source of large unstable variations in lateral characteristics. This is shown quite dramatically in Figure 35. Consequently, a compromise must be made during the design of a slender wing between maximum lift, which varies directly with LEX area, and lateral stability, which necessitates a limit to LEX size.

FIGURE 27. FLOW CHARACTERISTICS ON A FORWARD
SWEPT WING (NORTHROP WATER TUNNEL)

FIGURE 27. FLOW CHARACTERISTICS ON A FORWARD
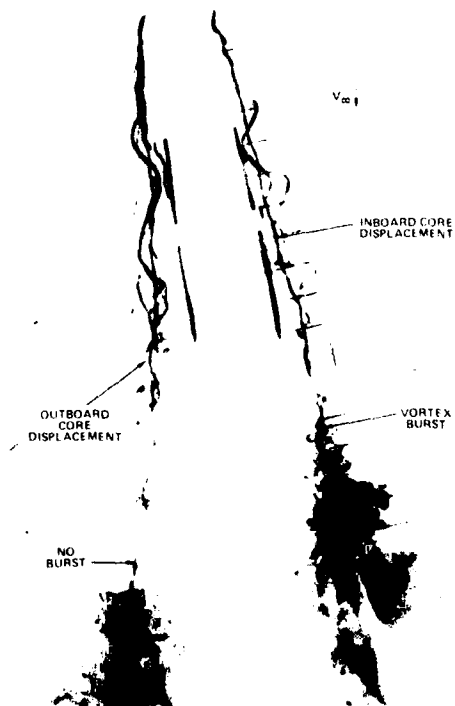SWEPT WING (NORTHROP WATER TUNNEL)
(Continued)

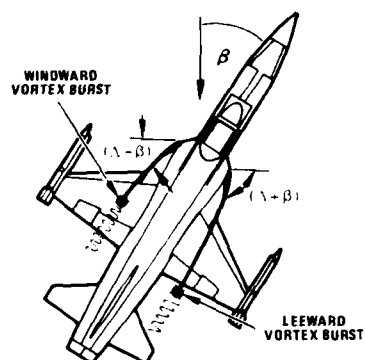FIGURE 28. ASYMMETRIC LEX VORTEX BREAKDOWN
IN SIDESLIP

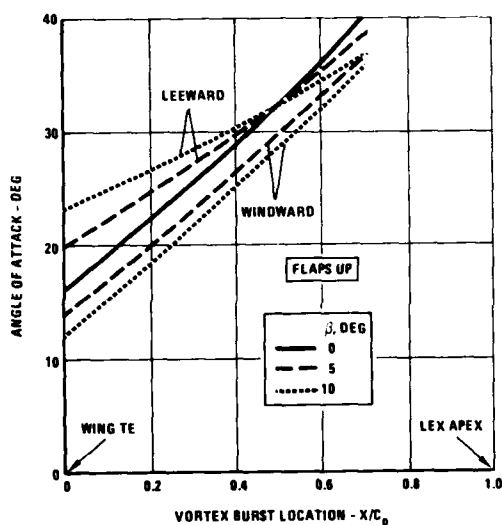FIGURE 29. ASYMMETRIC VORTEX BURSTING
DUE TO SIDESLIP

FIGURE 30. VORTEX BREAKDOWN POSITIONS IN
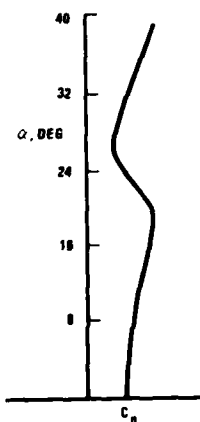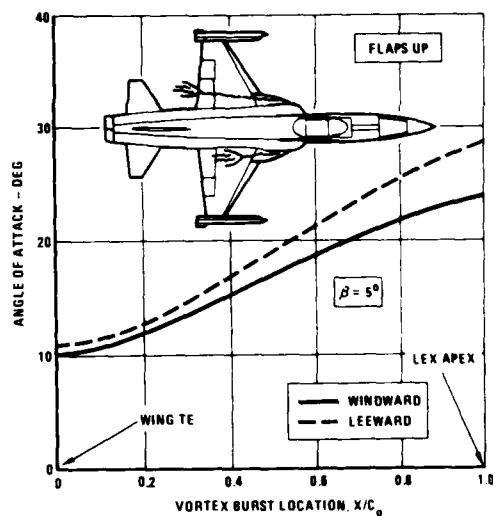SIDESLIP ON A FIGHTER MODEL WITH
SMALL LEX (WATER TUNNEL)

FIGURE 31. VORTEX BREAKDOWN POSITIONS IN
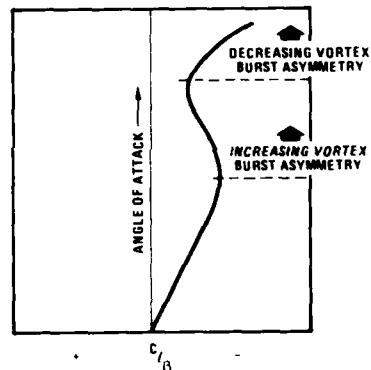SIDESLIP ON A FIGHTER MODEL WITH
LARGE LEX (WATER TUNNEL)

FIGURE 32. LATERAL STABILITY TRENDS
OF A FIGHTER AIRCRAFT WITH
LEADING-EDGE EXTENSIONS

FIGURE 33. YAWING MOMENT VARIATION
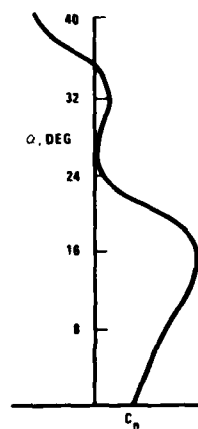WITH AOA: FIGHTER AIRCRAFT
MODEL WITH SMALL LEX

FIGURE 34. YAWING MOMENT VARIATION
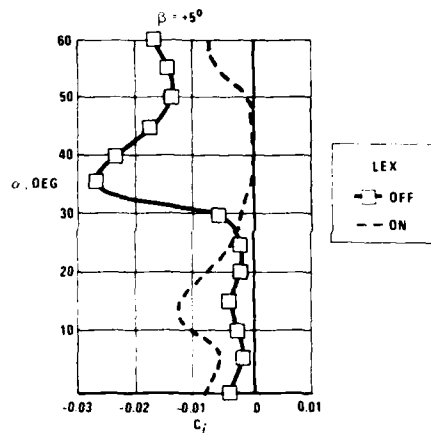WITH AOA: FIGHTER AIRCRAFT
MODEL WITH LARGE LEX

FIGURE 35. LEX EFFECTS ON ROLL AND YAW MOMENT
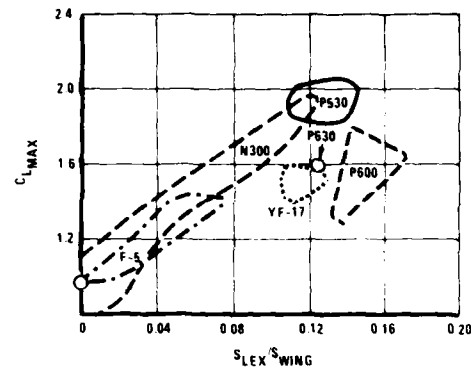VARIATIONS WITH AOA AT CONSTANT SIDESLIP

FIGURE 36. LEX AREA EFFECTS ON LIFT
(FROM REFERENCE 19)

The effects of LEX area on the lift characteristics of fighter configurations are shown in Figure 36 (from Reference 20). Concurrent with the lift increase due to increased LEX area is an improvement in LEX vortex stability at a given AOA, as shown in Figure 37 (LEX vortex behavior also depends on planform geometry). Theoretical and experimental studies (Reference 21) have shown that LEX shapes characterized by leading edge suction distributions that peak at the tip, i.e., "gothic" planforms, develop vortex flows of increased stability at high AOA relative to a triangular shaped planform. A comparison of vortex behavior on such LEX shapes is shown in Figure 38, which depicts smoke flow visualization in a wind tunnel of a fighter aircraft model. Abrupt variations in local leading edge sweep angle can, in
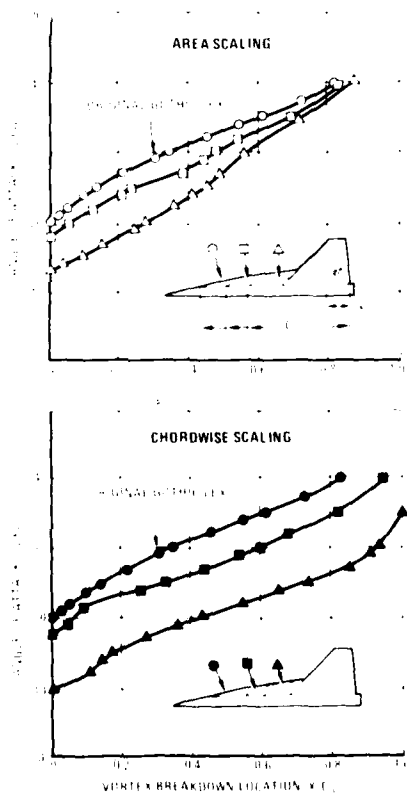

FIGURE 37. EFFECT OF AREA AND CHORDWISE
SCALING ON VORTEX BREAKDOWN
CHARACTERISTICS OF GOTHIC LEX

FIGURE 38. EFFECT OF LEX PLANFORM CURVATURE ON
VORTEX STABILITY: a = 30 DEGREES

some cases, promote the development of multiple vortices. In the extreme, a double-delta wing is an example of an abrupt discontinuity in the vortex-feeding mechanism, causing more than one vortex to be shed along the span. The presence of LEX boundary layer bleed slots, which are intended to prevent ingestion of low-energy boundary-layer fluid into side-mounted, under-wing engine inlets, can also result in multiple-vortex shedding, even on a LEX planform of continuous sweep variation. Slot flow entrainment effects can be of such a magnitude that available lower surface fluid, which separates at the leading-edge to "feed" into the LEX vortex, is severely restricted. The local reduction in vorticity shedding is similar to the effects associated with a planform with leading-edge sweep discontinuities. LEX vortex behavior can also be influenced by LEX thickness and camber and leading-edge radius which, when increased, delay flow separation and hence reduce vortex strength at a given AOA. LEX dihedral anhedral and LEX incidence angle relative to the wing plane are all means by which vortex behavior can be affected.

Comparison of vortex breakdown characteristics determined in a water tunnel with subsonic wind tunnel data indicates that a highly swept planform integrated with a higher-aspect-ratio main-wing surface develops maximum lift at an AOA at which breakdown of the forward panel (or LEX) vortex occurs near the LEX-wing junction or LEX apex, depending on LEX area. On F-18-type LEXs the former applies, whereas the latter appears applicable to F-5-type LEXs. Figures 39 through 41 present measured lift and pitching moment characteristics along with vortex breakdown progression for double-delta; general, reflective LEX-wing combinations; and a specific fighter configuration.
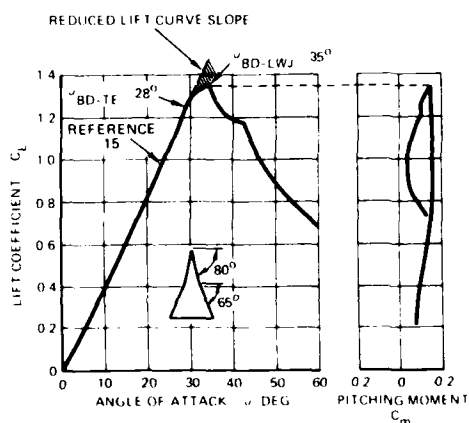

FIGURE 39. LIFT AND PITCHING MOMENT
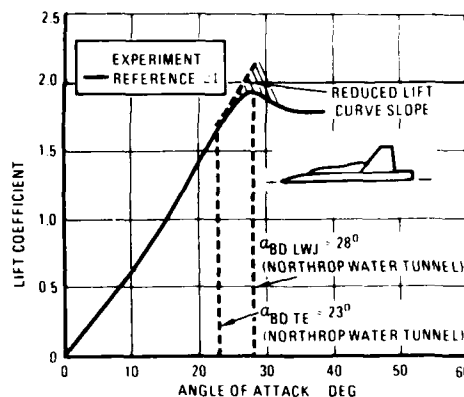CHARACTERISTICS OF A DOUBLE
DELTA WING

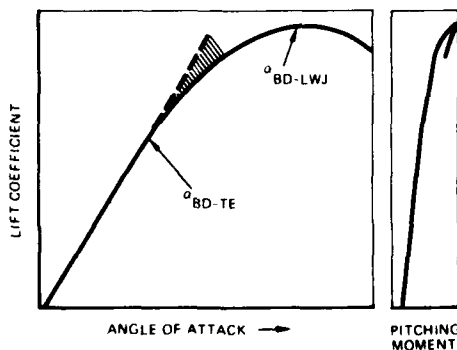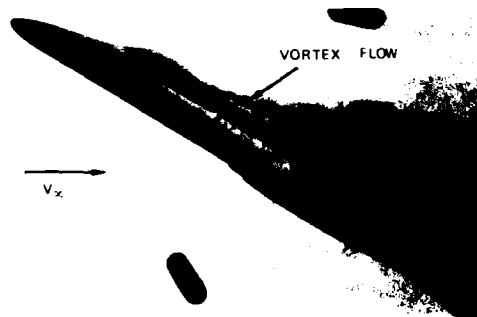FIGURE 40. LIFT CHARACTERISTICS OF LARGE
REFLEXIVE LEX/WING CONFIGURATION

FIGURE 41. LIFT AND PITCHING MOMENT TRENDS OF A FIGHTER AIRCRAFT

2.6 Leading and Trailing Edge Flap Effects

Deflection of a leading edge flap has a stabilizing influence on the leading edge vortex since it reduces the pressure peak and the associated positive pressure gradient near the wing nose. This effect is illustrated in the water tunnel flow visualization photographs of a slender wing in Figure 42. Concurrent with an increase in vortex stability is a change in vortex trajectory, as seen in the plan views in Figure 42.
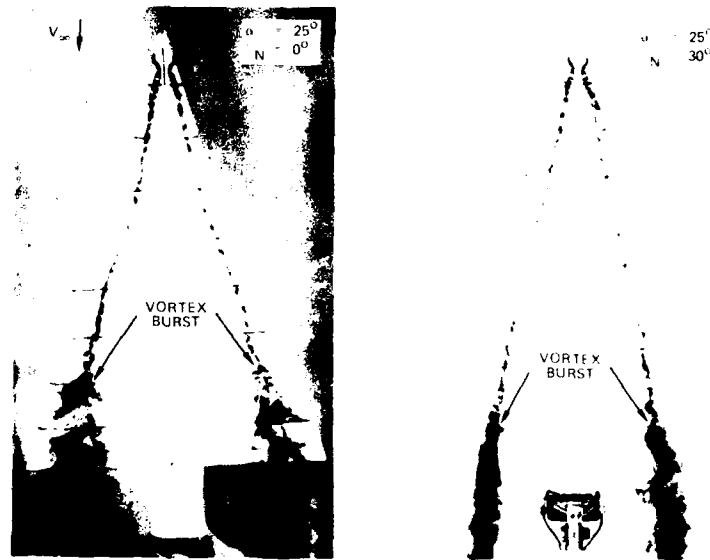

FIGURE 42. EFFECT OF DEFLECTED LEADING-EDGE FLAPS ON SLENDER WING VORTEX BEHAVIOR (NORTHROP WATER TUNNEL)

Similar effects are evident on LEX wing geometries, where deflection of the main wing leading edge flap can result in a significant increase in AOA for vortex bursting at the trailing edge of the wing. Results obtained on a 12 percent scale model of the Northrop P 530, where LEX vortex burst was visualized by smoke injection, are shown in Figure 43 (Reference 20).

A deflected leading edge flap reduces the vortex induced lift, i.e., the vortex strength is reduced at a given AOA. This effect can be viewed in a qualitative manner in a water tunnel facility by observing the less tightly wound vortex flow with flaps down. Improvement of wing efficiency by leading edge camber will reduce LEX effectiveness. This is analogous to the reduced effectiveness of spanwise blowing near the leading edge for vortex enhancement due to deployment of leading edge flaps.

A promising means of improving drag characteristics at cruise and maneuver conditions is to "force" the flow to separate in a controlled manner at the leading edge, roll up into a discrete vortex core, and confine the vortex to a region near the leading edge by suitable contouring of the wing profiles. Drag benefits are thus made possible by allowing the vortex to run along a sloping surface with a forward-facing component in streamwise projection, as shown in Figure 44. Utilization of vortex flow for drag reduction is based on experimental and theoretical observations on wings at high AOA at which flow separation occurs at the flap leading edge. The subsequent formation of a primary leading edge vortex on the deflected flap can result in induced drag benefits due to the vortex suction pressures acting on the forward-facing surface.

Such concepts were examined at Northrop during the development of the YF-17 leading edge extension (Reference 20) and in water tunnel studies of slender wings suitable for supercruise fighter designs (unpublished data), at NASA Langley Research Center on supercruise configurations (Reference 7), and at Boeing on commercial SST and supercruise fighter configurations (Reference 9).

Vortex flows are not easily controlled, however, due to the sensitivity of the core to external disturbances. For example, concurrent with vortex core trajectory changes due to leading edge contouring is a reduction in vortex stability. Furthermore, attainment of drag benefits by "forcing" the vortex to act on a sloping surface is, in general, accompanied by a reduction in vortex-induced lift.

For the 74 degree delta wing shown in Figure 45, a leading-edge tab was added to the deflected flap so that the tab deflection was zero relative to the wing plane. The resultant leading edge flap arrangement is similar to the "vortex flap" concept discussed in Reference 9. Water tunnel observations on this "stepped wing" arrangement shown in Figure 45 indicate that the primary apex vortex stability increase associated with the deflected leading-edge flap is lost when the tab is present. This is due to

the reduction in vorticity available for feeding into the primary apex vortex pair. Water tunnel observations reveal the presence of a primary vortex flow commencing at low AOA within the confines of the flap arrangement. The "trapped vortex" tends to remain within this leading-edge channel for a limited distance downstream. The downwash induced by this vortex prevents flow separation from occurring at the flap hingeline. The resultant flow situation is similar to the flow about a wing with a large leading edge radius. As the vortex grows in size, however, the core trajectory abruptly turns streamwise, "escaping" the channel. A corresponding increase in drag would be expected due to this vortex "breakaway" phenomenon.
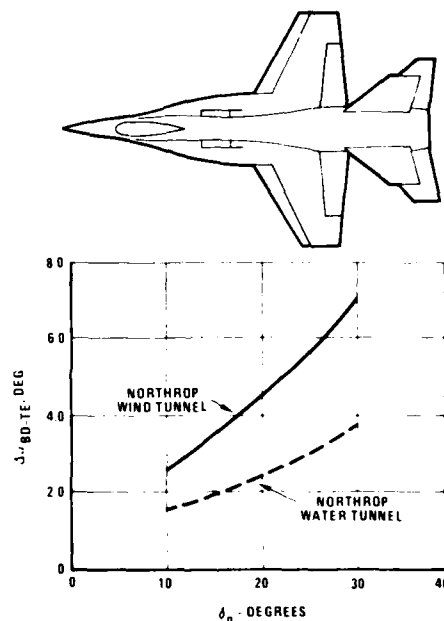
FIGURE 43. LEADING-EDGE FLAP EFFECTS ON LEX VORTEX BREAKDOWN AT THE TRAILING EDGE (WATER TUNNEL-DYE INJECTION; WIND TUNNEL-SMOKE INJECTION)
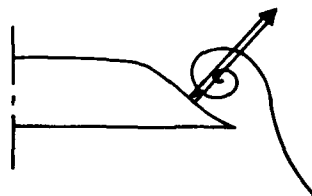
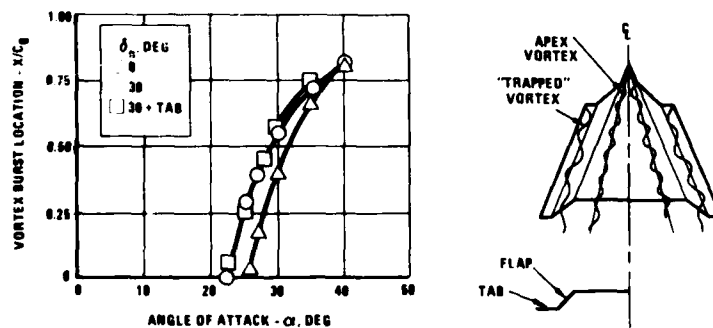FIGURE 44. LEADING-EDGE VORTEX ON A CONTOURED LEADING EDGE

FIGURE 45 "VORTEX FLAP" EFFECT ON 74-DEGREE DELTA WING APEX VORTEX STABILITY

Several vortex flap arrangements have also been assessed (Reference 8). It was found during low speed wind tunnel tests that the most favorable flap geometries produced total leading edge suction values approaching the optimum level predicted by theory (Reference 22).

A variation of the vortex flap concept features an extension of the leading-edge flap above the wing surface. This inverted leading edge flap arrangement has been investigated in References 23 and 24, for example. The purpose of inverted flaps is to generate vortex-induced lift increments at low AOA for takeoff and approach conditions. The problem associated with this concept, however, is that the increased vortex strength at low AOA is compromised to a certain extent by a displacement of the vortex away from the wing surface. This effect is more pronounced at higher AOA and, in addition, premature wing stall is promoted. Combining inverted leading-edge flaps with a propulsive lift enhancement concept has been shown (Reference 25), however, to generate very large vortex-induced lift increments over a wide range of AOA. In fact, the combination of inverted leading- and trailing-edge flaps with spanwise blowing promotes the formation of a dual-vortex system within the upper surface channel, as shown in the helium bubble photograph in Figure 46 (Reference 26). Comparison of experimental lift character istics with theoretical estimates of a very thick, highly cambered wing section (Figure 47) suggests that the dual vortex system induces an "effective" thickness and camber, as might be inferred from the flow visualization photograph.

"LOCKED VORTEX" WING EXPERIMENT (REFERENCE 25)
C_μ
○ 0
□ 0.3
△ 0.4

THICK, HIGHLY CAMBERED WING SECTION THEORY (INVISCID, INCOMPRESSIBLE) (REFERENCE 26)

——— 2-D

— — — 2-D CORRECTED TO 3-D
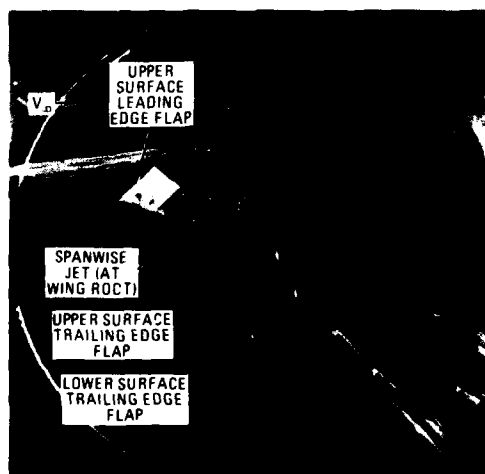
FIGURE 46. STREAKLINES ABOUT "LOCKED VORTEX" WING USING HELIUM BUBBLE FLOW VISUALIZATION TECHNIQUE: ⌐ = 20 DEGREES (FROM REFERENCE 26)
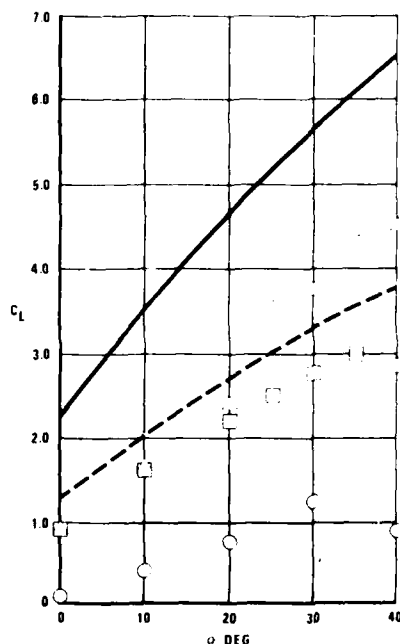
FIGURE 47. "LOCKED VORTEX" WING (UNSWEPT) LIFT CHARACTERISTICS AND THEORETICAL LIFT ESTIMATES FOR A THICK, HIGHLY CAMBERED WING SECTION

Vortex core trajectory and stability are also affected by downward deflection of a plain trailing edge flap. At low AOA, where the wing positive pressure gradients are not large, trailing edge flap deflection increases vortex strength without promoting vortex breakdown and, in addition, the vortex core tends to follow the curvature of the wing.

The latter effect is vividly illustrated in the wind tunnel smoke flow visualization photograph in Figure 48 (Reference 20). At high AOA, however, trailing-edge flap deflection sufficiently increases the adverse pressure gradients near the wing trailing edge to cause a reduction in vortex stability. The maximum vortex-induced lift increment is reduced since the vortices burst at a lower AOA. Increased trailing-edge flap deflection angle results in a further reduction in vortex stability at a given AOA, as illustrated in Figure 49. This flap effect is evident, in general, throughout the high-AOA range, which is indicative of the effective increase in AOA due to positive aft camber. Although the water tunnel observations in Figure 49 underpredict wind tunnel results due to viscous effects (Reference 16), the trends are representative.

It is not intended to leave the impression that a trailing edge flap deflection is undesirable. A deflected trailing-edge flap increases the potential flow lift so that, for a constant lift coefficient, less vortex lift and less AOA are required.

The premature vortex bursting at high AOA can promote an increase in lateral stability, as shown in Figure 50 for a twin jet fighter configuration. In sideslip conditions, water tunnel observations indicate that a deflected trailing edge flap tends to reduce vortex burst asymmetry at high AOA. The low speed wind tunnel data in Figure 50 are consistent with the flow surveys, revealing an increase in lateral stability due to flap deflection. Since the primary contributor to static lateral stability is the wing, the increase in lateral stability may be associated with a reduction in vortex burst asymmetry.

LEX VORTEX CORE
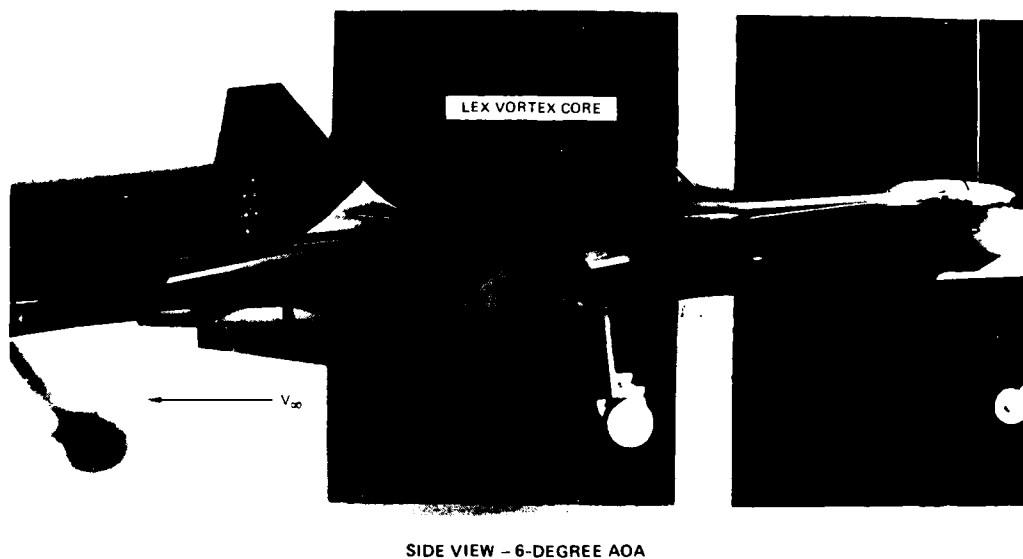
V_∞

SIDE VIEW – 6-DEGREE AOA

FIGURE 48. NORTHROP WIND TUNNEL SMOKE FLOW VISUALIZATION OF A LEX VORTEX CORE AT LOW AOA (FROM REFERENCE 20)
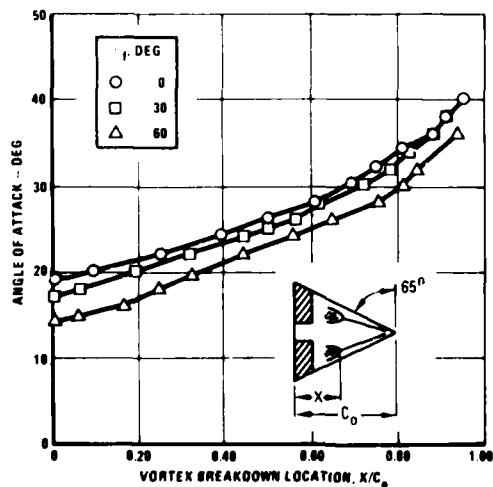

FIGURE 49. EFFECT OF DEFLECTED TRAILING-EDGE FLAP ON VORTEX BREAKDOWN CHARACTERISTICS OF 65-DEGREE DELTA WING.
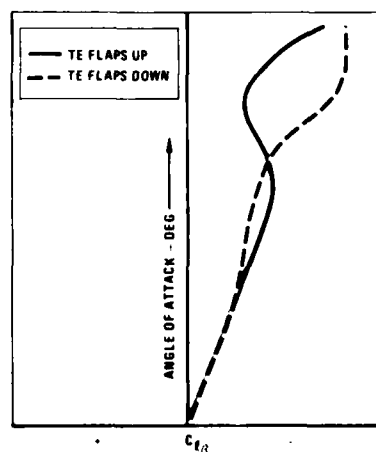

FIGURE 50. EFFECT OF DEFLECTED TRAILING-EDGE FLAPS ON LATERAL STABILITY TRENDS OF A FIGHTER AIRCRAFT.

It is noted that the beneficial effects on vortex stability due to deflected leading-edge flaps can be offset at high AOA by the early vortex breakdown promoted by a simultaneously deflected trailing-edge flap. This effect is illustrated in Figure 51 for a cranked wing planform.

2.7 Upper-Surface Fences and Leading Edge Discontinuities

Improvements in lift at high AOA and/or longitudinal- and lateral-directional stability may be achieved by incorporating certain features into the wing design (e.g., wing upper surface fences and leading-edge discontinuities, or "snags").

On a slender wing at high AOA, a wing snag promotes an earlier breakdown of the primary wing leading-edge vortex, shown in Figure 52, due to the abrupt discontinuity of the vorticity feeding mechanism along the leading edge. The snag creates two vortices that rotate in opposite sense. The vortex that forms at the notch has a sense of rotation that tends to inhibit outboard spanwise flow, causing a premature breakdown of the wing leading-edge vortex. A second primary vortex emanates from the snag leading edge and is of the same rotational sense as the wing vortex shed inboard of the leading-edge discontinuity. This outboard vortex improves the flow over the outboard wing panel and can provide an improvement to the induced lift and the longitudinal- and lateral stability due to delayed wing tip stall. Figure 53, from Reference 27, illustrates the effect of a snag on a fighter model with LEX-wing geometry.
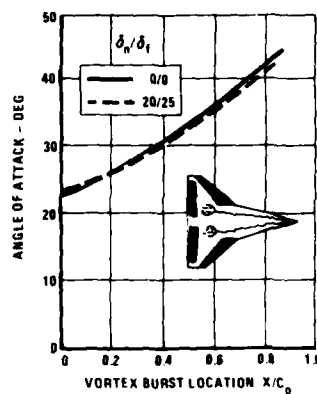
FIGURE 51. EFFECT OF SIMULTANEOUS
DEFLECTION OF LEADING- AND
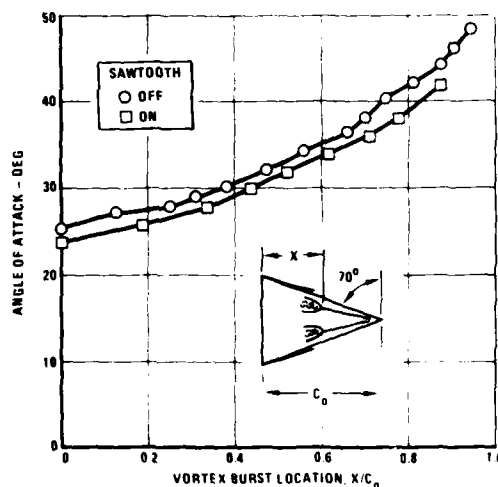TRAILING-EDGE FLAPS ON VORTEX
BREAKDOWN ON A SLENDER WING

FIGURE 52. EFFECT OF LEADING-EDGE SAWTOOTH ON
VORTEX BREAKDOWN CHARACTERISTICS
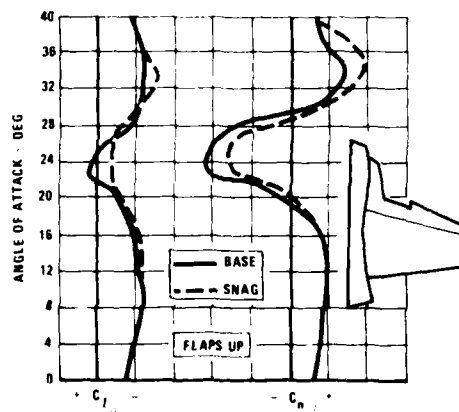OF 70-DEGREE DELTA WING

FIGURE 53. EFFECT OF SNAG ON LATERAL-DIRECTIONAL
STABILITY CHARACTERISTICS (FROM REFERENCE 27)

The development of spanwise-distributed vortices shed from several snags on a highly swept wing is, in theory, one means of providing a more uniform downwash distribution and, hence, improved drag characteristics. In practice, however, it is difficult to generate such a flowfield without adverse mutual interaction between the multiple shed vortices. A "scalloped" wing (Reference 28) may avoid such interaction but, in general, the development of several vortices shed from surfaces of short generating length appears less practicable than a single vortex emanating from a surface of long generating length. It is interesting to note, however, that upon microscopic examination of an owl's wing (Reference 29), much of its efficiency appears to be derived from a multiple vortex system shed from the leading-edge "hooked comb," which consists of a complex spanwise distribution of twisted and cambered leading edge "barbs."

The pylon vortex-generator devices developed in Reference 30 operate on a principle similar to the wing snags described above. A vortex shed from the upper edge of the lower surface pylon has been shown in water tunnel and wind tunnel tests (Reference 30) to pass over the wing at AOA and to induce strong downwash at outboard wing stations, thereby delaying tip stall.

Wing upper surface fences provide an aerodynamic effect very similar to wing snags (the snag notch vortex acting as a "fluid fence"). Like the notch vortex, the fence inhibits outboard spanwise flow and the corresponding boundary-layer buildup, and also promotes an early breakdown of the leading edge vortex. This effect is illustrated for a slender wing in Figure 54. The fence also promotes a less asymmetric vortex breakdown in sideslip, thereby improving lateral stability, as shown in Figure 55. Above stall AOA, the effect of the fence diminishes as it is immersed in the separated flow over the wing.
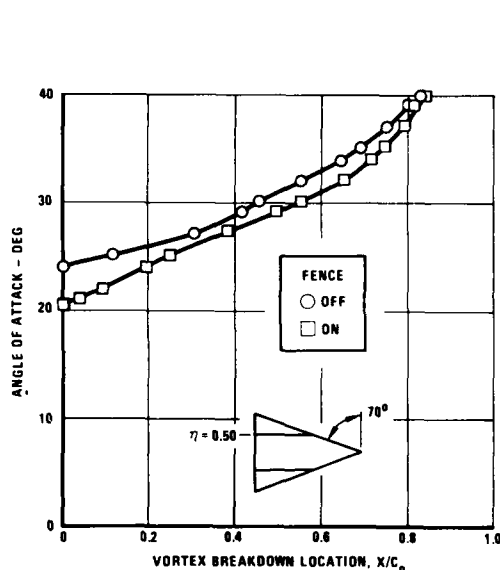

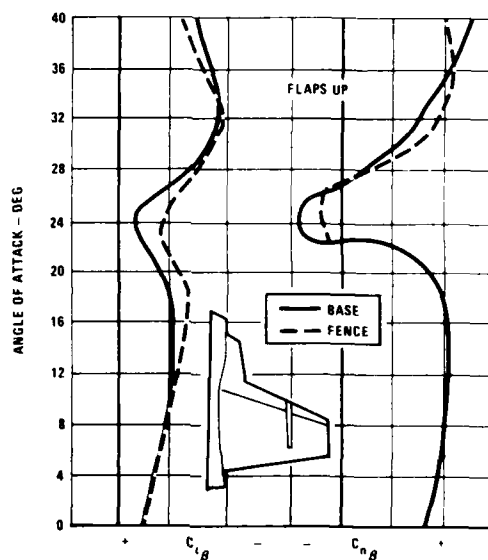**FIGURE 54. EFFECT OF WING FENCE ON VORTEX BURST**

FIGURE 55. EFFECT OF FENCE ON LATERAL-DIRECTIONAL STABILITY CHARACTERISTICS

2.8 Horizontal and Vertical Tail Effects

As shown in Figure 48, at low AOA a discrete LEX vortex core can be tracked aft of the wing trailing edge to interact with downstream airframe components such as horizontal and vertical tails. The change in LEX vortex trajectory due to wing flap deflection can cause the vortex to pass on either the upper or lower surface of the horizontal tail, depending on wing flap angle, tail location relative to the wing, and tail incidence angle. In addition, the pressure field imposed by the tail may promote vortex breakdown. It is evident, then, that lift characteristics and longitudinal stability can be affected by vortex interaction with the tail surfaces.

At high AOA, however, the horizontal tails appear to have a lower-order effect on vortex behavior due to the dominating effect of the wing pressure field. For example, the wind tunnel data in Figure 56, obtained on a twin-jet fighter configuration, reveal negligible effect at high AOA on rolling moment variation with AOA due to horizontal tail incidence angle or even removal of the tail surfaces.

Several current fighter aircraft feature twin vertical tail arrangements in order to maintain directional stability in the extended AOA range attainable with LEX-wing geometries. Twin vertical tail placement can influence LEX vortex stability in a manner similar to that observed with downstream obstacles placed in the path of the vortex core. Improper placement of the vertical tails can promote premature vortex bursting and, consequently, limit the attainable $C_{L_{max}}$ and influence longitudinal- and lateral-directional stability levels.

LEX vortex behavior can be very sensitive to tail location, incidence, and cant angle for example, particularly in a sideslip condition where the windward vortex can pass on either side of the windward tail surface and/or breakdown in the presence of the tail. To illustrate, the unstable "break" in the yawing moment data in Figure 57 is associated with the appearance of vortex breakdown at the windward vertical tail.
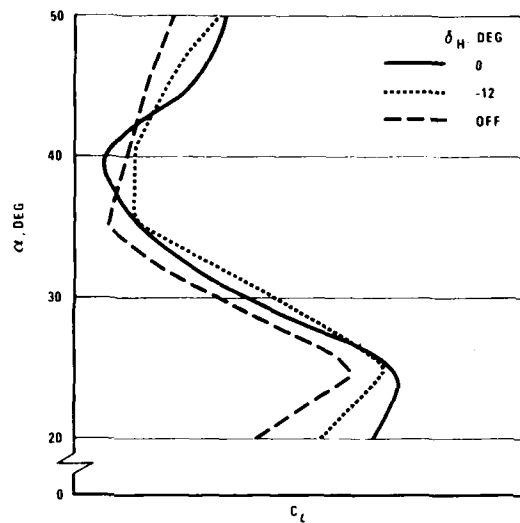
FIGURE 56. EFFECTS OF HORIZONTAL TAIL DEFLECTION
ON ROLLING MOMENT VARIATIONS WITH AOA
ON A LEX-WING FIGHTER
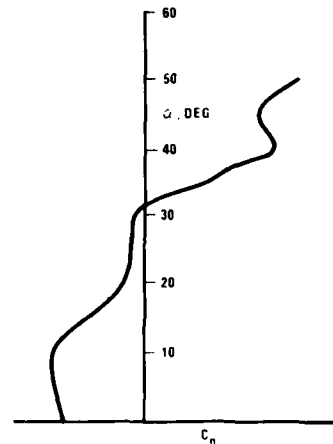
FIGURE 57. VARIATION OF YAWING MOMENT
WITH AOA ON A LEX-WING FIGHTER
WITH TWIN VERTICAL TAILS

A basic example of the effect of twin-tail location on vortex stability is presented in Figure 58 for a slender wing in sideslip. Tip-mounted tails have essentially no effect on vortex stability, whereas the inboard-mounted tails are seen to have a large influence on vortex core behavior. Supersonic cruise fighter designs featuring "cranked" or arrow wing planforms with outboard wing mounted vertical tails will require careful consideration of vortex-induced effects, particularly when more than one leading-edge vortex is shed along the span.
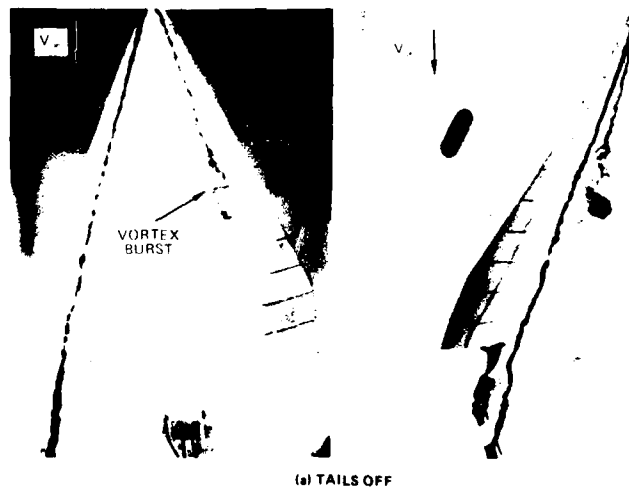
(a) TAILS OFF

FIGURE 58. EFFECT OF VERTICAL TAIL LOCATION ON VORTEX STABILITY AT 20-DEGREE
AOA AND 10-DEGREE SIDESLIP ANGLE (NORTHROP WATER TUNNEL)
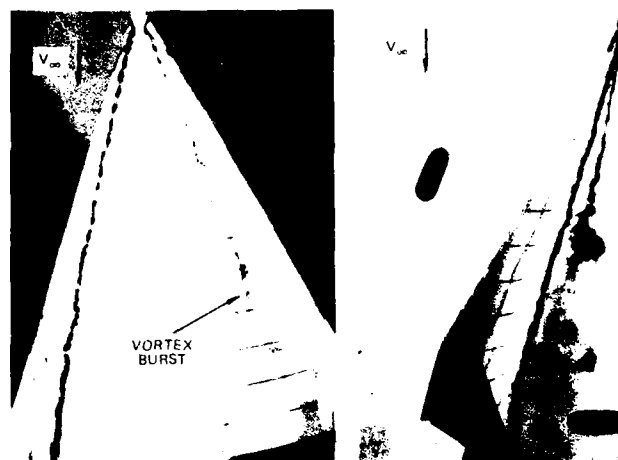
(b) TIF-MOUNTED TAILS
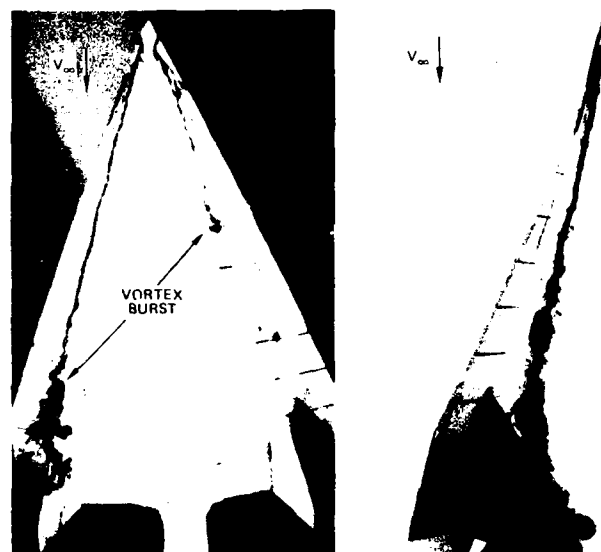
(c) INBOARD TAILS

FIGURE 58. EFFECT OF VERTICAL TAIL LOCATION ON VORTEX STABILITY AT 20-DEGREE
AOA AND 10-DEGREE SIDESLIP ANGLE (NORTHROP WATER TUNNEL) (CONTINUED)

3.0 FOREBODY DESIGN

3.1 Vortex Flows in the Leeside of a Forebody

In the post stall AOA region, aircraft stability can be strongly influenced by the forces developed on the fuselage forebody (Reference 27). In addition to the well-understood negative effect of forebody side area on directional stability, a more complex and dominant effect is produced by the system of vortices shed from the forebody at high incidence. This vortex system can generate very strong yawing moments both through direct action of forces on the forebody and through interaction with other aircraft components. The forebody vortices are shed in either a symmetric or asymmetric manner. For sufficiently slender forebodies, they can align in an asymmetric orientation in the sense that the core of the vortex from one is located above the core of the other. This results in asymmetric yawing moments in a symmetric flight condition (zero side slip angle).

As an example, Figure 59 schematically illustrates typical forebody vortex shedding patterns at both low and high AOA. Figure 60 shows dye patterns of forebody vortices at high AOA, recorded in a hydrodynamic research facility. An asymmetric vortex pattern is clearly shown. Characteristically, the forebody vortex system includes a pair of primary apex vortices emanating from the tip of the nose, which tear away from the body, plus a second, weaker vortex pair arising from the separated flow along the fuselage side. Figure 61 shows an example of this vortex arrangement.

HIGH ANGLE OF ATTACK
(ASYMMETRIC)

LOW ANGLE OF ATTACK
(SYMMETRIC)

FIGURE 59. FOREBODY VORTEX PATTERNS

FIGURE 60. ASYMMETRIC FOREBODY VORTEX SHEDDING AT ZERO SIDESLIP

FIGURE 61. CONCENTRATED VORTEX CORES ON A SLENDER BODY
(NORTHROP WATER TUNNEL)

Asymmetric forces and moments generated by asymmetric vortex shedding can greatly impact the departure and spin resistance of fighter aircraft. Aerodynamic asymmetries tend to reduce aircraft departure resistance 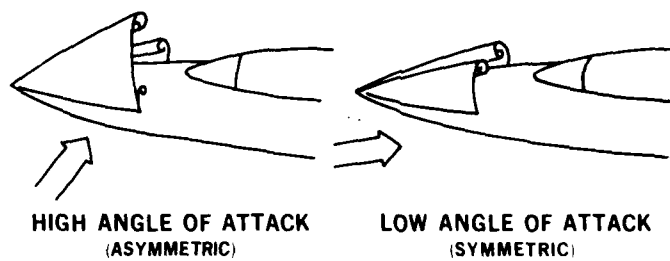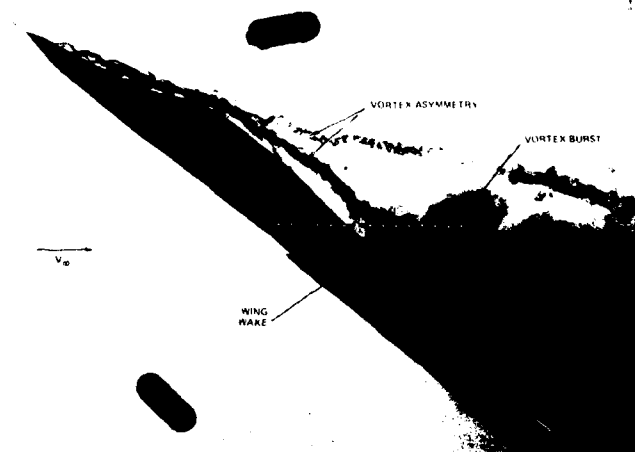and promote spin entry, and can determine the direction and rate at which an aircraft will spin. It is extremely important to include these asymmetries in the computer simulations used to assess the predicted departure and spin characteristics of aircraft with long, slender forebodies. Figure 62 illustrates the magnitude of the effect aerodynamic asymmetries can have on the critical yaw rates, which lead to a spin entry.
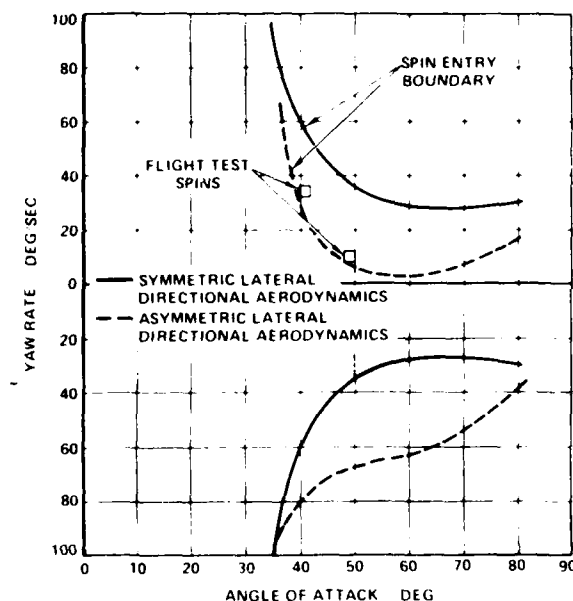

FIGURE 62. EFFECT OF AERODYNAMIC ASYMMETRIES

When these asymmetries are not included in the aerodynamic model, the calculated spin boundary is symmetric and indicates a false level of spin resistance; when the asymmetries are included, a strong bias is evidenced. Flight test results of two measured spin entry conditions are also shown (see Reference 31), underscoring the importance of including aerodynamic asymmetries in an analytical simulation of high AOA characteristics.

Proper forebody design can significantly reduce the magnitude of aerodynamic asymmetries. In addition, forebodies can be designed so that they also provide a favorable contribution to aircraft directional stability at high AOA. This second fact was first clearly evidenced by work conducted by researchers at NASA Langley Research Center on an F-5A nose shape (Reference 32). The results, shown in Figure 63, indicate the forebody to be the major contributor to the directional stability of the test aircraft at post-stall AOA. The primary cause of this stability was found to be the unique orientation that the forebody vortex system assumes in sideslip, which is caused by the forebody's elliptical cross section. An example of the development of this vortex system on a water tunnel model of the F-5F is shown in Figure 64.

One goal of the aircraft designer should be to generate a functional forebody shape with good aerodynamic performance, including acceptable lateral-directional characteristics at high AOA, without adverse impact on the performance of major aircraft systems (e.g., radar). More detailed discussion of the effects of forebody shape on radar performance will follow. Several geometric parameters related to the forebody shape have been identified as being important in determining the aerodynamic characteristics of forebodies. These geometric parameters will be discussed in the following sections and can be used as general design guidelines.

3.2 Forebody Fineness Ratio Effects

One of the primary geometric parameters that influences forebody aerodynamics is the forebody fineness ratio, which is defined as the forebody length divided by its maximum diameter. The forebody length used in determining the ratio depends on the aircraft planform geometry. For aircraft with long forebodies, the convention is to draw a reference line four body diameters forward of the wing trailing edge. The forebody length is the length forward of the reference line. This convention (from Reference 33) is illustrated in Figure 65 (a). For aircraft with shorter forebodies or with large wing-body strakes (LEXs) or large inlets that extend fairly far forward, a modified definition of forebody length is used, as shown in Figure 65 (b).
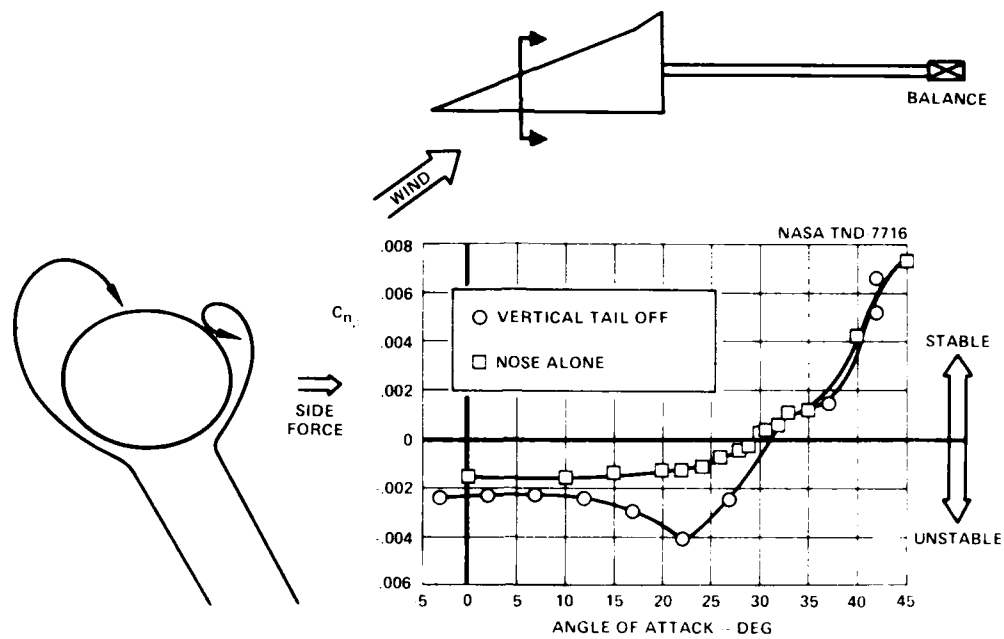
4-28

FIGURE 63. NOSE EFFECT ON STABILITY

FIGURE 64. F-5F FOREBODY VORTEX ORIENTATION IN SIDESLIP
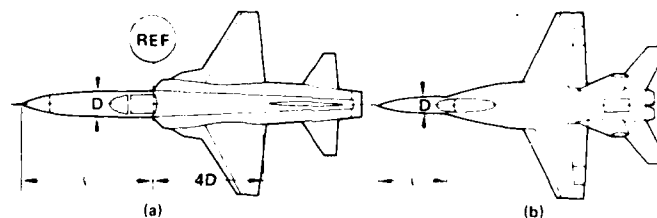(NORTHROP WATER TUNNEL)

FIGURE 65. DEFINITION OF FINENESS RATIO

Figure 66 shows the variation in yawing moment coefficient at zero sideslip as a function of fineness ratio. The trend shown was developed from an analysis of data representing several aircraft whose fineness ratios varied approximately from 3.5 to 6.0. Also shown in Figure 66 is the variation of onset AOA (from Reference 33). Increasing the forebody fineness ratio produces larger asymmetric yawing moments and lowers the onset angle at which they occur.
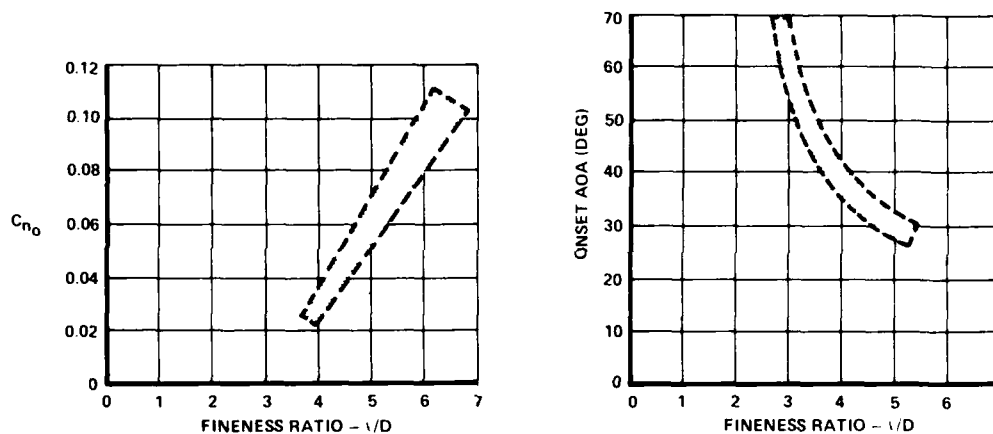
FIGURE 66. EFFECT OF FINENESS RATIO (FROM REFERENCE 33)

For any forebody shape of given fineness ratio, it is desirable to have zero yawing moment at zero sideslip throughout the operating AOA range. Realistically, for forebodies having large fineness ratios, even optimally designed forebodies will probably have some asymmetrical aerodynamic characteristics; therefore, it is important for the designer to determine the level of asymmetry that can be compensated by aerodynamic control.

3.3 Forebody Cross Sectional Shape Effects

Fuselage cross-section shape, from the apex aft two to three diameters, has a significant effect on directional stability at high AOA. Figure 67 (from Reference 19) illustrates this effect. The data presented were obtained from a number of fighter aircraft configurations with vertical tail removed for an AOA range up to 60 degrees. These configurations represent a full range of cross-sectional shapes, including ellipses in vertical and horizontal orientation. All configurations are unstable at low AOA and remain unstable up to an AOA of approximately 25 degrees. Above 25 degrees, cross sectional effects are evident; the horizontal ellipse cross-sectional shape becomes stable while the vertical ellipse shape becomes even more unstable.

Figure 68, also from Reference 19, further illustrates the effect of cross-sectional shape on directional stability at post stall AOA. Directional stability for several aircraft at a 35 degree AOA is shown as a function of nose ellipticity ratio. Although some scatter is present in the data, the trend conforms to the previous conclusion that a flat, elliptical nose section is required to produce positive directional stability at high AOA.

Directional stability attributed to properly shaped forebodies at low speed can be strongly influenced by compressibility effects at transonic Mach numbers (Figure 69). As shown, directional stability is reduced as the Mach number approaches transonic values.

Geometric changes in the shape of the aircraft forebody that affect lateral directional stability have also been found to affect the aircraft longitudinal stability under nonzero sideslip conditions. This effect is shown in Figure 70 for two different types of elliptical nose shapes. The results indicate that nose shapes with a stabilizing directional stability component also have an unstable, nose-up pitching moment contribution in sideslip. ($C_{m_{\beta}}$). The converse is true of forebodies with a destabilizing directional force component.
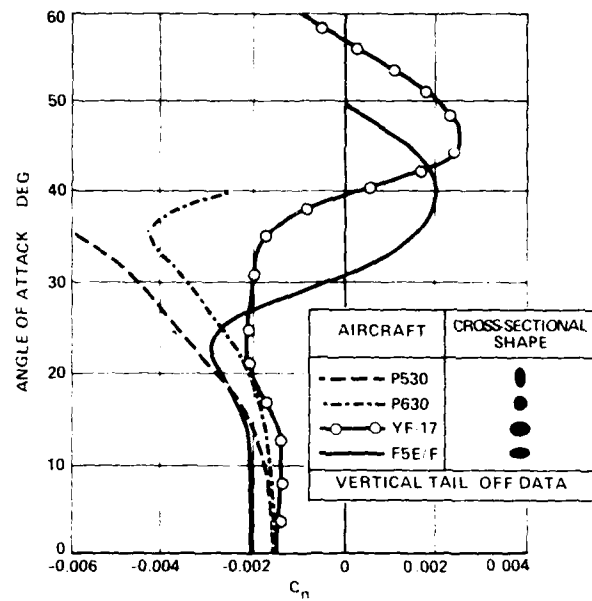
FIGURE 67. EFFECT OF NOSE SHAPE ON STABILITY (FROM REFERENCE 19)
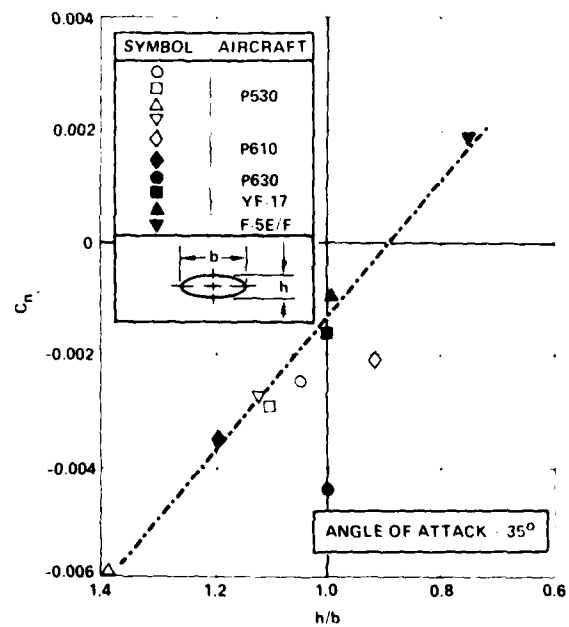
FIGURE 68. EFFECT OF NOSE ELLIPTICITY ON C_{n_β}
(FROM REFERENCE 19)
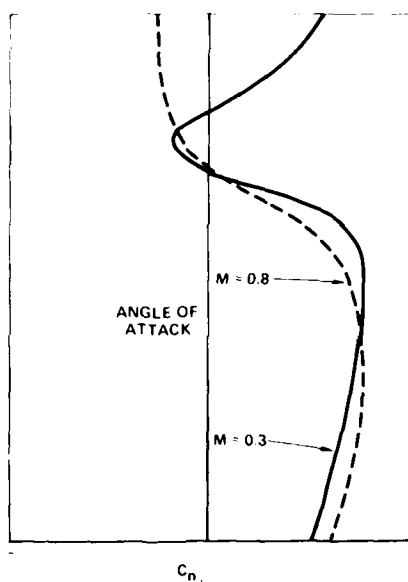
FIGURE 69. TRENDS IN DIRECTIONAL STABILITY

SYMBOL	AIRCRAFT	CROSS SECTIONAL SHAPE
⊸◦⊸	P610	
⊸△⊸	P600	
⊸●⊸	F5F F	

ANGLE OF ATTACK – DEG
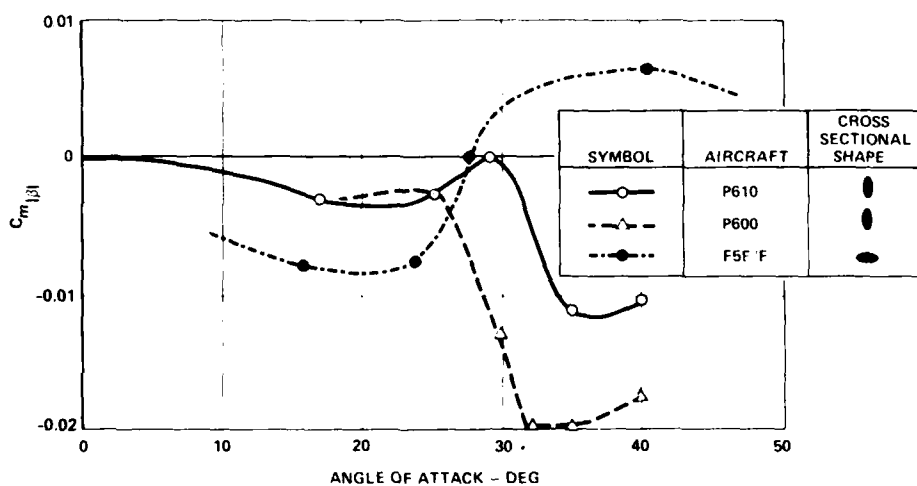
FIGURE 70. PITCHING MOMENT DUE TO SIDESLIP

3.4 Forebody Bluntness Effects

Fuselage apex radius is another geometric parameter that has an effect on aerodynamic asymmetries at high AOA. The results of research conducted by NASA (Reference 34) are presented in Figures 71 and 72. The data show that bluntness affects both the overall magnitude and the onset AOA at which directional asymmetries occur at zero sideslip. As the apex bluntness is increased, the onset AOA is delayed to higher angles and the aerodynamic asymmetry is reduced. Northrop results on the F 5F, which agree well with the NASA data, are presented in Figures 73 and 74. The data support the trends that nose bluntness raises the onset AOA and also has an important effect on the peak asymmetric yawing moment at zero sideslip.
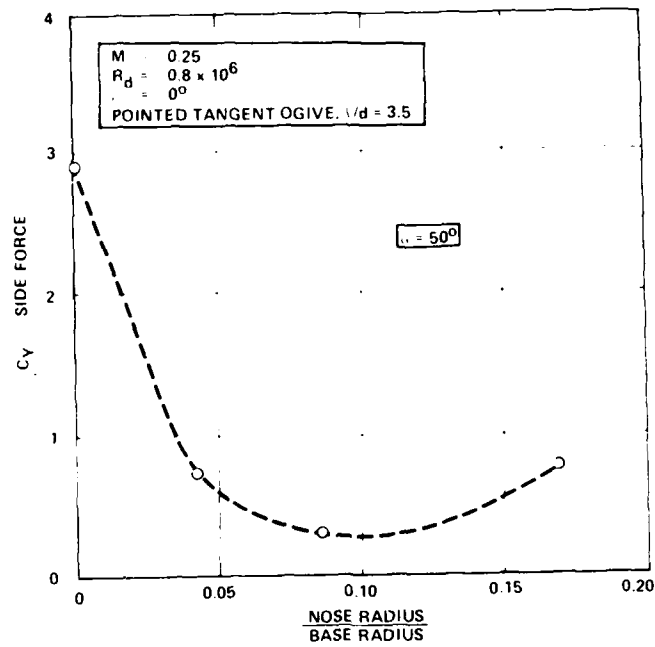
FIGURE 71. EFFECT OF NOSE BLUNTNESS ON SIDE FORCE
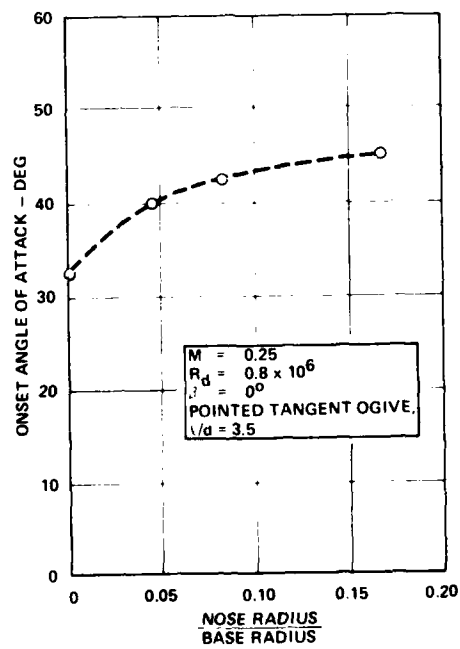
FIGURE 72. EFFECT OF NOSE RADIUS ON ONSET AOA
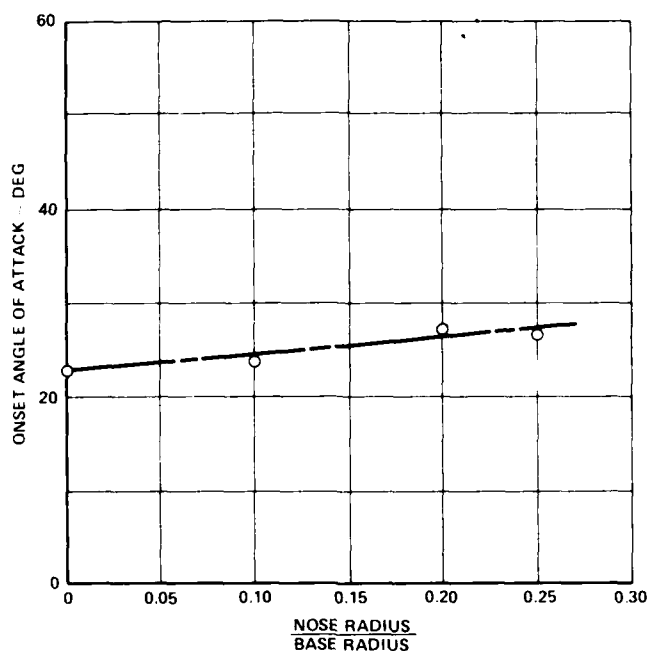
FIGURE 73. EFFECT OF NOSE RADIUS INCREASES ON
ONSET ANGLE OF ATTACK
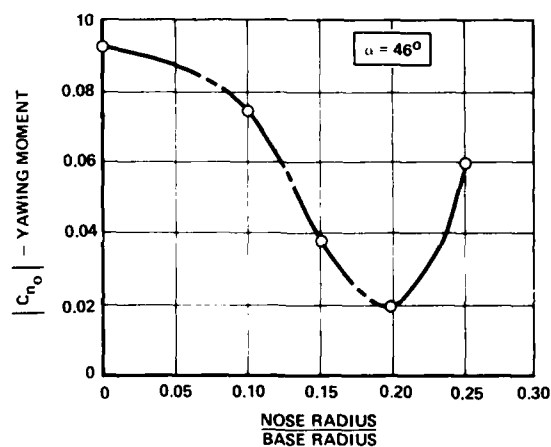
FIGURE 74. EFFECT OF NOSE RADIUS ON PEAK
ASYMMETRIC YAWING MOMENTS

3.5 Forebody Strake Effects

A common means of ensuring that the forebody vortices will shed symmetrically at zero sideslip has been the use of thin strakes placed on the sides of the forebody. Unfortunately, in many cases, while effectively reducing asymmetrics at zero sideslip, the strakes can adversely affect the directional stability contribution of the forebody. They can also prevent the formation of the unique forebody vortex orientation in sideslip that is responsible for the positive directional stability at high AOA. This effect is illustrated on the F-5E/F configurations in Figure 75 and 76. As with most aerodynamic phenomena, the effect of forebody strakes is not always consistent. An example of an aircraft on which directional stability was improved by the addition of nose strakes is the YF-17. The addition of the flight test nose boom destabilized the basic configuration in yaw. Nose strakes were added, and directional stability was improved, as shown in Figure 77 (Reference 20).
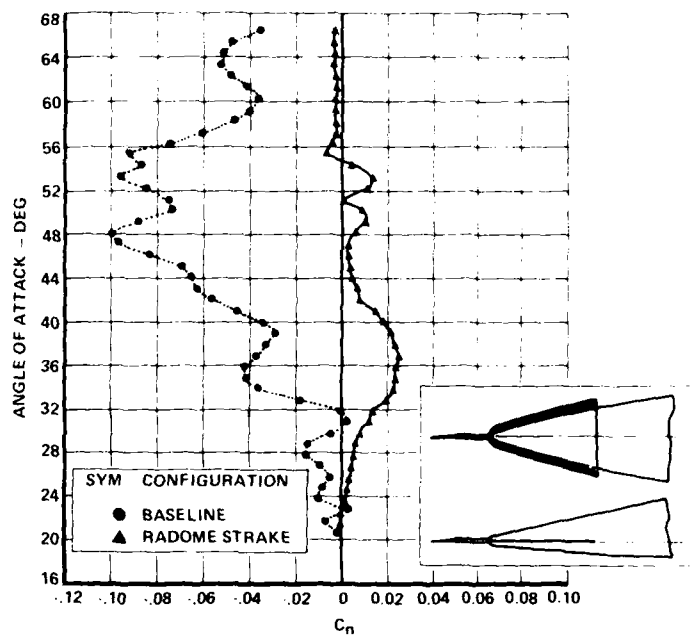
FIGURE 75. STRAKE EFFECT ON AERODYNAMIC ASYMMETRIES
AT ZERO SIDESLIP
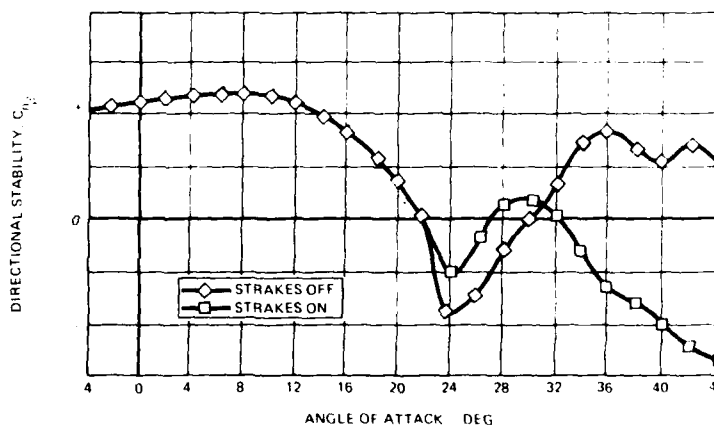
FIGURE 76. STRAKE EFFECT AT NONZERO SIDESLIP

Nose strakes can also strongly affect lateral stability through interaction with downstream components such as the wing and vertical tail. The effect on lateral stability can be so positive as to overcome the degradation in directional stability. This point will be expanded in Section 4.0 of this paper.

3.6 Flight Test Nose Boom Effects

Flight test requirements often result in the addition of a large instrumentation boom to the nose of the aircraft. This boom is usually equipped with a pitot-static system and vanes to measure AOA and sideslip. The nose boom modifies the nose shape and alters the forebody vortex system, which can significantly affect the lateral-directional stability of the configuration and alter the departure characteristics and recovery capability from those without the boom.
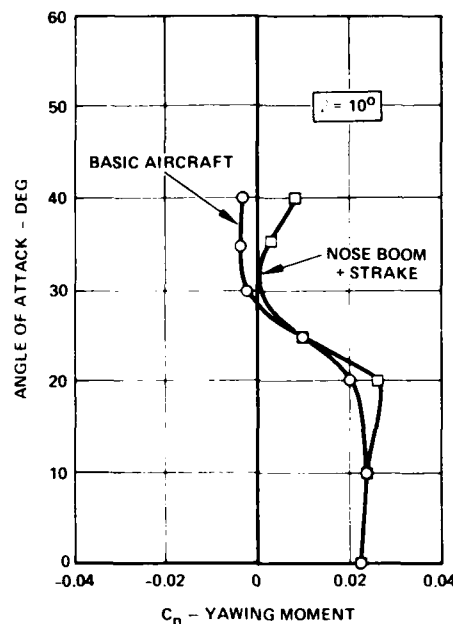
FIGURE 77. EFFECT OF NOSE BOOM AND STRAKE

A long nose boom attached to a short forebody increases the effective fineness ratio, which results in a lower onset AOA for vortex asymmetry. Studies conducted in the Northrop water tunnel on a tangent ogive of fineness ratio 3 showed that the onset AOA was reduced from 30 to 23 degrees by the addition of a long tapered nose boom. Moreover, the vortex asymmetry was significantly amplified by the nose boom, as shown in Figure 78. To further substantiate this trend, Figure 79 (from Reference 35) shows the effect of a nose boom added to an F-15 model. The F-15 configuration has a relatively short forebody of fineness ratio 4.3. The data shows that adding the nose boom reduced the onset of the vortex asymmetry by 10 degrees in AOA.

(a) CLEAN FOREBODY   (b) TAPERED NOSE BOOM

FIGURE 78. EFFECT OF NOSE BOOM ON AN l/d = 3.0 TANGENT OGIVE WITH l/d = 4.5 AFTERBODY:
α = 40 DEGREES, β = 0 DEGREES

The effect of adding a flight test nose boom to the F-5F configuration is presented in Figure 80. The F-5F has a long, slender forebody of fineness ratio 6. The data show that the onset AOA was essentially unaffected; however, asymmetric yawing moments became oscillatory rather than biased in one direction. The oscillatory nature of the yawing moment data suggests switching in the forebody vortex system orientation induced by the wake from the nose boom. Another example of adding a nose boom to a long forebody is shown in Figure 81. These data (from Reference 35) are for a research model based on an F-15 configured with a long forebody. Like the F-5F, no effect is seen in onset AOA while the peak yawing moment is reduced by a factor of 2.
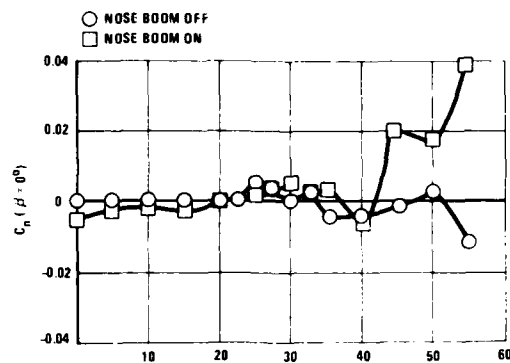
FIGURE 79. EFFECT OF NOSE BOOM ON PRODUCTION
FOREBODY (FROM REFERENCE 35)
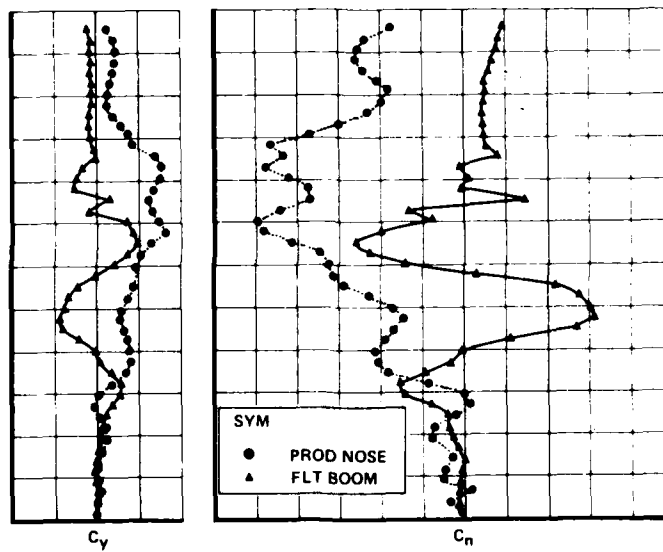
FIGURE 80. EFFECT OF FLIGHT TEST NOSE BOOM
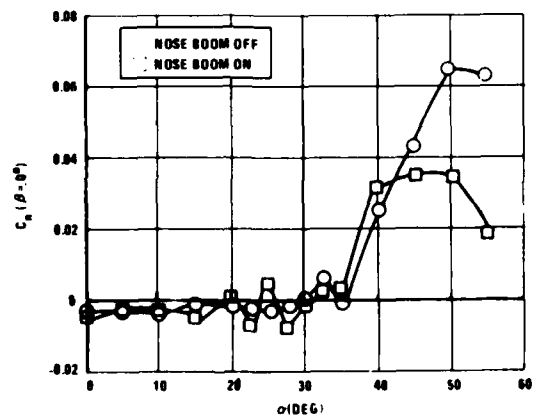
FIGURE 81. EFFECT OF NOSE BOOM ON LONG FOREBODY

3.7 Shark Nose Design

Development of the Northrop Shark Nose is an example of how the forebody design guidelines just discussed can be applied. The Shark Nose is an optimum F-5 forebody geometry developed as a part of Northrop's ongoing research into high AOA aerodynamics. This configuration acquired its name because of its broad, flat, elliptical nose, which resembles that of a shark (Figure 82). The nose planform and cross-sectional shape were developed to attenuate asymmetric vortex formations while enhancing the favorable directional stability effects at nonzero sideslip.
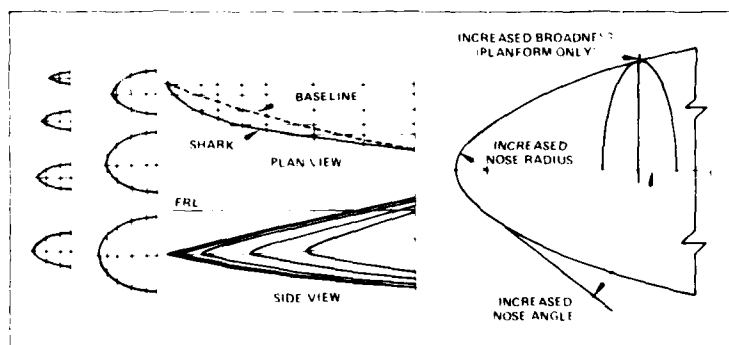
FIGURE 82. SHARK NOSE GEOMETRY

The Shark Nose is shown alongside the basic unmodified nose in Figure 83. Figure 84 shows the effect of the Shark Nose on asymmetric yawing moment; an order of magnitude reduction is indicated. Figure 85 shows the effect of the Shark Nose on directional stability at an AOA of 46 degrees. Figure 86 shows the improved directional stability as a function of AOA.
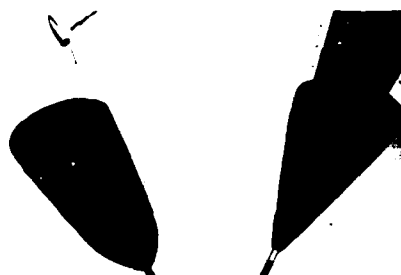
FIGURE 83. COMPARISON OF SHARK NOSE AND BASELINE NOSE

The Shark Nose was subsequently evaluated in a flight test program. The test configuration, shown in Figure 87, was found to have improved handling qualities at high AOA as compared to the unmodified configuration (Reference 36). Resistance of the Shark Nose configuration to departure and spin was dramatically improved. A derivative of the Shark Nose, optimized for a coherent radar, is a design feature of the latest number of the F-5 family of fighter aircraft, the F-5G Tigershark (Figure 88).

3.8 Reynolds Number Effects on High Angle-of-Attack Side Forces

The effects of Reynolds number on the development of forebody side forces at high AOA have been the subject of much debate since about 1970. Many previous experimenters measured large side forces on slender aircraft and missile bodies at zero sideslip in subscale wind tunnel testing at low Reynolds number. In the absence of any conclusive evidence of the existence of these forces at flight Reynolds numbers on a full scale vehicle, the tendency was to believe that the side forces measured in wind tunnels were an anomaly associated with the test technique, i.e., that the effects of minute geometric imperfections were being amplified to large proportions by the turbulence in the tunnel free-stream and the low Reynolds number.
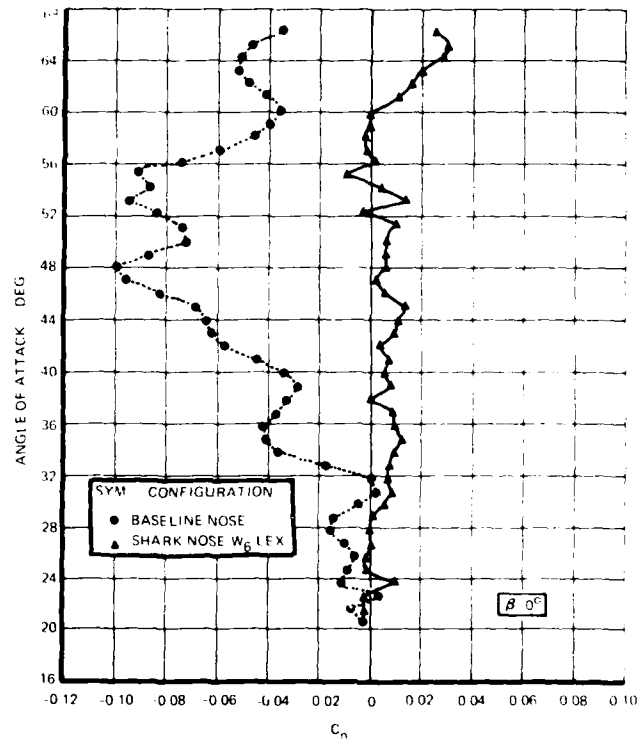
FIGURE 84. SHARK NOSE EFFECT ON AERODYNAMIC ASYMMETRIES
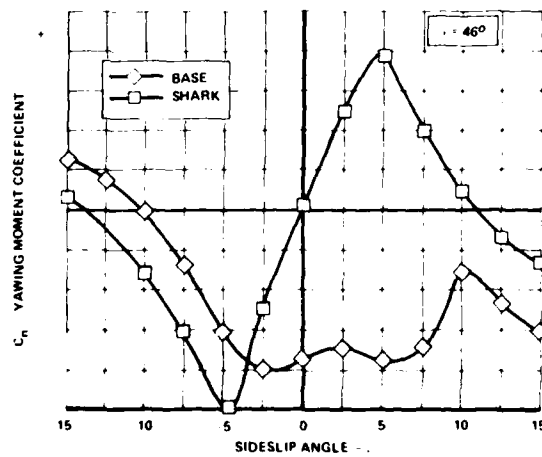
FIGURE 85. SHARK NOSE EFFECT ON STABILITY
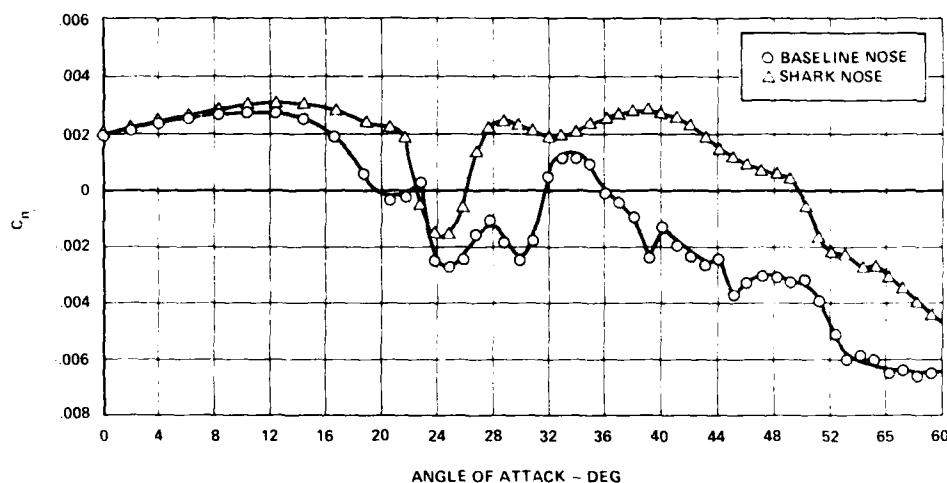
FIGURE 86. EFFECT OF SHARK NOSE ON STABILITY
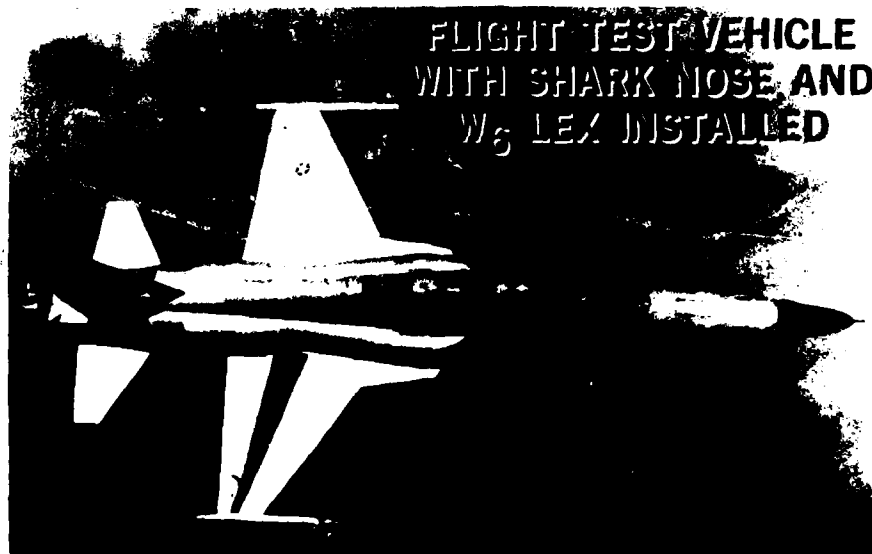
FIGURE 87. FLIGHT TEST VEHICLE WITH SHARK NOSE AND W_6 LEX INSTALLED

In 19   Kow and Til'riga (Reference 37) presented data showing that the asymmetric yawing moments generated by .!'; forebody side force at high AOA and zero sideslip do exist on a fighter aircraft at full scale Reynolds number. By analyzing the results of an abrupt symmetric pitch maneuver conducted during spin tests of the F-5F, it was shown that the asymmetric yawing moments on this aircraft begin at essentially the same AOA and develop the same peak magnitude in flight at a Reynolds number of 7×10^6 and in the wind tunnel at a Reynolds number of 1.5×10^6. Figure 89 presents the results of this analysis. These data indicated that the forces generated by the forebody vortex system might be independent of Reynolds number or at least not dominated by Reynolds number effects and that the asymmetric nature of the vortices might be due to an instability in the wake. Asymmetric vortex patterns in the leeside of a highly swept thin delta wing ($\Lambda > 80$ degrees) observed in wind tunnel and water tunnel tests (Reference 17) lent further credence to the tentative conclusion that Reynolds number was not a driver. The main effect of testing at low Reynolds number appeared to be confined to the difficulty of obtaining repeatable results.

In 1980 Lamont (References 38 and 39), presented data from a series of experiments conducted under stringently controlled conditions to study the development of forebody side forces in some detail over a wide spectrum of Reynolds numbers. These data show that over the AOA range from approximately 40 to 70 degrees, large side forces are developed both at low Reynolds numbers with laminar separation on the body and at high Reynolds numbers where the separation is fully turbulent. The data also showed that the distribution of side force along the body was well structured in both the laminar and the turbulent cases.

4-40

FIGURE 88. NORTHROP F-5G WITH MODIFIED SHARK NOSE
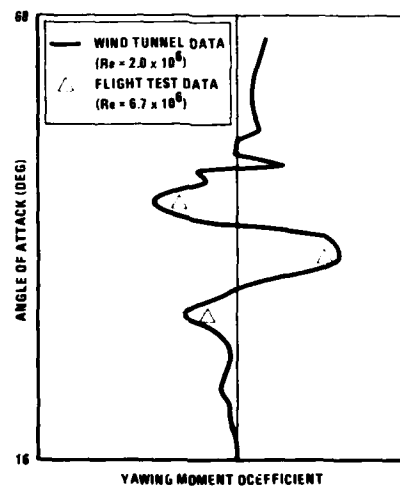
FIGURE 89. WIND TUNNEL/FLIGHT TEST CORRELATION

The laminar and the turbulent side forces were found to have similar magnitudes and distributions but were produced by altogether different pressure distributions along the body. Figure 90 illustrates the variation of side forces with Reynolds number at a constant AOA. It is possible that the reduction in side force seen in these data at an AOA of 55 degrees in the intermediate Reynolds number range may occur at a different Reynolds number at a lower AOA, although this possibility is arguable. Lamont's data (Reference 38) suggest that the onset of transitional behavior is largely independent of AOA but that the upper limit, where fully turbulent separation occurs, increases with the AOA. At transitional Reynolds numbers the side forces were significantly reduced, with a minimum near zero, and their distributions were poorly structured.

As to data repeatability, these tests illustrated that under identical conditions, excellent repeatability can be obtained in both the laminar and the turbulent regions but that only moderate repeatability exists for transitional separation. The unfortunate fact is that most wind tunnel tests on fighter aircraft are conducted in this transitional region. Under all conditions, the measured side forces were sensitive to minute geometric imperfections in the model, as evidenced by Figure 91, which shows the variation in side forces at high AOA that were induced by rolling of the axisymmetric model.
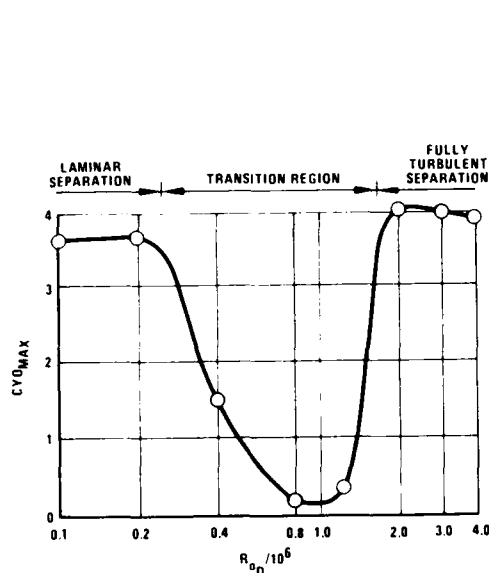
FIGURE 90. EFFECT OF REYNOLDS NUMBER ON MAXIMUM FORCE: α = 55 DEGREES
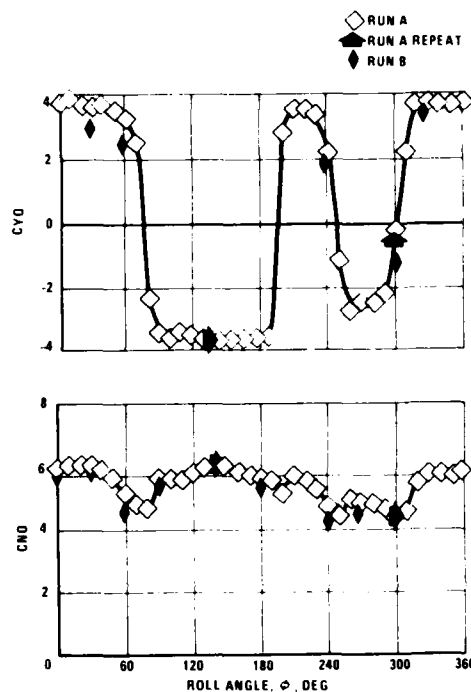
FIGURE 91. VARIATION OF OVERALL FORCE COEFFICIENTS WITH ROLL ANGLE

In contrast to Lamont's results, Ericsson and Reding (Reference 40) claim that the largest side forces can be developed in the transitional regime due to the possibility of different boundary layer states and, therefore, different separation characteristics on the two sides of the body. They further suggest that this difference in separation lines can be aggravated by the dynamics of the body motion (e.g., by symmetric pitching or by rolling the body). If this postulate were correct, a method of ensuring turbulent flow over most of the forebody (by artificial means) would appear to be useful for obtaining data at low Reynolds number that would be representative of high-Reynolds-number conditions. Very little data exists to guide an experimentor in this area, and what data does exist suggest that traditional means of causing a boundary layer to transition to a turbulent profile (such as grit) may actually cause the forebody flowfield to be extensively altered.

The following conclusions/recommendations can be offered:

1. Extreme caution should be used when conducting tests at high AOA in the transitional Reynolds number range $(0.2 \times 10^6 \lesssim Re_D \lesssim 4 \times 10^6)$.

2. Test and flight Reynolds numbers should be matched as closely as possible (difficult in practice).

3. Note: The validity of using grit or other artificial means to simulate high Reynolds-number conditions on slender bodies has not been established.

3.9 Effect of Forebody Shape on Radar Performance

When designing a forebody for a fighter that will engage in maneuvering at high AOA, it is important that there be a close interaction between aerodynamic requirements for good stability and low drag, electromagnetic requirements for good radar performance, and requirements for some aircraft systems. This interaction can result in several competing design considerations. The primary geometric factors that affect radar performance are:

1. The location of a pitot-static boom (and sometimes α/β vanes) in front of the radome

2. High fineness ratios resulting from aerodynamic shaping of the forebody for low drag

3. Aerodynamic shaping of the forebody cross section for good high-AOA directional stability.

\ radome mounted pitot static boom, with or without ⍺ β vanes, scatters the transmitted electromagnetic waves from the antenna and increases the sidelobe levels. Any large mass that is added to the radome to provide support for the pitot-static boom and its associated hardware will greatly attenuate and scatter transmitted electromagnetic energy.

Efficient transmission of electromagnetic waves from the radar antenna depends upon the incidence angle, polarization of the antenna, curvature of the radome surface, and blocking structures. Incidence angle is defined as the angle formed by the surface normal vector and the vector indicating the flow direction of the electromagnetic energy. The plane formed by these two vectors is referred to as the plane of incidence (Figure 92). Although there is an optimum thickness of each incidence angle, it is unlikely that a single point on the radome will have only one incidence angle as the radar antenna sweeps. In fact, at low incidence angles the maximum transmission efficiency is less sensitive to variations in thickness from the optimum than at higher incidence angles (Figure 93). Therefore, the "ideal" radome shape for optimum radar performance should be axisymmetric with a profile somewhere between a hemisphere and a low caliber tangent ogive. Any deviation from this shape results in a degradation in radar performance. However, if a high fineness ratio is required in order to provide lower drag, a thickness taper based on the average incidence angle at each station should make the degradation in radar performance less severe.
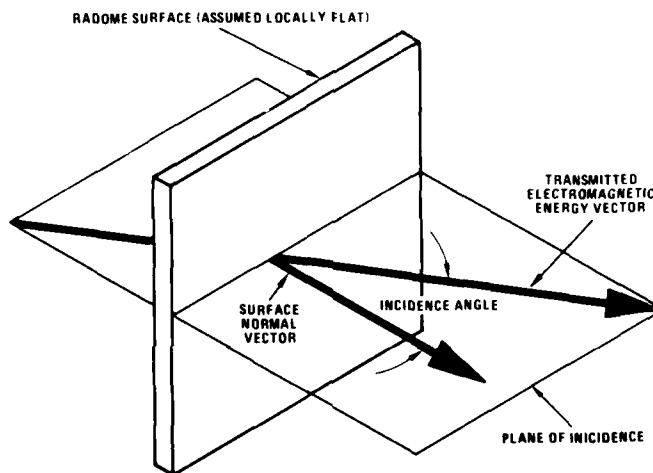
FIGURE 92. RADAR ENERGY INTERACTION AT RADOME SURFACE
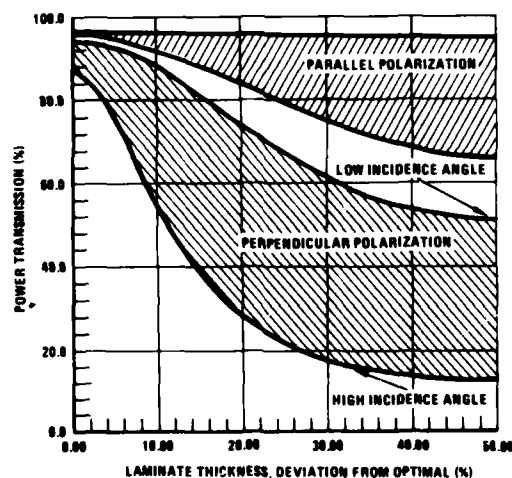
FIGURE 93. EFFECT OF RADAR ANTENNA POLARIZATION ON POWER TRANSMISSION EFFICIENCY FOR DIFFERENT RADOME THICKNESSES

The effect on radar performance of forebody cross-sectional shaping for good high AOA stability can be minimized by some electrical design considerations. The forebody or radome is a protective shell in which the radar antenna is located. The main goal in the electrical design is the maximum transmission of electromagnetic energy from the antenna through the radome. The reflected energy and the energy trapped on the radome surface propagate back to the antenna to increase the sidelobe level on the antenna. This causes clutter to appear with the target radar return and is most critical at look-down angles at which the increase in sidelobe level increases the false alarm rate and therefore reduces the detection range.

Deviations from axial symmetry of the radome also cause difficulty in optimum electrical design and usually result in reduced radar performance. Rapid change in the radome radius of curvature degrades the radar performance more than a milder change. Discontinuities in the radome (e.g., adding thin strakes to control the shedding of the forebody vortices at high AOA) can degrade radar performance by scattering the electromagnetic wave. If the primary mode of the radar is look down, however, strakes located above the maximum half-breadth will cause less sidelobe increase and, consequently, preserve the radar detection range.

Shaping of the forebody cross section into an ellipse with the major axis horizontal has been shown above to be beneficial to the directional stability of the aircraft at high AOA. The polarization of the radar antenna has a direct influence on the degree of ellipticity that can be allowed in the radome cross section. The electric field intensity from the radar antenna can be separated into two components, one parallel and the other perpendicular to the plane of incidence. The parallel component transmits more efficiently even at large deviation from optimum thickness at all incidence angles, as shown in Figure 93. The polarization of a radar antenna is chosen to match the mission requirements of the aircraft. If a ground-mapping mode is primary, for instance, a horizontally polarized antenna is most suitable. For a radar whose primary mode is air-to-air, the best antenna polarization is vertical.

Figure 94 illustrates three of approximately a dozen radome profiles analyzed by Northrop for the F-5G. The ogive profile was analyzed with a nearly circular cross section. The Shark I radome has a flat, elliptical shape, especially near the tip. The Shark II profile has a less elliptical cross-sectional shape than Shark I. None of these radomes has a pitot-static boom or α/β vanes mounted in front. The ogive profile is optimum for radar performance; it has high drag and slightly degrades high-AOA directional stability. The Shark I shape, which is optimum aerodynamically, was discussed above; it provides positive directional stability above the stall AOA and is low in drag. The Shark II is a compromise shape (the results of this comparison are shown in Figure 95). These data illustrate that the Shark I radome dramatically reduces the radar detection range due to its higher sidelobe level developed by the extremely flat shape near the tip. The Shark II shape has much of this flatness removed, although it is still very elliptical overall. This example illustrates that it is possible to tailor a radome shape to provide low drag and excellent high AOA directional stability without adversely affecting radar performance.

4.0 FOREBODY/WING VORTEX INTERACTIONS

Current-generation, highly maneuverable aircraft with hybrid wing planforms and slender forebodies can have strong interactions between the forebody and wing/LEX vortex systems. These interactions can often affect the aerodynamic characteristics of an aircraft to a greater degree than the direct effects of the forebody and wing vortices discussed above.

4.1 Long-Coupled Forebody/LEX Vortex Interactions

The F-5 configured with a Shark Nose and W_6 LEX is an example of a favorable forebody and wing LEX vortex interaction improving lateral-directional stability. The W_6 LEX, denoted by its wind tunnel part number, is shown in Figure 96, which illustrates how the LEX vortex breakdown location over the wing varies with AOA. It can be seen that near the stall AOA (approximately 24 to 25 degrees), the W_6 LEX causes the vortex breakdown to be delayed by 2 to 3 degrees. Figure 97 shows how this delay in vortex breakdown delays the AOA at which loss of directional stability occurs in the stall region by approximately 2 degrees in AOA.

Figure 86 showed how the addition of the Shark Nose alone improved directional stability in the stall region; the point at which directional stability was regained occurred at a lower post-stall AOA compared to the unmodified forebody.

Figure 98 shows the effect of the Shark Nose in combination with the W_6 LEX. The separate effects of the more stable LEX vortex and the stronger forebody vortices are seen to overlap. The favorable vortex interaction has a synergistic effect that results in positive directional stability throughout the entire stall region.

4.2 Short-Coupled Forebody/LEX Vortex Interactions

Strong forebody and wing/LEX vortex interactions have been noted on other advanced configurations that employ large amounts of vortex lift at high AOA. This is illustrated in Figure 99 for an F-18L model at a 32-degree AOA at zero sideslip. The proximity of the large LEX to the forebody, in addition to the disparity of vortex strengths between the LEX and forebody vortical flows, results in a strong suckdown of the forebody vortices onto the wing upper surface. The manner in which the forebody primary vortex pair interacts with the LEX vortex flows depends on such parameters as forebody cross-sectional shape and fineness ratio, LEX planform and LEX size, and AOA and sideslip angle. Near $C_{L_{max}}$ the forebody and LEX vortices are of sufficient strength that, depending on the vortex orientations, the levels of lateral-directional stability can be significantly affected. It is interesting to note that the forebody vortex orientation in sideslip

4-44

on the F-18L wing LEX model is opposite to the vortex patterns observed on the Northrop F-5F, which features a less-coupled forebody and LEX surface arrangement. The F-5F exhibits a windward body vortex in proximity to the fuselage, while the leeward body vortex "shears" away from the fuselage. In contrast, the F-18L model, due to the coupling of the forebody and LEXs, develops a leeward body vortex that is strongly entrained into the leeward LEX vortex whereas the windward body vortex tends to shear away from the fuselage (Figure 100). It is the sensitivity of the forebody LEX vortex flow interactions at high AOA that promotes highly nonlinear variations in lateral directional stability. For example, a favorable body vortex interaction with the LEX wing flowfield can delay wing stall, which in turn can promote an increase in lateral stability and, due to a reduction in wing wake, increase vertical tail effectiveness and thus directional stability. A slight perturbation to the forebody vortex orientation, however, can cause a complete reversal of the above trends. It is evident that the design of hybrid aircraft intended to operate effectively at high AOA requires careful consideration of the global impact of the flow developed on the various surface components.
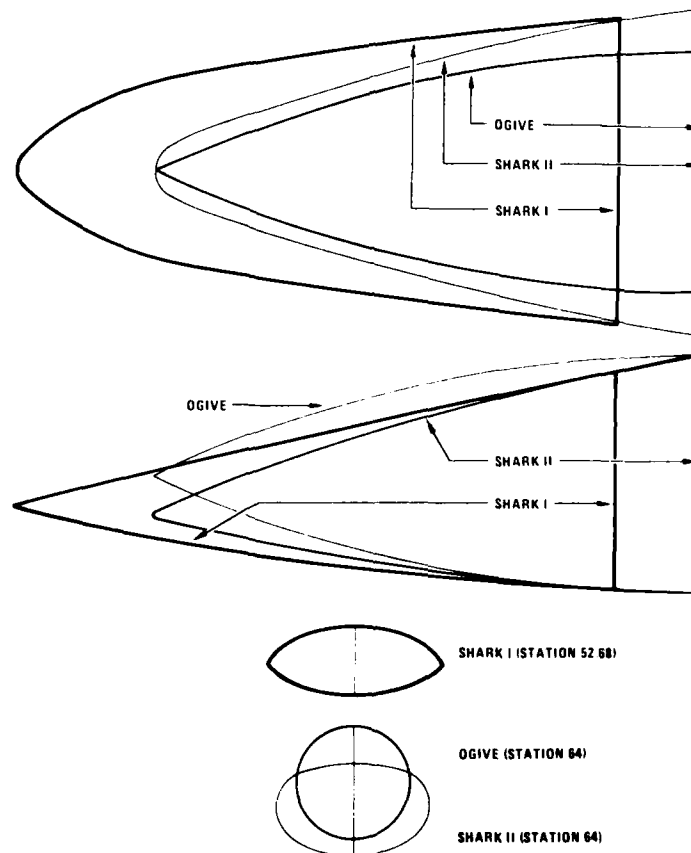
CROSS SECTIONAL VIEW 12" FROM THE RADOME TIP

FIGURE 94. ALTERNATE RADOME SHAPES

Forebody strakes have been found to cause strong forebody and wing/LEX vortex interactions for some fighter configurations. As an example, Figure 101 shows the effects of nose strake radial location (ϕ) on the lateral-directional characteristics of a current fighter configuration. These data are for an AOA of 35 degrees and sideslip angles from -12 to 12 degrees. The results reveal a high degree of sensitivity of lateral and directional stability characteristics to strake radial location. For example, the most directionally stable configuration is obtained with the strakes located at the maximum half-breadth ($\phi = 0$ degrees); however, the corresponding lateral stability is quite low. Flowfield surveys in a water tunnel have shown that strakes mounted in this position disrupt the forebody primary vortex pair development at high AOA due to the discontinuity in vorticity shed along the fuselage sides and to the wake shed by the strakes. In terms of dynamic directional stability, defined as

$$C_{n_{\beta_{dyn}}} = C_{n_\beta} \cos \alpha - (I_z/I_x) C_{l_\beta} \sin \alpha$$
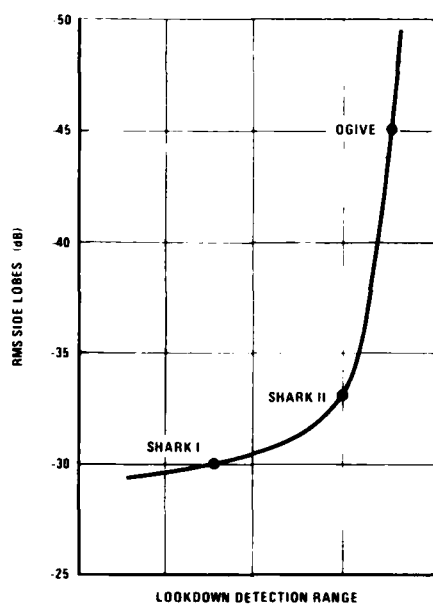
FIGURE 95. EFFECT OF RADOME SHAPE
ON DETECTION RANGE
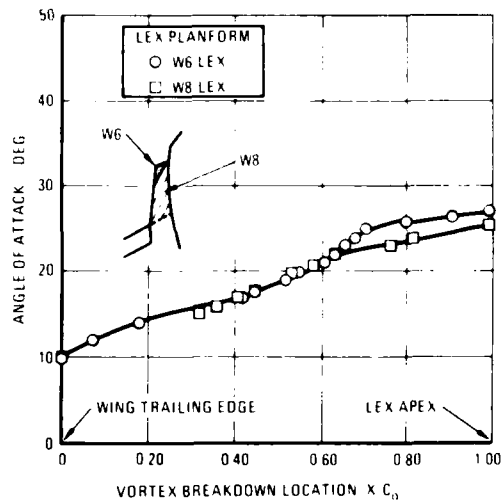
FIGURE 96. F-5F W_6 AND W_8 LEX VORTEX
BREAKDOWN CHARACTERISTICS
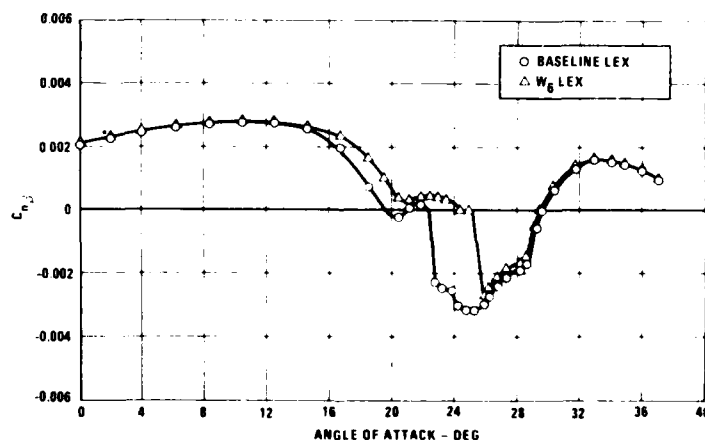
FIGURE 97. EFFECT OF W_6 LEX ON STABILITY

the most favorable strake location is at $\phi = 40$ degrees. At this strake location the negative directional stability is more than offset by the large positive lateral stability and large ratio of yaw-to-roll inertia. The changes in directional and lateral stability with strake position are, in large part, a result of variations in forebody and wing/LEX vortex interactions. The effect of nose strakes on directional stability is a direct one; that is, the strakes directly alter the forebody vortex flowfield. The primary airframe contributor to lateral stability, however, is the wing, by virtue of its large area and spanwise extent. Any changes in lateral stability due to nose strakes are therefore indicative of a change in the interactive behavior of the forebody and wing flow fields. Water tunnel studies of this configuration indicate that strakes positioned 40 degrees above the maximum half-breadth are embedded in a region of low local AOA and, as a result, shed discrete vortices even at AOA in excess of 40 degrees. Because the strake position is nearly coincident with the forebody primary boundary layer separation lines along the nose region, the strake vortices "feed" directly into the forebody primary vortices. Consequently, the body vortex pair is of increased strength and is resistant to asymmetric orientation in sideslip. The resultant strongly coupled forebody vortex pair enhances the windward wing flow by promoting a strong vortex-induced sidewash. Because the body vortices are in proximity, the flow field tends to be slightly unsteady. This unsteady vortex flowfield can result in "wing rock," a phenomenon exhibited by most fighter aircraft.
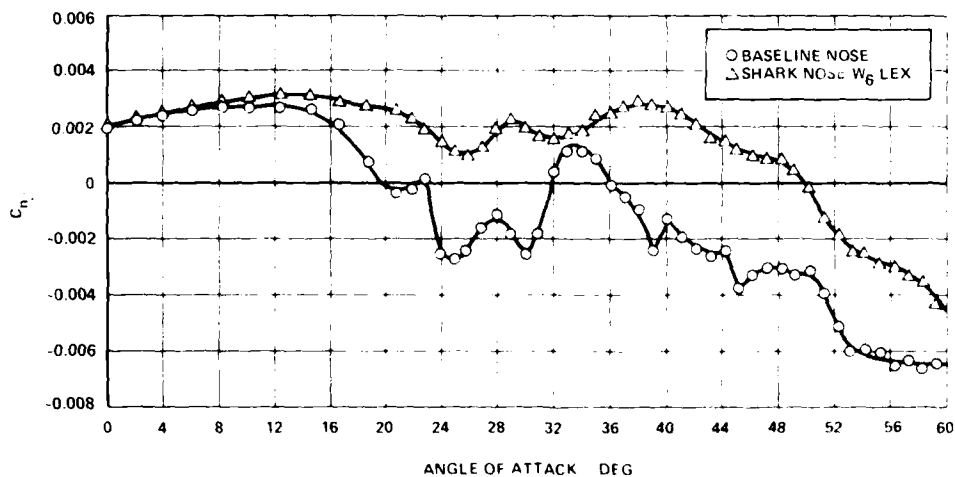
FIGURE 98. EFFECT OF SHARK NOSE W_6 LEX ON STABILITY

FIGURE 99. FOREBODY-WING-LEX VORTEX FLOW
INTERACTION AT HIGH ANGLE OF ATTACK
(NORTHROP WATER TUNNEL)
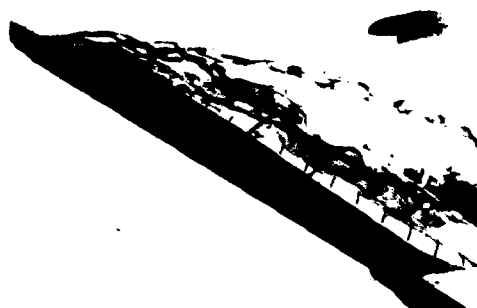
FIGURE 100. NORTHROP WATER TUNNEL FLOW
VISUALIZATION OF THE STRONG COUPLING
BETWEEN THE FOREBODY AND WING-LEX
VORTEX FLOW FIELDS AT SMALL ANGLE
OF SIDESLIP

4.3 Interactions With a Non-Vortical Wing Flowfield

In addition to nose strakes, forebody shape can strongly influence forebody and wing flowfield inter actions on a configuration with little vortex lift at high AOA. This was found on a scale model of the F 15 tested with two lengthened forebodies with modified cross-sectional shapes (see Reference 35). One forebody tested was the Northrop Shark Nose, and the other was a cambered forebody (Figure 102). The results, shown in Figure 103, sh v that the Shark Nose and cambered nose produced similar high levels of direc tional stability. The cambered forebody produced only slight changes in lateral stability from that of the short forebody of the basic F-15. In the Shark Nose, however, there was a sharp loss of lateral stability. This results from an interaction between the leeward Shark Nose vortex and the wing/glove vortex system. The cambered forebody has a forebody vortex orientation that has minimal interaction with the wing/LEX flowfield.

4.4 Forebody/Wing Vortex Interactions in a Rotational Flowfield

When an aircraft yaws at high AOA and at low forward speeds, as in a nose-slice or yaw departure. the vortical flowfield around the forebody becomes skewed or biased. This bias affects the forces devel oped by the forebody and can alter the interaction of the forebody flowfield with downstream components. Similarly, when an aircraft develops a rolling motion at high AOA and low airspeed, such as wing-rock, the vortices emanating from a LEX or from the wing leading edge are affected to some degree, as is the influence of upstream vortices. Forebody strakes and, to a lesser degree, forebody cross-sectional shape can have a dramatic effect on the damping characteristics which an aircraft exhibits in a rotational flowfield at high angles of attack.

(a) – DIRECTIONAL CHARACTERISTICS

(b) – LATERAL CHARACTERISTICS
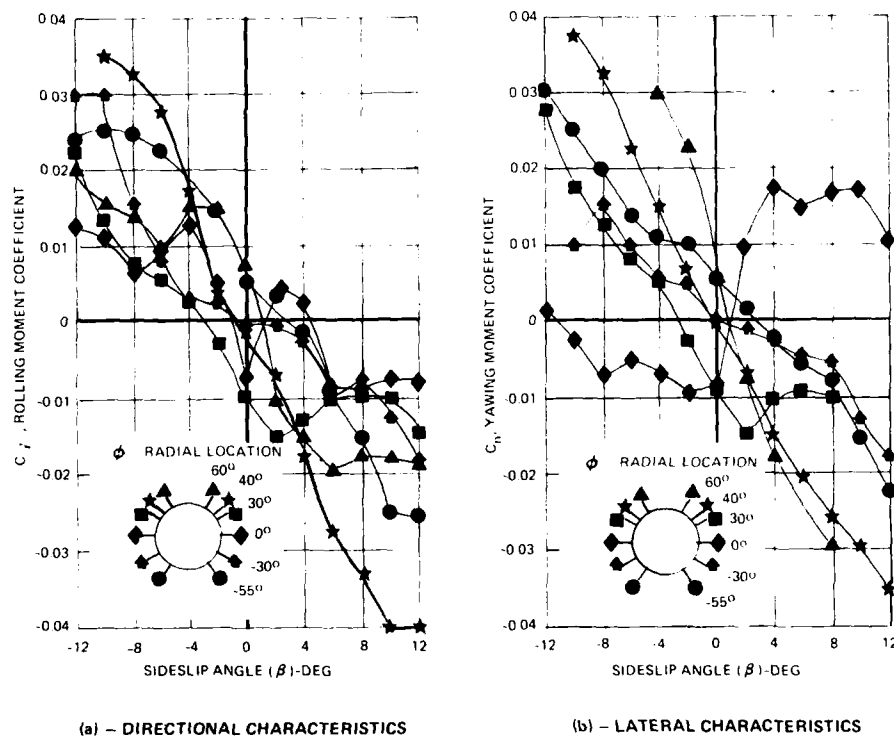
FIGURE 101. EFFECT OF NOSE STRAKE RADIAL LOCATION ON LATERAL-DIRECTIONAL CHARACTERISTICS: α = 35 DEGREES
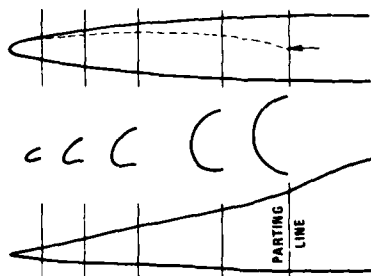
FIGURE 102. CAMBERED FOREBODY GEOMETRY

Rotary balance wind tunnel tests of an F-5 model at NASA Langley have indicated that thin strakes placed on the forebody in the vicinity of the primary vortex separation line can greatly increase the damping in yaw of the aircraft at angles of attack above 40 degrees.

Further tests of this configuration at low speeds mounted on an aft sting and unconstrained in roll indicated that the limit-cycle wing rock exhibited by this aircraft could be greatly attenuated, presumably by an increase in roll damping due to a more favorable interaction between the forebody and wing vortex systems developed by the rolling motion.

The reader is reminded that the effects of similar strakes on this aircraft were found to be destabilizing above α = 30 (see Section 3.5). Further study is required to determine whether the net effect on the aircraft departure and spin resistance is positive or negative. Accepted criteria for departure resistance, such as $C_{n_{\beta dyn}}$ and LCDP, may have to be modified to account for variations in both yaw and

roll damping.

5.0 CONTROL SURFACE DESIGN

Achieving adequate controllability at high AOA is a very difficult design problem, and as AOA for maneuvering become increasingly large, the design problem becomes even more difficult. Sizing and placement of tail surfaces is critical for both stability and controllability at high AOA.
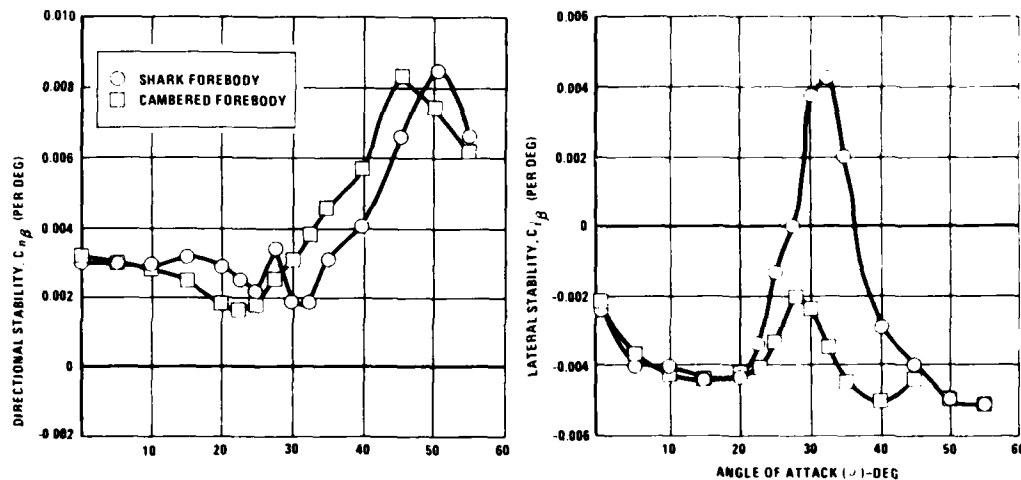
FIGURE 103. EFFECT OF FOREBODY SHAPE ON STABILITY

5.1 Lateral Directional Controls and Stabilizing Surfaces

In the past the designer's job in sizing a vertical tail was relatively simple. The flight conditions that established the tail geometry were straightforward, such as low speed (rigid body) directional stability and control adequate for cross wind landing, and high speed (elastic body) directional stability adequate for good flying qualities.

These criteria were usually achieved by providing an adequate vertical tail volume coefficient, the required value of which was based on a large, very consistent empirical design data base. Wind tunnel tests were utilized mainly for verification of the final value of directional stability.

For modern fighter aircraft, which operate regularly at post-stall AOA, vertical tail sizing and placement are more complex, more "cut and try." For fighters with large amounts of vortex lift at high AOA, generated by the wing, the LEX or wing body strake, or by the forebody, the vertical tail must be carefully placed in this vortical flowfield. A significant augmentation in terms of directional stability can, in fact, be achieved if the placement of the vertical tail takes full advantage of the concentrated energy contained in a wing or LEX vortex. Large increases in high AOA directional stability and in directional control effectiveness were achieved on both the YF-17 and on the F-5G by moving the vertical tail(s) forward on the body, into closer proximity to the LEX vortex flowfield, even though this significantly reduced the tail volume coefficient. In considering the placement of the vertical tail in a vortical flow, however, the trajectories of the vortices in the flowfield under nonzero sideslip conditions must be accurately known. Care must be exercised to ensure that these vortex trajectories do not cause an abrupt loss of directional stability at high sideslip angles.

Another characteristic difficult to achieve is roll control at high AOA. Traditional aileron controls lose much of their effectiveness at AOA near stall and can produce adverse yaw during a rolling maneuver, which can cause roll rate reversal and departure from controlled flight. Differential deflection of an all moving aft tail can be more effective in producing adequate roll control at high AOA, although adverse yaw is a consideration in the design of these "rolling tails" as well.

Whatever means of roll control the designer chooses to employ, the aircraft should be designed to achieve a coordinated roll about the velocity vector rather than about the body axis at high AOA. Examination of the kinematics of a high-AOA roll clearly illustrates why this is the case, minimizing the buildup of adverse sideslip, which reduces the peak roll rates and can cause roll reversal.

Roll reversal can be accurately predicted using the lateral control departure parameter (LCDP) or the aileron alone divergence parameter (AADP), as shown in References 37 and 41. The LCDP parameter has been used in various forms for different purposes and is derived from the simplified rolling and yawing moment equation. As a lateral control departure parameter, it predicts roll reversal or the point at which rolling moment due to adverse yaw overcomes the aileron power.

$$\text{LCDP (AADP)} = C_{n_\beta} - \left(C_{n_{\delta_a}} / C_{l_{\delta_a}} \right) C_{l_\beta} \quad \text{(no rudder)}$$

$$\text{LCDP} = C_{n_\beta} - C_{l_\beta} \left(C_{n_{\delta_a}} + K C_{n_{\delta_r}} \right) / \left(C_{l_{\delta_a}} + K C_{l_{\delta_r}} \right) \quad \text{(with rudder)}$$

In addition, at high AOA the kinematics of aircraft motion are different from those at low AOA in that the aircraft is designed to be maneuvered in roll about the flight path vector rather than about the body axis. Were this not the case, very large adverse sideslip angles would develop, which would greatly reduce roll effectiveness. Due to this tendency (by design) of the aircraft to roll about the flight path, a large body axis yaw rate is generated, which will couple with the commanded roll rate to create a very strong inertial pitching moment.

This inertial pitching moment, developed by aggressive roll maneuvering up to α_{max}, must be accounted for in designing the control system and in the sizing of the control surfaces. As previously illustrated, at higher maximum AOA, there is generally less pitch controllability to work with, so two obvious solutions present themselves to a designer sizing a pitch control system. The first is to size the control to prevent high AOA pitch departures for a given level of inertial roll yaw coupling and for a given α_{max}. The second solution is to reduce α_{max}, either through increases in the aircraft static stability or through active limiting with the control system feedback loops, so that adequate pitch control capability exists with a smaller surface or with less deflection.

A third, less obvious option also exists: Since rolling at high AOA could be considered the root cause of the problem, actively limiting the roll capability of the aircraft as a function of AOA, again using control system feedback loops, could be included in the basic design, thereby reducing the inertial pitch coupling. However, since the ability of a fighter pilot to rotate the lift vector of his aircraft in offensive or defensive ACM is a key agility parameter, roll limiters should be considered only as a last resort.

When maneuvering at AOA at or beyond stall, many fighter aircraft experience a loss of roll damping and possibly a reduction in lateral stability. These factors can contribute to an oscillation in roll known as "wing rock." This can lead immediately to a rolling departure if a post stall AOA is maintained, or the motion may become a bounded, limit-cycle oscillation.

For an aircraft with a limit-cycle wing rock at high AOA, an interaction can develop between the lateral directional and the longitudinal axes. This interaction is initiated by the kinematic interchange of AOA and sideslip that occurs during wing rock and is manifested by the static derivative $C_{m_{|\beta|}}$

Depending on the specific aerodynamic characteristics, $C_{m_{|\beta|}}$, varies with AOA and may be positive or negative. Forebody cross-sectional shape appears to be the dominant geometric parameter that influences the sign of this derivative. A flat, elliptical forebody cross section, known to be good for high AOA directional stability, usually produces a nose-up $C_{m_{|\beta|}}$. A vertically oriented elliptical shape tends to produce nose-down $C_{m_{|\beta|}}$ but degrades directional stability. Figure 105 presents an example of how C_{m} varies for a fighter aircraft with a flat, elliptical forebody cross section. Figure 106 schematically illustrates how this derivative can cause peak AOA in a sustained, post-stall maneuver to increase well beyond the static, trimmed value.
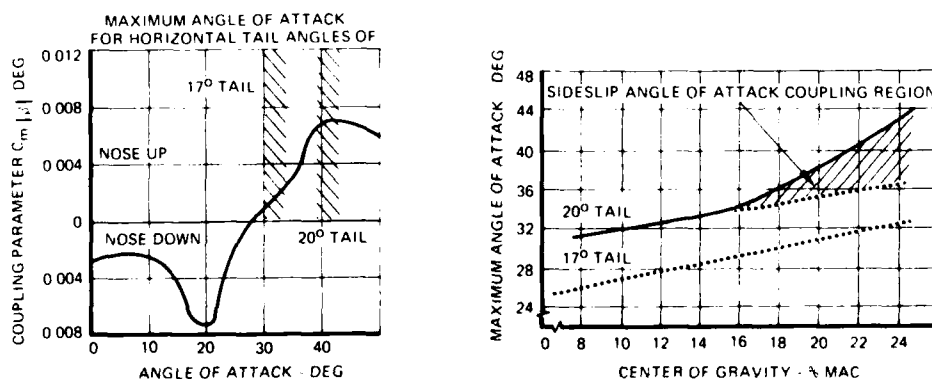
FIGURE 105. EFFECT OF LIMITING TAIL AUTHORITY ON SIDESLIP/AOA COUPLING PARAMETER

The effects of pitching moment due to sideslip and the effects of inertia coupling at high AOA must be superimposed on the basic airframe longitudinal stability when determining the pitch control system design. Figure 107 shows how consideration of both kinematic ($C_{m_{|\beta|}}$) and inertial (pxr) coupling can drastically affect the allowable aft center of gravity of a fighter aircraft with an aft, all moving horizontal tail. After subtracting the basic airframe controllability for the effects of pitching moment due to sideslip and the effects of inertial coupling, a net -0.05 nose-down pitching moment must remain to achieve adequate controllability at α_{max}. This amount of net nose-down moment, though not large, will assure that AOA overshoots can be minimized, even at airspeeds as low as 100 knots.

$C_{m_{|\beta|}}$

C_m

$\alpha = 35^\circ$

SIDESLIP ANGLE — DEG

10   20   30   40
ANGLE OF ATTACK — DEG

α
DEG

TIME

β
DEG

TIME

$\dot{q}$
DEG SEC^2

TIME
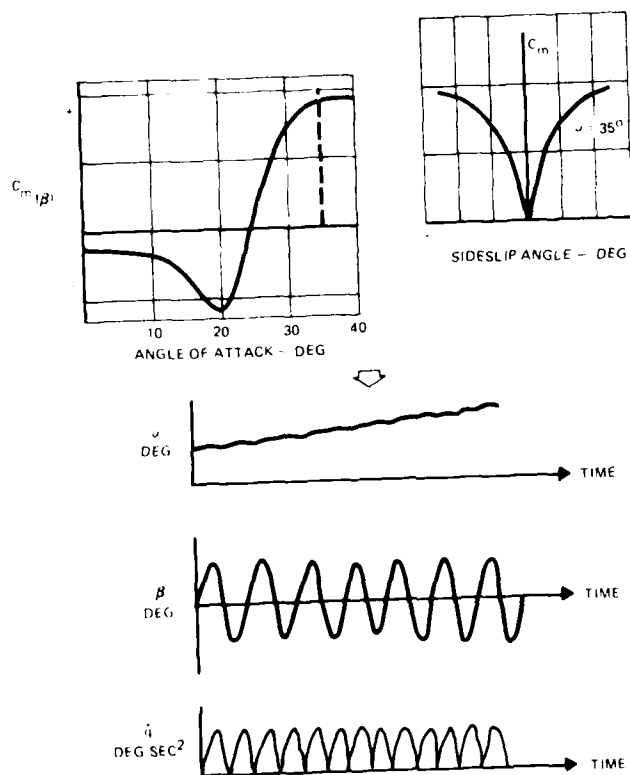
FIGURE 106. EFFECT OF $C_{m_{|\beta|}}$ DURING OSCILLATORY
LIMIT-CYCLE WING ROCK

HIGH-AOA AFT CG LIMIT

LOW-AOA AFT CG LIMIT

CG POSITION

0.05 MINIMUM
CRITERION

$\alpha_|\beta$ + MILD INERTIA COUPLING

WITH α/β COUPLING

STATIC

PITCHING MOMENT COEFFICIENT, C_{m_*}
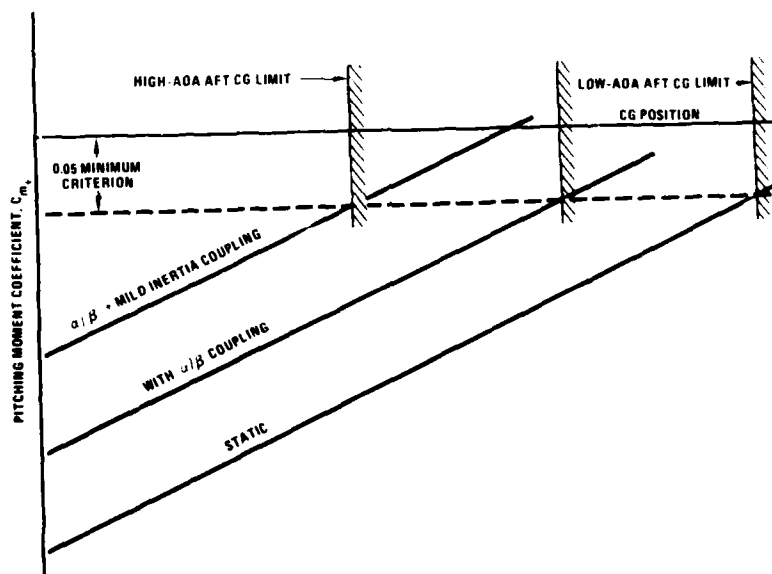
FIGURE 107. EFFECT OF KINEMATIC AND INERTIAL COUPLING
ON AFT CG LIMIT

4-52

6.0 INLET AIRFRAME INTEGRATION CONSIDERATIONS AT HIGH ANGLES OF ATTACK

Due to the considerable extension of the operating AOA range of modern, highly maneuverable fighter aircraft, the difficulties of integrating a propulsion system into the airframe are made more formidable. The designer wishes to maintain relatively uniform dynamic pressure contours across the engine compressor face since the distortion caused by nonuniform contours reduces the surge margin of the engine and can cause compressor stall and flameout.

6.1 Induction System High Angle of Attack Flow Quality Requirements

Maintaining a low level of dynamic distortion is the primary induction system requirement at high AOA. When the peak AOA is 40 degrees or higher, it becomes virtually impossible for the designer to preclude massive separation at the inlet. The key to keeping distortion at the engine compressor face low is not to delay separation, but rather to control the development of the separation region. A long inlet duct can help to attenuate distortion that originates at the inlet lip. The designer must maintain acceptable dynamic distortion levels up to the maximum design AOA.

The designer also wishes to maintain a high level of pressure recovery through the induction system to maximize the installed thrust available. At high AOA, maintaining high recovery while simultaneously maintaining low distortion can lead to conflicting design requirements or to a highly complex variable geometry inlet that tries to satisfy both requirements. As it turns out, low levels of pressure recovery at high post stall AOA have a negligible effect on the specific excess power (P_s) a fighter can develop. The negative P_s at post stall AOA is dominated by airframe drag due to lift, which is typically four to five times greater than the available thrust. Providing that a high enough pressure is developed at the engine face to ensure satisfactory engine operation, high pressure recovery through the induction system is an important design consideration only up to the AOA at which a constant energy turn can be performed. This turn rate is the maximum steady state turn rate (ω_{ss}). Figure 108 illustrates that at two subsonic Mach numbers, the maximum instantaneous turn rate and the specific excess power at that condition are essentially constant whether the inlet is operating at 70 percent recovery or even at 100 percent.
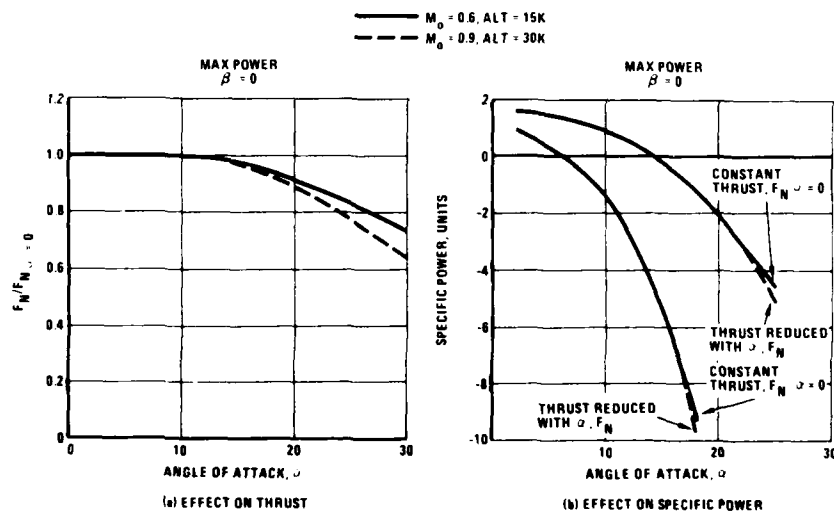
FIGURE 108. INSTALLED THRUST VARIATION WITH INLET RECOVERY AT HIGH AOA

The designer must also ensure that the induction system exhibits no flow instabilities over the entire aircraft engine operating envelope. At high Mach numbers, an external compression inlet can encounter shock boundary layer interactions, which can trigger a flow instability called "inlet buzz." Inlet design features to preclude buzz can cause compatibility problems at high AOA at low speeds (e.g., separation over a ramp leading and lower edge thus causing a vortex to be ingested by the inlet). At low mass flow rates (idle flow or less), separation off of a ramp edge or from the inlet lip can cause a duct to develop an instability or resonance at the theoretical organ pipe frequency. Figure 109 illustrates the development of this resonance with AOA on a 1/5-scale model of the F-5G induction system. By contouring the lower edge of the ramp and making it more conformal to the fuselage, the resonance was eliminated at zero sideslip and greatly attenuated at nonzero sideslip.
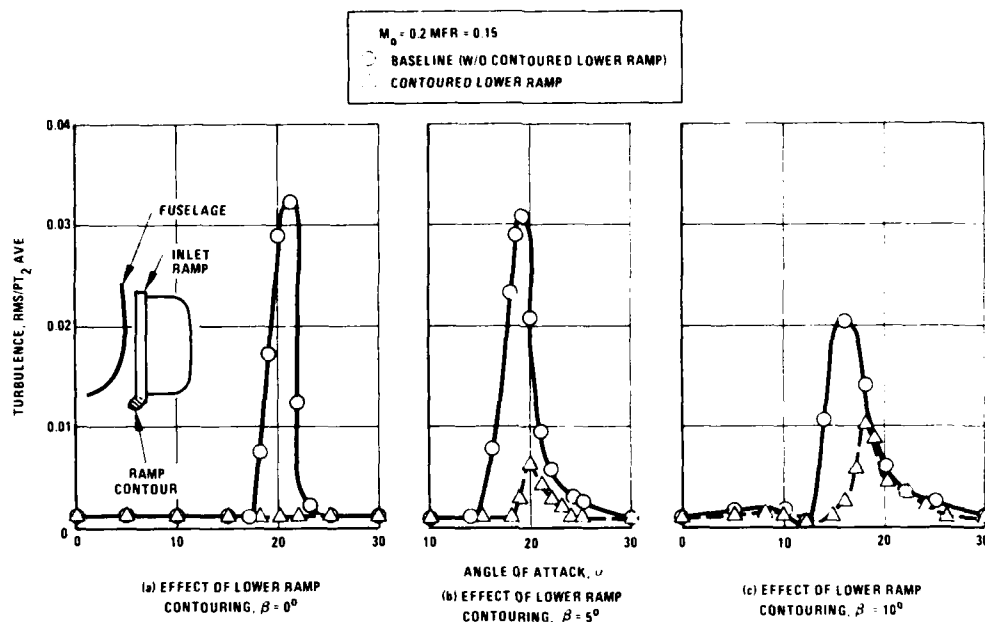
FIGURE 109. INLET RESONANCE AT LOW MASS FLOW RATIO

6.2 Inlet Placement Relative to Fuselage/Wing

Inlet geometry and location is typically a compromise selected to accommodate various design, mission, and operational requirements. Figure 110 presents representative fighter configurations with a variety of possible inlet integrations.

When considering the requirements for operation at high AOA, the designer may wish to locate the inlets where they are shielded from high flow angularity (e.g., beneath the fuselage or the wing). Any reduction in flow angularity at the inlet will improve the high AOA induction system characteristics. This may not be possible because other design constraints may finally dictate the location. These constraints can be clearance above the runway to minimize foreign object damage; water, slush, or steam ingestion; reduction in frontal or lower hemisphere radar echo for mission survivability; or simply placement to reduce total induction system complexity. Inlet location can have an adverse effect on aircraft stability, and these effects can even be a function of inlet mass flow. This is especially evident if the inlet is in close proximity to a LEX or highly swept leading edge of a wing. Inlet mass flow can alter the vortex burst characteristics and can degrade lateral-directional stability.

A top mounted inlet is perhaps least suitable for operation at high AOA. However, Williams and Hunt (Reference 42) have shown that by careful integration of the inlet on the fuselage to take maximum advantage of the sweeping action of the vortical flows from the LEX at high AOA, the pressure recovery and dynamic distortion can be controlled and can have values comparable to more traditional inlet locations, as shown in Figure 111.

6.3 Bifurcated Duct Effects

When an engine is fed by a bifurcated duct, flow instabilities set up by external disturbances due to nonzero sideslip can be important. If the bifurcated duct included separate inlets, one on the windward and one on the leeward side of the aircraft in a sideslip condition, a beneficial interaction that can ameliorate the otherwise adverse effects of sideslip can develop. Figure 112 illustrates how average engine face pressure recovery remains essentially constant at an AOA of 30 degrees as sideslip is increased 10 degrees. At high AOA, the windward inlet recovery improves at the same rate at which the leeward inlet recovery deteriorates. At lower AOA, the average recovery decreases with sideslip since at zero sideslip recovery is higher and true potential improvement in the windward inlet is reduced.
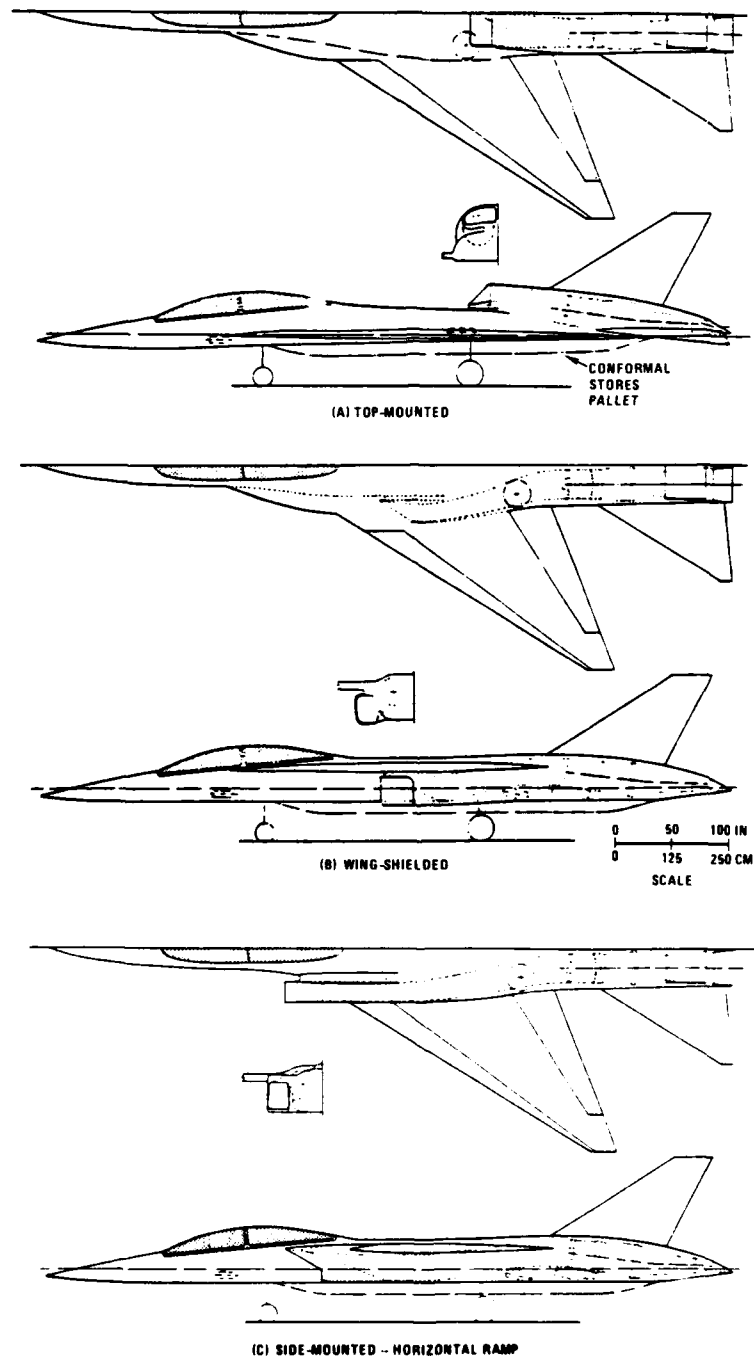
(A) TOP-MOUNTED

CONFORMAL
STORES
PALLET

(B) WING-SHIELDED

| 0 | 50 | 100 IN |
| 0 | 125 | 250 CM |

SCALE

(C) SIDE-MOUNTED – HORIZONTAL RAMP

FIGURE 110. INLET/AIRFRAME INTEGRATION OPTIONS

(D) FUSELAGE-SHIELDED
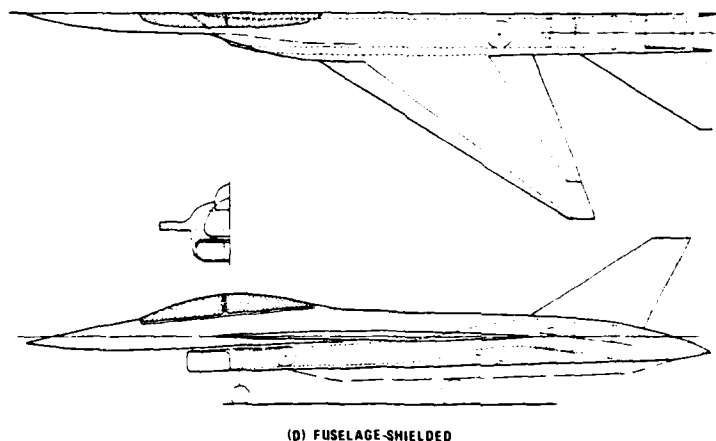
FIGURE 110. INLET/AIRFRAME INTEGRATION OPTIONS (CONTINUED)

──────── TOP-MOUNTED (NASA/NORTHROP VATOL)

••••••••• FUSELAGE-SHIELDED (GENERAL DYNAMICS YF−16, REF 8)

—•—•—•— WING-SHIELDED (NORTHROP YF-17)

— — — — SIDE-MOUNTED (ADVANCED NORTHROP FIGHTER CONFIGURATION,
2-D EXTERNAL COMPRESSION RAMP INLET, VERTICAL RAMP)

ANGLE OF ATTACK (DEGREES)
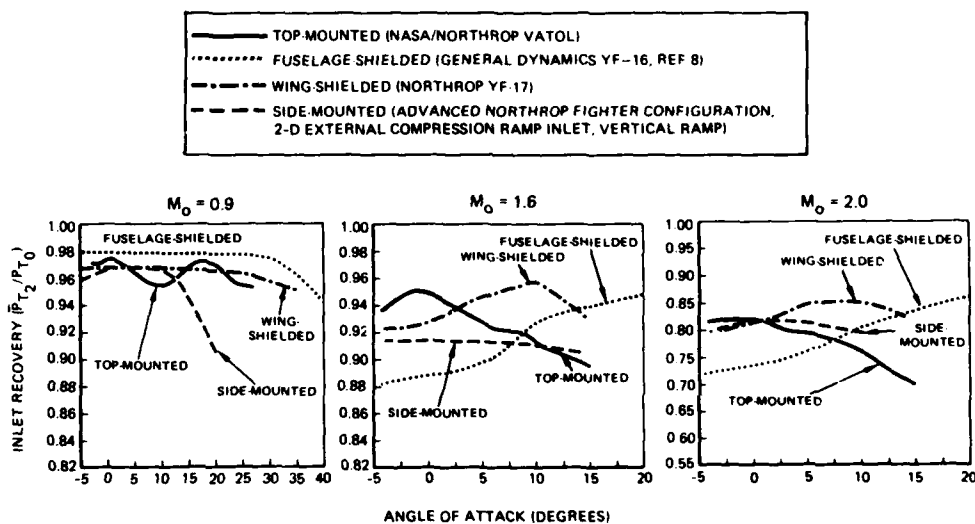
FIGURE 111. A COMPARISON OF INLET RECOVERY CHARACTERISTICS FOR
TOP AND CONVENTIONAL INLET INSTALLATIONS

7.0 SUMMARY: HIGH-ANGLE-OF-ATTACK DESIGN CRITERIA

This discussion has dealt with the factors that affect the flow over wings, bodies, control surfaces, and inlets of fighter aircraft at high AOA. Most of these factors are related to the geometry of the aircraft although some are related to the conditions of the free stream through which the aircraft moves. Fluid mechanics development around the aircraft was shown to have a direct effect on the flight mechanics, which relate to stability, controllability, and departure resistance at high AOA. A consistent relationship can be shown between some aircraft geometric features or characteristics and the handling qualities of the vehicle, and these features can be developed into some useful design guidelines.

1. Airframe Stability:

a. $(C_{n_{\beta_{dyn}}} > 0.0040$ up to α_{max}

b. C_{n_β} (body axis) $\quad 0$ up to α_{max}

c. C_{l_β} 0 up to σ_{max}

d. C_{n_0} $(\beta - 0$ degrees) 0.0100 up to α_{max}

2. *Controllability*:

a. LCDP 0 up to α_{max}

b. Net C_m more negative than -0.05 up to α_{max}
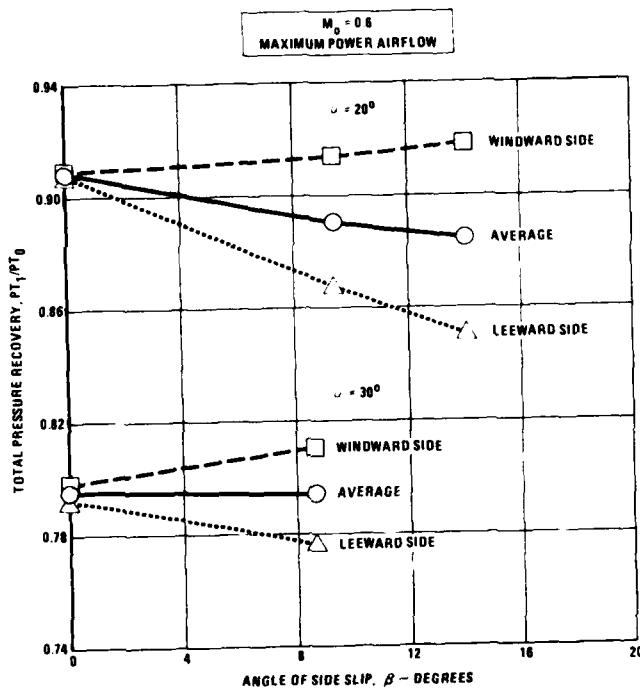
FIGURE 112. EFFECT OF SIDESLIP ON INDUCTION SYSTEM RECOVERY

3. Inlet Airframe Compatibility:

a. Fixed throttle dynamic distortion indices within engine limits up to σ_{max}/β_{max}

b. Variable throttle (full body) dynamic distortion indices within engine limits up to $\sigma C_{l_{max}}$

c. High inlet recovery only up to $\sigma_{\psi_{ss}}$

Figure 113 shows the correlation between expected post-stall behavior as a function of $C_{n_{\beta_{dyn}}}$ when no lateral/directional control inputs are considered. Figure 114 shows the correlation between $C_{n_{\beta_{dyn}}}$, LCDP, and post-stall behavior when lateral/directional controls are considered.
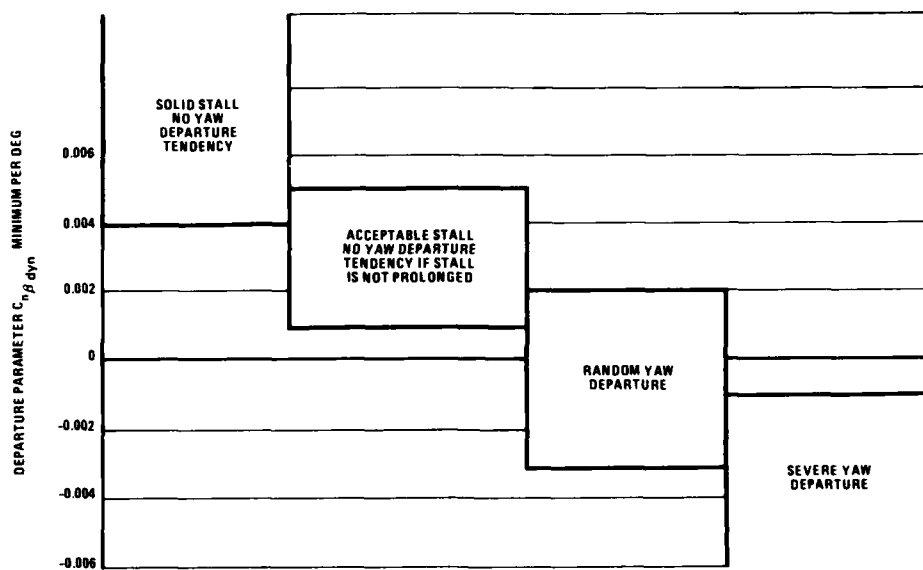
FIGURE 113. EXPECTED STALL BEHAVIOR AS A FUNCTION OF $Cn_{\beta_{dyn}}$

	REGION (A): NO DEPARTURES SOLID STALL
WEISSMAN CRITERIA	REGION (B): MILD ROLLING DEPARTURES ACCEPTABLE STALL LOW SPIN SUSCEPTIBILITY
	REGION (C): MODERATE ROLLING DEPARTURES – MODERATE SPIN SUSCEPTIBILITY
	REGION (D): STRONG ROLLING DEPARTURES HIGH SPIN SUSCEPTIBILITY
NORTHROP CRITERIA	REGION (E): RANDOM YAW DEPARTURE MODERATE SPIN SUSCEPTIBILITY
	REGION (F): SEVERE YAW DEPARTURES HIGH SPIN SUSCEPTIBILITY

FIGURE 114. COMBINATION OF WEISSMAN AND NORTHROP DEPARTURE CRITERIA

REFERENCES

1. Polhamus, E.C., "A Concept of the Vortex Lift of Sharp-Edge Delta Wings Based on a Leading-Edge Suction Analogy," NASA-TN-D-3767, December 1966.

2. Lorincz, D.J., "Space Shuttle Orbiter Flow Visualization Study," NASA-CR-163092, February 1980.

3. Küchemann, Dietrich, "The Aerodynamic Design of Aircraft," Pergamon Press, 1978. p. 360.

4. Werlé, Henri, "Le Tunnel Hydrodynamique an Service de la Recherche Aerospatiale," ONERA Publication 156, 1974.

5. Aviation Week and Space Technology, Vol. 111, No. 1, 2 July 1979, pp. 20-21.

6. Aviation Week and Space Technology, Vol. 114, No. 25, 22 June 1981, p. 18.

7. Lamar, J.E., Schemensky, R.T., and Reddy, C.S., "Some Applications of Vortex Flow Analysis Methods Related to the Design of Slender Cambered Wings," AIAA-80-0327, January 1980.

8. Rao, D.M., "Leading-Edge 'Vortex Flaps' for Enhanced Subsonic Aerodynamics of Slender Wings," ICAS-80-13.5, 1980.

9. Tinoco, E.N., and Yoshihara, H., "Subcritical Drag Minimization for Highly Swept Wings with Leading-Edge Vortices," AGARD-CP-247, October 1978.

10. Johnson, F.T., et al., "An Improved Method for the Prediction of Completely Three-Dimensional Aerodynamic Load Distributions on Configurations With Leading-Edge Separation," AIAA-76-417, 1976.

11. Lambourne, N.C., and Bryer, D.W., "The Bursting of Leading-Edge Vortices - Some Observations and Discussion of the Phenomenon," Aeronautics Research Council R&M 3282, Vol. 22, April 1961, p. 775.

12. Chigier, N.A., "Measurement of Vortex Breakdown Over a Delta Wing Using a Laser Anemometer," NEAR-TR-62, June 1974.

13. Hummel, Dietrich, "Experimental Investigation of the Flow on the Suction Side of a Thin Delta Wing," Z. Flugwiss., Jahrg. 13, Heft 7, July 1965, pp. 247-252.

14. Lowson, M.V., "Some Experiments with Vortex Breakdown," J. Roy. Aero. Soc., Vol. 58, No. 343, 1964.

15. Wentz, W.H., "Effects of Leading-Edge Camber on Low-Speed Characteristics of Slender Delta Wings," NASA-CR-2002, October 1972.

16. Erickson, G.E., "Vortex Flow Correlation," AFWAL-TR-80-3143, January 1981.

17. Shanks, R.E., "Low-Subsonic Measurements of Static and Dynamic Stability Derivatives of Six Flat-Plate Wings Having Leading-Edge Sweep Angles of 70° to 84°," NASA-TN-D-1822, 1953.

18. Lorincz, D.J., "Flow Visualization of the HiMat RPRV," NASA-CR-163094, July 1980.

19. Headley, J.W., "Analysis of Wind Tunnel Data Pertaining to High Angle of Attack Aerodynamics," Vol. 1, AFFDL-TR-78-14, 1978.

20. Gerhardt, H.A., "The Aerodynamic Development of the Wing Root Leading Edge Extension of the P530 Airplane Configuration," Northrop Report NOR 73-71, 1972.

21. Lamar, J.E., and Luckring, J.M., "Recent Theoretical Developments and Experimental Studies Pertinent to Vortex Flow Aerodynamics - with a View Towards Design," AGARD-CP-247, October 1978.

22. Lamar, J.E., and Gloss, B.B., "Subsonic Aerodynamics Characteristics of Interaction Lifting Surfaces with Separated Flow Around Sharp Edges Predicted by a Vortex-Lattice Method," NASA-TN D-7921, 1975.

23. Marchman, J.F., "Aerodynamics of Inverted Leading Edge Flaps on Delta Wings," AIAA Journal of Aircraft, Vol. 18, No. 12, December 1981, pp. 1051-1056.

24. Rao, D.M., "Leading Edge Vortex-Flap Experiments on a 74° Delta Wing," NASA-CR-159161, November 1979.

25. Westesson, R.A., and Clareus, V., "Turbulent Lift: Comments on Some Preliminary Wind Tunnel Tests," Saab-Scania Report TP-74-51, March 1974.

26. Erickson, G.E., and Campbell, J.R., "Flow Visualization of Vortices Locked by Spanwise Blowing over Wings Featuring a Unique Leading- and Trailing-Edge Flap System," NASA-TM-X-72788, December 1975.

27. Skow, A.M., Titiriga, A., Jr., and Moore, W.A., "Forebody/Wing Vortex Interactions and Their Influence on Departure and Spin Resistance," AGARD-CP-247, October 1978.

Lamar, J.E., "Summary of Some Recent Studies of Subsonic Vortex Lift and Parameters Affecting the Leading-Edge Vortex Stability," AIAA-76-414, July 1976.

29. Hertel, Heinrich, Structure-Form-Movement, Reinhold Publishing Corp., New York, 1963.

30. Rao, D.M., and Tingas, S.A., "Subsonic Balance and Pressure Investigation of a 60° Delta Wing with Leading-Edge Devices (Data Report)," NASA-CR-165806, November 1981.

31. Edwards, O.R., "F-5F Stall/Post-Stall/Spin Susceptibility Flight Tests," Northrop Report NOR 77-91, August 1977.

32. Grafton, S.B., Chambers, J.R., and Coe, P.L., Jr., "Wind Tunnel Free-Flight Investigation of a Model of a Spin-Resistant Fighter Configuration," NASA-TN-D-7716, June 1974.

33. Jorgensen, L.H., and Nelson, E.R., "Experimental Aerodynamic Characteristics for Slender Bodies with Thin Wings and Tail at Angles of Attack from 0° to 58° and Mach Numbers from 0.6 to 2.0," NASA-TMX-3310, March 1976.

34. Chapman, G.T., Keener, E.R., and Malcolm, G.N., "Asymmetric Aerodynamic Forces on Aircraft Forebodies at High Angles of Attack - Some Design Guides," AGARD-CP-199, June 1976.

35. Carr, P.C., and Gilbert, W.P., "Effects of Fuselage Forebody Geometry on Low-Speed Lateral-Directional Characteristics of Twin-Tail Fighter Model at High Angles of Attack," NASA-TP-1592, December 1979.

36. Edwards, O.R., "Northrop F-5F Shark Nose Development," NASA-CR-158936, October 1978.

37. Skow, A.M., and Titiriga, A., Jr., "A Survey of Analytical and Experimental Techniques to Predict Aircraft Dynamic Characteristics at High Angles of Attack," AGARD-CP-235, May 1978.

38. Lamont, P.J., "Pressure Distributions on an Ogive-Cylinder at High Angles of Attack With Laminar, Transitional or Turbulent Separation," AIAA-80-1556, August 1980.

39. Lamont, P.J., "The Complex Asymmetric Flow Over a 3.5D Ogive Nose and Cylindrical Afterbody at High Angles of Attack," AIAA-82-0053, January 1982.

40. Ericsson, L.E., and Reding, J.P., "Steady and Unsteady Vortex-Induced Asymmetric Loads on Slender Vehicles," AIAA-80-0181R, January, 1980.

41. Weissman, R., "Preliminary Criteria for Predicting Departure Characteristics/Spin Susceptibility of Fighter-Type Aircraft," AIAA Journal of Aircraft, April 1973.

42. Williams, T.L., and Hunt, B.L., "Top Mounted Inlet System Feasibility for Transonic-Supersonic Fighter Applications," AIAA-80-1809, August 1980.

ACKNOWLEDGEMENT

MODERN MISSILE DESIGN FOR HIGH ANGLE-OF-ATTACK

Gregor Gregoriou
Messerschmitt-Bölkow-Blohm GmbH
Dynamics Division
Ottobrunn/Munich, Germany

SUMMARY

This paper deals with aerodynamic problems associated with the design of modern missiles for high angles of attack. The design consideration that have to be given by the aerodynamicist to develop the external configuration are exemplified. It is shown how the information available from existing literature on in-plane and out-of-plane forces and moments of the single missile components wing, body, tail or of complete configurations is of influence on the aerodynamicists decisions during the design process. In addition the effect of the mostly rather complex aerodynamic characteristics on other missile components (i.e. propulsion or control system, etc.) is mentioned. Finally methods for the theoretical and experimental determination of aerodynamic coefficients are discussed and critically assessed.

1. SYMBOLS

b	missile total span
L	missile total length
L_N	length of missile
D	body diameter
X	axial coordinate
AR	wing or tail aspect ratio
λ	wing or tail taper ratio
V	free-stream velocity
Ma	free-stream Mach number
Ma_Q	Mach number of the cross flow
α	angle of attack
ϕ	roll angle
Re_D	Reynolds number based on diameter
h	altitude
c_{z_1}	local normal-force coefficient
c_z, c_y	normal-force and side-force coefficients
c_m, c_n	pitching-moment and yawing-moment coefficients
c_1	rolling-moment
x_{CP}	center of pressure
$c_{N1...4}$	individual panel forces
CCR	roll-yaw cross-coupling rate
t	time

Reference area for the coefficients is $\pi D^2/4$

Reference length for the coefficients is D

ABBREVIATIONS

B,W,T	body, wing, tail

2. INTRODUCTION

On reviewing the missile development of recent years a tendency towards high angles of attack is apparent. This trend of development is being fostered on the one hand by the demand for higher maneuverability and, on the other hand - due to a mission's special features - by specific requirements on flight behaviour. Moreover, this tendency is amplified by the ever increasing requirement of decreasing the overall wingspan to a minimum. Favourable aspects are the decrease in missile-mass and missile-cost, fewer storage problems under the aircraft-carrier or within a dispenser, decrease in missile drag and logistic and structural advantages. Nowadays there are several fields of missile design that involve high angles of attack, e.g.:

- vertically launched missile

- store separation from aircraft top-side

- submunition launched from aircraft container

- one-man anti-tank weapon (attack on upper surface of tanks)

- air-to-air and air-to-ground short range missile.

In all these cases high angles of attack are reached at subsonic Mach numbers. In some cases the flight Mach number range is very wide and extends from low subsonic speeds to high supersonic speeds. In such a vast variation of flight conditions the flow pattern around the missile is subject to considerable changes and important aero-dynamic characteristics such as static margin and trimm-performance are affected.

The challenge for the design aerodynamicist now is to develop a favourable external configuration which fulfills the flight mechanic and other requirements successfully. In doing so the aerodynamicist needs to be informed about the manifold and partially rather complex flow behaviour at high angles of attack as well as about the effects on the in-plane and out-of-plane forces and moments since the static and dynamic flight-characteristics of the missile are thereby considerably changed. This in return bears great influence on the missile's geometric layout, the design of the autopilot, controls and actuator, the choice of the seeker and the propellant's characteristics. The mutual interference of all of these components is fairly large and necessitates close contact between the specialised staff of the various design fields already at the commencing stage of a missile project.

To begin with, in the paper presented, a few missile missions with high angles of attack involved will be exemplified. Subsequently, a review of high angle-of-attack aerodynamics suited for the design-aerodynamicist's needs will be presented. Consi-deration will be given to both the in-plane and out-of-plane forces and moments. In addition, the most relevant effects of the vehicle motion will be mentioned. Subsequently some aerodynamic characteristics of bodies with non-circular cross section will follow. The aerodynamic effects at high angles of attack on other missile components will be discussed in a separate paragraph. The paragraph following deals with the prediction of aerodynamic coefficients, both with the aid of theoretical methods and experimental investigation. At the end the most important conclusions for missile design at high angles of attack are summed up into a design guideline.

The high angle-of-attack region is characterized by a strong flow separation. This is indicated by a pronounced non-linear characteristic of the in-plane coefficients and the appearance of out-of-plane forces and moments. As a lower limit of high angles of attack an angle of $\alpha \approx 20^o$ might be assumed in this context. The canard configuration, however, is an exception in so far that particularly with control deflection, strong non-linearities occur also at small angles of attack.

3. MISSILE MISSIONS WITH HIGH-ANGLES-OF-ATTACK OCCURRENCE

There are numerous missile projects under development that operate at high angles of attack even if it is only for a short period of time. Some examples are illustrated in Fig. 1 - 6.

VERTICALLY LAUNCHED MISSILES

Vertical launch is an old launch technique, well known from historical missiles such as V2 and many of its successors. It is now gaining increasingly in significance as far as many new guided missile concepts for ground-to-air or sea-to-air defence as well as for sea-skimmer defense are concerned. Here the most frequent type of launch was aimed launch from a launcher adjustable in azimuth and elevation. This technique became questionable in modern systems where requirements exist as to

- multiple target engagement for simultaneously attacking aircraft

- complete 360° coverage without blind arcs

- obstacle clearance: trees, hills, buildings, ship superstructures.

It becomes evident that these requirements cannot be reached by moving a heavy mul-tiple launcher but they can easily be satisfied if the missiles are fired vertically from a container. Experimental missiles such as "Sinner" of "Velarc" have proved the feasib-ility of this technique.

Two trajectory types occurring in the case of a vertical launch are sketched in Fig. 1, ref. 1, which also indicates the inclination of the missile with respect to the trajectories. As a rule, the design of vertically launched missiles is based on the fact that thrust vector control is required to turn around the missile after ejection from the container, ref. 2. However, it is also conceivable that purely aerodynamic control is sufficient, depending on the weapon system mission requirements. In Fig. 2 the different trajectories resulting from aero control and jet-vane plus aero-control are shown. The altitude attained with JVC is generally lower and the minimum mission range is herewith more favourable. Also shown in Fig. 2 is the time history of the elevation θ, accelleration a_z/g, control deflection η and angle of attack α.The example reveals that the aero controls operate for a relatively long time at full deflection,whilst the jet vanes require the maximum deflection only briefly. It is important to consider, however, when designing the aerodynamics for such a wingless configuration, that the angle of attack extends up to 50°, irrespective of the type of control. Missile aerodynamics in the subsonic and transonic range at such angles of attack are characterized by the so-called out-of-plane forces and moments which, as is well known, occur due to the asymmetrical vortex shedding of the body. An existing wing could drastically change the situation due to the asymmetric breakdown of its own vortex system and the interference with the tail. These will be described in more detail in the following paragraphs.

A small wing span is required for a missile which is to start from a container in order to minimize the container's dimensions. Additional requirements for low missile mass and low costs frequently leads to a wingless configuration with wrap-around or jack-knife control panels.

STORE SEPARATION FROM AIRCRAFT TOP-SIDE

The over-aircraft carriage and launch of weapons/external stores is receiving a new interest because of its ability to solve some of the major problems associated with the delivery of weapons/stores from extremely low altitudes in order to increase aircraft survivability. Conventional stores release during a terrain following attack would lead to a damage of the carrier since it does not have the time to leave the blast zone of the detonating store. With the top-side release technique it is important that store and aircraft separate quickly, as due to the stores rapid pitching motion there is the danger of collision. This requires careful matching of normal force and pitching moment, ref. 3. In Fig. 3 some suitable shapes of weapons for top-side release together with calculated launch trajectories are illustrated. The angle of attack thereby exceeds 45°.

SUBMUNITION LAUNCHED FROM AN AIRCRAFT CONTAINER

For the attack of area targets (e.g. tank formations, runways) small bombs are increasingly being used - mostly orientated perpendicular to the flight direction - and jettisoned from a container. In Fig. 4 such a mission and its typical α-characteristic are shown.

ONE-MAN ANTI-TANK MISSILE

Regarding the anti-tank weapons there is a known development of a one-man missile consisting of a body only and controlled by means of BLTVC (Boundary Layer Thrust Vector Control), ref. 4. In Fig. 5 typical characteristics of trajectory and angle of attack are illustrated.

SHORT-RANGE AIR-TO-AIR AND AIR-TO-GROUND MISSILE WITH LARGE OFF-BORESIGHT ANGLE

The requirements for short range air-to-air and air-to-ground missiles have undergone a radical change. This becomes apparent in Fig. 6 where the firing envelope of the Sidewinder is compared with the previously designed Agile missile. The high turn-around capability of the Agile requires at low speeds high angles of attack and the use of TVC (gimmballed nozzles). Although the development of Agile was terminated at an early stage some of its design principles live on in the ASRAAM missile, a European project. The utilization of missiles at large off-boresight angles has been made possible due to the increase of seakers search capability. In the extreme case of a rearward launched missile, Fig. 6, with an off-boresight angle of 180° the angle of attack may reach $\alpha = 180^\circ$.

4. BRIEF REVIEW OF HIGH ANGLE-OF-ATTACK AERODYNAMICS

The important phenomenon of high angle-of-attack aerodynamics is the flow separation on body, wing and tail and the shedding of free vortices, Fig. 7 . These vortices cause additional forces and moments on the missile. The predominant features of flow separation and their effects will be discussed in this paragraph which should serve as a source of information for the design-aerodynamicist.

The onset of flow separation is distinguishable by the characteristics of the aerodynamic coefficients, namely by the pronounced non-linearity of the in-plane coefficients with respect to angle of attack and also by the occurrence of out-of-plane forces and moments. The following provides a brief review of in-plane and out-of-plane forces and moments of bodies, wings, body-tails and body-wing-tail combinations and of some important parameters of influence.

FLOW SEPARATIONS AND THEIR EFFECTS ON BODIES

The body has proven to be the dominating missile component concerning flow separation and its resulting effects. Intense research during the last decade has yielded the result that the flow behaviour around a body is at least phenomenologically known. However, there are still shortcomings in many cases as regards the understanding and insight into the

physics of this particular nature of flow dynamics. The key to the solution apparently lies in the up to now insufficient explanatory behaviour of the boundary layer.

In Fig. 8 flow patterns about ogive-cylinder bodies at various angles of attack and the corresponding characteristics of normal force and side force are schematically shown, ref. 5 (see also Fig. 9 for the onset boundaries). At small angles of attack and as long as the flow is attached, the normal-force characteristic with angle of attack is linear. With increasing angle of attack the flow starts to separate on the leeward side of the body and a system of two or more pairs of symmetric vortices are generated. Due to the influence of the free vortices the increase in normal force is more than linear. At angles of attack beyond $30°$ mostly asymmetric shedding of vortices occurs which causes side forces on the body. In this region the flow is generally steady. However, it has been reported of wind-tunnel investigations with the observation of unsteady vortex shedding - mostly at angles of attack of approx. $50°$. This phenomenon can be described as the formation of asymmetric, alternating pairs of vortices that alter the direction of the side force. Experimental investigations have shown that asymmetric separation is mainly possible if the cross-flow component $(Ma_0 = Ma \cdot \sin \alpha)$ is less than $Ma_0 = 0.5$. Finally, at angles of attack beyond $60°$ the flow becomes unsteady and the boundary layer is shed in the form of a random wake (high Reynolds numbers) or of a von Karman vortex street (low Reynolds numbers). The mean side force decreases toward zero. The normal force has a decreasing characteristic, too.

IN-PLANE FORCES AND MOMENTS OF BODIES OF REVOLUTION

At high angles of attack the normal force and pitching moment (or center of pressure) depend a great deal on Mach numbers and Reynolds numbers. Examples relating to this are given in Fig. 10, 11 and 12, ref. 6, 7. There is a mutual dependency between Mach numbers and Reynolds numbers as long as the cross-flow Mach number equals $Ma_0 = 0.45$. For higher Mach numbers Ma_0 there is a dependency on Mach number only. This is also evident in Fig. 11 and 12. The region with Reynolds number dependency is quite wide at $Ma = 0.5$ and appreciably smaller at $Ma = 0.8$. It disappears completely at $Ma = 1.7$.

There is little information available about the effect of body shape on the in-plane aerodynamics at high angles of attack. Generally speaking there is a dependency of roll orientation on normal force at high angles of attack which, however, is not so distinguished as the dependency concerning the side force (see Fig. 14). The dependancy on roll orientation of both coefficients was to be expected, considering that both are influenced by separated vortices.

OUT-OF-PLANE FORCES AND MOMENTS OF BODIES OF REVOLUTION

The side forces and yawing moments may impose a rather complex autopilot or may impair the mission and are therefore extremely inconvenient for the aerodynamicist. The side forces cause a miss-distance, whereas the yawing moments are of a dentrimental nature to stability and maneuverability. Comparisons with the normal force indicate that side forces may even take on higher values under certain conditions, Fig. 13 . The task for the aerodynamicist, in taking any given geometry constraints into considerations, is to minimize these out-of-plane forces and moments. They depend, as known from numerous experiments, on parameters such as shape of body, Reynolds number or Mach number. In addition there is the rather unpleasant experience that obviously small unavoidable surface asymmetries may be of detrimental effect. Some relating examples of these effects are given in Fig. 13 - 19. More details with respect to the high-angle-of-attack aerodynamics of bodies of revolution are given in the references 8, 9, 10, 11, 12, 13, 14, 15.

IN-PLANE AND OUT-OF-PLANE FORCES AND MOMENTS OF WINGS

The flow behaviour becomes more complex with increasing angle of attack not only around a body but also around a wing. The flow pattern for a wing at higher α's is characterized by the development of two symmetric vortices (primary separation) on the leeward side with their origins at the wing leading edge, Fig. 20 . Due to a secondary separation two additional vortices can develop, possessing opposite sense of rotation relative to the first pair of vortices.

All of these vortices cause a non-linear increase of normal force and usually burst behind the wing. The position of the vortex bursting moves upstream with increasing angle of attack and finally comes to lie within the wing planform, which causes a diminution of the normal force - however, it is well known that at high α's an asymmetrical vortex bursting occurs which causes a rolling moment (Fig. 21 for triangular wings). Fig. 22 demonstrates the lift coefficients of triangular wings and Fig. 23 the normal force coefficients of rectangular wings. The effect of Mach number on the normal force of a slender rectangular wing is shown in Fig. 24. More details on wing characteristics are given in ref. 14, 21, 22.

INTERFERENCE BETWEEN INDIVIDUAL COMPONENTS

The vortex structures of the complete missile can be constructed by superimposing those of the isolated components. This results in a vortex system as shown in Fig. 7. Body vortices interact with wings and tails, wing or canard vortices with tails. The interaction can be very strong if a vortex passes very close to a tail surface. For a missile which is allowed to fly at different angles of attack and roll such a situation certainly occurs.

The wing seems to be of little influence to the body vortices upstream of the wing-body junction. Aft of this point, body vortex strengths are reduced and their paths are perturbed as the experimental investigation of ref. 23 has shown for body-wings in subsonic flow.

In Fig. 25 a few examples of the normal force of tail-panels as a function of roll angle are shown. On adding canards the panel forces change little, even when the canards are deflected, ref. 24 . Here the influence of the body vortices is obviously dominating. The example in Fig. 26 shows the normal-force distribution induced by the wing on the body at roll angles of $\emptyset$ = 0° and 45°, ref. 25 .

At supersonic speeds interaction between the nose-snockwave and the fin-shockwaves may occur at $\emptyset$ = 22.5° or 45°, thereby reducing the effective flow velocity on the windward fins and consequently resulting in a loss of fin efficiency (fin choking, ref. 26).

Finally, in ref. 27 it was reported, that in the transonic speed range appreciable losses of efficiency of the windward fins at certain roll angles may occur, the reason of which is unknown ("Roll stall").

IN-PLANE FORCES AND MOMENTS OF BODY-TAIL AND BODY-WING-TAIL COMBINATIONS

As a rule a missile composed of a body only would show aerodynamic instability. Fins, which are used to provide stability, lose their efficiency at high angles of attack. A body-tail combination suffers a large shift of center of pressure and therefore is adverse to the design of the autopilot. An example is shown in Fig. 27, ref. 28. The application of additional long strakes increases the normal force and the static margin, but can hardly suppress the shift of center of pressure with angle of attack. Not until higher supersonic attack numbers are reached the shift of the center of pressure is diminished, Fig. 28, ref. 29 . With the application of wings of high aspect ratio the tail loses its efficiency almost completely at small angles of attack, but gains in efficiency with growing angle of attack, Fig. 29, ref. 30 . For a missile, a realistic center of gravity providing, a large shift of center of pressure can mean that the sign of the pitching moment may change several times by widely varying the angle of attack, Fig. 30, ref. 31 .

Moreover, as far as body-tail and body-wing-tail configurations are concerned, the roll angle can be of important influence on normal force and pitching moment, Fig. 31, 32, 33 . Generally speaking, missiles at $\emptyset$ = 45° show less normal force and static stability than at $\emptyset$ = 0°. This difference is particularly characteristic and of appreciable magnitude when using long strakes. Out of the examples illustrated in Fig. 31, 32, 33 the configuration with strakes possesses the most unfavourable pitching moment characteristic versus α with regard to the design of the autopilot.

OUT-OF-PLANE FORCES AND MOMENTS OF BODY-TAIL AND BODY-WING-TAIL COMBINATIONS

The adding of a wing and/or a tail has, in general, relative little influence on the maximal side forces and their related centers of pressure, Fig. 34, 35 . In ref. 29, however, some examples do indicate double the amount of the body-only side force due to the addition of a tail. Illustrated in Fig. 35, 36, 37 there are the in-plane and out-of-plane coefficients of a body-tail combination, a missile with strakes and a canard-controlled configuration for different roll angles and Mach numbers. There, particular attention has to be paid to the induced rolling moments. In general, the maximum rolling moment occurs at $\emptyset$ = 22.5°, Fig. 38, ref. 32 and takes on quite appreciable values. With wings of high aspect ratio the magnitude of the rolling moments may even be too great to achieve the necessary roll-controllability. With configurations utilizing strakes the maximal induced rolling moments are generally lower.

An interesting possibility for a missile having small-span wings and controls to operate at high angles of attack offers the bank-to-turn flight mode which allows the choice of a preferred maneuver orientation. The preferred orientation yields the maximum lift and control authority in the desired maneuvering plane, a minimum of out-of-plane forces and moments and a minimum of roll-yaw control cross-coupling. A satisfactory autopilot design usually requires that the cross-coupling rate CCR (unwanted to wanted roll and yaw) remains less than 0.5. Fig. 39 shows the cross-coupling rate CCR for a missile in + - and x-position ref. 33 . The maximum values are about the same but at different angles of attack. According to ref. 33 an optimum bank-to-turn configuration consists of a planar wing and interdigitated controls in x-position. Interdigitated controls cause the lowest minimum induced rolling moment as indicated in Fig. 40.

INFLUENCE OF BODY CROSS SECTION ON THE IN-PLANE AND OUT-OF-PLANE FORCES AND MOMENTS

Regarding quite a number of missile configurations, there are specific requirements concerning the body cross section. For example, a rectangular cross section is usually best for the stowage of subminution. In order to establish the effect of the body cross section on the aerodynamic characteristics, comprehensive wind tunnel investigations were performed at DFVLR, ref. 34. Part of the results is shown in Fig. 41. It can be seen that the rounding off of the edges has a diminishing effect on the normal force. The maximal normal force is obtained with a quadratic cross section at $\emptyset$ = 45° roll position. Regarding aerodynamic stability the bodies with sharp-edged corners are advantageous since, with decreasing corner radius the center of pressure moves toward the base of the body. In ref. 35 a report is given on a comprehensive wind-tunnel study on missiles with quadratic cross sections.

Another category of missiles uses bodies of elliptic cross sections. In comparison with axi-symmetric bodies the elliptic cross section bodies are advantageous in so far that they deliver higher normal force and less side force - both at subsonic and at supersonic speeds, Fig. 42 - and a more favourable storage under the carrier aircraft. The advantages just mentioned, however, depend largely on the roll position and hold

mainly for the $\emptyset = 0°$ position. This is the reason, why elliptic cross sections are usually found with missiles that utilize the "bank-to-turn" steering technique.

The example of a configuration with an axi-symmetric and an elliptic cross section is shown in Fig. 43, ref. 36. The span and tail size being equal, the elliptic configuration results in a 25 % gain in normal force and indicates improved maneuverability in the pitch-plane and yawing-plane, Fig. 44 . Also the out-of-plane forces and moments at low Mach numbers are more favourable, Fig. 45 . A further example was shown in Fig. 3. More information on elliptic cross sections is available from ref. 37, 30.

COUPLING BETWEEN VEHICLE MOTION AND VORTEX GENERATION

The coupling between vehicle motion and vortex generation could be very significant. This is mainly the case if the Reynolds number is such that already minor changes of speed have a significant effect on the separation of the boundary layer.

The side forces of a rotating body are almost independent of the rotative speed, Fig. 46, ref.38 . However, unguided missiles may adopt the so called "roll lock-in" motion at high angles of attack. The "lock-in" motion is characterized by oscillations in the roll angle that dampen into a roll trim angle. These oscillations indicate the presence of an induced rolling moment. Roll lock-in may occur with body-tail and body-canard-tail combinations, Fig. 47, 48 .

Primarily on aircraft the asymmetric separation of the wing vortices causes what is known as the wing rock phenomenon, ref.40,41 . The aircraft thereby undergoes an oscillating motion in roll, yaw and pitch. The hysteresis of the vortex bursting when changing the angle of attack thereby plays a part. An example concerning the change in aerodynamics due to the pitch rate is given in ref. 40 . This kind of aerodynamic characteristic has not yet been discovered with missiles but it can not be ruled out that this might also exist with missiles having large wings.

THE EFFECT OF HIGH ANGLE-OF-ATTACK AERODYNAMICS ON MISSILE COMPONENTS

There are, however, not only advantages associated with high angles of attack but also drawbacks and some problems involved in missile design for high angles of attack are explained in this paragraph.

The search capability of the seeker has to be high in order not to lose sight of the target. This fact necessitates a very complex and rather expensive seeker.

The large shift of center of pressure with angle of attack causes an unfavourable variation of pitching moment and of its slope. Consequently, the natural pitch frequency is subject to a wide variation, too. However, the upper limit of the pitch frequency is determined by the structural vibration frequency and the roll frequency (pitch-roll-resonance). The danger of resonance frequency is further increased by the utilization of new structural materials (e.g. CFC), the lower structural stiffness of which leads to a lower natural frequency. The wide band of natural frequency as well as the intense cross-coupling effects of the controls make the design of the autopilot more difficult. The latter does not permit simplification of the autopilot by means of separated treatment of pitching and yawing motion.

The intense structural loads and their frequently unfavourable distribution on the body, tails and wings often lead, with the missile mass in mind, to structures with minimal structural stiffness. Consequently, effects of aeroelasticity may play a role.

Due to the effect of the body-vortices on the controls of body-tail and body-canard-tails configurations there are considerable changes of the load distribution on the fins (depending on a , $\emptyset$ and Ma) and consequently to the hinge moments. This may necessitate powerful and rather heavy actuators.

With vertically launched missiles the turnover at high angles of attack and low speeds is usually achieved by utilizing TVC. In order to keep the rolling moments hereby as small as possible the wing has to be of small span.

The relatively largely widespread uncertainty concerning the aerodynamic coefficients at high angle of attack impedes the application of the observer technique and the development of a optimal guidance law. Usefull information regarding this problem is available in ref. 43, 44, 45, 46, 47, 48, 49, 50, 51.

6. THE PREDICTABILITY OF AERODYNAMIC COEFFICIENTS

In general, the prediction of the aerodynamic characteristics of missiles at very high angles of attack is rather difficult for both the theoretical and experimental determination. These difficulties concern the in-plane and even more severely the out-of-plane characterstics. The highest problems arise with the determination of that amount of coefficient that is induced by the asymmetric body vortices, and especially with the determination of the rolling moment. In the following some prediction methods will be presented, which have been developed during the last couple of years.

In ref. 29 a semi-empirical method is described, valid for bodies, body-tail and body-strake-tail combinations and applicable to a's up to $180°$ and Mach numbers from 0.6 to 3.0. Some examples of comparison between theory and experiment are illustrated in Fig.28. This method only predicts the in-plane characteristics for the +-position and is based on

a data base consisting of wind tunnel data. The applicability of this method is thus limited by the range of data contained in the data base. In ref. 52 it has been reported of an extension of this method regarding the roll angle (up to 45°) for body-tail combinations. The results in Fig. 49 however indicate that the accuracy of the prediction of the center of pressure and the rolling moment at $\emptyset = 45°$ is insufficient. The comparison between theory and experiment for the normal force seems to be reasonably well.

In ref. 53 the multi-vortex method of Thomson (ref. 54) to describe the asymmetric vortex structure above a body of revolution at high angles of attack has been incorporated into an engineering method for the determination of the in-plane and out-of-plane characteristics of body-tail combinations. In principle, this method may be applied to arbitrary Mach numbers, angles of attack and roll angles. A comparison between theory and experiment is given in Fig. 50. Another similar method is discussed in ref. 55.

The method of ref. 30 allows the determination of the in-plane forces and moments of bodies isolated or in combination with wings and tails, with circular or elliptic cross-section, for the +-position. The method is based on the coefficient synthesis (similar to the N-P-K method for slender missiles) and utilizes the crossflow theory for the estimation of the non-linear terms at higher angles of attack. The range of the applicability is $0.6 < Ma < 2.9$ and $0° < \alpha < 180°$ for the body alone and $0.6 < Ma < 2.0$ and $0° < \alpha < 60°$ for combinations with wings and tails.

The most sophisticated methods for the treatment of wing-body-tail combinations at arbitrary Mach numbers, roll angles and angles of attack of approx. 40° have been developed by NEAR, Inc. These methods yield both the in-plane and the out-of-plane characteristics of missiles with circular or elliptical cross section, including the consideration of control deflections of canards or tail, ref. 56, 57 . A comparison between theoretical results (programs MISSILE, MISSILE 2, DEMON 2) and experimental results is carried out in ref. 58, Fig. 51.

Numerous computing methods, among them many of non-empirical character, are available for the treatment of isolated bodies. There are also attempts with great analytical effort involved in order to take the behaviour of the boundary layer into account. The most extensive methods are based on the complex Euler or Navier-Stokes equations. However, it has not yet been possible to achieve the quality of results by calculation as the experimental results shown in Fig. 14.

All the methods mentioned so far are insufficiently accurate concerning mainly the computation of the out-of-plane characteristics and it has to be proceeded with caution if these methods are to be used for design purposes. Quite often the accuracy criteria of aerodynamic coefficients as derived from performance and other design parameters can not be met. In Fig. 52 an example of a missile design, ref. 59, is given whereby the calculated yawing moment coefficient exceeds the allowable magnitude at high angles of attack.

However, even the experimental investigation of the aerodynamic coefficients at high angles of attack is not always accurate. In Fig. 53 for instance it is exemplified how the coefficients of an axi-symmetric body-tail combination differ when the model is rotated by 90°-steps. This is to be ascribed to the asymmetric body vortices, similar to the body-alone case shown in Fig. 14. As a rule, the experimental results have to be carefully corrected to free-flight conditions, with the frequently differing Reynolds number having the greatest effect on the coefficients regarding body and body-tail combinations. Moreoever, the effects of the wind-tunnel turbulence level, ref. 60 , the wall interference and the model support interference, ref. 61, are to be taken into consideration, since they may cause a decisive change to the vortex system by affecting the very sensitive boundary layer.

In practice, the aerodynamic coefficients of a missile together with the scatter of the results and their probability are obtained from wind-tunnel tests. For the control and structural requirements the maximal values, and for the missile accuracy the most probable values are considered. Regarding wind tunnel testing, it is to be noted that the measuring of coefficients of configurations with long strakes is easier than that of body-tail configurations, since a great deal of the problems caused by the asymmetric body vortices is suppressed by the strakes.

7. SOME GUIDELINES FOR MISSILE DESIGN AT HIGH ANGLES OF ATTACK

The analysis of numerous wind tunnel investigations of missiles at high angles of attack has led to significant results that may well be regarded as guidelines for the missile design at high α's.

The effect of the asymmetric body vortices (and herewith the generation of severe out-of-plane forces and moments) may be reduced by means of:

Choice of a low-fineness-ratio body nose; blunting of the body nose; utilization of small strakes on the body nose, Fig.54(for roll-stabilized missiles only); utilization of helical or straight body trips at the body nose (for roll-stabilized missiles only); utilization of small spikes at the nose tip; increase in flight Mach number (see ref.62).

Bodies alone show an extensive shift in center of pressure with respect to angle of attack and are generally aerodynamically unstable at small α's. By means of wings with higher aspect ratio the shift in center of pressure can be kept reasonably small. Tail fins in combination with strakes are very effective at small α's but lose efficiency

with increasing α . This characteristics of the tail may be reversed if they are combines with wings of higher aspect ratio.

Missiles with long strakes show a strong dependency of the pitching moment with respect to roll angle.

The induced rolling moments of missiles with wings can become very large and the maximal values usually occur at $\emptyset = 22.5°$. A reduction in wing aspect ratio generally means a reduction of the maximal rolling moment.

It is advantageous to fly in the bank-to-turn mode since this provides the possibility of a preferred roll orientation for which the center of pressure, the out-of-plane forces and moments and the cross-coupling effects turn out favourably.

The compensation of the induced rolling moments of canard configuration proves to be rather difficult. The rolling moments can be kept small if the tail span is less than the canard span. Another approach to the solution of this problem is the use of a free-rolling tail-fin afterbody or the utilization of a ram-air-spoiler to provide roll-stabilization, ref. 63, 64 .

For vertical launch missiles with the maneuver-capability of turning around at low speeds TVC-control is generally necessary.

Missiles with long strakes prove to be advantageous in many respects, e.g. stowage inside containers or under the carrier-aircraft is facilitated, reduced missile weight and simplified logistics. Another favourable aspect of long-strake configurations is the fact that the determination of the aerodynamic coefficients by means of wind tunnel testing is usually easier.

8. REFERENCES

1. Gregoriou, G. and Knoche, H.-G.: High Incidence Aerodynamics of Missiles during Launch Phase. AIAA Paper 80-371
2. Giragosian, P.A.: Theoretical and Experimental Aerodynamic Correlation of Jet Vane Control Effectiveness. AIAA Paper 81-1897
3. King, H.A. and Wedon, B.W.: Topside Weapons Release. An Analytical Study. AIAA Paper 81-1655
4. Hessmann, F.W.: An Airslew Anti-Armor Weapon Concept. AIAA Paper 81-0288
5. Chapman, G.T. and Keener, E.R.: The Aerodynamics of Bodies of Revolution at Angles of Attack to 90°. AIAA Paper 79-0023
6. Nelson, R.C. and Fleeman, E.L.: High Angle-of-Attack Aerodynamics on a Slender Body with a Jet Plume. J. Spacecraft, Jan. 1975
7. Hartmann, K.: Über den Einfluß der Reynoldszahl auf die Normalkräfte schlanker Flugkörperrümpfe. DFVLR Report No. 251 76A20, 1976
8. Keener, E.R. and Taleghani, J.: Wind Tunnel Investigations of the Aerodynamic Characteristics of Five Forebody Models at High Angles of Attack at Mach Numbers from 0.25 to 2. NASA TM X-73, 076, Dec. 1975
9. Lamont, P.J.: Pressure Measurements on an Ogive-Cylinder at High Angles of Attack with Laminar, Transitional, or Turbulent Separation. AIAA Paper 80-1556
10. Keener, E.R., Chapman, G.T., Cohen, L. and Taleghani, J.: Side Forces on a Tangent-Ogive Forebody with a Fineness Ratio of 3.5 at High Angles of Attack and Mach Numbers from 0.1 to 0.7. NASA TM X-3437, Febr. 1977
11. Pick, G.S.: Investigation of Side Forces on Ogive-Cylinder Bodies at High Angles of Attack in the M = 0.5 to 1.1 Range. AIAA Paper 71-570
12. Ericsson, L.E. and Reding, J.P.: Vortex-Induced Asymmetric Loads in 2-D and 3-D Flows. AIAA Paper 80-0181
13. Wardlaw, A.W. Jr.: High-Angle-of-Attack Missile Aerodynamics. AGARD-LS-98, 1979
14. Peake, D.J.: Three Dimensional Flows about Simple Components. AGARD-LS-121, 1982
15. Lamont, P.J. and Hunt, B.L.: Prediction of Aerodynamic Out-of-Plane Forces on Ogive-Nosed Circular Cylinders. J. Spacecraft, Jan. 1977
16. Wendt, J. and Wedemeyer, E.: Flow around a Rectangular Low Aspect Ratio Wing and the Effect of Compressibility on it. VKI Rep. 1981-29, June 1981
17. Polhamus, E.C.: Prediction of Vortex-Lift Characteristics by a Leading-Edge Suction Analogy. J. Aircraft, Apr. 1971
18. Wentz, W.H. and Kohlman, D.L.: Wind-Tunnel Investigations of Vortex Breakdown on Slender Sharp-Edged Wings. Univ. of Kansas, Center of Research, Rep.No. FRL 68-013, 1968
19. Winter, H.: Flow Phenomena on Plates and Airfoils of Short Span. NASA-TM-798, 1936
20. Esch, H.: Wind Tunnel Tests on Wings of Different Planforms. DFVLR Rep. (to be publ.)
21. Wendt. J.: Compressibility Effects on Flows Around Simple Components. AGARD-LS-121, 1982
22. Stallings, R.L. and Lamb, M.: Wing Alone Aerodynamic Characteristics at High Angles of Attack. AIAA Paper 81-0008
23. Grosche, F.R.: Wind Tunnel Investigation of the Vortex System Near an Inclined Body of Revolution with and without Wings. AGARD, Aerodynamic Interference, 1971
24. Allen, C.Q., Schwind, R.G. and Malcolm, G.N.: Canard-Body-Tail Missile Test at Angles of Attack to 50° in the Ames 11-Foot Transonic Wind Tunnel. NASA TM 78441, Sept. 1978
25. Esch, H.: Experimentelle Untersuchungen zur Interferenz zwischen Rumpf und Leitwerk an einem Flugkörper in +- und x-Lage. DFVLR Rep.Nr. IB 351-76/21, 1976
26. Stallings, R.L. Jr., Lamb, M., Watson, C.B.: Effect of Reynolds Number on Stability Characteristics of a Cruciform Wing-Body at Supersonic Speeds. NASA TP 1683, July 1980
27. Nielsen, J.N.: Nonlinearities in Missile Aerodynamics. AIAA Paper 78-20
28. Baker, W.B. Jr.: An Aerodynamic Coefficient Prediction Technique for Slender Bodies With Low Aspect Ratio Fins at Transonic Mach Numbers and Angles of Attack to 180 Degrees. Dissertation, Univ. of Tennessee, Aug. 1976

29. Aiello, G.F. et al.: Aerodynamic Stability Technology for Maneuverable Missiles, Vol. I: Configuration Aerodynamic Characteristics. NTIS AD/A-070250, March 1979
30. Jorgensen, L.H.: Prediction of Aerodynamic Characteristics for Slender Bodies Alone and With Lifting Surfaces to High Angles of Attack. AGARD-CP-247, 1979 (also NASA-TR R-474, Sept. 1977)
31. Mifsud, L.: Caractéristiques Aérodynamiques de corps de résolution munis d'ailes d'allongements divers. AGARD-CP-247, 1979
32. Le Beau, R.P.: The Effect of Angle of Attack on Induced Rolling Moment for a Low Aspect Ratio Missile. AGARD-CP-71
33. Droning, H.D. Jr.: Aerodynamic Design for Slender Missiles for Bank-to-Turn Flight at High Angles of Attack. AIAA Paper 81-289
34. Schneider, W.: Experimental Investigations on Bodies With Noncircular Cross Section in Compressible Flow. AGARD-Symposium on Missile Aerodynamics, Norway, 20-22 Sep.1982
35. Yechout, T.R. and Zollars, G.J.: Experimental Aerodynamic Characteristics of Missiles with Square Cross-Sections. AIAA Paper 81-0144
36. Graves, E.B.: Aerodynamic Characteristics of a Monoplanar Missile Concept With Bodies of Circular and Elliptical Cross-Sections. NASA TM 74079, 1979
37. Sawyer, W.C. and Sangiorgio, G.: Stability and Control Characteristics of a Monoplanar Elliptic Missile Model at Mach Numbers From 1.6 to 2.86. NASA TP 1352, Feb. 1979
38. Kruse, R.L.: Influence of Spin Rate on Side Force of a Axisymmetric Body. J. Spacecraft and Rockets, Apr. 1978
39. Hardy, S.R.: Nonlinear Rolling Motion of a Canard-Controlled Missile Configuration at Angles of Attack from 0 to 30 Degrees in Incompressible Flow. AIAA Paper 78-61
40. Chintsun Hwang and Pi, W.S.: Some Observations on the Mechanism of Aircraft Wing Rock. J. Aircraft, June 1979
41. Schmidt, L.V.: Wing Rock Due to Aerodynamic Hysteresis. J. Aircraft, March 1979
42. Smith, L.H. and Nunn, R.H.: Aerodynamic Characteristics of an Axisymmetric Body Undergoing a Uniform Pitching Motion. AIAA Paper 75-838
43. Arrow, A. and Yost, D.J.: Large Angle-of-Attack Missile Control Concepts for Aerodynamically Controlled Missiles. J. Spacecraft, Oct. 1977
44. Nesline, F.W. and Nabbefeld, C.N.: Design of Digital Autopilots for Homing Missiles. AGARD-LS-101, 1979
45. Gonzalez, J.: New Methods in the Terminal Guidance and Control of Tactical Missiles. AGARD-LS-101, 1979
46. Ericsson, L.E.: Aeroelasticity, Including Dynamic Effects of Separated Flow. AGARD-LS-114 , 1981
47. Schiff, L.B., Tobak, M., Malcolm, G.N.: Mathematical Modelling of the Aerodynamics of High-Angle-of-Attack Maneuvers. AIAA Paper 80-1583
48. Orlik-Rückemann, K.J.: Sensitivity of Aircraft Motion to Cross-Coupling and Acceleration Derivatives. AGARD-LS-114, 1981
49. Orlik-Rückemann, K.J.: Effect of High Angles of Attack on Dynamic Stability Parameters. AGARD-CP-247, 1979
50. Uselton, B.L. and Jenke, M.L.: Experimental Missile Pitch- and Roll-Damping Characteristics at Large Angles of Attack. J. Spacecraft and Rockets, April 1977
51. Murphy, C.H.: Symmetric Missile Dynamic Instabilities - A. Survey, AIAA Paper 80-0320
52. Devan, L.: Aerodynamics of Tactical Weapons to Mach Number 8 and Angle of Attack 180°. Part I, Theory and Application. NSWC TR 80-346, 1980
53. Fidler, J.E. and Bateman, M.C.: Asymmetric Vortex Effects on Missile Configurations. AIAA Paper 75-209
54. Thomson, K.D.: The Estimation of Viscous Normal Force, Pitching Moment, Side Force and Yawing Moment on Bodies of Revolution at Incidences up to 90°. Australian Weapons Res. Est. WRE-Report-782, 1972
55. Nikolitsch, D. and Waxweiler E.: Berechnung der Rollmomentenbeiwerte von Flügel-Rumpfkombinationen bei hohen Anstellwinkeln im Unterschall. MBB TN AE12-5/81
56. Blair, A.B. Jr., and Rapp. G.H.: Experimental and Analytical Comparisons of Aerodynamic Characteristic of a Forward-Control Missile. AIAA Paper 80-0374
57. Smith, C.A., and Nielsen, J.N.: Prediction of Aerodynamic Characteristics of Cruciform Missiles to High Angles of Attack Utilizing a Distributed Vortex Wake. NEAR TR 208, Nielsen Engineering and Research, Inc., Mountain View, California, January 1980
58. Allen, J.M.: Comparison of Analytical and Experimental Supersonic Aerodynamic Characteristics of a Forward Control Missile. AIAA Paper 81-0398
59. Krieger, R.J. and Williams, J.E.: Accuracy Criteria for Evaluating Supersonic Missile Aerodynamic Coefficient Prediction. AIAA Paper 81-1894
60. Hartmann, K.: Einfluß der Windkanalturbulenz auf die aerodynamischen Beiwerte von Flugkörperrümpfen bei Anstellwinkeln bis zu 90°. Privat Communication, DFVLR
61. Canning, T.N. and Nielsen, J.N.: Experimental Study of the Influence of Supports on the Aerodynamic Loads on an Ogive Cylinder at High Angles of Attack. AIAA Paper 81-0007
62. Ericsson, L.E. and Reding, J.P.: Alleviation of Vortex-Induced Asymmetric Loads. J. Spacecraft, Nov.-Dec. 1980
63. Blair, A.B. Jr.: Remote Control Canard Missile With a Free-Rolling Tail Brake Torque System. AIAA Paper 81-0146
64. Blair, A.B. Jr.: A Ram Air-Spoiler Roll Stabilization Device for Forward Control Cruciform Missiles. AIAA Paper 78-24.
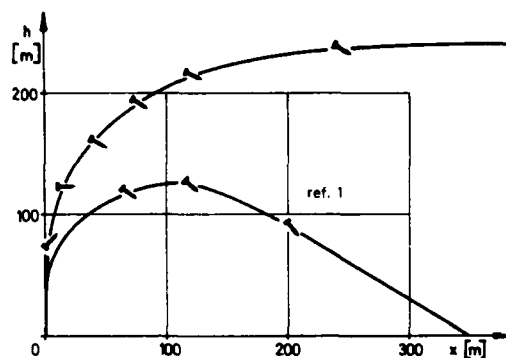
Fig. 1: Vertical-launch trajectories a-
gainst aircraft and sea-skimmer
targets
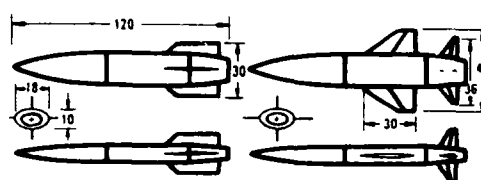
Config. 1   Config. 2

t_{final} = 1.4 SECS

STORE POSITION
SHOWN FOR EQUAL
TIME STEPS

ref. 3

Config. 1

Fig. 3: Favourable configurations and cal-
culated trajectory for top-side
release
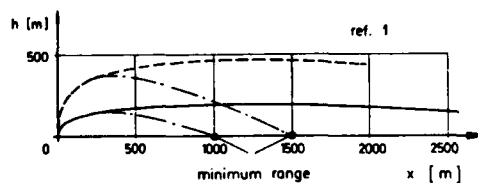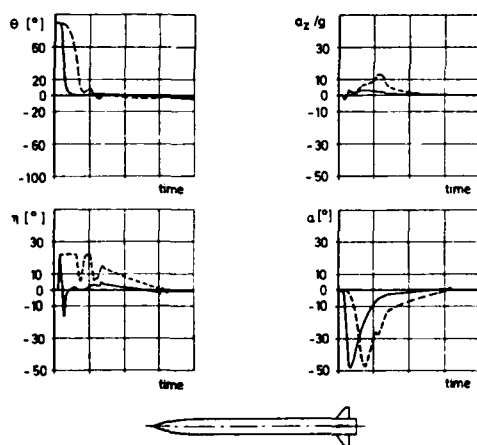
Fig. 2: Vertical launch with jet vanes +
aero-control   (————)
aero-control only (-----)
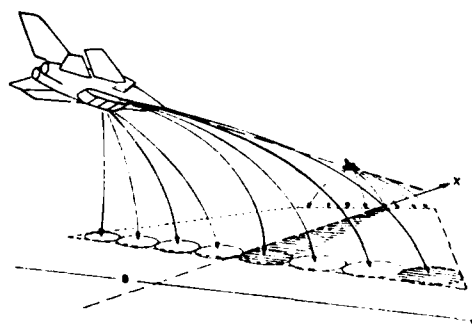
Fig. 4: Submunitions against area targets
and typical angle-of-attack cha-
racteristic
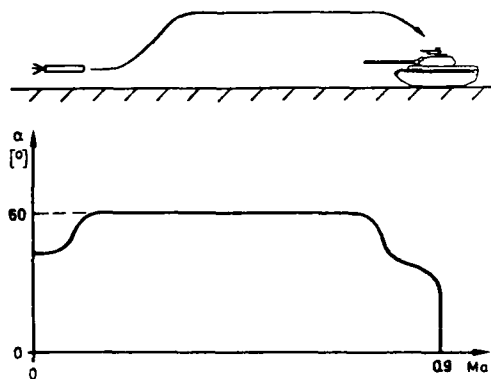
Fig. 5: Trajectory and schematic angle-of-attack characteristic of an anti-tank missile

Fig. 7: Vortex shedding on a missile at high angles of attack

Sidewinder

2850 mm

AGILE

N20 — 200

2643 mm

6 fins

~ 2700 mm

ASRAAM

~ 170 mm

Fig. 6: Firing envelopes of short-range air-to-air missiles

CROSS SECTION A-A

VORTEX FREE FLOW

SYMMETRIC VORTEX FLOW

STEADY ASYMMETRIC VORTEX FLOW

WAKE-LIKE FLOW

ref. 5

(a)

NORMAL FORCE   SIDE FORCE

VORTEX FREE FLOW

SYMMETRIC VORTEX FLOW

STEADY ASYMMETRIC VORTEX FLOW

WAKE-LIKE FLOW

ANGLE OF ATTACK

(b)   ref 5
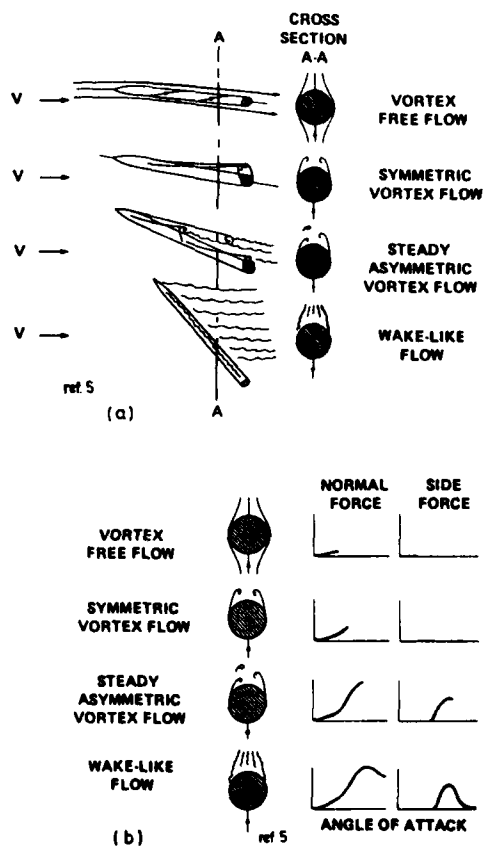
Fig. 8: Flow types (a) and forces regimes (b) for increasing angle of attack on ogive-cylinder
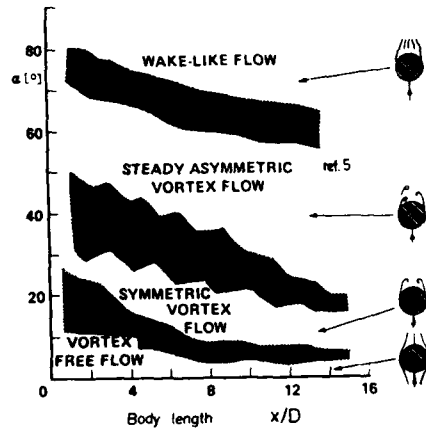
Fig. 9: Onset boundaries for ogive-cylinders
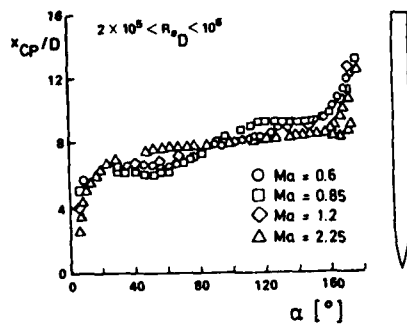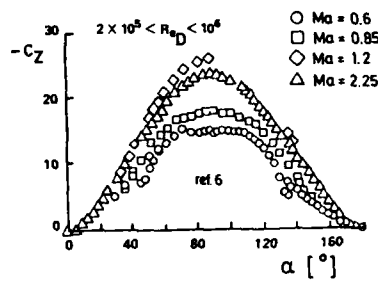
Fig. 10: Influence of Mach number on normal-force coefficient and center of pressure for an ogive-cylinder
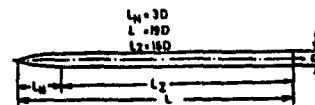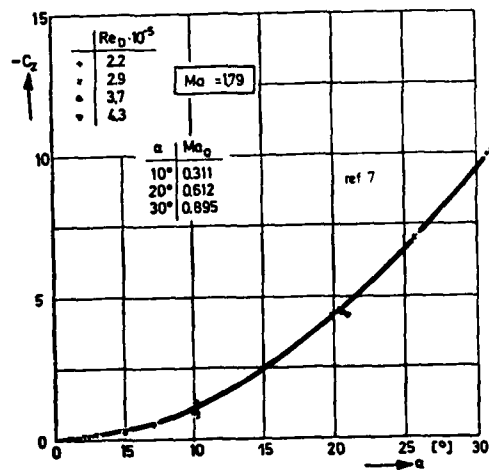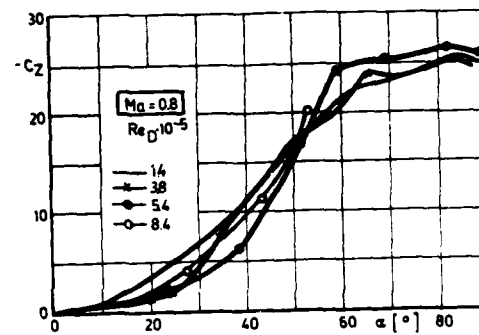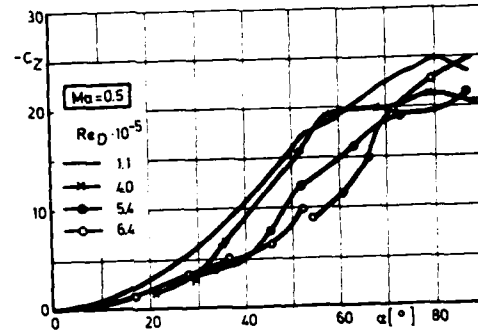
Fig. 11: Influence of Reynolds number on normal-force coefficient of ogive-cylinder for different Mach numbers

Fig. 13: Normal-force and side-force coefficients of an ogive nose

Fig. 14: Variation of normal-force and side-force coefficients with roll angle
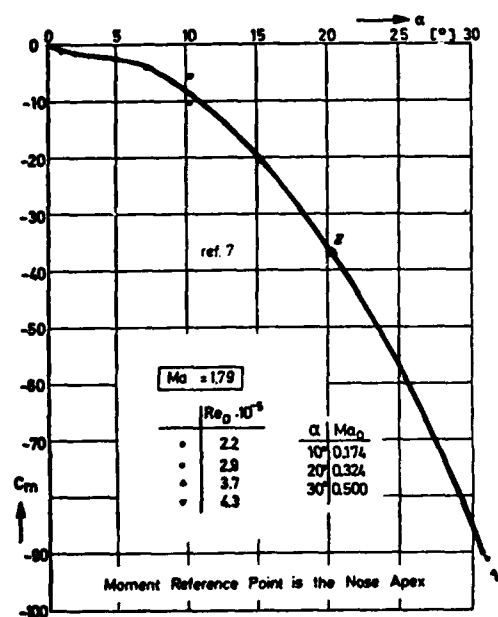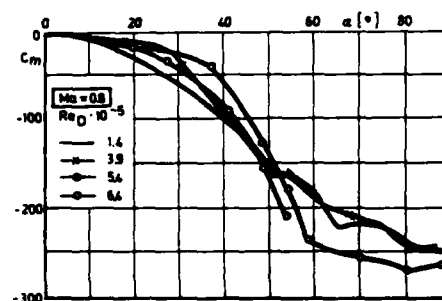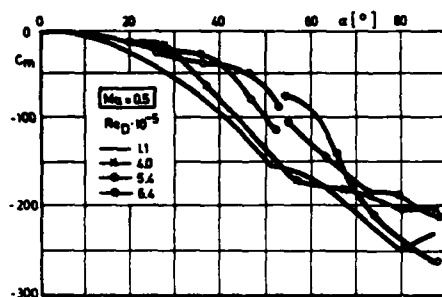
Fig. 12: Influence of Reynolds number on pitching-moment coefficient
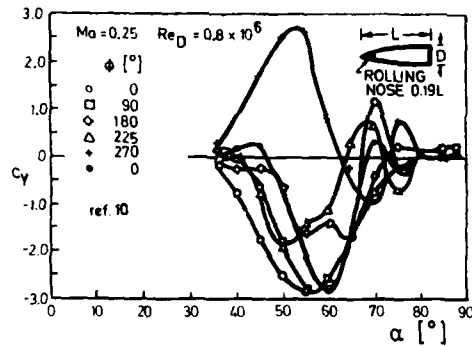
Fig. 15: Effect of roll angle on side-force coefficient (3.5 caliber ogive nose)
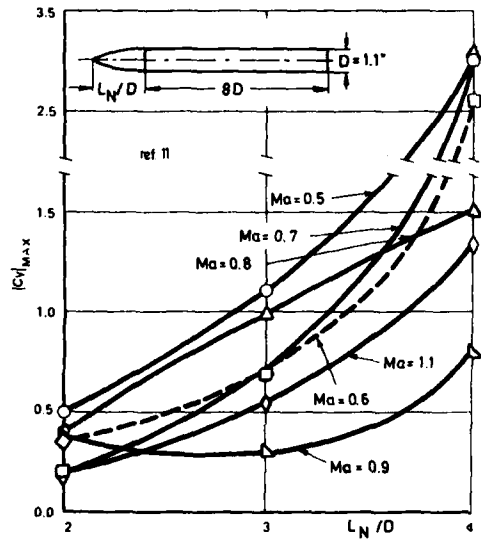
Fig. 16: Influence of the nose fineness ratio on the maxim. induced side-force coefficient
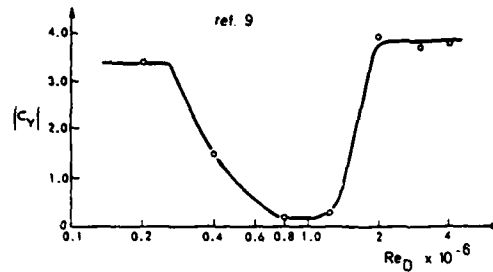
Fig. 17: Effect of Reynolds number on maximum side-force coefficient at $\alpha = 55°$
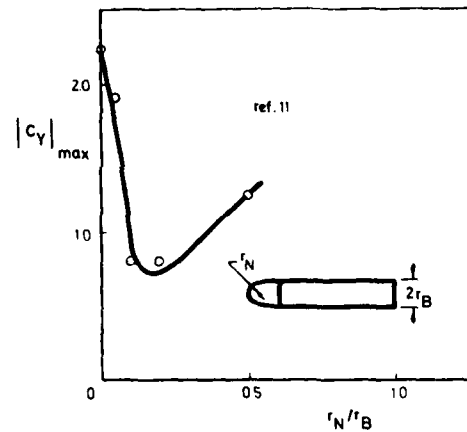
Fig. 18: Effect of nose bluntness of the side-force coefficient on an ogive-cylinder
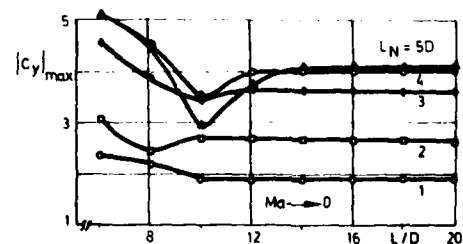
Fig. 19: Maximum side-force coefficients for ogive-cylinders at Ma →0 (laminar separation)

Fig. 21: Vortex structures on delta wings
in incompressible flow
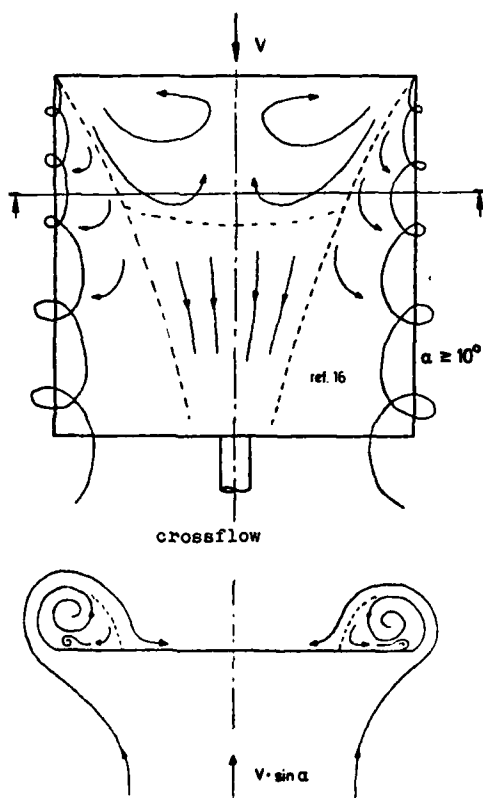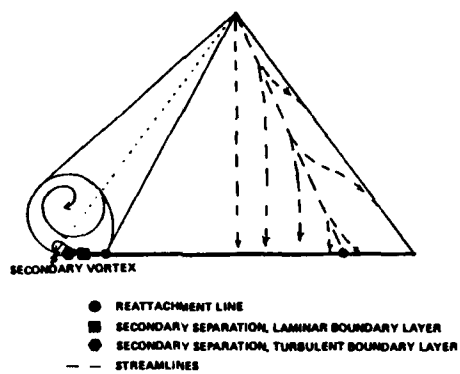
Fig. 20: Vortex structure on the lee side
of a delta and a rectangular
wing
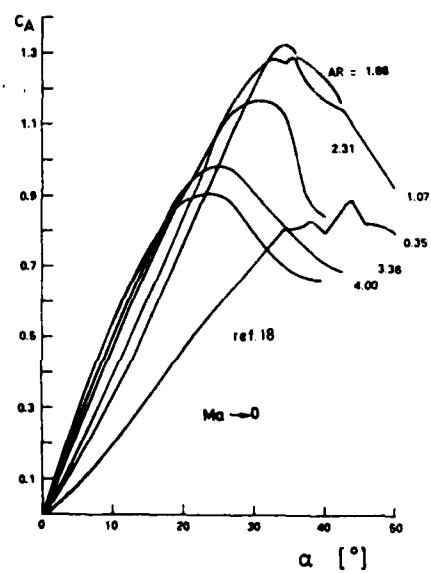
Fig. 22: Lift coefficients of delta wings
in incompressible flow
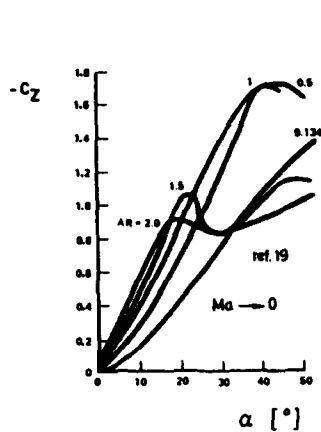
Fig. 23: Normal-force coefficients of rectangular wings in incompressible flow
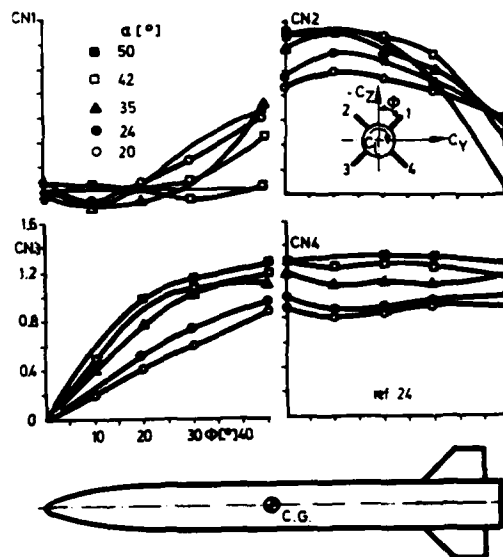
Fig. 25: Individual panel forces of a body-tail combination at Ma = 0.8
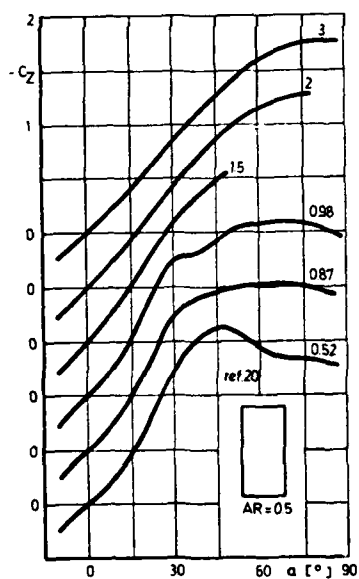
Fig. 24: Influence of Mach number on the normal-force coefficients of a rectangular wing
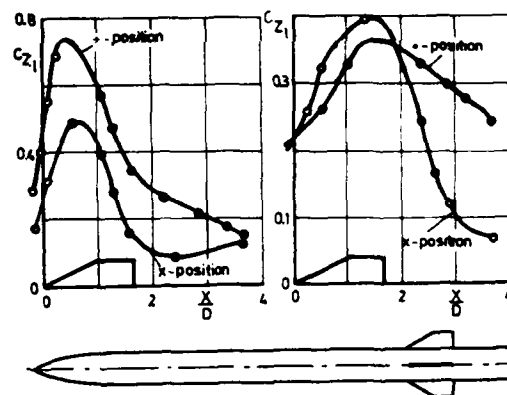
Fig. 26: Normal-force distribution on a body in the presence of a wing at α = 20°
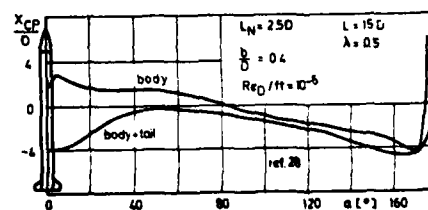
Fig. 27: Center of pressure of a body and a body-tail combination at Ma = 0.8

Fig. 29: Distance from missile nose to center of pressure for body, body-wing and body-wing-tail combination ($Re_D = 3.8 \ 10^5$)
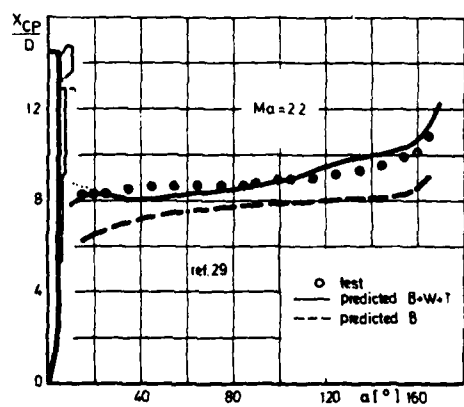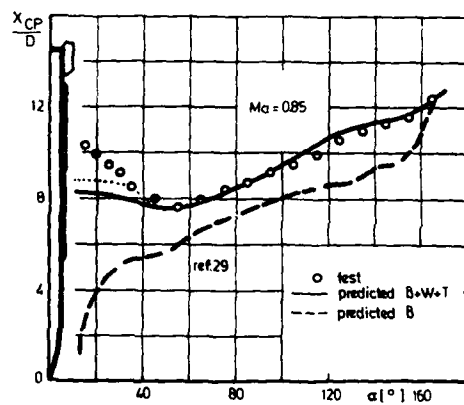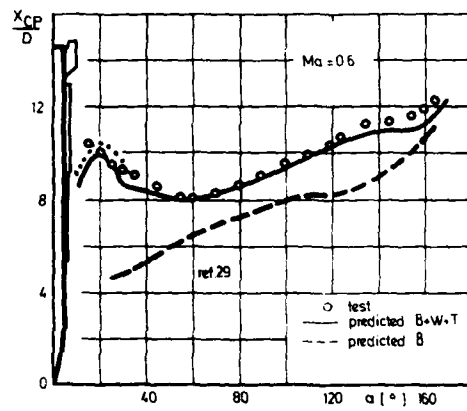
Fig. 28: Center of pressure of a body and body-wing-tail combination
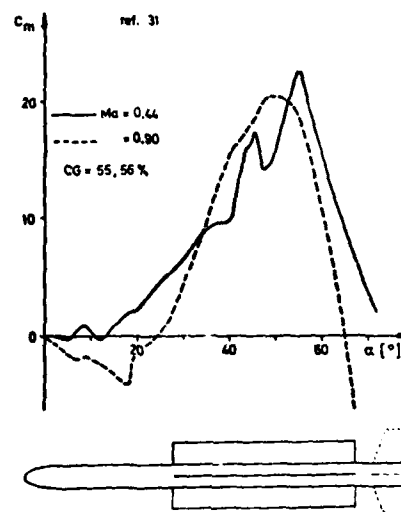
Fig. 30: Pitching-moment coefficient of a missile with low aspect ratio wing
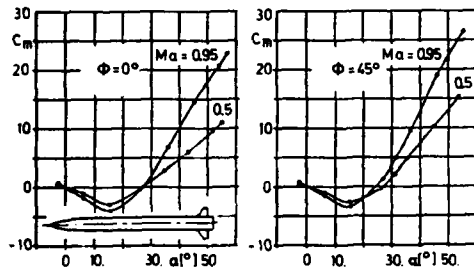
Fig. 31: Influence of roll angle on the pitching moment coefficient of a body-tail combination

Fig. 34: Side-force and its center of pressure for a body, body-wing and body-wing-tail

Fig. 32: Influence of roll angle on the pitching moment coefficient of a missile with a low-aspect-ratio wing
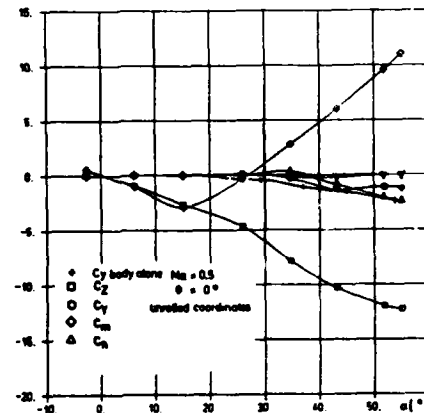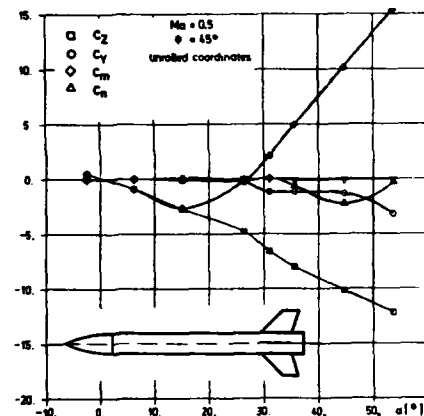
Fig. 35: In-plane and out-of-plane coefficients of a body and a body-tail combination

Fig. 33: Influence of roll angle on the pitching moment coefficient of a canard configuration
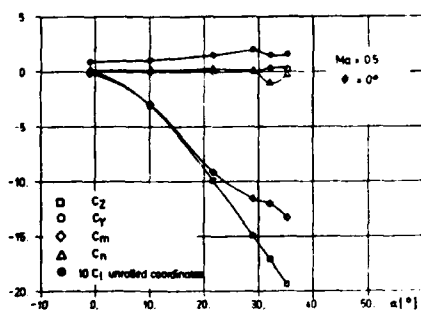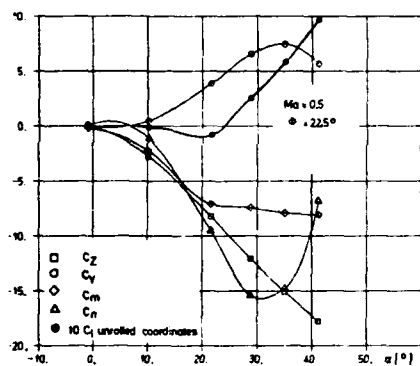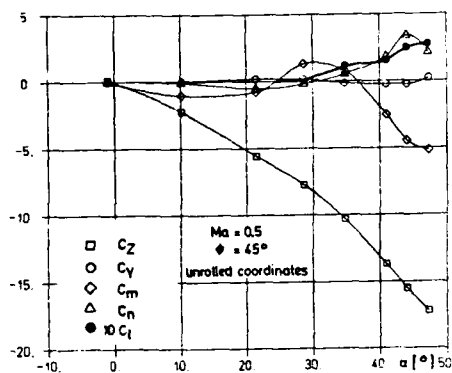
Fig. 36: In-plane and out-of-plane co-
efficients of a missile with
strakes
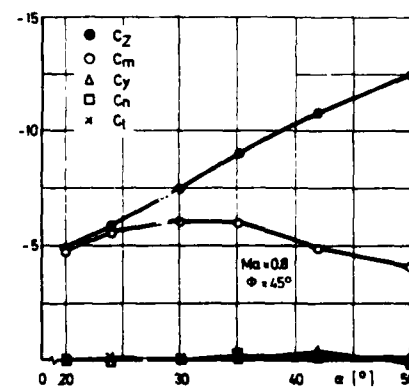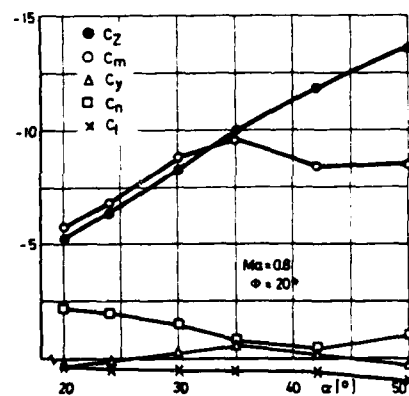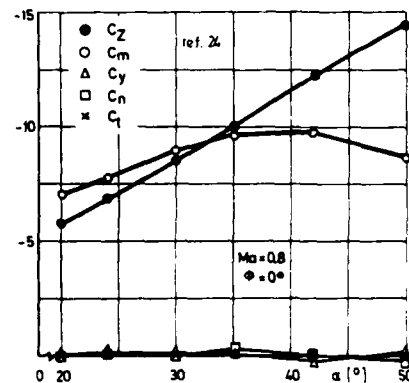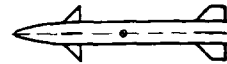
Fig. 37: In-plane and out-of-plane co-
efficients of a canard confi-
guration
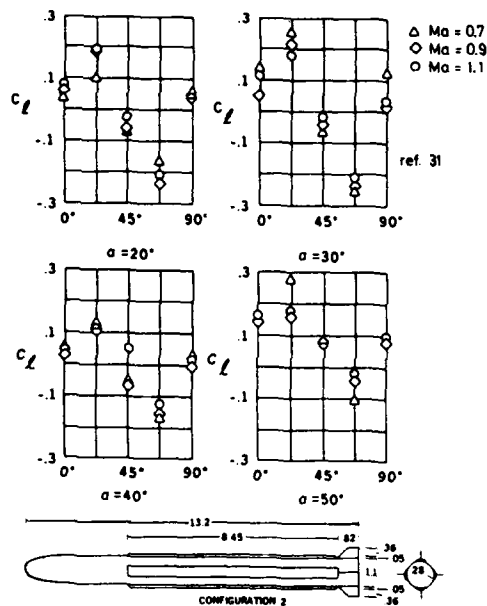
Fig. 38: Rolling moments for missiles with strakes
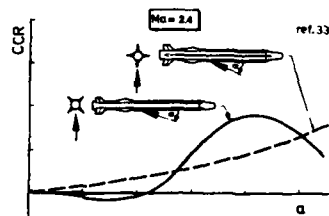
Fig. 39: Cross-coupling rate CCR of cruciform missiles
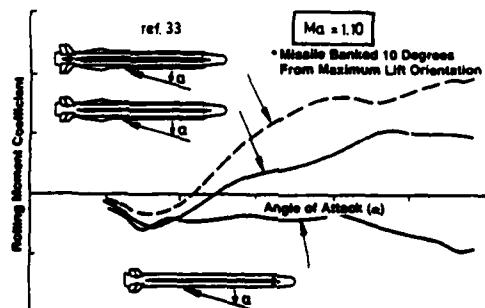
Fig. 40: Induced roll comparison for different missile
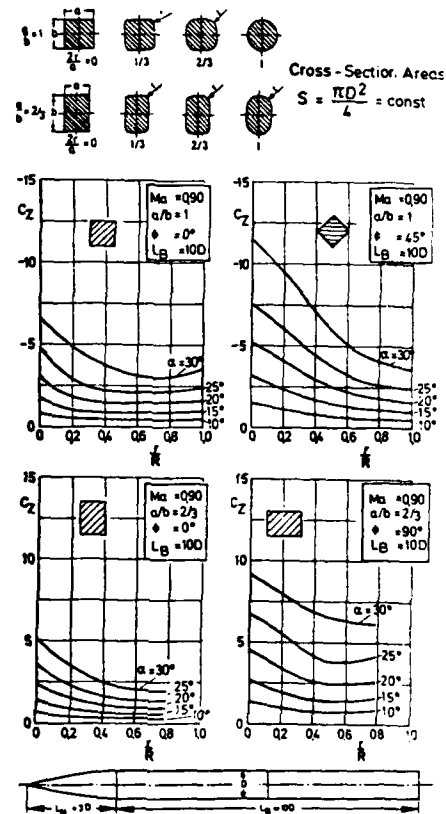
Fig. 41: Normal-force coefficients versus radius of corner rounding for bodies with rectangular cross section
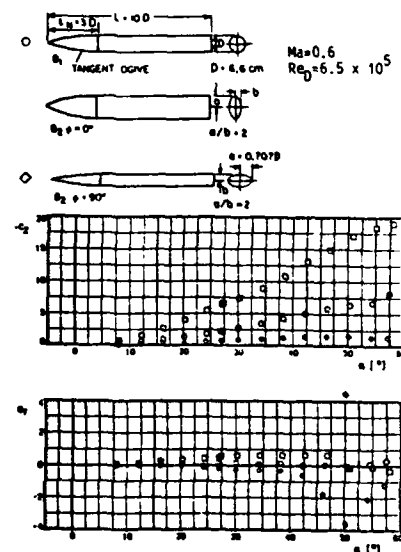
Fig. 42: Normal and side force of bodies with elliptical and circular cross section

(a) Circular BWT (reference length, 0.712 m)

(b) Elliptical BWT (reference length, 0.712 m)
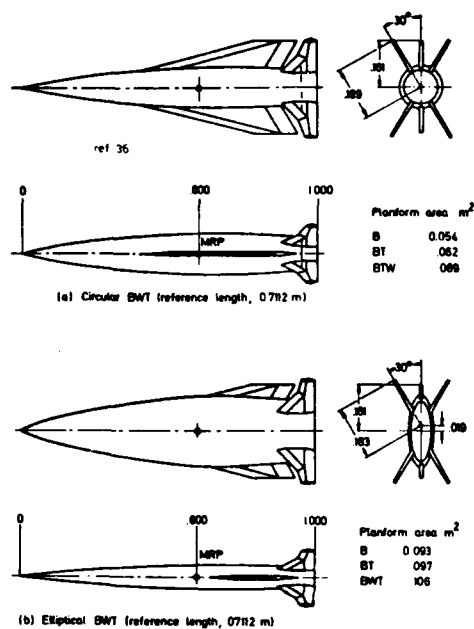
Fig. 43: Geometry of a missile with circular and elliptical cross section

Fig. 45: Out-of-plane forces and moments of a missile with circular and elliptical cross section

Fig. 44: Normal-force comparisons for a missile with circular and elliptical cross section
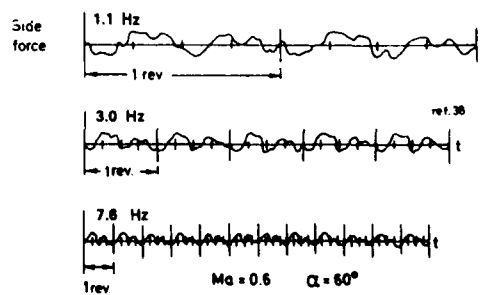
Fig. 46: Effect of spin rate on side force of 10° half-angle cone
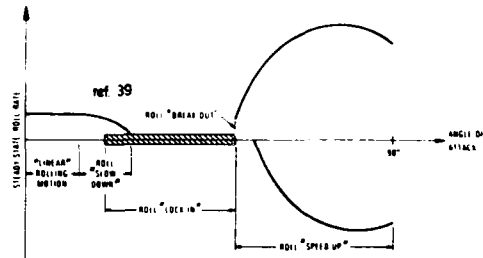
Fig. 47: Rolling motion characteristics of unguided cruciform body plus tail missile

Fig. 49: Comparison between computed and experimental results for the Air Slew Demonstrator

= 30° - BODY + TAIL
x OBSERVED(EVERY 4TH PT PLOTTED)
- COMPUTED

ref. 39

a = 30° - CANARD+BODY+TAIL (B = 0°)
x OBSERVED(EVERY 4TH PT PLOTTED)
- COMPUTED
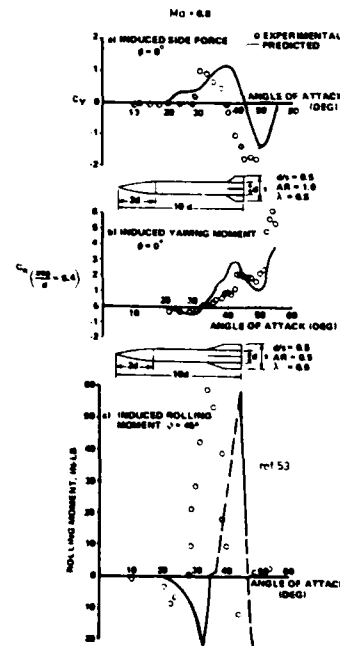
Fig. 50: Comparison between computed and experimental results for a body-tail combination

Fig. 48: Comparison plots of observed and computed roll angle versus time for a body-tail and a body-canard-tail configuration at angles of attack from 0 to 30°
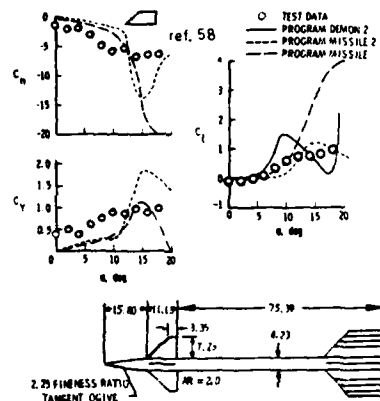
Fig. 51: Comparison of measured and predic-
ted induced lateral characteris-
tics for a canard missile

Fig. 52: Comparison between prediction
and required accuracy for a mis-
sile design

Fig. 53: Influence of the roll angle on
the aerodynamic coefficients of
a body-tail combination
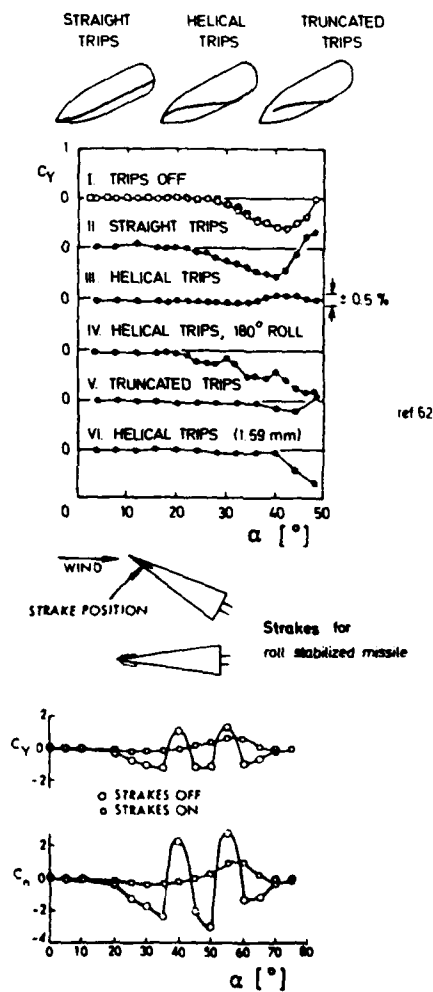
Fig. 54: Alleviation of vortex-
induced side forces

THE ROLE OF COMPUTATIONAL FLUID DYNAMICS IN HIGH ANGLE-OF-ATTACK AERODYNAMICS

Barry Hunt, M.A., F.I.M.A.
Section Leader, Theoretical Methods Applications,
Aerodynamics Dept.,
British Aerospace, Aircraft Group,
Warton, Preston, PR4 1AX, U.K.

SUMMARY

Recent advances in computers and in numerical algorithms have brought forward the possibility of per-forming, relatively economically, accurate calculations of the flow over realistic representations of air-craft and missile geometries. The present indications would appear to be that most of the problems assoc-iated with shock waves in the flow are now starting to be resolved - or at least acceptable compromises are in sight. The outstanding difficulty is connected with vortex flows and related effects which make high α aerodynamics particularly complicated.

A wide class of problems can be simulated adequately by inviscid models of the flow - particularly flows involving separation from sharp edges such as wing leading and trailing edges, and tips. In many cases the simulation can be further improved by coupling the inviscid calculation with a simplified viscous model of boundary-layer type.

In some cases, however, the flow is viscous-dominated and a more comprehensive scheme is required. In these circumstances, recourse to the Navier-Stokes equations is the usual alternative, but solution of these equations is difficult and computationally expensive. A more serious difficulty is that for certain aero-dynamically-relevant problems, including body-vortex flows and wing stall, the key physical phenomena (e.g. vortex switching) may be triggered by non-deterministic effects such as external turbulence and surface vibration; in such cases the deterministic Navier-Stokes equations will not be appropriate. Possibly an infinite number of unstable states may satisfy the conditions of the problem; in a theoretical calculation, numerical bias may force an arbitrary selection of one of these states or prevent a steady state being attained. Analogous difficulties will exist for an experimental approach.

Following a discussion of the overall design task for a modern military aircraft and the position of aerodynamic excellence in the hierarchy of design objectives, this paper discusses the prospects of high α aerodynamics prediction via theoretical methods and will discuss some of the methods in detail, with particular emphasis on panel methods (including rolling and coning motions), discrete vortex dynamics calculations for the incompressible Euler and Navier-Stokes equations, and the new generation of field methods for the compressible Euler equations.

PART ONE: DESIGNING AIRCRAFT AND ALGORITHMS

1.1 The writer's dilemma

When asked to define the role of computational fluid dynamics (C.F.D.) in high-angle-of-attack aero-dynamics, the initial feeling of the writer was that it would be difficult to keep the paper to a reasonable length, so great had been the progress in recent years. This progress, the paper would start by saying, was due to the tremendous growth in the speed, capacity and economy of electronic computers. The paper would go on to describe a few of the writer's favourite algorithms with details of their convergence rates, numer-ical accuracy, etc. Some carefully selected examples would demonstrate the ability of these algorithms to reproduce *some* of the features of vortex-dominated flows for a number of cases where the flow is sufficiently simple to have allowed a systematic comparison to be made between theory and experiment. Some equally care-fully chosen examples would demonstrate the deficiencies of the traditional experimental approach, and add further fuel to the already heated debate about the relative merits of these two *"alternative"* approaches to the prediction problem.

The reality of preparing a paper to fit the title, however, has proved much more difficult than anti-cipated. This title relates to the *role* of C.F.D. - not to its *potential* - and by implication to the aero-dynamics of real shapes such as military aircraft and missiles, not to circular cylinders, square cavities and so on. To make matters more difficult, the subject relates to the high-α regime, and not to the familar "attached flow" state where C.F.D. really has started to pay dividends.

The theme adopted for the paper will *at first sight* delight the traditionalists (those who unswervingly support the wind-tunnel approach), and confound the proponents of computer-based theoretical methods (or at least those who advocate this approach *instead* of the wind-tunnel). This is in fact not the intention of the writer, as may become clear as the theme is developed. The basic theme of the paper is that, if we omit those so-called C.F.D. methods which are actually little more than computerised data-sheets or empirical correlations, then :

the present generation of C.F.D. methods is incapable of giving an accurate prediction of the air forces on a conventional aircraft shape at high angle of attack. In most cases, predictions based on properly-conducted wind-tunnel tests will be nearer to the reality of actual flight.

It is not even clear to what extent, or over what time scale, these statements will remain true as C.F.D. continues to evolve.

The counter-argument is that the traditional experimental approach is itself stretched to or beyond its limits by the physical processes involved in the high-α flow of air over an aircraft shape. Furthermore, the trend towards increased cost of "properly conducted" wind-tunnel experiments, in the face of ever more

stringent demands on the aircraft designer (tighter constraints on performance, wider range of flight regimes, lower lead-times), *requires* that computer-based theoretical methods play a substantial and increasing part in the aircraft design process - including the high-α regime.

The designer is therefore obliged to adopt some form of compromise; the nature of this compromise is motivated by the accuracy which is in fact *required* of predictions of high-α behaviour. This requirement differs in some respects from the accuracy of prediction needed for other parts of the flight envelope.

1.2 The nature of high-α prediction requirements

For civil aircraft, and for conventionally-configured military aircraft under cruise conditions, the current generation of C.F.D. methods allows a computer-based *design* to be achieved with some confidence. A number of fundamental design guidelines exist, including those which point to certain desirable forms of pressure distribution compatible with good drag rise characteristics, or stall progression, or minimum induced drag, and so on. It is now becoming possible to compute with some accuracy (including boundary layer effects), *the shapes* which will produce these target pressure distributions, subject to certain fundamental constraints on that shape.

At high α, and especially for non-conventional layouts, the complexity of the shapes involved, and the extreme nonlinearity of the flow phenomena, mean that this possibility does not exist, and almost certainly never will.

There is, for example, a set of "rules-of-thumb" pointing to desirable fin and tailplane placements which experience shows lead to acceptable spin-recovery properties; other empirical rules may be motivated by a desire to give the pilot an unmistakable warning of impending stall via a progressively increasing buffet amplitude (this being an important objective in the case of a "basic trainer" aircraft. The need does not exist in this regime for an *exact* attainment of ideal target pressure distributions. The role of C.F.D. will at best be confined during the initial design stage to subsequently confirming that the shape first designed by "rules-of-thumb" actually does produce *the right sort* of behaviour. In the event that it does not, C.F.D. may be of further assistance in suggesting modifications that will rectify the problem.

- Even when the configuration layout has been decided, an accurate prediction of high-α air forces is not always necessary or useful; an indication of trends or a signalling of some potentially catastrophic flow situation will generally suffice. This is particularly true during the intermediate phase of a project, after the basic lines of the configuration have been decided but before the detailed shapes have been frozen.

- Where accurate predictions are required, more refined computations or a limited series of specialised wind-tunnel tests may be performed.

- Only under limited circumstances is the designer concerned with accurate details of the air flow over a *conventional* aircraft shape at high α; the phenomena which can occur (such as stall, vortex bursting, etc.) are generally undesirable and the aim is usually to avoid their occurrence. If such undesirable flows should occur, the aim is usually to recover from them, and an estimate of their approximate maximum magnitude is then desirable in order to allow adequate control power to be installed to allow recovery from that condition (spin, etc.).

- For certain military aircraft, one of the primary design aims is a high degree of manoeuvrability. Some of the aircraft shapes to achieve this would not generally be regarded as "conventional". For such shapes, the air flow can still be "ordered", or predictable, even though the angle of attack is "high"; in the case of highly-swept leading-edges, or strakes, the aim is to achieve ordered separation of the flow from the leading edges, and to utilise the effect of that separation in controlling the flow over other parts of the configuration. Canards are another means of meeting "unconventional" requirements. For such ordered flows, C.F.D. in its current state can produce very useful predictions and can significantly reduce the number of wind-tunnel tests which would otherwise be required.

- Despite the above difficulties, the high-α regime is a vitally important part of the flight envelope of a modern fighter aircraft; the aircraft will be required to generate large normal accelerations by generating high lift in the presence of "non-ordered" separations of the trailing-edge type and body-vortex type. These can produce large effects on fins and other downstream surfaces. Reasonably accurate predictions of the forces and moments *and* an understanding of the associated flow patterns are required during the design stage. The wind-tunnel approach has a number of deficiences in such cases: during high-g manoeuvres, where aeroelastic distortion is large, the required shape of the wind-tunnel model will not be known accurately; separations of the above type can be very sensitive to Reynolds number effects; in order to rectify some undesirable feature, an *understanding* of the flow behaviour will be required, and this is very difficult to acquire from the wind-tunnel approach; at high-α, and especially for canard-configured layouts with strong interaction betwen the canard wake and the main wing, wind-tunnel wall constraint and support-strut interference effects can be significant but difficult to estimate.

In the light of the above observations, this paper will discuss the deficiencies of "classical" computational methods for high-α predictions, outline the capabilities of some current methods (from the viewpoint of not only their physical realism but also of their usability as routine design tools), and go on to discuss whether there really is a need to develop very much more complex theoretical methods for high-α aerodynamics.

To put these arguments into perspective, however, it appears relevant to attempt first to locate the aerodynamic design process in the hierarchy of priorities governing the overall military aircraft design process, and secondly to give some indication of how the subject of C.F.D. has rapidly grown from the seeds sown by Lanchester, Prandtl, Glauert, Lighthill, et al, to a monstrous new science of almost unmanageable proportions. The task of designing and constructing new computer programs, based on state-of-the-art algorithms and models of fluid-dynamics phenomena, has now become comparable in some respects to the aircraft design process itself: the elapsed timescales (but not the man hours!) can be similar; both require a wide range of

disciplines; there will be a number of contrasting requirements, all of which it is not possible to satisfy optimally at the same time. The next two sections of the paper summarise some of the features of these two design processes.

1.3 Objectives in military aircraft design

For a number of clearly-identifiable reasons, the overall design process for military aircraft differs substantially from that for almost any other engineering product. Although the set of basic objectives may be very similar to those involved in designing and marketing, say, a television set, the relative priorities are quite different.

The predominant differences lie in the magnitude of the task (and especially the number of disciplines involved), in the associated lead-time (i.e. time from initial concept to commercially-available hardware - typically ten years for current military aircraft), and life expectancy demanded of the product (which increases as a function of the sophistication and cost of the product). The financial commitment and high risk involved in a new aircraft project now demand decisions at a national rather than a company level, and have been the main motivation behind the large number of multi-national projects which have been undertaken over the last two decades. This frequent international collaboration, whilst inevitably giving rise to numerous difficulties, produces the added benefit of widening the potential market for the new product. In the unlikely event that it suddenly became possible to reduce the lead-time and costs associated with a new aircraft project by, say, an order of magnitude, then the relative priorities of the basic objectives in the overall project would almost certainly change dramatically.

Such a transformation has indeed taken place, for example, in the case of television manufacture. Fundamental research in abstract physics, followed by the vital element of intuitive advances in component design and more recently by the computer-aided design and verification of circuits, has revolutionised this technology. This revolution has not only significantly improved the standard of performance of the product (i.e. the T.V. set) but has increased its reliability and maintainability, and (by virtue of mass production and sales) reduced its retail cost. This in turn has led to a perceptible change in customer attitude; the television set has become an expendable product, replaced at frequent intervals as new models with appealing new facilities become available.

Similar revolutions are taking place in other industries able to take advantage of electronic technology - watches, motor cars, communications, etc. In some cases the very foundations of these industries have changed almost overnight; those manufacturers who have failed to respond accordingly have quickly run into hardship. It is therefore hardly surprising that this revolution in electronics is also playing a fundamental part in the overall design concept for the next generation of military aircraft.

Unlike the television industry, however, the aircraft design process is directly affected by parallel progress in a wide variety of other, quite unconnected, technologies. These include:

- *materials:* modern aircraft designs now incorporate an increasing number of components fabricated from unconventional materials such as carbon or boron fibres, new alloys etc. These may be chosen for their weight, strength, durability, electrical or magnetic properties, etc. Their behaviour may be quite different from that of conventional materials, and in some cases positive advantage may be taken of this (e.g. "aeroelastic tailoring" wherein the anisotropic stress-strain relationship of certain materials can be used to make a wing distort in some controlled, favourable manner under certain loading conditions).

- *manufacturing and maintenance:* the processes involved and the skills required have changed subst-antially in recent years; the reasons include the use of new materials (as above), and the intro-duction of computer-driven machining processes. Ease of manufacture and of repair or maintenance (and thus the associated cost to the customer) can in some cases outweigh almost all other consider-ations.

- *active controls:* the development of onboard computers and "active" controls allows aircraft to fly with automatic control under conditions where it would be unstable according to conventional philos-ophies. The relaxation in the conventional stability constraints is of considerable advantage with respect to other design aspects. It may be expected that the "fly-by-wire" concept will play an increasingly important role from now on; this in turn means, however, that further attention will have to be applied to airframe construction materials and their electromagnetic shielding properties, to avoid adverse effects due to extraneous electromagnetic fields such as those associated with nuclear explosions.

- *electromagnetic detection:* the increased sophistication of ground-based and aerial detection systems has made conventional aircraft much more susceptible to early detection. Detectability can be reduced by a choice of suitable construction materials, use of radar-absorbent materials and, to a lesser extent (except in certain critical details), by a careful choice of aircraft shape. This has led to a set of new criteria - in addition to those relating to aerodynamic performance - on which overall and detailed aircraft shapes and construction materials should be based. The improvement in detection systems has also led to a modified set of possible aerodynamic requirements, including manoeuvrability, (e.g. for missile avoidance), terrain-following capabilities, air-to-air combat tactics, etc. Detectability also needs to be considered when the weapon-carriage strategy is being planned (tip missiles, under-fuselage conformal carriage, etc.).

- *engine technology:* the integration of airframe and propulsion unit is an exceedingly complicated business and necessarily involves making a number of less-than-optimal compromises. During the initial design process, attention has to be given not only to the installation of adequate power to meet all tactical needs, but also to vulnerability, detectability, possible deleterious effects of hot engine efflux on downstream surfaces (particularly when lightweight materials are involved), fuel economy, etc. During static engine runs or taxying movements on the ground, as well as at high angle of attack, the flow into the intake can be subject to swirl induced by vortex effects.

This can, under certain circumstances, adversely affect the operation of the engine.

Design, for intake/engine compatibility is especially difficult at high α; in addition to the problems of swirl, there can be serious difficulties associated with flow distortion (with respect to total head as well as flow speed and direction). Under the most severe conditions, the air in front of the intake can have a tendency to actually flow away from it, thus preventing the engine from operating just when thrust is most needed. A limited number of modern military aircraft have variable intake geometry in order to overcome some of these problems.

It is clear, then, that in the overall design process for a military aircraft, aerodynamic excellence is by no means the sole criterion. It has to be balanced against a growing list of other criteria, not all of them consistent with optimal aerodynamic properties. *We are in fact dealing with the design of an overall weapon system, and not merely a highly efficient and versatile flying machine.* We are certainly dealing with an optimisation problem subject to a large number of constraints, rather than a straightforward aerodynamic optimisation problem.

This is even more true at high angle of attack. Current dogfight tactics occasionally require consistent, predictable and controllable high-performance aerodynamic characteristics at angles of attack which would have been inconceivable in earlier generations of aircraft. These manoeuvres are often associated with high-g turns which lead to very large inertial and aerodynamic forces, producing large distortions of the wing and of the structures supporting missiles and other stores. These lead to further structural and weight constraints not present for level flight.

The roles which a military aircraft is required to fulfil themselves evolve as a function of the enemy's (assumed) capabilities. These requirements are usually decided at multi-national government level, and the level to which these requirements can be met in practice then depends on the final terms in the equation: *cost and timescale.* There is little point in designing and constructing an aircraft with the maximum possible aerodynamic performance, if the lead time is so long that the requirement in the meantime becomes obsolete, or if the non-aerodynamic features are below par, or if the cost is beyond the reach of the customer. (Unlike television sales, the potential market for military aircraft is strictly limited). If a rival aircraft is able to meet the requirements *adequately,* but is available sooner, or is significantly cheaper, then it stands a good chance of winning the market (though the presence of political bias is a factor which cannot be ignored!)

Bearing in mind all the above arguments, and the increasingly tight performance requirements stipulated by customers, it is reasonable to conjecture that *the difficulty of the design task increases by about an order of magnitude with each new aircraft project.* It can be likened to the problem of attempting to reach a temperature of absolute zero. *As the ultimate goal is approached, the amount of work needed, and the new technology required to bring about further improvement, increase indefinitely.* Based on the use of only traditional tools (i.e. wind-tunnels and flight test in the case of aerodynamic design) it would therefore be impossible to progress much further than the aerodynamic capabilities of current military aircraft, whilst still observing the need to reduce timescales and costs.

The aerodynamic-design element, however, is by no means the weak link in the overall weapon-system design chain. In view of all the other constraints, our ability to achieve *adequate* aerodynamic performance with the traditional tools is arguably good enough as it stands now, *if we disregard the cost and timescale elements.*

The primary objective of computational fluid dynamics is thus *to achieve a given overall standard of aerodynamic design more cheaply than can be achieved by traditional methods alone.*

If at the same time C.F.D. is able to lead to a *better* product, then this must be regarded as a bonus. Such a bonus will not be won easily: the difficulties of progressively improving the engineering product (the overall weapon system) are at least matched by the difficulties of developing and applying progressively more sophisticated C.F.D. programs.

1.4 Theoretical method development for high-α predictions: theory and practice

Like stress analysis, electromagnetic wave theory and quantum mechanics, *theoretical fluid dynamics* is one of the many branches of theoretical physics. It is almost certainly one of the branches with the longest history of development, with the widest range of subdivisions, and with the greatest technical difficulty.

Theoretical physics generally involves the consideration of some physical process, constructing some model (usually expressed as a system of differential equations) which closely matches some of the key features of that process, and then analysing the behaviour *of that model* in order to attempt to predict the behaviour of the real process under a given set of conditions.

In some cases the model provides a very close simulation of the real process, diverging perceptibly from it only under extreme conditions. Examples of this are provided by Newtonian mechanics and by Maxwell's equations. So successful are these models that they are taught and applied without question, and are even accepted as being the exact equations governing real-world behaviour.

In contrast, most of the models devised to simulate the behaviour of moving fluids are applicable over only a narrow range, and even than often fail to give a full simulation of all the phenomena of interest. For example, even though the working medium is nominally the same, the models used in meteorology bear little resemblance to those used in aerodynamics. The physical processes dominating the overall behaviour of the air in these two cases are very different: gravity and thermal effects are the prime movers in meteorology but play an insignificant part in most flows of aerodynamic interest.

The two fields do share one common property, however; whilst the models used in the respective fields generally work well under "normal" conditions, *they can fail catastrophically when pressed to produce predictions where they are most needed.*

Non-deterministic factors control "unsettled" weather on a day-to-day basis (at the time this paper was being written, the U.K. was suffering almost unprecedented and certainly unpredicted freak winter weather conditions!). As will be discussed in this paper, these factors are matched by equally non-deterministic factors, but with smaller length- and time-scales, in the off-design flow of air over an aircraft. In both these cases, the mismatch between model-based prediction and actual behaviour is not wholly attributable to deficiencies in the model, but also lies in the inability to describe sufficiently accurately the *boundary conditions* which complete the definition of the problem.

At high angle-of-attack, the governing phenomena - vortex interactions - are often unstable and sensitive to small details such as freestream turbulence, surface roughness, surface vibration, etc. Small changes in these can cause gross differences in the flow pattern (e.g. vortex switching). In these small details, a real-life flow is not as repeatable as a carefully-controlled experiment, and consequently a number of the most important high-α phenomena are in effect non-deterministic. This fact causes problems for prediction either by theory or by experiment, and for this type of phenomenon gives rise to a "principle of uncertainty" which at present is not sufficiently acknowledged.

This does not mean that there is no part to be played by C.F.D. for high-α prediction - indeed these phenomena also demonstrate the inadequacy of the experimental approach used in isolation.

It does emphasise, however, the futility of attempting to construct a "black box" computer program for C.F.D. predictions in the high-α regime (or any other off-design part of the flight envelope). Any user of a C.F.D. program for aerodynamic predictions *must* be aware of the limitations *inherent in the models* used in the program. This applies for any C.F.D. program, past, present or future, for all parts of the flight envelope. It is the opinion of the writer that no single computer program will ever be able to predict, *automatically and with sufficient accuracy*, all the relevant aerodynamic properties of a real military aircraft. (The fact that a model yields good predictions for flow over a circular cylinder, or some other simple shape, does not imply that the same model will work equally well for a realistic shape!)

It should be clear, then, that in order to judge the future role of C.F.D. in aircraft design, we need to estimate the extent to which a user of any such program will be able to anticipate and allow for its deficiencies - without knowing the answer in advance. Unfortunately it seems to be the case that as C.F.D. models evolve towards greater realism, this ability on the part of the user is decreasing in proportion.

Just as with cookery, or any other skill-based activity, an unsophisticated tool in the hands of an experienced and enlightened user can often produce more acceptable results than the most complex system in the hands of one with inadequate skills. Unlike in the case of cookery, however, the reason lies not so much in the decreasing skill level of those involved, as in the immense increase in the complexity not only of the task, but also of the tool. To understand this requires an appreciation of the *computational* side of C.F.D.

In the early days of aerodynamic design, the only models with which it was possible to perform any predictions of any value - in the absence of today's computing capabilities - were of necessity very simple. They were, moreover, usually phenomenological, often being originated and developed by engineers rather than mathematicians. Lifting line theory, boundary layer theory and their variants were easy to learn and understand, easy to apply and easy to adapt, and in the majority of cases were *adequate* for the problems (i.e. aircraft shapes and speeds) for which they were used. Equally importantly, their limitations were immediately apparent; these simple models were *expected* to give only approximate simulations.

As aircraft speeds increased, however, and as the requirement for more precise predictions of more complicated flows became more pressing, these simple models were found to give either an inadequate simulation of the real physics, or were too difficult for the engineer to adapt manually to the more complicated geometries in question.

In a number of cases it has been possible to take advantage of the power of computers to *automate* the adaptation of a simple model to a more complex geometry, without essentially changing the nature of the model itself. The well-known vortex lattice method provides a good example here. When applied within its range of validity (which is in fact wider than often supposed), and when its results are correctly interpreted (which is by no means always the case) this method is capable of very useful predictions. Such a model, however, has two independent types of serious limitation, the first physical, the second numerical.

The physical limitations of a model become apparent when the assumptions (adopted deliberately or otherwise) about the features of the physical process are seriously violated; these features can change with flow speed, body attitude, scale etc., in a sometimes unpredictable manner. For example, the role played by viscosity at high angle of attack can be quite different from that at low α. A model such as a vortex lattice is in such a case incapable of simulating the key physics of the problem without modification - no matter how accurate the numerical calculation itself may be. To model the phenomena in question, it may be sufficiently accurate to modify the simple model by allowing vorticity to somehow escape from the surface into the fluid. If this level of approximation is not adequate for the problem in hand, a more complicated model may be required, taking more account of the actual physics involved; for example, a solution of the Navier-Stokes equations, based on totally different numerical principles, may be required.

The *numerical* limitations of a particular model, on the other hand, may be much more difficult to identify and to rectify. The limitation may be on *accuracy*; for example, the classical vortex lattice method *cannot* give an accurate value for the local velocity or pressure on a body surface; this is an inherent limitation of the numerical formulation. Alternatively, the limitation may be on *stability*; for example, a time-evolutionary vortex-lattice type representation of a separated viscous layer (vortex sheet) can diverge to chaos for purely numerical reasons. For entirely different numerical reasons, certain finite-difference representations of the spatial derivatives in the partial differential equations describing a flow model can lead to divergence of the solution when the local flow speed exceeds the local sonic value. (Mathematical arguments can be put forward to explain this numerical phenomenon).

The above problems, some of which are in no way related to aerodynamics or even to fluid dynamics, have necessitated the application of the techniques of *Numerical Analysis*. Computational fluid dynamics is now

one of the most active fields of research and development in applied numerical analysis.

Some of the most recent and successful programs for the solution of rotational flow over complete aircraft, for example, are based on the use of the classical Runge-Kutta algorithm for proceeding through pseudo-time to attain the required steady state asymptotically. The latest C.F.D. techniques based on "multi-grids" or on "approximate factorisation" or "operator splitting" are little more than classical Numerical Analysis techniques under a different name.

The majority of C.F.D. programs reduce to approximating the differential (or integral) equations describing the model by a large system of linear equations with many hundreds, often many thousands, of degrees of freedom. In some cases the associated matrix may be sparse (e.g. tridiagonal) and in many cases it may be full (e.g. with a panel program). It may or may not be "well-conditioned". It would be impossible to solve these large systems without the well-established tools of Numerical Analysis, though in most cases these tools have to be adapted to the particular requirement.

In addition, whilst some modern C.F.D. techniques proceed directly from a numerical discretisation of the differential equations expressing the model, a number of other techniques involve some quite advanced *mathematical* analysis before any discretisation is introduced. Such is the case with the current generation of boundary integral formulations ('panel methods'), including those adapted for high angle-of-attack simulation.

Another field in which abstract mathematics may be helpful is that of turbulence. Long considered as a random process, requiring random elements to be introduced into the equations describing the motion, there is now some evidence that the phenomenon may have a deterministic interpretation. Recent work led by Zeeman at the University of Warwick, U.K., shows that greater understanding of turbulence may be obtained via the relatively new mathematical concepts of topology.

Another form of mathematical preconditioning which is often introduced, prior to numerical discretisation, consists of *transforming* or mapping the differential equations from the original physical region to a fictitious domain in which the equations can be more readily handled, at the cost of having to deal with unfamiliar concepts such as Jacobians and metrics.

All the above processes have the effect of converting the original model of the physical process (with all its inherent limitations, which the engineer or aerodynamicist was at least able to recognise) into a highly abstract, impenetrable form in which the original model and its physical limitations are not only obscured, but confused with numerous artificial properties belonging to the particular mathematical and numerical techniques employed to investigate the model. Anyone attempting to interpret the predictions of a particular model of viscous vortices shed from a surface at high angle-of-attack may first have to contend with concepts such as the "random walk" (a process used to *simulate viscous* diffusion within a vortex, its use being based on numerical convenience and having nothing whatever to do with the physical process being simulated).

A more major problem is presented by the fact that the differential equations expressing a model may, for given conditions, possess a multiplicity of solutions. Only one of these may be possible physically, the others corresponding to non-physical circumstances not allowed for in the approximating model. A good example of this is provided by the possibility of non-physical "expansion shocks" in isentropic models approximating transonic flow. A variety of artifices have been devised to suppress such violations of the Laws of Thermodynamics. These include *artificial viscosity* (which introduces into the numerical formulation an element of dissipation which is absent from the basic inviscid model) and such obscure concepts as *penalisation* and *regularisation* which were originally motivated by events in totally unrelated branches of engineering and physics. Again, anyone wishing to familiarise himself with the details of such a model, or of a number of them in order to perform a relative assessment, is obliged to first become familiar with such unfamiliar ideas.

It is an interesting observation that the so-called finite-element method for analysing the behaviour of continuous media, which was largely developed in the U.K. in the field of stress analysis, was originally formulated by engineers using intuitive arguments. The method involved familiar engineering concepts which were readily accessible to any traditionally-trained graduate engineer. A quick glance at current technical journals reveals, however, just how far this method, in the recent forms developed for fluid mechanics, has moved away from its "classical engineering" roots. It is now a highly abstract and esoteric subject, employing all the jargon and mysteries of Sobolev spaces, topology, etc. It is by no means readily accessible to a classically-trained aerodynamicist.

What has happened to the finite element method has happened to a similar extent to most of the models and techniques which were originally conceived in the pre-computer era. It would be extremely interesting to see just how well the past-masters - Prandtl, Lighthill, Glauert, Lanchester, et al - would cope with the present generation of C.F.D. methods!

The above arguments have been developed at some length to emphasise the fact that although computers have enabled potentially extremely powerful tools to be placed in the hands of the aerodynamicist, this does not in fact make his job any easier. To extract the maximum value from these tools, the user certainly needs a much wider range and greater depth of talents than was the case before these tools became available. *In this field at least, the introduction of advanced computers has increased, not decreased, the skill and academic attainment level requir 1 of the engineer.*

This is every bit as true with regard to the *developer* of C.F.D. programs. In addition to the above list of skills required - advanced fluid mechanics, advanced mathematics, advanced numerical analysis - must be added the ability to develop advanced computer programs and data-processing facilities (especially interactive graphics, without which the modern generation of computer programs, generating vast amounts of numerical output, is severely limited).

Although opinions vary in this matter, it is the writer's opinion that the programming stage is an integral part of the overall task. Since algorithm development is itself an evolutionary process, it is virtually impossible to deliver a C.F.D. "program specification" to be programmed by some other specialist agency. The subject of where, and by whom, C.F.D. programs can most effectively be developed is discussed,

together with some of the above topics, in Ref. 1a . The writer's conclusion is that the user-industry should be the source of such programs.

The important conclusion must be that the future role of C.F.D., especially in high-α aerodynamics where the key phenomena are so difficult to model, will be governed not so much by developments in computers as by the ability of the user-industries to develop and retain staff with the requisite levels of skill, both for method development and application. The practical and logistic difficulties of meeting this requirement are also discussed in Ref. 1a .

PART TWO: C.F.D. AS A HIGH-α PREDICTION TOOL

2.1 Methods for conventional flight prediction

Modern C.F.D. techniques based on the use of powerful computers are now relatively well-established as design tools for the "simple" part of the flight envelope.

Foremost among the methods used is the *panel method* for subsonic fl.w; analogous programs for (linearised) supersonic flow are now also reaching fruition, though here the model is less representative of real physics than in the subsonic case, and requires very careful use and interpretation.

Also heavily used are the *transonic small perturbation* (T.S.P.) programs. Again the model (i.e. the T.S.P. equation) gives only a limited representation of the features of the real flow. There is the added problem that the aircraft geometry is represented only approximately and this in turn leads to a number of extra, purely numerical, spurious effects near wing leading edges, and to a severe limitation in the aircraft configurations which can be treated. The use of this method, however, is bolstered by the fact that experience has been gained in its use and that its range of application has been widened by the development of "inverse" versions (calculating the shape for a prescribed pressure distribution, to within the limitations of the model) and "viscous" versions (coupled with a boundary layer code). Its application will henceforth be progressively curtailed as more realistic models are developed.

In the short term, programs based on the *full potential* equation will find more application, partly as a consequence of their "better" physical modelling and partly due to their ability to treat more realistic geometries. Their inability to represent rotational flow, however, limits their value in the longer term.

The very recent developments in solutions of the so-called *Euler equations* (Refs. 2,3) are taking C.F.D. into a new era of realism (both of shock representation and of inviscid rotational flow simulation). The prospects are particularly exciting in view of the new generation of numerical algorithms which at the same time are bringing the computational costs down very substantially.

The application of these Euler methods may be expected to become as routine (for the *entire* speed range) as that of the panel methods is for *subsonic* flow. Indeed, the parallel progress in mesh generation programs is already allowing geometries to be treated which are as complex as those which hitherto have been accessible only to panel methods. It is conceivable, (but not yet certain) that the Euler programs may shortly supplant *all* the above-named methods both on the grounds of physical realism and of economy of computation.

Methods based on even more realistic models of the physics (e.g. the Navier-Stokes equations) are starting to be used for simple shapes, but as yet are far from being routine tools for complete aircraft calculations. The use of the above inviscid methods, plus *boundary-layer type simulation*, is unlikely to be challenged by such programs for the foreseeable future, for the "simple" part of the flight envelope.

A discussion of the process whereby the various C.F.D. programs are progressively adopted as routine tools in a practical engineering environment is given in Ref. 1b . In addition to the stages of model and algorithm development, further vital stages in this process consist of *numerical validation* (confirming that the program actually does give an accurate representation of the model) and of *evaluation* (performing systematic comparison with experiment to determine the conditions under which the model succeeds in giving an acceptably accurate simulation of the real physics). This process is relatively well advanced for the methods named above (though the Euler and Navier-Stokes codes are still at the numerical validation stage). The situation is by no means so clearly defined in the high-α regime, however. For these conditions the main design tools continue to be the simple methods outlined in the following section.

2.2 Simple methods of predicting high-α aerodynamics

The basic models used in the above methods (with the possible exception of the Euler and Navier-Stokes methods) fail to give a realistic simulation of the features of high-α flow. The extent to which this failure has been rectified in a number of current schemes will be examined in Section 2.3.

Apart from a number of new methods currently under development, the design process for high-α flight is still based on the use of simple approximate methods. The final design is validated by wind-tunnel testing, with appropriate rectification of undesirable properties once these have been detected from the measured characteristics.

The weaknesses in this procedure, apart from the elements of cost and time, were indicated earlier: the correct distorted shape of the model for simulating high-α manoeuvres is not known; the vortex phenomena may be Reynolds-number sensitive and therefore incorrectly simulated in the wind tunnel; it is difficult to establish the root cause of an undesirable property, purely on the basis of wind-tunnel tests; at high-α, wind-tunnel interference effects can be particular troublesome.

As was also mentioned earlier, however, the high-α behaviour of a modern fighter is such an important part of its overall function that at least a limited form of aerodynamic optimisation (subject to all the constraints detailed in Part 1) has to be attempted, with the tools actually available, before any wind-tunnel tests of the prototype configuration are performed. These tools are essentially two-fold:

empirically-based approximation and the experience of the designer.

In the case of "classical" aircraft shapes, (and "basic trainer" aircraft usually fall into this category), the high-α flight characteristics are dominated by two types of phenomena: body vortex flows (which may be symmetric or asymmetric), and conventional 'wing stall', frequently of the trailing-edge separation type. The primary aim of the design process for high α will be to attempt to ensure that these vortex effects do not lead to a potentially catastrophic situation; there is generally no need to ascertain precise details of such a flow should one arise, except in the case of a basic trainer. Usually it is the aim here to achieve a design whereby the pilot is warned of the approach to such a situation, e.g. stall or deep stall, by progressive growth of an associated phenomenon (e.g. buffet). In the case of a basic trainer it is usually also essential to design for regular spin characteristics and easy recovery. For this to be possible it is vital that these two types of vortex flow do not cause the aerodynamic control surfaces to become ineffective, or to possess unpredictable or discontinuous characteristics. The latter property can arise, for example, if during some manoeuvre a vortex (e.g. from the aircraft nose) undergoes a progressive change in position, until it switches from one side of a control surface (e.g. a fin) to its other side. To predict this will require some knowledge of the behaviour of such vortices. This itself requires that, as far as possible, these vortex properties be repeatable, which in turn points towards designing fuselage shapes which favour *symmetric* vortex shedding. To some extent this can be achieved (subject to other constraints such as the influence of shape on supersonic drag) by judicious choice of nose shape. Where this is impractical, other devices such as strakes on the front fuselage surface may be considered.

Initial design for good spinning characteristics is traditionally accomplished by selecting a configuration layout which previous experience has shown to be favourable. Spin tunnel and analytical (transient response calculation) methods are subsequently employed to *assess* the acceptability of the initial design; if necessary, modifications may then be introduced and further tests conducted. For use in the above transient response calculations, the motion in a spin is derived by integrating the equations of motion on the basis of aerodynamic data estimated by using a combination of, say, static wind tunnel test data with rotary derivatives calculated by strip theory. This approach requires a knowledge of the wing's sectional aerodynamic characteristics (essentially C_L and C_D as a function of local incidence for the two-dimensional section, with some allowance for 3-D effects). These will be available from datasheets, or from previous experience with the appropriate wing sections. Such approaches generally ignore the interference between the various components. An extreme example of this is provided by the practice, frequently used during approximate initial studies, whereby characteristics of two simple wings with different taper ratios may be combined, via strip theory, to give an approximate model of a straked or cropped double-delta wing.

For unconventional layouts, for example those involving canards, wing strakes, twin fins, etc., the above approach can only be used with extreme caution. In such cases the interference between different components can be large, and a much more sophisticated procedure than the above is desirable. It is of little comfort to the designer to find that a spin prevention system through the F.C.S. (flight control system) is required for a new aircraft with unconventional layout. This in itself is difficult, but additionally some knowledge of spin characteristics and associated recovery procedures are still required for test flying as a guarantee against system failure. Thus with maximum incidences, where 35°, say, is often regarded as conservative, the demands on design engineers, C.F.D. method developers and wind-tunnel engineers are obviously very high.

For all types of modern combat configuration, improvements in weapon agility and lethality mean that there is no escape from close air combat once it has been engaged. This places heavy emphasis on manoeuvrability, particularly on sustained (thrust limited) and attained (lift limited) turn rates. There is also some additional benefit due to 'pointability' beyond maximum lift to allow snap-shot firing opportunities. This emphasis on performance at high incidence involves design for controllable flight in conditions of extensive separated flow. In past and present generations of combat aircraft, flight in such conditions has been limited by "cliff edge" phenomena such as stall, spin, pitch up and other forms of uncontrollable behaviour. For the next generation of combat aeroplanes we are aiming to design for *carefree manoeuvring*. This means augmenting natural stability with active controls and moderating the pilot's ability to generate manoeuvres which would cause departure. In effect we intend to erect a safety barrier in place of the cliff edge.

Design for carefree manoeuvring, as well as requiring adequate margins of control power up to and beyond the stall, involves modelling aircraft behaviour under conditions of extensive separated flow to enable F.C.S. design to be undertaken with confidence. The tools available to the aerodynamicist are conventional static wind tunnel tests and free-flight tests in the vertical wind tunnel and with helicopter-drop models. Added to this we at BAe Warton, foreseeing the need for such data, have developed rotary rigs for measurement of aerodynamic coefficients in coning motions at high incidence, both at low speed and at transonic speeds.

However, these tests suffer from the inherent limitations associated with wind tunnel testing techniques, i.e. doubts about Reynolds number effects, the correct geometric representation etc. This reinforces the need for development of C.F.D. methods. A limited number of separated-flow predictions are already possible with the current generation of C.F.D. methods, as indicated in the next section.

2.3 Current computer-based high-α prediction methods

In Part 3 a number of recent concepts and developments will be described. Even now, some of these can be, and are, used (with caution) to give useful indications for practical aircraft problems. However, they are generally not yet sufficiently well developed or evaluated to allow their routine use in an industrial environment.

The programs which are currently used in an attempt to predict high-α flows are mostly semi-automated extensions of simple models, and are strictly limited in their range of application. This section will give an outline of some modifications to a *panel program* which have extended its applicability to certain high-α problems.

2.3.1   The basic concept of a panel program

The mathematical basis of the "boundary integral" or "panel" method is described in detail in Refs. [4], [5] and [6].   The method consists of calculating "singularity" strengths on panels representing the aircraft surface, such that the prescribed conditions of the problem are satisfied.   The surface velocities and pressures, and thus the loading, then follow immediately.   These singularity distributions usually comprise simple source or vorticity distributions on each panel.   The model is applicable to very complicated geometries such as that in Fig. 1 .   For such a geometry it is possible by this method to obtain accurate solutions of the Prandtl-Glauert equation, which is a linearised approximation of the exact equations governing inviscid, irrotational, compressible flow.   For zero Mach number, it degenerates to Laplace's equation, and this is applicable both for steady and unsteady flows.

Rotational flow is supported to the extent that vortex separations from the aircraft surface are allowed by inserting into the flow field sheets of vorticity issuing from the separation lines.   (A zero thickness *sheet* is exactly representative of a shear *layer* in the limit of infinite Reynolds number).

When this separation line is a sharp edge, the so-called Kutta condition states that the flow must physically leave such an edge smoothly, i.e. that the velocity must be everywhere finite.   It is then possible to automate the calculation process, the strength of the separated vorticity distribution being controlled by the Kutta condition.

Most such programs deal automatically with lifting aircraft by extending the definition of the wetted surface (on which boundary conditions are required to complete the definition of the problem) to include the wake surfaces described by the vortex sheets leaving sharp trailing edges of wings.   The need to prescribe boundary conditions over this entire wake surface is removed if the unknown wake geometry is approximated by some simple, fixed surface proceeding downstream from the trailing edge.

The boundary conditions applied on the aircraft surface usually state that the normal component of the velocity is zero at the centre of each panel, i.e. that the surface is solid and stationary.   However, it is straightforward to specify a non-zero normal velocity;   this allows either a permeable boundary or a moving solid boundary to be treated.   The permeable-boundary option allows finite intake-flow velocities to be simulated, or boundary-layer effects to be modelled economically.   The moving-boundary option allows unsteady flow problems, including rolling and coning motions, to be treated.   In turn this allows the associated aero-dynamic derivatives to be computed automatically.   This will be discussed further in Section 2.3.3.

The flow field in which the aircraft is situated may simply comprise a uniform stream, or it may in part be generated by independent sources and vortices embedded in the fluid.   In a coupled iterative scheme, these can be progressively updated in strength and position to satisfy some required condition.   This can be used to model a variety of phenomena associated with, for example, high-α aerodynamics.   Some current capabilities will be indicated later.

The mathematical and numerical analysis involved in modern formulations of the panel method is as difficult as in any other branch of C.F.D., and not easily accessible to the user-engineer.   However, the fundamental "singularities" employed (and this is especially true of vortex lines and sheets) have a direct physical relevance which is apparent and natural to any aerodynamicist.   This certainly aids the engineer to manipulate the programs, and to interpret their output (particularly when this has been post-processed to give graphical presentations).   This intuitive "feel" is absent with most other current methods, and to a considerable extent makes panel programs one of the "safer" types of program to use;   the experienced user can usually detect erroneous computations quite readily.   Indeed it can be argued that the panel program is the vehicle which brings up to date the "classical" ideas of lifting-line theory - probably the most important single model for pre-computer aerodynamic predictions.   This point will be reinforced in Section 2.3.2.

It should first be emphasised, though, that in common with all other inviscid models, and with models using a simple boundary-layer simulation of viscous effects, panel programs exhibit deficiencies in regions where viscous effects are significant, even at low α.   These include:

* *wing trailing edges:* for attached flow the effect of viscosity, on most of a simple wing, is generally small as far as the lift is concerned.   The boundary-layer displacement effect is comparable to the effect of a small change in thickness and camber, *except* at the trailing edge. The biggest contribution to the viscous lift loss is attributable to the change in circulation associated with local vorticity-induced effects at the trailing edge.   If this local effect is not properly modelled, then it is futile attempting to have an accurate simulation of displacement effects over the rest of the wing.   This is true even if the concept of displacement thickness remains valid near the trailing edge - in practice the classical boundary layer assumptions become very dubious in this region.

* *wing tips:* the viscous flow near a wing tip, even at low α, is by no means as simple as the models usually adopted.   The flow does not leave the trailing-edge in a thin shear layer near the tip, neither does the fluid inside the viscous region flow in simple fashion round the tip from lower surface to upper surface.   Rather, there is a diffuse region of vorticity enveloping the tip region, which can actually cause the local flow, on the wing upper surface near the trailing edge at the tip, to be orientated *towards* the tip, (see Ref. [7]).   This flow, and the associated tip pressures, cannot be represented by simple boundary layer models, and certainly not by a potential flow model.   Without some form of correction, the aerodynamic parameters sensitive to tip modelling (such as rolling moment) will be inaccurately predicted.

* *junctions:* the wing root represents a region where the relatively simple boundary layers of the wing surface and the fuselage combine to form complex secondary flows involving pairs of contra-rotating vortices.   Such vortices lie in both the upper-surface and lower-surface junctions, and downstream of the trailing edge of the wing they continue along the length of the fuselage.   The overall system is sometimes called a "scarf vortex system".   It gives rise to a discontinuity in the spanwise

distribution of circulation, at the wing root, of unknown magnitude. This, combined with the complex viscous flow at the downstream end of the fuselage, means that the circulation distribution across the fuselage is not known. It is usually modelled as being a uniform continuation of the circulation at the wing root. Although this is a totally arbitrary choice, there is absolutely no way of deriving a more general model, at present, without resorting to empiricism.

Similar modelling difficulties exist in connection with junctions between pylons and wings. Concentrated vortices of unknown strength can continue in the wake downstream of such a junction.

These uncertainties relating to the model of circulation distribution continue as Reynolds number is increased (the vortices simply becoming more concentrated) and presumably remain in the limit of infinite Reynolds number – which is taken to be a potential flow. The usual theorems of uniqueness of solutions do not apply for potential flows containing such discontinuities. Simple boundary layer theory can offer no assistance in determining these unknown features.

· *Afterbody separation:* even with isolated bodies of revolution, simple potential-flow-plus-boundary layer modelling is incapable of modelling the separated flow which inevitably occurs at the downstream end of a body. Such methods are thus incapable of predicting overall forces, i.e. lift, moment and pressure drag.

The above list of deficiencies becomes considerably longer and more serious when high-α flows are considered.

2.3.2 Wake and vortex relaxation

As stated in the previous section, it is standard practice in a panel program to approximate the unknown wake surface by some fixed surface, with no boundary conditions applied on that surface, except perhaps at the trailing edge. The resulting flow will be such that the vorticity distribution on this wake surface will sustain a pressure difference inconsistent with physical flow.

Now, in the case of an isolated wing at moderate incidence, the pressure distribution computed on the wing will be relatively insensitive to the location of the fixed surface chosen to approximate the wake position. If this wake passes close by another surface downstream, however, the flow induced at that surface will not be insensitive to the position selected for the wake. This can lead to inaccurate prediction of the loads on close-coupled lifting surfaces such as canard/wing configurations, or to inaccurate simulation of wind-tunnel interference effects if a wind-tunnel geometry is also included in the theoretical calculation.

In such cases, it is therefore highly desirable to place the vortex sheet in a position representative of the physical wake location. Since this is not known in advance, it must be relocated iterately until appropriate conditions on the sheet are satisfied. In the limit of infinite Reynolds number, the correct conditions are that at each point of the shear layer there be no pressure difference across the wake, and that the wake surface be a stream surface. It is easy to show that for zero Mach number both these conditions are satisfied simultaneously if the vorticity vector in the shear layer is aligned with the mean of the two velocity vectors on the two sides of the sheet (see Ref. [8]).

One simple means of approximating the above condition consists of representing the distributed vortex sheet as a set of discrete line vortices of constant strength along the streamwise length of the wake, and representing each semi-infinite line as a finite chain of straight line segments of constant strength. The relaxation process then consists of iteratively adjusting the end-points of each segment until every segment is aligned with the velocity computed at its midpoint. In this computation, the velocity induced by each segment at its own midpoint is reckoned to be zero. This is the correct limit for the self-induced velocity at the centre of a cylindral segment with circular cross-section, carrying uniform volume vorticity parallel to the axis of the cylinder, as the radius of the cylinder decreases to zero. (It is also the correct limit for the self-induced velocity of a square surface patch of vorticity, of which the line segment represents a far-field approximation).

This type of calculation has a tendency to become chaotic for numerical reasons. It can be stabilised by a number of methods. In the program described in Ref. [8] this is achieved by:

· *the order of segment relaxation:* all the segments at one station in a row across the wake are relaxed simultaneously. All downstream segments of each line are then given the same vector shift as the downstream node on the just-relaxed segment in that line. All segments in the next streamwise station are then relaxed simultaneously, in accordance with the velocities induced at their midpoints by all the segments in the wake in their most recently shifted position (plus the freestream velocity, plus the velocity induced by the current aircraft singularities). After each sweep of the wake, the aircraft singularities are recomputed. The entire process is repeated until convergence is attained (generally three or four sweeps).

· *core amalgamation:* when the most outboard vortex strip has undergone a twist (about the streamwise direction) of more than three-quarters of a complete revolution, the remaining downstream segments of the two line vortices forming that strip are amalgamated into a single line vortex at their centroid of vorticity.

· *spiral acceleration:* when a vortex is close to a surface there is a tendency for each node on that line to converge to its final position along a spiral trajectory. The process can optionally be accelerated by computing the form of the spiral on the basis of three consecutive positions of the node, and then putting the node at the centre of that spiral.

· *velocity computation:* the velocity field induced by the wake in its relaxed position is computed by converting the line vortex approximation to a higher-order approximation (piecewise-constant surface vorticity). In particular, this has the effect of restoring the finite tangential velocity jump across the wake.

This *algorithm has been* found to be particularly stable and accurate. An example of comparison with experiment is given in Fig. 2. An example of its application to a complex configuration performed recently at B.Ae Warton is shown in Fig. 3. The problem here involved estimating the wind-tunnel constraint effect on the loading on a wing-body canard configuration. The picture shows the computed wakes from the canard and wing at α = 7° with a canard setting of 10°, inside the wind tunnel. The figure demonstrates the effect on the wing loading due to the presence of the canard wake, and secondly shows the effect of wind-tunnel constraint effects on the computed canard and wing loading distributions for the complete configuration. The other highly peaky, curve shows the wing loading in the presence of an *unrelaxed* canard wake continued linearly from the canard trailing edge, parallel to the freestream direction (i.e. with the canard wake in a plausible but "wrong" position). Now the wind-tunnel walls modify the canard wake position, and therefore modify the wing loading over-and-above the constraint effect associated with a simple wing body. In addition to this the canard lift and trailing-vortex strength are modified by the tunnel. The combination of these effects demonstrates the difficulty of estimating the effect of tunnel constraints on the loading of both the wing and the canard, and in particular on the pitching moment.

The process described above for relaxing each line in the model of the wake is of course equally applicable to a single line vortex. Such a vortex forms a plausible model of a diffuse vortical structure separating from a slender body (e.g. a front fuselage), or of the rolled-up core of a wing wake.

Fig. 4 shows the result of the relaxation of a canard wake over a lifting wing. In the case presented here the wing incidence is 6°, with a canard setting of 0° relative to the wing. An example of core amalgamation (see earlier) is clearly visible.

Fig. 5 shows a simple line vortex model adopted to represent the canard and its wake. In the calculation shown here the bound vortex is in two fixed ("rigid") segments; the first is along the wing quarter chord to about ¼ semispan (this figure is not critical); the second segment then proceeds chordwise, terminating at the canard trailing edge. The remainder of the trailing line vortex could either be held rigid or allowed to relax. The strength of the vortex was estimated by a very simple calculation using the value of the maximum circulation on the canard obtained from a wing-body-canard calculation with fixed wake.

The figure shows a side view of the relaxed and rigid shapes of the vortex. The pressure profiles plotted for the inboard part of the wing show the different results obtained for wing-alone, wing with fixed canard vortex, and wing with relaxed canard vortex. The differences are substantial on the inboard part of the wing. The corresponding results for a full canard with relaxed wake are not plotted, but are virtually indistinguishable from those shown for the relaxed vortex representation. Fig. 6 shows the inboard portion of the spanwise loading distribution on the wing. The spurious results given by the rigid vortex and by a calculation using a full canard with a rigid wake, are clearly visible.

The conclusion is that, even for close-coupled calculations of this kind, a line vortex simulation of a canard wake is adequate as far as the wing flow field is concerned. Whether such a line representation or a full wake is used, however, relaxation is essential. In the case of a line vortex simulation, an estimate of the vortex strength has to be made, and this weakness has to be balanced against the advantage of a saving in computation time. It can thus be seen that, as indicated in Section 2.3.1, the panel program with vortex relaxation represents a very natural but very powerful extension of the classical lifting line model. Unlike most other modern C.F.D. methods, such programs have an intuitive "feel" in the hands of an experienced aerodynamicist.

Thus the relaxation of trailing-edge wakes or of simple line vortices is now a relatively routine matter. The same is not true of wakes issuing from sharp leading edges or from smooth surfaces, where the coupling between the relaxing vortices and the generating surface is much stronger. A considerable amount of effort is currently being directed towards these problems, and an outline of some of this work will be given in Part 3.

2.3.3 Unsteady flow and prediction of aerodynamic derivatives

There are numerous flows of interest to the aerodynamicist in which the aircraft is not in uniform motion relative to the ground, but where the flow is steady (though apparently rotational) when viewed in aircraft axes. Examples are provided by

- Rolling motion about the direction of flight; the general case of this corresponds to coning motion, the degenerate case being simple rolling motion. This last case includes the case of a propellor or windmill with axis parallel to the airflow direction, if asymmetric body effects are ignored.

- Steady spins.

Motions of this kind are often of interest in their own right; they also constitute basic motions fundamental to the *definitions* of some of the so-called aerodynamic rate derivatives (which are based on *partial* derivatives of the aerodynamic forces and moments with respect to angular velocities about each of the three reference x, y, z axes). Rigid-body motions of this kind can always be instantaneously expressed as a linear combination of the three basic translations along the x, y and z axes and the three basic rates of rotation p, q, r about these axes. In the case of inviscid (steady or unsteady) flow at zero Mach number, the governing equation for the velocity potential is Laplace's equation, expressed in ground axes. If an instantaneous solution of the equation (i.e. the ground-based velocity field) is determined for each of the above 6 basic motions, then the instantaneous velocity field for any linear sum of these motions is the corresponding linear sum of these basic solutions. In the case of a lifting aircraft this statement is restricted to flow combinations for which the circulation does not vary with respect to time, otherwise wake-history effects must also be considered.

The solution (i.e. the perturbation velocity in either ground or aircraft axes) for each component motion is obtained, as outlined in Section 2.3.1, by requiring the ground-based velocity component of the fluid in the direction normal to the local surface to be instantaneously equal to the known normal component of the ground-based velocity $\vec{V}_s$ of the physical surface at that point. In each case this is obtained simply by

adding an extra "right-hand side" to the matrix equation system to be solved.

At any point on the aircraft surface or in the external air, the resultant velocity is then obtained as the sum of the unperturbed freestream velocity and the perturbation velocity due to the *instantaneous singularity distribution* on the aircraft and its wake.

If a wake relaxation is being performed – whether this be trailing edge or leading edge or body vortex – then the relaxation is valid only for that single (steady) motion. The relaxed solution for that motion cannot then be obtained by superposition of relaxed basic solutions but must be calculated iteratively as before, using a single definition of the body motion. The boundary condition to be satisfied on the wake (with the flow steady in aircraft axes, again) is the direct analogue of that in the standard case of Section 2.3.2 – the vorticity vector must be parallel to the local mean velocity (mean of the velocities on the two sides of the sheet) defined in the (moving) aircraft frame.

It is worth noting that once the relaxed wake position has been determined for a particular composite *motion*, then that wake position can be regarded as fixed and used in the same way as a "rigid" approximation of a trailing-edge wake is normally used (see Section 2.3.1). Solutions could then be obtained for different aircraft motions, using this rigid wake. This wake would of course *not* satisfy the physical conditions for these other motions. However, the motions for which such rigid-wake solutions are derived could be the basic components (translations and rotations with respect to x, y, z) of the *composite motion* in question (i.e. for which the wake relaxation was performed. The appropriate linear sum of these component rigid-wake solutions *would* then satisfy the relaxed-wake conditions. Advantage will be taken of this fact later, in the definition of a method of approximating the aerodynamic derivatives for flows involving separation.

The computation of the velocity field is thus straightforward for flows which are steady relative to the aircraft. (In some cases the argument can be extended to compressible flow, but extra care is then needed). Once the velocity field has been determined, in the compressible or incompressible case, it then remains to determine the pressure field and hence the loading on the aircraft. A simple method developed recently at B.Ae. Warton, for obtaining the pressure from the velocity by using the unsteady compressible form of Bernoulli's equation, will be described below. This is particularly simple to implement in the case of a panel program, but the idea is equally applicable to other types of potential flow computation. In the case of a panel program, it has the further advantage of allowing the aerodynamic derivatives to be obtained automatically.

For inviscid flow the quantity

$$\tfrac{1}{2}U^2 + \frac{\partial\phi}{\partial t} + \int \frac{dp}{\rho}$$

is constant along a streamline, with U = local flow speed, ϕ = velocity potential (see below), p = local pressure, ρ = local density. If we use the isentropic relation (p/ρ^γ = constant) in this expression, then use the equation of state (p/ρ = RT), noting that $a^2 = \gamma RT$ (with a = speed of sound) it then follows that

$$\frac{\gamma-1}{2}\left(U^2 + 2\frac{\partial\phi}{\partial t}\right) + a^2$$

is constant along any fluid-particle trajectory. If we now say that the flow is steady in ground axes at infinity, then $\frac{\partial\phi}{\partial t}$ = 0 at infinity. It then follows that we can write

(1)
$$\frac{T}{T_\infty} = 1 + \frac{\gamma-1}{2a_\infty^2}\left(U_\infty^2 - U^2 - 2\frac{\partial\phi}{\partial t}\right) = F, \text{ say,}$$

where ϕ is now the *perturbation* potential, since the unperturbed freestream potential is independent of time. Thus

(2)
$$\bar{U} = \bar{U}_\infty + \nabla\phi = \bar{U}_\infty + \bar{u}$$

where the gradient operator ∇ and the aircraft-singularity-induced perturbation velocity $\bar{u}$ may be derived with respect to the aircraft, but are expressed with respect to the reference (ground) system.

Now we can obtain an expression for the pressure coefficient C_p based on some reference speed U_{REF}, as follows:

$$C_p = \frac{p - p_\infty}{\tfrac{1}{2}\rho_\infty U_{REF}^2} = \frac{(p/p_\infty) - 1}{\tfrac{1}{2}(\rho_\infty/p_\infty)U_{REF}^2} = \frac{2[(T/T_\infty)^{\frac{\gamma}{\gamma-1}} - 1]}{\gamma U_{REF}^2/a_\infty^2}$$

i.e., using (1)

(3)
$$C_p = \frac{2}{\gamma M_{REF}^2}[F^{\frac{\gamma}{\gamma-1}} - 1] \quad \text{with}$$

(4)
$$F = 1 + \frac{\gamma-1}{2M_{REF}^2}C_{pI} \quad \text{and} \quad M_{REF} = U_{REF}/a_\infty$$

where C_{pI} is an "incompressible" pressure coefficient defined in the traditional manner as

(5)
$$C_{pI} = \frac{U_\infty^2 - U^2 - 2\frac{\partial\phi}{\partial t}}{U_{REF}^2}$$

Note that U_{REF} is left arbitrary: this allows us to include *the case with* $U_\infty = 0$, as would occur in the case of a non-translating propellor or helicopter. The definition used in the B.AE Warton panel program is that U_{REF} is the amplitude of the vector $\overline{U}_\infty - \overline{V}_c$ where $\overline{V}_c$ is the translational velocity of the aircraft origin (see later); if this vector has zero amplitude, then a user-defined value, or the value unity, is used.

It can thus be seen that the unsteady case is equivalent to the steady case with U^2 replaced by $U^2 - 2\partial\phi/\partial t$. We therefore need to calculate the time-derivative $\partial\phi/\partial t$ of the perturbation at each point P in the field. However, to achieve this it is *not* necessary to use a time-stepping process. For each point P, this instantaneous time-derivative can be determined directly, by considering what happens at P when viewed in the two frames of reference relative to the ground and relative to the aircraft.

Now the point P (which in the ground system is a fixed point at which the perturbation potential, the perturbation velocity and the static pressure *vary in time*) coincides instantaneously with a point S (which in the *aircraft* axis system is a fixed point at which, for the flows considered, the total potential, the total velocity and the static pressure are *independent* of time). After an infinitesimal interval of time dt, the point P coincides instantaneously with a new point S', again considered fixed in the aircraft frame. The difference between the perturbation potentials $(\phi_{S'} - \phi_S)$, evaluated in the aircraft system, represents the change in total potential at the fixed point P over the time interval dt.

Now the vector displacement $\overline{SS'}$ is clearly equal to $\overline{V}_s\,dt$ (with $\overline{V}_s$ equal to the velocity of the point S relative to the ground). It therefore follows immediately that the difference in perturbation potential between S' and S is equal to the scalar product $-\nabla\phi \cdot \overline{V}_s\,dt$. Thus the time derivative of the perturbation potential (and therefore of the total potential) at the fixed point P in the ground-based system is given by:

$$(6) \qquad \frac{\partial\phi}{\partial t} = -\nabla\phi \cdot \overline{V}_s = -\overline{u} \cdot \overline{V}_s$$

where $\overline{u}$ is the perturbation velocity at P due to the singularity distribution representing the aircraft and its wakes; this velocity is computed automatically by the panel program for the motion in question.

We may now use this relation to obtain an expression for the pressure at P. Inserting (6) into (5) we obtain

$$C_{pI} = \frac{U_\infty^2 - U^2 + 2\,\overline{u} \cdot \overline{V}_s}{U_{REF}^2}$$

which can be rearranged as

$$C_{pI} = \frac{(\overline{U}_\infty - \overline{V}_s)^2 - (\overline{U}_\infty + \overline{u} - \overline{V}_s)^2}{U_{REF}^2}$$

or

$$(7) \qquad C_{pI} = \frac{\tilde{U}_\infty^2 - \tilde{U}^2}{U_{REF}^2} \qquad \text{with} \quad \tilde{U}_\infty = \overline{U}_\infty - \overline{V}_s \;, \quad \tilde{U} = \overline{U} - \overline{V}_s$$

where $\tilde{U}_\infty$ is an equivalent "unperturbed" freestream velocity at P, *relative to the moving point* S, and $\tilde{U}$ is the total (perturbed) local air velocity at P, relative to S. With this new definition of a local *relative* free-stream velocity (which varies from point to point) we thus have a definition of unsteady compressible C_p which is totally analogous in form to the steady-state definition. The value of C_p is obtained by inserting (7) into (3) via (4).

Suppose that the aircraft is executing a six-degree-of-freedom motion such that the aircraft origin C is translating at $\overline{V}_c$ and the aircraft has a vector rotational speed $\overline{\Omega}$ about C. Then any point S (fixed in the aircraft reference frame but not necessarily on its surface) has a velocity $\overline{V}_s$, relative to the ground, given by

$$(8) \qquad \overline{V}_s = \overline{V}_c + \overline{V}_\Omega \qquad \text{with} \quad \overline{V}_\Omega = \overline{\Omega} \times \overline{r} \;,$$

where $\overline{r}$ is the vector from C to S.

As indicated earlier, $\overline{V}_c$ and $\overline{\Omega}$ can be decomposed into linear sums of basic motions u_c, v_c, w_c, p, q, r with respect to the reference x, y, z axes. Solutions obtained for each of these motions can then be superposed to give the solution for any composite motion. In addition to the advantage that this approach allows any number of composite motions to be analysed on the basis of six basic motions, it also forms the basis of the following method for calculating stability derivatives.

Aerodynamic derivatives:

The contributions to the vector force and moment due to aerodynamic pressures acting on a sub-component J of a complete aircraft, for some arbitrary flight condition, may be written as $\overline{F}_J$ and $\overline{T}_J$. These have components (X_J, Y_J, Z_J) and (L_J, M_J, N_J) relative to a fixed set of axes (x, y, z).

Within the usual level of approximation used in a panel program, the vector force $\overline{F}_I$ acting on panel number I (measured relative to the ambient state in which the unperturbed, uniform, static pressure is p_∞) may be written as

$$\overline{F}_I = -(p_I - p_\infty)\,\hat{n}_I\,A_I$$

where A_I, $\hat{n}_I$ and p_I are the area, unit exterior normal and static pressure at the centroid of panel I.

The corresponding contribution $\overline{T}_I$ to the vector moment about the origin may be written as $\overline{r}_I \times \overline{F}_I$, or

$$\overline{T}_I = -(p_I - p_\infty)(\overline{r}_I \times \hat{n}_I)\, A_I$$

where $\overline{r}_I$ is the position vector of the centroid of panel I.

We can therefore write the components X_I, Y_I, Z_I of $\overline{F}_I$ and the components L_I, M_I, N_I of $\overline{T}_I$ in the single generalised form

$$C_I = (p_I - p_\infty)\, B_{C_I}$$

where, for example, when C_I corresponds to M_I, we have

$$B_{C_I} = -(\overline{r}_I \times \hat{n}_I)\cdot\hat{j}\, A_I$$

with $\hat{j}$ the unit vector in the y direction.

Summing over all the panels I in the sub-component J we thus have the generalised form for the quantity C_J (i.e. the contribution from region J to the overall aerodynamic force or moment component):

(9)
$$C_J = \sum_J C_I = \sum_J (p_I - p_\infty)\, B_{C_I} \ .$$

Now the quantity C_J will vary with respect to the motion of the aircraft. We shall consider here its rate of change w.r.t. each of the six degrees of freedom U_R, V_R, W_R, p, q, r. The first three of these quantities are the x, y, z components of the relative translational unperturbed velocity $\overline{U}_{\infty R}$ defined by

(10)
$$\overline{U}_{\infty R} = \overline{U}_\infty - \overline{V}_c$$

(as discussed earlier, $\overline{U}_\infty$ and $\overline{V}_c$ are respectively the undisturbed freestream velocity and the translational velocity of the aircraft origin C, relative to a fixed frame of reference). The quantities p, q, r are the rates of rotation of the aircraft about C, measured relative to the fixed frame.

We can write the six quantities U_R, V_R, W_R, p, q, r in the single generalised form s. To evaluate the generalised derivative $\partial C_J/\partial s$ (which has 36 different possible forms) we therefore need to differentiate (9) with respect to s, giving

(11)
$$\frac{\partial C_J}{\partial s} = \sum_J \frac{\partial}{\partial s}(p_I - p_\infty)\, B_{C_I} \ .$$

Now from (3) and (7) we can write

(12)
$$p_I - p_\infty = p_\infty\left\{\left(1 + \frac{\gamma-1}{2a_\infty^2}G\right)^{\frac{\gamma}{\gamma-1}} - 1\right\} \qquad \text{with}$$

(13)
$$G = (\overline{U}_\infty - \overline{V}_s)^2 - (\overline{U}_\infty - \overline{V}_s + \overline{u})^2$$

Also, we have

(14)
$$\frac{\partial}{\partial s}(p_I - p_\infty) = \frac{\partial}{\partial G}(p_I - p_\infty)\,\frac{\partial G}{\partial s} \ .$$

But by differentiating (12) we obtain (see (4)):

(15)
$$\frac{\partial(p_I - p_\infty)}{\partial G} = \frac{\rho}{2} = \frac{1}{2}\rho_\infty F^{\frac{1}{\gamma-1}}$$

Also, combining (8) and (10), (13) can be written,

$$G = (\overline{U}_{\infty R} - \overline{V}_\Omega)^2 - (\overline{U}_{\infty R} - \overline{V}_\Omega + \overline{u})^2$$

which after differentiating with respect to s and rearranging, using (7), (8) and (10), gives

$$\frac{\partial G}{\partial s} = -2\left\{\dot{U}\cdot\frac{\partial\overline{u}}{\partial s} + \overline{u}\cdot\left(\frac{\partial\overline{U}_{\infty R}}{\partial s} - \frac{\partial\overline{V}_\Omega}{\partial s}\right)\right\}$$

Inserting this and (15) into (14) and then into (11) gives

(16)
$$\frac{\partial C_J}{\partial s} = -\rho_\infty \sum_J (\dot{U}\cdot\overline{u}_s + \overline{u}\cdot\overline{V}_{S_s})\, F^{\frac{\gamma}{\gamma-1}}\, B_{C_I}$$

with, as before, $\overline{U} = \overline{U}_{\infty R} - \overline{V}_\Omega + \overline{u}$.

In writing (16), use has been made of the fact that $\partial\overline{u}/\partial s$ is simply the local perturbation velocity induced by the surface singularities, for unit value of the parameter s; this is denoted by $\overline{u}_s$ (remembering that s is one of U_R, V_R, W_R, p, q, r). Also the value of $\partial\overline{U}_R/\partial s$ is simply the unit vector in the direction

of x, y or z when s is respectively U_R, V_R or W_R, and equal to zero otherwise. Similarly, $\partial V_w/\partial s$ is simply minus the local rigid-body velocity vector associated with unit value of s when s is equal to unit value of p, q or r, and equal to zero otherwise. Since only one of the six parameters will be varied in any one derivative, the above vector is denoted by the single vector $\overline{V}_{Ss}$.

Equation (16) after appropriate non-dimensionalisation, expresses the contribution from region J to all of the above-named aerodynamic derivatives, for any required flight condition.

It should be noted that this approximation ignores the contribution due to changes in the wake geometries which would in practice occur if any of the six degrees of freedom were varied. Furthermore those derivatives which are sensitive to, say, tip effects, will be relatively less accurate than the others.   It may be possible to establish correct procedures to allow for such deficiencies of the potential flow model.

Examples of the predictions of the method for a very simple wing-body and for a wing (both with attached flow) are given in Fig. 7.   The good level of agreement with the traditional datasheet predictions indicates that the method may be of value for more complex shapes for which a datasheet method is not strictly applic- able. At the present time, the method has not been proved for high-α flows involving separations.

2.4   Body vortex flows, symmetric and asymmetric

At the present time, the mainstream tools used for predictions of body-vortex effects are primarily of the empirical type;   these will not be discussed here. However, a simple theoretical method developed at B.Ae Warton can also be used, with care, to give some useful indications for simple body shapes such as missiles. More importantly, perhaps, this method forms the basis of a much more powerful tool (the "hybrid method") which is under development for application to complex aircraft shapes and is capable of producing nominally-exact numerical 3-D solutions (i.e. for the assumed model of the vortex system used within the program).   This method will be outlined in Section 2.5.

The underlying simple theoretical model is based on the use of slender body theory and is described in detail in Ref. 8.   In this model a 2-D panel program is used to calculate the cross-flow at each x (i.e. longitudinal) station. At each x station the panel program uses a fixed source distribution on the body contour to simulate locally the cross-flow (y,z) velocity perturbation due to the coupling between the axial freestream component U_x and the longitudinal rate of change of the body's polar radius (i.e. there is a *known* non-zero external normal velocity).   The program then calculates the 2-D surface vorticity distribution required to maintain the above external normal velocity in the presence of the freestream cross-flow component and of any separated vortices at that station.

For the calculation of the velocity induced at the surface, the separated vortices are modelled locally as 2-D line vortices, connected to the body surface by a feeding sheet which is postulated to carry only vorticity in the cross-flow plane. This sheet, within the local 2-D approximation, induces no (y, z) velocity in the crossflow plane. There is thus no jump in the (y, z) velocity components across this sheet, but the implied jump in x velocity gives rise to a pressure jump across the sheet.

There is also a force on each separated vortex if this (in a quasi-3-D sense) is not locally aligned with the resultant flow. If the 3-D vortex is defined by the line joining the vortex points in successive cross-flow planes, this line will generally not intersect a cross-flow plane perpendicularly.   The 3-D line vortex will thus possess a component in each cross-flow plane. This will couple with the longitudinal (freestream) velocity component to produce a force within the cross-flow plane. Similarly the longitudinal (i.e. the 2-D) vortex component will couple with the resultant cross-flow velocity component to produce a further force within the cross-flow plane.

The program calculates the trajectory of the vortex by satisfying the condition that in each cross-flow plane the vortex position is such that the total force on the vortex-plus-cut system is equal to zero. The local inclination of the vortex, as mentioned above, is estimated on the basis of its locations in the current and the *previous* cross-flow plane. There is thus an element of downstream bias built in to the method.

The vortex strength in each cross-flow plane is obtained from the extra condition that the separation point (i.e. the foot of the cut carrying the vorticity from the surface to the vortex) is postulated to be a stagnation point for the surface cross-flow velocity component in each plane. This condition is formulated along with the equations for the surface vorticity densities on the body in that cross-flow plane.

The "correct" positions of the separation points in each cross-flow plane are not known, unfortunately, and these have to be chosen empirically. The sensitivity of the flow to this separation line is illustrated in Fig. 8.   This figure shows the longitudinal variation of the nonlinear (vortex-induced) normal force on a simple ogive-cylinder body at α = 15° and M = 0.3.   (For attached flow the normal force would quickly reach a level of zero on the cylindrical region of the body). Results are shown for two different separation assumptions: 46° and 54° respectively from the horizontal diameter. It can be seen that the change in normal force is comparable to that observed experimentally when the Reynolds number changes from 0.44 x 10^6 to 3 x 10^6. Further details are given in Ref. 8.

In these calculations, both the separation line and the positions of the separated vortices were forced to be symmetric. However, some more recent work at B.Ae Warton, with the same program, has demonstrated an interesting feature: such a method is capable of calculating asymmetric vortex trajectories, *even with symmetric separation lines*.   The *physical* relevance of these calculations is not yet fully understood; however, there is little doubt that, within the inherent approximations of the model used, the program succeeds in calculating solutions which satisfy all the *stipulated* conditions of the problem.

There are two questions to be resolved here. The first question is whether the asymmetry is possible only within the 2-D cross-flow assumption.   The writer's present guess is that the phenomenon will persist when a more realistic (but still, of course, approximate) 3-D model is used;   work in hand at B.Ae Warton will investigate this question using the "hybrid" concept outlined in Section 2.5.   Recent unpublished work at RAE Farnborough by Fiddes has indicated similar possibilities under the assumptions of inviscid conical

flow theory.

The second question is connected with the fact that the inviscid approach outlined here in fact gives rise to an *infinite number* of different possible asymmetric states. The solutions calculated are actually only particular samples selected, quasi-randomly, by the numerical process used to solve the equations. It may well be the case that in a physical flow such a range of possible states can exist in principle; more probably, other constraints absent from the present theoretical model may favour only a restricted number of such states in the physical viscous flow. Certainly, as discussed elsewhere in this Lecture Series, the possibility of *vortex switching* is present in a real flow over a slender body at high angle of attack. In this phenomenon a vortex pair can possess at least two asymmetric equilibrium states. Similar "switches" between equilibrium states can arise with other physical phenomena, such as vortex bursting. The flow can be switched from one equilibrium state to the other by external events such as freestream turbulence. A discussion of the aerodynamic phenomenon of wing rock is given on the basis of bifurcation theory by Schiff et al in Ref. 9.

The fact that the *switching* phenomenon is associated with random external events almost certainly precludes its prediction by C.F.D. Nonetheless, the fact that asymmetric equilibrium solutions have been demonstrated by the present simple scheme is worthy of some comment.

As mentioned earlier, the algorithm used within the present slender-body approximation is based on the use of a 2-D panel method using surface vorticity as the unknown singularity distribution. Now, in the case of such a distribution on a *closed* 2-D section, *eigensolutions* of the boundary-value problem can exist. Such solutions modify the overall flow whilst still satisfying the prescribed boundary conditions. In this case, the vorticity eigensolution for a body of circular cross-section consists of a uniform vorticity distribution around the circle. This produces a nett external circulating field which decays to zero with distance from the body and which satisfies the surface boundary condition of zero normal velocity. *Any multiple* of this eigensolution satisfies these conditions. This means that the influence matrix, expressing the linear equations which approximate the model of the flow, is strictly singular.

However, under certain circumstances the numerical scheme used to solve these equations is able to "home in" on a solution containing some particular but arbitrary multiple of this eigensolution. The multiple selected depends on quite arbitrary factors, such as the order in which the equations are solved, the panelling arrangement, numerical discretisation error, etc.

It is clear that if a pair of independent vortices lie in the cross-flow plane external to the surface vorticity distribution, these will *necessarily* have to take up asymmetric locations, or have unequal strengths, if they are to be associated with symmetric separation lines.

One extra physically-based ingredient which needs to be injected into the above algorithm relates to the rules governing creation and conservation of vorticity. We are clearly dealing with a viscous flow, and the rules governing such flows are by no means as simple as those for the "inviscid" (infinite Reynolds number) approximation. The Navier-Stokes equations indicate that the *total* rate at which vorticity is injected into the fluid from the overall, closed surface must be exactly zero at any instant. This tells us nothing about what *must* happen in any one cross-section, without considering the whole of the rest of the surface. In the fuselage-type flows in question, it is conceivable that whatever happens in relation to the vorticity created on the upstream portion of the body, can be countered by what happens at the downstream base of the body. In the present state-of-the-art, details of the flow in this region are not accessible to computation. It is not clear, therefore, which physical features, if any, can be built into a modified inviscid model in order to arrive at only physically-plausible asymmetric vortices.

One important quantity of interest to the aerodynamicist is the asymmetric side-force generated on the body by the asymmetric vortices. It has been observed on the basis of the above model that, contrary to intuitive physical reasoning, the side force will not necessarily be orientated towards the body side facing the nearer vortex of an asymmetric pair. It is more frequently in the opposite direction. The reason for this is that the extra suction generated at the near-vortex surface is more than counteracted by the region of more positive pressure in the region of the near-vortex separation line. This observation has previously been made in unpublished work by Fiddes (RAE Farnborough) in connection with flows over a cone.

The outstanding difficulty associated with this type of body-vortex calculation, both for symmetric and for asymmetric vortex configurations, is the estimation of the separation lines, as indicated earlier. It may be possible (though currently this is the subject of heated debate) to couple the inviscid calculation, giving the surface pressures and inviscid streamlines, iteratively with a 3-D boundary layer code which would then predict the separation line for the next iteration of the inviscid calculation.

The limiting streamlines calculated (on the basis of an attached potential flow solution) on the surface of a prolate spheroid with axis ratio 4.3 : 1 at $\alpha = 20°$, Re = / x 10^5, are shown in Fig. 9, together with the external streamlines. The limiting streamlines were calculated using a 3-D turbulent boundary layer code developed at B.Ae Brough by Coleman and Cross. These figures, and other figures relating to higher values of α, display a remarkable qualitative agreement with independent experimental flow visualisations (not shown here). Further work is necessary to achieve a satisfactory coupling of the calculation with an inviscid flow model simulating the separated vortices. At present it is not possible to say whether such a method can be developed to produce predictions of acceptable engineering accuracy.

2.5   Leading-edge vortex flows;   the hybrid method

Leading-edge vortex flows are simpler to compute than body vortex flows, in the sense that the separation line is known in advance. However, the coupling with the wing is very strong because the vortex is directly linked with the prime lift-producing mechanism of the wing - its circulation.

A simple, approximate method is often used to estimate leading-edge separation effects - the so-called leading-edge suction analogy associated with the name of Polhamus (Ref. 10). This technique, although undoubtedly successful for a number of simple cases, will not be considered here as it falls more into the

category of empirical methods than of C.F.D.

In contrast to this simple method, an extremely large and complex program based on a higher-order panel-method concept has been developed at Boeing, see Ref. 11. This program, known as PANAIR, has been developed for treating linearised subsonic and supersonic flow; amongst its numerous novel features is the ability to compute leading-edge vortex separations.

In the model employed, a limited portion of the spiral structure is represented as a number of curved segments carrying a vorticity distribution. The inner part of the spiral is replaced by a concentrated line vortex with a feeding sheet, similar to that mentioned in Section 2.4. Some of the features of a model of this type are discussed in Ref. 12.

In this model, the unknown functions are not only the doublet densities characterising the vorticity on the aircraft surface and the separated vortex sheet, but also the parameters defining the unknown location of that free vortex sheet. The boundary conditions to be satisfied on the vortex sheet correspond to those defined in Section 2.3.2: the vorticity vector must be aligned with the local mean velocity vector at a finite set of control points on the sheet. The resulting system of equations to be solved is nonlinear as well as being very large, and special techniques have had to be developed to solve this system. The singularity distribution is discretised so as to enforce the vorticity flux conservation law across panel and "carpet" boundaries. This has also required a number of special techniques to be developed.

An alternative method of solving the same problem, based on the use of a low-order (piecewise-constant) panel method, was proposed and demonstrated a number of years ago at B.Ae Warton, and further development of the method has recently started again. This method is known as the "hybrid" method and is described in Ref. 8. The basic concept consists of iterating between a 3-D panel method and a slender-body program of the type described in Section 2.4. The 2-D velocity field normally used as an onset flow in each plane in the (n+1)th iteration of the slender-body calculation is replaced by a 3-D non-uniform flow field $\tilde{U}^{n+1}$ defined at that plane. This is defined by

$$\tilde{U}^{n+1} = \overline{U}^n_{3D} - \overline{U}^n_{2D} .$$

The field $\overline{U}^n_{3D}$ is a 3-D field evaluated at the control points in that plane, obtained from a 3-D panel program calculation applied to the complete aircraft configuration in the presence of the nth estimate of the vortex system (i.e. trajectory and strength). $\overline{U}^n_{2D}$ is the previous estimate of the 2-D velocity field at that plane, as calculated in the previous slender-body sweep.

In this (n+1)th iteration of the slender-body calculation, the new 2-D field $\overline{U}^{n+1}_{2D}$ at that plane is calculated which, when added to the field $\tilde{U}^{n+1}$, satisfies the required *three-dimensional* boundary conditions at the control points in that plane. In the simplest formulation, these proper 3D conditions are replaced by the quasi-3D conditions indicated in Section 2.4. The quantities computed during this stage comprise the 2D singularity strengths on the body surface and the vortex strength and position, in that cross-flow plane.

A number of variants of the scheme are possible. In one variant, the surface strengths as well as the vortex parameters calculated in each plane in the slender-body calculation are passed on to the next iteration of the 3D program and interpreted as local values of the required 3D parameters. In another variant only the vortex parameters are passed through to the 3D panel program, the surface strengths being determined in the standard manner within the 3D program. The important point is that the difficult part of the calculation, the determination of the strength and location of the separated vortices, is performed *outside* the time-consuming 3D panel-program part of the computation. It is performed using a modified form of a process which has been developed and which has proved reliable and economical in connection with another, more approximate scheme: the slender body approximation.

The basic algorithm for the iterative computation of the 3D field can be expressed schematically as

$$\overline{U}^{n+1}_{3D} = \tilde{U}^n + \overline{U}^{n+1}_{2D} = \overline{U}^n_{3D} - \overline{U}^n_{2D} + \overline{U}^{n+1}_{2D} .$$

When convergence is reached, typically after 3 or 4 complete iterations, the last two terms are identical in each plane, and the erroneous 2D (or "slender body") contribution to the solution vanishes completely. The associated computation time is little more than that for an attached-flow panel program calculation for the same configuration. The 3D computation can extend, of course, over parts of the configuration which are not even represented in the geometry treated in the quasi-2D parts of the computation; the *presence* of these other regions is conveyed to the 2D computations, of course, in the definition of the non-uniform onset flow U.

The model used to represent the separated vortex structure can be as simple or as complicated as required. In the simplest formulation, a vortex-plus-cut model of the type described in Section 2.4 is used. Results obtained by applying this model to a straked wing with separation from the strake leading edge, are shown in Fig. 10. The calculation includes the computation of the trajectory of the unfed vortex over the down-stream portion of the wing. In this calculation, in order to achieve a reasonably representative loading form near the wing trailing edge, it was necessary to also perform, in the 3D panel program part of the calculation, a partial relaxation of the trailing edge wake in the presence of the leading-edge vortex. In this computation the wake surface was held fixed in the plane of the wing, but the wake was unloaded, approximately, by relaxing the vorticity within that surface until a zero *normal* loading condition was achieved.

It is acknowledged that a simple line-plus-cut representation of the vortex structure of the type described earlier, is incapable of producing an accurate simulation of the pressure distribution near the wing leading edge. Nonetheless, the hybrid technique allows more advanced models to be used, taking advantage of the considerable amount of progress which has been achieved in the numerical modelling of *two-dimensional* vortex sheets. Some of the techniques used for stabilising and increasing the accuracy of such models are

described in Refs. 8, 12.

One technique currently being investigated at B.Ae. Warton allows a curved vortex of finite diameter and arbitrary vorticity distribution to be modelled using a variant of the "hybrid" concept. The local effects inside the vortex are computed by treating the local vortex structure as the cross-section of a 2D vortex with the same vorticity distribution. The velocity field associated with the latter can be computed analytically. The error due to neglect of longitudinal curvature is then removed (approximately) by subtracting the erroneous contributions from remote segments of the "2D" vortex (now represented as a pair of semi-infinite line vortices) and adding in the contribution from the correctly-positioned remaining segments of the curved vortex (these segments also being represented as line segments). It is hoped that this technique may not only offer a more realistic simulation of a rolled-up vortex core than the vortex-plus-cut model, but also allow calculation of effects associated with impingement of a vortex upon a down-stream surface (e.g. a tailplane). Such a calculation is not possible with a line vortex model.

2.6   Modelling of trailing-edge separation

A model developed by Maskew et al (Ref. 13) allows a plausible simulation of extensive separation from the upper surface of an aerofoil. Recent work has been aimed at extending the model to 3D wings (Ref. 15).

In this model the interface between the potential flow region and the separated rotational-flow bubble is simulated as a simple shear layer, which is taken to be a stream surface of the flow. The separated rotational region inside the bubble is interpreted by Maskew as a potential flow region with a reduced value of the total head.

Another interpretation is possible, by assuming that the volume vorticity is uniform in this region - as is plausible on the basis of approximate physical reasoning. The locally rotational velocity field induced by this volume distribution can then validly be interpreted as a supplement to the truly potential residual field, induced by surface singularities on the aerofoil and separated shear layer. The velocity induced by the volume vorticity distribution can be computed on the basis of equivalent, known, source and vorticity distributions on the boundary of that volume, i.e. on the shear layer and on part of the aerofoil surface. The necessary relationships are derived in Ref. 14. At the present time, this approach has not been used in any practical computations.

In Maskew's interpretation, the total-head loss is simply related to the vorticity in the shear layer. The shear layer is relaxed iteratively until it is force-free, for a given estimate of the separation point. The process is completed by iteratively updating the estimate of the position of this separation point on the basis of a boundary-layer computation.

Although the method requires further development before it can be regarded as a reliable prediction tool, it already appears to have been used in a number of interesting applications, yielding predictions of C_L and C_D up to and beyond C_{Lmax}.

Fig. 11 taken from Ref. 15 shows a particularly interesting example of application, compared with experimental measurements. The aerofoil in this experiment was at a critical value of α where the real flow switched randomly between an attached state and a separated state (the trigger being presumably the turbulence in the tunnel). The pressure profile was measured over a finite time interval and the measurements are distributed randomly between the two different types of profile. The figure shows the computed attached-flow and separated-flow profiles.

It is quite clear that a model of this type could readily be extended to 3D on the basis of the "hybrid" scheme described in Section 2.5. Such a process has not been attempted at the present time.

PART THREE: FUTURE PROSPECTS OF HIGH-α PREDICTION

3.1   Global Navier-Stokes calculations

The methods defined in Part Two are already capable of giving useful predictions for high-α flows, and all have substantial development potential for application to complete aircraft configurations. These methods generally require the location of the separation line to be estimated independently, e.g. by using the boundary-layer approximation (which is strictly not applicable in region of separation) or by resorting to empiricism. For smooth surfaces, the location of this line is Reynolds-number dependent. These methods also generally model the physical vorticity distribution as a line or as a thin sheet. For ordered separations where such models are reasonably representative of real flow, the physical vorticity will be distributed, via the physical process of diffusion, over regions with finite cross-section. The thickness of these regions is Reynolds-number dependent.

It may therefore appear essential, in order to account properly for the real effects of diffusion, to resort to solutions of the Navier-Stokes (N-S) equations. However, this is not yet a practical proposition for realistic aircraft configurations, for a number of reasons.

The first reason is related to cost, both of developing user-orientated computer programs, and of running these programs on a routine basis. In the current state-of-the-art, solutions of the N-S equations for even simple problems (flow over a cylinder, the driven-cavity problem) are computationally very expensive, and technically difficult to obtain;   each problem requires individual attention: turbulence model, grid generation, etc. There is at present no technical prospect of such programs being extended to allow their routine application to high-α calculations for real aircraft, or to allow their use on economic grounds even if they became available.

The second main reason for discounting the possibility of N-S solutions for high-α calculations is based on the nature of the phenomenon of turbulence. The range of length scales is so wide (a factor of about 10^5

between the largest and smallest eddies) that direct calculation of the time-dependent motion of the smallest eddies (which affects, and is affected by, the large eddies) is out of the question. Some form of modelling, essentially time-averaging, has to be employed for these small eddies. Considerable effort is currently being applied to this problem, much of it centred on Stanford; some of this work is described by Ferziger (Ref. 16). Most of the older models (e.g. those based on a mixing-length theory) are now falling out of favour for practical problems. Furthermore, different models are required for different phenomena: separation regions, shock regions, vortex bursting etc. Any program attempting to model flows involving such phenomena would need to be able to recognise the need to select a particular turbulence model. Some years ago there was some indication that it might be possible to split the eddies into two scales: "large" and "small"; the large eddies would be determined directly by calculation at low Reynolds number, and their properties would transfer unchanged to the high Reynolds number situation; the remaining small eddies would be *modelled* to complete the high-Re solution. This type of picture does not now enjoy popular support.

A third reason for lack of optimism in the N-S area is related to the fact that many of the phenomena in question are sensitive to parameters which are not accessible to the modeller or the aerodynamicist: free-stream turbulence, surface vibration, heat transfer effects at the surface, surface roughness, etc. As mentioned earlier, some of the phenomena can exhibit a number of stable states: asymmetric vortex shedding, vortex bursting, etc. External disturbances can trigger a switch from one state to the other. Although N-S calculations may increase our understanding of this type of event, they will not be able to predict what will actually happen to a particular aircraft shape under particular (and only approximately known) flight conditions. Their value as prediction tools for the aerodynamicist is highly questionable.

It will be argued in the next section that many of the flow phenomena which are apparently viscous-dominated are in fact dominated by inviscid-flow effects. Viscosity actually plays a secondary, though very important, role; in particular, viscosity will control the *strength* of free-vorticity distributions, via its role in moderating the location of separation lines from smooth surfaces. Possibly the most important task of N-S solvers could be to supply the ingredient which is missing from the models described in Part Two and from those in the following section: the location of separation lines.

3.2 Inviscid modelling of rotational flow

3.2.1 The vortex dynamics method

Fig. 12a shows experimentally-measured properties behind a delta wing with leading-edge separation. The pictures would at first sight appear to indicate a viscosity-dominated flow pattern. However, Fig. 12b shows the wake development predicted using a very simple inviscid model (Ref. 17). The qualitative agreement is quite remarkable.

In this calculation the streamwise evolution of the 3D wake was likened to the timewise evolution of a 2D vorticity distribution which at the initial instant t - 0 was defined to have the same form as that estimated at the trailing edge in the 3D problem. The vorticity distribution was replaced by a series of point vortices which were moved in a series of discrete timesteps in accordance with the instantaneous velocity induced at each vortex by all the other vortices (with some approximate account being taken, in the calculation, of the downwash field due to the bound vorticity on the wing in the experiment). The calculation was stabilised by redistributing the vortices along the computed curve after each step, so as to maintain a uniform spacing along that curve.

The evolution process used here is quite different in principle from the wake-relaxation methods described in Part 2. In these latter models, the vorticity is considered as being a property belonging to a particular point in space, and not to particular air particles; it is analogous to the property of "illumination", involved in visualising flows by directing a fixed beam of light at the region of interest so as to instant-aneously illuminate (dust) particles carried through that region; the properties associated with a particular point in space are constant once a steady state is attained. In contrast, in the calculation used here, the property of vorticity is considered to belong to a particular group of air particles which move together as a flexible "block". The point vortex is a discrete representation of the vorticity property which in reality is distributed over that group of air particles. Since diffusion is ignored in these calculations, the total vortex strength associated with any single group of particles remains constant as that group convects through the flow, distorting in shape as it proceeds. This type of approach is known as the *Langrangian* approach, in contrast to the *Eulerian* approach used in Part 2. The scheme described above is a particular example of the "vortex dynamics" or "vortex blob" method. The simulation of the diffusion process will be discussed briefly later in this section.

A second example of this type of method, this time involving a 3D inviscid calculation, is shown in Fig. 13, taken from Ref. 18. In this calculation each scalar component of the vector vorticity is preserved. The pictures show computed "streaklines" at two instants in the time-evolution of the tip-edge and trailing-edge wakes of an impulsively-started rectangular plate at α - 30°. Again the level of agreement with experimental observations (not shown) is remarkable. More importantly, perhaps, the calculations became chaotic after a certain time, and it was not possible to attain a steady-state solution. At this same α, the vortices present in corresponding water-tunnel studies "burst". At α - 14.5°, however, both theory and experiment eventually displayed similar, well-organised and steady vortex structures.

In this calculation, the surface boundary conditions on the wing were satisfied by using a simplified form of panel method. The flow field induced at the wing by the vortex particles in the wake is computed in an "Eulerian" fashion totally analogous to the method described in Part 2 for "Eulerian" wake relaxation. (In the limit of steady flow, the two methods are of course simply different ways of looking at the same thing).

During the panel program calculation, the conditions satisfied include the (inviscid) Kutta conditions at the sharp edges. The rate at which vorticity is released into the fluid is determined from the flow calculated at these edges. It is easy to show that the nett amount of vector vorticity leaving the surface by crossing unit length of an edge, in unit time, may be approximated by one half of the product of the

surface vector vorticity $\tilde{\gamma}_s$ and the component of the inviscid (boundary-layer edge) tangential velocity component normal to that edge, U_s. This quantity, scaled by the appropriate time interval Δt, is concentrated into a vortex "particle" of strength $\frac{1}{2} \tilde{\gamma}_s U_t \Delta t$. During each time step, each particle is convected in accordance with the velocity induced at its location by the freestream, all the other vortices, and the wing itself. In the calculation described here, it is assumed that each particle originally leaves the trailing edge with a velocity equal to the mean of the upper and lower surface boundary-layer edge velocities, these being computed during the panel-program stage of the calculation. It is shown by Maull in Ref. 19, on the basis of a 2D argument for separation from a single surface, that a more appropriate value would be 2/3 of the velocity at the boundary-layer edge. Nonetheless, the results demonstrate that apart from a few doubts relating to the vortex-shedding mechanism *at even a sharp edge*, the inviscid vortex dynamics method is capable of capturing some of the essential features of a viscous flow.

It should be mentioned that a considerable amount of work, mainly in two-dimensional flows, has been done in connection with *viscous* vortex dynamics calculations. The basic concepts are explained in the numerous works by Wu (e.g. Ref. 20), Leonard (e.g. Ref. 21) and Chorin (e.g. Ref. 22). The numerical process is essentially the same as that outlined above for the inviscid model, with the extra element that an attempt is made to allow for the effects of diffusion on the vorticity $\bar{\omega}$ carried by each group of air particles. The equation governing the incompressible diffusion process, written relative to the moving (Lagrangian) reference frame of the group of air particles, is:

$$\frac{d\bar{\omega}}{dt} = \nu \nabla^2 \bar{\omega} \quad (\nu = \text{kinematic viscosity coefficient}).$$

This is derived directly from the incompressible Navier-Stokes equations. It is of the same form as the classical diffusion equation governing heat-conduction and numerous other physical processes.

The solution of the diffusion equation is usually expressed in relation to the point vortex particles normally used in the vortex dynamics method. The effect is to produce finite "blobs" rather than points; it is the writer's opinion that the success of a number of the methods developed on this basis, however, is not due in any way to a proper simulation of diffusion effects, but merely to the fact that the finite "blobs" remove the destabilising effect introduced (in totally unrealistic fashion) by the decision to use *point* vortices in the first place. It does not seem to be appreciated universally that it is a straightforward and economic process to use distributed surface vorticity (e.g. piecewise constant) as the basic discretised form, instead of point vortices. This avoids the problems of spurious infinite velocities induced in the immediate vicinity of the point vortices. The supporting logic and influence expressions are given in Ref. 6.

It may be noted that, *in two dimensions*, the time-dependent solution of the diffusion equation corresponds at any instant t to a vorticity distribution $\omega(r, t)$:

$$\omega(r, t) = \Gamma_0 \exp(- r^2/4\nu t)/4\Pi \nu t$$

which is sometimes referred to as a "Lamb vortex". In this expression Γ_0 is the total vortex strength associated with the original particles.

Chorin avoids calculating its explicitly-known influence by observing that the mathematical form of the vorticity distribution given above is identical to the form of the probability distribution of a random variable; he exploits this similarity by replacing *the evaluation of the* velocity field induced in the interior of the above vorticity distribution by the evaluation of the mathematically-simpler field induced by a small number of randomly-located point particles with the same total strength. In the limit of an infinite number of such particles, the computed velocity field should be identical to that of the Lamb vortex. The technique used by Chorin to determine the random placements is termed a "random walk"; the process may be likened to the *classical Monte-Carlo technique*.

An alternative method consists of computing directly the influence of the "Lamb vortex". This gives the value of the circumferential velocity V_θ at radius r as:

$$V_\theta(r, t) = \Gamma_0(1 - \exp(- r^2/4\nu t))/2\Pi r.$$

Various other methods are also used to smooth the (spurious) influence of a point vortex particle, including approximation by a uniform distribution over a finite radius.

If a sheet vorticity distribution were used instead of point particles, the simulation of the diffusion process would require a "sheet diffusion" model instead of the above "point diffusion" model. The appropriate mathematical expressions are given by Batchelor in Ref. 23. An example of application of this idea for a boundary layer calculation is given in Ref. 24.

The most useful application of the above ideas is probably in connection with events at the solid surface from which the whole of the vorticity originally diffuses; in particular, this type of treatment is in principle capable of predicting the details of viscous separation. At a solid surface, the physical no-slip condition means that laminar diffusion is the predominant process in that region. The local rate of vorticity diffusion must be exactly sufficient to preserve the no-slip condition in the presence of all the singularities representing the flow in question. The appropriate rates of vorticity creation may be derived from the N-S equations as a function of the local surface pressure gradient. Discussions of the relevant details are given in Refs. 20, 21, 22, 25.

It is the writer's opinion that a local application of the concepts outlined above may be useful in determining local details of the flow near a separation line, in a global calculation which is otherwise performed with an appropriate inviscid model (the diffusion process is probably unimportant *except* at the surface). Such a method may be an acceptable means of resolving, for example, the difficulties still associated with the correct specification of the Kutta condition at a trailing edge. The writer is not aware of any efforts in this direction at present.

3.2.2 Solution of the compressible Euler equations

As a final example of the prediction of rotational flow by an *inviscid* method, we consider the compressible-flow problem depicted in Fig. 14. This computation relates to an arrow wing with a leading-edge sweep of 71.2°, at $\alpha = 12°$ and $M = 0.4$. The wing section possesses a *rounded* leading edge.

This computation was performed during the last few weeks of 1981 (i.e. just before the present paper was written) by Schmidt at Dornier, Friedrichshafen, using the latest generation of Euler solver. Codes for solving the compressible Euler equations are now undergoing intensive development at numerous establishments around the world, but those developed by Schmidt in conjunction with Professor A. Jameson are outstanding from the standpoints of both accuracy and economy. A number of recent developments, including the use of multi-grid algorithms, Runge-Kutta time-stepping and special far-field boundary conditions, have enabled very significant advances to be made in the last few months.

The primary motivation for developing Euler solvers has hitherto been related to the need to compute transonic flows, involving strong shocks, over complex aircraft shapes. As indicated in Section 2.1, earlier generations of codes aimed at this problem have solved the so-called T.S.P. or the full-potential approximations of the transonic-flow equations. These have the disadvantage of not giving a proper representation of shocks, as a consequence of their inability to model the rotational flow which physically must exist downstream of a curved shock wave. This has the second, equally important, effect of producing erroneous conditions downstream, at the trailing edge of a wing, and thereby giving an incorrect value of the circulation (and therefore of flow conditions *upstream* of the shock, and so on). The Euler codes, in contrast, allow the correct (Rankine-Hugoniot) jump conditions to be generated across a shock (except at its foot, *where viscous interactions produce effects which cannot be adequately simulated without some form of viscous modelling*).

The Euler codes are also more "forgiving" than potential formulations, with respect to the regularity required of the space-grid on which the equations are discretised and solved. Calculations are now possible for very complex aircraft shapes, via "box-type" schemes wherein a set of subgrids are generated in a number of topologically-simple regions in the space around the aircraft.

It has recently been discovered that, *by a most happy accident*, Euler codes of the type used here are capable of automatically capturing not only shocks, but also certain types of vortex flow which are not directly associated with shock waves. The example shown in Fig. 14 is a case in point. *There is no supersonic point present in the converged solution shown here.* Nonetheless the flow directions plotted in the vertical plane just downstream of the trailing edge clearly demonstrate the presence of vortical regions. These vortices arise at the leading edge. Furthermore, the surface isobar pattern indicates that the flow over the inboard part of the leading edge is attached; flow separation commences at a finite distance outboard.

The mechanism of the vortex formation at these rounded surfaces is not yet fully understood, but it would appear to lie in the (quasi) time-evolution process used to solve the equations (the steady state is attained asymptotically in a manner analogous to the vortex-dynamics schemes outlined earlier). During the early iterations before vorticity formation, the flow accelerates around the leading edge and reaches the state where a shock must form to avoid expansion to a vacuum. These shocks produce rotational flow downstream of the shock, *associated with fixed regions of space*. The associated vorticity persists, distorting the inviscid streamlines and decelerating the flow along them in subsequent iterations, until an equilibrium state is attained where the flow can negotiate the curved edge without needing any longer to form a shock. Finally, a steady state solution, presumably unique, *is* reached which satisfies the Euler equations at all points of the flow, and satisfies all the stipulated boundary conditions. The vorticity formed during the calculation will of course be aligned with the local streamlines. The effect of this vorticity is to modify the flow such that at the appropriate points on the surface the flow stagnates and "separation" is evident. (If viscosity were present in the calculation, this would induce further deceleration of the flow near the surface, and separation would then occur further upstream than in the foregoing infinite-Reynolds-number calculations).

In another one of many Euler solutions performed by Schmidt (not shown here), a 2D flow over a circular cylinder at transonic Mach number demonstrates a symmetric pair of strong shocks. Downstream of these shocks, the fully-converged solution demonstrates a pair of contrarotating, closed, vortical bubbles trapped in the "base" region. An interesting debating point is whether these bubbles genuinely represent the infinite-Re limit of shock-induced separation. It should be noted that calculations performed by the writer, using a panel method, have shown similar results for a half-cylinder in a horizontal infinite flat plate in a horizontal onset flow carrying a uniform shear, at zero Mach number. In this case, the vorticity is already present in the unperturbed flow (i.e. a constant value equal to the shear gradient); the effect of the cylinder-induced irrotational perturbation is merely to produce a total flow in which closed streamlines are visible, enclosing vortical bubbles. In the case of the Schmidt calculation, however, the shear is not present in the unperturbed flow, but is generated (in accordance with the equations governing the flow) at the shock surface.

The vital point is that, unlike panel methods, these Euler codes do not require vorticity to be *put* into the field in accordance with the instinct of the modeller; the vorticity is available within the Euler equations and just like a shock, can appear automatically *wherever* the flow requires it - whether this be at a sharp trailing edge or at a smooth surface.

This vorticity will be *automatically* aligned with streamlines ("relaxed"). The implications of this statement are far-reaching; it means that in calculations of complete aircraft, vorticity will be generated at the edges of, say, canards, and convected in correct fashion past *downstream surfaces*; all interactions between the vortices and these surfaces will be automatically included.

It must be said, of course, that body vortices and other genuinely viscosity-dominated flows will not be predicted by the above type of inviscid scheme. Nonetheless there is every prospect that if separation lines are stipulated on smooth surfaces (or calculated by iterative coupling with a boundary-layer code), then the

6-22

Euler codes should be capable of calculating the associated separated flow. It may be expected that calculations of this kind will be undertaken very shortly.

The above three examples were chosen to demonstrate that a number of flows which were previously considered viscous - and therefore accessible only to Navier-Stokes calculation - are in fact essentially inviscid; the effect of viscosity is merely to moderate the essentially-inviscid phenomena.

CONCLUDING REMARKS

- Aerodynamic excellence has to be balanced against a wide variety of other, often-conflicting, criteria in the overall design process for a modern military aircraft.

- High-α phenomena do not generally need to be predicted in fine detail. Most are so complex, and sensitive to unknown external parameters, that accurate prediction is impossible either by theory or experiment. Confirmation by flight-test will always remain a vital element of the total process.

- The primary role of C.F.D. at high α is to attempt to obtain predictions of reasonable quality more quickly and cheaply than can be obtained by traditional techniques.

- Development of more powerful C.F.D. techiques is an exceedingly complex process, the timescales being on a par with those of the aircraft design process itself. The state of diminishing returns has probably been reached in high-α C.F.D. method development. It is questionable how much more effort should be directed towards attempting to develop complete Navier-Stokes solutions for full aircraft, even if these become technically feasible with the next generation of computers.

- Many of the most interesting phenomena previously assumed to be dominated by viscosity are essentially inviscid. Viscosity plays only a moderating role in such cases. Such phenomena can often be adequately predicted by minor development of the current generation of computer models. The latest generation of Euler codes is particularly interesting in this respect.

- The vortex dynamics method may offer a means of predicting viscous effects by concentrating attention on the regions where it is most needed, and in particular on the flow in the vicinity of separation lines.

REFERENCES

[1] Hunt, B., Marchbank, W.R., Hewitt, B.L. (a) "The strengths and weaknesses of computational fluid mechanics in aerodynamic design and analysis". Part I: background and philosopy. Presented at Workshop-cum-Seminar on C.F.D., VSSC, Trivandrum, India, Dec. 1981.

(b) As above. Part 2: Detailed examination of the strengths and weaknesses of C.F.M.

[2] Schmidt, W., Jameson, A. et al(a)"Finite volume solution for the Euler equations for transonic flow over airfoils and wings including viscous effects".

AIAA Paper 81 - 1265, Palo Alto, June 1981.
(b) "Numerical solutions of the Euler equations by finite volume methods using Runge-Kutta time-steepping schemes".

AIAA Paper 81 - 1259, Palo Alto, June 1981.

[3] Rizzi, A., Eriksson, L.-E. "Computation of vortex flow around wings using the Euler equations". Proc. IV GAMM Conf. on Num. Meth. in Fluid Mech., Paris, Oct. 81.

[4] Hunt, B. "The panel method for subsonic aerodynamic flows; a survey of mathematical formulations and numerical models, and an outline of the new British Aerospace scheme".

VKI L.S. 1978-4 on Comp. Fl. Dyn., March 13-17, 1978.

[5] Hunt, B. "Recent and anticipated advances in the panel method. The key to generalised field calculations?"

VKI L.S. 1980-5, March 24 - 28, 1980.

[6] Hunt, B. "The mathematical basis and numerical principles of the Boundary Integral Method for incompressible potential flow over 3-D aerodynamic configurations".

In: Numerical Methods in Applied Fluid Dynamics, (Editor: Hunt) Academic Press, London, N.Y, 1980.

[7] Francis, S.M. and Kennedy, D.A. "Formation of a trailing vortex".

J. Aircraft, Vol. 16, No. 3, 79-4038.

[8] Jepps, S.A. "The computation of vortex flows by panel methods".

VKI L.S. 1978-4 on Comp. Fl. Dyn., March 13-17, 1978.

[9] Schiff, L.B. et al, "Mathematical modelling of the aerodynamics of high-angle-of-attack manoeuvres".

AIAA Paper 80-1583.

[10] Polhamus, E.C. "A concept of the vortex lift of sharp-edged delta wings based on a leading-edge suction analogy". NASA TN D-3767, Dec. 1966.

[11] Johnson, F.T., Tinoco, E.N. "Recent advances in the solution of 3D flow over wings with leading edge separation".

AIAA Paper 79-0282, Jan. 1979.

[12] Smith, J.H.B. "Vortical flows and their computation".

VKI L.S. 1980-5, March 24-28, 1980.

[13] Maskew, B. and Dvorak, F. "The prediction of $C_{L_{max}}$ using a separated flow model".

Journal American Helicopter Soc., April 1978.

[14] Hunt, B. "Relationships between volume, surface and line distributions of vorticity, source and doublicity"
B.Ae. Warton Note Ae/384, Nov. 1977.

[15] Maskew, et al. "Prediction of aerodynamic characteristics for wings with extensive separations".

AGARD Symp. on Comp. of Viscous/Inviscid Interactions, Colorado Springs, Oct. 1980. AGARD CP 291, Paper 31.

[16] Ferziger, J.H. "Higher-level simulations of turbulent flows".

Report TF-16, Thermosciences Div., Dept of Mech. Eng., Stanford Univ.

[17] Jepps, S.A. "Theoretical calculations of the wake behind a delta wing with leading edge separation".

B.Ae. Warton Note Ae/A/583, Nov. 1978.

[18] Guiraud-Vallée et al. "Numerical studies of unsteady viscous flows at ONERA".

In: Numerical Methods in Applied Fluid Dynamics, (Editor: Hunt). Academic Press, London, N.Y., 1980.

[19] Maull, D.J. "An introduction to the discrete vortex method".

In: Practical Experiences with Flow-Induced Vibrations, IAHR/IUTAM Symp., Karlsruhe 1979, Springer-Verlag (Berlin, Heidelberg, New York), 1980.

[20] Wu, J.C. et al   a) "Numerical boundary conditions for viscous flow problems". AIAA Journal, Vol. 14, No. 8, Aug. 1976.

b) "Method for numerical solution of turbulent flow problems". AIAA Jnl, Vol. 16, No. 9, Sept. '78.

c) "Separate treatment of attached and detached flow regions in general viscous flows". AIAA Paper 79-1451.

[21] Leonard, A. "Vortex methods for two- and three-dimensional flow simulations".

VKI L.S. 1980-5, March 24-28, 1980.

[22] Chorin, A.J.   a) "A vortex method for the study of rapid flow".

In: Proc. 3rd Int. Conf. on Numerical Methods in Fluid Mech. Springer, 1972.

b) "Numerical study of slightly viscous flow".

Journal of Fl. Mech. Vol. 57, Part 4, 1973.

[23] Batchelor, G.K. "An Introduction to Fluid Dynamics".

C.U.P., 1967, pages 187 ff.

[24] Telionis, D.P. and Tsahalis, D.T. "Response of separation to impulsive changes of outer flow".

AIAA Jnl., Vol. 12, No. 5, May 1974.

[25] Sod, G.A. "Computational fluid dynamics with stochastic techniques".

VKI L.S. 1980-5, March 24-28, 1980.
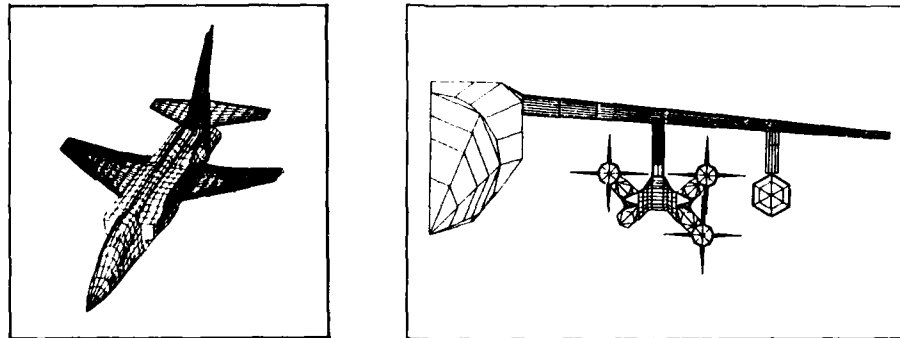
Fig. 1 : Examples of complex geometries investigated by B.Ae panel program (attached flow).
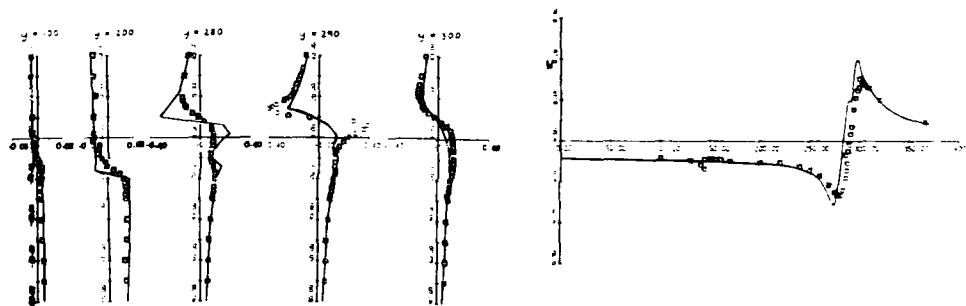
Fig. 2 : Comparison (taken from Ref. [8]) of sidewash (on left) and downwash (on right), 2.75 chords behind a rectangular wing of $R = 6$ at $a = 7.5^o$. Line shows theory (B.Ae panel program with wake relaxation), squares show experiment (Maskell, RAE). Lateral shift near wing tip is due to error in tip vortex initial position).

$a = 7^o$, $\eta_c = 10^o$
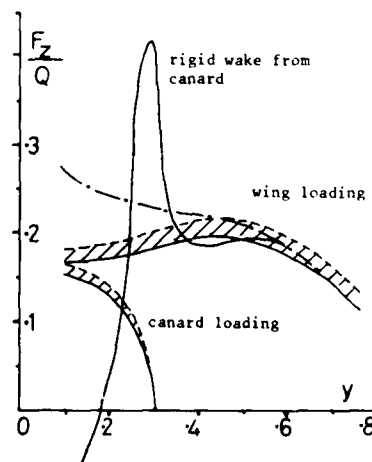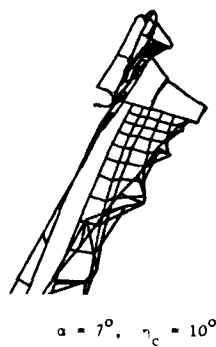
Fig. 3 : Wake relaxation for wing/body/canard configuration. Curves on right show spanwise loading for different canard wake assumptions. Dash-dot line : canard off; solid lines : relaxed wake in freestream; dashed line : relaxed wake in wind tunnel; highly peaky curve shows result for rigid planar wake from canard. Loading shown for $a = 4^o$, $\eta_c = 10^o$.
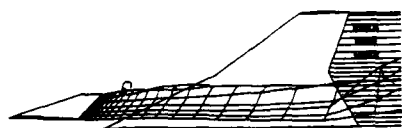
Fig. 4 : Relaxation of canard wake over wing.
α = 6°, η_c = 0°.
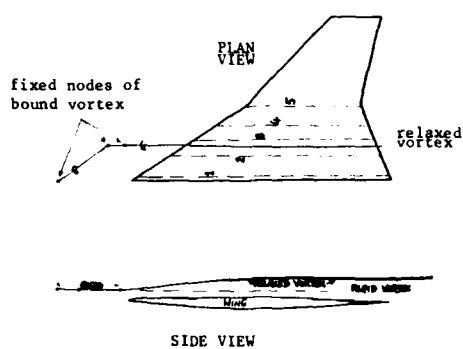
Fig. 5 : Line vortex model of canard wake, α = 6°, η_c = 0°.
Profiles on right show results for wing alone,
wing with rigid and with relaxed vortex (identical
to results with relaxed canard wake - not shown).
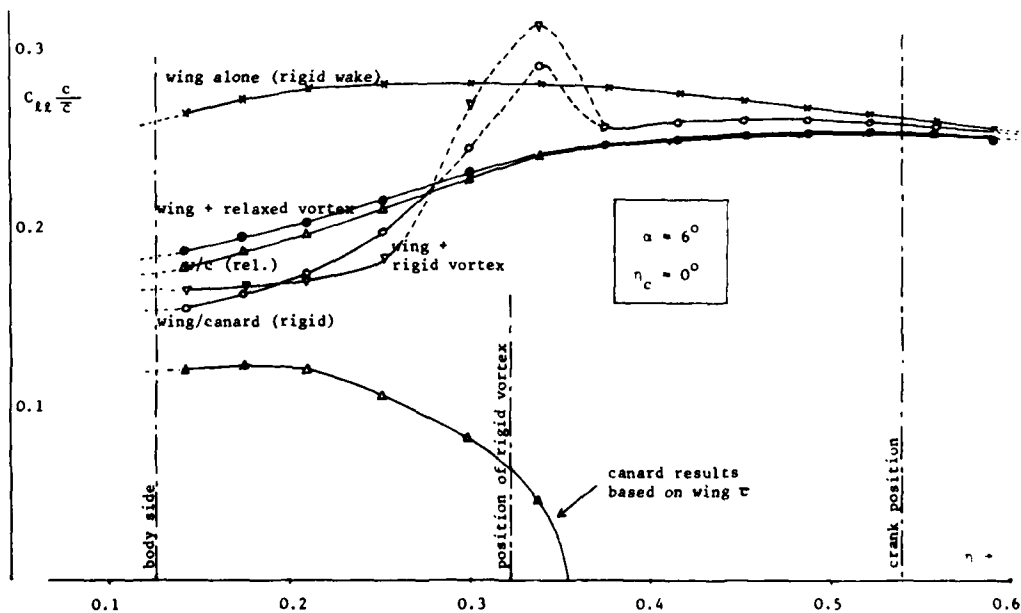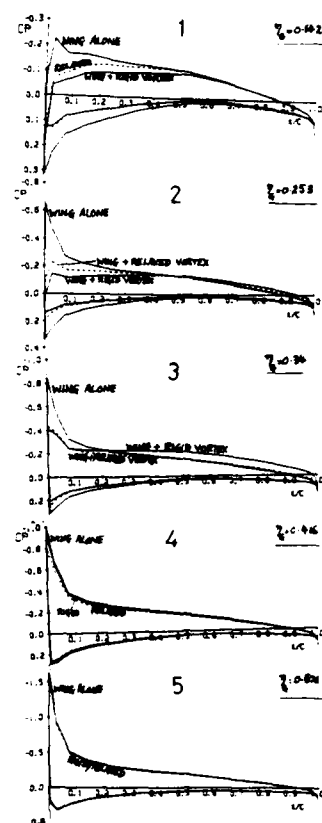
Fig. 6 : Spanwise loading on wing/body/canard with various canard wake representations.
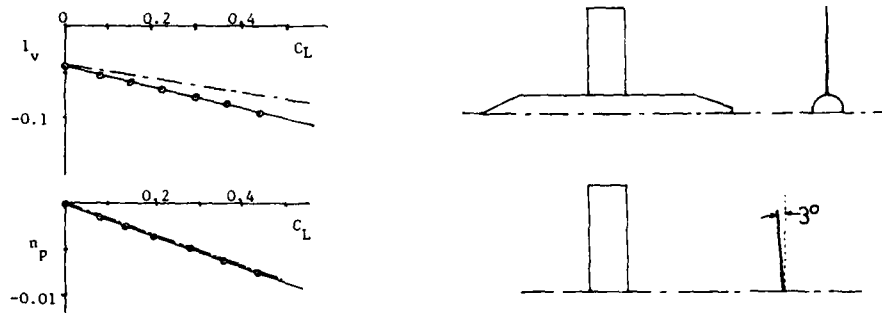
Fig. 7 : Samples of panel-program (B.Ae Mark 2) predictions of aerodynamic derivatives. Comparison with predictions of DATCOM datasheets.
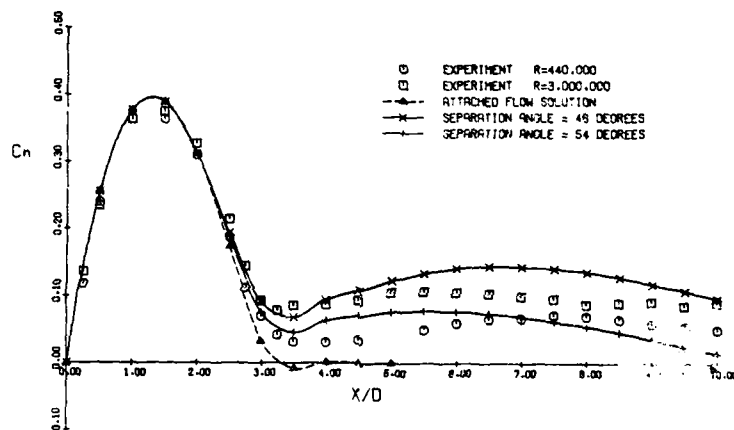
Fig. 8 : Normal force distribution on an ogive-cylinder. M = 0.3, α = 15°.   (Ref. 18.).

top view

side view

bottom view

top view

side view

bottom view   N.B. Hatch lines show
separation region.
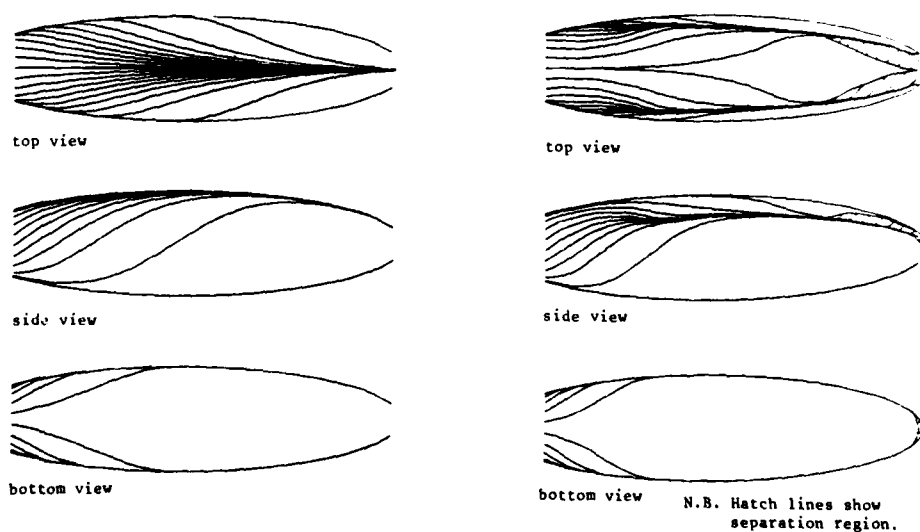
Fig. 9 : External streamlines (on left) and surface streamlines (on right) on a prolate spheroid of axis ratio 4.3:1 , α=20°, Re=7x10⁵. (B.Ae Brough 3D b.l. program).

$\alpha = 14.32°$
$M = 0$
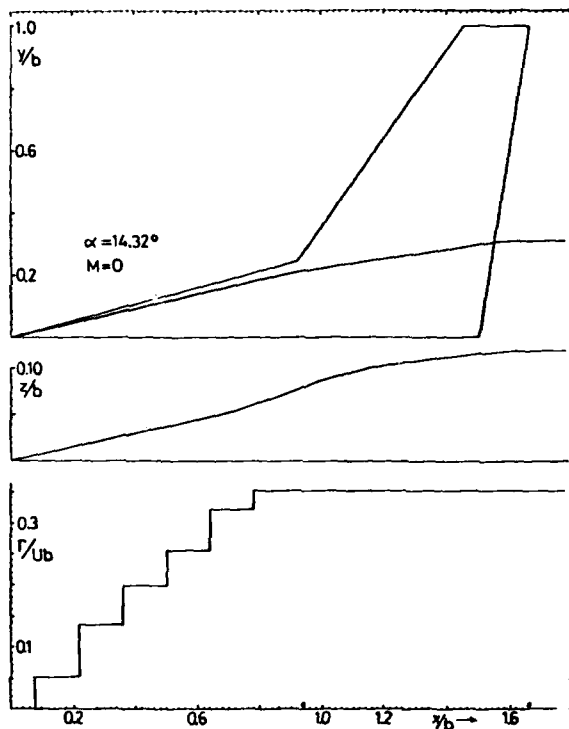
Fig. 10 : The "hybrid" method.
Computation of vortex fed from
strake leading edge and then con-
vecting over main wing.   Equal-
pressure wake from trailing edge
held in plane $z = 0$. (Ref. [8]).

lateral position of vortex core.

height of core above wing.

strength of core (piecewise
constant, fed from strake l.e.)

Fig. 11 : Comparison of attached flow model
and separated flow model with experiment.
The experimental measurements show random
switching between the two states.

(Maskew, Rao and Dvorak, AGARD CP-291, 1980)

------ Attached flow (theory)

——— Separation at
       x/c = .06 (theory)

●   Upper surface (experiment)

▲   Lower surface (experiment)

       $\alpha = 21.38°$
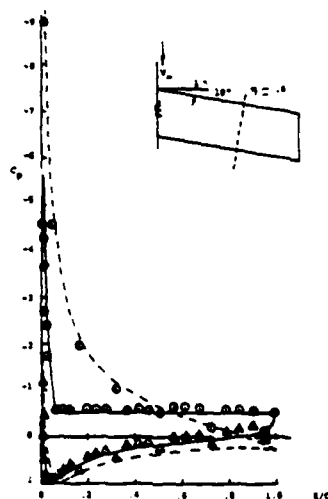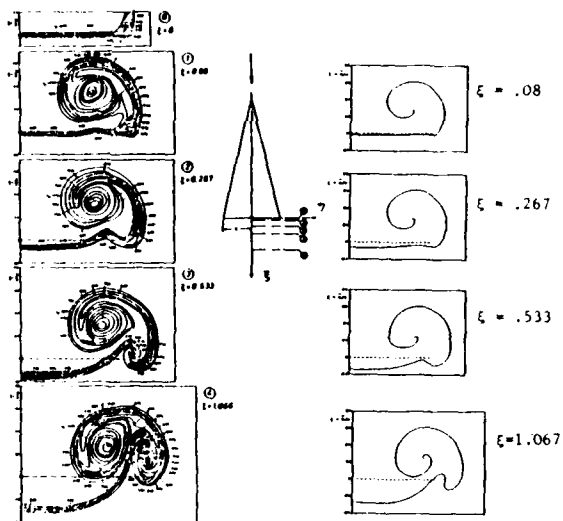
Fig. 12 : Experimental and theoretical wake
roll-up behind a delta wing of unit R.

The experimental curves on the left show
contours of total pressure (Hummel).

The theoretical curves on the right show
the evolution of an inviscid vortex sheet.
(Taken from Ref. [8]).

The dashed line shows the projection of the
wing trailing edge.

$\xi = .08$

$\xi = .267$

$\xi = .533$

$\xi = 1.067$
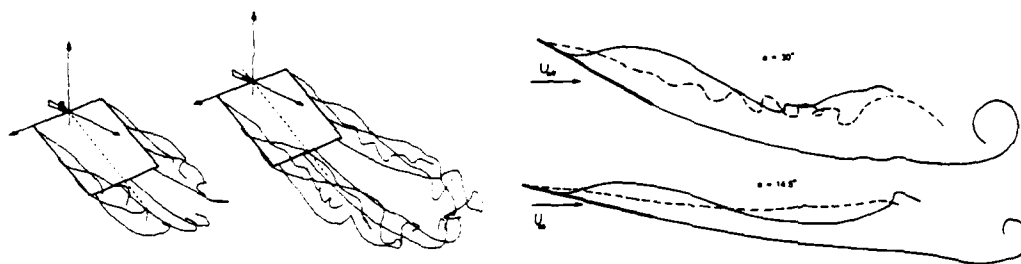
Fig. 13 : Three-dimensional vortex dynamics calculations (ONERA, Ref [18]) for impulsively-started plate.
The figures on the left show streak lines for $a = 30°$ after $\tau = 1$ & $\tau = 2$ ($\tau = $ chord/U_∞).
The figures on the right show streaklines after $\tau = 2.8$ for $a = 30°$ (unstable) and $a = 14.5°$ (stable).
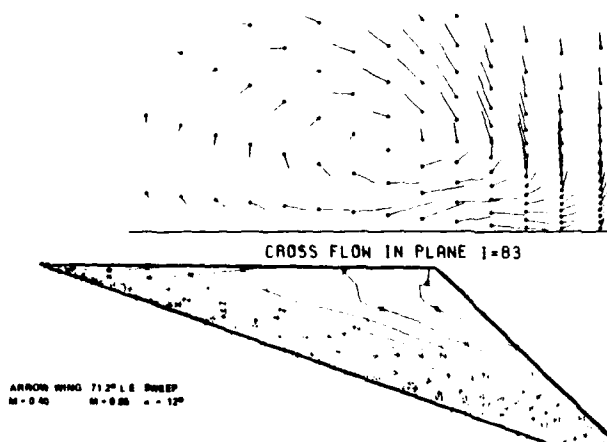
Fig. 14 : Leading-edge vortex flow
from fully-subsonic inviscid solution
of Euler equations (Schmidt, Dornier).

The upper picture shows flow directions
immediately downstream of trailing edge.

The lower picture shows the isobar
pattern. The separation initiates at
a finite spanwise position along the
curved leading edge.

CROSS FLOW IN PLANE I=83

ARROW WING 71.2° L E SWEEP
M = 0.40   M = 0.85   a = 12°

COMPRESSIBILITY EFFECTS ON FLOWS AROUND SIMPLE COMPONENTS

J. F. WENDT

von Karman Institute for Fluid Dynamics
Chaussée de Waterloo, 72
B - 1640 Rhode Saint Genèse, Belgium

SUMMARY

The effects of compressibility are considered on the flow fields and overall aerodynamic characteristics of low aspect ratio, sharp-edged planforms - rectangular, trapezoidal, and delta - and long ogive-cylinders at high incidence. Emphasis is placed on the leeside vortex-dominated flow structure, including vortex bursting. Both subsonic and supersonic regimes are included; unsteady effects are not considered.

NOTATION

AR	wing aspect ratio, $= b^2/S_c$
b	wing span
c	wing chord
$\bar{c}$	mean chord
C_L	lift coefficient, $= \dfrac{L}{q_\infty S_c}$
C_{M_z}	pitching moment coefficient, $= \dfrac{M_z}{q_\infty S_c L}$
C_N	normal force coefficient, $= \dfrac{N}{q_\infty S_c}$
C_p	pressure coefficient, $= \dfrac{p-p_\infty}{q_\infty}$
C_Y	side force coefficient, $= \dfrac{S}{q_\infty S_c}$
d	body diameter
L	lift force or characteristic length: chord for wings, body diameter for bodies and wing-body combinations
ℓ_N	length of nose
ℓ_A	length of afterbody
M_z	pitching moment
M_N	Mach number normal to leading edge
M_∞	free stream Mach number
N	normal force, or nodal point
p	static pressure
p_∞	free stream static pressure
q_∞	free stream dynamic pressure, $= \frac{1}{2} \rho_\infty U_\infty^2$
Re	Reynolds number, $= \dfrac{U_\infty L}{\nu_\infty}$
s	wing semi span
S	saddle point, or side force
S_c	characteristic area : planform area for wings, maximum cross sectional area for bodies or wing-body combinations
U_∞	free stream velocity
U'	axial component of vortex velocity
x,y,z	coordinate system fixed in wing
α	angle of incidence
α_n	angle of incidence normal to leading edge
δ_N	semi apex angle of nose
ν_∞	free stream kinematic viscosity
ρ_∞	free stream density
λ	taper ratio
ϕ	sweep angle

1. INTRODUCTION

Combat aircraft will be expected to fly at high incidence in a controlled manner throughout the subsonic and transonic regimes; missiles will add the supersonic regime to their range of operation. The objective of this paper is to examine compressibility effects on the flow field and aerodynamic characteristics of simple components. The dis-cussion will focus on shapes which are characteristic of missile wings and bodies . low aspect ratio planforms of zero camber with sharp leading edges and ogive-cylinder bodies; the former case constitutes an excellent example of controlled separation, the latter an example of uncontrolled or free separation.

This paper is divided into five sections according to geometry : rectangular, trape-zoidal and delta wings, the strake-wing combination and ogive-cylinders. In each section a brief review of the incompressible characteristics is provided followed by a discussion of compressibility (subsonic and supersonic) effects. The paper is far from exhaustive and the interested reader is urged to consult reference 1 for more detail, a large list of references, and considerable discussion on the hypersonic case. However, the author hopes that some insight into the surprisingly complicated three dimensional flow fields produced by extremely simple geometric shapes will be provided. With the exception of the strake-wing combination, interference effects are neglected - a definite shortcoming since at high incidence these effects can play an important role.

2. RECTANGULAR WINGS

While low aspect ratio rectangular wings find less application than wings with moderate sweep, nevertheless they represent a useful starting point for a discussion on the flow around simple components and the effects due to compressibility. As the emphasis in this paper will be on missile components, the case of sharp-edged low-aspect ratio flat plates is considered. Two basic features are evident: separation at the leading edge which leads to an increasingly large separation bubble at high incidence, and separation at the side edges which results in side-edge or tip vortices. Water tunnel studies using dye injection and oil flow surface visualization indicate a complex highly three-dimensional flow even at low incidence. Figure 1 shows an oil flow picture of an AR = 1 wing at 16° incidence. A sketch of the resulting skin friction lines is shown in the same figure (Ref. 2). A heated wire coated with light oil and placed at various locations relative to the leading edge has produced smoke streamlines which confirm the essential elements of the sketch showing a large rotational system on each side of the centerline (Ref. 3). This separation bubble remains attached until at least 20° incidence. The Reynolds number would be expected to play an important role in the development of this flow because it will influence transition of the free shear layer and thus the location of the reattachment line. However, the essential features should be preserved. Pressure distributions shown in figure 2 on a low aspect rectangular wing at low speeds (Ref. 4) lend support to the flow picture described above. The leading edge separation bubble is clearly seen as well as its three dimensional reattachment region and the effect of the side-edge vortices is marked even at low incidence. The peak suction moves from the region of the centerline at low incidence to the leading corners at high incidence. Normal force coefficients from the same reference, shown in figure 3, exhibit the expected behavior of a separated flow with vortex lift: a favorable non-linear lift curve followed by a reduction in the effects of the side vortices due to breakdown, and finally the opening of the separation bubble at the trailing edge. The effect of aspect ratio is also illustrated and attention is drawn to the abrupt changes in normal force for aspect ratios less than unity at very large incidence; the moment curves show the same characteristic shape. This may be due to a bursting of the separation bubble which, for low aspect ratio wings, could be stabilized up to a certain incidence by the presence of the side-edge vortices.

Compressibility effects have been examined (Ref. 2) by means of pressure distributions for Mach numbers from 0.55 to 0.95 and incidences up to 30°. A sample of the pressure coefficient variation on the suction side of an AR = 1 sharp-edged plate is shown in figure 4. The separation bubble grows with increasing Mach number and a small increase of the overall suction level is also noted; however, the suction peak near the leading edge decreases with increasing Mach number. At incidence angles less than 5.5°, the suction peak is at the centerline, as noted in reference 4. If the Mach number is of order 0.9, then at low incidence the supersonic expansion is strong enough to attach the leading edge flow and separation occurs downstream due to a shock-boundary layer inter-action. At higher incidence (>10°), leading edge separation again occurs and a shock wave can be seen imbedded in the flow near the trailing edge (Ref. 2). The integrated effect of this compressible three dimensional flow can be seen in the overall force and moment coefficients. The normal force coefficient for an aspect ratio one wing is shown in figure 5. A number of points are worth mentioning:
- In the subsonic range, C_N increases only slightly with Mach number up to about 20° incidence. This result is in agreement with other experiments (Ref. 5).
- Above 20°, the effect of increasing Mach number is to reduce the (first) maximum value of C_N and to shift it to lower values of incidence. In particular, the dramatic drop in C_N at large incidence shown in figure 3 for the incompressible case diminishes markedly as the Mach number increases.
- In supersonic flow (Ref. 6), C_N decreases with increasing Mach number, as expected; the side-edge vortices also are seemingly very weak according to the pressure distribu-tions plotted in the same reference.
The effect of aspect ratio on the aerodynamic coefficients in subsonic flow is similar to that observed in incompressible flow; i.e., an increase in aspect ratio leads to a larger C_N for a given incidence at low values of incidence and a peak C_N at a lower incidence.

Increasing Mach number again acts to smooth the peaks in the C_N α curves (Ref. 7). Super-
sonic Mach numbers lead to the same result, except that C_N increases monotonically with
incidence (Ref. 6).

The subsonic aerodynamic characteristics of rectangular wings are well predicted by
inviscid theory. For example, the lifting surface can be represented by a bound-vortex
sheet, approximated by discrete vortex lines arranged to form a lattice (Ref. 8). Com-
pressibility transformations are introduced through a modified Prandtl-Glauert rule; thus
the results are valid only for small incidence at large Mach numbers, e.g., 10-12° at
Mach 0.8.

In summary, the flow around low aspect ratio rectangular wings, while quite complex
in detail, results in well-behaved aerodynamic coefficients to high incidence in compres-
sible flows. Theoretical predictions to nearly 15° incidence are quite accurate. An
interesting problem area which remains is to find an explanation for the abrupt, in fact
dramatic, behavior of low aspect ratio wings at high incidence in incompressible flow and
the reason behind their increasingly acceptable behavior as compressibility becomes impor-
tant.

3. TRAPEZOIDAL WINGS

As the sweep angle of a sharp -edged rectangular wing at incidence increases from
zero to some finite value, the flow field on the resulting trapezoidal wing changes only
moderately from its original state (Ref. 9). At low incidence, the flow appears to re-
attach near the centerline and remains separated outboard as seen on figure 6. The sepa-
ration bubble induces a sidewash. Side edge vortices persist (although they are not in
evidence on this figure because of the absence of pressure taps near the wing tips), but
act over a smaller area of the wing as the sweep angle increases. At higher incidence
(15° and above), the pressure distribution is seen to be nearly uniform over the entire
wing indicating a fully separated flow. Thus, as sweepback angle increases, full separa-
tion with no reattachment occurs at low angles of incidence.

The effect of increasing (subsonic) Mach number is to decrease the incidence at which
a fully separated flow occurs, as may be seen by comparing the pressure distributions of
figures 6 and 7 and the C_N α curve of figure 8. Just as in the case of the rectangular
wing, the (first) maximum value of C_N occurs at a lower incidence and has a lower absolute
value as the Mach number increases.

In supersonic flow, the same trends as observed for the rectangular wing are noted;
they are also indicated on figure 8. In fact, measurements show that two wings of the
same aspect ratio, one of which is rectangular ($\lambda=1.0$) and the other trapezoidal ($\lambda=0.5$),
have nearly the same C_N curve (Ref. 5); further evidence that the supersonic flow field on
moderately tapered trapezoidal wings and rectangular wings is quite similar (The increas-
ing importance of the windward flow field at supersonic conditions should be noted).

On the theoretical side, the vortex lattice technique with compressibility factors
of the Prandtl-Glauert type again offers an accurate means of predicting the aerodynamic
coefficient as shown in figure 9 (Ref. 8). While no data were available at subsonic Mach
numbers for comparison, the trend is clearly correct as seen in figure 8. The limitations
of this technique must be recalled : small incidence for high subsonic Mach numbers, larger
incidence ($\sim15°$) at lower Mach numbers.

4. DELTA WINGS

When the sweepback angle of a sharp-edged trapezoidal wing at incidence exceeds about
50°, a highly stable leading edge vortex appears. It is formed by the flow emanating from
the windward side which cannot negotiate the infinite curvature at the leading edge and
hence separates and rolls up into a tightly coiled vortex as shown schematically in fig-
ure 10. While the overall flow picture is essentially independent of Reynolds number due
to the controlled nature of the separation, the detailed structure exhibits a secondary
(and possibly a tertiary) vortex lying outboard of the primary one; as it stems from a
separation on the lee surface, its characteristics will depend on the state of the attached
boundary layer inboard and hence on the Reynolds number. A typical pressure field on a low
aspect ratio delta wing at incidence is shown in figure 11 (Ref. 12). The primary suction
peaks on the lee side are due to the high induced velocities of the vortices and flow vis-
ualization photos show that they indeed lie just below the centerline of the primary vor-
tices. Secondary vortices near the leading edges may also be deduced. The suction peaks
decrease in the streamwise direction, but those further aft affect ever larger areas of
the surface. Conical flow may be observed, to first order. That the Reynolds number plays
a role in the pressure distribution is clearly as shown in figure 12. (Ref. 14). The
observed variation can be explained by examining the state of the suction side boundary
layer. At high Reynolds numbers, the boundary layer is turbulent; it penetrates the adverse
pressure gradient, established by the primary vortex, virtually to the leading edge before
separating to form the secondary vortex. At sufficiently low Reynolds numbers, the boun-
dary layer is laminar and therefore separates further inboard forming a larger and more
inboard-located secondary vortex. The effect is to displace the primary vortex inboard
and upward, thus shifting the peak suction point inboard and diminishing its magnitude.
As the aspect ratio decreases, the suction drops as shown in figure 13, all other parame-
ters being equal (Ref. 15). As a result, normal force will also decrease with decreasing
aspect ratio. This is illustrated in figure 14 by lift (and moment) plots (Ref. 16). At
low incidence, the lift and moments are linear, but above about 5°, the typical nonlinearity
due to the presence of strong vortices on the suction side is manifested. At modest

incidence, increasing aspect ratio means increased lift. However, at an incidence which increases with decreasing aspect ratio, a departure from the observed non-linearity in lift and an abrupt change in pitching moment take place. The origin of these effects is a bursting or breakdown of the vortices over the wing, a phenomenon which will be discussed later. At increased incidence, as shown on figure 15 the leeside flow affects the delta wing in the same manner as on the rectangular or trapezoidal wing; i.e., the normal force decreases at an angle which increases with decreasing aspect ratio and the rate of decrease in normal force reaches a maximum at a specific value of the aspect ratio (in the case of the delta wing, at an aspect ratio of about 2).

Compressibility effects are already noted in the flow structure at free-stream Mach numbers as low as 0.5. The suction is reduced and the vortices move slightly inboard as M_∞ reaches unity according to figure 16 (Ref. 14). Laser doppler velocimeter measurements (of a preliminary nature)(Ref. 18) show that the vortices become somewhat more flattened in shape and lie slightly closer to the surface as the Mach number increases from 0.4 to 0.8. An example of the cross flow velocity vector field is shown in figure 17; the cross flow velocities are seen to exceed the free-stream velocity by as much as 20% in some regions. In the same reference, the maximum axial velocity at a given chordwise station decreases from a value larger than the free stream velocity at Mach 0.4 to a value less than the free stream velocity at Mach 0.8. When the free stream Mach number exceeds unity, depending on incidence and aspect ratio, a detached shock will form. The large scale lee-side vortices will still be present at moderate supersonic conditions, but as the Mach number increases further, a supersonic expansion around the leading edge will occur (when the Mach number normal to the leading edge exceeds unity) and the flow will not separate at the leading edge but rather inboard of it resulting in smaller vortices and less vortex lift. Finally, at large Mach numbers, the shock will be attached at the leading edge. These regimes have been studied extensively (Ref. 19) and are shown schematically in figure 18. These changes in flow structure for finite Mach numbers are reflected in the overall aero-dynamic coefficients. Even though the leeside suction decreases with increasing value of M_∞, the increasing values of the windward pressures more than compensate as shown in figure 16 and the net result is an increasing value of the normal force coefficient, C_N in the subsonic regime as shown in figure 19. At high incidence the behavior is similar to that already noted on other planforms. In the supersonic regime, the trend is clear - decreasing C_N with increasing M_∞ and less and less influence from the leeside flow field.

From the point of view of numerical predictions, the work of reference 8 may again be cited as providing good agreement with experimental results as long as the limitations of the Prandtl-Glauert small perturbation potential equation are observed. The vortex-sheet method, based on the same equation, gives comparable results (Ref. 20). An analogy with the unseparated flow around a leading edge and the resulting suction force has been used to calculate forces and moments around a variety of planforms which agree well with experiments (Refs. 21 and 22). However, neither flow field structure nor surface pressure distribution can be computed. A good summary of the available inviscid numerical models for flow separation from sharp leading edges is given in reference 23. All these models suffer from common failings: the inability to deal with secondary vortices, high subsonic conditions at high incidence, and vortex bursting.

We now return to the subject of vortex bursting, by which is meant the transformation of a highly ordered vortical structure, whose axial velocity component may substantially exceed that of the free stream, into a large diffuse slowly rotating structure with a low axial velocity component. An example is shown in figure 20 which is the result of a laser Doppler velocimetry spanwise survey at two chordwise locations on a delta wing in incompressible flow (Ref. 24). The ordinate plots the (nearly) axial component of the velocity and the dramatic stagnation of the flow is clearly seen. As the angle of incidence increases further, the location of the vortex bursting point moves toward the apex as shown in figure 21 (Ref. 25), gradually reducing the effect of the vortical flow on the lift curve (The discrepancies between the results observed in air and in water should be noted; undoubtedly they may be ascribed to a difference in Reynolds number, although differences in the definition of the location of bursting may have played some role). No complete theory of vortex breakdown is available at present. However, it has been shown that a stable leading edge vortex entering a region of increasing pressure eventually is transformed into a highly unstable vortex (Ref. 28). This explanation is consistent with a number of experiments (see e.g. Ref. 15) in which the introduction of a probe into the vortex core may induce breakdown, depending on wing incidence, and the presence of a burst vortex on a delta wing has been noted just upstream of an imbedded shock in high subsonic flows. More recently a different point of view has been taken (Ref. 29). One asks under what conditions can a stable vortex exist near the apex of a delta wing. A stability boundary has been derived outside of which the leading edge vortex can no longer be stable. The theory does not predict how far downstream from the apex bursting will occur; only whether or not an instability is present. Figure 22 shows the essential results and compares them with experimental observations (Ref. 17). The theoretical and experimental trends are clearly in good agreement and quantitative agreement may be said to exist for AR ≤ 1.5. As the theory is based on the slender body assumption, and as this assumption is less valid at larger aspect ratios, the divergence between theory and experiment is not surprising.

Compressibility has a marked effect on the phenomenon of vortex bursting on delta wings, as reported first in reference 30 and later in references 15 and 31. These authors noted that at high subsonic Mach numbers, the bursting point literally "jumps" to mid-chord at an incidence angle which, as usual, depends on aspect ratio. The effect is illustrated on figure 23 by the variation with incidence of the pressure coefficient for each of 5 pressure taps located on the 60% ray of a sharp-edged wing of AR = 2. Increasing the

incidence to 16.8° resulted in the expected increase in suction; at 16.9° the vortex on the lift side suddenly burst, markedly affecting the suction up to the 50% chord. At the same angle, within experimental error, a similar force model exhibited a marked change in normal force and pitching moment. At 1.5° greater incidence the vortex on the right side burst at approximately the same location. On decreasing the incidence from an initially large value, a hysterisis was noted; the vortex which was the last to burst on increasing the incidence became the first one to suddenly reestablish its low-incidence character. An example of its effect on C_N is shown in figure 24 (Ref. 31). A summary of the results for different aspect ratios and Mach numbers is shown in figure 25 (Ref. 31). It may be concluded that an increase in Mach number and a decrease in aspect ratio amplify these effects. In the study described above, one vortex (the same one) always burst prior to the others. With the thought that this might reflect an initial yaw angle, a series of tests were carried out at different yaw angles. With sufficient yaw (a few degrees), the opposite vortex would indeed burst first. However, we were never able to have both vortices burst simultaneously. The unstable nature of the vortex bursting phenomenon was exemplified by a process which the author of reference 15 called "flickering"; i.e., at the critical angle for which the vortex bursting point suddenly appeared on the AR = 2 wing, we frequently could observe, both by means of pressure measurements, balance output, and schlieren, a random fluctuation between the two extreme cases of trailing edge burst and mid-chord burst. The term "flickering" was coined because the switching from one extreme to the other appeared as a sudden change in illumination level on the schlieren screen, which was not unlike that of a flickering lamp. It is interesting to note that this effect could not be observed on an AR = 1.26 wing. Finally, since good agreement on the critical angle for bursting was found for both the force model supported by a straight rear sting and the pressure model supported by a blade, the influence of the support was evidently small.(Support effects can be important in studying the vortex bursting phenomena as emphasized in reference 32).

To the best of the author's knowledge, no theoretical description of vortex bursting which takes into account compressibility effects has been developed.

In summary, a good understanding of compressibility effects on simple sharp-edged delta wings is now available at incidences up to the point at which vortex bursting occurs. That phenomenon, as well as the very high incidence fully-stalled flow, remains a source of research work, even in the incompressible case.

5. STRAKE-WING COMBINATION

Although not strictly a "simple" shape, the flat sharp-edged strake-wing combination is composed of two simple planforms discussed previously: the delta wing and the trapezoidal wing, and its importance in high angle-cf-attack aerodynamics is well known. Recent reviews may be found in references 25, 33 and 34. At low incidence, i.e., 3°-5°, the sharp-edged flat-profile strake-wing shown in figure 26 exhibits the typical vortex shed from the leading edge of the strake. When the vortex reaches the junction between the strake and the main wing, it is partially entrained along the leading edge. As discussed in references 29 and 35, the sidewash induced by the strake vortex at the leading edge "kink" (the junction between the strake and wing leading edges) increases the effective sweepback-angle of the main wing. The sidewash triggers, at somewhat higher angles-of-attack, e.g. 6°-12°, a new vortex generated at the kink which moves downstream making a larger angle to the freestream than the strake vortex. This "kink" vortex is clearly seen on figure 27 (Ref. 36) and its effect on the flow field is quite pronounced as seen in pressure plots at different chordwise locations on a strake (77.5° sweepback) - wing (27° sweepback) examined in reference 9. One example appears in figure 28; it should be compared with figure 6 which was recorded for the same wing without strake. At about 18° incidence, the effect of the strake and kink vortices suddenly disappears, possibly due to the bursting of the strake vortex.

Compressibility alters the flowfield in a way which is not easy to quantify. As shown in figure 29, again from reference 9, the suction by the strake itself is reduced, as expected; however, the kink vortex is reinforced. A close examination of pressure plots at numerous incidence angles leads one to conclude that compressibi'ity also changes the range of incidence in which the effects described earlier occur; e.g., as the Mach number increases, the kink vortex produces its maximum suction at lower angles-of-attack. The overall result of the leeward and windward pressure distributions is shown in figure 30 in the form of a normal force coefficient. The beneficial effect of the strake (whose area is only 10% of the wing area) is clearly seen. Compressibility acts to increase C_N, at least to 20° incidence, and the largest fractional increase in C_N with a change in Mach number from 0.42 to 0.83 occurs in the vicinity of 7°, which is consistent with the pressure plots shown earlier.

While the flow on a simple planform such as strake-wing represents an interesting example of synergism in that the two components together exhibit enhanced aerodynamic characteristics, the final application always involves a volume element which will produce additional favorable or unfavorable interference effects. Long forebodies and/or wings whose span relative to the body diameter is not very large may lead to flow fields on the main wing and overall aerodynamic characteristics which are different from those described above. An example, typical of a missile application because the total span is only three times larger than the body diameter, is shown in figure 31. The forebody, an ogive cylinder has an r/d = 12 upstream of the strake apex and the strake area is 10% of the wing area (Ref. 38). Again, the beneficial effect of the strake is clearly seen, but now the influence of the body vortices, discussed in the next section, and the body-wing interference must also be considered. Compressibility effects are less important for the full

configuration than for the strake-wing alone as may be seen by a comparison with figure 10.

6. OGIVE-CYLINDER BODIES

The flow around bodies of revolution at incidence is considerably more complex than the flow considered in the earlier sections because separation is not fixed at a salient edge. Thus, the Reynolds number plays a dominant role, in particular by determining whether the separation is turbulent or laminar and thereby influencing its location. A long slender body pitched through the range of incidence from 0° to 90° will give rise to four distinct flowfields as shown in figure 32 (Ref. 39). At very low incidence, the flow is largely attached over virtually the entire body, with the exception of the base, and linear inviscid aerodynamics provides a reasonable prediction of such quantities as normal force and center of pressure. As the incidence is increased, the crossflow component becomes important and this leads to boundary layer separation and the formation of symmetric vortices which give rise to a nonlinear lift component. At still larger incidence, the crossflow component dominates the axial component and the vortices become asymmetric. Since their effect on the leeside surface is also asymmetric, side forces and moments appear at zero sideslip. Finally, as the incidence approaches 90°, the boundary layer is shed as periodic von Karman vortices or as an unsteady wake; in this regime, unsteady side forces will be experienced by the body. The boundaries for the onset of these regimes depend on the length of the body as shown in figure 32 and more specifically on the fineness ratios of both the nose and the body as illustrated in figure 33, also from reference 39. Figure 34 is a visualization of such flows in a water tunnel (Ref. 41). The change in the trajectories of the vortices with incidence is clearly noted, and the question posed for the designer of aft-mounted control surfaces is evident from the cross-flow photos: how to predict the strength and location of these vortices in the asymmetric case so that their effect on the control surfaces can be estimated?

A number of reviews on the subject of nose-cylinder flows at high incidence have appeared in recent years, among them references 42-44. The authors point out the important influence of nose geometry; surface roughness in the nose-tip region; body spin, coning, and pitching; Reynolds number and Mach number in predicting the boundary between the symmetric and asymmetric vortex regimes, as well as the aerodynamic effects in the asymmetric regime. Only the effect of the latter parameter will be summarized here. Figure 35 illustrates the effect of Mach number on the leeside flow regimes experienced by a circular body of approximately 10 d length (Ref. 42). As the crossflow Mach number approaches unity, the vortices near the base become elliptic and, at larger Mach numbers, change into free shear layers. The shed vortices are clustered near the nose. The leeside surface pressures become progressively smaller at high supersonic Mach numbers and thus, even though the flowfield may be quite complex, its effect on the resulting forces and moments becomes small. The normal force coefficient, shown in figure 36 (Ref. 45), has the typical variation with incidence and Mach number that we have come to expect in flows with leeside vortices: a linear region up to $\sim$5 degrees incidence followed by a nearly $\sin^2 \alpha$ dependence to approximately 50 degrees after which important unsteady wake effects dominate the picture. C_N increases with increasing Mach number to about $M_\infty = 1.2$ and decreases with increasing supersonic Mach number. However, a recent study suggests that the dependence is somewhat more complicated; namely, C_N increases with M_∞ to a least Mach 2 (the limit of this study) for $\alpha < 30°$ but reaches its peak value at Mach 1.5 for $\alpha > 30°$ (up to at least 58°) for values of nose fineness from 1.5 to 3.5 on a 13 d body (Ref. 46). The interesting features of this flow are observed when the vortices become asymmetric. While the Mach number has little influence on the angle of incidence at which the asymmetric vortices and the resultant side forces first appear (the "onset" angle), it has a strong effect on the maximum value of the side force as seen in figure 37 (Ref. 47) and figure 38 (Ref. 39). It is clear from the former that the maximum side force, which seems to be associated with the shedding of the first vortex (Ref. 48), for long-nosed bodies decreases markedly with Mach number, and from the latter that the rate of disappearance of this effect depends strongly on the nose fineness ratio. One explanation that has been offered (Ref. 42) is that at a crossflow Mach number above 0.4 the supercritical/subcritical geometry for asymmetric separation cannot be formed because the asymmetric leeside flow cannot communicate its influence to the separation region through the local supersonic pockets. In summary, vortex-induced side loads on ogive-cylinder bodies decrease with increasing subsonic crossflow Mach numbers above 0.4 and become negligible when the crossflow Mach number is supersonic.

7. CONCLUSIONS

This paper has considered the flows around bodies of very simple shapes; for the most part they are characterized by separation from a salient edge. Nevertheless, due to the relatively small aspect ratios and large incidences, the resulting flow fields are highly three dimensional, frequently involving a strong interaction between vortices and separation bubbles - both closed and open. While remarkable progress has been made in developing computational techniques to predict the relevant aerodynamic characteristics, practical codes are still restricted to Prandtl-Glauert-type applications; i.e., modest incidences at modest Mach numbers, and viscous effects, secondary separation, vortex cores, etc, are neglected. Thus, considerable latitude remains for the clever experimentalist and the wind tunnel design engineer.

Fortunately, Mach number does not generally play a dominant role in determining flow field structure, except in highly supersonic flows where the leeside conditions are of much less importance in determining overall aerodynamics. As such, water tunnels and low speed tunnels will continue to be used extensively. There are, however, two phenomena

which seem to be sensitive to Mach number and deserve further study: vortex bursting and the very high incidence stall regime on low aspect ratio wings. In these cases, the water tunnel must be supplemented by good flowfield visualization techniques in high speed tunnels. Because of the sensitivity of these phenomena to adverse pressure gradients and other free stream non-uniformities, non-intrusive measurement techniques should be used for quantitative studies and sting/tunnel interference effects should be carefully examined.

8. REFERENCES

1. Peake, D.J. & Tobak, M.: Three dimensional interactions and vortical flows with emphasis on high speeds. AGARDograph 252, July 1980.

2. Van Westerhoven, P.: Flow around a rectangular low aspect ratio wing and the effect of compressibility. Addendum on Flow Visualization. VKI PR 1981-29, June 1981.

3. Foerster, W.: Flow visualization in the separation bubble of a rectangular low aspect ratio wing using a smoke wire technique. VKI SR 1981-14, September 1981.

4. Winter, H.: Flow phenomena on plates and aerofoils of short span. NACA Report 798, 1937.

5. Yermolenko, S.D.: Nonlinear theory of wings of small aspect ratio. NASA TT-F 10,915, June 1967.

6. Stallings, R.L. & Lamb, M.: Wing-alone aerodynamic characteristics for high angles of attack at supersonic speeds. NASA TP 1889, July 1981.

7. Kavsaoglu, M.: Unpublished VKI data. December 1981.

8. Kandil, O.A.; Mook, D.T.; Nayfeh, A.H.: Effect of compressibility on the nonlinear prediction of the aerodynamic loads on lifting surfaces. AIAA Paper 75-121, AIAA Aerospace Sciences Meeting, 20-22 January 1975.

9. Vigevano, L.: Effects of strakes on low aspect ratio trapezoidal wings for missile configurations in compressible flow. VKI PR 1979-5, June 1979.

10. Movassaghie, B.: Experimental study of a wing with strake for a missile configuration in high subsonic and transonic flows. VKI PR 1976-3, June 1976.

11. Work of Jacob taken from Gersten, K.: Calculation of non-linear aerodynamic stability derivatives of aeroplanes. AGARD Report 342, 1961.

12. Hummel, D.: Zur Umströmung scharfkantiger schlanker Deltaflügel bei grossen Anstellwinkeln. Zeit. Flug. Wiss., Vol. 15, 1967, pp 376-385.

13. Smith, J.H.B.: Improved calculations of leading-edge separation from slender delta wings. Proc. Roy. Soc., Lordon, A 306, 1968, pp 67-90, also RAE TR 66070, 1966.

14. Stahl, W.; Hartmann, K.; Schneider, W.: Force and pressure measurements on a slender delta wing at transonic speeds and varying Reynolds number. in Facilities and Techniques for Aerodynamic Testing at Transonic Speeds and High Reynolds Number. AGARD CP 83-71, August 1971, pp 9-1 to 9-12.

15. Muylaert, J.: Effect of compressibility on vortex bursting on slender delta wings. VKI PR 1980-21, June 1980.

16. Hummel, D. & Srinivasan, P.S.: Vortex breakdown effects on the low speed aerodynamic characteristics of slender delta wings in symmetrical flow. J. Roy. Aero. Soc., Vol. 71, 1967, pp 319-322.

17. Earnshaw, P.B. & Lawford, J.A.: Low-speed wind-tunnel experiments on a series of sharp-edged delta wings. ARC R&M 3424, 1966.

18. Vorropoulos, G. & Wendt, J.F.: Preliminary results of LDV surveys in the compressible leading edge vortex of a delta wing. VKI TN 137, September 1981.

19. Squire, L.C.: Flow regimes over delta wings at supersonic and hypersonic speeds. Aero. Quart., Vol. 27, February 1976, pp 1-14.

20. Johnson, F.T.; Lu, P.; Tinoco, E.N.; Epton, M.A.: An improved panel method for the solution of three dimensional leading edge vortex flows. NASA CR 3278 and 3279, July 1980.

21. Polhamus, E.C.: Predictions of vortex-lift characteristics by a leading-edge suction analogy. J. Aircraft, Vol. 8, No. 4, 1971, pp 193-199.

22. Lamar, J.E.: Vortex flow characteristics of wings. J. Aircraft, Vol. 13, No. 5, 1976, pp 379-381.

23. Smith, J.H.B.: Inviscid fluid models, based on rolled-up vortex sheets, for three-dimensional separation at high Reynolds number, in Three Dimensional and Unsteady Separation at High Reynolds Number, AGARD LS 94, February 1978, pp 9-1 to 9-27.

24. Anders, K.: Measurement of velocity distribution in delta wing vortices using laser doppler velocimetry. VKI PR 1981-03, June 1981.

25. Lamar, J.E. & Frink, N.T.: Experimental and analytical study of the longitudinal aerodynamic characteristics of analytically and empirically designed strake-wing configurations at subcritical speed. NASA TP 1803, June 1981.

26. Wentz, W.H. & Kohlman, D.L.: Wind tunnel investigation of vortex breakdown on slender sharp-edged wings. NASA CR 98731, 1968.

27. Headly, J.W.: Analysis of wind tunnel data pertaining to high angle of attack aerodynamics. Vol. 1, AFFDL TR-78-94, July 1978 and ADA069 646.

28. Ludwieg, H.: Vortex breakdown. DFVLR Göttingen, DLR FB 70-40, 1970 and earlier publications in Z. Flugwiss., Vol. 10, 1962, pp 242-249 and Vol. 13, 1965, pp 437-442.

29. Wedemeyer, E.H.: Stable and unstable vortex separation, in High Angle of Attack Aerodynamics, AGARD CP-247, January 1979, pp 13-1 to 13-10.

30. Stahl, W.: Zum Einfluss eines strakes auf das Strömungsfeld eines deltaflügel (AR=2) bei schallnahen Geschwindigkeiten. DLR Mitt. 73-04, 1973, pp 113-136; also (in English) ESA TT 175, 1975.

31. Duprez, V.: Etude expérimentale de l'éclatement des tourbillons sur des ailes delta: influence du coefficient d'allongement. Travail de fin d'étude, University of Brussels, May 1981.

32. Ericsson, L.E.: Support interference, in Dynamic Stability Parameters, AGARD LS 114, May 1981, pp 8-1 to 8-26.

33. Stahl, W.H.: Aerodynamics of low aspect ratio wings, in Missile Aerodynamics, AGARD LS 94, February 1979, pp 3-1 to 3-64.

34. Lamar, J.E. & Luckring, J.M.: Recent theoretical developments and experimental studies pertinent to vortex flow aerodynamics - with a view towards design, in High Angle of Attack Aerodynamics, AGARD CP 247, January 1979, pp 24-1 to 24-31.

35. Fiddes, S.P. & Smith, J.H.B.: Strake induced separation at moderately swept leading edges. RAE TR 77128, 1977.

36. Demurie, F.: Investigation of the interference effects in the flow field around a body-strake-wing missile configuration. VKI PR 1980-23, June 1980.

37. Stahl, W.; Movassaghie, B.; Brohez, G.: Aerodynamic characteristics of a missile configuration featuring a wing with strakes. DFVLR-Göttingen DLR 77-34, 1977; also VKI Preprint 1977-2.

38. Akçay, M.; Richards, B.E.; Stahl, W.H.; Zarghami, A.: Aerodynamic characteristics of a missile featuring wing with strakes at high angles of attack, in High Angle of Attack Aerodynamics, AGARD CP 247, January 1979; also VKI Preprint 1978-7.

39. Chapman, G.T. & Keener, E.R.: The aerodynamics of bodies of revolution at angles of attack to 90°. (Written version unavailable, graphs taken from Ref. 40). AIAA Paper 79-0023, January 1979.

40. Malcolm, G.N.: Impact of high-alpha aerodynamics on dynamic stability parameters of aircraft and missiles, in Dynamic Stability Parameters, AGARD LS 114, March 1981.

41. Werlé, H.: Hydrodynamic visualization on streamlined bodies of vortex flows particular to high angles of attack. Presented at International Symposium on Flow Visualization, Bochum, Germany, September 1980.

42. Wardlaw, A.B.: High-angle-of-attack missile aerodynamics, in Missile Aerodynamics, AGARD LS 98, March 1978.

43. Peake, D.J. & Tobak, M.: Three dimensional interactions and vortical flows with emphasis on high speeds. AGARDograph 252, July 1980.

44. Ericsson, L.E. & Reding, J.P.: Steady and unsteady vortex-induced asymmetric loads on slender vehicles. AIAA J., Vol. 18, No. 2, 1981, pp 97-109.

45. Fleeman, E.L. & Nelson, R.C.: Aerodynamic forces and moments on a slender body with a jet plume for angles of attack up to 180 degrees. AIAA Paper 74-110, 1974.

46. Kruse, R.L.; Keener, E.R.; Chapman, G.T.; Claser, G.: Investigation of the asymmetric aerodynamic characteristics of cylindrical bodies of revolution with variations in nose geometry and rotational orientation at angles of attack to 58° and Macn number to 2. NASA TM 78533, September 1979.

47. Paul, B.P.: An investigation of the flow about an ogive cylinder at high angles of incidence. VKI PR 1981-21, June 1981.

48. Yanta, W.J. & Wardlaw, A.B.: Flowfield about and forces on slender bodies at high angles of attack. AIAA J., Vol. 19, No. 3, 1981, pp 296-302.

9. ACKNOWLEDGEMENTS
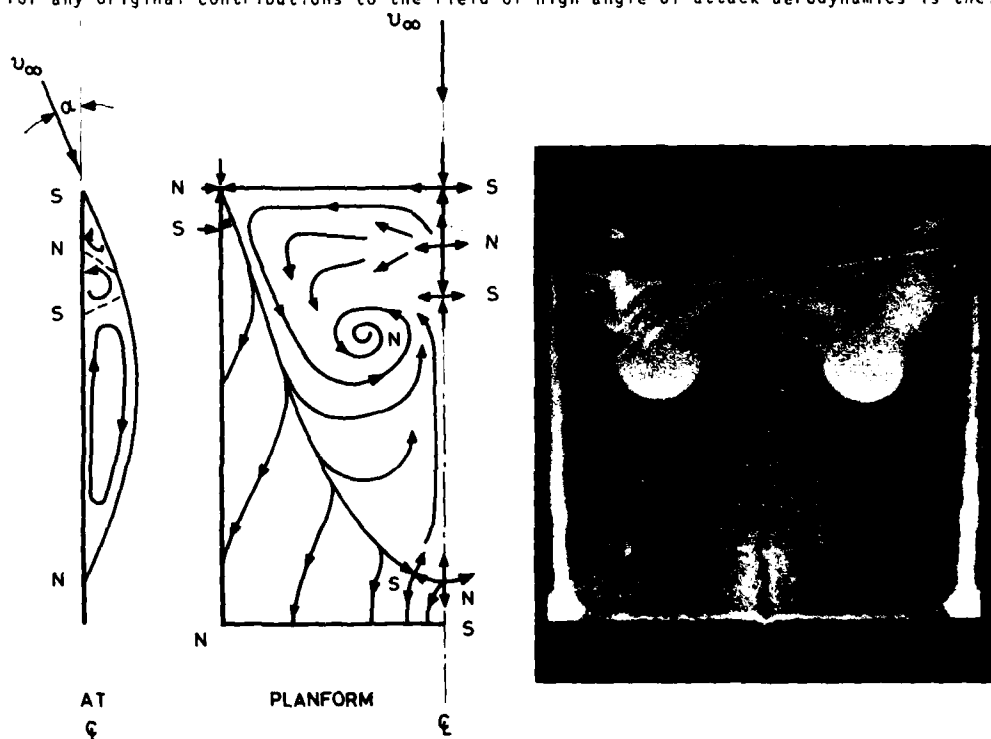
FIG. 1 - Oil flow and skin friction lines on an AR=1 rectangular plate at 16° incidence (Ref. 2).

FIG. 2 - Leeside pressure distribution on an AR=1 rectangular plate (Ref. 4)
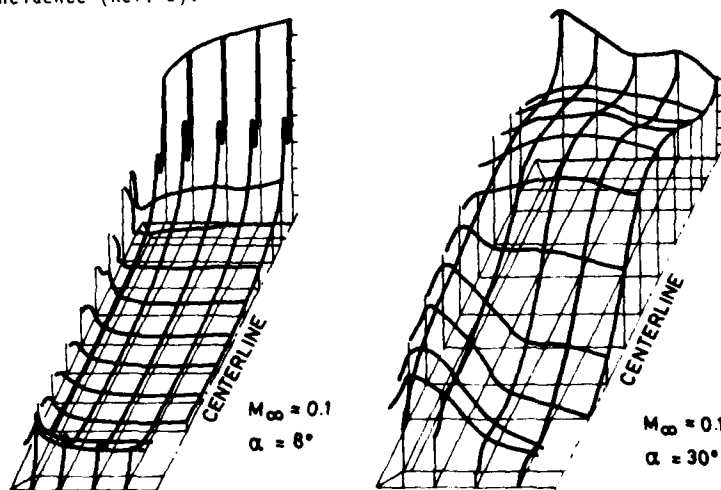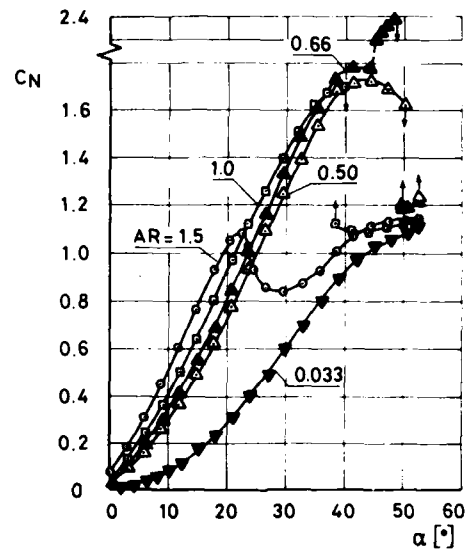
FIG. 3 - Normal force coefficients for rectangular plates of various aspect ratios
(Ref. 4)
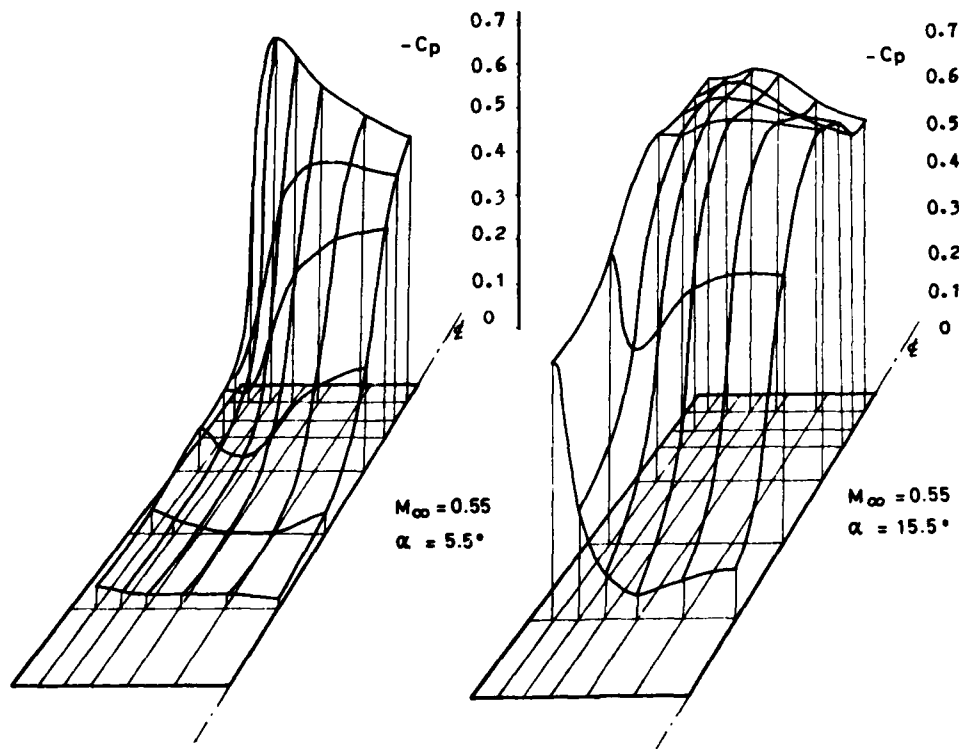
FIG. 4 - Pressure distribution on the leeside of an AR=1 rectangular plate showing
the effects of Mach number and incidence. $Re_L = 3 \times 10^5$ (Ref. 2)

$M_\infty = 0.86$
$\alpha = 5.5°$

$M_\infty = 0.85$
$\alpha = 15.5$
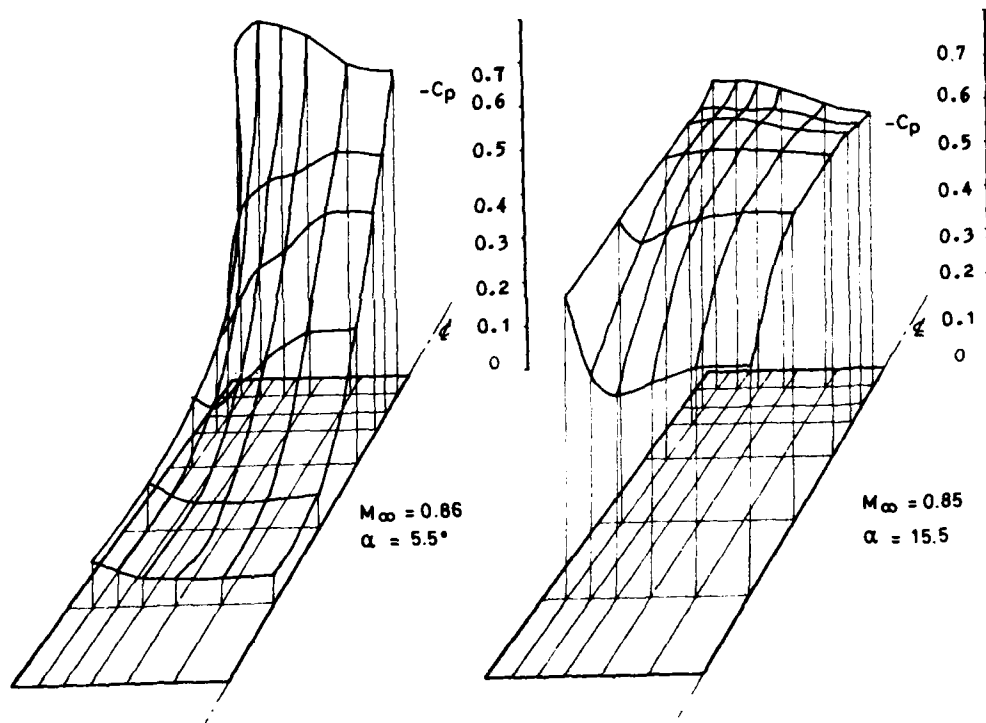
FIG. 4 (continued)
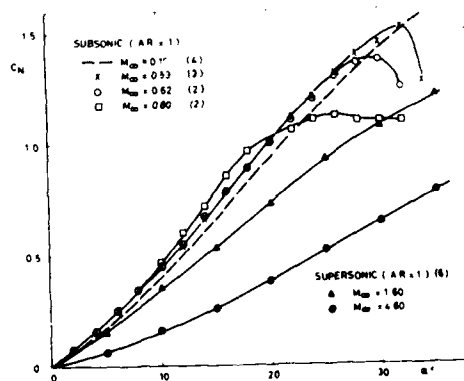
FIG. 5 - Normal force coefficient of a rectangular plate at incidence
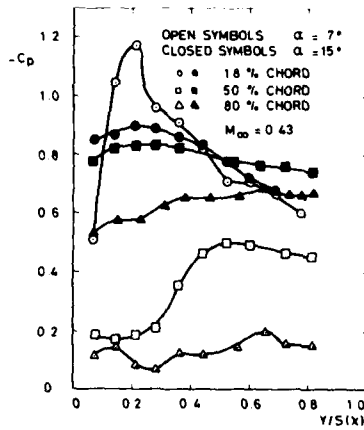
FIG. 6 - Pressure coefficient in the span-
wise direction at various chord-
wise locations on an AR=1 rectan-
gular flat plate. M∞=0.43 (Ref.2)
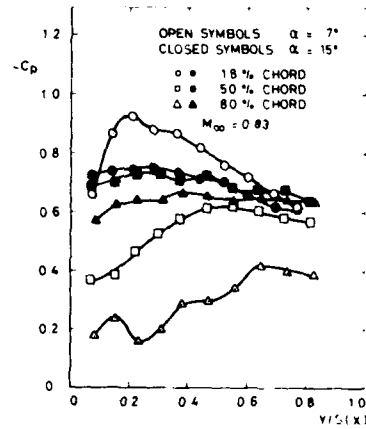
FIG. 7 - Pressure coefficient in the span-
wise direction at various chord-
wise locations on an AR=1 rectan-
gular flat plate. M∞=0.83 (Ref.2)
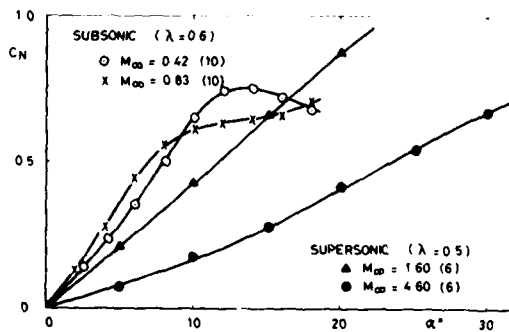
FIG. 8 - Normal force coefficients for trape-
zoidal wings as a function of incidence.
AR = 2.0
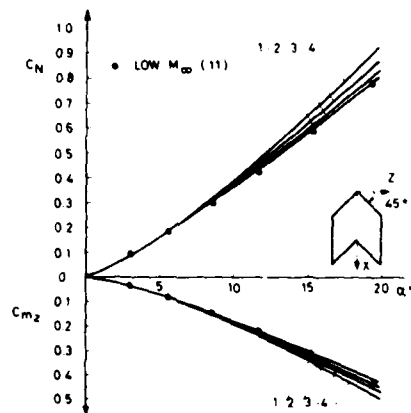
FIG. 9 - Predictions of normal force
and pitching moment using a
vortex lattice model (Ref. 8)
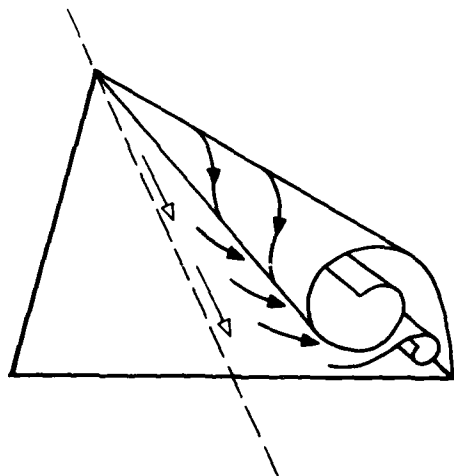
FIG. 10 - Schematic of leeside vortices
on a delta wing
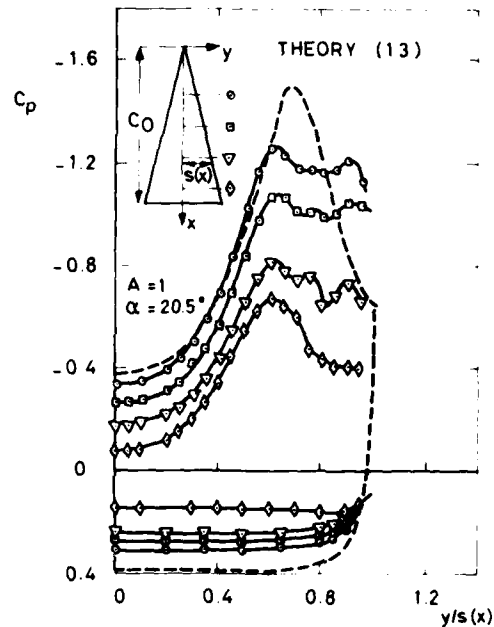
FIG. 11 - Pressure distribution on a delta
wing in low speed flow (Ref. 12)
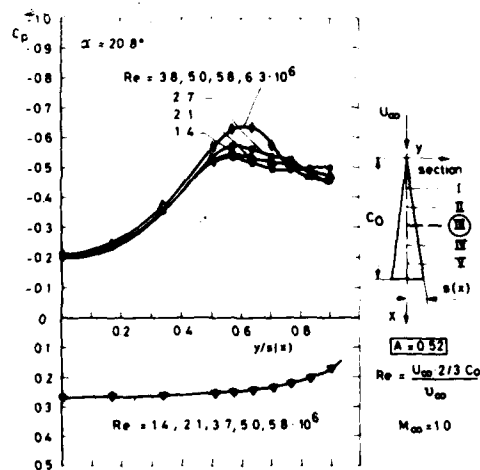
FIG. 12 - The effect of Reynolds number on
the leeside pressure distribution
of a delta wing (Ref. 14)
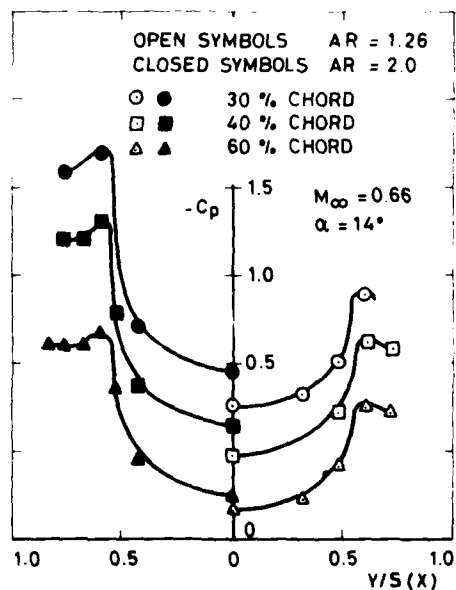
FIG. 13 - The effect of aspect ratio on the
leeside pressure distribution of
a delta wing (Ref. 15)
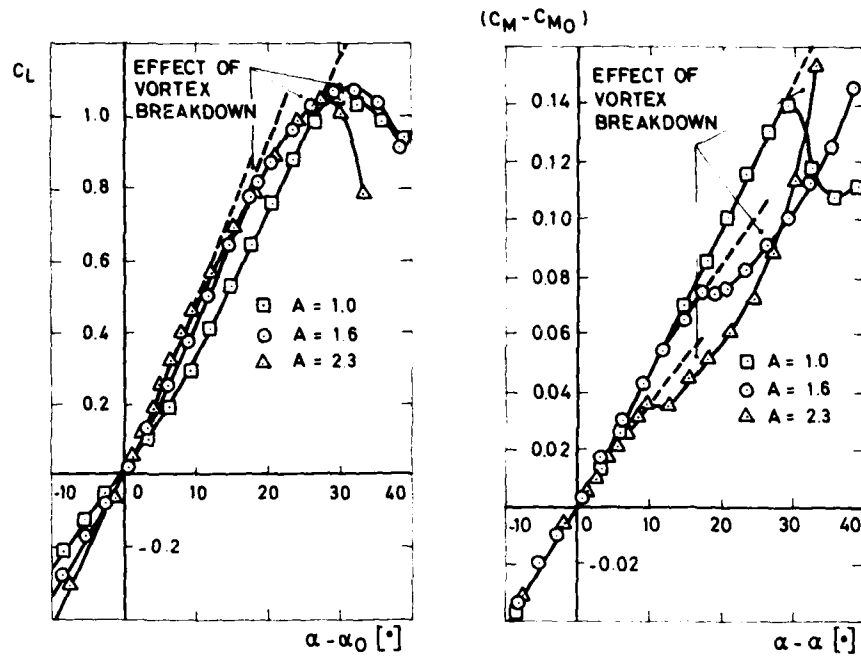
FIG. 14 - Lift and pitching moment of a delta wing in low speed flow for various
aspect ratios (Ref. 16)
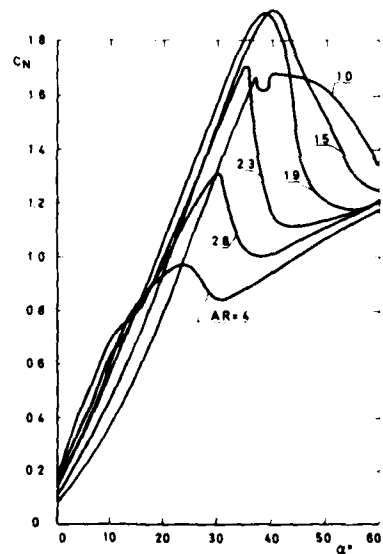
FIG. 15 - Normal force coefficient of a
delta wing for various aspect
ratios in a low speed flow
(Ref. 17)
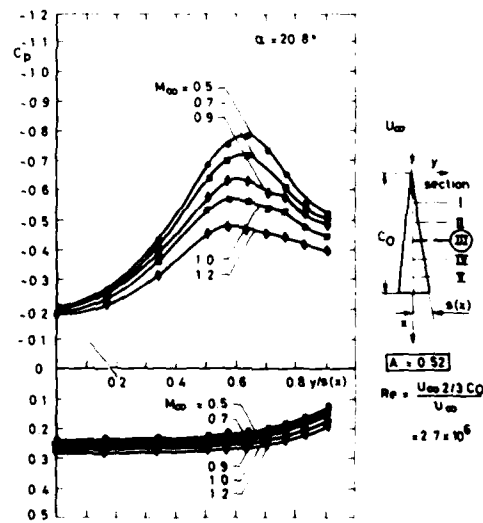
FIG. 16 - The effect of Mach number on the
leeside pressure distribution of
a delta wing (Ref. 14)

LENGTH OF U_∞ VECTOR FOR COMPARISON: ⊢——⊣

AR = 2.0
M_∞ = 0.62
α = 10°
X/C = 0.8
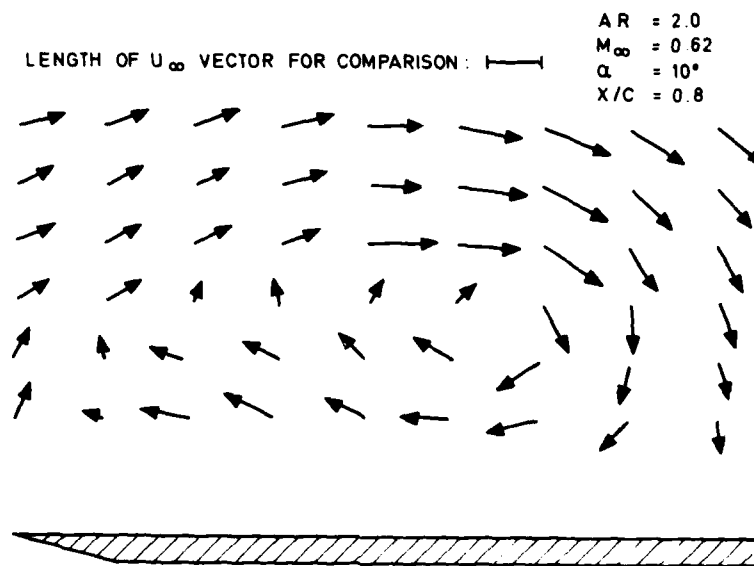
FIG. 17 - Cross flow velocities on the leeside of a delta wing in a compressible
flow as deduced by laser velocimetry (Ref. 18)
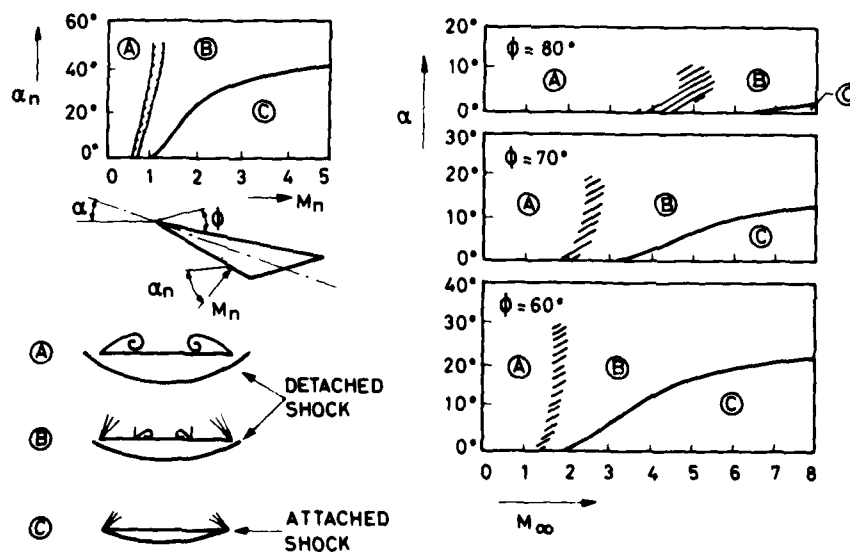
FIG. 18 - Flow fields on thin delta wings at supersonic speeds (Ref. 19)
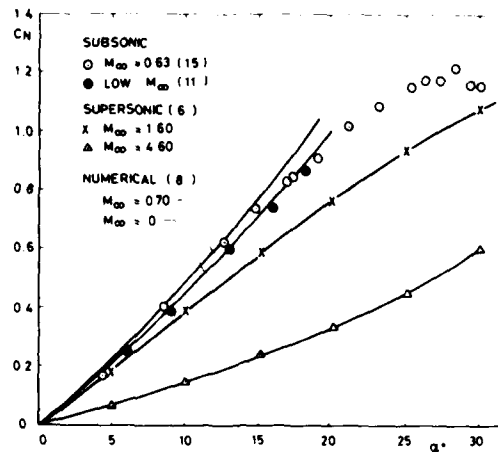
FIG. 19 - Normal force coefficient for a delta wing of AR=2 as a function of incidence for subsonic and supersonic Mach numbers
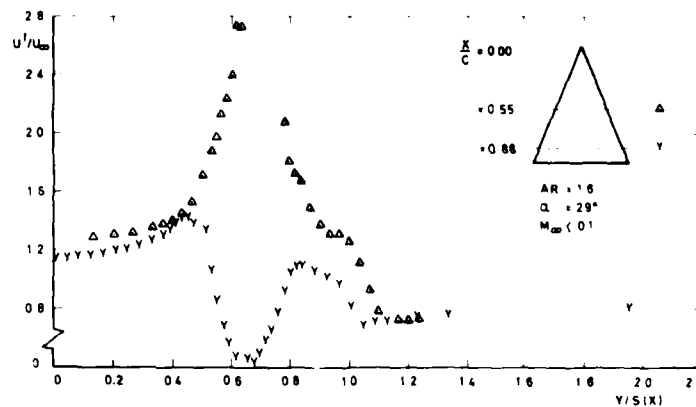
FIG. 20 - The spanwise variation of the (nearly) axial velocity component in a delta wing vortex at two chordwise locations, illustrating vortex breakdown (Ref. 24)
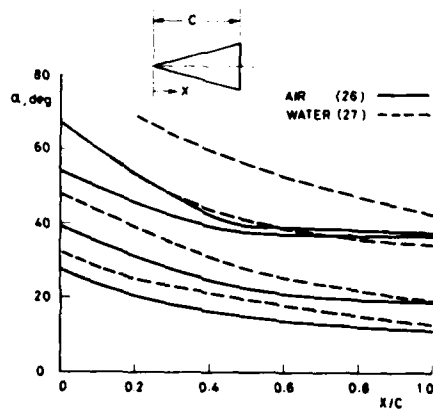
FIG. 21 - The location of the point of vortex breakdown as a function of incidence on delta wings of various sweepback angles (Ref. 25)
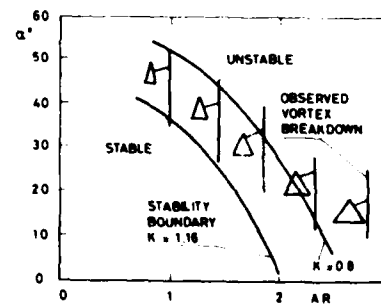
FIG. 22 - Stability boundary for vortex breakdown on a delta wing (Ref. 29)
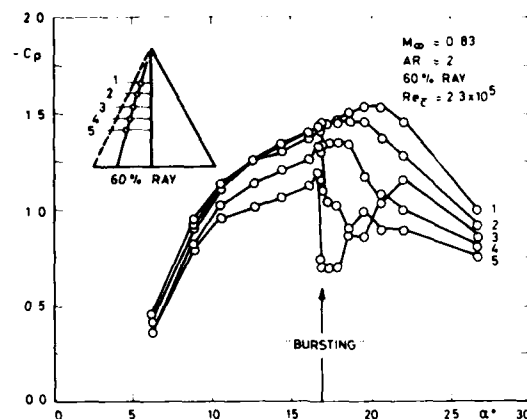
FIG. 23 - The effect of vortex bursting on the pressure distribution of a delta wing (Ref. 15)
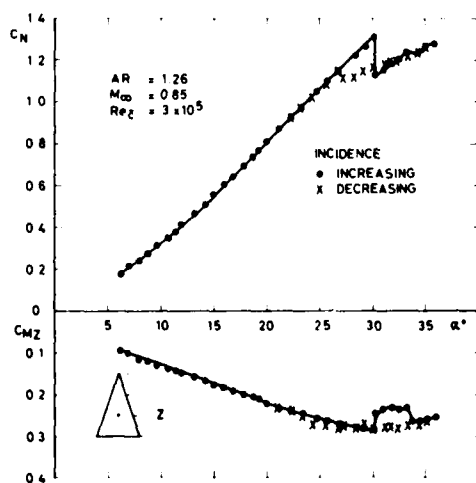
FIG. 24 - Hysteresis effect on normal force and pitching moment of a delta wing (Ref. 31)
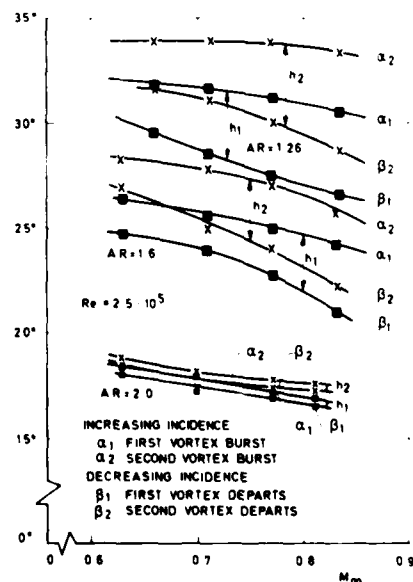
FIG. 25 - Vortex bursting and hysteresis effects on delta wings of varying aspect ratio (Ref. 15)
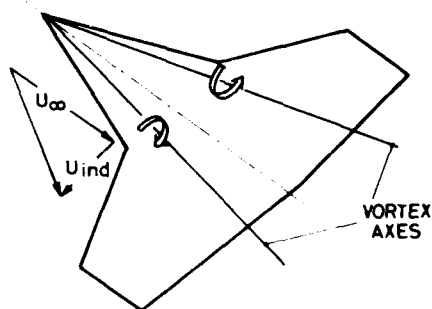
FIG. 26 - Schematic of a strake-wing

FIG. 27 - Strake and kink vortices as
observed in a water tunnel
(Ref. 36)
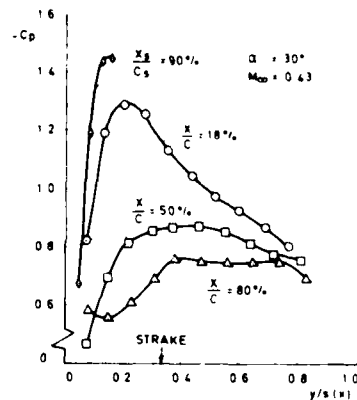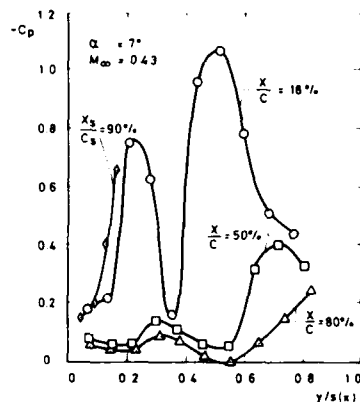
FIG. 28 - Surface pressure distributions on a strake-wing planform at 7° and 30° incidence
(Ref. 9)
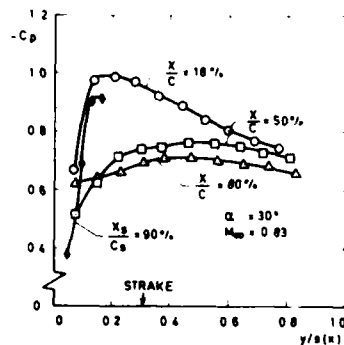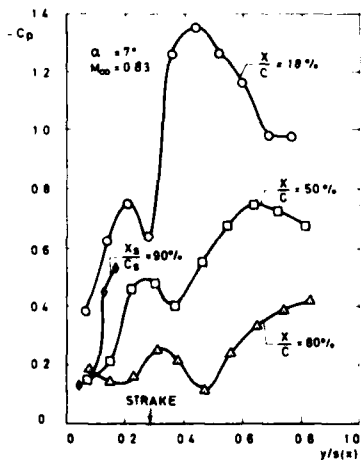
FIG. 29 - The effect of compressibility on the surface pressure distributions of a strake-
wing planform at 7° and 30° incidence (Ref. 9)
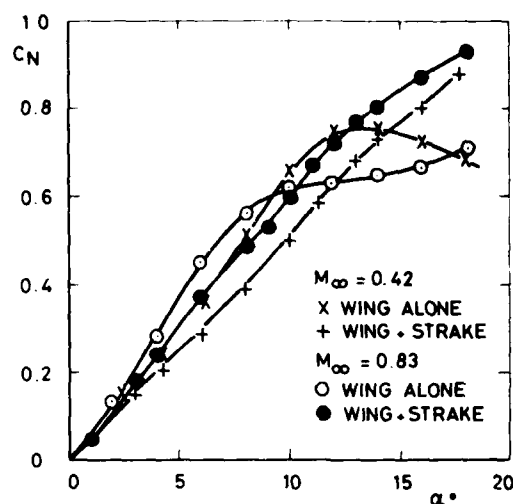
FIG. 30 - The effect of a strake on the normal force coefficient of a trapezoidal wing
Strake/wing area = 0.1
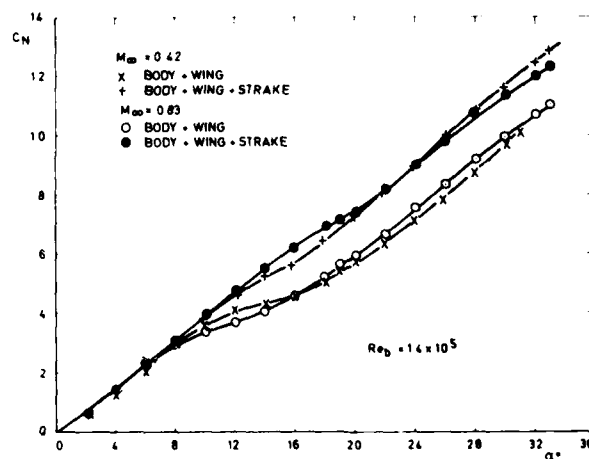
FIG. 31 - The effect of a strake on the normal force coefficient of a long-forebody
trapezoidal wing combination (Ref. 38)
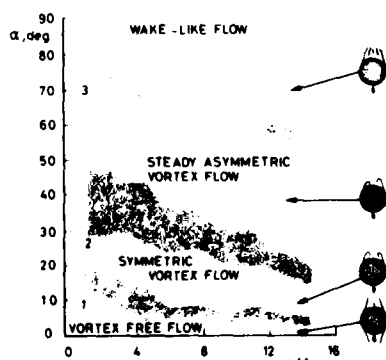
FIG. 32 - Flow field and onset boun-
daries for an ogive-cylinder
(Ref. 39)
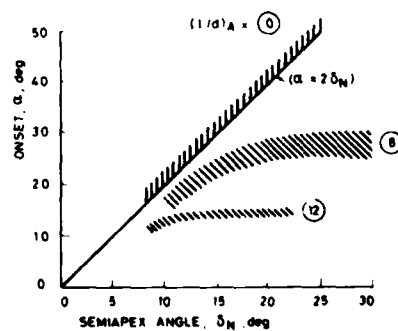
FIG. 33 - Boundaries for onset of aerodynamic
asymmetry for ogive-cylinders
(Ref. 39)

α = 20°

x/d = 11.6

α = 25°

x/d = 11.6

α = 30°

x/d = 11.6

α = 35°

x/d = 7.8
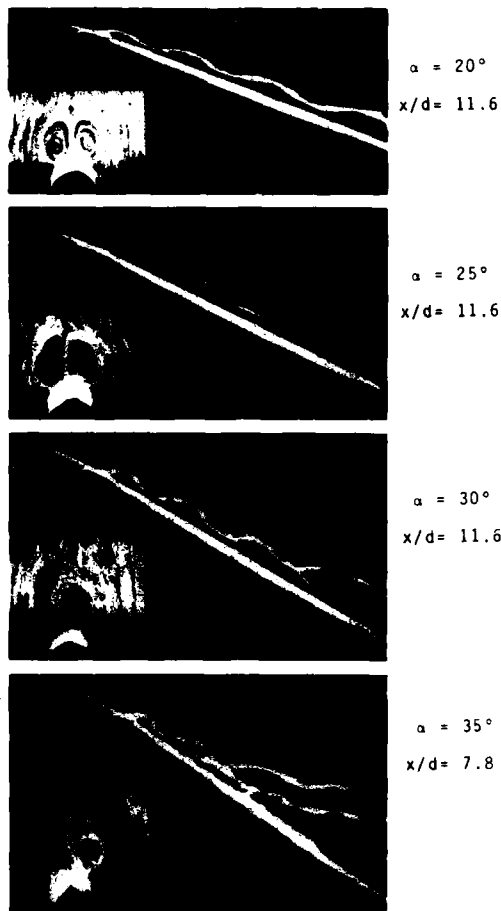
FIG. 34 - Flow around an ogive-
cylinder in a water tunnel
ℓ/d = 16   (Ref. 41)

FIG. 35 - The effect of Mach number on the
leeside flow field of an ogive-
cylinder body with ℓ/d ≈ 10 (Ref.42)
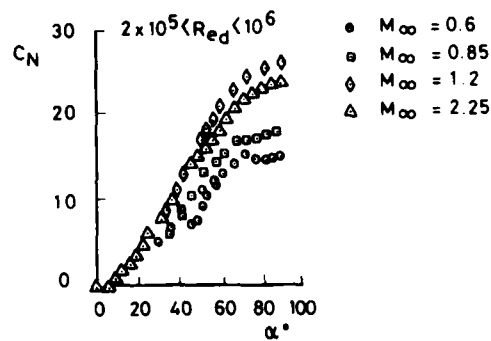
FIG. 36 - Variation of normal force coeffi-
cient of an ogive-cylinder with
incidence and Mach number;
ℓ/d ≈ 15   (Ref. 46)

FIG. 37 - Side force as a function of in-
cidence and Mach number on an ogive
cylinder (Ref. 47)
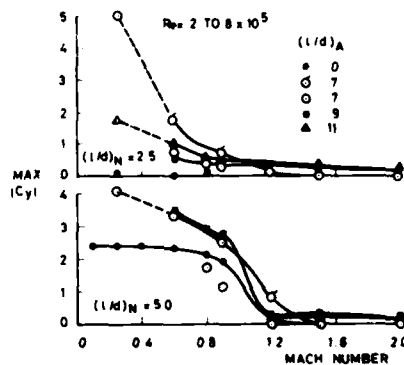
FIG. 38 - Maximum side forces on various
ogive cylinders (Ref. 39)

UNSTEADY AERODYNAMICS AND DYNAMIC STABILITY
AT HIGH ANGLES OF ATTACK

by

K.J. Orlik-Rückemann
Unsteady Aerodynamics Laboratory,
National Aeronautical Establishment,
National Research Council of Canada,
Ottawa, Ontario, Canada.

1. ABSTRACT

This lecture presents a review of some of the fluid dynamics phenomena that are associated with the oscillatory flight at high angles of attack, with particular emphasis on asymmetric shedding of forebody vortices, asymmetric breakdown of leading edge vortices, the oscillatory motion of such vortices, and the time lag between the motion of the vortices and that of the aircraft. These phenomena cause a number of important effects on the dynamic stability parameters at high angles of attack (high α), such as strong non-linearities with α, significant static and dynamic aerodynamic cross-coupling, large time-dependent effects and a strong configuration dependence. The importance of these effects on the prediction capabilities of aircraft behaviour at high α is discussed and some of the new wind tunnel testing techniques required to determine these effects are briefly described. The oral presentation is illustrated by several 16 mm movie films.

2. UNSTEADY AERODYNAMICS PHENOMENA

As already described in considerable detail in the other lectures in this series, an aircraft or a missile flying at high angles of attack experiences a variety of complex aerodynamic phenomena that usually are non-existent or have much less significance at lower angles of attack. These phenomena encompass all kinds of transitional, separated and vortical flows over the body, the wings and the control surfaces of the aircraft or missile. Of particular interest for this lecture are those flow phenomena that significantly vary with the angle of attack and that, at high enough values of that parameter, can cause asymmetric effects even if the aircraft itself continues to head symmetrically into the wind (i.e. has zero sideslip). Two of the most important phenomena of that kind are (1) formation and asymmetric shedding of forebody vortices and (2) formation and asymmetric bursting of wing leading-edge vortices.

The complexities of the development and the structure of vortical flows on stationary configurations at high angles of attack have already been discussed at some length in this Lecture Series. What makes the corresponding situation on oscillating configurations particularly involved is the introduction into this already complex picture of the time element. The forebody vortices will now change their lateral and vertical positions as functions of the angle of attack, which itself is a function of time. Similarly, leading-edge vortices will periodically vary the longitudinal location at which they burst. The various components of the aircraft or missile, such as the fin(s) and the horizontal stabilizer, will move in and out of the local flow regions in which they are embedded. To make matters even more complex, all these motions will take place not in a manner simultaneous with the motion of the aircraft, but with a certain delay, mainly due to the convective time lag. This delay is a function of the distance of the station under consideration (say, at the fin) from the station at which a particular flow phenomenon originates (say, at the vicinity of the nose, in the case of forebody vortices).

The response of the forebody vortices to the oscillatory pitching motion of a cone-wing configuration is illustrated by flow visualization motion pictures made in the NAE water tunnel. The periodic lateral motion of the vortices as well as the time delay between the motion of the vortices and that of the model are clearly visible. Another movie film, made in the Northrop water tunnel, shows the oscillatory longitudinal displacement of the location at which vortices emanating from the leading edges of a highly swept delta wing burst as the wing oscillates in roll (and as it thereby periodically increases or decreases the effective angle of attack on each half of the wing). The models in both these movie films are all the time at a zero angle of sideslip and the asymmetric phemonena just described occur only when the mean angle of attack is sufficiently high.

It should be noted that the above flight conditions are not the only ones under which asymmetric flow may occur on an aircraft. An additional, obvious flight condition of this kind is one when an aircraft flying at lower angles of attack is exposed to a finite angle of sideslip. Since this is encountered quite frequently, the remarks in this lecture that deal with the effects of flow asymmetries have a rather general application. As already discussed elsewhere in this Lecture Series the phenomenon of vortex burst is quite sensitive to the sweep angle of the wing and therefore is also strongly dependent on the angle of sideslip. An aircraft flying at an angle of attack sufficiently high for the occurrence of vortex bursts on the wings, will experience a differential longitudinal displacement of the vortex burst location on its two wings in response to a changing angle of sideslip, such as occurs during an oscillation in yaw, roll, or a lateral oscillation. Even if an aircraft flies at an angle of attack below the one for the onset of vortex bursts, an oscillatory variation in the instantaneous angle of

sideslip may under some circumstances cause a corresponding periodic occurrence and differential longitudinal displacement of the vortex bursts. In this regard a high angle of attack can to some extent be considered equivalent to a combination of a somewhat lower angle of attack and a finite angle of sideslip.

Similarly to what is the case in *steady* high-α flight conditions, also the *oscillatory* aerodynamic phenomena at high α exhibit significant dependence on both the Mach number and the Reynolds number. For instance, on a pointed slender body the vortex-induced lateral reactions decrease with an increasing subsonic crossflow Mach number above 0.4 and become insignificant at supersonic crossflow Mach numbers. The maximum such reactions occur at a critical Reynolds number where subcritical conditions prevail on one side and supercritical on the other. On a body at zero sideslip these vortex-induced asymmetric reactions can often be reduced and sometimes even eliminated by the use of small nose bluntness, nose boom, nose strakes or forebody trips. Reynolds number effects on vortex shedding can be further modified by the body motion, such as spin, coning or pitching, particularly so in situations where boundary layer transition is present.

3. EFFECTS ON DYNAMIC STABILITY PARAMETERS

The aforementioned high-α flow phenomena have large effects on all the aerodynamic characteristics of the aircraft including, of course, the static and dynamic stability parameters. For dynamic stability considerations, which are the subject of this lecture, the most important such effects are:

(a) large non-linear variations of stability parameters with angle of attack, angle of sideslip and rate of coning,

(b) significant aerodynamic cross-coupling between longitudinal and lateral degrees of freedom,

(c) time dependent and hysteresis effects,

(d) strong configuration dependence.

We will now discuss these effects in some detail, following - to a considerable extent - the presentation of Ref. 1 by the present author.

3.1 Non-linearities with Angle of Attack

Large variations with the angle of attack of the various complex flow features discussed in the previous section frequently cause significant non-linearities in the dynamic stability parameters. Some examples of these non-linearities are presented in Fig. 1. In the top row, the three damping derivatives are shown, as measured at NAE for a wing-body configuration at a Mach number of 0.7 (Refs. 2-3). The curves amply illustrate both the magnitude and the suddenness of the variations with angle of attack. It can be appreciated that if the angle of attack about which the oscillation takes place happens to be in the region where a sudden change in a derivative occurs, large effects of the amplitude of oscillation may be expected. In cases like this the derivative concept can only give an equivalent linearized description of the dependence of the aerodynamic reaction on the variable of motion and a better mathematical formulation may be needed.

Non-linear effects were also measured at NASA Langley (Ref. 4) for fighter aircraft at low subsonic speeds (Fig. 1b). The damping-in-yaw derivative exhibits a very sudden and very large unstable peak at angles of attack about 60°. This is usually the result of the vortex pattern that is associated with long, pointed forebodies. The damping-in-roll derivative shows marked irregularities and a large dependence on the amplitude of oscillation at angles of attack between 25° and 45°. The smaller the amplitude of oscillation, the more pronounced is the local instability in roll. It has also been observed (although not shown here) that a decreasing oscillation frequency sometimes has a similar destabilizing effect. These results are probably associated with the flow separation and loss of lift on the downward-moving wing and, in some cases, may be responsible for the occurrence of wing rock.

Equally dramatic non-linearities with angle of attack occur also in other dynamic derivatives, such as the familiar cross derivatives (Ref. 5) between the rolling and yawing degrees of freedom shown at the bottom of Fig. 1. It is interesting to note from Ref. 5 that the angle of attack at which these peaks occur is largely independent of both the wing sweep angle and the presence of vertical tails. (The height of the peak, however, is decreased when the vertical tails are off and when the reduced frequency is increased.) This suggests that the primary mechanism for these effects is associated with the existence and motion of the forebody vortices.

A set of yawing and rolling moment derivatives obtained from rotary-balance experiments for a current combat aircraft (Ref. 6) is shown in Fig. 2. The measured roll damping compares favourably with flight test data (up to 20°), but shows a non-linear behaviour at higher angles of attack which is different from estimates based on static wing pressure measurements. The measured yawing moment derivative, on the other hand, shows a much smoother variation with angle of attack than the predicted one, but exhibits a well pronounced peak totally absent in the estimates. In both cases the non-linearities are significant and, on the whole, not satisfactorily predicted.

3.2 Non-Linearities with the Rate of Roll (Spin, Coning)

Considerable non-linearities with spin rate, together with important effects of both angle of attack and Reynolds number are shown in Fig. 3, where the nose side-force coefficient for a model with a square forebody cross-section but with rounded corners is shown as a function of the spin rate at $\alpha = 75°$ and for various Reynolds numbers. These experiments, performed at Ames Research Center (Ref. 7), show a strong non-linear pro spin contribution at all but the two lowest Reynolds numbers investigated. No such pro-spin contributions were detected at $\alpha = 45°$.

Another example (from Ref. 8) of large non-linearities with spin rate is shown in Fig. 4. Pitching, rolling and yawing moments for a series of general aviation models at $\alpha = 60°$ are shown versus reduced spin parameter. The non-linearity is pronounced and the sense of the rolling and yawing moments can change with rotation rate from auto-rotative to damping. The pitching moment increases by as much as 50 percent over the static value, primarily due to the effect of the horizontal tail.

3.3 Non-linearities with Angle of Sideslip

An interesting set of rolling moment data as functions of the reduced roll parameter was recently obtained at the Langley Research Center (Ref. 9). The data were determined by means of rotary-balance experiments (in which the rotation takes place about the wind axis) at several values of the angle of attack (α) and of the angle of sideslip (β). Some examples of the results are shown in Figs. 5-7. It can be seen that the rolling moment varies linearly with the reduced roll rate at lower angles of attack but becomes non-linear at $\alpha = 30°$. The slope of the curves represents the damping in roll and is negative for positive (stable) damping and vice-versa. At $\alpha = 10°$ the damping is positive for all β investigated. At $\alpha = 20°$ and 30° the damping is negative at small β but positive at higher β. A set of curves (Fig. 8) constructed by combining the above results with the results of some forced-oscillation experiments shows the variation of the damping in roll with the magnitude of sideslip for different angles of attack. The damping in roll changes from unstable to stable in the range of 5° to 7° of sideslip. Concurrent flow visualization studies have indicated that this effect is associated with the upward displacement of the leeward vortex from the surface of the upgoing part of the wing, while the windward vortex remains close to the upper surface of the wing. A non-linear simulation using the data of Fig. 8 yielded a wing-rock motion in close agreement with the results of a free-to-roll experiment, as can be seen in Fig. 9 where the comparison is shown in terms of the limit cycle amplitude, $(\Delta\phi)_{WR}$, and the period, P_{WR}, of the wing rock observed at various angles of attack. Fig. 9 also shows the results of an approximate analytical solution based on a simplified linear variation of the damping in roll with the magnitude of sideslip.

3.4 Aerodynamic Cross-Coupling

The high-α flow phenomena discussed in Section 2 illustrate cases where (a) *lateral* aerodynamic reactions (such as those caused by the lateral motion of the forebody vortices) may occur on an aircraft as the result of some *longitudinal* motion such as pitching or vertical translation, and where (b) *longitudinal* aerodynamic reactions (such as those caused by the longitudinal motion of the vortex burst locations) may occur on an aircraft as a result of some *lateral* motion, such as rolling, yawing or lateral translation. Because of this relation between the longitudinal and lateral degrees of freedom, the above aerodynamic reactions can be said to represent the aerodynamic *cross-coupling* between the longitudinal and lateral degrees of freedom. As already mentioned, the cross-coupling reactions are in general shifted in time in relation to their causative motions and therefore will have components which are both in phase and in quadrature with these motions. When related to the causative displacements and their time rates of change, these components of the cross-coupling reactions become static and dynamic *cross-coupling derivatives*, respectively. (The term *cross derivatives* should, however, still be used to denote the traditional derivatives that relate two lateral degrees of freedom, such as roll and yaw.) It should be noted that the introduction of cross-coupling derivatives requires simultaneous consideration of *all* the equations of motion of an aircraft, rather than of separate groups of equations for the longitudinal and for the lateral motions, as often done in the past.

The concept of aerodynamic cross-coupling, especially in relation to the *dynamic* stability derivatives, was introduced only relatively recently (Ref. 10). New experimental capabilities had to be developed to permit the measurement of the pertinent derivatives. Some of these new apparatuses are briefly described in Section 6. So far, only relatively few measurements of this kind have been performed. Some examples of the dynamic cross-coupling derivatives obtained on simple wing-body-fin configurations (Refs. 3 and 11) are given in Fig. 10. From top to bottom, the dynamic yawing and rolling moment derivatives due to oscillation in pitch are shown, followed by the dynamic pitching moment derivatives due to oscillations in yaw and in roll. The angle of sideslip in these examples varies. In all cases, the derivatives are relatively small for low angles of attack but attain large values and display sudden variations at angles of attack between 15° and 20°, and - except for the bottom example, which was obtained for a slightly different configuration - become quite irregular at higher angles of attack, especially in the region between 32° and 38°. Both the levels attained and the suddenness of variations is larger for the derivatives of the lateral moments due to oscillation in pitch than for the pitching moment derivatives due to oscillations in yaw and in roll. It should be noted that these cross-coupling derivatives may be of the

same order, and sometimes even larger, than the corresponding traditional damping derivatives (except for the damping-in-pitch derivatives at high angles of attack), such as previously shown in Fig. 1. The same conclusion can also be reached when comparing, instead of the derivatives, the corresponding terms in the pertinent equations of motion (Ref. 2).

As can be expected from basic aerodynamic considerations, the direct and the cross derivatives should be symmetrical with respect to zero angle of sideslip, whereas the cross-coupling derivatives should change sign with the direction of sideslip. This is demonstrated in Fig. 11, where the three dynamic moment derivatives due to oscillation in roll are plotted as functions of the angle of sideslip. The antisymmetric variation of the cross-coupling derivative with the angle of sideslip is clearly visible. Another example of such a variation is given in Fig. 9 of Ref. 2.

3.5 Time-Dependent Effects

In addition to *quasi-steady* effects, such as represented by derivatives of various aerodynamic reactions due to angular velocities, we have to consider the existence of purely *unsteady* effects, such as those represented by derivatives due to the time rate of change of angular deflections, $\dot{\alpha}$ or $\dot{\beta}$. These derivatives have been known for many years, since they constitute part of the dynamic results obtained with standard wind-tunnel techniques of oscillation around a fixed axis, which always give composite derivative expressions such as $(C_{mq} + C_{m\dot{\alpha}})$. Up to now, however, it was standard practice to ignore the $\dot{\alpha}$ and $\dot{\beta}$ effects (or to introduce a simple correction for them) and to use the composite derivatives in place of the purely rotary ones. At low angles of attack the error introduced by such a procedure was often small and the simplification large enough to be justifiable.

At higher angles of attack, however, the $\dot{\alpha}$ and $\dot{\beta}$ effects unfortunately become quite substantial and can no longer be ignored or corrected for in a simple fashion. This is illustrated in Fig. 12, where the composite derivatives obtained from oscillatory experiments around a fixed axis are compared with purely rotary derivatives obtained from experiments in a curved or a rolling flow (Ref. 12). The difference between the two sets of results represents the unsteady effects due to the time rate of change of the angular deflection (in this case of the angle of sideslip) and becomes quite significant for higher angles of attack.

Derivatives due to the time rate of change of angular deflections are aero-dynamically equivalent (in the first approximation) to derivatives due to *translational acceleration* in the same plane of motion. This fact renders them of high interest for aircraft designs using direct-lift or direct side-force controls and also makes it possible to determine them experimentally using a translational oscillatory motion in the vertical or lateral direction. Because of this relation, $\dot{\alpha}$ and $\dot{\beta}$ derivatives are often referred to as *translational acceleration derivatives*.

3.6 Hysteresis Effects

High angle-of-attack flow phenomena such as asymmetric vortex shedding and vortex breakdown (burst) are frequently responsible for aerodynamic hysteresis effects. Such hysteresis is characterized by a double-valued behaviour of the steady-state aerodynamic response to variations in one of the motion variables such as angle of attack, angle of sideslip or spin rate. Fig. 13 shows an α-hysteresis in the variation of location of the vortex burst on a delta wing (Ref. 13) and an example of β-hysteresis in the varia-tion of lateral aerodynamic coefficients for an aircraft configuration (Ref. 14). Fig. 14 shows an example of an Ω-hysteresis in the side-force coefficient on a previously-mentioned (Section 3.2) square forebody with rounded corners (Ref. 7) rotating at $\alpha = 90°$ (flat spin). [This hysteresis effect was not observed at $\alpha = 75°$ and below, and even at $\alpha = 90°$ it occurred only in a relatively narrow range of Reynolds number.] Another illustration of hysteresis effects is the delayed lateral motion of the forebody vortices in response to pitching oscillation, as shown in the NAE water-tunnel movie films, referred to in Section 2.

In the presence of such hysteresis effects the dynamic characteristics of an air-craft can be expected to be strongly dependent on both the amplitude and the frequency of oscillation. When conducting experiments in the critical range of, say, $25° < \alpha < 40°$, it is advisable to obtain data (both static and dynamic) in very small increments of angle of attack. Dynamic data may have to be determined not only at the frequency of the primary motion but also at higher harmonics.

3.7 Configuration Dependence

The intricate vortex pattern that exists around an aircraft configuration at high angles of attack is very sensitive to even small changes in aircraft geometry. So is the behaviour of this vortex pattern on an oscillating configuration. The forebody vortices are greatly dependent on the planform and the cross-sectional geometry of the aircraft nose as well as on the presence of various forms of protuberances on the fore-body that may affect the stability of an existing vortex pattern, give rise to new vortices and create conditions for strong vortex interactions. The wing leading-edge vortices, in addition to being a strong function of the leading edge sweep as discussed before, are also known to be greatly affected by various leading-edge modifications, such as apex drooping, discontinuities or contouring, and by various modifications of the wing itself, such as addition of wing leeside fences and deflections of leading-

edge or trailing-edge flaps. All these variations of the geometry of a wing affect not only the position and the strength of the wing vortices but also the all-important location at which these vortices break down.

The most common modification of the aircraft geometry intended to eliminate or to delay the onset of asymmetric effects is the use of forebody strakes. These strakes are often combined with leading edge extensions (the so-called LEX) or with some suitable modifications of the shape of the forebody. An example is presented in Fig. 15, where the effect of a flat, broad nose (called the "Shark Nose") developed by Northrop (Ref. 14), on the variation with angle of attack of the dynamic directional stability parameter, $C_{n\beta_{DYN}}$, is shown. The Shark Nose geometry attenuates the unfavourable local reduction in that parameter and at the same time extends this favourable influence on stability to somewhat lower angles of attack. It has also been demonstrated in Ref. 14 (but is not shown here) that the presence of Shark Nose enhances greatly the directional stability at small non-zero angles of sideslip ($|\beta| < 5°$).

A common method of ensuring a symmetrical shedding of forebody vortices at zero sideslip is, of course, the use of forebody strakes. Although, when used alone these strakes often prevent the formation of a unique vortex pattern at non-zero sideslip, thereby seriously reducing the directional stability of the configuration, they can be amazingly effective when used in combination with a suitable nose geometry. Fig. 15 presents the effect of the Shark Nose used together with a particular leading edge extension (LEX), which can be considered to be a form of strake. It can be seen that the negative peak in $C_{n\beta_{DYN}}$ is almost totally eliminated and that the favourable influence on stability now extends to both lower and higher values of angle of attack.

The effect of strakes (or leading edge extensions) on various dynamic stability derivatives is presented in Fig. 16. In all cases the addition of strakes reduces the magnitude of derivatives, practically eliminates non-linearities with angle of attack in the range investigated (except for pitch damping derivative), and makes the derivatives independent of reduced frequency (Ref. 15). The dynamic yawing derivative due to rolling becomes essentially zero. The negative damping in roll (for $\alpha > 13°$), in pitch (for $12 < \alpha < 23°$) and in yaw (for $\alpha > 11°$) completely disappears. It should be noted, however, that the range of angle of attack investigated extends only to $\alpha = 25°$, and that the results have been obtained for only four values of α, leaving the possibility of existence of undetected peaks.

As is well-known, however, strakes do have certain disadvantages. Their success-ful development for a particular application may require much trial and error. They often adversely affect the directional stability. If mounted near the tip of the nose radome, they may disturb the radar operations. The strake vortices may adversely inter-act with aircraft components further downstream, such as air intakes or control surfaces. Therefore, alternative approaches continue to be of high interest.

4. SENSITIVITY OF HIGH-α AIRCRAFT MOTION TO DYNAMIC STABILITY PARAMETERS

Several studies have recently been carried out on the sensitivity of the predicted aircraft (or missile) motion at high angles of attack to the inclusion in the equations of motion of the cross-coupling and acceleration ($\dot{\alpha}$ and $\dot{\beta}$) derivatives and of the taking into account the various non-linear effects. These studies were reviewed in Ref. 16, from which some examples will be included in the present lecture.

Sensitivity studies are usually carried out (a) by programming, on a computer, a complete set of equations of motion pertinent to a particular configuration and particular flight condition, (b) by inserting a set of stability parameters, including – if required – some non-linear effects, (c) by varying those parameters in a pre-determined manner, and (d) by observing the responses of the variables of motion to some form of disturbance applied to the set of equations. The stability parameters are usually varied individually, but may also be studied in combinations. The difference between responses obtained for two different values of a parameter or for two different combinations determines the sensitivity of the aircraft behaviour to the variation of that particular stability parameter or that particular combination of parameters.

As already discussed, both the cross-coupling and the acceleration derivatives, and in fact most of the other derivatives as well, display significant non-linear effects at higher angles of attack. Since an analytical description of the variation of a derivative with angle of attack may be rather complex, it is often more practical to limit the range of angle of attack for which the analytical description is made to the immediate vicinity of the equilibrium angle of attack and to assume that the derivative varies linearly with α in that narrow range of angle of attack. Such a locally linearized derivative can then be written as a + b ($\alpha - \alpha_T$), where α_T is the trim (or equilibrium) angle of attack.

Dynamic derivatives that are subject to a sensitivity study are often varied in a relatively wide range, such as from zero to perhaps twice the nominal value including, in some cases, also a change of sign. It is important that during such a variation the remaining derivatives be kept at their nominal values rather than zero, otherwise gross misrepresentation and, in some cases, even an erroneous elimination of the effect of a given derivative may result. Sometimes there may be some interest in investigating the effect of a whole group of derivatives such as cross-coupling derivatives, by including

or excluding the entire group all at once. In cases involving composite derivatives it is often of interest to divide the total value between the two component parts in different proportions and to insert the resulting two derivatives at their proper place in the equations of motion, as purely rotary and purely time-rate-of-change or acceleration effects.

As already shown many years ago (Ref. 17), the inclusion or omission of the $\dot{\beta}$ derivatives in theoretical equations of motion can produce large differences in the calculated dynamic stability characteristics. In particular, it was shown that when composite derivatives obtained from oscillation experiments around a fixed axis were used in place of the pure angular-rate derivatives and when the $\dot{\beta}$ derivatives were assumed to be zero, the results varied significantly from the results obtained when all pure derivatives (both angular-rate and lateral-acceleration derivatives) were used at their proper place in the equations of motion. A further illustration of these results was provided in Ref. 18, where calculations - using three-degree-of-freedom linearized equations - were made for a hypothetical delta-wing fighter configuration in trimmed flight at $\alpha = 20°$ and $\alpha = 28°$. The purely rotary derivatives used were obtained by the curved-flow and rolling-flow test techniques, and the lateral acceleration derivatives by a lateral oscillation test technique.

The results are shown in the table in Fig. 17. In Case 1 the true values of the purely rotary derivatives were used and the $\dot{\beta}$ derivatives were omitted. In Cases 2 to 4, both the purely rotary and the $\dot{\beta}$ derivatives were correctly included. In Cases 5 to 7 the $\dot{\beta}$ derivatives were added to the purely rotary ones to form composite derivatives, similar to those that would result from oscillation around a fixed axis. These composite derivatives were then used in place of the purely rotary derivatives and the $\dot{\beta}$ terms in the equations were set equal to zero.

It can be seen from Fig. 17 that the inclusion and the proper use of the $\dot{\beta}$ derivatives, although of only minor significance at $\alpha = 20°$ where the $\dot{\beta}$ derivatives were rather small, had a very pronounced effect at $\alpha = 28°$ where these derivatives were relatively large. In particular, when the derivatives were used properly (Cases 2 to 4), the Dutch roll mode was absent, the roll mode was virtually neutrally stable, the spiral mode was very unstable and two additional aperiodic modes were indicated. This should be compared with Cases 5 to 7, where the improper use of the derivatives resulted in an erroneous indication of a highly unstable Dutch roll mode, highly stable roll and spiral modes, and no aperiodic modes.

The significance of cross-coupling moment derivatives was studied in Ref. 19 and is illustrated in Fig. 18. The measured values of composite derivatives were equally distributed between their rotary and acceleration parts. The non-linear effects were taken into account by local linearization. The cross-coupling derivatives due to oscillation in roll were unknown at the time of the analysis and therefore set equal to zero. The various angular rates ($p,q,r,\dot{\alpha}$ and $\dot{\beta}$) are shown as functions of time after an initial disturbance in the angle of attack (Fig. 18a) and angle of sideslip (Fig. 18b). The constant angular rates for the unperturbed case (p_o, q_o, r_o) are also shown. Had the cross-coupling derivatives not been included, the rates p, r and $\dot{\beta}$ in Fig. 18a and the rates q and $\dot{\alpha}$ in Fig. 18b would have remained essentially constant. It can be seen that the departures of p, r and $\dot{\beta}$ in Fig. 18a from their constant values is much larger than the corresponding departures of q and $\dot{\alpha}$ in Fig. 18b, indicating a much larger effect of the cross-coupling derivatives of the rolling and yawing moments due to pitching than of the cross-coupling derivatives of the pitching moment due to yawing. Fig. 18 pertains to a 2g turning flight at $\alpha = 33°$.

Although this lecture is mainly concerned with stability and motion of *aircraft*, a brief mention has to be included about the corresponding studies related to the motion of *missiles*. A comprehensive investigation of missile motion sensitivity to dynamic stability derivatives has recently been completed (Ref. 20). In that investigation the importance of dynamic stability derivatives for the simulation of motion of both bank-to-turn and yaw-to-turn missile configurations was examined, using a six-degree-of-freedom linearized stability programme.

Among the most pronounced effects due to the variation of a dynamic cross-coupling derivative was that due to the variation of C_{l_q} at high Mach number, high load factor and relatively low altitude. Sample results showing the influence of that derivative on the simulated motion of the yaw-to-turn missile are shown in Figs. 19 and 20. It can be seen that the short period (S/P), dutch roll (D/R) and roll (R) modes are quite sensitive to the variation of C_{l_q} over the range ±500 (per radian) and that the dutch roll sensitivity increases with an increasing load factor (Fig. 19). Even a variation of C_{l_q} within a much more narrow range (0 to -50) results in a large effect on the roll rate time history (four times higher roll rates at $C_{l_q} = -50$ than at $C_{l_q} = 0$), as shown in Fig. 20.

On the basis of sensitivity studies such as those described above and on the basis of some additional studies included in Ref. 16, it has been shown that the inclusion in the equations of motion of the cross-coupling derivative C_{l_q} (and to a lesser extent C_{n_q}) and of the acceleration derivatives $C_{l_{\dot{\beta}}}$ and $C_{m_{\dot{\alpha}}}$ may be important for the correct prediction

of the behaviour of aircraft and missiles at high angles of attack. It was shown in these studies that the aforementioned derivatives in some cases could have an effect on the predicted motion that was as large as that of some of the well-known damping and cross derivatives. It was also shown that it is important to be able to separate the purely rotary and the acceleration derivatives and use them in their proper places in the equations. Furthermore, it was found that the cross-coupling derivative C_{m_p} is

relatively important for missiles but less so for aircraft, and that the cross-coupling derivative C_{m_r} appears to be insignificant in both these cases.

5. MATHEMATICAL MODELLING

The mathematical modelling used in most countries at the present time to describe the aircraft flight history applies strictly to flight at small to moderate angles of attack, where non-linearities are small, time-dependent effects insignificant and aero-dynamic cross-coupling non-existent. In view of the complexity of the aerodynamic phenomena reviewed in Sections 2 and 3 and the effects on the forces and moments that govern the behaviour of flight vehicles at high angles of attack a much more sophisticated modelling is obviously required.

Substantial progress has recently been made in this area. A generalized formulation which includes the non-linear pitch-yaw-roll coupling and non-linear coning rates is now available (Ref. 21). Time-history and hysteresis effects have now also been included in that formulation (Refs. 22 and 23). Among things still to be done is an adequate modelling of the suddenness with which the aerodynamic reactions may vary with the angle of attack or sideslip, and a satisfactory verification of some of the more advanced mathematical models. The verification should be conducted by determining a complete set of stability parameters for a particular configuration, by predicting a series of maneuvers and by comparing them with the actual flight histories. One of the principal difficulties in conducting such a verification at the present time is the lack of complete static and dynamic aerodynamic data for the required test cases.

6. NEW DYNAMIC STABILITY TEST TECHNIQUES

The determination of a complete set of static and dynamic stability data for a test case of a high-angle-of-attack flight requires the development and the availability of novel test techniques with the following, greatly expanded capabilities:

· to test at high angles of attack, and to carry the associated high loads,

· to measure dynamic cross-coupling derivatives,

· to measure effects due to $\dot{\alpha}$ and $\dot{\beta}$,

· to measure effects due to coning and continuous rolling,

· to test at large amplitude of oscillation, particularly in the case of oscillation in roll

A fairly complete review of existing testing techniques for determination of dynamic stability parameters in a wind tunnel was given by the present author in Ref. 24. This review included the significant developments that have taken place in the last few years at several research establishments in various countries of the world, and notably those at NASA Ames, NASA Langley, AEDC, RAE Bedford, BAC Warton, DFVLR, ONERA and NAE. Since the development of experimental techniques plays such an important role in our progress towards obtaining better prediction capabilities of the aircraft behaviour in high-angle-of-attack flight, this topic clearly deserves to be mentioned in the present lecture. As an example, a brief account will be rendered of the techniques presently available at the National Aeronautical Establishment (NAE) in Ottawa, which may be considered as fairly representative of the new experimental trends in this field.

In Fig. 20 a list is presented of the presently available three full-model and two half-model apparatuses that can be used to study the primary oscillations in five degrees of freedom, providing means to determine all the moment derivatives and some of the force derivatives associated with these motions. Both static and dynamic derivatives are included and the list encompasses the direct, cross and cross-coupling derivatives, as discussed before. It should be noted that in all cases the derivatives are obtained from a *direct* measurement, which is based only on an assumed relation between the aero-dynamic reaction measured and the causative primary motion. Often this relation is linear, but can be replaced by a non-linear or higher order formulation, if the need arises. Since the motion is essentially in one degree of freedom, the measurement is independent of the remaining parts of the equations of motion and therefore the results may be expected to be valid for any formulation of these equations as long, of course, as the principle of superposition is still applicable, that is as long as the concept of stability derivatives can be used.

In all the full-model apparatuses the model is mounted on a balance that in turn is attached to an elastic support system capable of deflecting in the appropriate degree of freedom. The primary motion is imparted by an electro-magnetic drive mechanism which oscillates the model with a constant amplitude at the resonance frequency in the primary degree of freedom. Each balance has a multi-component capability (but always without

axial force) and is made in one piece - a most desirable feature for dynamic testing. Each drive mechanism utilizes a high-current coil (or coils) moving in a strong magnetic field that is generated by compact rare-earth permanent magnets. As a result, the apparatuses are relatively slender and permit testing of realistic models of current aircraft configurations. An example of the NAE oscillatory apparatuses is the present pitch/yaw apparatus, shown in Fig. 22.

The high complexity of the aforementioned techniques and the lack of any previous data on some of the recently identified dynamic derivatives made it necessary to develop a system that would independently verify the validity of the experimental technique and data-reduction methods employed. The same system was also conceived as a diagnostic tool to identify, on a regular basis, equipment faults or software errors. A pictorial view of such a system developed at NAE and called a *dynamic calibrator*, is shown in Fig. 23. The aircraft model is replaced on the dynamic stability apparatus by a special calibrating frame (or "rotor"), which is then oscillated in the primary degree of freedom by the drive mechanism of the apparatus. The inertia characteristics of the rotor duplicate, at least approximately, the inertia characteristics of the model, resulting in a similar dynamic response of the rotor and of the model in all three degrees of freedom. The three oscillatory aerodynamic moments, that act on the oscillating model during a wind tunnel test, are simulated by accurately known, electromagnetically induced, *alternating* loads, whose phase and amplitude can be adjusted at will. A comparison between the known applied loads and the outputs of the dynamic stability apparatus, obtained by processing the balance data and other relevant information by means of the same procedure as in the wind tunnel experiments, provides an overall calibration of the technique and of all the mechanical and electronic systems involved. Other dynamic calibrators, simpler but based on similar principles, have been developed for the half-model dynamic apparatuses.

A dynamic apparatus based on the principle of *orbital fixed-plane motion* (Ref. 25) is now being designed at NAE. An orbital motion is called a fixed-plane motion if the model is rotated in such a way that its transverse axis remains at all times in a plane that maintains a fixed orientation in the inertial frame of reference. The two special cases of that motion that are important for the determination of stability derivatives are illustrated in Fig. 24. These are:

(a) Pure Translation - the model performs a combination of a vertical oscillation *and* a lateral oscillation. The two motions are 90° out of phase. No rotation is involved. All the position angles are constant and all body angular velocities are zero. Only the aerodynamic angles are variable. With proper, rather complex, experimental procedures the dynamic derivatives due to $\dot{\alpha}$ and $\dot{\beta}$ can be determined.

(b) Pure Rotation - the model axis is tilted through the angle induced by the orbital motion; the model continuously follows the velocity vector during a circular translation. As a result, the model performs a combination of a pure pitching oscillation and a pure yawing oscillation. The two motions are again 90° out of phase. In the ideal case (not excessively large angles of attack), all the aerodynamic angles remain constant and the roll rate is zero. The dynamic derivatives due to pure pitching (q) and due to pure yawing (r) can be determined.

In addition, by suitably locking the model to the rotating sting, the apparatus may also be used for steady rolling and coning experiments. Thus, with a single apparatus and three experiments, it may be possible in the future to obtain all the moment derivatives due to p, q, r, $\dot{\alpha}$ and $\dot{\beta}$, i.e. the results for which at the present time three different apparatuses and five experiments are needed. With the model locked to the sting the apparatus will also be able to produce the aerodynamic coefficients as functions of rotation rate, i.e. the information normally obtainable from rotary-balance experiments.

7. CONCLUDING REMARKS

In this lecture a review was presented of some of the aerodynamic phenomena associated with the dynamic behaviour of an aircraft flying at high angles of attack and of the various effects that these phenomena have on the dynamic stability parameters of aircraft or missiles at those flight conditions. Although only very limited quantitative information on these effects is available at the present time, a tentative assessment was offered of the relative significance of the various effects and parameters. The deficiencies of the commonly-used mathematical models of the aerodynamics of high-angle-of-attack maneuvers were pointed out and the need was postulated for the development and verification of more sophisticated models, that would probably have to include significant non-linearities, aerodynamic cross-coupling and time-dependent effects. Finally, recent developments in the wind-tunnel techniques needed to provide the aerodynamic inputs required for such more advanced mathematical modelling were discussed and illustrated by examples of some of the novel techniques that have been and are being developed at the lecturer's laboratory.

8. REFERENCES

1. Orlik-Rückemann, K.J. "Dynamic Stability Parameters at High Angles of Attack", 12th Congress of the International Council of the Aeronautical Sciences, Munich, 12-17 October 1980, Paper 7.1, Proceedings, pp 265-277.

2. Orlik-Rückemann, K.J. "Aerodynamic Coupling Between Lateral and Longitudinal Degrees of Freedom", AIAA Journal, vol. 15, no. 12, pp 1792-1799, 1977.

3. Hanff, E.S., Orlik-Rückemann, K.J. et al. "New Oscillatory Roll Apparatus and Results on Direct, Cross and Cross-Coupling Subsonic Moment Derivatives for an Aircraft-Like Model", NRC, NAE LTR-UA-50, 1979.

4. Chambers, J.R., Gilbert, W.P. and Nguyen, L.T. "Results of Piloted Simulated Studies of Fighter Aircraft at High Angles of Attack", AGARD CP-235, Paper 33, 1978.

5. Grafton, S.B. and Anglin, E.L. "Dynamic Stability Derivatives at Angles of Attack From -5° to 90° for a Variable-Sweep Fighter Configuration with Twin Vertical Tails", NASA TN D-6909, 1972.

6. Matthews, A.W. "Experimental Determination of Dynamic Derivatives Due to Roll at British Aerospace, Warton Division", AGARD CP-235, Paper 4, 1978.

7. Malcolm, G.N. "New Rotation-Balance Apparatus for Measuring Airplane Spin Aero-Dynamics in the Wind Tunnel", Journal of Aircraft, vol. 16, no. 4, pp 264-268, 1979.

8. Birhle, W.,Jr. and Bowman, J.S., Jr. "Influence of Wing, Fuselage and Tail Design on Rotational Flow Aerodynamics Beyond Maximum Lift", Journal of Aircraft, vol. 18, no. 11, pp 920-925, November 1981.

9. Nguyen, L.T., Yip, L. and Chambers, J.R. "Self-Induced Wing Rock of Slender Delta Wings", AIAA-81-1883, August 1981.

10. Orlik-Rückemann, K.J. "Dynamic Stability Testing of Aircraft - Needs versus Capabilities", Proc. of International Congress on Instrumentation in Aerospace Simulation Facilities, ICIASF'73 Record, pp 8-23, 1973.

11. Orlik-Rückemann, K.J., Hanff, E.S. and LaBerge, J.G. "Direct and Cross-Coupling Subsonic Moment Derivatives due to Oscillatory Pitching and Yawing of an Aircraft-Like Model at Angles of Attack Up to 40° in Ames' 6' x 6' Wind Tunnel", NRC NAE LTR-UA-38, 1976.

12. Orlik-Rückemann, K.J. "Effect of High Angles of Attack on Dynamic Stability Para-meters", AGARD CP-247, Paper 1, 1978.

13. Lawson, M.V. "Some Experiments with Vortex Breakdown", J. Royal Aero. Society, vol. 68, pp 343-346, May 1964.

14. Titirega, A. and Skow, A.M. "Analytical and Experimental Techniques to Predict Air-craft Dynamic Characteristics at High Angle of Attack", AGARD CP-235, Paper 19, 1978.

15. Staudacher, W. et al. "Some Factors Affecting the Dynamic Stability Derivatives of a Fighter-Type Model", AGARD CP-235, Paper 11, 1978.

16. Orlik-Rückemann, K.J. "Sensitivity of Aircraft Motion to Cross-Coupling and Accelera-tion Derivatives", AGARD LS 114, Lecture 15, 1981.

17. Campbell, J.P. and Woodling, C.H. "Calculated Effects of the Lateral Acceleration Derivatives on the Dynamic Lateral Stability of a Delta-Wing Airplane", NACA RM L54K26, 1955.

18. Coe, P.L. Jr., Graham, B.H. and Chambers, J.R. "Summary of Information on Low-Speed Lateral-Direction Derivatives Due to Rate of Change of Sideslip, $\dot{\beta}$", NASA TN D-7972, 1975.

19. Curry, W.H. and Orlik-Rückemann, K.J. "Sensitivity of Aircraft Motion to Aerodynamic Cross-Coupling at High Angles of Attack", AGARD CP-235, Paper 34, 1978.

20. Langham, T.F. "Missile Motion Sensitivity to Dynamic Stability Derivatives", AIAA-81-0400, 1981.

21. Tobak, M. and Schiff, L.B. "On the Formulation of the Aerodynamic Characteristics in Aircraft Dynamics", NASA TR R-456, 1976.

22. Tobak, M. and Schiff, L.B. "The Role of Time-History Effects in the Formulation of the Aerodynamics of Aircraft Dynamics", AGARD CP-235, Paper 26, 1978.

23. Tobak, M. and Schiff, L.B. "Aerodynamic Mathematical Modelling - Basic Concepts", AGARD LS-114, Lecture 1, 1981.

24. Orlik-Rückemann, K.J. "Review of Techniques for Determination of Dynamic Stability Derivatives in Wind Tunnels", AGARD LS-114, Lecture 3, 1981.

25. Beyers, M.E. "A New Concept for Dynamic Stability Testing", AIAA-81-0158, 1981.

BIBLIOGRAPHY

1. "Unsteady Aerodynamics", AGARD FDP Symposium, Ottawa, Canada. AGARD CP-227, September 1977.

2. "Dynamic Stability Parameters", AGARD FDP Symposium, Athens, Greece. AGARD CP-235, May 1978.

3. "High Angle of Attack Aerodynamics", AGARD FDP Symposium, Sandefjord, Norway, AGARD CP-247, October 1978.

4. "Dynamic Stability Parameters", AGARD FDP Lecture Series, NASA ARC, USA and VKI, Belgium, AGARD LS-114, March 1981.

5. Ericsson, L.E. and Reding, J.P. "Unsteady Aerodynamics of Slender Delta Wings at Large Angles of Attack", Journal of Aircraft, vol. 12, no. 9, pp 721-729, September 1979.

6. Ericsson, L.E. and Reding, J.P. "Steady and Unsteady Vortex-Induced Asymmetric Loads on Slender Vehicles", Journal of Spacecraft, vol. 18, no. 2, pp 97-109, March/April 1981.

7. Levin, D. "A Vortex-Lattice Method for Calculating Longitudinal Dynamic Stability Derivatives of Oscillating Delta Wings", AIAA-81-1876, August 1981.

8. Ericsson, L.E. "A Preliminary Look at Vehicle Dynamics in Light of Recent High-α Test Results", WG on High α Missile Aerodynamics, October 1981.

9. Langham, T.F. "Aircraft Motion Sensitivity to Dynamic Stability Derivatives", AEDC-TR-79-11, 1980.

NON-LINEARITIES
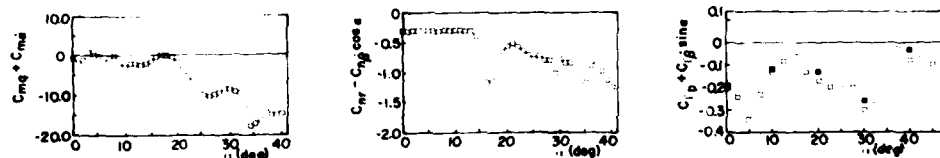
(a) Damping derivatives. Wing-body-fin configuration. M=0.7
(NAE)
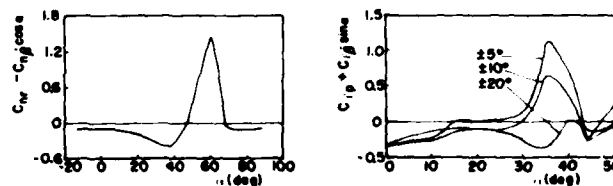
(b) Damping derivatives. Current fighter configuration. M<0.1
(NASA Langley)
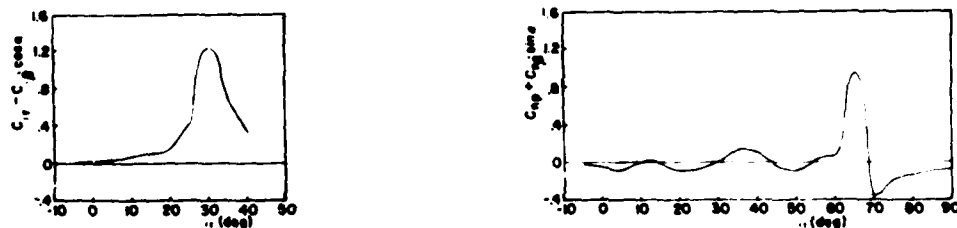
(c) Cross derivatives. Swept-wing fighter configuration. M<0.1
(NASA Langley)

Fig. 1 Examples of Non-Linearities in Damping and Cross Derivatives

ROTARY DERIVATIVE RIG DATA

AERODYNAMIC DEPT. ESTIMATES
(0<α<20° FLIGHT TEST DATA, M≤0·5
α>20° WING PRESSURE DATA)

$\delta_s = 9°$
$\delta_r = 0°$
$\eta_r = 0°$
$\beta = 0°$

(a) Pitching moment.

MODEL
A
B
C
D
E

(b) Rolling moment.

(c) Yawing moment. Ωb/2V

Fig. 4 Effect of rotation rate on moment
coefficients. General aviation
configurations. λ = 60°.
(NASA Langley)

ROTARY DERIVATIVE RIG DATA

AERODYNAMIC DEPT. ESTIM. ES
(0<α<20° FLIGHT TEST DATA, M≤0·5
α>20° THEORETICAL ESTIMATES)

$\delta_s = 9°$
$\delta_r = 0°$
$\eta_r = 0°$
$\beta = 0°$

Fig. 2 Rolling and yawing moment deriva-
tives due to rolling. Current
fighter configuration. M ≤ 0.5
(British Aerospace)

a = 75 deg
M = 0.25

$R_d/10^6$
O 0.16 △ 0.50
□ 0.32 △ 1.96
◇ 0.42 ◇ 1.90

(PROSPIN)

(ANTISPIN)

(PROSPIN)   (ANTISPIN)
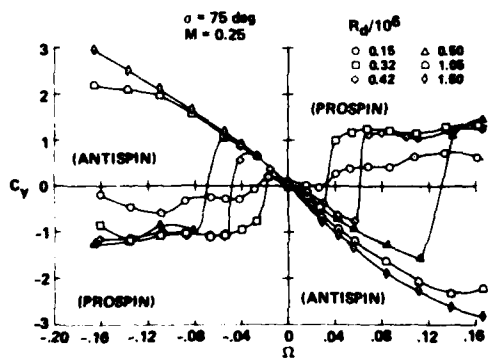
Fig. 3 Nose side-force coefficient versus
reduced spin rate. Square cross
section with rounded corners.
α = 75°.
(NASA Ames)

O β = 0
□ β = +5
◇ β = +10
△ β = +15

Ωb/2V

Fig. 5 Effect of sideslip on rotary
rolling moment. α = 10°.
(NASA Langley)
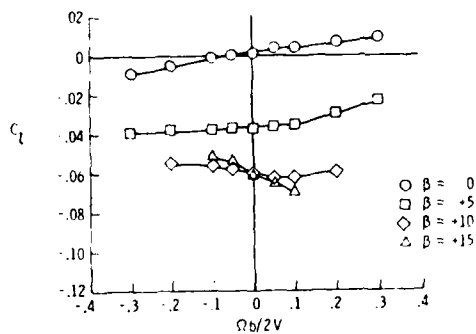
Fig. 6 Effect of sideslip on rotary
rolling moment. α = 20°.
(NASA Langley)
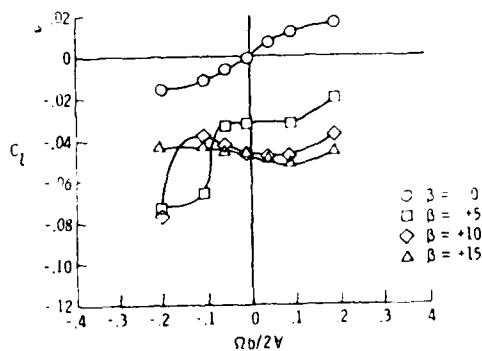
Fig. 7 Effect of sideslip on rotary
rolling moment. α = 30°.
(NASA Langley)
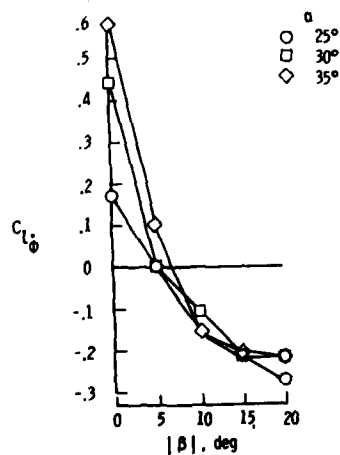
Fig. 8 Variation of roll damping deriva-
tive with sideslip used in non-
linear simulation of Fig. 9.
(NASA Langley)
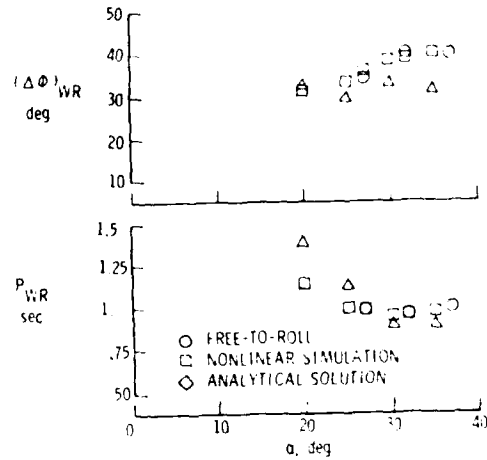
Fig. 9 Comparison of simulation and
analytical predictions of wing-
rock characteristics to experi-
mental results.
(NASA Langley)
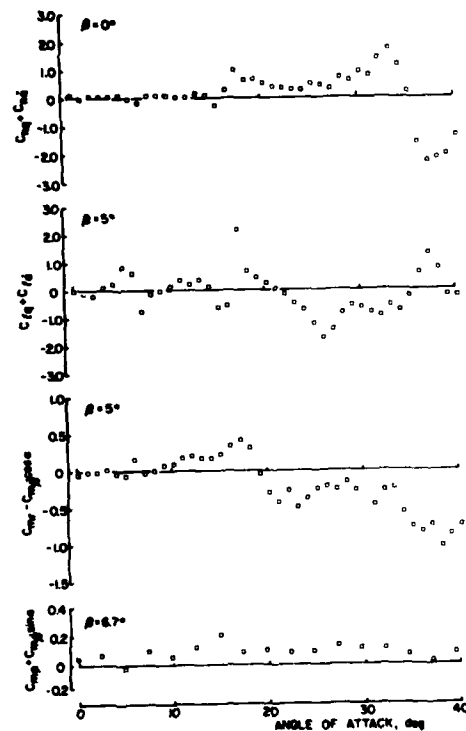
Fig. 10 Dynamic cross-coupling derivatives.
Wing-body-fin configuration.
M = 0.7.
(NAE)
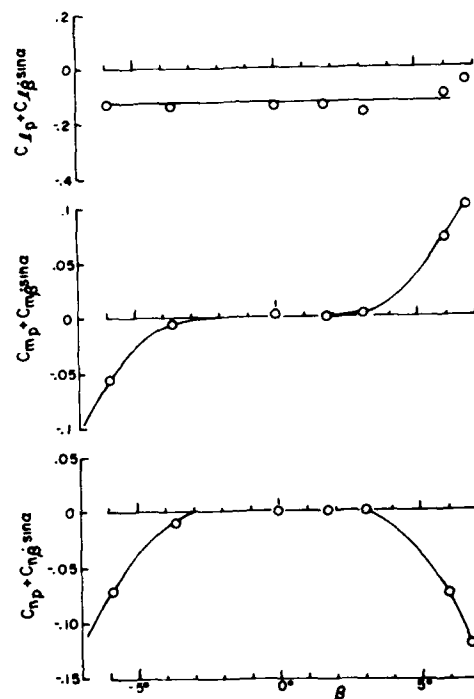
Fig. 11 Effect of sideslip on dynamic moment
derivatives due to oscillation in
roll. M = 0.7. α = 17.5°.
(NAE)

$\dot\beta$-DERIVATIVES
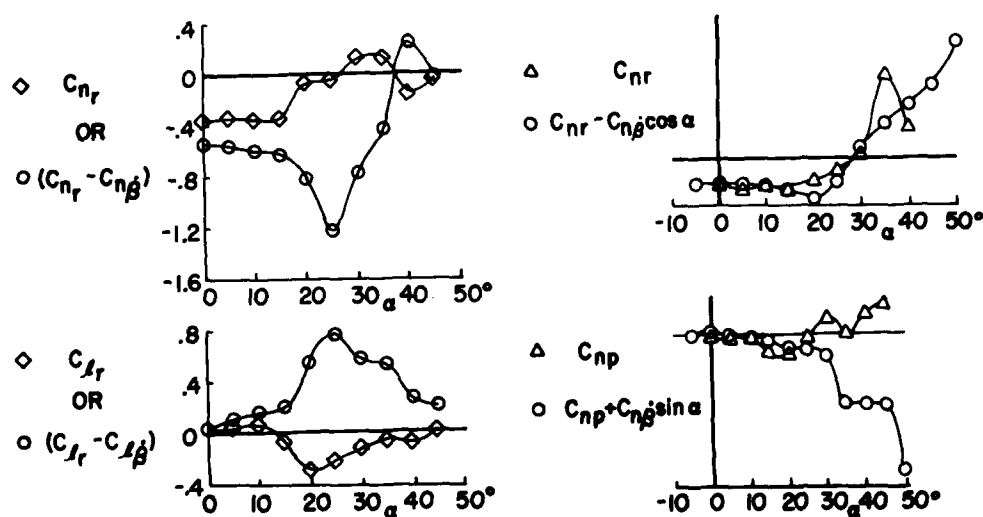
Fig. 12 Difference between purely rotary and oscillatory derivatives equal to deriva-
tives due to time rate of change of angle of sideslip.
(NASA Langley)

HYSTERESIS EFFECTS

POSITION OF VORTEX, x/c

Λ = 80°
M~0
DECREASING α

UNSTABLE REGION

UNSTABLE REGION

INCREASING α

α (DEG)
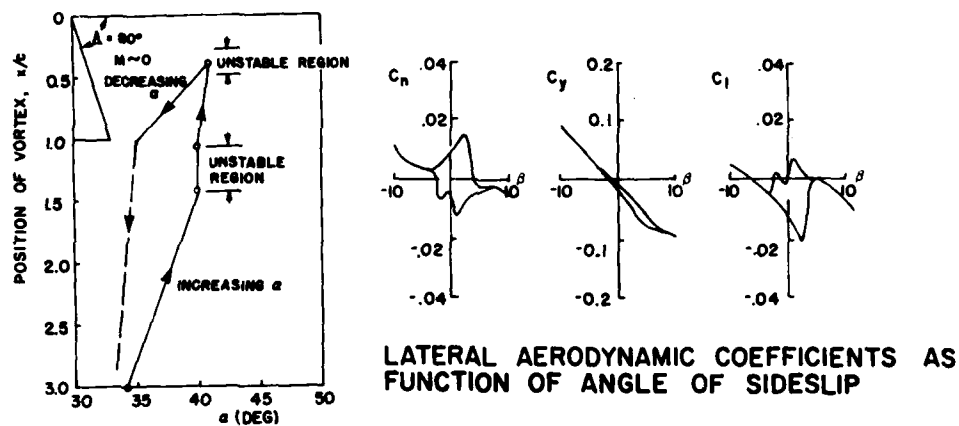
VORTEX BURST LOCATION ON A DELTA WING

LATERAL AERODYNAMIC COEFFICIENTS AS FUNCTION OF ANGLE OF SIDESLIP

Fig. 13 Aerodynamic hysteresis in a region of vortex breakdown.

CONFIGURATION DEPENDENCE

SHARK NOSE AND LEADING EDGE EXTENSION (LEX)
NORTHROP

SHARK NOSE GEOMETRY   **W_6 LEX GEOMETRY**

C_y

Ω
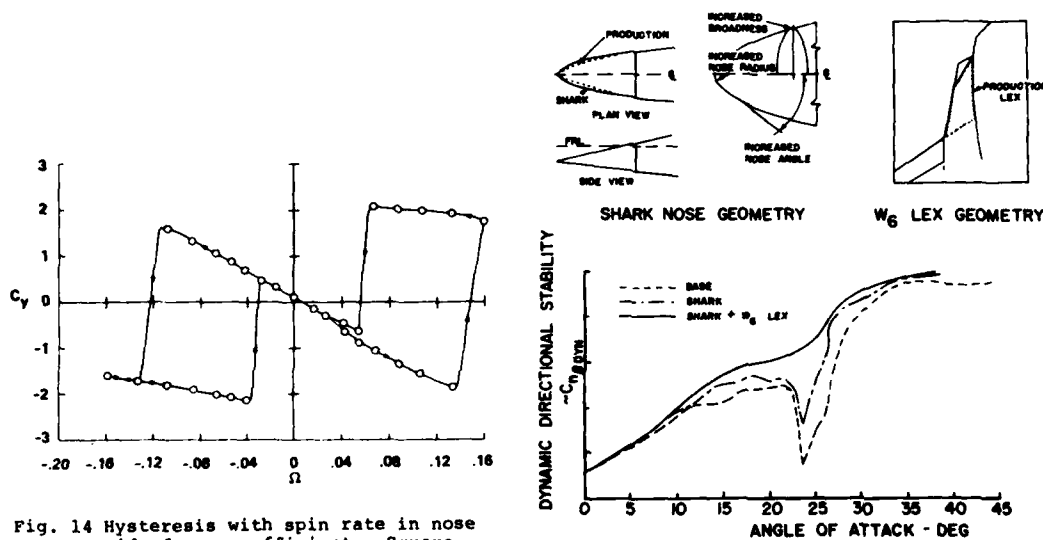
Fig. 14 Hysteresis with spin rate in nose
side-force coefficient. Square
cross-section with rounded corners.
$M = 0.25$. $\alpha = 90°$. $Re_d = 0.6 \ 10^6$.
(NASA Ames)

DYNAMIC DIRECTIONAL STABILITY $-C_{n\beta_{DYN}}$

BASE
SHARK
SHARK + W_6 LEX

ANGLE OF ATTACK - DEG

Fig. 15 Shark Nose and Leading Edge Exten-
sion (LEX).
(Northrop)

M = 0.3, Re = 1.8 · 10⁶ ... (graphs)
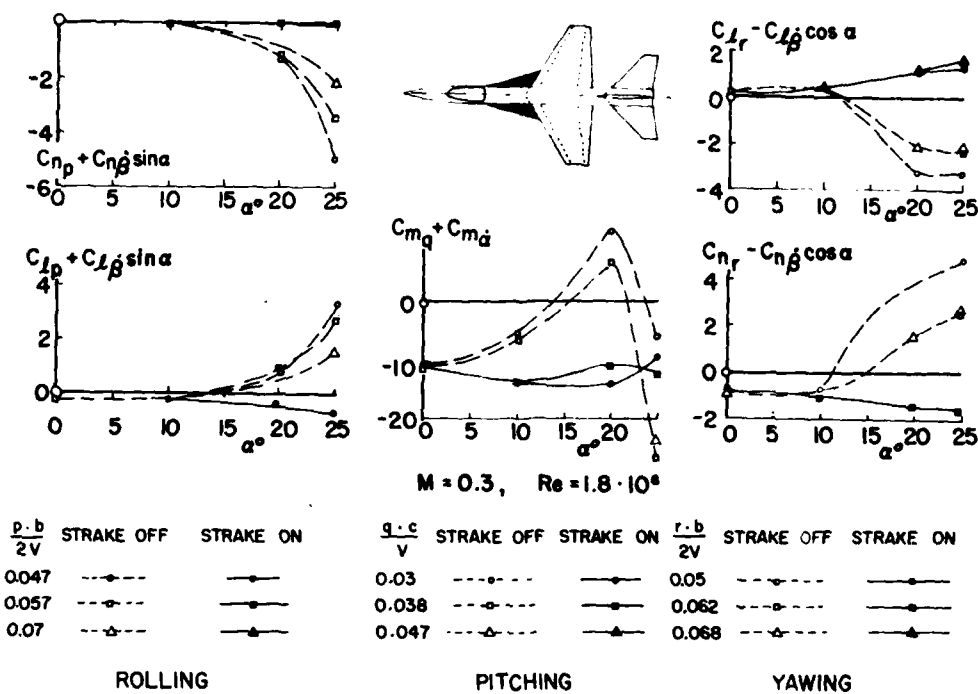
Fig. 16 Effect of strakes. M ≈ 0.3.
(MBB/ONERA)

(a) $\alpha = 20°$

Case	k	Aerodynamic derivatives											Results				
		C_{Y_β}	C_{n_β}	C_{l_β}	$C_{Y_{\dot\beta}}$	$C_{n_{\dot\beta}}$	$C_{l_{\dot\beta}}$	C_{Y_p}	C_{n_p}	C_{l_p}	C_{Y_r}	C_{n_r}	C_{l_r}	Dutch roll mode		Roll mode	Spiral mode	Aperiodic modes
														$t_{1/2}$, sec	k	$t_{1/2}$, sec	$t_{1/2}$, sec	$t_{1/2}$, sec
	(a)																	
1	----	-0.510	0.135	-0.155	0	0	0	0.239	-0.062	-0.168	0.513	-0.332	0.023	11.99	0.086	1.79	16.03	---	---
2	0.066					-.130	-.357							4.35	.086	1.79	16.10	---	---
3	.109					-.239	-.306							5.63	.086	1.79	16.10	---	---
4	.132					-.280	-.258		↓		↓		↓	6.97	.086	1.79	16.11	---	---
b5	.066					0	0		-.107	-.290		-.210	.358	4.42	.085	1.48	-19.63	---	---
b6	.109					0	0		-.144	-.273		-.107	.311	5.70	.086	1.46	-15.46	---	---
b7	.132	↓	↓	↓	↓	0	0	↓	-.158	-.256	↓	-.069	.265	7.02	.086	1.60	-15.49	---	---

[a] Reduced frequency at which $\dot\beta$ derivatives were measured.
[b] $\dot\beta$ derivatives combined with pure angular-rate derivatives.

(b) $\alpha = 28°$

Case	k	Aerodynamic derivatives											Results				
		C_{Y_β}	C_{n_β}	C_{l_β}	$C_{Y_{\dot\beta}}$	$C_{n_{\dot\beta}}$	$C_{l_{\dot\beta}}$	C_{Y_p}	C_{n_p}	C_{l_p}	C_{Y_r}	C_{n_r}	C_{l_r}	Dutch roll mode		Roll mode	Spiral mode	Aperiodic modes
														$t_{1/2}$, sec	k	$t_{1/2}$, sec	$t_{1/2}$, sec	$t_{1/2}$, sec
	(a)																	
1	----	-0.196	-0.121	-0.015	0	0	0	0.155	-0.011	-0.214	0.400	-0.280	-0.171	51.14	0.014	-1.15	---	---
2	0.066					.452	-1.940							----	----	46.21	-2.85	1.72	0.34
3	.106					.387	-.996							----	----	48.52	-2.00	1.48	.54
4	.132					.336	-.856		↓		↓		↓	----	----	48.88	-1.87	1.43	.62
b5	.066					0	0		.201	-1.125		-.659	1.542	-2.44	.019	.32	1.12	---	---
b6	.106					0	0		.171	-.683		-.602	.710	-2.36	.015	.52	1.05	---	---
b7	.132	↓	↓	↓	↓	0	0	↓	.147	-.817	↓	-.557	.586	-2.33	.013	.58	1.02	---	---

[a] Reduced frequency at which $\dot\beta$ derivatives were measured.
[b] $\dot\beta$ derivatives combined with pure angular-rate derivatives.

Fig. 17 Effect of $\dot\beta$ derivatives on calculated dynamic stability characteristics.
(NASA Langley)
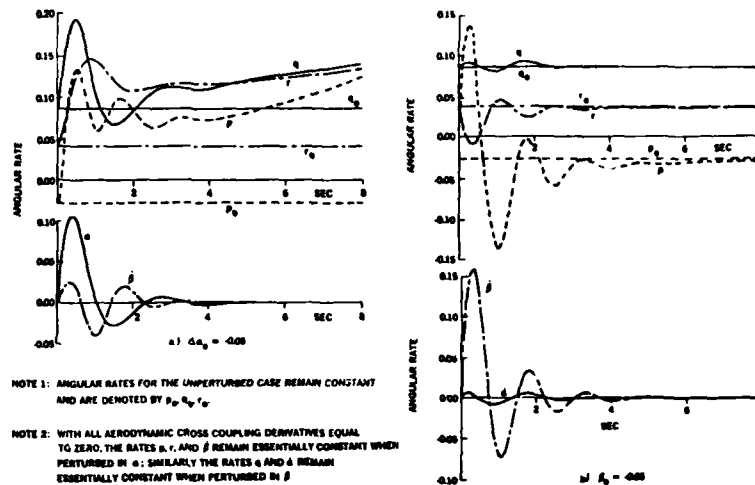
Fig. 18 Effect of including cross-coupling derivatives due to pitching and yawing on the angular rates for 2g turning flight.
(Sandia/NAE)
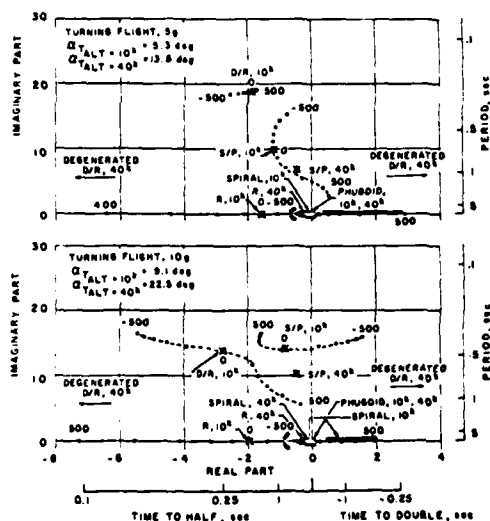
Fig. 19 Effect of variation of C_{l_q} derivtive. Yaw-to-turn missile in 10g turning flight. M = 3.
(AEDC)

b. Time response
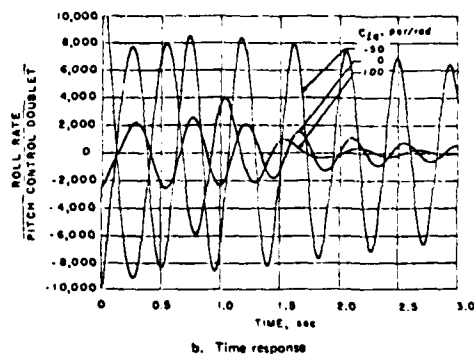
Fig. 20 Effect of variation of C_{l_q} derivative on roll rate time history. Yaw-to-turn missile in 10g turning flight. M = 3.
(AEDC)

APPARATUS	PRIMARY MOTION	STATIC DERIVATIVES	DYNAMIC DERIVATIVES
PITCH/YAW	PITCHING OSCILLATION	$C_{l\alpha}, C_{m\alpha}, C_{n\alpha}$	$C_{lq} + C_{l\dot{\alpha}}$ $C_{mq} + C_{m\dot{\alpha}}$ $C_{nq} + C_{n\dot{\alpha}}$
PITCH/YAW	YAWING OSCILLATION	$C_{l\beta}, C_{m\beta}, C_{n\beta}$	$C_{lr} - C_{l\dot{\beta}} \cos\alpha$ $C_{mr} - C_{m\dot{\beta}} \cos\alpha$ $C_{nr} - C_{n\dot{\beta}} \cos\alpha$
ROLL	ROLLING OSCILLATION	$C_{l\beta} \sin\alpha$ $C_{m\beta} \sin\alpha$ $C_{n\beta} \sin\alpha$ $C_{Y\beta} \sin\alpha$ $C_{N\beta} \sin\alpha$	$C_{lp} + C_{l\dot{\beta}} \sin\alpha$ $C_{mp} + C_{m\dot{\beta}} \sin\alpha$ $C_{np} + C_{n\dot{\beta}} \sin\alpha$ $C_{Yp} + C_{Y\dot{\beta}} \sin\alpha$ $C_{Np} + C_{N\dot{\beta}} \sin\alpha$
$\dot{\alpha}/\dot{\beta}$	PLUNGING OSCILLATION	$C_{l\alpha}, C_{m\alpha}, C_{n\alpha}$	$C_{l\dot{\alpha}}, C_{m\dot{\alpha}}, C_{n\dot{\alpha}}$
$\dot{\alpha}/\dot{\beta}$	LATERAL OSCILLATION	$C_{l\beta}, C_{m\beta}, C_{n\beta}$	$C_{l\dot{\beta}}, C_{m\dot{\beta}}, C_{n\dot{\beta}}$
PITCH (HALF-MODEL)	PITCHING OSCILLATION	$C_{m\alpha}$	$C_{mq} + C_{m\dot{\alpha}}$
PLUNGE (HALF-MODEL)	PLUNGING OSCILLATION	$C_{m\alpha}$	$C_{m\dot{\alpha}}$

Fig. 21 Dynamic stability testing capabilities at NAE.
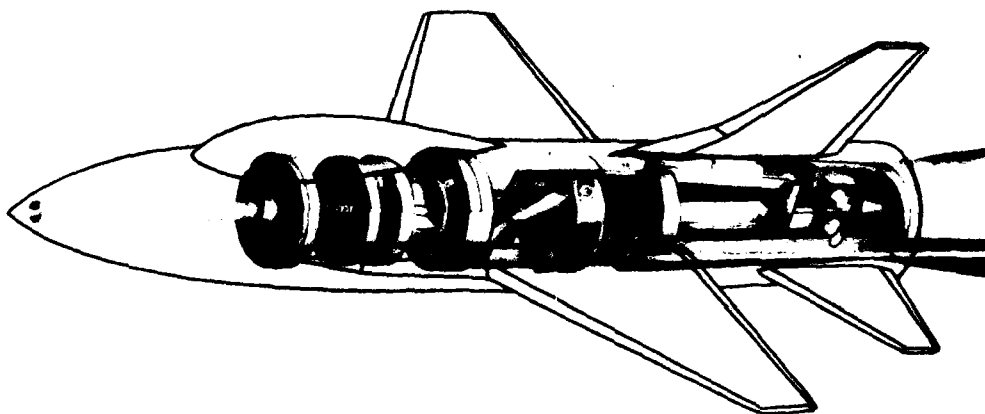
Fig. 22 Pitch/Yaw Oscillatory Apparatus.
(NAE)
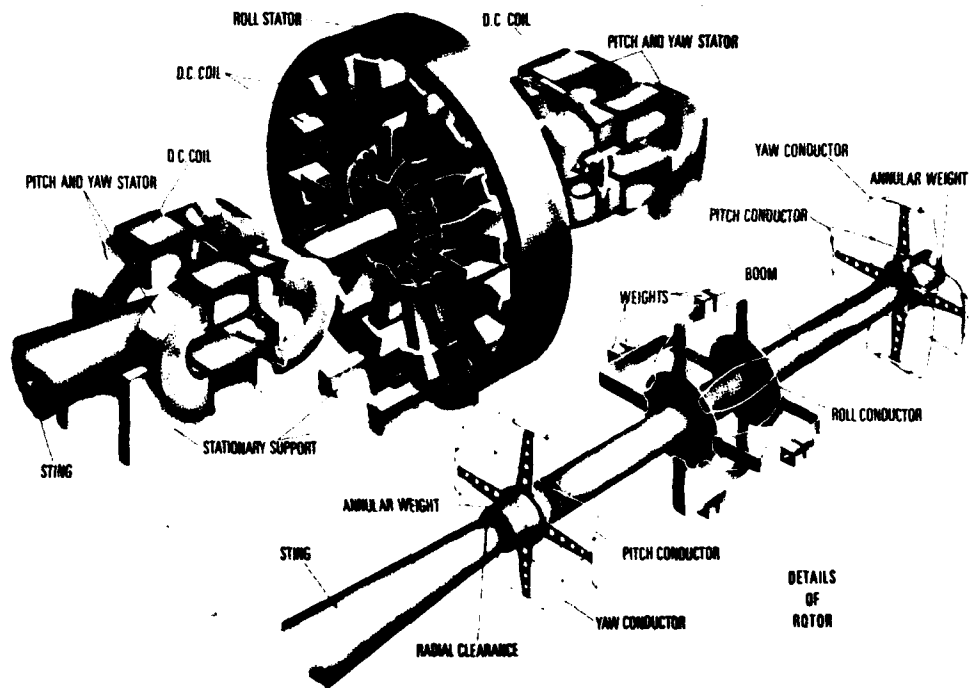
Fig. 23 Dynamic Calibrator.
(NAE)

(a) Translational motion   (b) Rotational motion
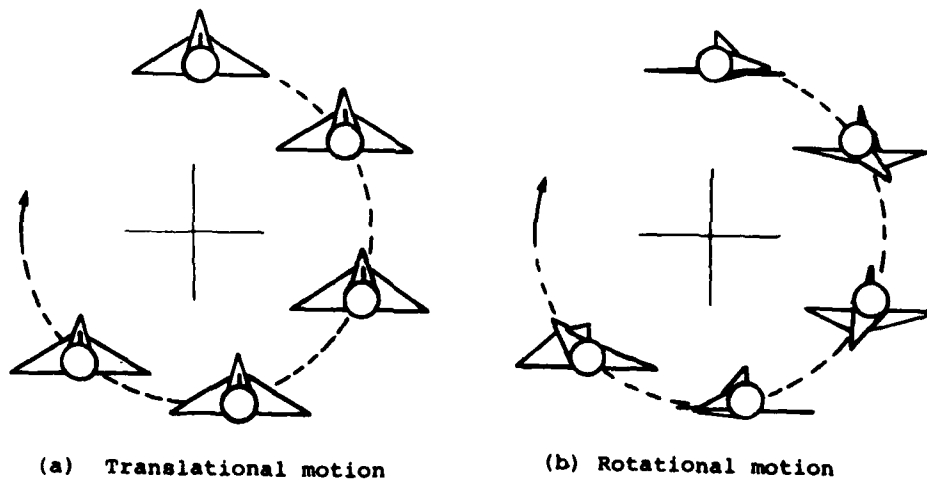
Fig. 24 Orbital fixed-plane motion.
(NAE)

VORTEX BREAKDOWN

E. Wedemeyer

DFVLR-Göttingen, Germany
VKI Visiting Professor 1980-1982

SUMMARY

The different forms of vortex breakdown are considered. Experimental results, theoretical explanations, and predictions are discussed with emphasis on vortex breakdown over wings with highly swept leading edges.

NOTATION

C_φ, C_z	non dimensional velocity gradients (eq. 20)
f	amplitude of disturbance wave (eq. 12)
h	(total head) $\cdot \frac{1}{\rho}$ (eq. 6)
k	circulation = rv (eq. 7)
K	profile parameter
ℓ_a	chord length
r, φ, z	radial, circumferential and axial coordinates, respectively
R	radius of the vortex core
S	momentum flux
u, v, w	radial, circumferential and axial velocity components, respectively
U, V, W	velocity components of the basic flow
z_E	distance of breakdown position from apex
α	angle of incidence
α, γ	wave numbers in axial and circumferential directions, respectively
Λ	aspect ratio of delta wing
φ	small perturbation of the stream function
φ_B	angle of sweep back
Φ	swirl angle, $\tan\Phi = \frac{v}{u}$
Φ_{max}	maximum swirl angle
ψ	stream function
Ω	angular velocity of rigidly rotating approach flow

1. INTRODUCTION

The term "vortex breakdown" denotes the abrupt change of the flow structure which is frequently observed in vortex flows. The phenomenon of vortex breakdown or vortex bursting, as it is sometimes called, was described first by Peckham & Atkinson (1957) who had observed the breakdown of leading edge vortices over wings with highly swept leading edges when the angle of attack exceeded a critical value.

Because of its unusual nature and its implications on aircraft performance, vortex breakdown has become a field of intense research. A typical example of vortex breakdown is shown in figure 1 which is a photograph of the flow over a delta wing taken in the hydrodynamic tunnel at ONERA by Werlé (1960). The flow has been made visible by the injection of dye near the tip of each of the leading edge vortices. Following the dye filaments as they move in tight spirals about the axis of the vortices we observe at a certain distance fromthe apex an abrupt change in the structure of the flow. The streamlines originally near the vortex axis suddenly change direction and begin to spiral anout an expanding body of stagnant fluid until finally the filament breaks up into large scale turbulence.

Vortex breakdown is known to occur in many other vortical flows as well, e.g., in swirling flows in ducts, in flame holders and combustion chambers and in the trailing vortices behind wings. Two examples of vortex breakdown of swirling flows in a circular duct are shown in figure 5. The flow is again visualized by a thin dye filament at the vortex axis. The two photographs in figure 5 show two different forms of vortex breakdown which are called the axisymmetric or bubble form (Fig. 5a) and the spiral form (Fig. 5b). The spiral form closely resembles the form of breakdown usually observed over deltz wings, wherea whereas the bubble form seems to reprnsent a completely different type of breakdown. In the bubble form the central filament reaches a free stagnation point from which it expands in a nearly axisymmetric flow about a body of recirculating fluid. The stream tube forming the envelope of the bubble almost closes in the wake of the bubble and, further downstream, becomes non-axisymmetric before it decays by the onset of turbulent motion.

It may be conjectured that the observed spiral form of breakdown only appears to be different fromthe bubble form as a result of some displacement of the dye filament away from the vortex axis which would, indeed, give the appearance of a spiral form after an axisymmetric breakdown. This possibility was carefully investigated by Sarpkaya (1971b) by changing the location of dye injection very near the axis. From all experimental evidence there seems to be no doubt that the spiral form of breakdown is real, i.e. that the

fluid particles originally at the vortex axis follow a trajectory of spiral form after breakdown.

The practical importance of vortex breakdown has motivated much experimental and theoretical work and has excited controversial opinions. Various explanations have been given for the breakdown phenomenon and theories have been developed with the goal of predicting the location of vortex breakdown or the conditions under which it may occur, but none of the proposed explanations has so far found general acceptance. Although the interest in vortex breakdown originally arose from its application to leading edge vortices, most of the more recent work - experimental and theoretical - has concentrated on investigations of the breakdown phenomenon exhibited by swirling flows in circular ducts. This may be partly due to the fact that the flow in ducts can be more easily controlled and is more nearly axisymmetric than the flow in the vortex core over slender delta wings. All existing theories of vortex breakdown assume - for reasons of simplifying the governing equations of motion - that the approach flow (upstream of breakdown) is axisymmetric. In fact, most investigators disregard the asymmetric features of breakdown altogether taking the point of view that vortex breakdown is an essentially axisymmetric phenomenon and that asymmetries are only secondary effects resulting from instabilities within the axisymmetric breakdown bubble. Another point of view is taken by Ludwieg (1962), (1965), (1970), who explains the spiral form of breakdown as a hydrodynamic instability of the approach flow against small helical disturbances. That is to say, there are at least two different mechanisms for vortex breakdown. In a review article on vortex breakdown Ludwieg (1970) emphasizes : "it cannot be expected that all sudden changes of vortex structure, which are called vortex breakdown, can be explained by one theory only".

In the following sections a description is given of the significant physical features of vortex breakdown followed by a discussion of the proposed explanations and the prevailing theories. Since this papers is one in a series about high angle of attack aerodynamics, it concentrates on the vortex breakdown of leading edge vortices over highly swept wings. Much theoretical work dealing with axisymmetric vortex breakdown will be discussed only briefly. Detailed surveys of this subject are found in review articles by Hall (1972) and Leibovich (1976).

Very few investigations of vortex breakdown have included compressibility effects. A discussion of these will be given in a separate lecture of this series.

2. EXPERIMENTS

Since Peckham & Atkinson (1957) discovered vortex breakdown over wings with highly swept leading edges, the phenomenon has been studied experimentally by a large number of authors. The breakdown over slender delta wings or highly swept flat plates was studied extensively by Werlé (1960, 1971), Elle (1960), Lambourne & Bryer (1961) and Lowsen (1964) using flow visualization techniques. In the experiments of Werlé (1960) a 60° delta wing was mounted in the ONERA hydrodynamic tunnel (Fig. 1). The flow was visualized by ejecting dye from the leading edges near the apex of the wing. The dye, marking the streamlines passing over the leading edge, formed a fine filament on or close to the axis of the leading edge vortices. Since the vortices are formed by rolling up of the separated vortex sheets, the fluid particles passing over the leading edge near the apex of the wing form streamlines near the vortex axis while streamlines passing over stations further downstream of the leading edge form a nearly cylindrical helix about the vortex axis.

The location of vortex breakdown is recognized by a sudden deflection or expansion of the central dye filament (Fig. 1).

In some cases the dye filament forms a bubble-like structure at the early stages of breakdown (Fig. 2) but the bubble is never closed or nearly closed as observed in vortex tubes. Figure 2 also shows the influence of suction on vortex breakdown : while the left vortex has burst already near the apex, the right vortex could be stabilized by suction near the vortex axis so that non breakdown occurs. The opposite effect is obtained by stagnation of the flow (Fig. 3). By placing an obstacle near the axis of the right vortex, the position of vortex breakdown is moved forward. The sensitivity of the vortex breakdown to solid bodies inserted near the axis, which was also observed by other investigators, implies severe limitations to the possibility of measuring the flow field within or near the breakdown region by means of probes. Lambourne and Bryer (1961) reported that the effect of a body on the breakdown position depends on the size of the body and its axial position relative to the natural bursting point and that useful probe measurements should be possible only with sufficiently small probes.

The effect of yaw angle is shown in figure 4 : for the case shown here, breakdown occurs only at the side which is turned into the flow direction. This is in accord with the observation that the tendency to breakdown increases with decreasing sweepback angle. Figure 6 shows the variation of the bursting point with angle of attack for a 75° sweepback delta wing : the position of the bursting point moves, with increasing incidence, towards the apex of the wing. The effect of sweep angle is shown in figure 7 : the angle of incidence has been adjusted so that breakdown occurs just ahead of the trailing edge. It is seen that the critical angle of attack decreases with decreasing sweepback.

The results obtained in the ONERA hydrodynamic tunnel (Werlé, 1971) are summarized and compared with the results of other investigators in a diagram reproduced in figure 8. The angle of incidence, α, is shown as a function of sweep angle for breakdown positions at the trailing edge ($z_E = \ell_a$) and midchord position ($z_E = \ell_a/2$). The diagram confirms what has frequently been observed : that the Reynolds number has no significant influence on the breakdown position.

Similar experiments have been performed by Lambourne & Bryer (1061), who observed the process of breakdown in much detail on a flat plate delta wing of 65° sweepback in wind tunnel and water experiments and on a flat plate with variable sweep angle in a wind tunnel. The results of these investigations largely confirm the results of the ONERA hydrodynamic tunnel. In addition, Lambourne & Bryer (1961) investigated the effects of acceleration and deceleration of the flow, and the effect of an axial pressure gradient produced by flaps and camber of the wing.

The authors emphasize that an essential feature for the occurrence of vortex breakdown is a region of low total pressure near the axis of the vortex. They conclude that vortex breakdown results from stagnation of the flow in the presence of an adverse pressure gradient. The required pressure gradient is attributed to the deceleration of the external flow and viscous effects. It is noted that a small change in the external flow is sufficient to produce a large pressure gradient at the axis because the pressure gradient is magnified towards the axis of the vortex. This explanation of the breakdown mechanism anticipates the essential part of most of the theories of axisymmetric vortex breakdown.

The physical mechanism for the retardation of the flow was later investigated by Hall (1965) who calculated numerically the variations of axial velocity and pressure along the axis and along an outer cylindrical stream surface. The result of this calculation is illustrated in figure 9, which shows that the variations of pressure and axial velocity along the vortex axis are much larger than along an outer stream surface. This magnification effects is brought about by the large radial pressure gradient present in swirling flows.

2.1 Experiments in vortex tubes

In the course of experimental studies of the vortex breakdown phenomenon, it became apparent that experiments could be performed more easily with swirling flows in tubes. The apparatus which was used by Harvey (1962) for his observations of vortex breakdown is shown schematically in figure 10. Air was drawn by a small fan through a transparent tube of 4 ft length and 3.5 in diameter. The swirl was imparted to the fluid as it moves radially inward over a set of adjustable vanes mounted in the inlet section. The ratio of swirl velocity to axial velocity could be increased by increasing the angle of the swirl vanes. In addition, the size of the viscous core of the vortex could be changed by boundary layer suction applied at an annular slot in the center body of the swirl generator (Fig. 10). In this way a family of velocity distributions of the approach flow (upstream of vortex breakdown) could be obtained.

Basically, similar apparatus for experiments in water were used by Sarpkaya (1971a,b, 1974) and Faler & Leibovich (1977, 1978). Escudier et al. (1980) used a vortex tube in which the flow enters the generator section of the tube through a tangential inlet slit. In all cases, velocity distributions of a similar kind were generated. The circumferential velocity distribution, v, can be represented approximate by Burger's vortex :

$$v(r) = \frac{K}{r} \left[1-\exp(-ar^2)\right] \tag{1}$$

which approaches a rigidly rotating viscous core near the vortex axis r = 0 and a potential vortex for large radial distances. The axial velocity component, w, has a jet-like profile with a maximum velocity at the vortex axis. It can be approximated (see Faler & Leibovich, 1977) by :

$$w(r) = w_1 + w_2 \exp(-ar^2) \tag{2}$$

It should be noted that these velocity distributions are quite different from those of leading edge vortices (eq. 18) although they may be similar within the region of the viscous subcore.

In Harvey's experiments, the flow was visualized by smoke which was injected into the center of the vortex through a hole in the tip of the center body of the swirl generator. For experiments in water, flow visualization was accomplished in a similar way by a central dye filament.

Observations

In all experiments with vortex tubes it was found that vortex breakdown occurs when the swirl component of the flow was sufficiently large. The amount of swirl can be characterized roughly by the maximum swirl angle Φ_{max} where the swirl angle Φ is defined by $\tan\Phi = v/u$. The swirl angle is one of the quantities that can be determined by observing the trace of a smoke filament injected into the flow field at a given distance from the axis. A radial distribution of the swirl angle of the flow just upstream of breakdown is shown in figure 11.

Vortex breakdown was found only if the maximum swirl angle Φ_{max} exceeded a critical value of about 45°-50° depending somewhat on the shape of the velocity profiles. The observed values of the critical swirl angle are in close agreement with the theoretical predictions discussed in section 3. In Harvey's experiments, only axisymmetric forms of breakdown were observed giving the impression that this form is typical for experiments in tubes where the approach flow is strictly axisymmetric. However, Sarpkaya (1971a,b, 1974) and later Faler & Leibovich (1977) found other forms of breakdown, especially the spiral form shown in figure 5b. Which form of breakdown actually occurred depended mainly on the amount of swirl.

Observing the flow in mildly diverging tubes, Sarpkaya obtained a sequence of breakdown patterns with increasing swirl. Schematic sketches of the observed patterns in the order of increasing swirl are shown in figures 12a to 12e. The shaded areas indicate regions of stagnant, reversed or turbulent flow. For the smallest amount of swirl at which breakdown first occurred, the dye filament assumed, after a sudden kink, the spiral form shown in figure 12a. Successively increasing the vane angle resulted at first in a distortion of the filament which tends to turn back towards the initial kink (Figs. 12b,c). For still larger vane angles the breakdown pattern approaches an axisymmetric form. Once a near-axisymmetric breakdown form is obtained, further increase of the vane angle does not change the flow pattern but only moves the location of breakdown further upstream. The flow downstream of the breakdown bubble becomes unsteady and non axisymmetric. In some instances, however, it was observed that the flow downstream of the bubble did not at once degenerate into unsteady turbulent motion but had a tendency to form a nearly closed bubble downstream of which a new central dye filament is observed. Figure 13 shows a configuration which was obtained by Harvey (1962) by acceleration of the flow downstream

of breakdown. The original flow is nearly restored behind the breakdown bubble until, further downstream, a second breakdown occurs. Figure 14 shows a formation of even three bubbles in succession which was observed by Serpkaya (1971b) when the vane angle was suddenly increased. The complete or partial recovery of the flow downstream of tne breakdown bubble leads Harvey (1962) to conclude that this type of breakdown is not due to the onset of some sort of instability. Hydrodynamic instability implies that initial small disturbances grow without return. Instead, the bubble form of breakdown gives the appearance of large amplitude standing waves.

Other forms of disturbances have been observed by Sarpkaya (1971b) and Faler & Leibovich (1977) in which the central filament deviates from the axis more smoothly forming a spiraling tape, eventually splitting into two branches forming a "double helix" as shown in figure 15. These disturbances are not really breakdowns as they have no free stagnation point and no reverse flow region. They may be considered as progenitors of the spiral form of breakdown as they occur at swirl rates just below the critical swirl for spiral breakdown.

Conditions leading to breakdown in vortex tubes

From observations of breakdown in tubes the following conclusions can be drawn :
1. Breakdown occurs only at high swirl rates with peak swirl angles of about $\Phi_{max} > 45°$.

2. A necessary condition for breakdown is an adverse axial pressure gradient appearing near the vortex core. Increasing swirl reduces the necessary pressure gradient and breakdown position moves upstream. The same upstream movement of the breakdown position is obtained by placing an obstacle into the flow downstream.

3. A condition related to adverse pressure gradient is a divergence of the streamtubes ahead of breakdown. Sarpkaya (1971b) obtained breakdown in a divergent tube at a 20% smaller peak swirl angle than that found by Harvey in a cylindrical tube. With increasing angle of divergence, the position of breakdown moved upstream (so long as no separation at the tube walls was present) (Sarpkaya, 1974).

3. EXPLANATIONS OF VORTEX BREAKDOWN

The various explanations given for the phenomenon of vortex breakdown can be classified into two categories :
1. Explanations which are not related to flow instability.
2. Explanations which relate breakdown to the onset of hydrodynamic instability of the approach flow.
If the approach flow is assumed to be stable, there is no reason why an originally axisymmetric flow should undergo a change into non-axisymmetric flow.

All explanations of the first category restrict themselves to the axisymmetric form of breakdown. Some authors (Lambourne & Bryer (1961), Benjamin (1962, 1967)) hold that observed asymmetries are secondary effects, caused by hydrodynamic instability of the flow within or downstream of the breakdown bubble.

Secondary instabilities are, indeed, observed downstream of axisymmetric breakdown where the flow becomes irregular and turbulent (see e.g., Garg & Leibovich, 1979). It is, however, not plausible that the spiral form of instability (shown e.g., in Fig. 1 or Fig. 5) should be an essentially axisymmetric phenomenon, since the flow, in this case, is asymmetric in the earliest stages of breakdown. It is more plausible to take the view, suggested by Ludwieg (1970), that not all forms of breakdown can be explained by the same mechanism. Although none of the proposed theories of vortex breakdown is generally accepted, it appears, at the present time, that stagnation of the low energy flow at the vortex center is an essential feature of vortex breakdown, whether axisymmetric or non-axisymmetric.

For reasons of simplicity, all theories of vortex breakdown assume that the approach flow is axisymmetric. It is not obvious that this assumption is not too restrictive in the case of spiral breakdown since an asymmetric breakdown pattern could be a consequence of asymmetries in the approach flow. However, in view of the fact that spiral forms of breakdown are observed in vortex tubes, where the approach flow is axisymmetric, it appears justified to consider only axisymmetric approach flows since these seem to contain all features relevant for non-axisymmetric as well as axisymmetric breakdown.

3.1 Theories not related to flow instability

The first attempt to derive a criterion for vortex breakdown was made by Squire (1960) who investigated the possibility of axisymmetric waves travelling upstream or downstream in a cylindrical swirling flow. Squire found that two different cases can be distinguished The two cases, which have subsequently been called "supercritical" and "subcritical" in analogy to flows in open channels, can be defined as follows :
(i) In "supercritical" flows, usually connected with low swirl velocities, only downstream travelling waves are possible.
(ii) In "subcritical" flows, connected with large swirl velocities, upstream travelling waves and standing waves are possible.
In the limiting "critical" case, which divides the subcritical and supercritical regions, standing waves first become possible for infinite wavelength or zero wave number respectively.

The "critical" condition, i.e., the condition that long upstream tavelling waves become possible, is proposed by Squire as a criterion for vortex breakdown. This criterion is based on the argument that, if standing waves can exist, disturbances which are present downstream could spread upstream and cause the breakdown. Although this argument is no real explanation for the phenomenon of vortex breakdown, it has drawn attention to the fact that the critical state has a decisive role in the evolution of breakdown. There is experimental evidence that the bubble form of vortex breakdown always occurs near the critical state (Harvey, 1962).

The critical state

Assuming inviscid stationary and axisymmetric flow, the equations of motion can be expressed by a single equation for the stream function $\psi(r,z)$, with :

$$rw = \frac{\partial \psi}{\partial r} ; \qquad ru = -\frac{\partial \psi}{\partial z} \qquad (4)$$

(r,z) are the coordinates and (u,w) the velocity components in radial and axial direction. The equation for $\psi(r,z)$ is :

$$\frac{\partial^2 \psi}{\partial r^2} - \frac{1}{r}\frac{\partial \psi}{\partial r} + \frac{\partial^2 \psi}{\partial z^2} = r^2 \frac{dh}{d\psi} - k \frac{dk}{d\psi} \qquad (5)$$

where h is the total head :

$$h = \frac{p}{\rho} + \frac{1}{2}(u^2 + v^2 + w^2) \qquad (6)$$

and k the circulation : $\qquad k = rv \qquad (7)$

In an inviscid stationary flow, total head and circulation are functions of ψ alone.

Equation (5) is in general a nonlinear equation for the stream function. In a cylindrical flow, ψ is a function of r only : $\psi = \psi(r)$. Considering now small axisymmetric disturbances of the basic cylindrical flow, the stream function may be written :

$$\psi = \psi(r) + \varphi(r,z) \qquad (8)$$

The linearized equation for the small perturbation $\varphi(r,z)$ becomes :

$$\frac{\partial^2 \varphi}{\partial r^2} - \frac{1}{r}\frac{\partial \varphi}{\partial r} + \frac{\partial^2 \varphi}{\partial z^2} + L(r)\varphi = 0 \qquad (9)$$

where

$$L(r) = \left\{ \frac{1}{r^3 W^2}\frac{dK^2}{dr} - \frac{1}{W}\frac{d^2 W}{dr^2} + \frac{1}{rW}\frac{dW}{dr} \right\} \qquad (10)$$

$K = rV$, and (V,W) are the velocity components (v,w) of the basic cylindrical flow. The boundary conditions require that φ vanishes at the axis and at $r \to \infty$ or, if the flow is confined in a cykindrical duct of radius R :

$$\varphi(0) = \varphi(R) = 0 \qquad (11)$$

Considering, with Squire, axisymmetric waves of the form :

$$\varphi(r,z) = f(r)\cos\alpha z \qquad (12)$$

one obtains an ordinary differential equation for f :

$$f_{rr} - \frac{1}{r} f_r + (L(r) - \alpha^2) f = 0 \qquad (13)$$

with boundary conditions : $\qquad f(0) = f(R) = 0 \qquad (14)$

Equations (13) and (14) constitute a Sturm-Liouville eigenvalue problem. It can be shown that there is always a maximum eigenvalue α_m^2. If $\alpha_m^2 < 0$ all α^2 are negative and, therefore, no standing waves are possible. This is the supercritical state.

If $L(r)$ is positive and sufficiently large in $0 \le r \le R$ (which is the case for sufficiently large circulation K), the Sturm-Liouville system, equations (13) and (14), eventually has a positive eigenvalue α_m^2; i.e., standing waves of the form of equation (12) exist and define a subcritical state.

The critical state is defined by $\alpha_m^2 = 0$, i.e., by the existence of standing waves with infinite wavelength. If standing waves of finite wavelength exist, it can be shown that upstream travelling waves also exist which have a large wavelength. (Solutions for travelling waves are derived from eqs. (9) and (10) if W is replaced by W-C where C is the wave speed and C > 0 represents downstream travelling waves).

As outlined above, Squire explains breakdown by the spreading of disturbances in upstream direction which is only possible for subcritical flows. Thus, according to Squire, subcritical flows are subject to vortex breakdown

Benjamin's theory

A quite different interpretation of the role of the critical state was given by Benjamin (1962, 1967) who proposed that vortex breakdown is a finite transition from a supercritical flow to a subcritical flow. Considering eq. (5) for the case of cylindrical flow $\psi = \psi(r)$:

$$\frac{\partial^2 \psi}{\partial r^2} - \frac{1}{r}\frac{\partial \psi}{\partial r} = r^2 \frac{dh}{d\psi} - k \frac{dk}{d\psi} \qquad (15)$$

Benjamin has shown that if h and k are specified functions of ψ, a pair of conjugate solutions $\psi_A(r)$ and $\psi_B(r)$ can exist, which satisfy eq. (15) with appropriate boundary conditions $\psi(0) = 0$, $\psi(R) = \psi_R$. It is possible also that more than one pair of mutually conju-

gate states exists, but Benjamin assumes that transition is always between a pair of "adjacent" conjugate states so that one state, e.g., ψ_A, is a supercritical and the conjugate state ψ_B is a subcritical state adjacent to the critical state.

Benjamin states "that supercritical flows are liable to undergo spontaneous transitions to the subcritical state". This transition is seen in close analogy to the hydraulic jump. It is shown that the subcritical state has a large value of the momentum flux :

$$S = 2\pi \int_0^R (\rho w^2 + p) \, r dr \tag{16}$$

In order to assure conservation of the momentum flux, small standing waves superimposed on the subcritical state are postulated which are shown to cancel the excess momentum flux. This appearance of small downstream waves is sufficient for mild transitions. For strong transitions it is proposed that turbulence must occur to establish the necessary equilibrium.

Benjamin's explanation of vortex breakdown does not give an account of the physical mechanism that brings about flow retardation and the formation of a breakdown bubble. The theory relates the upstream and downstream flow without considering intermediate states. In order to fill this gap, a number of attempts have been made to actually calculate the flow in the breakdown region.

Calculation of the flow in the breakdown region

Hall (1965, 1967) developed a method by which the flow can be calculated starting from an initial upstream condition and proceeding step by step in the downstream direction. In addition to the initial condition, a boundary condition - for example a pressure distribution - is prescribed at the edge r = R of the vortex core. The method is based on the assumption - similar to that used in boundary layer theory - that changes in the axial direction are small compared with variations in the radial direction. The corresponding approximation is called quasi-cylindrical. It is found that, as the calculations proceed downstream, eventually a point is reached where the quasi-cylindrical approximation fails, i.e., where calculations cannot be continued further downstream because the axial velocity gradients inside the vortex become infinite. This failure of the quasi-cylindrical approximation is analogous to the failure of two dimensional boundary layer calculations near the point of separation. In a similar way, Hall identifies the failure of the quasi-cylindrical approximation with the onset fo vortex breakdown.

For inviscid flow it can be shown (Ludwieg, 1970) that the point at which the quasi-cylindrical approximation fails is identical with the critical state. This suggests a new physical interpretation of the critical state : although the external flow changes only slowly, appreciable velocity gradients occur inside the vortex when the critical state is approached, indicating a rapid retardation of the flow which finally leads to stagnation and flow reversal.

Bossel (1969, 1971) made simplifying assumptions in order to be able to calculate the flow in the breakdown region. Considering a rigidly rotating approach flow $V = r\Omega$ with constant axial velocity W in a cylindrical duct, the (inviscid) equation of motion (eq. 5) becomes linear :

$$\frac{\partial^2 \psi}{\partial r^2} - \frac{1}{r}\frac{\partial \psi}{\partial r} + \frac{\partial^2 \psi}{\partial z^2} = \frac{2\Omega^2}{W} r^2 - \frac{4\Omega^2}{W^2} \psi \tag{17}$$

and can be solved by superposition. Prescribing a suitable downstream distribution of axial velocity and swirl a transitional flow is obtained which forms a bubble downstream of a free stagnation point. The shape of the bubble is in good agreement with experimental observations as shown in figure 16. Since Bossel's calculation assumes inviscid flow, it cannot be expected that correct results are obtained throughout the interior of the bubble where viscous effects must be important.

More recent approaches to vortex breakdown include theories of Mager (1972), Randall & Leibovich (1973), Bilanin (1973) and Huang (1974). The theory of Randall & Leibovich is based on an expansion for long axisymmetric waves (Leibovich & Randall, 1973). The authors consider flows in a slowly diverging tube allowing for acceleration flow. The flow is completely determined when the basic approach flow and the tube geometry are prescribed. The computations, which include viscous terms, have confirmed that bubble type flow patterns can be obtained if the upstream conditions are close to critical. The solutions are consistent with experimental observations although they contain inconsistencies such as reversed swirl in the interior of the bubble.

A number of investigators have numerically solved the full Navier-Stokes equations for Reynolds numbers from four to several hundred. Kopecky & Torrence (1973) considered the flow in a cylindrical tube for an initial swirl velocity given by eq. (1) and uniform axial velocity. Grabowsky & Berger (1976) consider a vortex core surrounded by an irrotational flow. The Navier-Stokes solutions are important insofar as they reveal the internal structure of the breakdown bubble which cannot be described properly by approximate theories. The numerical computations have shown that the Navier-Stokes equations admit of axisymmetric solutions with embedded regions of recirculating flow which resemble the bubble form of breakdown.

In spite of severe shortcomings of the various theoretical approaches, it seems possible now to construct at least a good qualitative explanation for the axisymmetric form of breakdown. An essential feature is the existence of a region of low energy flow in the viscous subcore near the vortex center. A small adverse pressure gradient in the external flow is magnified - as a result of swirl - towards the axis. The flow near the axis, having low total pressure, is decelerated rapidly. On reaching the critical state, finite gradients of the external flow produce infinite gradients near the vortex axis, indicating that the vortex core undergoes an abrupt change. A quantitative description of the flow in the breakdown region can only be obtained by solving the full nonlinear equations of motion.

3.2 Theories related to flow instability

Jones (1960), Petersohn (1970) and Ludwieg (1962, 1965) investigated the possibility that vortex breakdown is caused by hydrodynamic instability. The idea is that small initial disturbances grow, due to flow instability, and become large enough to cause strong distortion of the original vortex flow wich subsequently may lead to breakdown.

It is known that rotating flows are - similar to laminar boundary layers - subject to a number of flow instabilities. The two main types of flow instability in rotating flows are :
(i) A generalized inflection point instability.
(ii) An instability of the Rayleigh-Taylor type for rotating flows extended to account for an additional axial component.

All stability theories of vortex breakdown assume, for simplicity, that the approach flow is cylindrical, i.e., the slow conical growth in the streamwise direction is neglected, similar to the case of the stability theory of laminar boundary layers. It is also assumed that viscosity has no direct effect on flow instability, i.e., the stability of the approach flow is investigated with respect to small perturbations, neglecting viscous effects in the disturbance flow. This last assumption seems to be justified in view of the fact that the breakdown position is nearly independent of Reynolds number.

The structure of a leading edge vortex over a slender delta wing

The stability of the vortex flow depends, of course, on the structure of the vortex, i.e., on the velocity distributions of the circumferential (V) and axial (W) component.

Under simplifying assumotions, Hall (1961, 1966) derived a solution for the velocity distributions in leading edge vortices over slender delta wings. In particular, Hall assumed that the vortex core is slender, axisymmetric and conical and that the velocity distributions are smooth, i.e., that the original steps due to the rolled up vortex sheet are smooth out by viscous effects. Under these conditions, Hall (1961, 1966) finds for the velocity distributions of the vortex core :

$$V = C \sqrt{K + \frac{1}{2} - \ln \frac{r}{R}} \qquad \text{(swirl component)} \qquad (18a)$$

$$W = C (K - \ln \frac{r}{R}) \qquad \text{(axial component)} \qquad (18b)$$

$$U = -\frac{1}{2} C \frac{r}{R} \qquad \text{(radial component)} \qquad (18c)$$

where R is the radius of the vortex core (which, for conical flow, increases in proportion to the distance z from the apex of the wing). C and K are constants of integration, so that eq. (18) describes a two parameter family of velocity profiles. The constant K is a shape parameter for the velocity profiles while C determines essentially the magnitude of the velocities.

The velocity profiles V and W, given by eq. (18), are shown graphically in figure 17 for various values of the profile parameter K. The velocity distributions have a singularity at r = 0 where V and W become infinite according to Hall's inviscid solution. Clearly, viscous diffusion becomes appreciable near the vortex axis and changes the velocity profiles within a small viscous "sub-core". For laminar flow, Hall (1961) and Stewartson & Hall (1963) have derived a boundary layer type correction for the sub-core which is shown qualitatively by the broken lines in figure 17. Near the vortex axis, the velocity profiles approach rigid body rotation and constant axial velocity. Measurements of velocity distributions by Earnshaw (1961), Hummel (1965) and Anders (1981) have essentially confirmed the velocity distribution given by eq. (18) with viscous corrections. If a leading edge vortex is exposed to a pressure gradient (e.g., near the trailing edge of the wing), its structure must change, but Ludwieg (1962) has shown that the new velocity profile (except for the viscous subcore) is given again by a profile of the same family with a different value of K. The parameter K decreases in the direction of increasing pressure.

Stability analysis of Jones

Hydrodynamic instability as a cause of vortex breakdown was first suggested by Jones (1960). He investigated the stability of a leading edge vortex given by Hall's solution (eq. 18) with respect to axisymmetric disturbances. Jones made it plausible that Hall's vortex can become unstable but he did not succeed in providing any proof or in deriving a stability criterium. Even if instability with respect to axisymmetric disturbances could be demonstrated, this certainly could not account for the spiral type of vortex breakdown.

Ludwieg's stability criterion

A general stability criterion for helical flows (i.e., cylindrical flows having axial and circumferential velocities) was derived by Ludwieg (1960). According to Ludwieg's stability analysis, a helical flow is most unstable to spiral disturbances of the form :

$$\vec{V} = \vec{\underline{V}}(r) \exp i(\alpha z + \gamma \psi - \beta t) \qquad (19)$$

Ludwieg's criterion is a generalization of Rayleigh's criterion for rotating flows and, as in Rayleigh's criterion, it is a local stability criterion which attributes instability to a local unstable stratification of the flow. Local stability or instability depends on the non dimensional velocity gradients (C_ψ, C_z) where are defined by

$$C_\psi = \frac{r}{V} \frac{dV}{dr} \; ; \qquad C_z = \frac{r}{V} \frac{dW}{dr} \qquad (20)$$

The flow is stratified in an unstable manner if :

$$(1 - C_\psi)(1 - C_\psi^2) - (\frac{5}{3} - C_\psi) C_z^2 < 0 \qquad \text{(unstable)} \qquad (21)$$

and in a stable *manner if the left hand side* of eq.(21) is larger than zero. A stability diagram, showing stable and unstable regions in a (C_φ, C_z)-plane is shown in figure 18. For $C_z = 0$, the stability criterion reduces to Rayleigh's criterion which in this notation *reads*

$C_\varphi < -1$: unstable $\qquad\qquad\qquad C_\varphi > -1$: stable

It is seen that the radial gradient of the axial component, C_z, has a strong destabilizing effect. The stability criterion, eq. (21), was also experimentally verified by Ludwieg (1964). Although Ludwieg's criterion is derived, strictly, for flows in a small annular gap between concentric cylinders, it is believed that it applies, to a high degree of approximation, to more general flows. This was partly proved by Wedemeyer (1969) by investigating *the effect of gap-width and curvature of the velocity profiles on the flow stability.* These investigations have shown that - for helical flows - instabilities are *mainly due to* local unstable stratification, so that a general helical flow becomes unstable if it is locally unstable according to Ludwieg's criterion.

Ludwieg's theory of vortex breakdown

Applying Ludwieg's stability criterion to the flow field of Hall's vortex, the following results are obtained which can best be explained by use of the diagram in figure 18. The (C_φ, C_z)-values encountered in Hall's vortex (eq. 18) always lie on the lower half of the parabola $C_\varphi = - 1/2\, C^2$, which is shown in the diagram. The inner endpoint $C_\varphi = C_z = 0$ *corresponds to* the vortex axis (r=0), the outer endpoint is a function of the profile para-*meter K and correzponds to the outer edge of the vortex core. Various endpoints are denoted* in the diagram by the corresponding value of K.

Taking into account the deviation from the inviscid vortex within the "viscous subcore" the locus of the (C_φ, C_z)-points in the stability diagram is altered as shown by the broken line. The stability diagram shows that for leading edge vortices having a profile parameter smaller than K = 1.16, the outer parts of the vortex become unstable.

There is another instability, near (C_φ, C_z) = (1,0) which corresponds to a small region near the vortex center well within the viscous subcore. The latter instability, which is *present in every real vortex, was considered by Petersohn (1970) as the cause of vortex decay* which he had observed on vortices above delta wings. Petersohn fuund that within the unstable region of the viscous subcore, high turbulence levels exist. *The turbulence* spreads in the radial direction giving rise to further growth of the viscous subcore, which in turn inc·eases tlie unstable region. This process goes *on until the vortex is completely* transformed. The m··chanism described *above accounts well for the gradual decay of a vortex* core but it can certainly not explain the abrupt changes observed in vortex breakdown.

In contrast, Ludwieg (1962, 1965) attributes vortex breakdown to the instability of *the outer parts of the vortex.* Ludwieg shows that an originally stable vortex, having a profile parameter K > 1.16, is transformea in an adverse pressure gradient into a vortex with a smaller profile parameter which is less stable and eventually becomes unsteable if the profile parameter decreases below the value of K = 1.16. Once the vortex becomes un-stable, spiral disturbances of the form given by eq. 19 are amplified. Since the approach flow and initial disturbances are steady, preferably standing disturbance waves occur which are amplified in the streamwise direction. Among these waves are two-vortex modes, corres-ponding to a circumferential wave number γ = 1 and four-vortex modes, corresponding to γ = 2. Also high modes are possible but the lowest modes are probably the most unstable ones.

For the onset of vortex breakdown, only the two-vortex mode (γ=1) is responsible. Figure 19 shows, schematically, the disturbance flow generated by the two lowest modes and the resulting distortion of the original axisymmetric vortex : the vortex becomes eccentric and elliptical. Proceeding in the downstream direction, the distortion grows and - due to the spiral nature of the disturbance waves - the whole cross flow pattern rotates about the vortex axis. The eccentricity of the vortex increases rapidly so that the viscous sub-core is displaced from the center towards the circumference. *Figure 20 shows the effect* of this process schematically : the minima of total and static pressure are shifted rela-tive to each other resulting *in a flow field where a minimum of velocuty occurs beside the* maximum. Due to the exponential growth of the disturbances, the region of low velocity increases rapidly and the fluid in this region undergoes a rapid deceleration which subse-quently leads to an abrupt expansion or burst of the vortex. Naturally, this type of vor-tex breakdown is highly asymmetrical.

Ludwieg's theory of asymmetric vortex breakdown was experimentally verified by Hummel (1965) who measured the velocity and pressure distribution within a leading edge vortex at several axial positions before and after breakdown. Many details of Ludwieg's theory were confirmed by these measurements. In particular, breakdown was found to take place after the outer region of the vortex becomes unstable. Proceeding downstream the line of con-stant total pressure become distorted, clearly demonstrating the increasing eccentricity and ellipticity of the vortex. The lines of constant dynamic pressure, shown in Fig. 21 show the development of a minimum of the velocity beside the maximum and the rapid expan-sion of the region of low velocity which subsequently leads to bursting of the vortex. The experimental facts, observed by Hummel, make it highly probable that this form of vortex breakdown is caused by flow instability and that it develops essentially in the way envi-saged by Ludwieg.

Prediction of vortex breakdown on delta wings

It remains to relate the unstable flow conditions which lead to vortex breakdown to the geometric and aerodynamic parameters at which they occur.

Since vortex breakdown on slender delta wings occurs at first behind or near the trai-ling edge of the wing, Ludwieg assumes that the instability is brought forth by the pres-sure rise encountered at the trailing edge. In fact, Ludwieg (1962) has shown that an ad-*verse pressure gradient changes the velocity distribution so as to make the vortex more* unstable. We may, therefore, conclude that vortex breakdown occurs at or downstream of the trailing edge when the vortex flow over the forward part of the wing is stable and be-comes only unstable due to the pressure rise near the trailing edge. With increasing angle

of attack, the breakdown position moves from the trailing edge upstream towards the apex of the wing. This behaviour can be explained by assuming that with increasing angle of attack, the vortex becomes more unstable. The prediction of the breakdown position is, of course, extremely difficult. If breakdown occurs, its position depends on many unknown factors : the initial velocity distribution within the vortex, the axial pressure gradient, the existence of initial disturbances, and the rate at which the initial disturbances are amplified to the point where breakdown occurs. Considering a related but simpler problem, Wedemeyer (1979) investigated the conditions under which the vortex is stable over the forward part of the wing where the flow field is still conical and not influenced by the trailing edge. In order to be able to predict the stability of the vortex, its velocity distribution must be computed first. Assuming conical flow, the velocity distribution within the vortex core is one of the class of Hall's solutions with a profile parameter K, which is yet to be determined. The overall flow field is obtained by matching the solution for the vortex core with an "outer" solution which is computed by the method of Smith (1968).

In Smith's calculation of the outer solution, an approximate model is used where one or several outer turns of the spiral vortex sheet are computed, while the inner part of the vortex is represented by a concentrated line vortex at the vortex axis. The line vortex was introduced in order to avoid the numerical difficulties of handling an infinite number of turns. To join inner and outer solution, the line vortex is now replaced by a vortex core according to Hall's solution, having the appropriate core diameter and circulation to fit continuously into the outer solution. In this way, the profile parameter K is uniquely determined as a function of aspect ratio Λ and angle of incidence α of the wing. The leading edge vortex is considered to be stable if $K > 1.16$ and unsteable if $K < 1.16$ as suggested by Ludwieg's stability criterion.

Figure 22 shows the stability boundary so obtained, in the (Λ,α)-plane. The diagram shows that above a critical angle of incidence, which depends on the aspect ratio, no stable vortex exists. The critical angle of incidence decreases with increasing aspect ratio. Also shown in fig. 22 is the boundary corresponding to $K = 0.8$. For this K-value, the outer 50 percent of the vortex core (the outer 30 percent of the radius) has become unstable.

The theoretical predicitions are compared with experimental data for vortex breakdown observed by Earnshaw & Lawford (1964). The observed ranges of vortex breakdown for a number of delta wings are indicated in the diagram of fig. 22 as solid vertical lines. The lower endpoints of the line correspond to breakdown at the trailing edge, and the upper endpoints indicate the angle of incidence at which breakdown has reached the apex of the wing. For larger angles of incidence, no leading edge vortices were observed. The figure shows that vortex breakdown is observed only within the unstable region and that the range of vortex breakdown follows in general the theoretical stability boundary. For large aspect ratios, predicted and observed values for the stability boundary diverge. This can be explained by the fact that theoretical predictions are based on slender-body theory which is not applicable to large aspect ratio wings. Also the assumption of axisymmetric flow in the vortex core becomes inadequate for larger aspect ratios.

The good agreement observed for small and moderate aspect ratios is certainly a strong support for the stability theory of vortex breakdown.

4. CONCLUSIONS

The various explanations of vortex breakdown have been divided into two categories : theories which relate breakdown to flow instability and theories which do not. In the present paper, the view is proposed that the two forms of vortex breakdown - the bubble form and the spiral form - are essentially different phenomena, which admit of different explanations. This view is not generally accepted; some investigators hold that the principal mechanism of breakdown is exemplified in the axisymmetric form and that observed asymmetries are secondary effects resulting from initial asymmetries or instability of the breakdown bubble against asymmetric disturbances. The various explanations of vortex breakdown are consistent with many experimental observations : all theories predict vortex breakdown to occur within the observed range of swirl angles and the sensitivity of breakdown to an axial pressure gradient, nut none of the theories can predict the flow in the breakdown region and the location of breakdown with an accuracy sufficient to be checked against experimental observation. On the basis of present experimental evidence, it appears that the spiral form of breakdown is initiated by instability against spiral disturbances while the bubble form can apparently not be related to any flow instability.

The present paper does not consider the effect of vortex breakdown on the aerodynamic characteristics of the wing since this subjetc will be discussed in another paper of the lecture series. Experimental observations show that the lift increased due to vortex separation is always limited by the occurrence of vortex breakdown. There is, at present, no theory that should predict the effect of vortex breakdown on the lift of the wing.

REFERENCES

ANDERS, K. (1981): Measurement of velocity distribution in delta wing vortices using laser doppler velocimetry. VKI PR 1981-03.
BENJAMIN, T.B. (1962): Theory of the vortex breakdown phenomenon. J. Fluid Mechanics, Vol. 14, Part 4, pp 593-629.
BENJAMIN, T.B. (1967): Some developments in the theory of vortex breakdown. J. Fluid Mechanics, Vol. 28, Part 1, pp 65-84.
BILANIN, A.J. (1973): Wave mechanics of line vortices. Ph.D. Thesis, Massachussetts Institute of Technology.
BOSSEL, H.H. 1969): Vortex breakdown flow field. Physics of Fluids, Vol. 12, No 3, pp 498-508.
BOSSEL, H.H. (1971): Vortex computation by the method of weighted residuals using exponentials. AIAA J., Vol. 9, No 10, pp2027-2034.
EARNSHAW, P.B. (1961): An experimental investigation of the structure of a leading edge vortex. ARC R&M 3281.

EARNSHAW, P.B. & LAWFORD, J.A. (1964): Low speed wind tunnel experiments on a series of sharp edged delta wings. ARC R&M 3424.

ELLE, B.J. (1960): On the breakdown at high incidences of the leading edge vortices on delta wings. J. Roy.Aeron.Soc., Vol. 64, No 596, pp 491-493.

ESCUDIER, M.P.; BORNSTEIN, J.; ZEHNER, N. (1980): Observations and LDA measurements of confined turbulent vortex flow. J. Fluid Mechanics, Vol. 98, Part 1, pp 49-63.

FALER, J.H. & LEIBOVICH, S. (1977): Disrupted states of vortex flow and vortex breakdown. Physics of Fluids, Vol. 20, No 9, pp 1385-1400.

FALER, J.H. & LEIBOVICH, S. (1978): An experimental map of the internal structure of a vortex breakdown. J. Fluid Mechanics, Vol. 86, Part 2, pp 313-335.

GARG, A.K. & LEIBOVICH, S. (1979): Spectral characteristics of vortex breakdown flow fields. Physics of Fluids, Vol. 22, No 11, pp 2053-2064.

GRABOWSKI, W.J. & BERGER, S.A. (1976): Solutions of the Navier-Stokes equations for vortex breakdown. J. Fluid Mechanics, Vol. 75, Part 3, pp 525-544.

HALL, M.G. (1961): A theory for the core of a leading edge vortex. J. Fluid Mechanics, Vol. 11, Part 2, pp 209-228.

HALL, M.G. (1965): A numerical method for solving the equations for a vortex core. ARC R&M 3467.

HALL, M.G. (1966): The structure of concentrated vortex cores. Progress in Aeronautical Sciences, Vol. 7, pp 53-110.

HALL, M.H. (1967): A new approach to vortex breakdown. Proc. 1967 Heat Transfer and Fluid Mechanics Institute, Stanford U. Press, pp 319-340.

HALL, M.G. (1972): Vortex breakdown. Annual Review of Fluid Mechanics, Vol.4, pp 195-218.

HARVEY, J.K. (1962): Some observations of the vortex breakdown phenomenon. J. Fluid Mechanics, Vol. 14, Part 4, pp 585-592.

HUANG, J.H. (1974): The nonlinear interaction between spiral and axisymmetric disturbances in vortex breakdown. Ph.D. Thesis, Cornell U., Ithaca.

HUMMEL, D. & SRINIVASAN, P.S. (1967): Vortex breakdown effects on the low speed aerodynamic characteristics of slender delta wings in symmetrical flow. J. Roy. Aero. Soc., Vol. 71, No 676, pp 319-322.

HUMMEL, D. (1975): Investigation of vortex breakdown on a sharp edged slender delta wing. Paper presented at IUTAM Symposium on Concentrated Vortex Motions, Ann Arbor; also Z. Flugwiss., Bd 13, Heft 5, pp 158-168.

JONES, J.P. (1960): The breakdown of vortices in separated flow. U. Southampton, USAA Report 140; also "On the Explanation of Vortex Breakdown", paper presented at IUTAM Symposium on Vortex Motion, Ann Arbor.

KOPECKY, R.M. & TORRANCE, K.E. (1973): Initiation and structure of axisymmetric eddies in rotating stream. Computers & Fluids, Vol. 1, No 3, pp 289-300.

LAMBOURNE, N.C. & BRYER, D.W. (1961): The bursting of leading edge vortices - some observations and discussions of the phenomenon. ARC R&M 3282.

LEIBOVICH, S. & RANDALL, J.D. (1973): Amplification and decay of long non linear waves. J. Fluid Mechanics, Vol. 58, Part 3, pp 481-493.

LEIBOVICH, S. (1978): The structure of vortex breakdown. Annual Review of Fluid Mechanics, Vol. 10, pp 221-246.

LOWSON, M.V. (1964): Some experiments with vortex breakdown. J.Roy.Aeron.Soc., Vol. 68, No 641, pp 343-346.

LUDWIEG, H. (1960): Stabilität der Strömung in einem zylindrischen Ringraum. Z. Flugwiss. 8. Jhrg., pp 135-140; and Ergänzung zu der Arbeit "Stabilität der Strömung in einem zylindrischen Ringraum", Z.Flugwiss., 9. Jhrg., Heft 11, 1961, pp 359-361.

LUDWIEG, H. (1962): Zur Erklärung der Instabilität der über angestellten Deltaflügeln auftretenden freien Wirbelkerne. Z. Flugwiss., 10. Jhrg., Heft 6, pp 242-249.

LUDWIEG, H. (1964): Experimentelle Nachprüfung der Stabilitätstheorie für reibungsfreie Strömungen mit schraubenförmigen Stromlinien. Z. Flugwiss., 12.Jhrg., Heft 8, pp 304-309.

LUDWIEG, H. (1965): Erklärung des Wirbelaufplatzens mit Hilfe der Stabilitätstheorie für Strömungen mit schraubenlinienförmigen Stromlinien. Z. Fluwiss., 13. Jhrg., Heft 12, pp 437-442.

LUDWIEG, H. (1970): Vortex breakdown. DLR FB 70-40.

MAGER, A. (1972): Dissipation and breakdown of a wing-tip vortex. J. Fluid Mechanics, Vol. 55, Part 4, pp 609-628.

PECKHAM, D.H. & ATKINSON, S.A. (1957): Preliminary results of low speed wind tunnel tests on a gothic wing of aspect ratio 1.0. ARC CP 508.

PETERSOHN, E. (1970): The stability criterion for vortices by Ludwieg and its application to some experimental results. FFA Report 119.

POISSON-QUINTON, P. & ERLICH, E. (1965): Hyperlift and balancing of slender wings. NASA TT F 9523.

RANDALL, J.D. & LEIBOVICH, S. (1973): The critical state : a trapped wave model of vortex breakdown. J. Fluid Mechanics, Vol. 58, Part 3, pp 495-515.

SARPKAYA, T. (1971a): On stationary and travelling vortex breakdowns. J. Fluid Mechanics, Vol. 45, Part 3, pp 545-559.

SARPKAYA, T. (1971b): Vortex breakdown in swirling conical flows. AIAA J., Vol. 9, No 9, pp 1792-1799.

SARPKAYA, T. (1974): Effect of adverse pressure gradient on vortex breakdown. AIAA J., Vol. 12, No 5, pp 602-607.

SMITH, J.H.B. (1968): Improved calculations of leading edge separation from slender, thin delta wings. Proc. Royal Soc., A306, pp 67-90.

SQUIRE, H.B. (1960): Analysis of the "vortex breakdown" phenomenon. Part 1. Imperial Coll. London, Report 102; also in "Miszellaneen der angew.Mech.", 1962, pp 306-312; Akademie Verl.

STEWARTSON, K. & HALL, M.G. (1963): The inner viscous solution for the core of a leading edge vortex. J. Fluid Mechanics, Vol. 15, Part 2, pp 306-318.

WEDEMEYER, E. (1969): Stabilität spiraliger Strömungen in einem zylindrischen Ringraum. Mitt. Mx-Planck-Inst. für Strömungsf., Nr 44.

WEDEMEYER, E. (1979): Stable and unsteable vortex separation. in "High Angle of Attack
Aerodynamics", AGARD CP 247, pp 13-1 - 13-10.
WENTZ, W.H. & KOHLMAN, D.K. (1969): Vortex breakdown on slender sharp-edged wings.
AIAA P 69-778.
WERLE, H. (1960): Sur l'éclatement des tourbillons d'apex d'une aile delta aux faibles
vitesses. La Recherche Aéronautique, No 74.
WERLE, H. (1971): Sur l'éclatement des tourbillons. ONERA NT 175.
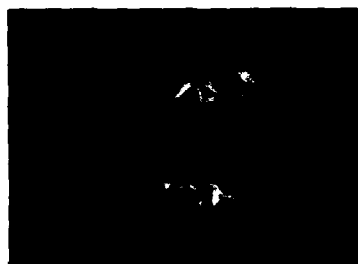
Fig. 1 Vortex breakdown on delta wing
φ_B = 60° (Werlé, 1960)

Fig. 2 Effect of suction on breakdown
(Werlé, 1960)

Fig. 3 Effect of stagnation on breakdown
(Werlé, 1960)

Fig. 4 Effect of yaw on breakdown
(Werlé, 1960)
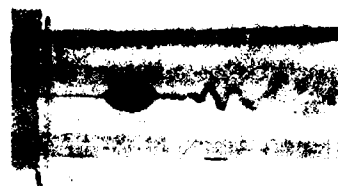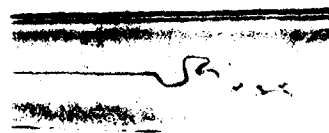
(a) Bubble form   (b) Spiral form
Fig. 5 Vortex breakdown in a vortex tube (Faler & Leibovich, 1977)
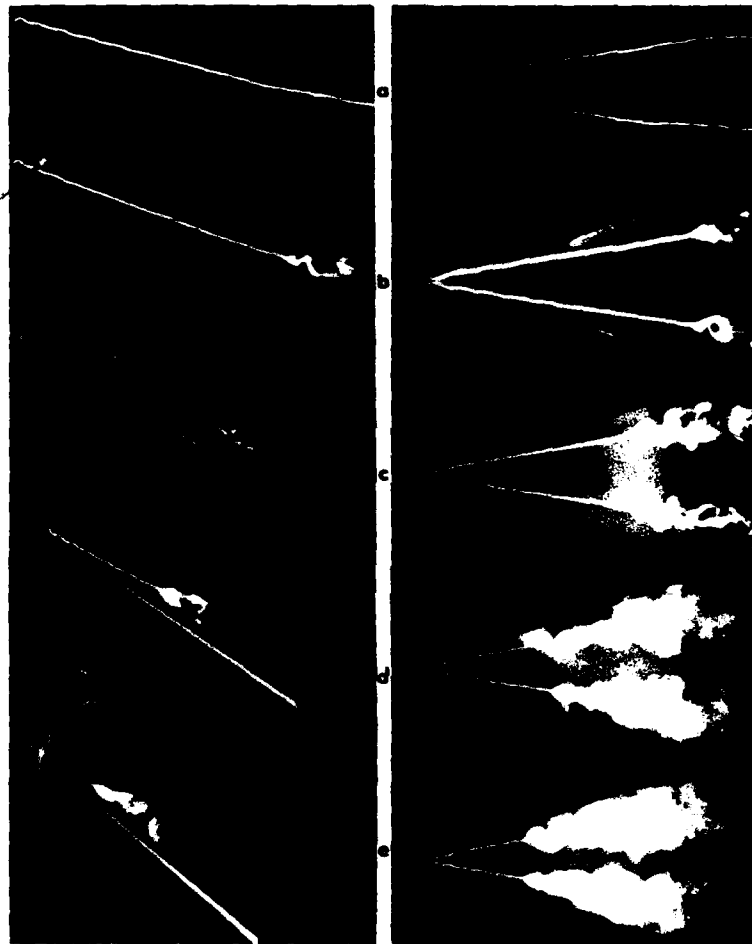
a) $\alpha = 21.6°$ $\varphi_B = 75°$ ANGLE OF SWEEPBACK
b) $\alpha = 27.2°$ α = ANGLE OF INCIDENCE
c) $\alpha = 32.6°$ Re = 2.10^4
d) $\alpha = 37.8°$
e) $\alpha = 42.6°$

Fig. 6 Effect of angle of incidence on the breakdown position
        (Werlé, 1971)

Fig. 8 The effect of sweep angle, φ_B, on the angle of incidence, α, for breakdown positions at the trailing edge $(\xi = l_s)$ and midchord $(\xi = \frac{1}{2} l_s)$ (Werlé, 1971)

Water tunnel test, $Re = 10^4$
●× Onera water tunnel

Wind tunnel tests, $Re = 10^6$
□ Poisson-Quinton & Erlich (1965)
● ○ Wentz & Kohlman (1969)
▲ Hummel & Srinivasan (1967)
▽ Earnshaw & Lawford (1964)
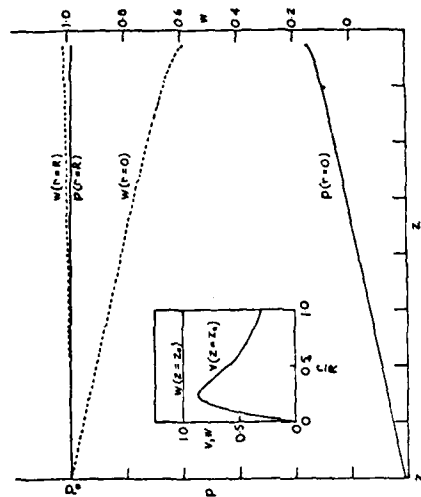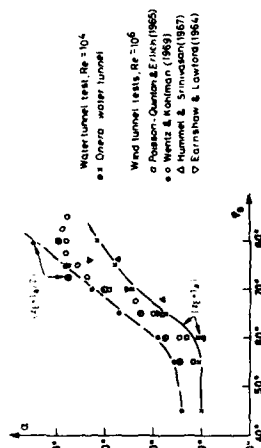
Fig. 9 Calculated (method of Hall, 1965) variations of pressure, p, and axial velocity, w, along axis $r=0$ and along outer cylindrical stream surface $r=R$ of vortex core (Hall, 1972)

$\varphi_B = 80°$ $\alpha = 35°$

$\varphi_B = 75°$ $\alpha = 32.5°$

$\varphi_B = 70°$ $\alpha = 27.5°$

$\varphi_B = 65°$ $\alpha = 22.5°$

$\varphi_B = 60°$ $\alpha = 13°$

Fig. 7 Effect of sweep back on the breakdown position (Werlé, 1971)
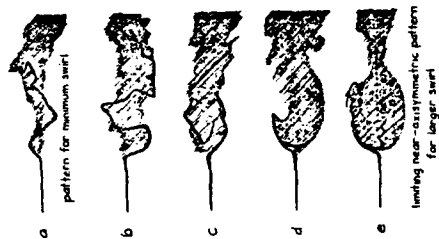
Fig. 12 Variation of breakdown pattern with increase of swirl (based on photographs of Sarpkaya, 1971) (Hall, 1972)

a
b
c
d
e   Involving near-axisymmetric pattern for larger swirl

pattern for minimum swirl

Fig. 13 Configuration obtained as a result of accelerating the flow downstream of the bubble (Harvey, 1962)
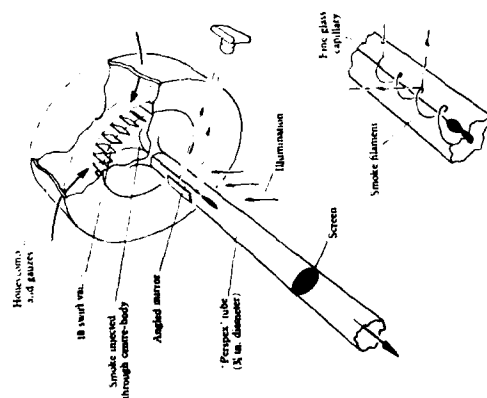
Fig. 10 A general view of the vortex tube (Harvey, 1962)
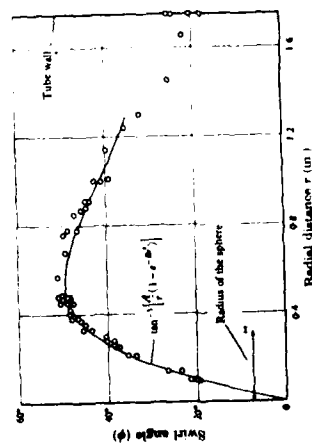
Fig. 11 The distribution of swirl angle measured ahead of breakdown (Harvey, 1962)

Fig. 16 Calculated (Bossel, 1967) and observed (Sarpkaya, 1971) bubble contours (Hall, 1972)
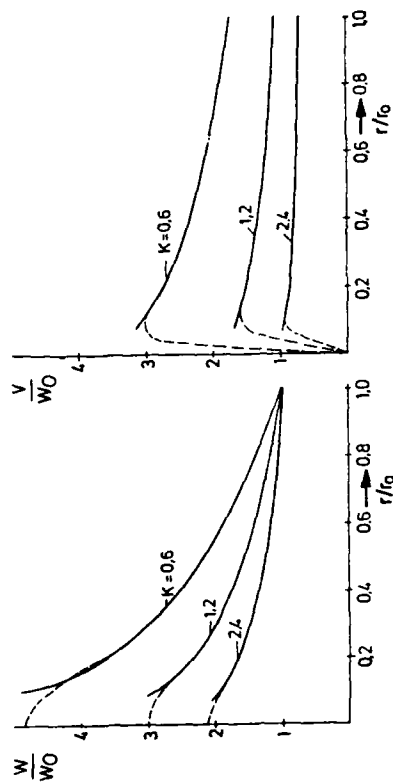
Fig. 17 Velocity distributions of Hall's vortex for various profile parameters K

(a) The formation of two bubbles and the increase of swirl angle

(b) The formation of three bubbles in rapid succession

Fig. 14 (Sarpkaya, 1971b)
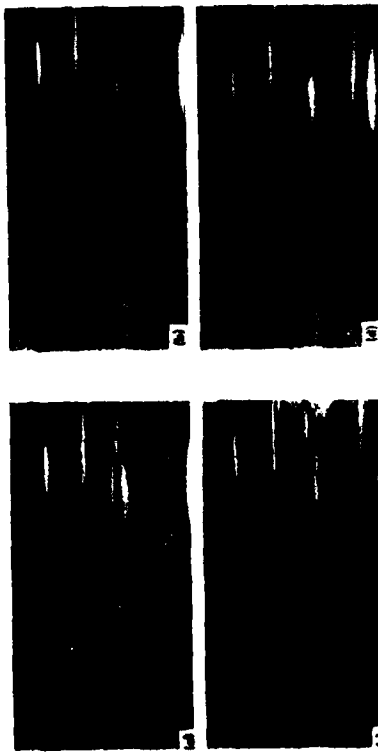
Fig. 15 Evolution of helical disturbances (Faler & Leibovich, 1977)
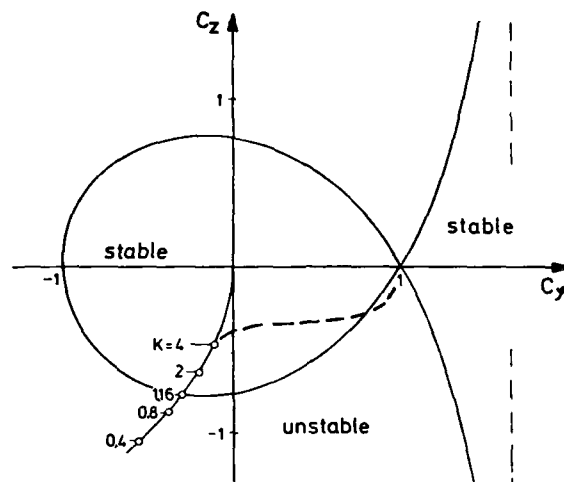
Fig. 18 Stability diagram for vortex flow. $C_y = \frac{r}{V}\frac{dV}{dr}$; $C_z = \frac{r}{V}\frac{dW}{dr}$; K = profile parameter

(a) Two-vortex flow

(b) Four-vortex flow
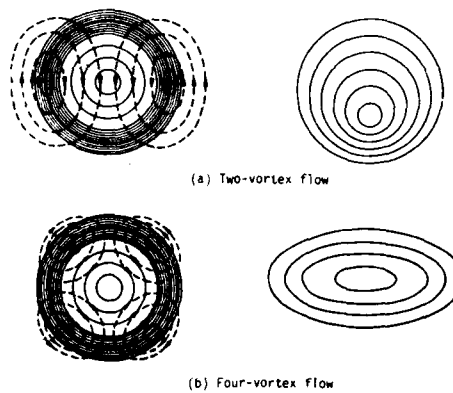
Fig. 19 Lines of constant total pressure (Ludwieg, 1970)
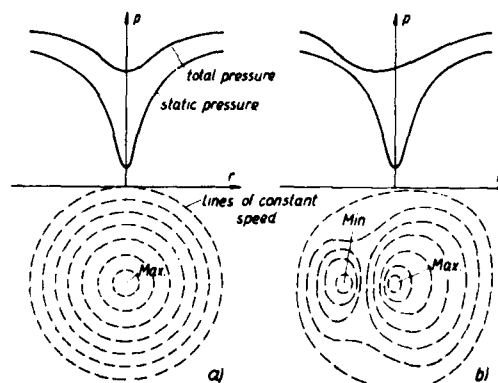
Fig. 20 Pressure and velocity distributions (schematic)
(a) Before beginning of breakdown
(b) After beginning of breakdown
(Ludwieg, 1970)
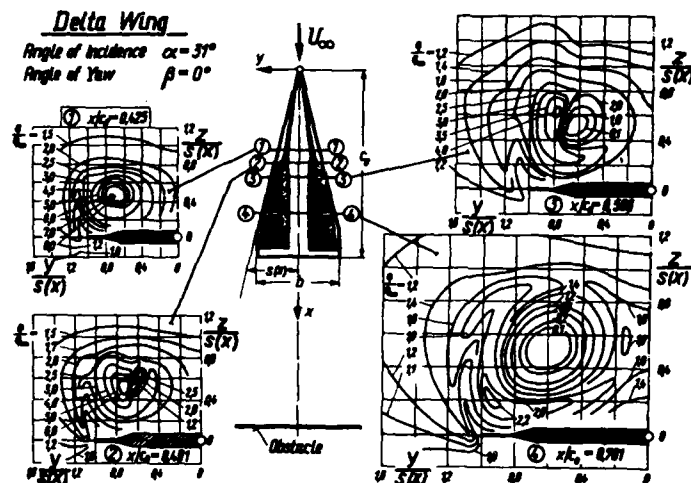
Fig. 21 Velocity distribution in four planes normal to the wing : lines
of constant dynamic pressure q/q_∞ (Hummel, 1965)
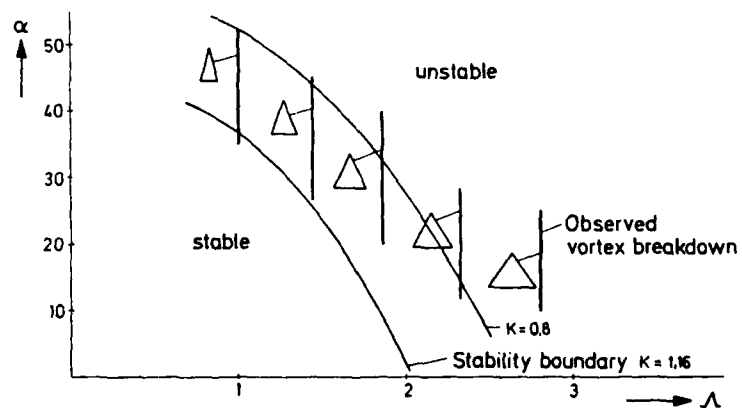
Fig. 22 Theoretical stability boundary and experimental ranges of vortex
breakdown in the (Λ,α)-plane
Λ = aspect ratio, α = angle of incidence
(Wedemeyer, 1979)

CONTROL OF THE FOREBODY VORTEX ORIENTATION BY ASYMMETRIC AIR
INJECTION: (PART A) APPLICATION TO ENHANCE DEPARTURE/SPIN
RECOVERY OF FIGHTER AIRCRAFT AND (PART B) DETAILS
OF THE FLOW STRUCTURE

by

A.M. Skow, Manager, F-5 Aerosciences
Northrop Corporation, Aircraft Division
One Northrop Avenue, Hawthorne, California 90250

D.J. Peake, Senior Research Scientist
NASA Ames Research Center
Moffet Field, California 94035

CONTENTS

SUMMARY

This paper describes a novel concept which has been developed to provide powerful directional control effectiveness for a fighter aircraft at high angles of attack, where more traditional controls have very limited capability. The concept utilizes the energy concentrated in the strong forebody vortices (which form on slender bodies at high relative incidence) by controlling the lateral orientation of the vortices with respect to the body.

A large volume of research which has been performed in recent years to attenuate the magnitude of the asymmetric forces and moments on slender bodies such as those on missiles and some fighter aircraft. This body of work showed that the forebody vortices on these configurations are very sensitive to small disturbances in the flow, such as would be caused by asymmetric surface imperfections on a body, especially near the apex of the nose.

The present concept grew out of this more general body of work and seeks to utilize the inherent sensitivity of the vortex positioning and its bi-stable nature to an advantage allowing control of the forces which are developed. As it turns out, the direction or sense of the asymmetric vortex pair is much easier to control than to attenuate.

Part A of this paper describes the work which was done to develop the concept for application to an aircraft and, as such, is directed toward the effects of the concept on aircraft forces and moments and on the flight mechanics of the aircraft during maneuvering at high angles of attack.

The objective of this part of the study was to utilize the side force associated with asymmetric vortices, in a controlled manner, to enhance the ability of the fighter to recover from a departure from controlled flight. The results from these water tunnel and wind tunnel experiments show that a small amount of tangential blowing along the forebody near the apex can effectively alter the forebody vortex system and generate large restoring yawing moments. Six-degree-of-freedom digital simulation results show that this concept can substantially enhance departure recovery characteristics of fighter aircraft with long, slender forebodies.

Part B of the paper describes the results of experiments which were conducted on a cone model, where the principal test objective was to develop an understanding of the fluid mechanics involved in the process of vortex control. Knowledge gained in these more generic tests should allow the concept to be applied to a wider range of configurations.

NOMENCLATURE

A1	primary attachment line	S1	primary separation line
A2	secondary attachment line	S2	secondary separation line

$C_p = \dfrac{P-P_\infty}{q_\infty}$ static pressure coefficient

$\tilde{x}$ longitudinal position (from apex)

Y_d nozzle lateral offset

C_{YB} side force coefficient from balance

α angle of attack, angle of incidence

C_{YP} side force coefficient from integrated surface pressures at $\tilde{x}/\ell = 0.87$

$\tilde{\sigma} = \alpha/\alpha_c$ relative incidence

C_μ blowing moment coefficient

α_T threshold angle of attack

β sideslip angle

d base diameter of forebody

ℓ axial length of forebody

θ_c semi-angle at apex of forebody

ℓ/d forebody fineness ratio

θ_n nose semi-apex angle

M_∞ free-stream Mach number

ϕ circumferential angle around cone surface, measured from windward generator: negative on port side

q_∞ free-stream dynamic pressure

ϕ_j jet position

Re Reynolds number

ϕ_R forebody roll angle (with roll degree of freedom)

r_n/d nose bluntness

A. APPLICATION TO ENHANCE DEPARTURE/SPIN RECOVERY OF FIGHTER AIRCRAFT

A.1 INTRODUCTION

For fighter aircraft that operate in the air combat maneuvering (ACM) arena, flight at high angles of attack (AOA), near the limits of controllability, is an inherent part of both offensive and defensive maneuvering. Reluctance to operate in this regime because of possible departure from controlled flight limits the capability of the man-machine combination to deliver its maximum performance. Pilot confidence is the key to effectively operating close to control boundaries, and pilot confidence is a function either of the aircraft system's natural resistance to departure or of the pilot's ability to easily recover from the occasional out-of-control condition associated with high-AOA maneuvering. Unfortunately, many aircraft in the inventories of the free world's air forces exhibit a high degree of susceptibility to departure and spin entry. Such aircraft have a departure threshold that is generally beyond maximum lift but well within the ACM gross maneuver envelope. Many of these aircraft also have poor departure recovery characteristics, and generally require the pilot to act quickly in order to regain control of his aircraft. Since most pilots spend relatively little time near control limits in training or in normal operational flying, they are often unprepared for their first departure. The standard out-of-control reaction is frequently one of panic, followed by ejection.

In an attempt to improve this situation, military training commands have instituted programs to better prepare the pilot for the disorientation he will experience in a departure and to give him a better chance of taking positive recovery action in a timely manner.

Engineers and scientists are also tackling the problem. One engineering approach has been to use motion and attitude sensors in conjunction with the aircraft's control system to "automatically" recover the aircraft from the departure. State-of-the-art sensors can determine whether the aircraft has departed from controlled flight and can determine the direction of motion much more quickly than the average pilot. Relatively simple control laws can be programmed into a control system to enable it to respond to these sensor inputs and place the control surfaces in position to optimize the chances of recovery. Such a control system would be much more reliable than the average pilot; the only drawback to concepts developed using this approach is that, for most aircraft, control effectiveness in the departure AOA region is severely degraded when compared to control effectiveness at lower AOA. This sometimes forces the designer to lower the threshold AOA for the automatic recovery system into a region in which it could be activated unnecessarily. If more effective control devices could be developed, however, this general approach could be used to design a system with the potential to dramatically reduce the loss of life and equipment resulting from out-of-control flight accidents.

Part A of this paper describes an analytical and experimental study undertaken to develop a novel control concept that is highly effective in the AOA region above stall, and could be mechanized in the manner outlined above. The vortex blowing control concepts tested in this study were designed to alter the asymmetric orientation of the forebody vortex system, taking advantage of the large aerodynamic forces produced by this asymmetry. The effects of these blowing concepts on the overall stability and control characteristics of an aircraft at AOA are reported in Part A of this paper and in Reference 1. Companion papers by Peake, Owen, and Johnson (References 2 and 3) discuss the fluid mechanics and topology associated with forebody blowing about a slender cone model.

A.2 BACKGROUND

A.2.1 Forebody Flowfields at High Angles of Attack

It is well known that an asymmetric vortex system forms on the leeside of aircraft and missile fore bodies at high AOA (References 4 through 9). The degree of asymmetry and the strength of the vortices depend on several parameters. the primary ones being AOA, fineness ratio (l/d), nose semi-apex angle (θ_n). and nose bluntness (r_n/d).

At incidences generally greater than twice the nose semi-apex angle, these asymmetric vortices be come strong enough to produce values of side force and yawing moment large enough to influence the de parture resistance of an aircraft (References 10 through 15). These asymmetric side forces may not only generate a departure from controlled flight but, once the departure has occurred. they may aggravate the tendency of an aircraft to enter a flat spin mode. In addition, since these vortices have been observed to remain in an asymmetric orientation even under coning conditions. they can oppose recovery from a spin (References 16 and 17).

These vortices have been observed to behave in a bistable manner, and are usually oriented in one of two mirror-image states (References 18 through 20); the mirror-image orientation assumed by a vortex is influenced by minute geometric imperfections, especially near the apex of the nose.

A.2.2 Asymmetric Vortex Control

The overall objective of the present study was to harness the power of this vortex system and use the side force generated by its asymmetric nature as a control device. Such a device would be effective in the AOA region beyond stall and could be used, with proper system design and following appropriate con trol laws, to greatly enhance the capability of an aircraft to recover from a departure from controlled flight.

A.2.3 Previous Research

The basic concept of controlling the yawing moments generated by long, slender forebodies to aid spin recovery was first proposed by Neihouse et al. in 1960 (Reference 10). These investigators pursued three means of controlling the yawing moments: strakes or spoiler strips placed along the inboard side of the nose (right side in a right spin), induced circulation about the forebody produced by rotating a conical nose section, and flap-type surfaces placed either on both sides or only on the inboard side of an aircraft nose. Each of these concepts proved effective in promoting rapid recovery from various types of spins on different models. Similar experiments using asymmetric nose strakes. reported by Chambers et al. in 1970 (Reference 21), showed equally promising results on a different aircraft configuration. Kruse conducted experiments on the effect of spinning an axisymmetric body about its longitudinal axis, and noted that the peak-to-peak variation of side force decreases with increased spin rate. His data also showed that the time averaged side force is reduced as the body is spun (Reference 22). Cornish and Jenkins conducted experi ments with symmetric tangential blowing near the nose of an aircraft but were unsuccessful in affecting the spin recovery characteristics of their particular configuration (Reference 23).

A.2.4 Present Studies

The present work concentrated on the experimental evaluation of concepts to control the forebody side force through asymmetric tangential blowing near the apex of the nose. The concept of augmenting the spin recovery capability of a fighter aircraft by controlling, through blowing, the side force produced by the nose was first proposed by Skow in 1977 (Reference 24).

Several pratical considerations were taken into account in order to screen out devices that would not be applicable to fighter aircraft regardless of their effectiveness. The screening criteria used were:

1. The tangential blowing concepts must be sufficiently effective to not require abnormally large quantities of air or unattainable mass flow rates.

2. The blowing nozzles must be located in a region aft of the radar antenna so radar performance would not be affected adversely.

A.3 EXPERIMENTAL APPARATUS AND TEST PROGRAM

A.3.1 Water Tunnel Tests

Preliminary tests of various forebody vortex blowing control concepts were conducted in early 1978 in the Northrop 16- by 24-inch diagnostic water tunnel on a 0.025-scale model of an F-5F aircraft. The Northrop water tunnel is a single-return, low-turbulence facility and is operated at a test section velocity of 0.1 meter per second (0.35 foot per second), which corresponds to a Reynolds number of approximately 1×10^5 per meter (3×10^4 per foot). The F-5F model was equipped with two parallel rows of dye injection orifices located on the lower surface of the fuselage forebody. Visualization of the forebody flowfield is achieved when the dye flows out of these orifices and is entrained into the separated shear layer or layers. which in turn roll up into well defined vortices.

The water tunnel tests were conducted to screen a large number of potentially useful blowing schemes by comparing, in a qualitative manner, the relative capability of each concept to control the forebody vortex orientation. The blowing concepts tested consisted of small nozzles located on the surface of the forebody at various locations. The angle of the blowing jet relative to the free-stream was also varied. Water was supplied to the blowing nozzle through a small tube running down the centerline of the model. Accurate mass flow rates were set by using a water flow meter in the supply line, external to the tunnel. Additional water tunnel tests were conducted on two tangent-ogive-cylinder bodies to determine the effect of vortex

blowing control on more generic shapes. The tangent ogive forebodies had fineness ratios (l/d) of 3.5 and 5.0. Each was tested with a common circular-cylinder afterbody (l/d = 4.5). Tangential blowing in a down stream direction was tested for a matrix of positions on the surface of both bodies.

The experiments were performed over an AOA range of 0 to 60 degrees. All water tunnel tests were performed at zero sideslip angle. Vertical and lateral positions of the vortex cores were determined at a fixed longitudinal station for the matrix of nozzle geometries at various blowing rates. In this manner the relative effectiveness of each concept was evaluated and optimum nozzle locations were determined.

A.3.2 Wind Tunnel Tests

Based on the results of the water tunnel tests, the most promising nozzle geometries were selected for proof-of-concept testing in the wind tunnel.

Testing was conducted in the Northrop low-speed wind tunnel. This tunnel is a horizontal, atmo spheric, single-return facility capable of test section Reynolds numbers up to 7.9 x 10^6 per meter (2.4 x 10^6 per foot) and dynamic pressures up to 9580 Newtons per square meter (200 pounds per square foot). The test section is 10 feet wide, 7 feet high, and 20 feet long. The tunnel has a contraction ratio of 12:1, which gives a streamwise turbulence level of less than 0.1 percent in the test section.

Tests were conducted using a 0.1-scale F-5F model equipped for asymmetric blowing at two fuselage stations on the upper surface of the forebody. A plenum chamber for the blowing system was located in the nose of the model. This plenum chamber was pressurized from an external source through an air supply line routed from a support near the back of the sting, forward along the top of the model, and buried just aft of the canopy. Care was taken to ensure that the supply line was nonmetric. Figure 1 shows the model installation in the tunnel and illustrates the blowing apparatus.

(A)   (B)

FIGURE 1. WIND TUNNEL TEST MODEL

The blowing nozzles were designed to provide choked flow at the nozzle exit plane. A nozzle calibration was performed to determine actual discharge coefficients. Plenum total pressure and temperature and nozzle mass flow rate were measured and used to compute nozzle jet velocity and, hence, the blowing momentum coefficient (C_μ).

Wind tunnel tests were performed at a dynamic pressure of 2494 Newtons per square meter (50 pounds per square foot), corresponding to a Reynolds number of 4.3 x 10^6 per meter (1.3 x 10^6 per foot). Plenum pressures for the blowing system ranged from 1.1 to 4.2 x 10^6 Newtons per square meter (165 to 615 pounds per square inch), yielding blowing momentum coefficients (C_μ) based on wing area of between 0.008 and 0.032. Data were taken over an AOA (α) range of 0 to 90 degrees in 2-degree increments and over a side slip (β) range of ±25 degrees in 5-degree increments.

A.4 DISCUSSION OF RESULTS

A.4.1 Water Tunnel Tests

A.4.1.1 Asymmetric Tangential Blowing Concepts

Water tunnel experiments performed with the 3.5l/d tangent-ogive forebody indicated that, for the range of longitudinal positions tested (approximately 1.0 to 2.0 body diameters aft of the apex of the nose), the most effective tangential blowing arrangement was with the nozzle directed aft and on the same side of the body as the higher primary vortex. (This would be on the side opposite to the direction of a departure or spin, since the driving side force is produced by the vortex in the closest proximity to the surface.) The topology of the asymmetric vortex development is discussed by Peake et al. in References 2 and 3.

As shown in Figure 2, with the model at zero sideslip angle, when a sufficient quantity of mass flow is directed in a concentrated jet beneath the high primary vortex, the asymmetric primary vortex system can be induced to form in its mirror-image state. The blowing coefficients shown are referenced to the

model base diameter. The blowing momentum required to induce a complete reversal of the vortex core posi tions (i.e., mirror-image state) was found to be a function of the longitudinal position of the nozzle relative to the apex of the nose, the radial position of the nozzle relative to the windward generator, and the model AOA. As seen in Figure 3, significant reductions in required momentum coefficient are noted as the nozzle is moved toward the apex of the nose at a constant nozzle lateral offset (Y/d). The approximate location of a typical radar antenna is shown for reference. Note that significantly higher values of jet momentum are required to produce reversal at higher AOA.
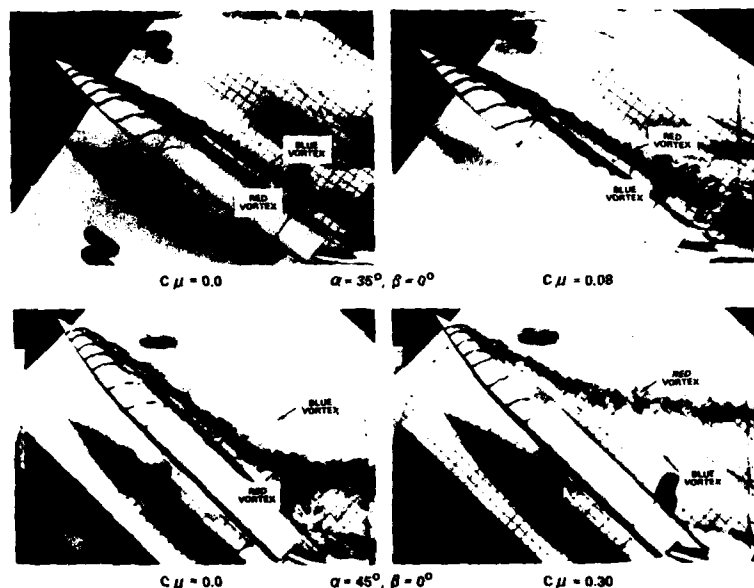
FIGURE 2. DEMONSTRATION OF VORTEX CONTROL ON A 3.5 CALIBER TANGENT-OGIVE MODEL
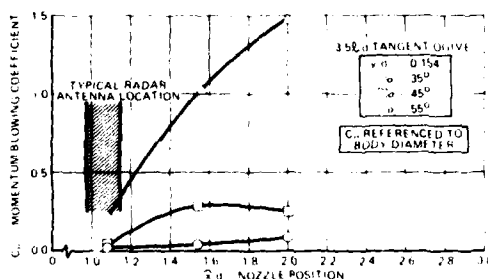
FIGURE 3. VARIATION IN BLOWING REQUIREMENTS WITH LONGITUDINAL POSITION OF NOZZLE

Figure 4 illustrates the effect of nozzle radial position on blowing control effectiveness. As the nozzle is displaced angularly away from the leeward generator at a constant longitudinal position, an increase in blowing effectiveness is noted. The optimum radial position appears to correspond to a lateral position slightly outboard of the center of the higher vortex core.

Water tunnel experiments performed on the F-5F model using the tangential, aft-blowing concept yielded the results shown in Figure 5. These results are consistent with those obtained with the tangent-ogive models and illustrate that, at zero sideslip angle, it is possible to induce the vortices to reverse orien-tation (i.e., mirror-image state) with sufficient quantities of blowing on a realistic fighter aircraft configuration.
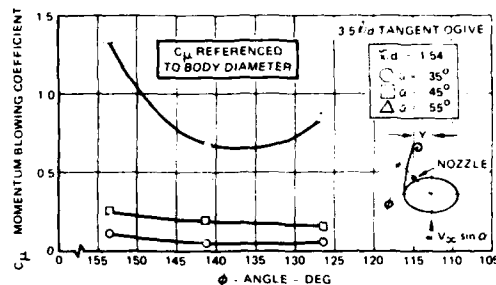
FIGURE 4. VARIATION IN BLOWING REQUIREMENTS WITH RADIAL POSITION OF NOZZLE

$C\mu = 0.0$ $\alpha = 35°, \beta = 0°$ $C\mu = 0.006$

$C\mu = 0.0$ $\alpha = 45°, \beta = 0°$ $C\mu = 0.018$
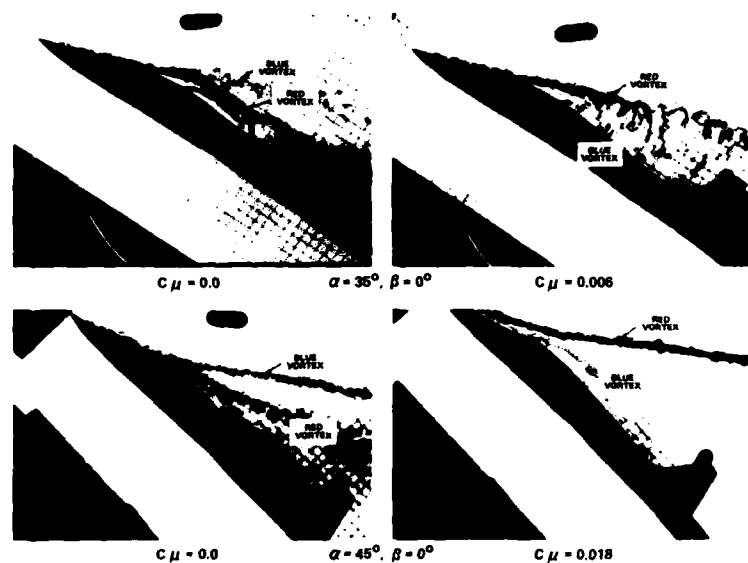
FIGURE 5. DEMONSTRATION OF VORTEX CONTROL ON A FIGHTER MODEL

A.4.2 Wind Tunnel Tests

From the results of the water tunnel tests previously discussed, the most promising vortex control schemes were chosen for proof of-concept testing in the low-speed wind tunnel. Two blowing nozzle locations were selected.

A.4.2.1 Vortex Blowing Control Concepts

Figure 6 presents the measured effect of aft tangential blowing on yawing moment at zero and ±5 degrees of sideslip for the F-5F aircraft. With blowing off, an asymmetry in the yawing moment at zero sideslip begins to develop at an AOA of approximately 32 degrees ($\sigma/\theta_n = 2.0$). With blowing on, even at the lowest jet momentum coefficient tested ($C_\mu = 0.008$), the asymmetry begins to develop slightly earlier, at an AOA of 24 degrees ($\sigma/\theta_n = 1.5$) and, at zero sideslip, forms in the opposite sense to the blowing-off case. The asymmetry in the side force or yawing moment is very easy to see at zero sideslip, but the asymmetric nature of the primary forebody vortex system applies a strong bias to the forces and moments at nonzero sideslip as well. Inspection of the data in Figure 6 at $\beta = \pm 5$ degrees indicates that the vortex blowing concept reverses the sense of the bias at AOA up to approximately 50 degrees.

At AOA beyond 24 degrees, the largest incremental change in yawing moment is obtained at the lowest momentum coefficient tested. The increment then increases approximately linearly as the jet momentum coefficient is increased, up to the maximum mass flow rate tested.
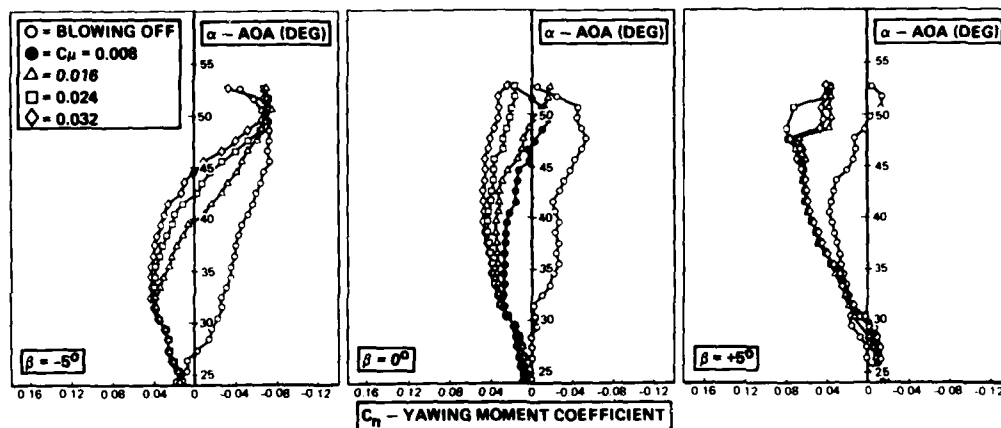
FIGURE 6. VORTEX BLOWING CONTROL EFFECTIVENESS

Figure 7 presents the incremental yawing moment generated by the vortex control system as a function of AOA. These data are compared with the incremental yawing moment produced by full deflection of the conventional rudder of the F-5F. Note that even the lowest jet momentum coefficient tested provides yawing moments in the AOA range from 35 to 55 degrees that are comparable to those produced by the rudder at very low incidences. Also, it is interesting to note that the vortex control effectiveness begins to increase in the same AOA region in which rudder effectiveness is declining rapidly. This leads to a rather interesting conclusion: at low AOA, directional stability and control are best provided by aerodynamic surfaces located behind the aircraft center of gravity. e.g., a vertical tail and a rudder, and at high post stall AOA, directional control as well as stability can best be provided by an aerodynamic device located ahead of the center of gravity, near the apex of the nose.
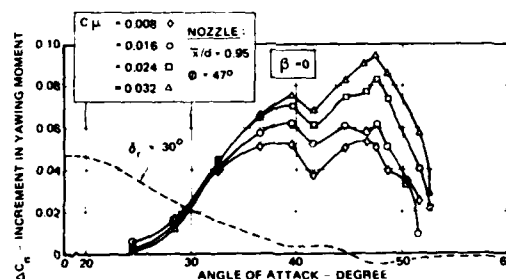
FIGURE 7. VORTEX BLOWING CONTROL EFFECTIVENESS

Figure 8 illustrates the effectiveness of the vortex blowing control device as a function of sideslip at a constant angle of attack (α = 47 degrees). These data indicate that over a very wide range of sideslip angles, the vortex blowing control device produces a significant incremental yawing moment (in this case a yawing moment to the left in opposition to the yawing moment produced by the blowing-off vortex asymmetry). The reversal in incremental yawing moment at a sideslip angle of 6 degrees caused some concern, but the impact of this phenomenon on the effectiveness of the device could not be assessed by inspection of the wind tunnel data only; simulation of the overall effectiveness was required.

A.4.3 Six-Degree-of-Freedom Simulation

The capability of the blowing concepts to augment the departure and spin recovery capability of an F-5F fighter aircraft was evaluated by means of a digital six-degree-of-freedom (6DOF) computer simulation. The baseline aerodynamic model used in this simulation has been validated by comparison of calculated and flight test trajectories of many coupled, high-AOA maneuvers flown during spin tests of this aircraft. An algorithm was developed to model the incremental forces and moments generated by the blowing devices, as determined from the low-speed wind tunnel experiments.

Maneuvers were simulated by specifying grossly aggravated control inputs, which were found during spin susceptibility testing to produce departures and spin entries. The departures and spins generated were found to be difficult to recover from using traditional recovery control inputs both inflight and in the simulation.
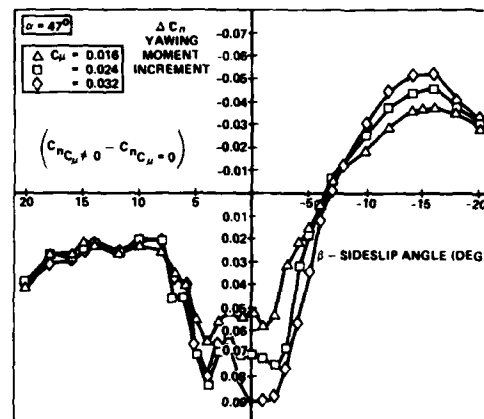
FIGURE 8. EFFECT OF SIDESLIP ON VORTEX BLOWING
CONTROL POWER

    The threshold AOA and yaw rate at which the device was activated were varied in the simulations. as was the blowing mass flow rate. The optimum yaw rate/AOA threshold and the general effect of blowing momentum were determined in this manner. Figure 9 presents a typical series of time histories at a given mass flow rate in which the threshold AOA was varied. Recoveries are seen to be significantly improved when the blowing device is activated early in the departure but severely degraded when the device is activated after the departure has been allowed to progress toward spin entry.
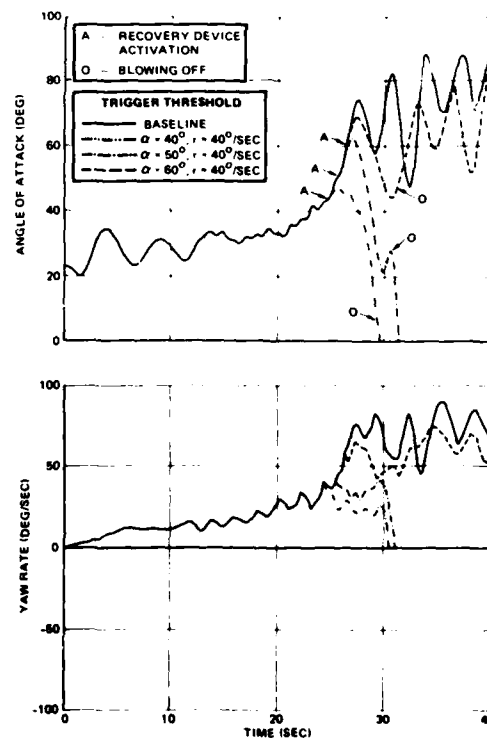
FIGURE 9. SAMPLE TIME HISTORY OF DEPARTURE RECOVERY
AUGMENTED BY VORTEX BLOWING

A blowing threshold angle of attack, a_T, of 40 degrees provides good recovery augmentation and is well beyond the AOA for maximum lift coefficient, and thus has no impact on the maneuvering capability of the F-5F aircraft. For each simulation a yaw rate deadband of ±40 degrees per second at an AOA of 40 degrees, decaying linearly to ±20 degrees per second at an AOA of 60 degrees, was used. In this manner the blowing device is not activated until the yaw rate exceeds the deadband limit.

Figure 10 illustrates the final blowing control device schedule superimposed on the ACM gross maneuver boundary for the F-5F. A sample trajectory of a typical ACM is also shown. The maneuver simulated is a high-speed, high-g, maximum rate windup turn to the left with the aircraft at an AOA near the maximum lift coefficient (C_{Lmax}). From this initial condition (indicated by ① on the figure), the pilot initiates a high-g turn reversal by applying full right rudder and aileron. Since most fighter aircraft are designed to roll about the flight path rather than the body axis, a large yaw rate develops in addition to the commanded roll rate (②). This yaw rate couples with the roll rate to produce a large nose-up pitch rate (③). The combination of yaw rate and high post-stall AOA produces a departure from controlled flight and a spin entry (④ and ⑤). At this point the pilot senses loss of control and initiates a conventional recovery, which is unsuccessful due to the reduced control effectiveness at high AOA; the aircraft enters a developed spin (⑥). For the case of a vortex blowing-assisted recovery, the blowing device is triggered when the maneuver trajectory crosses the activation threshold (Ⓐ). The blowing device generates a strong side force on the nose in opposition to the direction of yaw, allowing an immediate recovery (Ⓑ).
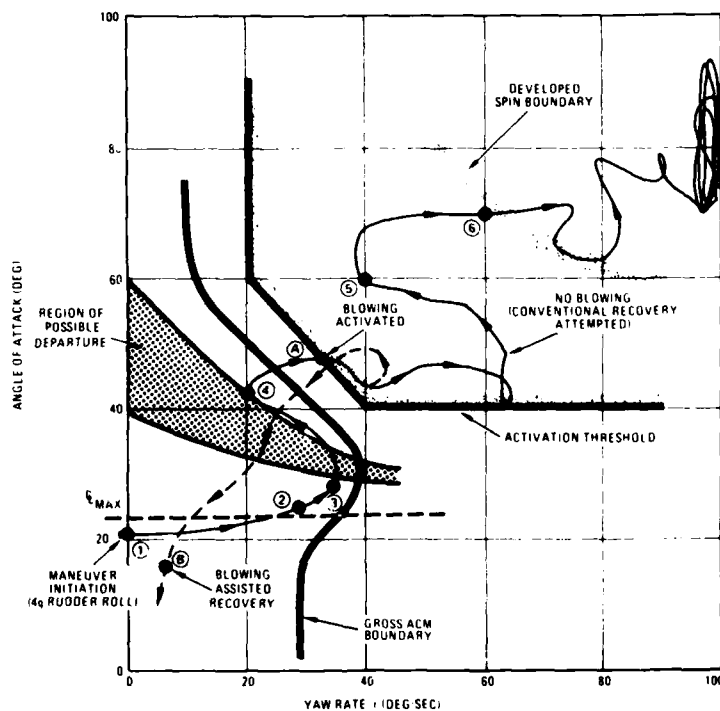
FIGURE 10. SAMPLE DEPARTURE TRAJECTORY

A.5 PRELIMINARY ASSESSMENT OF DESIGN FEASIBILITY

Using the results of the experiments and simulation discussed, some preliminary system design work was done to assess the feasibility of applying the blowing control concept to fighter or trainer aircraft. Factors considered in the feasibility study included effectiveness, reliability, complexity, impact on other systems, and suitability of the device for retrofit to in-service aircraft.

The wind tunnel experiments and 6-DOF simulatic showed that an acceptable level of departure recovery enhancement could be achieved at blowing coefficie ts ($C\mu$) of 0.015 to 0.025. The required duration of blowing was found to be between 3 and 5 seconds. In order to maximize the reliability of the system, engine bleed air was not considered as a potential source for the blowing jet, inasmuch as engine flameouts at high AOA and yaw rate are to be expected. A solid propellant system was chosen as the most attractive source of blowing. Figure 11 shows a schematic diagram of the proposed blowing system.
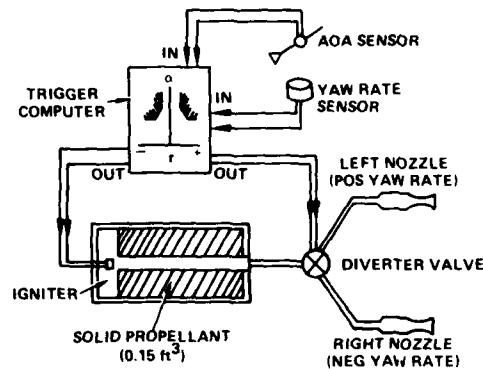
FIGURE 11. VORTEX BLOWING CONTROL SYSTEM SCHEMATIC

The solid propellant blowing system is estimated to require approximately 4.25×10^{3} cubic meters of propellant. The total system weight is estimated to be less than 9.1 kilograms.

Figure 12 illustrates the region of the flight envelope over which the system is designed to produce the required blowing momentum coefficients. This region encompasses the low speed transient area in order to provide maximum departure recovery enhancement, and is well outside of the primary ACM arena so that the maneuvering capability of the aircraft is not impacted adversely.
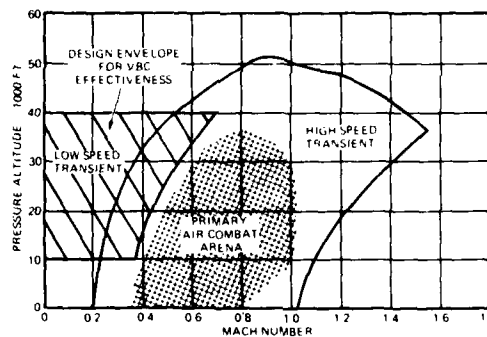
FIGURE 12. DESIGN ENVELOPE FOR VORTEX BLOWING CONTROL

A.6 CONCLUSIONS AND RECOMMENDATIONS

Based on small-scale water and wind tunnel experience, it has been shown that asymmetric tangential blowing along the surface of the forebody of an aircraft can be used to control the orientation of the lee side vortex system at high AOA. Further, it has been shown that the forces and moments produced by these vortices can be used, in a controlled manner, to greatly enhance the predicted departure recovery characteristics of an existing fighter aircraft configuration. Blowing rates required to produce these forces and moments were shown to be small owing to the fluid amplification afforded by vortex growth. Volume requirements are reasonable, and indicate that such a concept could be applied to a new aircraft or retro fitted to an existing aircraft with minimum impact on other aircraft systems.

Further experiments must be conducted on a large-scale free-flight model to substantiate the predictions. Further analysis should be done to determine whether this concept could be used not only as a departure recovery enhancement device but also as a departure inhibitor.

B. DETAILS OF THE FLOW STRUCTURE

B.1 INTRODUCTION

B.1.1 Asymmetric Vortex Wake About a Forebody at Incidence

Asymmetric vortices on the leeward of flight vehicles at high angles of incidence (References 8, 14, and 25 through 27) can cause severe stability and control problems. The asymmetric flow induces side forces on the forebody and consequent yawing moments that may overwhelm the counteractions available from control surface deflections. Analogous with the flow about most aircraft and missile forebodies at incidence, where crossflow effects dominate, is the flow about a slender cone. Having already established the structure of the symmetric separated flow about a circular cone at moderate incidence (References 3, 28, and 29), where free shear layers spring from primary and secondary separation lines to form well-organized, spirally coiled vortex motions, we may use the cone as a convenient vehicle to investigate the asymmetric flow complexities at elevated attitudes. Rather than destroying the asymmetric vortices to alleviate the induced side loads, our aim has been to retain the power of the vortices by controlling their orientation (References 1, 2, 3, and 24). The emphasis has been to acquire not only overall forces, pressures, and separation line locations on the cone, but to accompany these with laser vapor screens of the asymmetric vortex wake to produce a conceptual framework of the flow. The 1.4-meter (54-inch) long, 5-degree semiangle cone was sting-mounted on a roll gear in the Ames 1.8- by 1.8-meter (6- by 6-foot) closed-circuit wind tunnel. Two spherically tipped, interchangeable frusta were manufactured to fit the front of the model. One frustum was smooth, and the second had provision for blowing ports, as shown in Figure 13. The apparatus is described fully in References 2, 3, and 28.
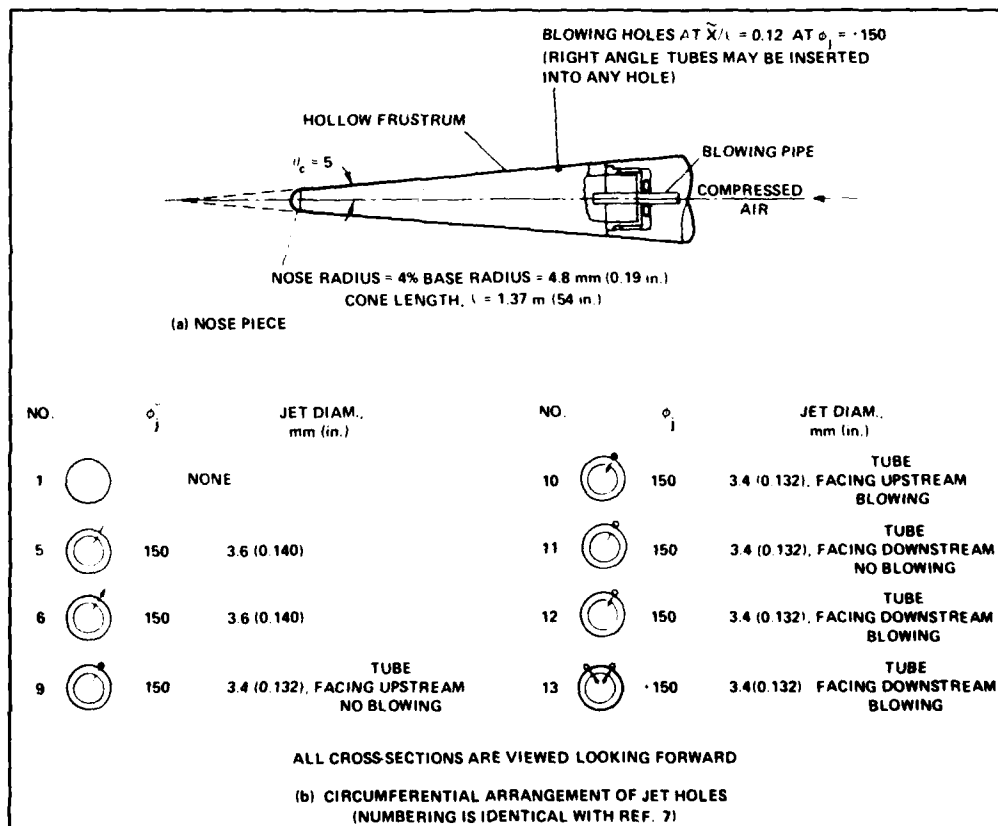
FIGURE 13. SCHEMATIC OF WIND TUNNEL MODEL AND BLOWING NOZZLE LOCATIONS

The onset of asymmetry for a forebody alone typically occurs when the forebody angle of incidence, α, exceeds twice the nose semiangle, θ_c. The ratio, α/θ_c, is called the relative incidence, $\bar{\sigma}$, an important parameter when comparing slender nose shapes of different θ_c. In wind tunnels it has been found that the onset phenomenon (References 8, 25, and 28) and the initial direction of the side force are responsive to small changes in geometry at the nose, Reynolds number, and free-stream Mach number. This sensitivity is detected up to relative incidences at which there are transonic conditions with embedded shock waves in the leeward crossflow, whereupon the side forces disappear (References 2, 25, 26, and 28).

A candidate mechanism for consideration to explain the initial development of asymmetry in the sub sonic vortex flow is related to the known susceptibility to instability (Reference 30) of inflexional velocity profiles. Such profiles exist in the vicinity of the primary vortices and the saddle type singular point that encloses the flow above the vortices in the crossflow plane (References 2 and 31). Some recent research is helpful in illuminating this instability mechanism. Nishioka and Sato (Reference 32) experimentally showed that the initially steady symmetric laminar flow about a two-dimensional circular cylinder becomes unstable beyond a certain (low) Reynolds number. Tne new flow produced is time-dependent and periodic, and develops into the Karman vortex street. A theoretical study accompanying the experiment suggests that the steady flow becomes unstable to anti-symmetric disturbances in the vicinity of the enclosing saddle point. Imagine the consequence of this result for impulsive flow development past the same two-dimensional cylinder. For Reynolds numbers less than this low value, the transient flow approaches a steady state as *time approaches infinity and this steady state is symmetric*, but for larger Reynolds numbers the transient flow is symmetric only at small values of t. As time approaches infinity, the steady *state to which this flow* is tending becomes unstable, with the result that antisymmetric disturbances can grow sufficiently large to once again promote the beginning of the Karman vortex street.

If we now invoke the impulsive-flow analogy and imagine a fixed plane through which a slender, circu lar cross-sectional, three-dimensional body passes with a downward velocity, one expects to see in this plane a flow development with time (i.e., the structure and mechanisms) similar to that of the impulsively started cylinder. Since the particular Reynolds number is low when the vortex street begins, we may postu late that all three-dimensional bodies tested would evidence the instability if they were sufficiently long. Its manifestation depends on the rapidity with which the velocity profile that becomes unstable is approached, as well as on the size or amplitude of the initial asymmetric disturbance. So far, then, we note that the candidate mechanism has been developed in accordance with observations of the laminar wake. References 7 and 33, however, illustrate that the structure of both the laminar and turbulent asymmetric wakes about slender bodies at incidence appear similar.

We therefore propose to extend the range of applicabilıty of the candidate mechanism to also explain the asymmetry phenome. n in fully developed turbulent flow. Furthermore, on the basis of this candidate mechr nism, we may predict that when leeward shock waves form in the crossflow about a three-dimensional body, the effects of vortex asymmetries in the wake will tend to disappear. Such an event is likely because there can be no direct transfer of the effects of amplified disturbances in the saddle point region to the body and vice ver-a.

About the cone, the local asymmetric flow perturbations developing about extremely small roughnesses at the nose may not only amplify downstream in the wake but may also goven the initial direction of the asymmetry. Near-mirror images of the side force/incidence performance of a slender cone, for example, are obtained at body roll angles of ± 90 degrees (Reference 2). The small surface irregularities may also lead to asymmetric transition (Reference 27). In the range of transitioi al Reynolds numbers, therefore, we may postulate an additional candidate mechanism in the existence of ı steady asymmetric mean flow (Reference 34). In the practical flow case of a slender body at incidence, we sʰall frequently be dealing with laminar, tran sitional, and turbulent flows, where both candidate mechanisms will be possibilities. Nevertheless, for our cone, laminar and transitional flows are restricted to the region close to the nose, so that we anticipate the character of the flow at the enclosing saddle point to dominate the wake development.

B.1.2 Control of the Asymmetric Vortices

Because the direction of the leeward asymmetry is sensitive to small irregularities in the surface at the nose, it is conceivable that the degree of asymmetry may be controlled by a single small strake to counter the vorticity imparted by the geometrical imperfection; or by spinning the nose, to remove altogether the sensitivity to nose perturbations (Reference 10). On the other hand, to perturb the flow in a controllable and repeatable manner without a "parasite" configuration penalty, we should like to make small but measure able changes to the effective forebody geometry near the nose by novel active means ʰo potentially alter the asymmetric leeward flow structure. Some recent results of Sharir et al (Reference 35) have demonstrated tne potential for control by air injection normal to the surface. They advised that blowing symmetrically from jets on the windward side of the nose of a missile configuration was effective in diminishing the side force. We propose that blowing from the leeward side, in the vicinity of the separation lines, should pro duce an even greater effect on the asymmetric flow development. For comparison with various jet configura tions employed in our experiments, the usefulness of passive devices such as an asymmetrically positioned strake and roughness elements has also been investigated (Reference 3).

B.2 EXPERIMENTAL RESULTS AND DISCUSSION

B.2.1 Structure of Asymmetric Vortex Wake

Up to relative incidences of more than 2 for our cone model, the leeward vortices remain symme trically disposed about the pitch plane, stemming from symmetric primary and secondary separation lines, S1 and S2, on the cone surface. At relative incidence slightly greater than 2.5 however, the leeward vortices take on an asymmetric pattern. Figures 14(a) to 14(e) illustrate the sequence of asymmetric flow field developments up to $\bar{a}$ = 3.6 at M_∞ ≈ 0.6, obtained in the wind tunnel using a vapor screen illu minated by an expanded laser line set normal to the cone surface. The view is towards the apex of the cone from the b·.e of the body; the roll orientation of the cone was fixed. Figures 15(a) to 15(e) are corresponding interpretations of the leeside vortex wake, as projections of the three-dimensional stream surfaces in the experimental external flow onto crossflow planes normal to the cone surface. These pro jections provide the continuous patterns of crossflow streamlines in association with a limited number of singular points (i.e., zero velocity points in the crossflow plane) that yield a conceptual framework of the fluid mechanics. Notice, in Figure 15(a), the following characteristic features: The primary vor tices result from the separation of the windward boundary layers at S1, and the induced boundary layer growth from the attachment line A1 near the leeward ray is eventually caused to depart from S2 as secondary vortices of opposite sign to, and tucked beneath, the primary vortices. Additional attachment

lines. A2. are found between the separation lines. S1 and S2. The characteristic convergence of skin friction lines towards a separation line, and divergence away from an attachment line, are displayed in Figures 16(a) and 16(b).

VIEW FROM BEHIND CONE BASE

VERY UNSTEADY

(a) $\alpha/\theta_c = 2.6$ (b) $\alpha/\theta_c = 3.2$ (c) $\alpha/\theta_c = 3.3$

(d) $\alpha/\theta_c = 3.4$ (e) $\alpha/\theta_c = 3.6$
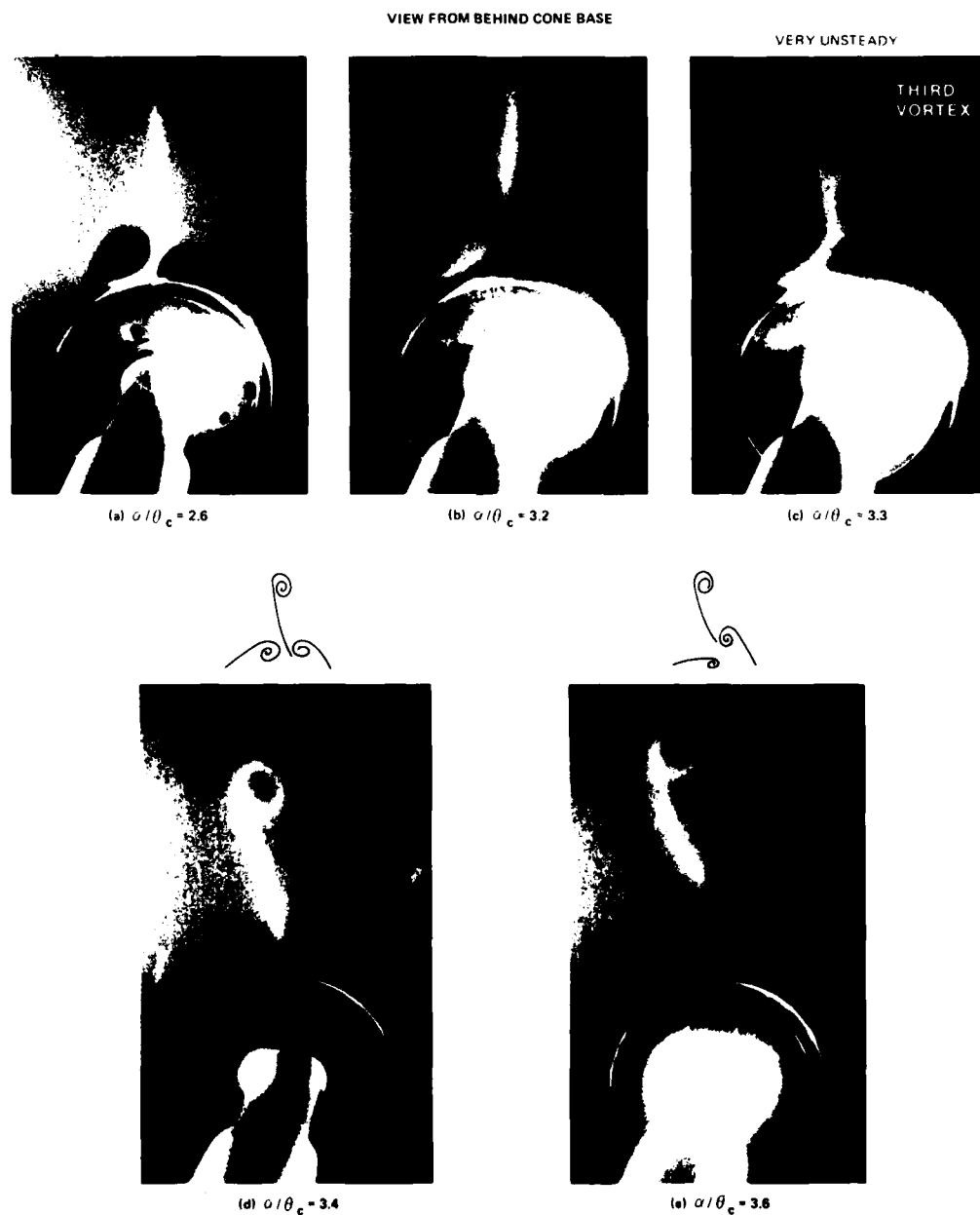
FIGURE 14. LASER VAPOR SCREEN – DEVELOPMENT OF VORTEX ASYMMETRY

ENCLOSING
SADDLE POINT

FORMATION
OF INTERIOR
SADDLE POINT

ENCLOSING
SADDLE POINT

PRIMARY
VORTICES

S_2 A_1 S_2
A_2 A_2
S_1 SECONDARY S_1
VORTICES

ATTACHMENT
LINE

A_1

(a) $\alpha/\theta_c = 2.6$

(b) $\alpha/\theta_c = 3.2$

(c) $\alpha/\theta_c = 3.3$

ATTACHMENT
LINE

(d) $\alpha/\theta_c = 3.4$

(e) $\alpha/\theta_c = 3.6$
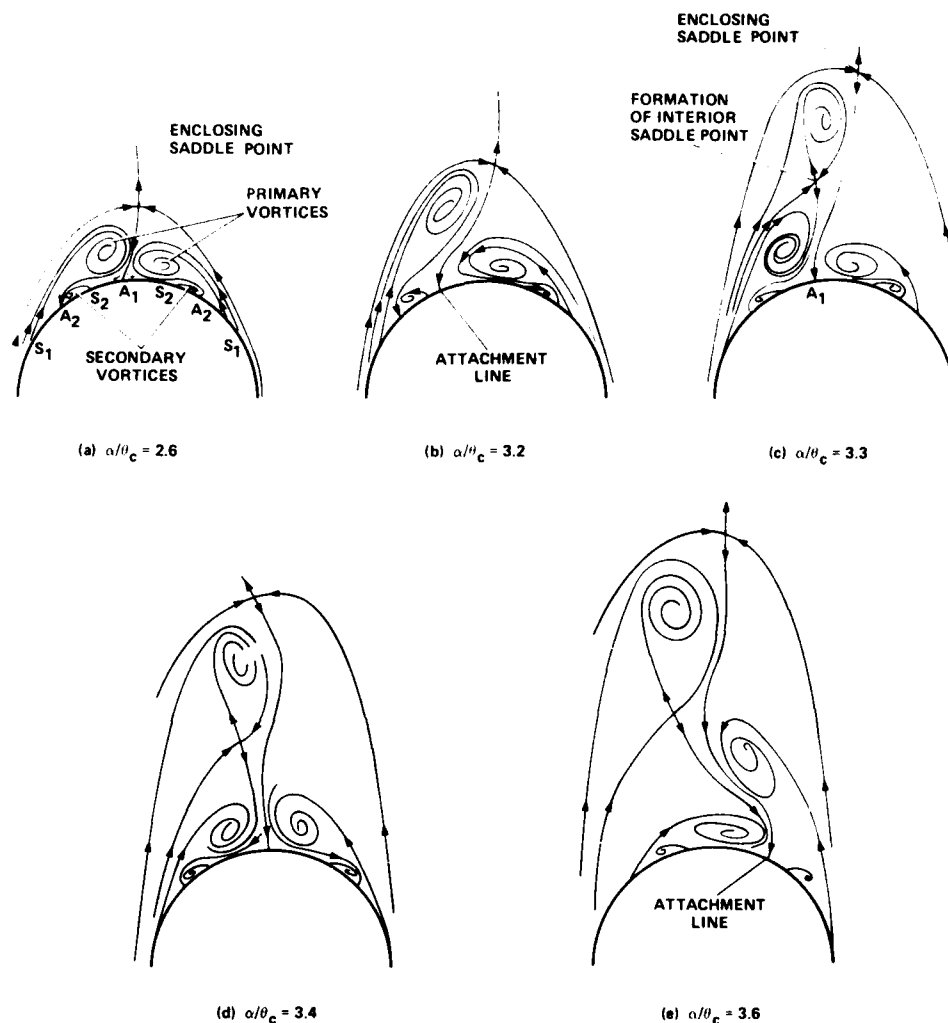
FIGURE 15. LEESIDE VORTEX WAKE STRUCTURE

Let us assume an asymmetric disturbance to originate at the nose, of the same rotation, say, as the port side primary vortex. If this disturbance amplifies in the vicinity of the enclosing saddle point as a consequence of instability of the inflexional velocity profiles, there will be an effective increase in the vorticity of the port side primary vortex. This vortex will enlarge slightly and move away from the surface as shown in Figures 14(a) and 15(a). As the relative incidence increases up to 3.2, the feeding shear layer continues to stretch, as shown in Figures 14(b) and 15(b). At a relative incidence of 3.3, in conjunction with the appearance of gross unsteadiness of the secondary vortices, the elongated shear layer itself passes through a shedding stage, as shown in Figure 14(c), until at a relative incidence of 3.4 there is definitive evidence of a third spiral vortex motion, as shown in Figure 14(d). In order that the two vortices of the same rotational direction be able to coexist in tandem on the left-hand side, the rules of topology (Reference 9) instruct us that a new saddle point must be inserted between them, as shown in Figure 15(c). As the relative incidence increases still further, the starboard-side primary vortex begins to grow, as shown in Figures 14(d) and (e) and 15(d) and (e), resulting eventually in the repetition of the shedding process for the opposite side; these incidences at which shedding occurs correspond with the maximum induced side loads. Note that the one crossflow streamline emanating from the enclosing saddle point to the body at A1 as shown, for example, in Figure 15(e), always partitions the left- and right-hand sides of the wake. Except during the shedding process, each flow field is constituted of well organized spiral vortex motions. In addition, scanning the plane of the laser vapor screen from the nose to the base of the forebody demonstrated virtually identical structure of the crossflow along the entire length of the cone.

(a) $\alpha/\theta_c = 3.0$

(A)

(b) $\alpha/\theta_c = 4.05$

(B)
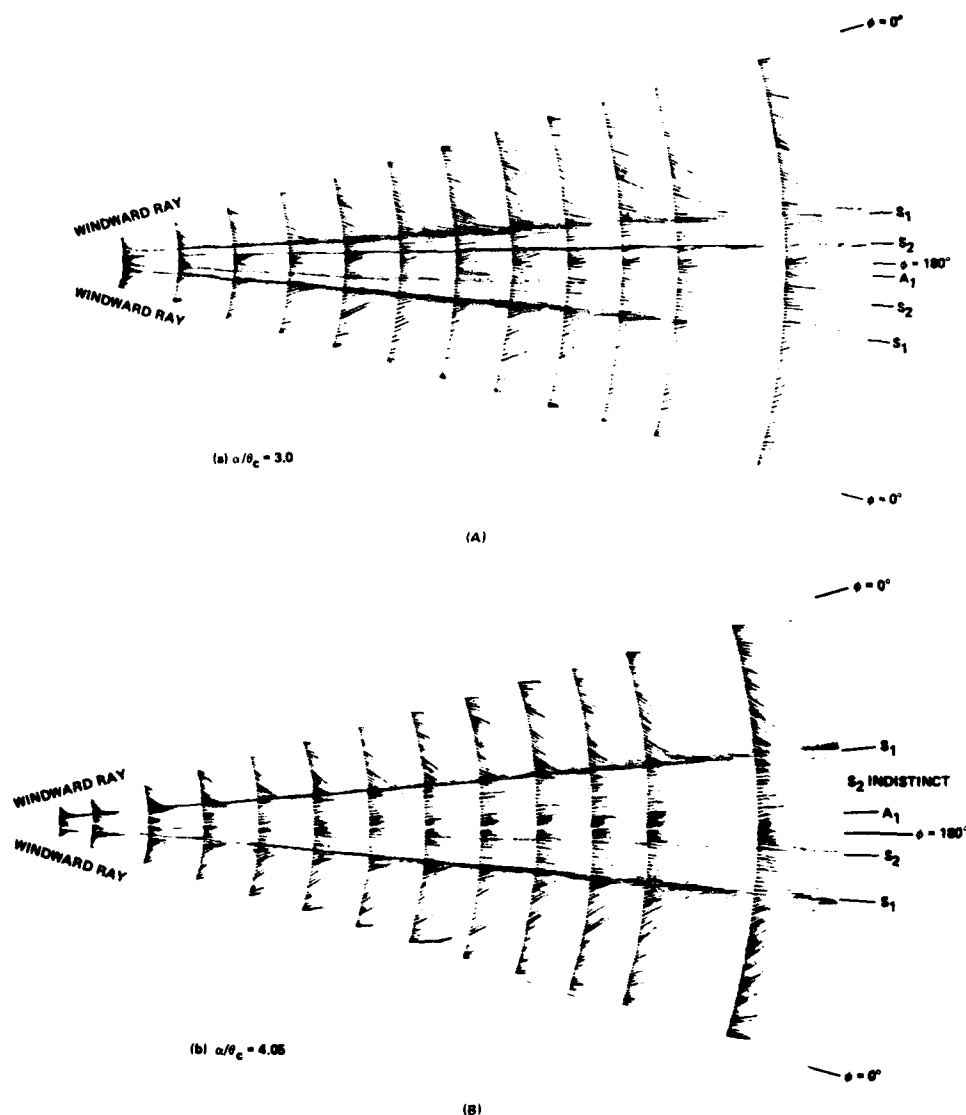
FIGURE 16. SURFACE SKIN FRICTION LINES

Figure 16(a) displays the unwrapped asymmetric skin-friction line pattern at a relative incidence of 3.0, corresponding with an external vortex pattern between Figures 14(a) and (b). We see, in Figure 16(a), that, as in the case of symmetric separation (Reference 3), the primary and secondary separation lines S1 and S2 remain coincident with certain conical rays, but now the entire surface pattern is skewed to the port side. The circumferential pressure gradient turns adverse closer to the windward ray on the port side than on the starboard side, causing substantial changes in the respective rates of skewing in the skin friction line development. At a relative incidence of 4, on the other hand, the skin friction line pattern is skewed to the right, as shown in Figure 16(b), consistent with the external flow photograph shown in Figure 14(c). Note that although we are not able to detect any circumferential movement of the windward attachment line at $\phi \sim 0$ degrees, the primary attachment line A1 does shift with respect to the leeward meridian, following the excursion of the overall flow structure towards, first, the port side and, second, the starboard side.

B.2.2 Control by Blowing of Asymmetry in the Leeward Flow

B.2.2.1 Flow Structure

Since the flow visualization results, allied with topological notions, have allowed us to develop a conceptual framework of the asymmetric flow, the next step is to ask how the flow orientation might best be controlled by active means. We have suggested that an amplified disturbance can be disruptive in the vicinity of the enclosing saddle point (again, see Figure 15). Let us now introduce a small but measured amount of

air, blowing as a controlled disturbance, into the stream near the nose but on the leeside. Let us also locate the jet between the primary and secondary separation lines S1 and S2 on one side of the leeward meridian, its disposition chosen to be situated beneath the primary vortex that initially lifts off the surface (Reference 1). Figure 17 illustrates a proposed model of the flow in terms of the crossflow streamlines in a plane near the base of the cone looking towards the apex. In the figure, the jet issuing normal to the surface is situated to the right of the leeward meridian. The ensuing interaction between the free stream and the jet plume penetrating downstream produces a new pair of skewed contrarotating vortices above the forebody vortices. In Figure 17, the median line of the jet efflux is depicted as a crossflow streamline commencing at the cone surface and terminating at the saddle point that interconnects the jet vortices. It is seen that the skewed orientation of the jet vortices must occur to attain a balance of forces on the four vortex cores. The model also shows that introducing the jet vortices into the crossflow plane moves the enclosing saddle point further into the free-stream, thereby reducing its influence at the surface. In addition, the reorganized interactive flow structure may prevent altogether the development of the shedding process that results in the formation of the third vortex.
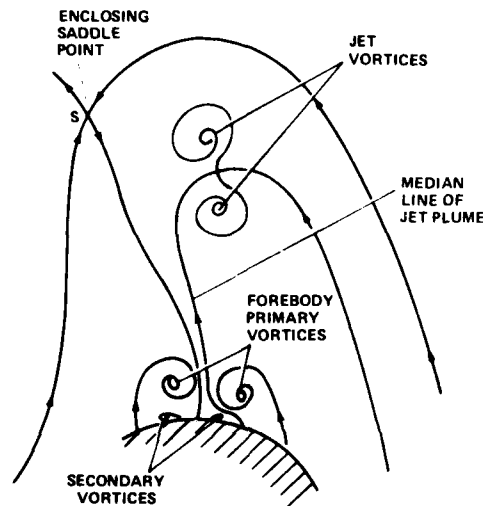
FIGURE 17. LEESIDE VORTEX WAKE STRUCTURE WITH
BLOWING JET

The candidate flow model of Figure 17 appears to be validated in the three laser vapor screen pictures shown in Figures 18(a) through 18(c) with normal blowing. The planes of illumination are at $\bar{x}$ / 0.87, with the views looking forward, and where 200 static pressure ports were situated around the surface. Although the two nose frusta in Figure 13(b) were manufactured to tight tolerances, we might still expect that the initial direction of the asymmetry for each nose would be unpredictable. Thus, for the particular nose frustum used in obtaining the results of Figure 18 (No. 6 in Figure 13), it so happens that, in the absence of blowing, the starboard vortex lifted off first (this is the mirror image, of course, of the flow development illustrated in Figures 14 and 15). Then holding the cone relative incidence constant at 3.3, slightly higher than the value at which shedding (production of the third vortex) was observed in Figure 14, the change in orientation of the forebody vortices as the blowing rate C_μ is increased, is shown in Figure 18(a), (b), and

(c). The jet orifice diameter is 3.6 millimeters (0.140 inch) and is located at ϕ_j 150 degrees beneath the

(initially) higher vortex. The forebody vortices are the bright oval blobs close to the cone, while the jet vortices in the kidney shaped bright zone are skewed at almost 90 degrees from the horizontal. At a blowing rate, C_μ, of 0.0014, Figure 18(b) shows that the initial asymmetric orientation is the same as that with

no blowing. The low port side vortex enhances the section pressures on that side, providing a side force to the left. As C_μ increases to 0.003, as shown in Figure 18(b), the surface pressure distributions about

each side of the meridian plane are almost coincident and there is no overall side force. With further addition of jet momentum flux, as shown in Figure 18(c), the orientation of the forebody vortices is the mirror state of Figure 18(a), and the side force is now to the right. Note that throughout this range of C_μ, at

this given relative incidence of 3.3, the skewness of the jet vortices changes little. As their strength increases with the increasing C_μ, their effect is reflected in the revised orientation of the forebody vortices, producing a stable flow configuration. The jet vortices alter the relative amounts of free-stream entrained into the forebody vortices, ultimately favoring the side opposite the blowing point. Finally, Figures 18(a) through 18(c) appear to demonstrate that the shedding mechanism and the production of the third vortex so evident in Figure 14(c) has been prevented. The picture appears much the same for all directions of blowing, but with the tangential modes the structure is less well defined.

(a) C_μ 0.0014

(b) C_μ = 0.003

FIGURE 18. LASER VAPOR SCREEN AND CIRCUMFERENTIAL PRESSURES FOR
C_μ = 0.0014, 0.0030, 0.0052
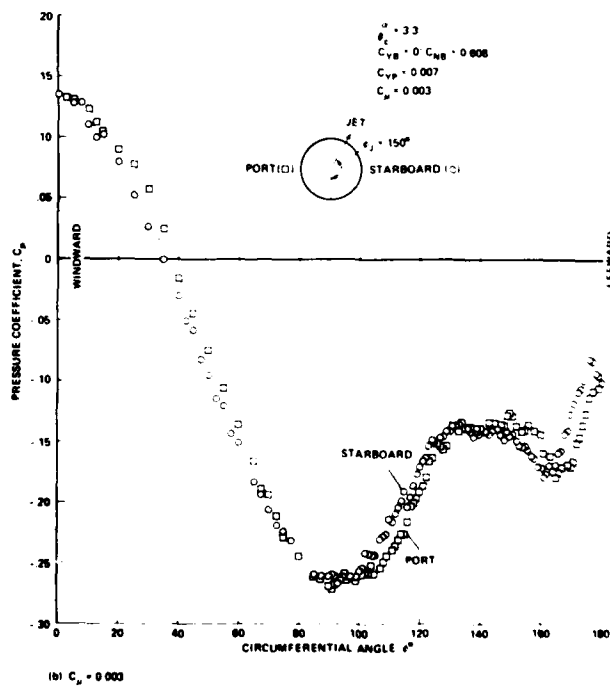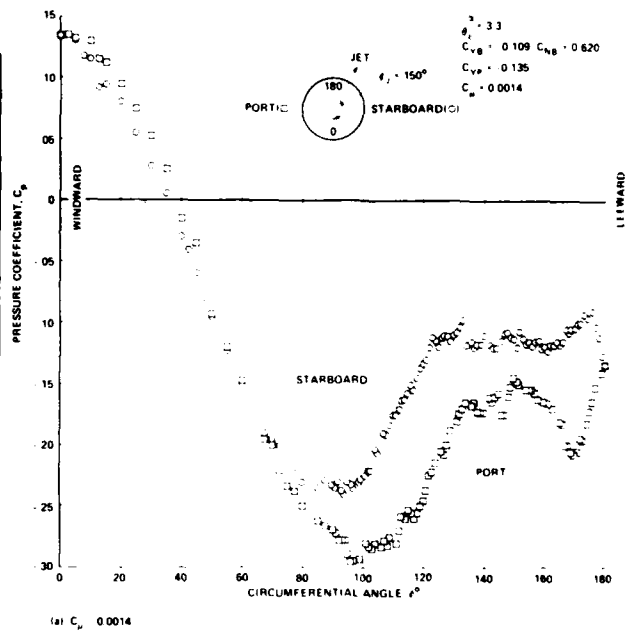
(c) $C_\mu = 0.0052$

FIGURE 18. LASER VAPOR SCREEN AND CIRCUMFERENTIAL PRESSURES FOR
$C\mu = 0.0014, 0.0030, 0.0052$ (Continued)

B.2.2.2 Effectiveness of Blowing in Changing Side Force Magnitude and Direction

The change in overall side force coefficient (C_{YB}, measured with the balance) as the rate of air injection C_μ grows, is depicted in Figure 19. The cone is at a constant relative incidence of 3.2, slightly less than the setting at which the vapor screen pictures of Figure 18 were taken and close to that at which shedding to form the third vortex was seen in Figure 14. Figure 19 provides force polars not only for air injected normal to the surface (Configuration 6 in Figure 13), but also for tangential blowing both upstream and downstream along a conical ray (Configurations 10 and 12 respectively).

Remembering that the objective of the blowing is to exert positive control over the orientation of the forebody vortices, we see how this might be achieved (Figure 19) for, first, yielding $C_{YB} \sim 0$ for a minimum blowing rate and, second, providing a range of side force that might be used for maneuvering (the different offsets at $C_\mu = 0$ are caused by the three different asymmetric blowing port arrangements). With regard to the former, the upstream pointed jet is the optimum arrangement at this particular relative incidence ($\bar{a} = 3.2$), but the downstream injection provides $C_{YB} \sim 0$ over an extensive range of C_μ ($0.0025 < C_\mu < 0.0055$). With regard to the latter, both normal and tangential injection perform creditably, but normal injection is preferred. Injection also suppressed the substantial fluctuations in side force (Reference 3).

Corresponding with blowing rates greater than 0.005 (see the right-hand side of Figure 19), Figure 20 presents the effect on the side force at constant C_μ as a is increased to 4. The effectiveness of upstream and downstream tangential blowing in delaying the onset of asymmetry and also in reversing the side force development relative to the no-blowing case is presented in Figure 20. Note also the degradation in controlling the direction of the side force when a pair of jets symmetrically disposed at $\phi_j + 150$ degrees about the leeward meridian is used, although the onset of asymmetry is usefully delayed. This offset in C_{YB} at low relative incidence occurred for all configurations. Whether this was due to angularity in the free-stream or model misalignment is speculative; in either event the offset has no bearing on the trends of the results.

CONFIG	JET POSⁿ	BLOWING	JET DIAM., mm (in.)
— ⟶	6	150	3.6 (0.140)
---⟶	10	150	3.4 (0.132)
-- --⟶	12	150	3.4 (0.132)
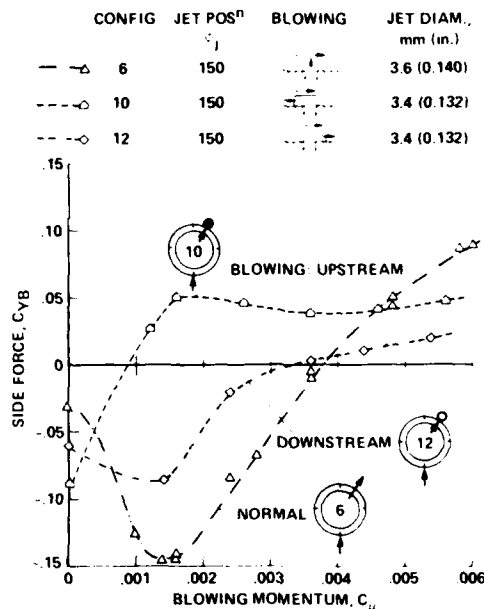
FIGURE 19. SIDE FORCE POLARS

Finally, a test was performed at a relative incidence of 3.2 to investigate the effect of rolling the model with the downstream pointed jet off (Configuration 11 of Figure 13) and then with the blowing rate at 0.0054 (Configuration 12). The circumferential positions of the blowing tube during the roll excursion are shown at the bottom of Figure 21, the view again looking forward from the base of the cone. The datum setting in roll angle of the body, $\phi_R = 0$ degrees, is when the jet is located 150 degrees from the windward ray, as shown

in the bottom left hand side of Figure 21. The side force continues to be measured in the wind axis system of coordinates. Rolling in an anticlockwise sense, we see, in the forebody roll angle range of 0 to 30 degrees, that the jet is able to reverse the direction of the side force in comparison with the no blowing case, this is the control exerted by blowing beneath the higher of the two primary vortices. Once past $\phi_R \sim 30$ degrees,

however, the ability of the jet to reverse the side force is lost. In the body roll angle range of 30 degrees $< \phi_R < 55$ degrees, the jet issues beneath the low vortex and exaggerates the side force magnitude, but

effects no control over side force direction. In the remainder of the body rolling sequence (30 degrees $< \phi_R < 180$ degrees) with the jet now positioned on the windward side, the blowing changes neither the side

force amplitude nor its direction to any significant extent. Thus, Figure 21 shows that the single air jet can only effect reversal of the side force when blowing beneath the high vortex (0 degrees $< \phi_R < 30$ de

grees and can only modulate the amplitude when blowing on the leeside (0 degrees $< \phi_R < 70$ degrees). When

blowing from the windward side, the jet's behavior is analogous to that of a solid roughness element.

B.3 CONCLUSIONS

Small quantities of air injected from a single orifice near the nose prevent shedding (i.e., formation of additional vortices) in the asymmetric vortex wake about a slender conical forebody. Injecting air also permits control of the magnitude of the induced side force at angles of incidence up to (at least) four times the semi nose angle. The blowing location was inboard of the primary separation line on one side of the lee ward meridian at 150 degrees from the windward ray.

When the jet is situated beneath the higher of the two asymmetrically disposed primary vortices, the control is additionally effective in reversing the direction of the side force.

The thrust coefficient, C_μ, based on the maximum cross sectional area of the forebody, is no greater than 0.006.

Asymmetric injection from the windward side of the cone proved ineffective in controlling either the magnitude or the direction of the side force.

The choice between blowing either normal to the surface or tangentially upstream or downstream is open. It would depend on the C_μ available and whether the objective was to provide either a nominally zero side force or a finite side force and prescribed direction for lateral control purposes, in the design range of incidence.

CONFIG.	JET POSⁿ. $\circ_j$	BLOWING	C_μ	JET DIAM., mm (in.)
9	150		0	3.4 (0.132)
10	150		0.0054	3.4 (0.132)
11	150		0	3.4 (0.132)
12	150		0.0056	3.4 (0.132)
13	·150		0.0102	3.4 (0.132)
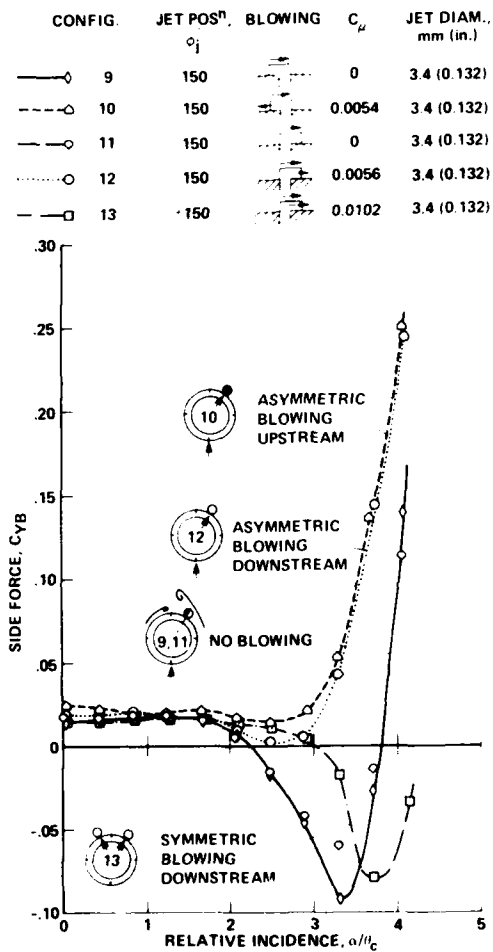
FIGURE 20. INCIDENCE – FORCE PERFORMANCE WITH
TANGENTIAL BLOWING

CONFIG. 11, σ_j = 150', JET DIAM. = 3.4 mm (0.132 in.).
TUBE FACING DOWNSTREAM
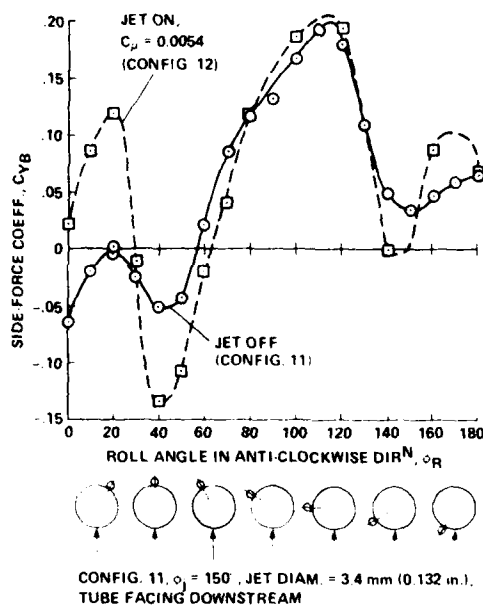
FIGURE 21. CIRCUMFERENTIAL PRESSURE DISTRIBUTIONS

C. REFERENCE

1. Skow, A.M., Moore, W.A., and Lorincz, D.J., "Forebody Vortex Blowing - A Novel Control Concept to Enhance Departure/Spin Recovery Characteristics of Fighter and Trainer Aircraft," AGARD-CP262-24, May 1979.

2. Peake, D.J., and Owen, F.K., "Control of Forebody Three-Dimensional Flow Separation," AGARD CP262-15, May 1979.

3. Peake, D.J., Owen, F.K., and Johnson, D.A., "Control of Forebody Vortex Orientation to Alleviate Side Forces," AIAA-80-0183, January 1980.

4. Nielsen, J.N., "Non-Linearities in Missile Aerodynamics," AIAA-78-20, January 1978.

5. Allen, H.J., and Perkins, E.W., "Characteristics of Flow Over Inclined Bodies of Revolution," NACA-RM-A50I.07, 1951.

6. Clark, W.H., Peoples, J.R., and Briggs, N.M., "Occurrence and Inhibition of Large Yawing Moments During High Incidence Flight of Slender Missile Configurations," AIAA-72-968, 1972.

7. Coe, P.L., Jr., Chambers, J.R., and Letko, W., "Asymmetric Lateral-Directional Characteristics of Pointed Bodies of Revolution at High Angles of Attack," NASA-TN-D-7095, November 1972.

8. Keener, E.R., and Chapman, G.T., "Onset of Aerodynamic Side Forces at Zero Sideslip on Symmetric Forebodies at High Angles of Attack," AIAA-74-770, August 1974.

9. Peake, D.J., and Tobak, M., "Three-Dimensional Interactions and Vortical Flows with Emphasis on High Speeds," NASA-TM-81169, March 1980.

10. Neihouse, A.I., Klinar, W.J., and Scher, S.H., "Status of Spin Research for Recent Airplane Designs," NASA-TR-R-57, 1960.

11. Greer, H.D., "Summary of Directional Divergence Characteristics of Several High-Performance Aircraft Configurations," NASA-TN-D-6993, 1972.

12. Anderson C.A., "Stall/Post-Stall Characteristics of the F-111 Aircraft," AGARD-CP102-18, April 1972.

13. Skow, A.M., and Titiriga, A., Jr., "A Survey of Analytical and Experimental Techniques to Predict Aircraft Dynamic Characteristics at High Angles of Attack," AGARD-CP235-19, May 1978.

14. Skow, A.M., Titiriga, A., Jr., and Moore, W.A., "Forebody/Wing Vortex Interactions and Their Influence on Departure and Spin Resistance," AGARD-CP247-6, October 1978.

15. Edwards, O.R., "Northrop F-5F Shark Nose Development," NASA-CR-158936, October 1978.

16. Tobak, M., Schiff, L.B., and Peterson, V.L., "Aerodynamics of Bodies of Revolution in Coning Motion," AIAA Journal, Vol. 7, No. 1, January 1969.

17. Schiff, L.B., and Tobak, M., "Results from a New Wind-Tunnel Apparatus for Studying Coning and Spinning Motions of Bodies of Revolution," AIAA Journal, Vol. 8, No. 11, November 1979, pp 1953-1958.

18. Lamont, P.J., and Hunt, B.L., "Pressure and Force Distributions on a Sharp-Nosed Circular Cylinder at Large Angles of Inclination to a Uniform Subsonic Stream," J. Fluid Mech., Vol. 76, Part 3, 1976, pp 519-559.

19. Lamont, P.J., and Hunt, B.L., "Prediction of Aerodynamic Out-of-Plane Forces on Ogive-Nosed Circular Cylinders," J. Spacecraft, Vol. 14, No. 1, January 1977, pp 38-44.

20. Hunt, B.L., and Dexter, P.C., "Pressures on a Slender Body at High Angle of Attack in a Very Low Turbulence Level Air Stream," AGARD-CP247-17, October 1978.

21. Chambers, J.R., Anglin, E.L., and Bowman, J.S., Jr., "Effects of Pointed Nose on Spin Ch acteristics of a Fighter Airplane Model Including Correlation with Theoretical Calculations," NASA TN-D-5921, September 1970.

22. Kruse, R.L., "Influence of Spin Rate on Side Force of an Axisymmetric Body," AIAA Journal, Vol. 16, No. 4, April 1978, pp 415-416.

23. Cornish, J.J. III, and Jenkins, M.W.M., "The Application of Spanwise Blowing to High Angles of Attack Spin Recovery," AGARD-CP247-9, October 1978.

24. Moore, W.A., Skow, A.M., and Lorincz, D.J., "Enhanced Departure/Spin Recovery of Fighter Aircraft Through Control of the Forebody Vortex Orientation," AIAA-80-0173, January 1980.

25. Peake, D.J., Rainbird, W.J., and Atraghji, E.G., "Three-Dimensional Flow Separations on Aircraft and Missiles," AIAA Journal, Vol. 10, No. 5, May 1972, pp 567-580.

26. Keener, E.R., Chapman, G.T., and Kruse, R.L., "Effects of Mach Number and Afterbody Length on Onset of Asymmetric Forces on Bodies at Zero Sideslip and High Angles of Attack," AIAA-76-66, January 1976.

27. Ericsson, L.E., and Reding, J.P., "Vortex-Induced Asymmetric Loads in 2-D and 3-D Flows," AIAA-80-0181, January 1980.

28. Peake, D.J., Owen, F.K., and Higuchi, H., "Symmetrical and Asymmetrical Separations about a Yawed Cone," AGARD-CP-247, October 1978.

29. Peake, D.J., Fisher, D.F., McRae, D.S., "Flight Experiments with a Slender Cone at Angle of Attack," AIAA-81-0337, January 1981.

30. Stuart, J.T., "Hydrodynamic Instability," in Laminar Boundary Layers, Ed., L. Rosenhead, Clarendon Press, 1963, pp 492-579.

31. Tobak, M., and Peake, D.J., "Topology of Two-Dimensional and Three-Dimensional Separated Flows," AIAA-79-1480, July 1979.

32. Nishioka, M., and Sato, H., "Mechanism of Determination of the Shedding Frequency of Vortices Behind a Cylinder at Low Reynolds Numbers," J. Fluid Mechanics, Vol. 89, Part 1, 1978, pp 49-60.

33. Werlé, H., "Tourbillons de corps fuselés aux incidences elevées," L Aéronautique et l'Astronautique, Vol. 6, 1979, pp 3-22.

34. Kamiya, N., Suzuki, S., and Nishi, T., "On the Aerodynamic Force Acting on a Circular Cylinder in the Critical Range of the Reynolds Number," AIAA-79-1475, July 1979.

35. Sharir, D., Portnoy, H., and Rom, J., "A Study of the Effects of Jets from a Slender Body of Revolution on the Side Forces Acting on It at Large Angles of Attack in Low Speeds," TAE-337, Technion, Israel Institute of Technology, May 1978.

INFLUENCE OF CONFIGURATION COMPONENTS OF
STATICALLY UNSTABLE COMBAT AIRCRAFT ON THE
AERODYNAMIC DESIGN FOR HIGH ANGLES-OF-ATTACK

DR. G. WEDEKIND
DORNIER GMBH, FRIEDRICHSHAFEN
GERMANY

1.   INTRODUCTION

With the design of future combat-aircraft new problems appear, which do not exist for
fighters flying today. These problems are caused by the fact, that one tries to design
these aircraft unstable in the longitudinal mode, to get improved performance. Further,
one intends to shift the upper limit of the maneuver range up to angles-of-attack which
are far beyond the angle for maximum lift. These two facts cause special problems at
high angles-of-attack, which will be discussed in this presentation.

Although these problems do not affect the main factors of design, they nevertheless
must not be neglected, because they have a large influence on the design.

In this presentation the influence of some aircraft components on the design of stati-
cally unstable aircraft will be shown in order, to give a certain insight into the ba-
sic problems of such aircraft. All tendencies related to aerodynamics, which will be
shown in this presentation, are derived from wind-tunnel tests.

Figure 1.1 shows a typical wing as an example of those which will be discussed here.
These wings have the following features:

- the span is mostly defined by the stationary turn-rate at transonic speed,
   the weight, and the thrust of the aircraft

- the aspect-ratio is relatively small, and the leading-edge is swept to get
   low supersonic wave-drag

These features lead to wing-planforms similar to that shown in figure 1.1.

Because the problems at high angles-of-attack have to be seen in connection with the ba-
sic requirements of the design, and because most of them cannot be understood without
having a general overview, the presentation will be built up as follows: (fig. 1.2):

1. Show the basic requirements for a combat aircraft, especially for an air-to-air
    combat fighter.

2. Show the effect of an unstable design on the performance of such an aircraft.

3. Show the limits of instability due to the control system.

4. Show the problems at high angles-of-attack due to longitudinal instability and lateral and directional stability.

The last point is the real topic of the presentation. The first three points are to be seen as an introduction.

2.   REQUIREMENTS OF A COMBAT AIRCRAFT

In figure 2.1 typical requirements of combat aircraft related mainly to air-to-air missions are listed:

- high sustained turn-rate is demanded at transonic speeds and at low supersonic speeds

- large maximum lift is required, because of a small corner speed

- to get high maneuverability, controllability is required at angles-of-attack above that of maximum lift. For instance the usable angle-of-attack region should exceed α_{CLmax} by at least five or ten degrees.

One can find the regions of these requirements in a diagram "angle-of-attack versus Mach number" as shown in figure 2.2. Only the main requirements are shown. There are additional requirements, such as high agility of the aircraft, which means that a high potential of acceleration is needed.
The discussions in this presentation however will be confined to the requirements shown above.

The following should be noted:

- For the stationary turn-rate at subsonic speed the induced drag coefficient (K-factor) and the wing area is of predominant influence

- For the stationary turn-rate at supersonic speed an additional influence is present due to the zero-lift drag.

- The maximum lift is a function of large trimmable C_{Lmax} and of course also the size of the wing area.

- Very many components have a larger influence on lateral and directional stability and control at high angles-of-attack, which often interfere with each other. It is therefore almost impossible to give a systematic overview of all influences.

To get high turn-rates and maximum lift, a destabilisation seems to give some advantage. In the following chapter will be shown how an unstable design affects the aircraft-performance.

3.   EFFECT OF AN UNSTABLE DESIGN ON AIRCRAFT PERFORMANCE

The effect of an unstable design can be demonstrated by means of a polar of a simple
tailless configuration with trailing-edge flaps (figure 3.1). The left side of the
figure shows the polar $C_L = f(C_D)$, for several flap-down deflections. The right side
shows the diagram $C_L = f(C_m)$, where the moment reference point is at the aerodynamic
center, which means that this diagram is valid for aircraft with neutral stability.

Such an aircraft is trimmed by a very small flap-deflection. As can be seen from the
polar $C_L = f(C_D)$ the drag-coefficient is relatively poor. The coefficients with a posi-
tive (down) deflected flap are much better. To trim these deflections, which give
a nose-down pitching moment, it is necessary to shift the center of gravity aft, so
that the wing itself balances this moment by a nose-up-moment. That means that the air-
craft has to be flown unstable. The optimum instability for tailless configurations
with small aspect ratio is in the order of a static margin SM $= (X_{cg} - X_{ac})/\bar{c} \sim -15$ %.
When a horizontal tail and leading-edge flaps are added, the problem becomes more com-
plicated. But in this case too, an unstable aircraft has better drag-coefficients than
a stable one.

3.1   Effect on sustained turn-rate

The effect, that the static margin has on the sustained turn-rate, can be seen better,
in a plot of $C_L \cdot S$ over $C_D \cdot S$ (figure 3.2). The maximum drag $C_D \cdot S$ or D/q for stationary
flight is equal to the maximum thrust T_{max}/q. From these values the maximum lift $C_{Lt} \cdot S$
for the stationary turn-rate can be found.

In addition to a low induced drag-coefficient, an appropriately large wing area is need-
ed to get a large $C_{Lt} \cdot S$.
In figure 3.2 the polars for a series of three configurations having different SM are
plotted for the same subsonic Mach number. The design with the smallest instability
(SM = 0 %) has a larger wing area as a compensation for the relatively poor induced
drag coefficient.

All three configurations are designed for the same sustained turn-rate at subsonic
speed. The small differences in $C_{Lt} \cdot S$ are related to different weights: The config;ca-
tion with the smallest instability, having the largest and heaviest wing, demands the
largest $C_{Lt} \cdot S$. The zero-lift drag differs slightly, but its influence on the sustained
turn-rate at subsonic speeds is quite small.

At supersonic speeds there is a different effect:
Because of the smaller maximum thrust T_{max}/q at that Mach number and the larger wave
drag, the zero-lift drag has much more influence. The wave-drag, depending on the maxi-
mum cross-section, is larger for the configuration having the larger wing.

So a remarkable advantage is to be seen for the most unstable design with the smallest
wing. In figure 3.3 the maximum sustained turn-rate for subsonic and supersonic speed
is plotted varying static margin and wing area independently. At subsonic speeds insta-
bility can be substituted by a larger wing area. At supersonic speeds this is not pos-
sible. Here the improvement due to enlargement of the wing area is almost compensated by
the increase of the zero-lift drag.

3.2   Effect on the corner-speed

The corner-speed V_c is the speed, where the load-factor at maximum lift equals the maximum possible load-factor due to structural limits (figure 3.4). The smaller V_c the more maneuverability an aircraft has at lower speeds or higher altitudes. Therefore a small corner-speed is favourable.

Varying static margin and wing area independently has a similar effect on V_c as on the sustained turn-rate at subsonic speeds: Instability can be substituted by wing area.

3.3   Conclusions

An unstable design provides large advantages only for aircraft which must have good performance at supersonic speeds. At a given sustained turn-rate at subsonic speeds the following can remarkably be improved by destabilisation:

- wave-drag
- sustained turn-rate at supersonic speeds.

4.   LIMITS OF THE UNSTABLE DESIGN DUE TO THE CONTROL SYSTEM

Instability is limited by several factors. On the one side the control system which has to stabilize the configuration artificially, has a certain reaction speed, which gives a limit to destabilisation. On the other hand there is a limit in the region of high angles-of-attack which will be discussed later.

4.1   Motion of an unstable aircraft

The motion of an unstable aircraft can be roughly derived from figure 4.1. (For more exact evaluations flight-mechanical calculations have to be made).
For an aircraft which can rotate around the pitch axis, the following equation of motion can be set up.

The acceleration of the increase in angle-of-attack, $\ddot{\alpha}$, multiplied by the product of mass m times the square of the inertia moment-arm r_y equals the moment due to the disturbance $\Delta\alpha$. For an unstable design $C_{m\alpha}$ is positive, and therefore the result is an accelerated motion which follows a cosh-function. The time to double t_2 is one of several variables, on which the needed reaction speed of the control system depends. The equation for t_2 shows, that the static margin is only one variable, which affects the time to double. From this equation the following conclusions can be drawn:

- An aircraft with a small wing, like a Starfighter for example, can bear a much larger static margin than one with a delta-wing.

- Because of the larger density of air the aircraft reacts quicker at low altitude than at high altitude.

- At high speed the time to double is smaller than at low speed, but at low speed the disturbances in α due to gusts are larger, so that at low speed (landing)

there are mainly the same problems related to artificial stabilisation than at high subsonic speed.

4.2 Conclusions

At this point the following facts can be summarized

- An unstable design gives improved performance especially to a supersonic combat aircraft

- To avoid a restriction of the maneuver angle-of-attack it is desirable to make the aircraft controllable above the α for maximum lift.

- Because the unstable design causes similar problems to the flight control system at low speed and high angles-of-attack as at high speed, the behavior at high angles-of-attack has a large influence on the design of an unstable combat aircraft. It can restrict the choice of the wing planform as will be shown later.

5. PROBLEMS AT HIGH ANGLES-OF-ATTACK

In the region of high angles-of-attack attention has to be paid to the following points:

- *limit of maximum usable instability*
- pitch-up problems
- problems due to lateral and directional instability
- problems related to roll and yaw control

The first two items are related to longitudinal motion, which are strongly influenced by instability. The last two are mainly independent of the static margin.

5.1 Limit of usable instability

At high angles-of-attack there is an additional limit of usable instability which is now explained more precisely (figure 5.1):

On this figure the maximum nose-down moment (flaps down) of a tailless configuration for different static margins is plotted over α. When destabilizing a configuration the following effects result:

- At low α the maximum nose-down moment reduces because the center of gravity approaches the aerodynamic center of the flaps

- the derivative $\partial C_m/\partial\alpha$ becomes more positive because of the unstable design

- Therefore, when increasing the instability, the $C_m = f(\alpha)$-curve points to more and more positive values at high angles-of-attack. That leads to a zero pitching moment at a certain static margin or even to a so called "trim gap" when destabilizing further. An aircraft with too much instability will pitch up when flying into this region and stay at the upper limit of the trim gap, which would be very undesirable. So, always a minimum pitch-down moment, a so called recovery moment

$C_{m\ rec}$, is needed. This fact gives an upper limit to the maximum usable instability, SM_{max}, which must not be exceeded.

It is assumed for this presentation that the minimum pitch-down moment be zero, and the recovery moment is produced by a vector nozzle or a similar device.

The maximum usable instability for a tailless aircraft is mainly a function of

- wing-planform, (which means: leading-edge sweep, aspect ratio, size of the wing-strake etc.)

- further parameters like the form of the vertical tail (twin or single), flap size and so on.

The influence of some of these parameters on the maximum usable instability will be shown in the following sections.

5.1.1   Effect of strake-size and leading-edge sweep

The increase of strake-size and leading-edge sweep has the effect that the nose-up tendency is increased as shown in figure 5.2 for the example of a strake-variation and for constant static margin (SM = -10 %). When increasing strake-size or leading-edge sweep, the maximum usable instability is reduced. If one wants to get similar instabilities for configurations with larger leading-edge sweep, one is forced to reduce strake-area down to negative strake-areas (which can be defined as "negative strakes") that means "gothic" wing-planforms. In figure 5.3 the result of a wing-trend is plotted. The maximum instability SM_{max} ($C_{m\ rec} \approx 0$) is shown as a function of strake-size for three leading-edge sweeps $\Lambda_o = 45°, 56°$, and $63°$.

To get a negative trailing edge sweep, which improves the pitch-down characteristics at high α, the aspect ratio is varied simultaneously. One can see the following:

- An increase in strake-area reduces instability

- an increase in leading-edge sweep reduces it too

- the larger the leading-edge sweep, the smaller the dependency of instability on strake-area.

One can assume that all the configurations, having roughly the same weight and the same engine, will have approximately the same span. Therefore the configuration with the largest leading-edge sweep will have the largest wing-area and the largest reference cord-length $\bar{c}$, and, from the point of flight control, its maximum instability has to be reduced in comparison to that with a wing having a smaller leading-edge sweep. Configurations with different wing-planform but equal time to double are marked with circles. When comparing different wing-planforms for highly unstable aircraft one should use such trends.

5.1.2 Effect of the form of the vertical tail

Vertical tails can be designed as single or twin tails. A twin vertical tail makes sense, when large strake areas are used, because they possibly reduce nonlinearities in lateral stability at higher angles-of-attack. Furthermore twin verticals - especially when canted - normally can improve lateral and directional stability at high α due to the V-tail-effect. But there is one big disadvantage of twin verticals on configurations without aft-tail, especially at a high-wing configuration: At higher angles-of-attack it seems that the flow breaks down in the region of the verticals, i.e. the pitch-up tendency is increased. Because of the reduction of maximum instability, related to pitch-up, a twin vertical tail reduces the maximum usable instability.

In the upper part of figure 5.4 this effect is shown for a tailless configuration. SM_{max} is reduced very much.

5.1.3 Effect of an aft-tail

When the vector nozzle, which can provide for the recovery moment, is replaced by a horizontal aft-tail, $C_{m\ rec}$ has to be produced aerodynamically. As shown in the lower part of figure 5.4 an aft-tail configuration can be designed for similar instabilities. The reduction in maximum usable instability related to a twin vertical tail is reduced.

5.2 *Maximum occuring instability*

5.2.1 Desired behaviour

A further effect at high angles-of-attack, which must not be overlooked is the possible occurence of a pitch-up. By this is not meant here the usual definition of pitch-up at stall conditions, breaking stable or breaking unstable in a $C_L = f(C_m)$ plot. By "pitch-up" is meant in this presentation an increased $\partial C_m/\partial \alpha$ at higher α relative to that at low α. As was already seen in the figure 4.1, $C_{m\alpha}$ is the important factor for the time to double and not the unstable static margin, defined as $SM = (X_{cg} - X_{ac})/\bar{c}$. Control has to be designed for the maximum $C_{m\alpha}$. If a maximum $C_{m\alpha}$ occurs in the region of higher angles-of-attack, as shown in figure 5.5, the aircraft will not any longer have an optimum performance, because the basic instability at low α has to be reduced. A more "optimum" $C_{m\alpha}$-function should possibly have a pitch-down at higher angles-of-attack, for example to reduce the problems at landing, when large flap deflections are needed to stabilize the configuration. Furthermore the center of gravity can shift backwards and thus increase the instability, when the aircraft fuel is exhausted, especially when the heavy engines are in the tail of the aircraft.

Maximum possible instability is a function of many factors; for example the design of the control system and hydraulic system, hinge-moments, and so on. So, maximum instability can't be evaluated except with realistic simulation.

Especially with configurations without aft tail, the $C_{m\alpha}$-problem can become aggravating: In figure 5.6 a typical flap-effectiveness ΔC_m is shown as a function of α and flap-deflection. This effectivity is reduced with increasing α, beginning at $\alpha \sim 20°$ up to $\alpha \sim 40°$. Unstable configurations are trimmed by a positive flap deflection in this α-region. This fact can result in an additional positive $C_{m\alpha}$ as shown in figure 5.7. Stable configurations, trimmed by negative flap-deflections, don't show this effect.

Especially configurations, which realize only small maximum instabilities are disadvant-
ageous: At low α there is a relatively large nose down moment and a relatively small
positive $C_{m\alpha}$. At high angles-of-attack $C_{m\ rec}$ is zero. So that the $C_{m\alpha}$-curve at low α
points to a "wrong" direction. Therefore there has to be a pitch-up somewhere at
medium α.

Two values for maximum pitch-up can be defined

- a trimmed maximum pitch-up, which should be analysed more extensively, because
  it is the more important value for the configuration (MPT)

- an untrimmed maximum pitch-up, which is always larger than the trimmed
  one (MPU).

Some results for the untrimmed maximum pitch-up are shown in the next section.
The trimmed pitch-up doesn't depend directly on the untrimmed one, but a configuration
with a large untrimmed pitch-up is suspected to have a large trimmed one too.

5.2.2   Untrimmed_maximum_pitch-up

5.2.2.1   Effect of basic static margin

The basic instability SM at low α itself has a certain influence on the pitch-up. In
figure 5.8 this dependency is shown for an example of a strake variation. The variable
MPU (maximum pitch-up untrimmed), defined as MPU = $C_{m\alpha\ max} / (C_{L\alpha})_{low\alpha}$, doesn't become
zero, when the basic instability SM goes to zero. This tendency is more or less valid
also for the trimmed pitch-up. That means that the basic instability has to be reduced
very much for a configuration with a large pitch-up tendency, when the maximum possible
instability is given by the flight control system. This figure further shows that the
maximum occuring instability can become very large.

5.2.2.2   Effect of leading-edge sweep and strake-size

Because of the fact, that the trailing-edge flaps provide for a pitch-up tendency at
unstable configurations, it is necessary to choose a wing-planform giving a pitch-down
tendency to balance the flap-effect.

The kind of wing-planforms required, will be analysed in the following section.

5.2.2.2.1 Effect of leading-edge sweep

Figure 5.9 shows the maximum pitch-up untrimmed (MPU) for configurations without strake
as a function of leading-edge sweep. The trailing-edge sweep is negative for all confi-
gurations from which this figure is derived. That means that the aspect ratio is varied
simultaneously with sweep. The following facts can be seen:

- All configurations with flaps up having a leading-edge sweep exceeding
  $\Lambda_o \sim 50^o$ show a pitch-up.

- With flaps down pitch-up occurs, when the leading-edge sweep exceeds an
  angle of $\Lambda_o = 45^o$.

- The smaller the sweep the larger the difference between the curves "flaps
  up" and "flaps down". At large leading-edge sweep this difference is small.

The last statement is only true, if leading and trailing-edge flaps are both deflected.
The dependency of the maximum pitch-up untrimmed (MPU) as a function of leading and trail-
ing-edge flaps separately deflected, shows figure 5.10: the maximum pitch-up untrimmed is
reduced very much by a leading-edge flap deflection.

One should be cautions with the absolute values shown here, because many more components
of the configuration have an influence. The last two pictures are valid for "well rounded
noses". For example a sharp nose results in a lower pitch-up, this influence is larger
the smaller the leading-edge sweep. A positive trailing-edge sweep intensifies the pitch-
up.

5.2.2.2.2 Effect of strake-size

In figure 5.11 the maximum pitch-up untrimmed (MPU) is shown for several wings with dif-
ferent strake-sizes. As can be seen, for the 45° and 50°-wing, a strake provides charac-
teristics of a wing with higher sweep:

- the pitch-up with flaps up is increased and the curves "flaps up" and "flaps
  down" approach.

Configurations having a large leading-edge sweep can have a low level in pitch-up or
even a pitch-down, as long as a "negative strake" is provided.

5.2.2.3   Effect of an aft-tail

For configurations with a horizontal aft-tail these problems can be reduced very much.
With a low tail the following effect occurs (figure 5.12): A trailing-edge flap deflect-
ed down causes a strong downwash at the horizontal tail. With increasing angle-of-attack
this downwash is reduced due to the flow separating at the flaps. Therefore the effective
angle-of-attack of the tail α_H is increased with increasing α, a fact that results in
a pitch-down tendency due to a low horizontal tail. This mechanism works as long as

- the flow isn't separated at the tail itself
- the tail is kept free of the wing's wake.

This is the case for normal trim-positions of an unstable aft-tail configuration over
the whole angle-of-attack region. Figure 5.13 shows this effect as tested in a wind-
tunnel. The tail-off configuration shows a slight pitch-up untrimmed (PU) when flaps
are deflected and a pitch-down-tendency when the horizontal tail is on.

If the position of the aft-tail is higher, irregularities in C_m can occur at higher
angles-of-attack, because the tail is within the wake of the wing.

5.2.2.4   Effect of a Canard

As can be seen in _figure 5.14_, a canard produces a certain pitch-up tendency. In the upper part of the figure the PU is shown as a function of C_L for a canard-off configuration with different flap deflections. The lower part shows corresponding results for the canard-on configuration with $\delta_{N,F} = 36^o/10^o$. The center of gravity is held at the same position, so that the basic instability SM at low α of the canard-on configuration is larger than that with canard-off. At higher lift the PU of the canard-off configuration with $\delta_{N,F} = 36^o/10^o$, which already shows a bad behaviour, is increased by the canard. This increment does not vanish, when the canard is deflected.

5.2.2.5   Effect of the form of the vertical tail

A twin vertical tail increases the pitch-up tendency as it decreases the maximum usable instability.

5.2.3   Trimmed maximum pitch-up

The maximum pitch-up trimmed (MPT) is defined in a similar way as the maximum pitch-up untrimmed (MPU). As already shown in figure 5.7 it has to be smaller than the maximum pitch-up untrimmed.

On the MPT relatively little information is available for the time being, because of the following facts:

- The MPT depends on the instability used

- In trend-studies many configuration variations were tested only with very few flap-deflections. It is therefore not possible to get trends of the maximum pitch-up trimmed, because it is necessary to test many flap-settings to evaluate the real maximum.

If one tries to get trends, as for a strake-variation for example, one is often forced to build up the various aerodynamic coefficients from different tests, which reduces the accuracy of the obtained pitch-up values.

For a configuration with a leading-edge sweep of 63°, such a build-up is shown in _figure 5.15._ The maximum pitch-up trimmed (MPT) is plotted as a function of the maximum usable instability SM, according to figure 5.3. The strake area is varied corresponding to SM. Two curves are plotted: one with nose-flaps down ($\delta_N = 20^o$) and one with flaps up ($\delta_N = 0^o$). As expected the "negative strakes" reduce the maximum trimmed pitch-up. But there is a reversed tendency related to the nose-flap effect: The untrimmed maximum pitch-up (MPU) with nose-flap up is larger, as can be seen in figure 5.10. Here the configuration with flaps up shows a smaller trimmed maximum pitch-up (MPT). The reason for it is not yet determined.

5.2.4   Conclusions

In summary:

- As one cannot allow a much larger instability at low speeds than at high speed, a pitch-up tendency as defined above is undesirable for a highly unstable configuration

- As a consequence, a highly unstable configuration without aft-tail is confined to certain wing-planforms: Wings having a small leading-edge sweep and a certain positive strake area up to those having a larger leading-edge weep with a "negative strake", which means "gothic" wing planforms.

- An aft-tail can improve behaviour in pitch very much

- A canard seems to cause some pitch-up tendency.

5.2.5   Cranked wings

It is striking, that this wing-trend for highly unstable aircraft doesn't include the so called "cranked wing" which is used on several current aircraft projects. Figure 5.16 shows some of these projects gathered from literature.

It is commonly assumed, that the cranked wing has several advantages.

- Unloading of the flow at the wing-tip relative to a mere delta-wing

- At high Mach numbers (M > 1.5) the aerodynamic center moves forward which results in a smaller stability at these Mach numbers.

Against these advantages there seems to be one big disadvantage: the behaviour in pitch. All tests with cranked wings (having a concave crank of the leading-edge), known to the author, show a pitch up as can be seen in (figure 5.17) for the F16-SCAMP configuration (ref. [1]).

This is a typical wing with a large pitch-up and a small usable instability. Although the configuration will be flown indifferently (at a $C_{m\,rec}$ = 0!), one can estimate that it has a maximum trimmed pitch-up (MPT) of about -10 %. But less extremly cranked wings also show a pitch-up. The phenomenon has not been analysed till now. The reason for it can be possibly explained by the Polhamus-analogy (figure 5.18). According to this analogy the vortex-lift equals the theoretical suction force normal to the leading-edge. The component of the suction-force in the direction of flow, C_T, is independend of leading-edge sweep. So the total suction force normal to the leading-edge grows with leading-edge sweep. That means that the suction force at a cranked wing is larger at the inner and more forward part of the wing. Because the suction force and the vortex-lift too has a quadratic dependency on α, there has to be a pitch-up tendency, beginning immediately at low angles-of-attack. Therefore cranked wing don't seem to be a good solution for a highly unstable aircraft.

5.2.6   Critical Mach-range related to pitch-up

As can be seen from HIMAT-data for example (ref. [2]), the most critical Mach range is the low Mach number region (figure 5.19), because at higher Mach-numbers a general trend

into the direction of pitch-down is found. As mentioned in [2], the HIMAT-configuration, when having a basic instability of SM = -10 % at low α and low Mach-number, destabilizes up to a MPT of -30 %. Because of this fact an angle-of-attack limiter was used already in the model, which was flown statically stable. To my knowledge the HIMAT-configuration hasn't flown unstable yet [3]. The reason for it is not the pitch-up problem, but the high reactionspeed caused by the smallness of the model (the fuselage length is about five meters). Therefore the flight control system was not able to stabilize this quick motion around the pitch-axis.

5.2.7 Pitch-up due to sideslip

Another variable, which must not be overlooked, is the pitch-behaviour at sideslip. As the recovery moment is relatively small, a large pitch-up due the sideslip cannot be allowed in the high-α region. Figure 5.20 shows such a pitch-behavior due to sideslip for a configuration with and without strake. For this example the strake gives a pitch-down tendency.

5.3 Lateral and directional stability at high angles-of-attack

The following section deals with some items about lateral and directional stability at high angle-of-attack. This stability is essentially independent of the longitudinal stability, but it depends strongly on many small components of the configuration.

It is very difficult to get a systematic overview about this theme, because of the large amount of details playing a role and interfering with each other.

The problematic range in angle-of-attack is that, where the flow is separated only partly. That is, the region roughly above the α for C_{Lmax} (α ∿ 30°) up to the α, where the flow is totally separated (α ∿ 40°). Above this angle-of-attack the problem disappears in most cases, and there is no big change in stability up to very high α any more. The reason for this problem seems to be that a flow being separated partly reacts strongly to small variations, so that an angle of sideslip can provoke strong aerodynamic forces, which need not have the same tendency as at low angles-of-attack. If one intends to fly up to the angle-of-attack for maximum lift or even slightly above it, this problem has to be resolved.

To give an example of the difficulty to estimate the lateral and directional stability of a configuration, figure 5.21 shows two almost similar configurations (from [4]). One of them is stable and the other one is unstable in lateral motion at high α. From this it can be seen, that one has to be very cautious in making general statements about stability in the high angle-of-attack region. But on the other hand this figure indicates, that it seems to be possible to stabilize many configurations by small variations as long as they don't have components destabilizing too strongly.

5.3.1 Common criteria related to lateral and directional stability

The so called dynamic directional stability $C_{n\beta dyn}$ is a value which predicts in the first approximation the stability of an aircraft at high α

$$C_{n\beta\ dyn} = C_{n\beta} \cdot \cos\ \alpha - \frac{I_z}{I_x} \cdot C_{1\beta} \cdot \sin\ \alpha$$

where $C_{n\beta}$ and $C_{1\beta}$ is the directional and the lateral stability (in body-axes) respectively and I_z/I_x is the ratio of the inertia moments around the roll (x) and the yaw-axis (z) respectively. This ratio normally is very large for combat aircraft (about 5 to 10), so that the lateral stability is the most important variable related to stability at high α. $C_{n\beta\ dyn}$ is the simplified coefficient E of the characteristic equation for lateral motion, which has to be positive when stable.

In [4] a very interesting comparison can be found between the divergence tendency of *contemporary aircraft* and the measured $C_{n\beta\ dyn}$ from their windtunnel models. For the most of these comparisons it could be shown, that the aircraft had no divergence tendency, when the $C_{n\beta\ dyn}$ was stable (positive) from windtunnel tests. For the most of the rest of the cases, where the comparison did not prove right, it could be shown that either $C_{n\beta\ dyn}$ was too small so that the simplification of coefficient E was not justified, or that there were local instabilities at small angles of sideslip.

Therefore the following requirements have to be met:

- positive $C_{n\beta\ dyn}$ over the whole angle-of-attack region used. (The coefficient should not go below a certain positive value, for example 0.2 rad^{-1})

- no local instabilities in the permitted region of sideslip angle, that means an essentially linear behavior in β, especially of C_1.

To get an idea of the reasons for lateral/directional stability of a configuration, flow-pictures in a water-tunnel should be taken. But it will be very difficult an needs much experience to take such pictures, which really show the reason for stable or unstable behaviour respectively. In the next section a description of the influence of different aircraft components will be attempted, based on force-measurements in wind-tunnels.

5.3.2   Effect of different aircraft components on lateral and directional stability

5.3.2.1   Leading-edge sweep

It is commonly assumed that an increasing leading-edge sweep results in an increased instability due to sideslip. At larger leading-edge sweeps, beginning at about $\Lambda = 55°$, a leading-edge vortex occurs at higher α, which will breakdown at a certain angle-of-attack, causing a certain unloading of the wing.

At a certain sideslip-angle β, the leading-edge vortex on the foregoing part of the wing will break down first, unloading this side of the wing. The result is a positive rolling-moment lowering the foregoing wing and causing an even larger side-slip-angle, leading to an unstable motion.

But from our experience, this effect does not seem to be so strong, that it cannot be overwhelmed by other effects. For example the SCAMP-configuration, having an extremly high leading-edge sweep, shows relatively good lateral stability (figure 5.22).

GREER [4] also presents a configuration (config. N) having a large leading-edge sweep, which remains stable in $C_{n\beta dyn}$ over the whole α range ($0° < \alpha < 40°$) tested.

5.3.2.2   Forebody

It seems that the forebody of a configuration, meaning all components in front of the
wing's apex including strakes, canards, air-intakes and the shape of the fuselage-nose,
has to be regarded as an unity, which has to be optimized as a whole. Here the inter-
ferences between the components are extremly large, and the whole forebody will influence
the flow over the wing in the critical α-range. Because of the complexity of these in-
fluences, only a small amount of trends can be shown here, which need not be valid in
every case.

5.3.2.2.1 Strake

A strake intensifies the vorticity of a leading-edge vortex. From this point of view one
tends to assume that it will destabilize the configuration at high angle-of-attack. But
tests about a strake-variation at a configuration having a leading-edge sweep of
$\Lambda_o = 45^o$ show that there seems to be a certain optimum strake-size for this configura-
tion (figure 5.23). To judge the performance of a configuration at high angles-of-at-
tack, one should look for the lateral stability $C_{1\beta}$. The best strake shown here is that
with an area of 4 % of the wing area. The largest strake causes a strong instability
between $\alpha = 30^o$ and 40°. But the 4 % strake is still not optimum. It produces an irre-
gularity at $\alpha \sim 33^o$.

Tests of a slightly different configuration have shown that a strake size of about 3 %
will be the best for this special wing (figure 5.24). Large strakes commonly stabilize
at low α and destabilize at high α.

5.3.2.2.2 Canard

A canard should have an effect similar to a strake, but it can be deflected when used
as a horizontal tail. Figure 5.25 shows tests of such a canard configuration.

Because a canard used as a horizontal tail always has a relatively large area
$(S_c \sim 5 %$ up to 10 %), all tests known to the author show the typical effect of a too
large strake: at low α a canard stabilizes and in the critical range of α it destabi-
lizes. Even a very large deflection of the canard of -30° (nose down) doesn't make the
destabilization vanish. A further effect of a canard of this size (and of large strakes
perhaps too) is a strong nonlinearity in rolling moment C_1 over β within the criti-
cal angle-of-attack range Figure 5.26 shows this effect at $\alpha = 35^o$. Without a canard
C_1 is an essentially linear function in β With canard on there is an extremly strong
instability within the range of $\beta \sim \pm 6^o$. At higher β the lateral stability of the
canard-off configuration is almost regained. Unfortunately the configuration was not
tested in both directions of β, because the strong assymetry of the $C_1 = f(\beta)$ curve
seems to show that there is a hysteresis in $C_1 = f(\beta)$.

These effects seem to be typical for close-coupled canards. The reason for it may be
seen from figure 5.27. The leading-edge vortex of the leeward wing is reinforced by
the tip vortex of the canard, while the leading-edge vortex of the foregoing wing
is not. Thus, this vortex breaks down first resulting in a strong lateral instability.
This would also explain the restabilization at higher side-slip angles: Both tip-vor-
tices of the canard would then not be rolled in.

Long coupled canards don't show this effect because the tip-vortices of the canard are too far away from the leading-edge vortices, so they can't be rolled in.

Very small canards as that on the Mirage 4000 for example can't be used as an empennage. Tests about this configuration are not known to the author. Possibly such a small canard may be optimum for this configuration.

5.3.2.3 Wing position

The difference of a high wing and a low-wing configuration in stability is shown at figure 5.28. The low wing is a little bit better in directional stability, but in lateral stability there is no clear tendency.

5.3.2.4 Shape of the leading-edge

Most of the variations of the wing's leading-edge have a large influence on the lateral and directional stability at high α. As already mentioned by Greer [4], this influence is reduced when increasing the leading-edge sweep. A large stabilisation is related to a deflected leading-edge flap as shown in figure 5.29. As can be seen, the lower part of the critical α-range is stabilized. A slat, as shown in the next figures 5.30 and 5.33 for two different configurations, has a different characteristic of stabilisation. In both cases lateral stability is improved over the whole tested high-α region.

5.3.2.5 Form of the vertical tail

A canted twin vertical tail can improve lateral and directional stability. As shown in figure 5.32 the stabilization is larger for larger cant-angle ν, of the verticals. Opposite to leading-edge flaps it stabilizes in the upper part of the critical α-range. The reason for this stabilization is that the foregoing part of the V-tail produces more lift and drag and therefore a stable rolling-moment, especially at high α.

5.3.2.6 Outboard stores

Outboard stores can have a large influence on stability. As an example, the influence of a store (3x Mavericks plus pylon) on a wing-station is shown in figure 2.33. There is a difference in behaviour between a high-wing and a low-wing configuration. The high-wing configuration is stabilized in $C_{l\beta}$ very much due to outboard stores (left side), whereas the low-wing configuration is stabilized only slightly and the pylons alone destabilize it a little bit. The stabilizing effect due to stores seems to be a function of their position in z direction. The lower the store the more it destabilizes. After [5] a center-line store (tested at a F5, a low wing configuration) destabilizes very much. Whereas outboard stores and landing gear all show a stabilizing effect.

5.3.3   Conclusions

The lateral and directional stability at high α can be influenced by a lot of small variations of the configuration. For some variations, like leading edge flap deflection for example, one can give a general trend: A deflected flap stabilizes. But for many other ones like strake variation it is almost impossible to predict the results. Perhaps one can state the following, considering the small extract of wind tunnel data shown here:

- Everything in front of the leading edge of the wing is suspected to have a strong influence on lateral stability (C_{l_β}), and the forebody of the fuselage including strake etc. has to be seen as an unity, which has to be optimized as a whole.

- Components which are more forward like the fuselage nose (not demonstrated here) will also have an influence on the yawing-moment at $\beta = 0^\circ$

- leading-edge flap and slats have generally a stabilizing effect.

- components being more aft only show a minor influence with one exception: A canted twin vertical tail, which is not located totally within the wing-wake, will stabilize at high α.

5.4   Controllability at high α

The controllability can become a big problem at high α, because in a normal case the efficiency of aileron and rudder becomes smaller in this region. The fact, that an aircraft is stable at high α, does not mean a controlled flight can be achieved in every case. For that, one needs a certain controllability.

5.4.1   Roll-control

For roll control ailerons are normally used, but these loose much efficiency at high α. In figure 5.34 are plotted the C_n and C_l of three different types of roll-control. At high α a part-span aileron has only a small efficiency. A full-span aileron has a relatively good efficiency, but one cannot use it, because one has to trim by flaps in a normal case. A good device for roll-control at high α seems to be the taileron. In the figure, there is shown the taileron-effectivity at a configuration with flap down and trimmed for SM = -8 %. One can see that it has its full efficiency at high angle of attack. It is possible to get even more C_l from it but then the adverse yawing-moment coupled to C_l becomes too large. For this evaluation a limit in C_n of +0.15 in the proverse direction and 0.1 in the adverse direction was used. At $\alpha \approx 35^\circ$ there is a minimum in C_L, which is related to the recovery moment of the unstable configuration. At this α the tail is loaded the most, so that there remains a minimum reserve for roll power.

5.4.2   Yaw-control

Yaw-control can become a problem too at high angles-of-attack. In figure 5.35 is shown the rudder-efficiency for a single and a canted twin vertical tail in a high-wing

configuration. Rudder-efficiency of the twin verticals begins to decay at about $\alpha \approx 20^{\circ}$ where that of the single vertical remains constant up to $\alpha \sim 40^{\circ}$. So the single vertical seems to be the best solution for a configuration at high angle-of-attack, but one also has to pay attention to the adverse rolling-moment caused by rudder deflection at $\alpha \sim 35^{\circ}$. This has to be compensated by roll-control. If this, for its part, has an adverse yawing-moment, roll-control and yaw-control can compensate each-other, so that there is no controllability at all.

6.   CONCLUSIONS

Problems in longitudinal motion occuring at high angles of attack, which are related to unstable design, were shown in this presentation. Although this α-range is not the region where the basic maneuvers of a combat aircraft are flown, problems can become so aggravating here, that they have a big influence on the design of such a configuration.

In the second part of the presentation some effects of configuration components on lateral and directional stability at high α were shown. Because of the complexity of these effects it is not possible to give an entire overview about this subject. But problems related to lateral stability at high α have to be solved if limitations in the maneuver-range of a combat aircraft are to be avoided.

7.   ACKNOWLEDGEMENT

FIGURES

1.1   Typical fighter-type wing

2.1   Typical requirements of combat aircraft
2.2   Requirements as a function of α, M

3.1   Polar of a tailless configuration
3.2 $C_L \cdot S \approx f(C_D \cdot S)$
3.3   Sustained turn-rate $= f(SM, S)$
3.4   Corner-speed $= f(SM, S)$

4.1   Motion around the pitch-axis

5.1   Limit of usable instability
5.2   Effect of strake-variation on C_m
5.3   Maximum instability for different wings
5.4 SM_{max} for tailless and aft-tail configuration
5.5 $C_{m\alpha} = f(\alpha)$
5.6 $\Delta C_m(\delta_F) = f(\alpha)$
5.7 $C_m = f(\alpha)$ (SM; MPT; MPU)

REFERENCES

[1]   General Dynamics   F16 SCAMP
FZP-1997-1
(Feb. 1980)

[2]   DEETS, D.A.,   Highly Manoeuverable
         CROTHER, C.A.   Aircraft Technology
AGARD-AG-234
(1978)

[3]   FLIGHT International
15 August 1981, p. 490

[4]   GREER, H.D.   Summary of Directional
Divergence Characteristics
of Several High-Performance
Aircraft Configurations
NASA TN-D-6993
(Nov. 1972)

[5]   TITIRIGA, A.   Design Technology for
      ACKERMAN, J.S.   Departure Resistance of
      SKOW, A.M.   Fighter Aircraft
                          AGARD-CP-199
                          (Nov. 1975)

SYMBOLS

AR   aspect ratio

$\bar{c}$ reference chord

c_D drag coefficient

c_{Di} induced drag coefficient

c_L lift coefficient

c_1 rolling moment coefficient

c_{Lmax} max. lift coefficient

c_{Lt} lift coefficient at turn-rate

$c_{L\alpha}$ $\partial c_L / \partial \alpha$

$c_{L\beta}$ $\partial c_1 / \partial \beta$

c_m pitching moment coefficient

$c_{m\ ac}$ c_m around the aerodynamic center

$c_{m\ cg}$ c_m around the center of gravity

$c_{m\ rec}$ recovery moment coefficient

$c_{m\alpha}$ $\partial c_m / \partial \alpha$

$c_{m\alpha\ max}$ max. $c_{m\alpha}$

c_n yaw-moment coefficient

$c_{n\beta}$ $\partial c_n / \partial \beta$

$c_{n\beta\ dyn}$ dynamic directional stability

c_S suction force coefficient

c_T thrust coefficient of the leading-edge suction

c_V vortex-lift coefficient

D   drag

K-factor	$C_{Di}/C_L^2 \cdot \pi \cdot AR$
L_H	lift of horizontal aft-tail
M	Mach number
m	mass
MPT	maximum pitch-up trimmed (in % $\bar{c}$)
MPU	maximum pitch-up untrimmed (in % $\bar{c}$)
n	load factor
n_{max}	max. load factor
PU	pitch-up untrimmed (in % $\bar{c}$)
q	dynamic pressure
r_y	inertia-moment arm
S	reference area
S_c	canard area (in % S)
SM	static margin
SM_{max}	max. instability (when $C_{m\ rec} = 0$)
S_{str}	strake area (in % S)
t	time
t_2	time to double
T_{max}	max. thrust
V	speed
V_∞	speed
V_c	corner-speed
X_{ac}	location of aerodynamic center
X_{cg}	location of center of gravity
α	angle-of-attack
$\alpha_{CL\ max}$	α of max. lift
α_H	α of horizontal aft-tail
$\dot{\alpha}$	acceleration in α

β angle-of-sideslip

δ_C deflection of canard

$\Delta C_m(\beta)$ pitch-up due to sideslip
$\Delta C_m(\beta) = C_m(\beta=10^\circ) - C_m(\beta=0^\circ)$

δ_F trailing-edge flap deflection

δ_H deflection of horizontal aft-tail

δ_N leading-edge flap deflection

$\delta_{N,F}$ deflection of leading- and trailing-edge flap

$\Delta\alpha$ disturbance in α

Λ_o leading-edge sweep

ζ rudder deflection
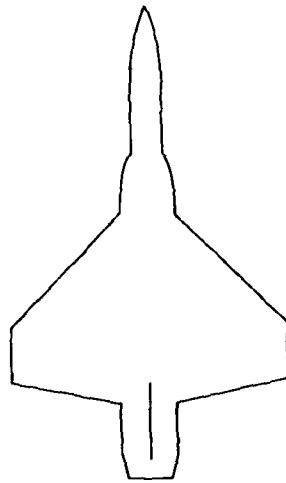
1.1 Typical fighter-type wing

- Basic requirements for a combat aircraft

- Effect of an unstable design on the performance

- Limit of instability due to the control system

- Problems at high angle-of-attack due to longitudinal instability and lateral and directional stability
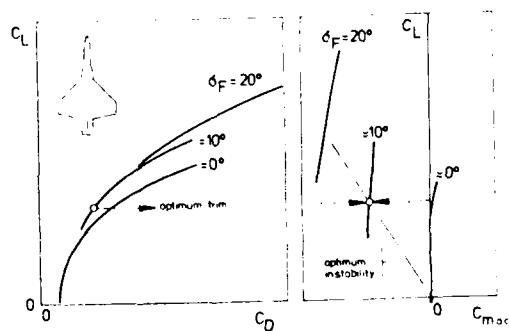
1.2

Typical requirements for combat aircraft

- high sustained turn-rate at subsonic and supersonic speed

- small corner-speed

- controllability at high angle-of-attack
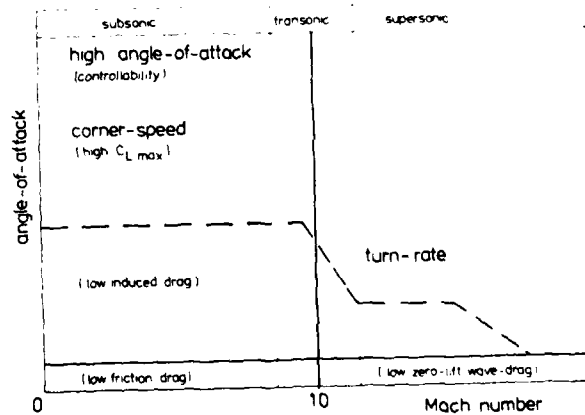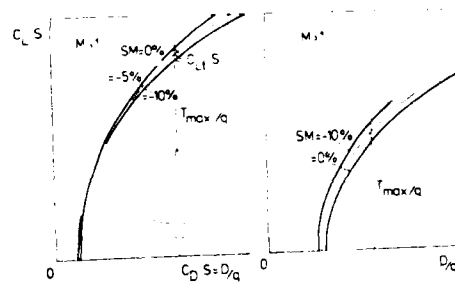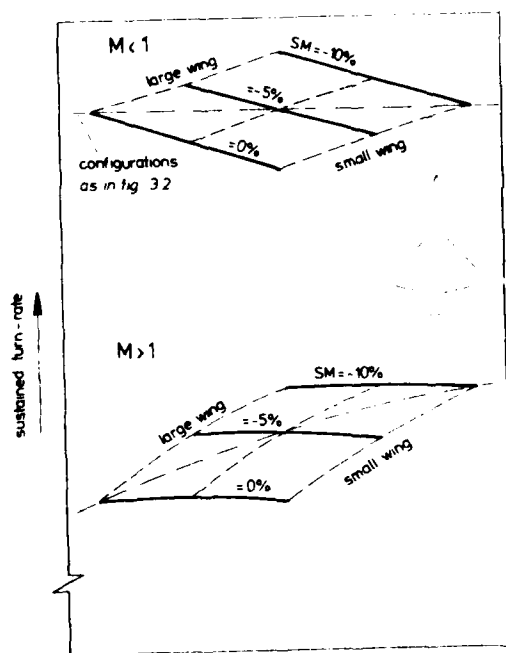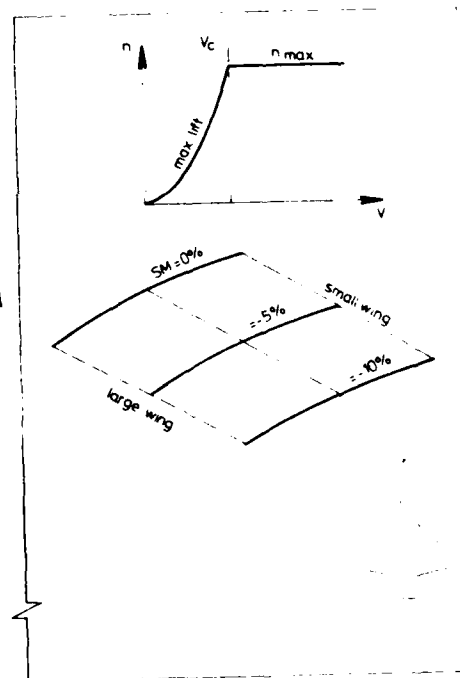

2.1 Typical requirements for combat aircraft

2.2 Requirements as a function of α, M

3.1 Polar of a tailless configuration

3.2 $C_L \cdot S = f(C_D \cdot S)$

3.3 Sustained turn-rate = f (SM,S)

3.4 Corner-speed = f (SM,S)

Equation of motion around the pitch-axis

$$\alpha\, m\, r_y^2 = \left[\frac{C_{m\alpha}}{-C_{L\alpha}\,SM}\right]\, q\,S\,\bar{c}\,\Delta\alpha$$

$$\alpha = \Delta\alpha_o \cosh\left(\sqrt{-C_{L\alpha}\,SM\,\frac{qS}{m}\cdot\frac{\bar{c}}{r_y^2}}\;t\right)$$

time to double

$$t_2 = \frac{\cosh^{-1}(2)}{\sqrt{-C_{L\alpha}\,SM\,\dfrac{qS\bar{c}}{2m\,r_y^2}}}\; v$$

4.1 Motion around the pitch-axis
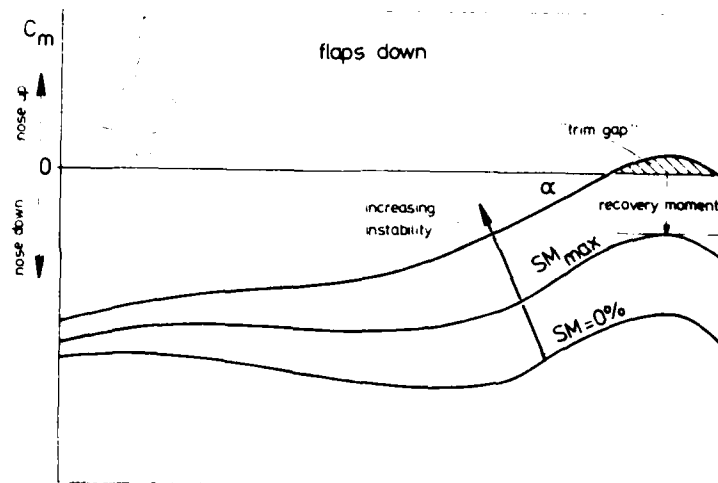
.1 Limit of usable instability
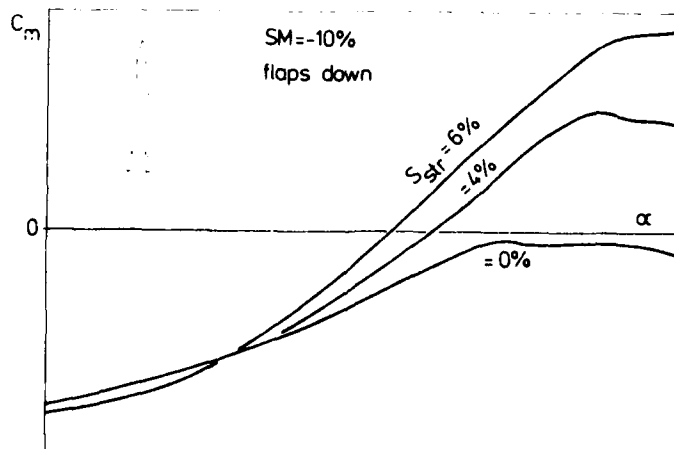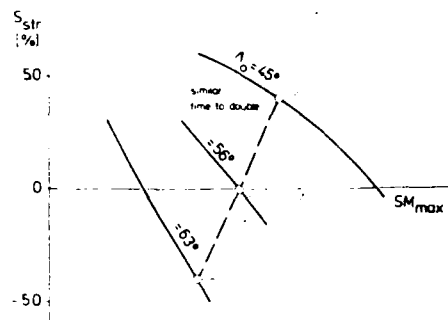
5.2 Effect of strake-variation on C_m

5.3 Maximum instability for different wings

5.4 SM$_{max}$ for tailless and aft-tail configuration

5.5 C$_{max}$ = f (α)

5.6 C$_m$ (δ$_F$) = f (α)

5.7 $C_m = f (\alpha)$ (SM; MPT; MPU)

flap-efficiency breaks down

0 $C_{m\alpha}$ (SM)

② $C_{m\alpha max}$ (MPT)

③ $C_{m\alpha max}$ (MPU)

$\delta_F = 20°$

large stroke

small stroke

no stroke

pitch up

5.8 Maximum pitch-up untrimmed (MPU)

SM = -10%
trailing-edge sweep negative

flaps down (δ_F = 20°)

flaps up

pitch down

leading- and trailing-edge flaps deflected
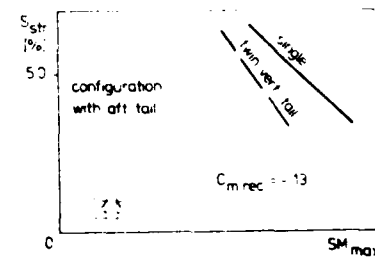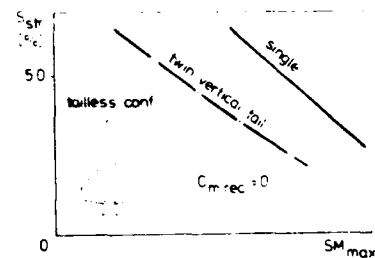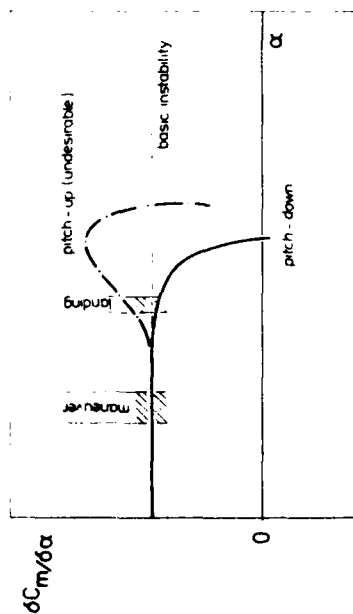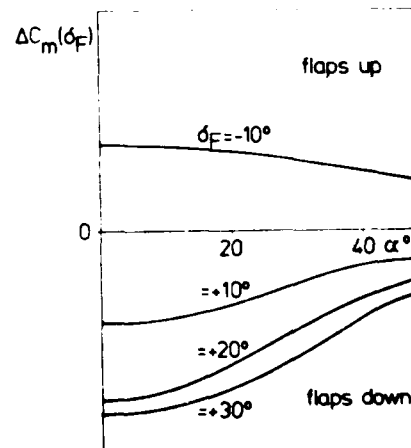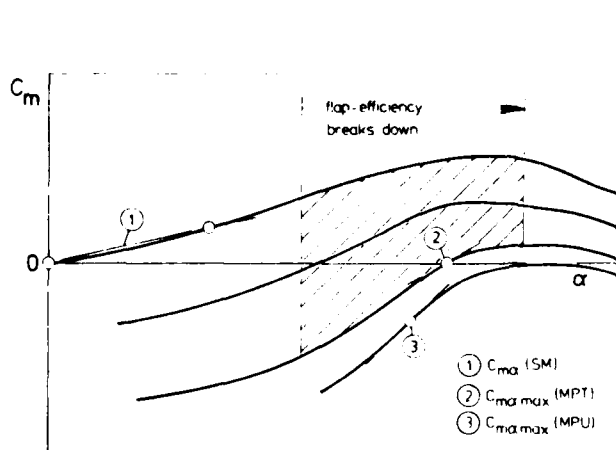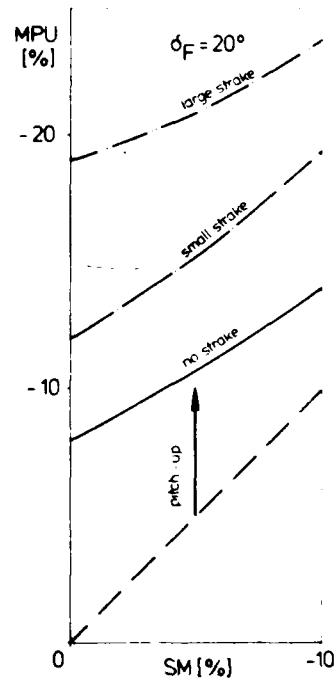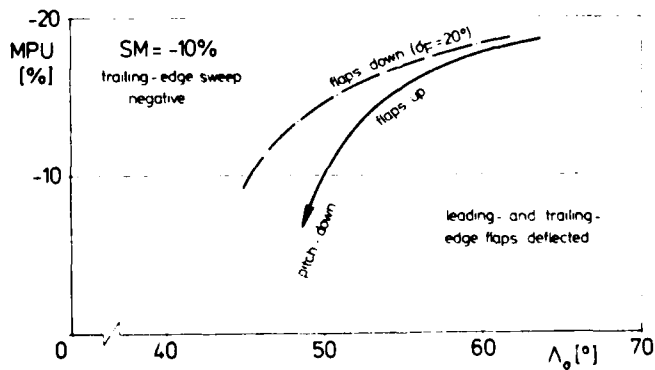
5.9 MPU as a function of leading-edge sweep

5.10 MPU = f (δ_N; δ_F)
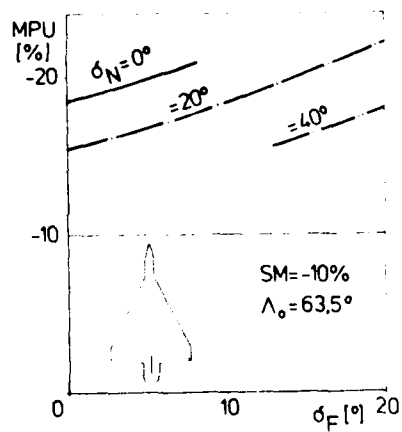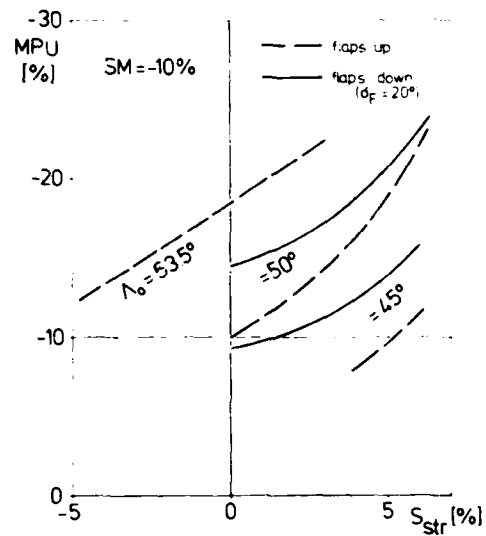
5.11 MPU = f (Λ_c, S_{str})
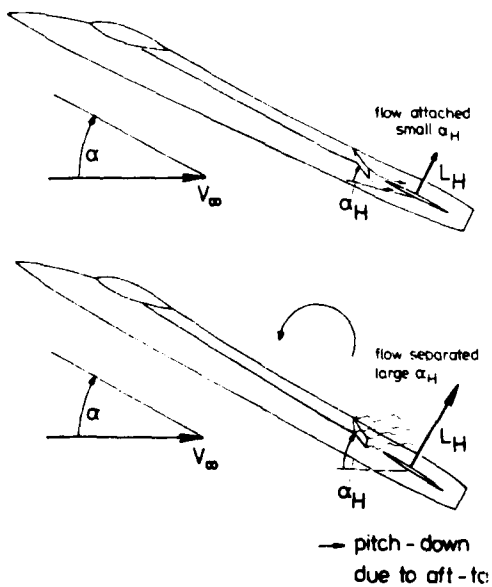
5.12 Pitch-down due to aft-tail
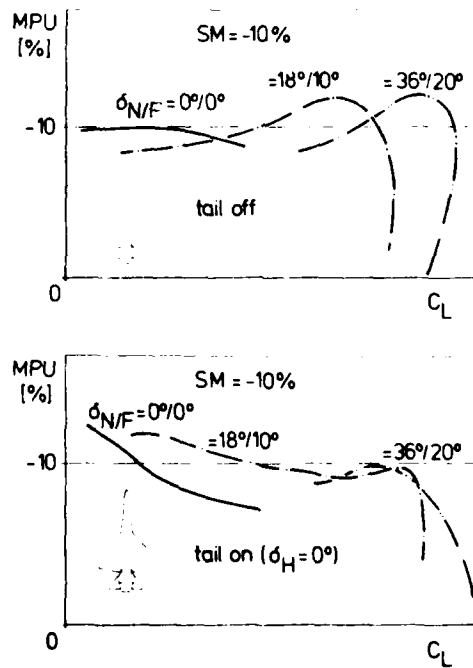
5.13 Pitch-down due to aft-tail (test)
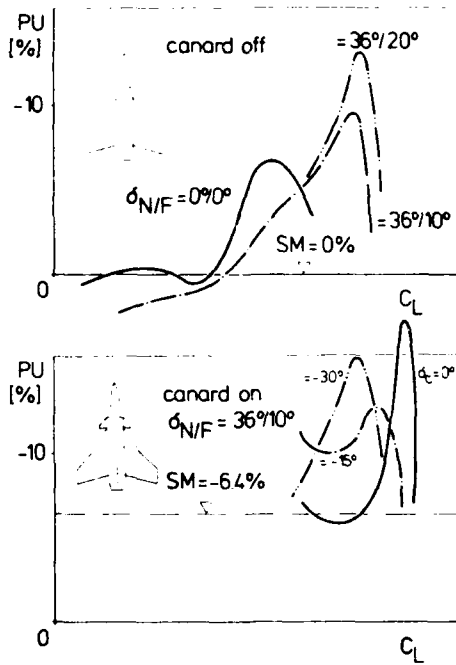
5.14 Pitch-up due to canard
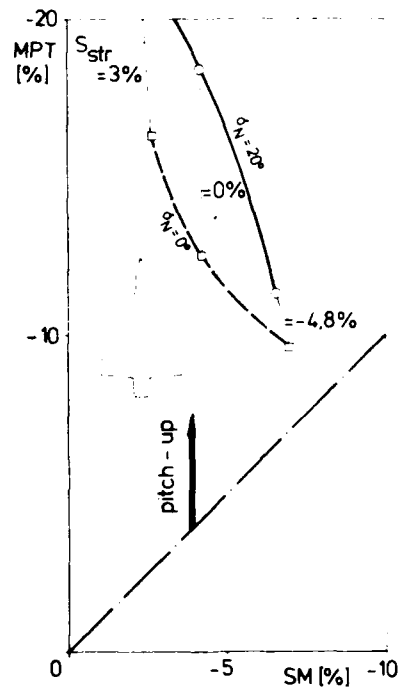
5.15 Maximum pitch-up trimmed (MPT)
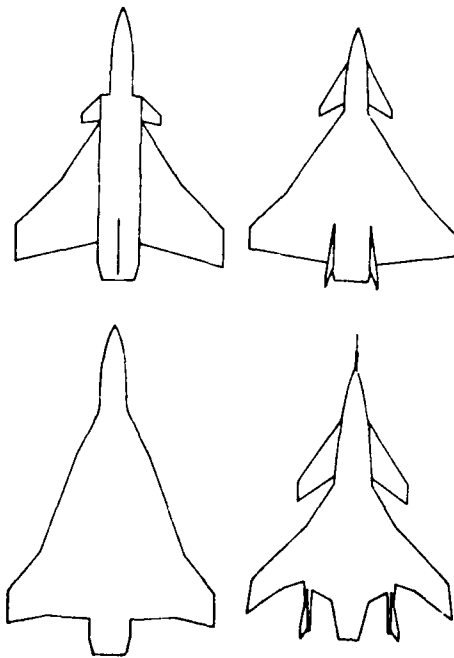
5.16 Cranked-wing configurations
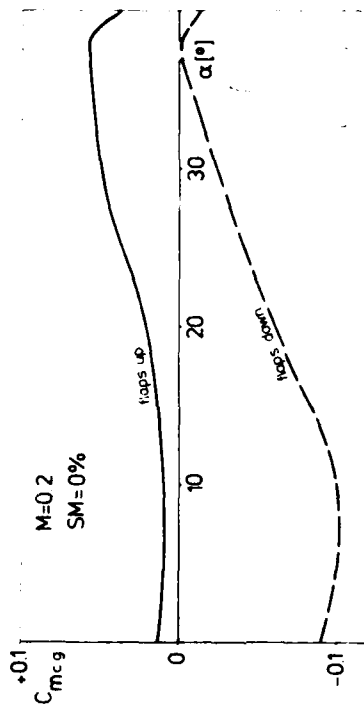
5.17 $C_m = f(\alpha)$; SCAMP-configuration

Polhamus - analogy
suction - force $C_S \sim$
vortex - lift $C_V \sim \alpha^2$

increased pitch - up

large

vortex - lift

small

Λ_o

C_S C_T

x_{ac}

x_{cg}
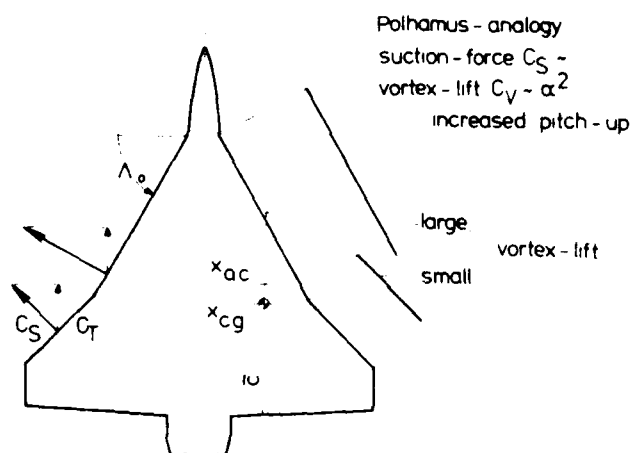
5.18   Pitch-up of a cranked wing according
to Polhamus-analogy

20

C_L

$M=07$

$M=0.2$

10

0   01   0.2 C_m 03
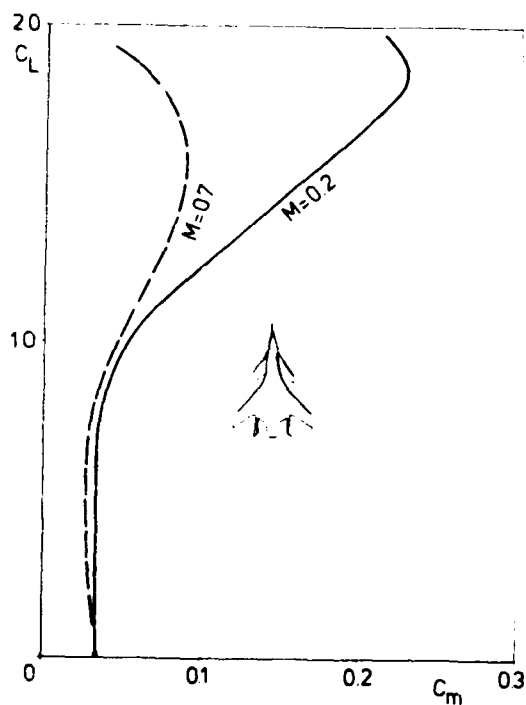
5.19 $C_m = f(C_L)$; HIMAT-configuration

α [°]

35

30

25

$SM = -10\%$
flaps down

$S_{str} = 0\%$

$S_{str} = 4\%$

pitch-up

$\Delta C_m(\Omega)$ 0
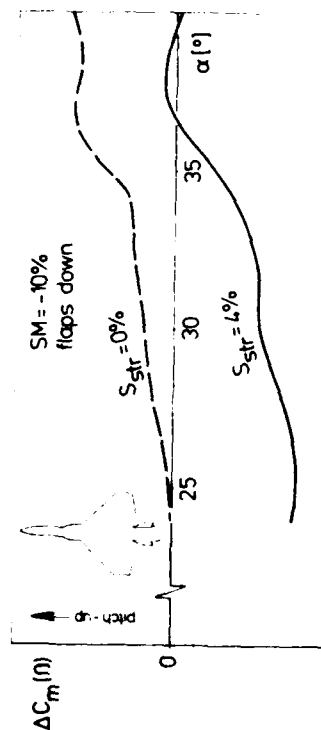
5.20   Pitch-up due to sideslip

unstable

stable
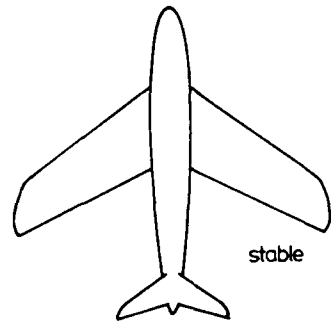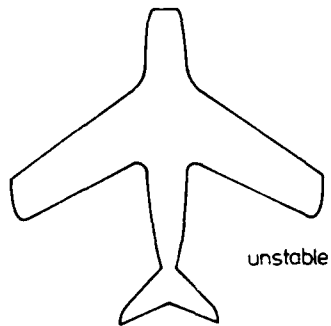
5.21 Two similar aircraft with different stability at high angle-of-attack
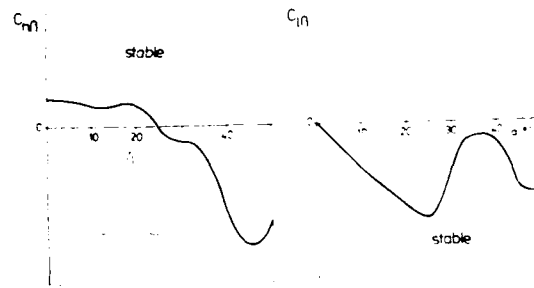
5.22 $C_{n\beta}$, $C_{l\beta}$ SCAMP-configuration
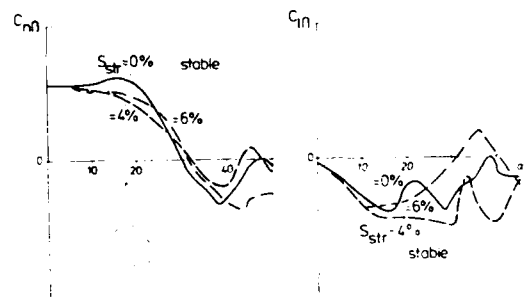
5.23 $C_{n\beta}$, $C_{l\beta}$ strake-variation
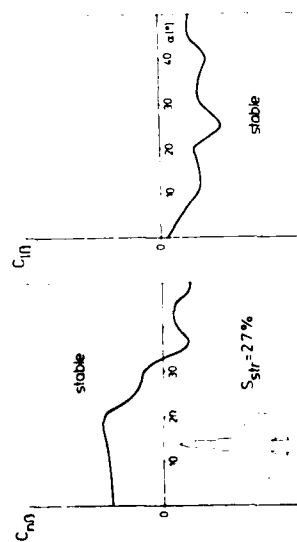
5.24 $C_{n\beta}$, $C_{l\beta}$ strake-variation (continued)
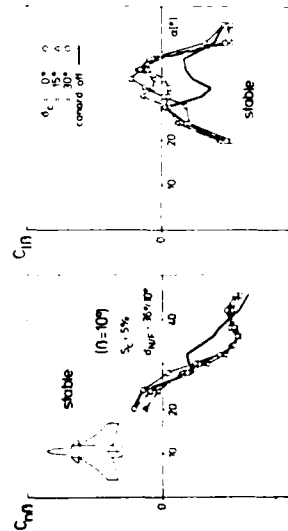
5.25 $C_{n\beta}$, $C_{l\beta}$ canard-configuration
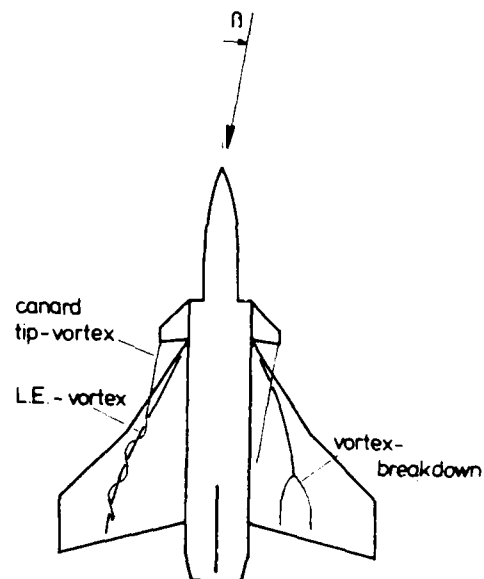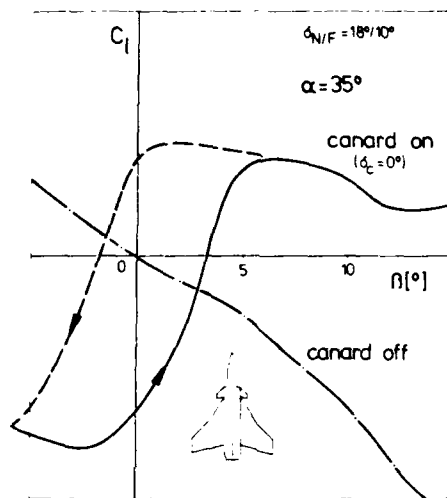
5.26 $C_l = f (\beta)$ canard-configuration

5.27 Influence of canard on vortex-system
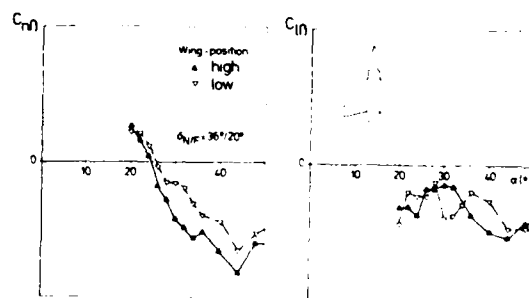
5.28 $C_{n\beta}$, $C_{l\beta}$ high wing/low wing
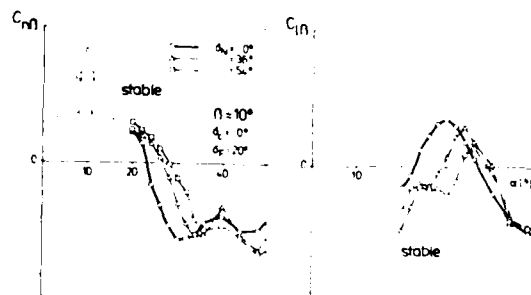
5.29 $C_{n\beta}$, $C_{l\beta}$ effect of nose-flap deflection
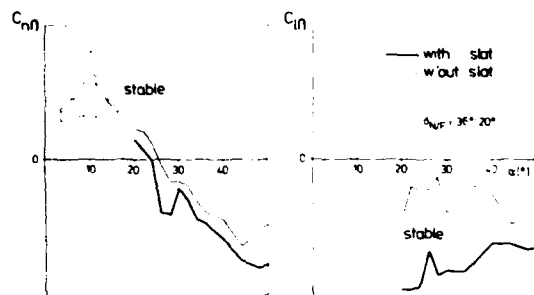
5.30 $C_{n\beta}$, $C_{l\beta}$ effect of slat
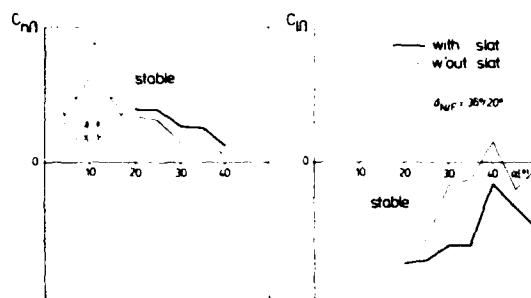
5.31 $C_{n\beta}$, $C_{l\beta}$ effect of slat
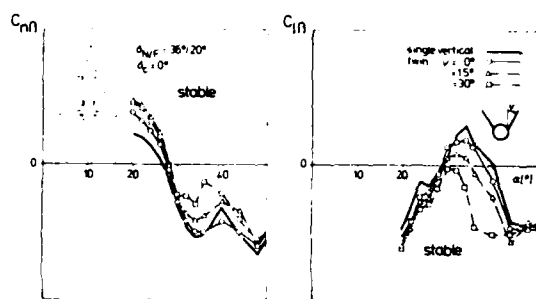
5.32 $C_{n\beta}$, $C_{l\beta}$ effect of vertical tail
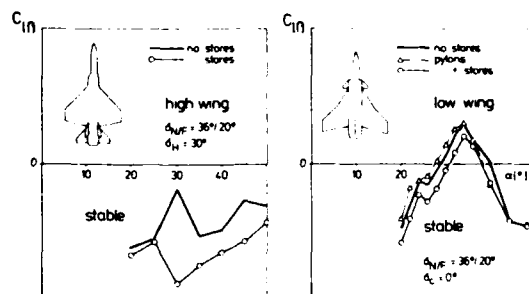
5.33 $C_{l\beta}$ effect of outboard stores
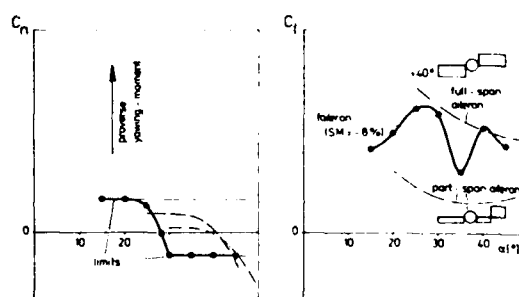
5.34 Roll-control
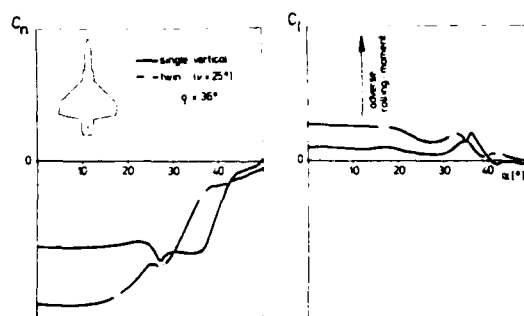
5.35 Yaw-control

MISSILE BODY VORTICES AND THEIR INTERACTION WITH LIFTING SURFACES

by

J. R. Deane,

Aerodynamics Research Department, FPC 67,

British Aerospace,

Dynamics Group,

Bristol,

BS12 7QW

U.K.

NOTATION

a	Body radius (local value)
c_r	Root chord length of a wing panel
c_1	Local chord length of a wing panel, or local chord for a cropped delta wing panel
c_p	Pressure coefficient $= \dfrac{p - p_\infty}{q}$
C_{Np}	Panel normal force coefficient based on body cross-sectional area
C_{Nv}	Vortex induced normal force coefficient
D	Body diameter (maximum value)
i	Vortex lift interference factor
K_{WB}	Wing body interference factor
L	Characteristic length for flow development used in impulsive flow analogy
$L(\xi)$	Non-dimensional spanwise loading function at ξ
	$(L(\xi) = \dfrac{c}{c_r} \int_{0}^{1} \Delta Cp \cdot d \left(\dfrac{x}{c_1}\right)$)
$L_T(v)$	Lift on a (tail) panel due to vortex interference
$(L_T)_\alpha$	Lift on a (tail) panel at incidence angle α
l_a	Afterbody length (i.e. body length excluding nose)
l_N	Nose length
M	Mach number
M_∞	Freestream value of Mach number
Re_D	Reynolds number based on body diameter and freestream speed
r	Distance from a vortex to a point at which velocity v is induced.
r_b	Radius of spherical blunting of a nose
r_T	Body radius at the (tail) panel location
r_{BV}	Radial location of a body vortex (See Fig. 6)
r_N	Radius of the body at the base of the nose
r_c	Radius of a viscous vortex core as suggested by Oberkampf's method
s_p	Semi-span of panel (gross)
s_T	Gross semi-span of a (tail) panel
s_w	Nett semi-span of a wing panel
V_c	Crossflow Velocity ($= V_\infty \sin\alpha$) or oncoming velocity relative to a cylinder in 2-dimensional flow
V_∞	Freestream flow velocity
v	Induced velocity due to a vortex
V	Flow velocity in working section
v_r, v_ϕ	Radial and circumferential velocities in the leeside wake
x	Distance along local chord of a wing panel
x	Distance along the body
x_s	Distance along the body at which first boundary layer separation/body vortex generation occurs
$\left(\dfrac{xcp}{D}\right)_v$	Centre of pressure of vortex induced load
y_w	Lateral distance across nett semi-span of a wing panel
y_{BV}, z_{BV}	Lateral and vertical position of body vortex core measured perpendicular to body longitudinal axis
y, z	General position coordinates
y_{cp}	Lateral panel centre of pressure position
α	Incidence angle (superscript r used when in radians)

α_1 Local value of incidence or angle of attack

β $\sqrt{M^2 - 1}$

Γ_{BV} Strength of a body vortex

Γ Circulation or vortex strength

$\Delta C_{N,v}$ Change of normal force coefficient on a body due to changes of positions of body vortices along the length of the body

θ_N Semi apex angle of a sharp-nosed body

θ_{BV} Polar coordinate of a body vortex (See Fig. 6)

ϕ Roll angle

ψ Circumferential angle of pressure tappings on the body

ξ Non-dimensional spanwise panel coordinate $(\xi = \dfrac{y_w}{s_w})$

SUBSCRIPTS

s   Sheet value   )

t   Total value   )   used in connection with circulation estimates

1. INTRODUCTION

This lecture is specifically concerned with the discussion of vortex generation from the body of a missile and with subsequent interaction or interference effects.

As well as outlining the results from various experimental studies it is important to discuss the development of prediction methods. In the case of body vortices this would be applied both to their initial generation, subsequent trajectories and consequent interaction effects. In general, the desire to predict any aerodynamic quantity, as opposed to having to measure it, has long been a requirement in missile aerodynamics. The available resources within the initial feasibility stages of a missile design are inevitably limited, probably precluding the acquisition of aerodynamic design data by testing the large parametric range of configurations which might be necessary. Thus prediction methods must be used.

In terms of the total normal force on a missile it can be argued that the importance of vortex interference terms can, in some cases, be quite small either because the interference loads themselves are small or because they may be generated on a wing or tail panel rolled into the leeside wake. The latter feature would mean that regardless of the size of the force generated on it, the component in the pitch plane direction due to the panel will be small due to a large angle through which it must be resolved. However, it must be recalled that not only the prediction of normal force is important. Side force and perhaps rolling moment must also be estimated and, for the latter especially, an adequate prediction of both the magnitude of load on a leeside panel and its spanwise distribution (or equivalently lateral centre of pressure) would be essential for high accuracy in the final answer.

The earliest work on vortex flow fields by BAe (DG) consisted of a compilation of a bibliography (Ref. 1) which sought to collate references on vortex effects available at the time (1975). This search was not limited to body vortex effects, but the next study (Ref. 2) was a specific experimental investigation of body vortex interaction with wing panels on a missile configuration at supersonic speeds. BAe (DG) involvement was then continued by a series of water tunnel and low speed wind tunnel experiments aimed at gathering more data, both qualitative and quantitative, on the same phenomena.

Supersonic investigations were continued with a short series of tests to complement the earlier work by the present author described in reference 2.

The studies have concentrated on the assessment of flow visualisation, force and moment and surface pressure data taken in a variety of experiments. Tests to quantify the flow field details by flow survey techniques have not been undertaken directly by BAe (DG). However, there has been close involvement with plans by the Royal Aircraft Establishment to undertake a comprehensive set of flow survey tests using yaw meters to explore leeside body vortex wake characteristics. As a forerunner to this programme a set of tests of a similar nature, but much less extensive, was carried out by Aircraft Research Association (Ref. 3).

Research interest on this topic is not confined to the U.K. Both in the U.S.A. and Europe investigators have been active in the field and, in general, similar lines of approach have been taken in response to similar demands for aerodynamic prediction method development and in the further understanding of flow fields. However, the number of references to the specific problem of body vortex interaction with lifting surfaces is not large.

Before proceeding it is worthwhile here to make three important general state-ments:

(a) The range of angles of incidence considered in this lecture has been deliberately chosen to ensure that, in the main, a body vortex system would be set up symmetrically disposed to the pitch plane.

(b) Whereas vortices from front fuselages are important to the aircraft aero-dynamicist, the aims of the <u>missile</u> designer have been uppermost in the thoughts of the author when considering material for this lecture.

(c) Only configurations with circular cross section bodies have been considered.

2. REVIEW OF THE LITERATURE

2.1 VORTEX CHARACTERISTICS OF ISOLATED BODIES OF REVOLUTION

2.1.1 Experimental Studies

The tests of Gowen, Perkins, Jorgensen, Gapcynski and Raney (Refs. 4 - 8) first explored what are, by now, the familiar characteristics of the contra rotating vortex pair, with large rotational areas in the flow field, significant local changes of dynamic and total pressures and, in compressible flows, the local Mach number. Such efforts at investigating the details of the flow fields were a natural extension to the efforts being made (Refs. 9 - 10) to formulate empirical prediction methods for the non-linear aero-dynamic (i.e. normal force and pitching moment) characteristics of slender bodies of revolution. Attention was mostly confined to supersonic speeds and incidence angles up to approximately 25°. Data was sought on the leeside flow behaviour as an input into such methods as that developed by Nielsen and Kaattari (Ref. 11) which considered inter-action phenomena on downstream surfaces.

Data from Jorgensen and Perkins (Refs. 7 - 8) is notable since it provided a source which was referred to by many later authors, for example Spahr (Ref. 12), who needed an input of body vortex characteristics. The locations and strengths were deduced from flow survey information and were then correlated using, effectively, the impulsive flow analogy as a basis to relate vortex development along the length of a three dim-ensional inclined cylinder at incidence to the development with time of the two dimensional flow about a cylinder set normal to an oncoming stream*.

The analogy had been used by Allen and Perkins (Ref. 13) and Kelly (Ref. 10) and required information on the drag characteristics of impulsively started two dimensional cylinders. Such data was available from Schwabe (Ref. 14) and latterly from Sarpkaya (Ref. 15). The generation of the flow in three dimensional situations could be visualised as the product of superposition of two mutually independent flow components, i.e. axial and crossflow. The flow characteristics evident in the latter plane could be considered to develop separately to those in the axial direction, except that the crossflow plane behaviour would be convected down the length of the body.

The reasons for the vortex generation in the crossflow plane are well known. The circular shape of the body cross section will mean that adverse, i.e. rising, pressure gradients are set up around the circumference from the shoulder. The boundary layer which develops on this surface is thus liable to separate on the leeside of the body at a point which is dictated very much by the state of the boundary layer (laminar or turbulent) and hence by Reynolds number with, for a compressible flow, the effects of crossflow Mach number also entering in. Inside the boundary layer there is an implicit rotational characteristic owing to the larger tangential velocities away from the surface than inboard arising from the velocity gradients in the boundary layer. On a simplistic level the formation of the two concentrated vortex cores on the leeside can thus be looked upon as a result of this rotational character or vorticity acting upon the separated boundary layer or feeding sheet. In the leeside wake this then rolls up in towards the plane of symmetry through the body axis resulting in two concentrated vortex cores. The flow velocities induced by the vortices will then be diverted back towards the leeside of the body and, underneath the cores, will be directed along the surface of the body in opposition to the main flow direction. This then means that an equivalent system of boundary layer development, separation and vortex formation is induced, but on a much smaller scale and with a consequent direction of vortex rotation in opposition to the main cores.

*NOTE: In reality there must be interaction between axial flow and crossflow. The impulsive flow analogy which assumes independence of these components must therefore be looked upon as a <u>convenient way of approximating</u> the flow development.

In a recent paper Wardlaw (Ref. 16) produced a graphic illustration of the complexity of the flowfield even with symmetric vortex generation. (Fig. 1). An important point to understand from such an illustration is the large area of the flowfield which is dominated by vortex effects, either in the main cores, feeding sheets or secondary vortices.

It was to gain an understanding of these phenomena in fixed crossflow planes and also how, if at all, the characteristics changed downstream that the early experiments were planned. It was found that for the angles of incidence they were concerned with, say up to approximately 25°, and for the relatively small overall fineness ratios (maximum about 13), the vortex patterns remained symmetrical and reasonably similar in their form in successive crossflow planes down to the base of the body. However, the strength would increase due to the continuous nature of the boundary layer separation (and hence vorticity feeding into the core) and the positions of the main vortex cores would move more upward and outboard relative to the body axis. An important aim of the early tests was, therefore, to quantify these variations and to establish whether they would be predictable for new configurations. At the time of Perkins and Jorgensen's work this could most sensibly be achieved by an empirical technique so they correlated their data on vortex paths and strengths for their range of angles of incidence, and longitudinal body station.

In their original reference they presented plots which correlated vortex strength and vortex positions against $\frac{x - x_s}{a}$. a .

It can be observed by reference to the original data of Jorgensen and Perkins that the correlation was by no means perfect (See Fig. 2) although the superposition of Raney's results supported the general form. This was commented upon in the reports which discussed this work and other early data (e.g. Ref. 18) and various reasons put forward relevant to the problems of actually measuring the appropriate vortex characteristics.

One particular problem lies in the assessment of the longitudinal position at which first separation or vortex formation occurs. Data on this can only be obtained from surface flow visualisation or pressure distribution measurements and neither will provide great accuracy; in the former case due to the problems of interpreting the flow patterns and, in the latter case, due to the practical difficulties of having a close enough spacing of pressure tappings. Jorgensen and Perkins presented their results as a separation zone (See Fig. 3).

The range of data in References 19 - 31 on symmetric body vortex characteristics made available since the tests of Jorgensen and Perkins and up to 1975 can be most easily reviewed by reference to the report of Mendenhall and Nielsen (Ref. 17). They followed the general procedures of Jorgensen and Perkins in forming empirical correlations of vortex strength and position against a non-dimensional parameter slightly modified from that which had been used in Reference 8. $\left(\frac{x - x_s}{r_N} . \sin a \text{ instead of } \frac{x - x_s}{a} . a\right)$.

Mendenhall and Nielsen obviously had access to extra data to supplement the earlier work and in particular there was now enough information to be able to suggest a form of Mach number dependency for the vortex paths and strengths and also to identify separately the vortex separation phenomena for sharp and blunt noses. Tinling and Allen's work (Ref. 23) had, for example, provided equivalent subsonic data to that measured by Jorgensen and Perkins.

It must be remarked here that although the range of data available was more extensive its greater quantity did not correspond to a closer correlation of the variables. This can be seen from Figures 4 and 5. On the latter figure the empirical fits which Mendenhall and Nielsen suggested should be used to specify body vortex starting point have been superimposed. The equations are:

(for sharp bodies) $\qquad \frac{x_s}{r_N} = 32 \left(1 - \sqrt{\frac{a - 4}{\theta_N - 4}}\right)$

(for blunt bodies) $\qquad \frac{x_s}{r_N} = \frac{10}{a - 4} + 2$

It was at about the time of the publication of Reference 17 that, judging from the literature, there was a resurgence of interest in exploring body vortex characteristics. This arose mainly due to increased project interest in the use of body dominated configurations which might operate at extremely high angles of attack thus experiencing the problems of asymmetric body vortex development with the generation of out-of-plane forces. As an offshoot of studies into these extremely high angles of attack more data has become available at those lower values where symmetric body vortex formation is maintained. Additional experimental techniques also have become available, notably Laser Doppler Velocimetry, which could be exploited to probe these flowfields, the latter technique having the great merit of not disturbing the flow being measured. The majority of such flow survey studies were performed in the U.S.A. (Refs. 32 - 36).

One study performed in the U.K. in this period but which had to make use of the well established yawmeter probe system of acquiring flow field data was that performed at ARA (Ref. 3) and the subject of subsequent analysis by the present author. (References 37, 38). If it is recalled that, at the time of the experiments, the most up-to-date and comprehensive source of information was that of Mendenhall and Nielsen, it could be demonstrated that there was a need to extend the data range. The test results collated by Mendenhall and Nielsen had concentrated on the low speed and supersonic ends of the spectrum with little in between. This was especially serious since transonic speeds represent highly important practical areas of application for missile designs. The range of body shapes was also quite limited in scope. The ARA tests thus attempted to supplement the previous experimental coverage. It was shown that the empirical results of Mendenhall and Nielsen were generally valid for the new body shapes and Mach numbers but that errors could be encountered when assessing the vortex starting point using the empirical correlations for sharp-nosed bodies. Another result to be found from analysis of the ARA data was that the importance of the feeding sheet was highlighted.

The general conclusion regarding the importance of considering the flow field as consisting of a much more complex structure than two line vortices was supported by data taken in the same general period by Oberkampf et al in the U.S.A.

This has been documented in various papers (Refs. 39 - 41) and in a formal report (Ref. 42). Using a single yawmeter mounted on a highly manoeuvrable traverse mechanism the flow field in the leeside of an ogive-cylinder body was explored but at higher Mach numbers (2 and 3) and Reynolds number (Re_D up to 1.7 x 10^6) than had been considered by previous investigators. The results obtained by Oberkampf et al showed that the feeding sheet was of great importance with up to 60% of the total circulation contained within it. Additionally the general form of the vortex induced velocity pattern was shown to lose much of its circular characteristic since the vortex wake was found to be highly elongated and diffused in the crossflow direction.

One unusual feature of the flow field which Oberkampf et al deduced from their results was the presence of "nose vortices" emanating from the very forward part of the nose and having a circulation of opposite sign to the main conventional vortex pair. Oberkampf and Bartel, in their discussion of these results, referred to previous tests by Hsieh, Wang and Werlé (Refs. 43 - 46) in which they also had hypothesised that a nose vortex system should arise not through the conventional action of crossflow separation but dictated more by separation of the axial flow on relatively blunt noses. Since the possibility of generating different forms of forebody vortex is by no means well understood it is fortunate that due to their positioning they are likely to be well clear of any downstream surface with which they could interfere. Ramaswamy and Rajendra (Ref. 47) have also investigated this phenomenon.

The majority of experimental information referred to in this section (certainly all that of American origin) has been collated by Wardlaw in Reference 16. He also attempted to correlate the vortex position and strength data on the basis that the flow would develop from the very tip of the nose. Thus his correlating parameter reduced to the form $x \tan\alpha$. Examination of his results, which are presented in the form of a

vortex position specified by polar angle and radius (See Fig. 6) will show that the same degree of scatter was evident in his results as was shown by Mendenhall and Nielsen. However, as would be expected, the general trends with speed or distance along the body are the same.

The current situation regarding availability of experimental information on symmetric body vortices is that, to the present author's knowledge, nothing of a large scale nature has been published since Oberkampf and Bartel's work. However, certain items of work in progress will yield further data in due course. There is a large programme to investigate body vortex flow fields in the U.K. at the Royal Aircraft Establishment, Bedford, in which yawmeter probe surveys are conducted in the 8 ft x 8 ft wind tunnel at subsonic and supersonic speeds. Data from the first test entry is at the stage of preliminary reduction and analysis. Experiments such as those recently done by Yanta and Wardlaw (U.S. Naval Surface Weapons Centre) to investigate asymmetric vortex behaviour at high angles of incidence, in this case by LDV techniques, may also provide information at those more moderate values where body vortex symmetry is maintained.

2.1.2 Theoretical Methods

In the early methods the "NACA Vortex Model" was developed. This sought to model the flow around the inclined cylinder as if it had two line vortices attached. These would start as some axial station and would follow trajectories with strengths varying along their lengths according to empirically determined rules. Thus the data of Jorgensen and Perkins was employed to provide the necessary information. The problems of specifying flow characteristics at any point then reduced to that of calculating two dimensional potential crossflow with image vortices suitably positioned to ensure that no flow was predicted to go through the body surface. Figure 7 illustrates the flow model.

The basic model could be modified in relatively small ways by, for example, attaching viscous cores to the line vortices in which the induced velocities decayed linearly to zero at the centre or by using feeding sheet representations.

Mello (Ref. 21) provided such an approach. Relatively large changes to the methods, perhaps revising their basic concepts, were not forthcoming until the 1970's. One major problem of the more complex methods has been, and is, the need to specify the boundary layer separation characteristics of the body. This can be very difficult since, unlike the problem of a sharp edged slender wing, the separation line is not fixed by a definite geometric feature.

The method of Bryson (Ref. 48) was an early attempt to calculate the flow around circular cylinders and cones at incidence. The vortices were represented in the flow model by the use of idealised line vortices connected to the body surface by a feeding sheet of negligible strength. The appropriate vortex position was then calculated by finding a solution to the problem when the load on the feeding sheet became zero. Wardlaw (Ref. 49) took the method of Bryson and extended it into the computation of asymmetric vortex flows, although his development was of course still capable, under the appropriate conditions, of yielding symmetric vortex flow results. A drawback to Wardlaw's method was however, that the use of the technique required the empirical input of many different parameters defining the vortex system, e.g. initial strength, position, degree of asymmetry etc. To do this successfully necessitated some prior experience in the application of the method.

Wardlaw uses relatively high strength concentrated vortices in this method. A departure from this was made by Angelucci (Ref. 50) and Marshall and Deffenbaugh (Ref. 51, 52) who developed techniques incorporating large numbers of elementary discrete vortices fed into the flow field. These were tracked downstream under the influence of the general potential flow and the velocities induced on one another. Different algorithms were employed to account for decay of vortex strength or discrete vortex coalescence but in general efforts were made, especially by Marshall and Deffenbaugh, to reduce to an absolute minimum the number of empirical inputs necessary in a method. Angelucci's technique still required the separate specification of vortex separation lines. Recent developments (Refs. 53 - 55) by both the original author and others have sought to improve the Deffenbaugh technique. An example of such a development is included in the recent paper by Shivananda and Oberkampf (Ref. 56) in which the extension of Deffenbaugh's technique into the compressible flow regime is described.

Shivananda and Oberkampf's method is capable of predicting out-of-plane forces and moments although the limited comparisons shown indicate that it is not very successful at the relevant high angles of attack. For lower values, however, it has been employed to predict symmetric vortex characteristics and the test case employed is the data of the present author's paper (Ref. 38). The method gave a reasonable approximation to body vortex strength (i.e. the sum of core and feeding sheet values) and a similarly reasonable approximation to vortex position for the supersonic speed data (M1.15). The effect of Mach number was however, over estimated, since the change in vortex strength as predicted by the method in going from incompressible speed to M1.15 was less than that shown by the experimental data in changing from M0.7 to M1.15.

Another very recent publication (Ref. 47) deals with the calculation of supersonic body vortex characteristics via the solution of Euler equations. Klopfer and Nielsen's work was itself an extension of an earlier study (Ref. 58) on wing body combinations.The latter was (in terms of calculating the vortex flows) in some ways an easier problem due to the prescribed separation line at the leading edge of the surface. For work on bodies this is a more difficult quantity to define and Klopfer and Nielsen have approached the task by empirical inputs of data. The results of their methods have been compared with the supersonic body vortex wake measurements of Oberkampf (Ref. 42) and have been demonstrated to yield better agreement with data than the vortex cloud theory of Mendenhall (Ref. 59) in which the body leeside wake is modelled by a large number of low strength discrete vortices, which group together to form the "cloud" which represents the body vortex, core and feeding sheet.

As an alternative to complex theoretical methods there is still room for the development of much more simple methods and for the validation of existing techniques such as the use of a viscous core around a vortex or the attachment to it of a feeding sheet. Such an examination of various methods using the ARA flow survey data as a basis was done by Kitson (Ref. 60). More recently still, a paper by Weihs (Ref. 61) has reverted to simple theoretical considerations to define the positions of symmetric vortex cores in the leeside of a body.

2.2   BODY VORTEX INTERACTION WITH LIFTING SURFACES

2.2.1   Experimental Studies

Grosche (Ref. 62) measured the flow field characteristics around a slender body with and without delta or rectangular lifting surfaces attached. Using a single yawmeter probe six crossflow planes perpendicular to the body axis were surveyed at equal inter-vals along the length of the body and the crossflow vectors and total pressure loss isobars derived and plotted. Trajectories for the body vortices were found to correlate reasonably well with data from other investigators' previous subsonic tests.

The main item of interest here, however, was the behaviour when the thin (t/c < 10%) monoplane wing panels were attached. From the flow survey results performed aft of the trailing edge of the wings it was deduced that the wings had a significant effect on the body vortex positions by, in the case of the delta wing, moving them down almost from the point of which the vortices crossed the leading edge of the panel. For the rectangular wing there was again a downward movement aft of the trailing edge but not until after the body vortices had first been induced to move slightly upwards relative to their positions for the body in isolation. (Figure 8 illustrates the vertical changes in trajectory found by Grosche). A partial explanation for the changes in body vortex trajectory was attempted by reference to the bound and trailing vortex system of the rectangular wing inducing a upwash ahead of itself and a downwash behind. The leading edge system of the slender delta wing panels was also thought to explain the downwards movement of the body vortex core as it passed by the wing panel (See Fig. 9).

Downwash behind the trailing edges was also thought to explain the other major feature of the flow patterns. This was the marked change of rotational characteristics within the crossflow. For the case without wings a strong and concentrated body vortex existed. However, when the wings were fitted the flow vectors display by no means as much concentrated rotational behaviour, i.e. the vortex effect has become much more diffused. Grosche interpreted this as a sign of the downwash field behind the wings cutting off the feeding of the body vortices so that at a given axial station along the body past the wings, the vortices will not have developed as much as they would have on the body in isolation.

Grosche's experiments were confined to zero roll angle, and in a set of tests at Cranfield Institute of Technology the present author sought to explore a more general flow situation. This work was reported in Reference 2. A cruciform cropped delta wing-body model was tested at supersonic speed (M = 2). (See Fig. 10 for model geometry). The model was equipped with a pressure tapped wing panel whose section shape was a wedge. Measurements were taken over an incidence angle range of 15 to 22.5° with panel roll angles in the leeside quadrant of between 60° and 80°. The Reynolds number for these tests was 0.09 x 10⁶. The surface pressure measurements were complemented by flow visualisation tests using both the surface oil flow, vapour screen and schlieren techniques.

Results from the surface pressure tests were used to produce both spanwise loading distributions and values of the total integrated normal force coefficients for the panel. The former were shown to be highly non linear (see Fig. 11 for example) and the latter could display reversals in sign at a particular combinations of incidence and roll angle. The flow visualisation experiments were used to derive the trajectories of the body vortices. It was found that these were somewhat further outboard than the positions suggested by the empirical method of Mendenhall and Nielsen.

In the concluding remarks of Reference 2 it was stated that it would be useful to attempt further investigations of the body vortex interaction problem by directly measuring the vortex effects on two types of configuration. First there would be the long forebody shape as tested before whose geometry would ensure a well developed body vortex pattern at the wing panels and then there would be a "minimum length forebody" shape designed to minimise the vortex generation. Models with such geometries were constructed (see inset to Fig. 10) with an improved wing panel design to allow concurrent measurement of upper and lower surface pressure distributions on the wing panel. Results from that test programme (Ref. 63) have only been partially analysed and are unpublished but indicated that the use of a minimum length forebody did indeed reduce the vortex interference phenomena, since the spanwise loading distributions were not as much non linear. It had been the interpretation from the earlier test series that the strong non linear behaviour was a sign of body vortex-induced downwash inboard and induced upwash outboard of the spanwise location at which the local loading changed direction.

Recent experimental work on vortex interactions at the Von Karman Institute has studied the aerodynamic characteristics of various missile type wings with and without strakes in subsonic and transonic flow including pressure and force measurements and flow visualisation. Water tunnel tests were also performed for flow visualisation (See Refs. 64 - 70). Experiments (Refs. 66, 69, 70) were conducted with a cropped delta wing body combination not too dissimilar in planform shape from the configuration tested by the present author at Cranfield and elsewhere. (See Fig. 12 for geometry of VKI model). The VKI tests were however, limited to a monoplane missile configuration at zero roll angle. Body in isolation tests were also performed.

From a review of the literature there appears to have been very few tests in the U.S.A. to specifically explore body vortex/wing panel interaction since research efforts have been directed more to the problems of isolated bodies. However, one example available to the author is Reference 71. As a part of an effort (Ref. 72) to develop methods for calculating pressure distributions including vortex effects on supersonic configurations this has included the assessment of body vortex effects. Reference 71 states that these are handled by an empirical technique for bodies with circular cross section. To check out the prediction methods employed for the vortex effects, a series of supersonic flow visualisation experiments were performed using the vapour screen technique on a cruciform wing-body-tail combination at various incidence and roll angles

with different control deflections. Qualitative comparisons made in Reference 71 showed that the agreement was reasonably good.

Variation of body vortex trajectory adjacent to the wing panel was accounted for but not any variation of strength. Experimental data showed that the body vortex which was in close interaction with the wing panel which was rolled into the leeward side was reduced in strength by its passage past the wing panel. The program dealt solely with concentrated vortex core representations and no attempt was made to model feeding sheets or distributed vorticity. The latter possibility has now subsequently been considered in Reference 73.

In their general review papers on vortex effects both Erlich and Werlé (Refs. 74 and 46) have shown results for the body vortex behaviour around missile-type shapes. However, these have mostly been biased towards the very low aspect ratio form of strake lifting surface with a long root chord.

Various investigators have explored the nature of interaction between vortices and downstream surfaces by somehow generating a vortex from a separate upstream position and then letting it flow back and over the surface under consideration.

An early reference to such a study was by Smith and Lazzeroni (Ref. 75) who used an upstream half wing to produce a trailing vortex which interacted with a rectangular half wing mounted on a reflection plate. Patel and Hancock (Ref. 76) also performed similar experiments, following a theoretical investigation by Hancock (Ref. 77), but the subject wing was, in their case, two dimensional with either an aerofoil or flat plate section. Such studies are evidently still favoured since Gillerlain and Yanta have recently reported in Reference 78 an experimental programme of a similar nature but which included investigation of the vortex-fin interaction flow field using a Laser Doppler velocimeter.

British Aerospace (Aircraft Group) have also been active in this type of study. (Ref. 79, 80). Using a small rectangular wing mounted upstream in a wind tunnel to generate a trailing vortex, interaction was investigated by allowing the vortex to pass by a downstream body or wing-body combination. The shapes involved were naturally aircraft-oriented.

2.2.2 Theoretical Methods

Turning now to the calculations or prediction of vortex effects on downstream surfaces it was recognised (Ref. 81) at an early stage that some way had to be found to allow for the modification of loads on a wing or tail panel due to the presence of a vortex. In most of the early reports the prime application in mind appears to have been the interaction of a rolled up wing trailing vortex with a downstream tail panel with the equivalent problem of canard to wing interference also dealt with. The early references did not make much mention of the possibility or importance of body vortex interactions. Thus Morikawa (Ref. 82) considered the interference between a wing and tail near zero angle of incidence with a semi infinite body. Sacks (Ref. 83) did consider body-wing-tail combinations and derived formulae for the vortex induced loads in terms of the change in complex coordinate of the vortices. This was taken further in a later report (Ref. 84) when non zero roll was allowed in the theory but again the emphasis was on wing-tail interference. Viscous core concepts were introduced into the equations and experiments were conducted for wing-tail combinations (no body). Spreiter and Sacks (Ref. 85) and Sacks (Ref. 86) also investigated vortex or wake interference effects by the use of slender body theory which could be exploited to write equations for the vortex induced loading distributions on slender wings or tails to superimpose on the existing effects of incidence or sideslip. Such studies were also used in the compilation of the overall prediction technique of Pitts, Nielsen and Kaattari (Ref. 87) and also the more specific reference by Spahr (Ref. 12).

Pitts, Nielsen and Kaattari's method was intended to apply over a wide range of geometrical shapes in terms of wing planform and freestream speeds but at only small angles of incidence or control deflection and zero roll angle. Thus body vortex generation is not considered but charts are provided to calculate the lift interference effects of a line vortex on a pair of wing or tail panels. This was meant for use in connection with fully-rolled-up trailing vortices from upstream wing panels but can, of course, be used for any vortex provided it is assumed that it is adequately modelled by a two dimensional line.

The charts mentioned above present values of a lift interference factor, "i", which is a function of the wing planform, relative size of wing span and body radius, and vortex position vertically and laterally relative to the surface. Pitts, Nielsen and Kaattari assessed two different theories for the calculation of the interference factor. The theory of Alden and Schindel (Ref. 88) was examined but in general found to be too complex to apply on a routine basis. It was however, observed that the use of a much simpler strip theory (i.e. assuming adjacent strips were mutually independent and assigning a local angle of incidence to each with the appropriate lift curve slope) would not introduce too great an error and would, under certain conditions, give the same result as Alden and Schindel's linear theory. The interference factors are negative,

thus indicating a general reduction of lift on a wing due to the presence of a vortex, and become very large when the vortex approaches the surface and, indeed, infinite if it intersects the tip on a planform which has a non-zero tip chord. This arises due to the infinite predictions for induced angle of attack at the tip position.

Spahr's report (Ref. 12) also considers two alternative methods of computing the vortex induced load. The first approach is via the equations of slender body theory which are used to compute the path of a concentrated line vortex past a cruciform or monoplane wing body combination at combined angles of pitch and yaw (or incidence and roll). Having done this the induced pressure coefficients can be calculated and, via integration, the loading distributions or total induced load on a component of the missile could be calculated. If the result for the total induced load on the complete missile was the only one required this could be calculated directly by the vortex impulse theorem once the vortex trajectories had been calculated. As an alternative to this procedure the linearised theory of wing panels in conjunction with a reverse flow theorem was assessed. This required the assumption that the vortices would not be deviated in their trajectories past the wing panel and that they would only induce a spanwise variation of local angle of attack. On the basis of these assumptions and using simple spanwise loading distributions for the wing in reverse flow charts of the interference factor 'i' were derived in the same manner as Reference 87 (See Fig. 13). However, Spahr removes the need for a symmetrical vortex disposition relative to the wing panel and presents results for a single vortex acting on a single panel. Thus asymmetric vortex positions relative to the wing due to roll angle, for example, can be taken into account.

It can be seen that the basic assumption concerning the structure of the vortex which interfered with the panels was, in both References 87 and 12, that it could be adequately modelled as a line and that it would induce velocities according to two dimensional potential flow i.e. $v = \dfrac{\Gamma}{2\pi r}$. Mendenhall and Nielsen (Ref. 17) followed such a procedure but then applied more sophisticated lifting surface techniques to compute the actual load on the wing panel itself. Up to the panel leading edge the body vortex was constrained to follow empirically derived paths and thereafter was tracked by conformal mapping methods, in the same manner as Spahr's slender body theory method. No change of strength was assumed as the vortices passed by the panels. With the vortex path obtained the local flow velocities at control points in the wing surface were calculated as inputs into a lifting surface technique which effectively calculated wing-in-isolation characteristics in a non-uniform flow.

The general approach of the previous methods by which a single core vortex model has been used to generate local flow velocities and angles of attack as input to a panel loading method has been departed from by Oberkampf (Refs. 89 - 91). In these three references he describes the use of a relatively simple flow model which incorporates the representation of a feeding sheet as a line of low strength vortices joining a separation point on the body to the vortex core. In his original paper with Nicolaides, Oberkampf suggests a form of vortex model shown in Figure 14. The low strength vortices representing the sheet were spaced equally along a circular arc joing an empirically derived separation location and the core location specified by experimental data from Mello and Fiechter. An experimental form of decay function was used inside the region of the vortex core area (whose size again was specified from experimental data). This was used to compute flow velocities at the panel location. In Reference 89 Oberkampf assumes that the variation of local normal force coefficients of a rectangular element of wing panel will be the same as the variation of normal force coefficients of a square panel which was tested in uniform flow in a normal wind tunnel experiment.

An empirical spanwise and chordwise loading function is then introduced to predict the local values across the panel surface. To test his theory Oberkampf compared data from his flow model with Mello's results and also summed his individual panel loads to yield rolling moments which he compared with experimental data. For the body with a square cruciform tail which he considered, he found reasonable agreement, both for the flow distribution and for the variation of rolling moment with incidence and roll angle. A further discussion of the prediction of rolling moment, this time in supersonic flow, was the subject of Reference 90. The same general procedure was adopted to calculate the crossflow vectors, which it should be noted are strictly applicable only to incompressible flow, but a different local loading procedure was used for supersonic wing characteristics. As for the subsonic speed case reasonable agreement was demonstrated for the limited range of experimental data which Oberkampf considered.

In the final reference of this series, Oberkampf returned to a consideration of subsonic flow but this time considered wing panels of much more general planform than the square ones of Reference 89. The empirical loading distribution function of the earlier reference was maintained but the normal force variation with incidence of a small element, although still assumed to be of the same form as that of the complete wing, was now extended to be a non linear function of incidence as predicted by an empirical load estimation method. Comparisons were presented for predicted and measured panel load coefficients for a cropped-delta tail body combination and also the result for configuration rolling moment. Quite good agreement was found over most of the angle of attack and roll range (See Fig. 15). Also presented was a predicted spanwise loading distribution for the four tail panels of the cruciform set when at combined incidence and roll angle.

Noteworthy is the reversed loading distribution apparent on the panel rolled near the body vortex. Such a pattern is in reasonable qualitative agreement with the data for supersonic speeds in Reference 2.

A useful feature of Oberkampf's paper was a discussion, based on his flow model, of the sensitivity of configuration rolling mount and side force characteristics to relative positioning of the panels and body vortices. Dependent on whether the latter were inside or outside the radius of the tip of the wing panels the rolling moment characteristics could exhibit highly different functional relationships with incidence or roll angle. Putting this another way, if, for a generalised configuration, an accurate prediction of rolling moment was required then the body vortex position and its induced loading effects would need to be highly accurately estimated.

A final reference in this review of past theoretical investigations of, or prediction method development for, body vortex interaction effects is the paper by Smith, Nielsen and Hemsch (Ref. 92). This paper briefly reports extensions of the NEAR prediction method described in References 93 and 94 (a more comprehensive reference is No. 95). It is of particular interest since it puts forward the idea that "afterbody vortex" generation is possible. This means that aft of a forward lifting surface which may locally interrupt the body vortex feeding a new body vortex system may begin to grow. In modelling such effects for inclusion in their prediction method the authors state that this is most effectively undertaken with a collection of vortices or a vortex cloud and that when a tail panel is in such a position that it would be affected by an afterbody vortex this would not be well modelled by a single vortex.

3. SOME RECENT EXPERIMENTAL STUDIES AT LOW SPEEDS

The review of earlier work described in the previous section illustrated that there was little information available on the specific problem of body vortex interaction with lifting surfaces for missile applications. This section will describe series of tests which have sought to improve this situation by yielding data on flow situations specifically chosen to highlight and explore the vortex interaction phenomena.

It will be observed that a common thread runs through the studies which have been performed by the present author. This is the choice of a standard model geometry for the experimental work. The configuration chosen was a cropped-delta cruciform wing-body combination. The aspect ratio of the wing panels was 1.02 and taper ratio 0.59. These could be positioned on the body of longitudinal stations of 7.67 or 4.10 body diameters aft of the apex of the sharp tangent-ogive nose which had a fineness ratio of 3.

Especially with the wings in their aft position it was expected that the long forebody ahead of the wing panel leading edges would ensure the production of a strong well developed body vortex system which would interact with the downstream surfaces. With the wings set in their forward position a long afterbody was available on which to study the body vortex generation phenomena as affected by the presence of upstream surfaces.

3.1 WATER TUNNEL TESTS

The combinations of incidence angle and roll angle chosen for the water tunnel experiments was such that a strong body vortex flow was apparent from the forebody of the model. Various wing panel roll angles were then set up to bring the panels into close proximity to the oncoming vortex. For successful visualisation by the dye line method the flow speed in the working section was 90 mm/s for the present tests, giving a Reynolds number based on body diameter of approximately 2000, which is obviously much lower than any value likely to be encountered in a wind tunnel test or in full scale flight. Consequences of such a difference will be discussed in a later section.

Output from this test programme was a series of simultaneous side and top views of the flow patterns.

3.2 LOW SPEED WIND TUNNEL TESTS

It was considered essential that quantitative data should be acquired on the problem of body vortex interaction with lifting surfaces to complement the completely qualitative data available from the water tunnel experiments at Warton. The model used for the low-speed wind tunnel testing in this programme was of a geometrically similar shape to the water tunnel model previously described. The scale was however much larger with a body diameter of 0.11 m. Facilities were available to obtain pressure distribution data on one wing panel of the model (both upper and lower surfaces concurrently) and around three circumferential rows at different points along the body's length. A general assembly of the model is shown as Figure 16 which illustrates the different builds. Force and moment information was also recorded in the test programme, as well as qualitative flow visualisation tests by the smoke, surface oil and tuft methods. Combinations of incidence and roll angle compatible with earlier water tunnel tests were chosen. Reynolds number was of course, much higher (approximately 4 x 10^5).

4. DISCUSSION OF RESULTS FROM WATER TUNNEL TESTS*

4.1 FLOW PAST THE BODY IN ISOLATION

The classic dye line flow pattern was clearly evident. The combination of the rotational velocity field set up in the leeside of the body by the vortex pair and the general axial flow results in a helical dye line trace where the dye particles move around the vortex centre and downsteam simultaneously. These patterns were steady, maintaining their vertical and lateral locations relative to the body centre line provided the oncoming flow was steady. Thus although the results shown in photographs are necessarily the instantaneous positions as recorded by a still camera, there was no evidence that these patterns would shift their position either vertically or laterally.

Evident from the side and top views is the large area affected by the vortical flow as shown by the large spread of the helix. As an indication of the practical importance of such a large affected area it should be remembered that many tail surfaces of conventional missiles have nett semi-span dimensions of the same order as the diameter of the body.

The predicted vortex trajectories resulting from the method of Reference 17 have been superimposed on composite tracings of the dye lines, both for side views and top views. The prediction is reasonably accurate. Vertical vortex positions appear to be more accurately predicted than lateral ones. Looking at this conclusion in a converse sense, and remembering that Mendenhall and Nielsen's method arises from a compilation of data taken in wind tunnels over a wide range of speed and Reynolds number, it can be stated that, from these sets of tests at least, the water tunnel results taken at low Reynolds number have provided a reasonably reliable guide to aerodynamic behaviour at much more realistic conditions.

One obvious feature which needs to be highlighted at this stage is how the dye line traces and hence the body vortices maintained their smooth appearance and well ordered structure without drastic changes of trajectory as far aft as is visible in the field of view, or in other words past the base of the model. This behaviour, will, in due course, be contrasted with changes of structure and position as the body vortex flows past a downstream wing surface.

4.1.1 Comparison of Results with those from other Investigations

Three VKI reports which post date the present author's original paper and report (Refs. 98, 99) have described experiments on body-alone or wing-body combinations and have contained data on body vortex paths and interaction effects. These three reports (Refs. 66, 69, 70) have used References 98 and 99 as a source and have extracted data for comparison purposes. Demurie, Muylaert and Wendt (Ref. 69) have measured the body vortex core positions on their body-alone model in a series of water tunnel experiments. Following the earlier examples of Mello , Fiechter and Grosche, (Refs. 21, 26, 28 respectively), these data have been expressed in body centred polar coordinates, i.e. with a circumferential angle and radial dimension, and were shown to agree quite closely (i.e. within the experimental error bands) with the earlier subsonic wind tunnel information from Grosche. However, not surprisingly, agreement was not so good with the higher speed data of Mello.

Comparisons of vortex position data were also made in Reference 69 with the original data correlations of Mendenhall and Nielsen. This showed good agreement generally although the standard for lateral position was relatively worse than for the vertical vortex location. This conclusion followed that expressed by Deane in References 98 and 99 although the differences between vertical and lateral standards of agreement were more exaggerated in the latter two references. Note that in assessing the quality of correlation with Mendenhall and Nielsen's data Demurie, Muylaert and Wendt had to assume a value of first separation location (or first longitudinal location for body vortex production). This was taken equal to zero ($x_s = 0$).

4.2 FLOW PAST THE WING-BODY COMBINATIONS

Photographs are available which illustrate the various flow patterns observed in the water tunnel around the wing body combinations BW_A and BW_P at different combinations of incidence and roll angle. Both these configurations were assembled with the sharp-nose body. The same nominal flow velocity was used for these experiments as for the body in isolation thus yielding a value of Re_D approximately equal to 2000.

The most notable feature of these flow patterns is that the body vortex system undergoes a change of trajectory adjacent to the wings away from what it would have followed if no wings had been fitted and, most important of all, undergoes a dramatic change or breakdown of structure at some axial station near to the trailing edge of the wing panel. (A tracing is included in this text as Figure 17).

---

* Illustrated in the lecture by a series of colour slides

It was quite obvious from the visual observation of the water tunnel flow patterns (and, indeed, this has been recorded on the ciné film taken during these tests) that the flow patterns were steady up to the wings, even when being deviated, but this was in sharp contrast to the unsteady eddying flow area after the point of breakdown. This would occur at axial stations between a position about half the chord behind the leading edge's apex and the trailing edge. This transition from steadiness to unsteadiness was also evident for those cases when the panels were rolled.

If the results for the isolated body at the same angles of incidence are considered it will be recalled how the vortex patterns stretched along the body as far as could be seen in the field of view in the water tunnel, with no sudden deviations of trajectory and certainly no breakdown in the smooth vortex structure. To confirm that the deviations of vortex trajectory are indeed due to the presence of the wing panel consider now how the results for both the BW_A AND BW_F configurations are generally the same, in that the body vortex does not pass by the wing panel without being broken down in structure.

For the zero roll angle cases illustrated it is clear that, prior to the breakdown of the vortex structure, then the vortex cores are deviated both down towards the upper surface of the adjacent horizontal panel and also laterally away from the body centre-line. The point at which breakdown occurred was seen to move forward as incidence angle increased.

Comparison of the dye line traces for the wing-body and the body-in-isolation cases for those parts of the flowfield upstream of the wing leading edge showed that the presence of the wing has very little effect on the body vortex position.

For those configurations with wings set forward on the body there is, of course, a long afterbody on which vortex generation could be investigated. Attemps to visualise any afterbody vortices were made in exactly the same way as for the forebody vortices. Whereas the vortices from forward on the body were immediately visible, no equivalent clear vortex structure could be observed on the afterbody.

The importance of the various experimental observations is underlined when current missile aerodynamic prediction methods are considered. Within the U.K. missile Industry at least, routinely applied techniques model the body vortices as idealised lines which follow empirically defined paths based, for example, on the correlations of Reference 17 up to the leading edge station of the wing panel. Using the vortex vertical and lateral locations appropriate to this station interference factors are then derived using such methods as the linear theory charts of Spahr (Ref. 12) to predict either a direct change to the panel load of the surface in the presence of a vortex or, equivalently, a change to the effective angle of incidence of the panel. These methods do not either explicitly or implicitly take account of any variation of vortex position adjacent to the wing panels.

Examples of flow patterns for $\emptyset = 70°$ and $\emptyset = 45°$ will be presented here for the BW_A configuration at an angle of incidence of 25°. It is obvious from these illustrations that the $\alpha = 25°$, $\emptyset = 70°$ case represents one of close interaction between the body vortex and the wing panel and also that, for these combinations of incidence and roll angle, and for this particular model geometry, the body vortex will not pass by the panels undisturbed but as at zero roll, is either broken down or is radically deviated in its trajectory.

4.2.1 Comparison of Results with those from other Investigations

Reference 103 reports the use of a modified version of the present author's model in an attempt to investigate the possibility that different flow patterns might be observed around a wing-body combination if the wing panel was of a different shape to the cropped delta originally used. It had been speculated that the panel planform shape might be a critical factor since it would dictate the flow field in its immediate vicinity and thus could quite radically affect the vortex interaction phenomena. The particular question was addressed of whether the use of a very slender wing, which would provoke a strong leading edge vortex system, as opposed to the original lower sweep angle cropped-delta wing which was apparently giving a completely separated random eddying flow on its top surface, would have any significant effect on the phenomena previously observed. Would the interaction of the body vortex with a better defined, more ordered flow structure, result say in deviations of trajectory but not the breakdown of the body vortex structure?

A new cruciform wing set was constructed which had the same aspect ratio and span to body diameter ratio as the previously used cropped delta set but due to its delta planform had a much longer root chord. The results may be summarised by remarking that the same kinds of vortex deviations and breakup phenomena were observed as had been evident for the cropped delta case.

The tests by Swaby, although yielding results different in detailed character, indicated that the present author's water tunnel results regarding the phenomenon of vortex breakdown, which was hitherto unexpected and certainly not accounted for in prediction methods, were not isolated and unrepresentative since fair qualitative agreement was achieved.

4.   DISCUSSION OF RESULTS FROM WATER TUNNEL TESTS*

4.1   FLOW PAST THE BODY IN ISOLATION

The classic dye line flow pattern was clearly evident. The combination of the rotational velocity field set up in the leeside of the body by the vortex pair and the general axial flow results in a helical dye line trace where the dye particles move around the vortex centre and downsteam simultaneously. These patterns were steady, maintaining their vertical and lateral locations relative to the body centre line provided the oncoming flow was steady. Thus although the results shown in photographs are necessarily the instantaneous positions as recorded by a still camera, there was no evidence that these patterns would shift their position either vertically or laterally.

Evident from the side and top views is the large area affected by the vortical flow as shown by the large spread of the helix. As an indication of the practical importance of such a large affected area it should be remembered that many tail surfaces of conventional missiles have nett semi-span dimensions of the same order as the diameter of the body.

The predicted vortex trajectories resulting from the method of Reference 17 have been superimposed on composite tracings of the dye lines, both for side views and top views. The prediction is reasonably accurate. Vertical vortex positions appear to be more accurately predicted than lateral ones. Looking at his conclusion in a converse sense, and remembering that Mendenhall and Nielsen's method arises from a compilation of data taken in wind tunnels over a wide range of speed and Reynolds number, it can be stated that, from these sets of tests at least, the water tunnel results taken at low Reynolds number have provided a reasonably reliable guide to aerodynamic behaviour at much more realistic conditions.

One obvious feature which needs to be highlighted at this stage is how the dye line traces and hence the body vortices maintained their smooth appearance and well ordered structure without drastic changes of trajectory as far aft as is visible in the field of view, or in other words past the base of the model. This behaviour, will, in due course, be contrasted with changes of structure and position as the body vortex flows past a downstream wing surface.

4.1.1   Comparison of Results with those from other Investigations

Three VKI reports which post date the present author's original paper and report (Refs. 98, 99) have described experiments on body-alone or wing-body combinations and have contained data on body vortex paths and interaction effects. These three reports (Refs. 66, 69, 70) have used References 98 and 99 as a source and have extracted data for comparison purposes. Demurie, Muylaert and Wendt (Ref. 69) have measured the body vortex core positions on their body-alone model in a series of water tunnel experiments. Following the earlier examples of Mello , Fiechter and Grosche, (Refs. 21, 26, 28 respectively), these data have been expressed in body centred polar coordinates, i.e. with a circumferential angle and radial dimension, and were shown to agree quite closely (i.e. within the experimental error bands) with the earlier subsonic wind tunnel information from Grosche. However, not surprisingly, agreement was not so good with the higher speed data of Mello.

Comparisons of vortex position data were also made in Reference 69 with the original data correlations of Mendenhall and Nielsen. This showed good agreement generally although the standard for lateral position was relatively worse than for the vertical vortex location. This conclusion followed that expressed by Deane in References 98 and 99 although the differences between vertical and lateral standards of agreement were more exaggerated in the latter two references. Note that in assessing the quality of correlation with Mendenhall and Nielsen's data Demurie, Muylaert and Wendt had to assume a value of first separation location (or first longitudinal location for body vortex production). This was taken equal to zero ($x_s = 0$).

4.2   FLOW PAST THE WING-BODY COMBINATIONS

Photographs are available which illustrate the various flow patterns observed in the water tunnel around the wing body combinations BW_A and BW_F at different combinations of incidence and roll angle. Both these configurations were assembled with the sharp-nose body. The same nominal flow velocity was used for these experiments as for the body in isolation thus yielding a value of Re_D approximately equal to 2000.

The most notable feature of these flow patterns is that the body vortex system undergoes a change of trajectory adjacent to the wings away from what it would have followed if no wings had been fitted and, most important of all, undergoes a dramatic change or breakdown of structure at some axial station near to the trailing edge of the wing panel. (A tracing is included in this text as Figure 17).

* Illustrated in the lecture by a series of colour slides

Illustrations of the flow patterns included in References 66, 69, 70 have also shown how similar the results obtained by VKI were compared to the present author's. A very smooth and well ordered flow pattern was seen for the case of the body-in-isolation but when lifting surfaces were attached the body vortex was deviated down towards the upper surface of the panel and then broken up in structure. This was most noticeable, as might have been expected, for the higher incidence results shown by Demurie, Muylaert and Wendt in Reference 69 for cases with and without a strake fitted. (Results without a strake were the subject of a footnote in Ref. 69). The wing panel shape also approximated that of the one used by the present author with a leading edge sweepback angle of 27°, a nett aspect ratio of 1.99 and a nett span to body diameter of 1.0.

The lower incidence angle cases shown by Demurie (Ref. 70), which contained a series of photographs for a constant angle of incidence but with various wing sweepback angles, showed that as the sweepback angle increased, or alternatively the size of the wing decreased (the semi span dimension was fixed) the phenomenon of body vortex breakdown was prevented. Thus, for the results with a wing leading edge sweep angle of 30°, breakdown was definitely visible, whereas for the higher sweep angles of 40°, 50° and 60° it was not apparent.

The other investigators have, however, contributed information which indicates that the phenomenon is likely to be dependent on total incidence angle and planform shape except at the higher angles where apparently the breakdown will definitely occur. The VKI results showed, for example, breakdown aft of the trailing edge of a wing-strake-body combination without any significant prior deviation of trajectory which was a different result to that shown by the recent results of the present author, but nevertheless the same ultimate breakdown effect occurred.

4.3   GENERAL COMMENTS ARISING FROM THE WATER TUNNEL TESTS

Prior to the water tunnel tests it had been anticipated that their major value would lie in yielding a qualitative appreciation of the changes in flow direction and hence body vortex trajectory adjacent to wing panels. The possibility of such dramatic changes of flow structure as have been subsequently found was certainly not expected. Similarly, the tests have shown that significant interaction effects can occur at combinations of incidence and roll angle other than those for which the simple geometry of the situation would indicate a "close approach" between body vortex and wing panel.

Thus vortex deviation and breakdown effects have been noted for zero roll angle cases when the body vortex originally starts some distance from the wing panel but is drawn towards the upper surface.

The next section will discuss the results from wind tunnel experiments, designed to provide a more immediately representative set of data but it should be remarked that for the configurations dealt with here, the great difference in Reynolds numbers of the test programmes was not felt to be too much of a problem. The important feature as far as the wing flow field is concerned is the sharp leading edge. At the high angles of incidence considered this will definitely fix the separation of the wing flow along the leading edge and thus it is felt that this aspect of the problem at least should be well modelled. As far as the body flow itself is concerned there is no equivalent salient feature to fix separation and thus it is quite likely that the vortex disposition might be different in the low Reynolds number range compared to high Reynolds number wind tunnel tests or full-scale applications. Even so the comparison of results derived from the water tunnel with those from other test sources (as correlated by Mendenhall and Nielsen) has indicated that the low Reynolds number results are not grossly in error since the previous (wind tunnel) and more recently acquired (water tunnel) data was not too much different in lateral or vertical vortex coordinate.

Before concluding this sub-section it is worthwhile to discuss further some aspects of the vortex breakdown phenomenon, which is shown adjacent to wing panels.

Various wind tunnel and water tunnel studies have been performed in the U.S.A. which have investigated the onset of vortex breakdown above isolated slender wings (mostly deltas). These have shown that as incidence angle is increased so the vortex breakdown will move forward across the trailing edge of the wing surface. Results, for example, by Erickson (Ref. 104) include wind tunnel and water tunnel data which are compared for the phenomenon of vortex breakdown at the trailing edge position. They are shown to correlate and thus are another example which can be referred to in the justification of the usefulness of water tunnel techniques to represent flows at higher Reynolds numbers.

Erickson has presented a comparison of vortex breakdown onset for delta wings as a function of angle of attack. These data have been acquired for wings in isolation and to apply them to the cases of interest here, i.e. wing-body combinations, some thought must be given to how the results can be read across to such shapes. The basic effect which must be taken into account is the increase of effective angle of attack of a panel attached to a body due to the upwash around the body. This effective change may be predicted (strictly for small angles of incidence) by the use of slender-body theory

whereby a wing-body interference factor (K_{WB}) is calculated.

Although it is rather "stretching" the application of this theory it can now be proposed that if vortex breakdown can be predicted to appear adjacent to the trailing edge of a wing panel in isolation at angle of attack a_0, then this should appear at the lower angle of attack a_0/K_{WB} for a wing-body combination. This rather gross assumption can be tested by an examination of the results of Swaby. The wing used in the experiments reported in Reference 103 had an aspect ratio of 1.02 and a gross span to body diameter ratio of 3.56, with a leading edge sweep angle of 76°.

Erickson's plot indicates an angle of incidence of approximately 33° for vortex breakdown at the trailing edge for a delta wing in isolation. K_{WB} for this model is approximately 1.23. Thus if this theory is correct evidence of vortex breakdown should be visible adjacent to, or forward of, the trailing edge for model incidence angles in excess of 27°.

The flow visualisation results of Swaby showed clear evidence of flow breakdown adjacent to the trailing edge at higher angles of attack but not at angles lower than 27°; thus it seems that the concept of applying the wing alone vortex breakdown characteristics to wing-body combinations is not totally unreasonable.

Consideration must now be given to the application of such an idea to configurations with non-zero roll angle. As before a very simple approach will be adopted in predicting the effect of roll angle by crudely modelling the effect on local angle of attack due to the flow components being resolved through the roll angle $\emptyset$. On a "first order" basis it can be shown that at a geometric incidence angle a and a roll angle $\emptyset$ the local angle of attack of a panel in the flow field would be $a\cos\emptyset$, neglecting wing-body upwash effects. If the latter were to be included the angle would be increased to $K_{WB}a\cos\emptyset$. Taking a crossover between the flow regimes with and without vortex breakdown for the delta wing of Swaby from the data for Erickson, one obtains a critical value of $K_{WB}a\cos\emptyset = 33°$. On this basis a crude diagram illustrating the flow regimes, (Figure 18) may be constructed with $K_{WB} = 1.23$.

Thus as roll angle of the subject wing increases so the angle of attack of the wing-body combination must increase for the leading edge vortex of the wing itself to break down at or before the trailing edge. This is what has been observed in practice in the water tunnel flow visualisation experiments. Deviations of the body vortex pattern in proximity to the wing leading edge vortex were observed either for low a (in which case the deviations could be quite small) at zero roll angle, or at higher angles of incidence when the panel was rolled into the leeside quadrant.

The problem remains of how to apply such results quantitatively rather than qualitatively to the cropped delta wing-body combination used in these experiments. What are basically required are data on the vortex breakdown positions for the same shape of wing in isolation.

5.   DISCUSSION OF RESULTS FROM THE LOW SPEED WIND TUNNEL TESTS

5.1   PRESSURE DISTRIBUTIONS ON THE BODY OF THE WING-BODY COMBINATIONS

Pressure data was recorded at three different longitudinal stations for both configurations BW_A and BW_F, Figure 16 illustrates the positions which are termed as "Front, Mid and Rear". Consider first the BW_A configuration at $\emptyset = 0°$ or 70° and $a = 30°$ (Figs. 19 and 20).

Examination of the data for the front and mid tapping rings will show that the latter are greater than the values expected from simple crossflow considerations. The magnitude of variation of the whole pressure distribution pattern around the body is also increased. It therefore, appears that the lifting action of the wing panels is to induce, forward of themselves, an upwash which increases the local angle of incidence.

The general circumferential form of the pressure distributions is indicative of a turbulent separation with it roughly constant pressure coefficient value after a circumferential angle (ψ) of 135°. Data from forward and mid tapping rings shows such a characteristic with it being emphasised for the cases with high local angles of incidence i.e. either $a = 30°$ for the complete model or for the mid tapping ring. Such behaviour, typical of normal body vortex generation, is however, completely lost for the rear tapping ring. For this station, one calibre aft of the wing trailing edge, the pressure tappings rotate with configuration roll angle such that for the $\emptyset = 0$ and $\emptyset = 70$ cases data is available at different ψ values. However, enough is available in appropriate places to be able to deduce that crossflow separation is not occurring. There is no noticeable pressure fall and recovery as for the other two tapping rings and the magnitudes of the pressure coefficients are much smaller. Thus it can be said that little modification to the flow magnitude is going on from the oncoming freestream direction.

The effect of the wing panel's wake on the local angle of incidence distribution aft of the wing is emphasised for the long afterbody inherent in configuration BW_F. Figures 21 - 22 include data for this model. Notice, how for the front tapping ring, which in this case is 1 calibre aft of the wing trailing edge, the crossflow separation characteristics are suppressed but that, if the general angle of incidence is high (30°),

or the distance along the body increases towards a point near the base, then "normal crossflow behaviour" re-establishes itself with a relatively high positive C_p on the windward generator followed by a fall to a low minimum and recovery to a near constant value for $v > 135°$. It should be however, noted that, on the afterbody, a pressure coefficient distribution indicative of crossflow separation is never as pronounced as on the forebody of the model.

The evidence of the pressure distributions is that crossflow separation, absent at the front tapping station, re-establishes itself by the mid and certainly by the rear tapping rings (although it is felt that the results for the rear station are somewhat affected by model base and support interference).

5.2   PRESSURE DISTRIBUTIONS ON THE WING PANELS

Figures 23 - 25 contain a selection of wing panel pressure coefficient data for both spanwise and chordwise distributions on configurations at incidence angles of 15° and 30° and roll angles of 0° and 70°. Both windward and leeward surfaces values are plotted.

The general characteristics may be summarised as follows:

(i)   For either configuration (BW_A or BW_F) at low a (i.e. 15°) and $\emptyset = 0°$ a suction peak is evident near the leading edge at the root, on the leeward surface.

(ii)   As incidence increases to 30° the general suction level rises but the suction peaks are lost resulting in a much more even distribution of pressure both across and along the panel.

(iii)   Pressure distributions on the windward surface are much more uniform than those on the leeward surface.

(iv)   The major contributor to normal force for panels at $\emptyset = 0°$ is the suction on the leeward surface.

(v)   At non-zero roll angles ($\emptyset = 70°$) both the suction and pressure levels on both wing surfaces are much reduced and in some cases can, over much of the wing planform, approach very close to one another thus resulting in a zero normal force loading on that part of the wing surface.

(vi)   Spanwise distributions of load are much more uniform than chordwise distributions. The predominant chordwise loading occurs near the leading edge of the wing.

5.2.1   Maximum Suctions Observed on the Wing Panel Upper Surfaces

It is worthwhile to pay attention to the flow conditions for maximum upper surface suction since this will yield some indication regarding the state of the wing upper surface flow field. If it retains a well ordered structure, perhaps with a leading edge vortex present, then it is likely that high suctions will be seen at points on the surface. If however, the upper surface flow breaks down into a random eddying turbulent flow then these suction peaks will disappear and the pressure distributions will become more uniform.

The minimum pressures were usually measured near the leading edge junction with the body but as $\emptyset$ increased this minimum could move outboard across the panel leading edge. After the decrease in maximum suction level the point at which this occurred could move rearwards slightly.

It was observed experimentally that the configuration angle of incidence a at which the sudden decrease in maximum suction was seen to occur, was higher for high $\emptyset$ than for low $\emptyset$. This coupled to the previously obtained water tunnel flow visualisation evidence has given rise to the concept that the breakdown of flow over the upper surface of the wing panel which leads to the loss in maximum suction, is dictated by the local geometric angle of attack which may be approximated to $a\cos\emptyset$. To test the validity of such an assumption, correlations have been made of minimum pressure coefficient on the wing panel's leeward surface with $a\cos\emptyset$. It can be seen on Figure 26 that a rough correlation exists with a peak in C_p (min) occurring around $a\cos\emptyset = 20°$ for both BW_F and BW_A. Even for the two different wing-body combinations, with their probably quite different vortex strengths at the wing leading edge station and hence vortex induced velocity or angle of attack values, the general result is very much similar. This would seem to point to the conclusion that for the purposes of assessing when wing flowfield breakdown occurs it is not necessary to include any vortex induced velocities, or, equivalently, it indicates that the body upwash and wing basic induced flowfield itself are the important parameters.

This conclusion is at variance with that implicit in the work of Hemsch et al reported in Reference 93. There, some attention is paid to the problem of representing body vortex interaction with lifting surfaces in order to predict panel loads on configurations at arbitrary combinations of incidence and roll angles. Embedded in their method was a procedure which required the specification of the vortex induced velocity on a fin panel attached to a body. Even with their "best choice" of $\dfrac{V_{max}}{V_a}$ from one wing

panel shape Hemsch et al admitted that their flow model would not necessarily give good predictions for a range of other shapes. They referred to the causes for poor estimates as including the possibility of vortex bursting adjacent to a panel and lateral changes of vortex position adjacent to the wing panel.

Returning now to the direct comparison of flow breakdown onset angles for these shapes it can be seen from Figure 26 that an approximate boundary lies at $\alpha\cos\emptyset = 20°$. The results may now be compared with those arising from the consideration of the water tunnel flow visualisation. In Section 4.2 it had been suggested that a boundary between body vortex breakdown adjacent to a panel or no breakdown would exist for a delta wing-body combination of the same aspect ratio and span to diameter ratio as the cropped-delta wing tested here, at combinations of incidence and roll angle defined by $\alpha\cos\emptyset = 27°$. Erickson has shown that the action of adding area to the front part of a wing is to decrease the angle of attack at which breakdown would occur. For a basic 70° leading edge sweep angle wing the reduction of breakdown angle going from the pure delta to a convex shape was shown to be approximately 4°, which will probably represent an under-estimate of the change for the cropped-delta wing considered here which has a 45° straight leading edge. This reduction in wing-vortex-burst angle of incidence due to change of shape is however offset by an increase in necessary angle of incidence to yield vortex breakdown at the leading edge which apparently is the phenomenon which dominates the subsequent flow past the wing.

A more detailed investigation of the vortex breakdown characteristics of the particular design of cropped-delta wing would be needed before it was possible to make a definite conclusion. However, it appears that the boundaries between vortex breakdown or no vortex breakdown for the wing-body combinations seem to be in qualitative agreement. A reasonable mechanism has been illustrated to explain the breakdown of the well ordered body vortex structure, adjacent to the wing panels. A cautionary note must however be recorded regarding the general opinion over the use of water tunnel results for vortex breakdown : see References 108 and 109.

5.3   DERIVED SPANWISE LOADING DISTRIBUTIONS

Examples of the results for various roll and incidence angle combinations are shown in Figure 27. The general features of the spanwise loading distributions mirror those of the pressure distributions in terms of a decrease in magnitude as the roll angle increases. This reflects the reduction in local angle of incidence.

The form of the distributions is also such that for cases of zero roll angle the shape is near elliptic as would be expected from a wing panel in subsonic flow and the magnitude of the local loadings are scaled in proportion to the angle of attack i.e. the spanwise shape of the loading distribution is not radically altered. For non-zero roll angle, however, the basic shape of the loading distributions does change with α and $\emptyset$. For high values of α and $\emptyset$ the shape can be highly irregular in the spanwise direction displaying a large increase to a maximum outboard, falling away again at the tip. The experimental results have also showed the possibility of a local reversal of sign of the local loading direction (e.g. $\alpha = 30°/35°$, $\emptyset = 70°$). Results for the BW_A configuration are not radically different from those for BW_F.

It is notable that the data measured in the tests now reported do not show the spanwise changes to be so drastic as those evident in the earlier data. The conventional explanation for the sudden changes in spanwise loading is that a body vortex will induce an increase of local angle of attack on a wing panel outboard of its spanwise location and conversely a decrease of local angle of attack inboard. These local increases and decreases would be reflected in proportionate increases and decreases in local loading. The apparent change of behaviour for the spanwise loading distributions could thus be associated with the breakdown of the well defined body vortex structure for the present tests whereas in the earlier investigations no mention was made of this possibility adjacent to the wing or tail panels of the configurations under study.

5.4   ASSESSMENT OF THE OIL FLOW PATTERNS FOR THE WING-BODY COMBINATIONS

Two effects are important. Firstly, the flow a little way upstream of the point at which the leading edge joins the body is evidently given an extra crossflow increment to its velocity due to forward interaction of the wing flow field. It can be seen that the traces of the flow visualisation indicate a local flow direction approaching more and more the crossflow direction as the leading edge position is approached. Once this region has been passed, i.e. immediately over the leading edge area of the wing panel, the flow evidently turns down towards the adjacent surface of the wing panel as shown by the large predominantly white area in the photograph.

Behaviour of the body flow field beind the wing's trailing edge must inevitably be somewhat distorted by the presence of the base and the transverse support structure, but it is of interest to note that the local angles of attack are much reduced aft of the wing as compared to the situation forward of it. Connected with this is the absence of any obvious evidence that body crossflow separation re-establishes itself on the relatively short afterbody of this configuration.

Oil flow patterns will be shown for configuration BW_F for $\emptyset = 0°$ and $\alpha = 30°$. Ahead of, and adjacent to, the cruciform wings the surface flow pattern characteristics are in good qualitative agreement to the BW_A case, with the same general features of flow deviation shown in two cases. One particularly noteworthy point is the obviously well-established character of the body vortex flow ahead of the wings for this wings-forward case. In this case for a relatively slender nose at high incidence the empirical techniques of Mendenhall and Nielsen (Ref. 17) would, in fact, predict $x_S = 0$. Thus the predictions for this aspect of the flowfield would not be in too much error.

The major item of interest is the flow pattern developed around the wing and on the long afterbody of the model. The local angle of incidence approaches 90° near the leading edge of the wing but is very much lower (of the order 20°) aft of the trailing edge. This angle then increases as distance increases along the length of the body. Similarly it is only on the extreme end of the afterbody that there is any clear evidence of body vortex formation re-establishing itself in the same general form as was shown on the forebody or ahead of the wings for the BW_A configuration.

The reasons for a change of flow pattern are not difficult to appreciate. The physical presence of the wing cuts off the feeding into the body vortex which has started upstream on the body. The structure is then disrupted adjacent to the wings which also must, necessarily, impart an axial direction to the local flow directions immediately aft of the trailing edge as the flow comes off the wing. However, beyond this point it could then be expected that the crossflow would re-assert its influence on the general flow pattern and re-establish crossflow separation. The failure to do this can simply be interpreted in terms of a downwash field aft of the lifting wing panel. This will result in a reduction of local angle of attack aft of the wing trailing edge. If the body-wing combination is at high angle of incidence then as distance along the body increases so the wing wake will pass further up and away from the body. Thus the induced downwash characteristics are reduced further aft on the afterbody. The local angles of incidence will, therefore, increase with distance along the body making the possibility of flow separation more likely.

It is of interest to consider the evidence of the present tests in the light of the suggested method of predicting afterbody vortex development as suggested by Hemsch, Nielsen and Dillenius (Ref. 101). Their method, which was intended for use with quite arbitrary onset flow attitudes and upstream canard deflections, is constructed to deal with the possibility that a computed flow direction aft of the canard position in the absence of body vortex effects could, depending on the combination of angles of incidence, canard deflection and roll, be anywhere in a 360° coverage, and might have any arbitrary magnitude. They recommend that if the local flow vector calculated by the superposition of effects due to the canard trailing vortices and the crossflow, yields a local angle of incidence greater than 4° and that this vector is not rotated more than 90° from the freestream crossflow direction, then afterbody vortex generation will begin at the trailing edge of the canard panel.

For the case considered here the application is quite simple. The wing panel replaces the canard and since it is undeflected, and since the configuration is at zero roll, the induced flow vectors will be in the same direction as the freestream flow vector. Instead of calculating the magnitudes of the induced velocities at the body centreline without the body present as Hemsch et al suggest it is here intended to interpret the oil flow visualisation photographs to yield the necessary information. Given the local flow angles on the periphery of the body of approximately 20° then it should not be too much in error to state that the 4° value at the centre line would be exceeded. However, at this point vortex formation on the afterbody is certainly not obvious. It would thus appear that Hemsch, Nielsen and Dillenius's method can predict afterbody vortex formation forward of the point at which it is observed to occur on this configuration. It is felt that their conclusions regarding afterbody vortex development might possibly be more appropriate to the type of case with which they were primarily concerned, i.e. canard configurations, for which the size of the lifting surface relative to the body is relatively smaller than the large wing type of models considered here.

5.5 ASSESSMENT OF FLOW PATTERNS ILLUSTRATED BY THE OTHER TECHNIQUES

The flow visualisation tests were completed by tuft spinner and smoke probe experiments.

Uncertainty regarding the location of a vortex core arose because of the subjective nature of deciding when the centre was reached and also due to the problems using a hand-held probe and trying to maintain its position. However, even allowing for this, the results of Figure 28 show how, for configuration BW_A at $\alpha = 30°$, $\emptyset = 0°$, the vortex is seen to move down towards the upper surface of the horizontal wing panel as it passes the leading edge. Lateral movement is less well defined but the re-drawing of the vortex positions in the crossflow plane (left-hand sketch of Fig. 28) does make it clearer that, accompanied by the initially upwards movement well forward of the wing panel, there is a inwards movement (Positions 1 - 5). When the vortex begins to move down it also begins to move out (Positions 8 - 9). This behaviour is in qualitative agreement to that shown in the water tunnel tests, but the vortex core locations as deduced from the wind tunnel experiments appear to be closer inboard upstream on the body than those from the water

tunnel, i.e. the vertical and lateral vortex coordinates are both less.

Whereas the body vortex structure was quite clearly evident ahead of the wings on either BW_A or BW_F the tuft spinner showed that, at some point along the length of the wing panel, the characteristic rotation was lost and replaced by an irregular motion with the mean tuft position directed down towards the adjacent horizontal wing panel. On the afterbody there was no evidence of any new body vortex development until the very end of the long afterbody of configuration BW_F, at the highest angles of incidence which were tested.

5.6   GENERAL COMMENTS ARISING FROM THE LOW SPEED WIND TUNNEL TESTS

The most useful way to review the results of the various low-speed wind tunnel tests is to consider these as an inter-related set and to consider how the conclusions from one type of experiment have supported conclusions reached from another. Examples include:

(i)   The flow visualisation and pressure distribution tests have indicated that the phenomenon of afterbody vortex formation may not be so prevalent as previous investigators have indicated. The importance of considering the local angles of attack in the assessment of whether afterbody vortex formation will take place has been emphasised.

(ii)   Upstream influence of the wings as evidenced by changes in surface oil flow patterns has been borne out by the pressure distributions.

(iii) The results for panel spanwise loading distributions have been found to be quite regular except for combinations of high α and β where loading direction reversals have been observed. Comparison of results with those of the water tunnel suggests that the general levelling out of spanwise loading distribution occurs for those cases where vortex breakdown adjacent to the wing panels has occurred.

5.6.1 Correlation between Low-Speed Wind Tunnel and Water Tunnel Results in these Tests

The results for vortex trajectories on a body in isolation have shown good agreement.

The general flow behaviour adjacent to the cruciform wing panels of a wing-body combination have been duplicated between the water tunnel and wind tunnel experiments. Loss of body vortex structure and change of direction have been seen in both sets of experiments. Detailed effects on the wing panel such as areas of stagnant or highly spanwise flow have been observed in both sets of tests. On the body, forward and aft of the wings panels, the same effects have been seen. Areas of high flow curvature immediately upstream of the wing leading edge - body junction have been duplicated. Aft of the trailing edge the lack of any obvious coherent afterbody vortex structure has been noticed.

For the present test programme, therefore, involving configurations with large areas of separated flow on the body and wing panels with sharp edges, the low Reynolds number available in the water tunnel tests has not been a problem.

6.   RESULTS FROM AN ASSOCIATED TRANSONIC EXPERIMENTAL STUDY

6.1   EXPERIMENTAL DETAILS

Tests performed by Aircraft Research Association covered two body shapes. Fitted to a common afterbody was either a short tangent ogive nose ($l_N = 1.215D$) or an ellipsoidal nose ($l_N = 1.0D$). The use of the former meant that the previous geometric coverage was enhanced since the nose semi-apex angle of the sharp tangent ogive nose (which Mendenhall and Nielsen had deduced was an important parameter) was much greater in this test series than for the data previously collected. (See Fig. 29). The models were pitched to angles of incidence of 8.1, 15.1 and 20.7 degrees. Freestream Mach numbers for the tests were 0.7 and 1.15 and the Reynolds numbers (based on freestream speed and model diameter) were 1.46 and 1.70 x 10^6 respectively. Flowfield information i.e. velocity vectors and magnitudes of total pressure, was gathered in the leeside wake of the bodies using a rake of 16 five-hole yawmeter probes.

The data available from the ARA flow survey tests was in the form of flow vector plots. (Reference 37 contains the complete set). Corresponding results could be deduced for the distribution of circulation around the small segments of the flowfield bounded by the circumferential paths of the yawmeter probes as they roll around the body axis. (Fig. 30). Note that in certain areas the segments can become quite large.   This reflects the sparse coverage of basic flow data.

6.2   ASSESSMENT OF THE RESULTS

Before proceeding to a detailed discussion of such quantities as the vortex position and strength as derived from the experimental data it is worthwhile making the general point concerning the relatively large area of the leeside flowfield which can be dominated by vortex effects.

6.2.1 Vortex Locations

From the flow vector plots body vortex core locations could be deduced subjectively by observing where the most rapid changes in crossflow velocity vectors occurred and where the magnitudes of these vectors decreased to a minimum. Implicit in this is the assumption of a viscous vortex core in which tangential induced velocities are reduced (ideally to zero) as the core position is approached. The results showed that in general, at a given incidence angle and for a given flow survey station, the body vortex core would lie slightly further away from the body axis (both laterally and vertically) at supersonic speed compared to subsonic speed. The effect of changing the nose shape from the short sharp tangent ogive to the ellipsoid is minimal. An examination of the results also showed that the underlying trend due to either increasing incidence angle or the distance along the body from the apex was to have an increasing value of $\frac{y_{BV}}{D}$, $\frac{z_{BV}}{D}$ and

$\frac{\Gamma_t}{*DV}$. It can be remarked that changes in vertical location were always more pronounced

than changes in the lateral direction.

6.2.2 Vortex Strength

To assess the strength of the body vortices, contour integrals have been done about the largest boundary possible in the leeside quadrant. Results have been derived for the quantity $\frac{\Gamma_t}{*DV}$ where Γ_t is the total circulation captured in this fashion. It must be remarked that for certain cases Γ_t may well represent a low estimate of the total vortex strength in the leeside since some vorticity may lie above the area covered by the rake traverse. The distributions of the total circulation over a quite large area of the flowfield make it obvious that the concept of a flow model containing only line vortices (in which Γ_t would be concentrated at a point) is inadequate. It can also be seen how the majority of the circulation which is not found adjacent to the core itself is distributed along a region joining the core to the body surface. The typical shape, and position of a body vortex feeding sheet is thus illustrated.

The relative importance of the feeding sheet compared to the core has been assessed in a crude way by estimating which segments contribute to each and then forming a ratio of the relative strengths. It has been shown that the ratios Γ_s Γ_t are quite closely grouped mostly between 0.21 and 0.35. Thus, even allowing for errors in the definition of this ratio, one feature is clear. The circulation of the feeding sheet is by no means negligible with respect to the total enclosed in the whole leeside quadrant.

An examination of the results also showed how the non-dimensional vortex strength increases both with distance along the body and with angle of incidence. For a given incidence or axial station non-dimensional vortex strengths in supersonic flow are also greater than those for equivalent conditions in subsonic flow.

Changing the nose shape from ogive to ellipsoidal has very little effect on $\frac{\Gamma_t}{*DV}$.

6.2.3 Comparison of Experimental Data with Predicted Results

The method of Mendenhall and Nielsen (Ref. 17) is available for the prediction of body vortex characteristics on an empirical basis. Comparison of the method with the experimental data deduced from the ARA flow survey tests has illustrated one particularly important feature connected with the prediction of vortex starting position.

Consider the equation Mendenhall and Nielsen suggest for vortex starting point on a sharp nosed body:

$$\frac{x_s}{r_N} = 32 \left(1 - \sqrt{\frac{\alpha - 4}{\theta_N - 4}} \right) \qquad\qquad A$$

For the ARA model $\theta_N = 44.7°$. Applying equation A one calculates x_s as a function of incidence angle alone. The significant feature of the results is that the vortex starting point is predicted so far aft. Indeed for $\alpha = 8.1°$ and 15.1° the starting point is predicted to be behind the aft flow survey station. However, for the forward flow survey location the flow vectors clearly showed a well developed body vortex system at $\alpha = 15.1°$ and 20.7°. Obviously, the Mendenhall and Nielsen method of equation A is mis-leading for the particular quantity of vortex starting point on sharp nosed bodies for high values of θ_N, since x_s should take a value equivalent to a point much closer to the apex. The reason for this result is quite clear. Mendenhall and Nielsen's empirical method is founded on a basis of data for quite slender nose shapes (maximum $\theta_N = 20°$). Thus applying equation A with $\theta_N = 44.7°$ is simply using it outside its intended range of application and thus misleading results are not unexpected.

In their description of the calculation of induced rolling moments (Ref. 101) Hemsch, Nielsen and Dillenius refer to the use of equation A and suggest that for $\theta_N > 30°$ the nose should be treated as if it were blunt. By this procedure equation B is used:

$$\frac{x_s}{r_N} = \frac{10}{\alpha - 4} + 2 \qquad\qquad B$$

This equation yields values which are much more reasonable than those from equation A.

Figure 31 shows some plotted comparisons of data where the predicted results of Reference 17 have been superimposed on the measured results. In general the trends of changes in vortex location and strength are reasonably well predicted. Note that there is no predicted Mach number dependency of vertical vortex location $\frac{z_{BV}}{D}$. The results of Figure 31 should be viewed in the light of the underlying uncertainty of any results obtained from Mendenhall and Nielsen's technique. Reference to the original source will immediately show that there was a large amount of scatter displayed in the correlations which make up the prediction scheme. In an effort to quantify the effects of this underlying scatter error bars have been superimposed on the predicted results of Figure 31. Having done this it is more easily concluded that the ARA data recently obtained is in general agreement with the earlier correlation of Mendenhall and Nielsen for the various trends of incidence, Mach number and axial position. Only a fraction of the results lie outside the general error bands mostly at M1.15 and the higher incidence angles (15.1° and 20.7°). Even then the discrepancies are not great.

7. PREDICTION OF WING PANEL CHARACTERISTICS IN THE PRESENCE OF BODY VORTICES

Following the experimental determination of previously unsuspected flow phenomena regarding body vortex interaction with lifting surfaces it was though necessary to consider how aspects of this behaviour might be accounted for in a suitable manner for inclusion in missile aerodynamic prediction methods. This section will review such an attempt at deriving a calculation procedure using as a basis the method of Oberkampf (Ref. 91)*.

7.1 EXPERIMENTALLY OBSERVED FEATURES OF THE FLOW WHICH NEED TO BE CONSIDERED

The ARA flow survey tests have shown that the feeding sheet and diffuse nature of the vortex core are important. This should be taken into consideration.

The water tunnel and wind tunnel tests have shown that, at particular combinations of incidence and roll angle, vortex breakdown adjacent to the wing panels can occur. This should be accounted for in a manner which allows the prediction of the spanwise loading distributions which may be quite regular or highly non-uniform depending on the roll and incidence angle combination.

The method of Oberkampf was considered to be a sensible basis from which to work since the examples shown in Reference 91 had included the prediction of a non-uniform spanwise loading characteristic. Additionally the presence of a feeding sheet was modelled in the method. However, even in the absence of any previously unexpected flow phenomena it was felt necessary to change various details of Oberkampf's method prior to incorporating any modifications to allow for vortex breakdown. In this form, incorporating DATCOM and Mendenhall and Nielsen techniques for the isolated wing and body vortex definitions respectively it will be referred to as the "hybrid method". (Refs. 107 and 17).

The method was implemented for a variety of flow conditions (i.e. combinations of incidence and roll angle) and the spanwise loading distributions calculated. Some results are shown in Figures 32 - 33. The first figure emphasises how irregular the onset local angle of attack distribution can be even when a viscous core and feeding sheet representation is used in the hybrid flow model.

It will be seen how, using the hybrid technique, reasonable results are given for the distribution of spanwise loading for $\emptyset = 0°$ and 45° but how for $\emptyset = 70°$, i.e. in the vicinity of the body vortex, agreement between experiment and prediction is virtually non-existent. Even for $\emptyset = 0°$ and 45° the accuracy could be much better especially near the wing-body junction ($\zeta = 0$) but at least the correct trends of loading are predicted. It is evident that attention needs to be paid to the case of $\emptyset = 70°$ to improve the results but before considering possible courses of action Figures 34 - 35 should be examined. These show the results of integrating the spanwise loading distribution to yield a predicted panel load and to give the lateral centre of pressure. These results should be compared with the superimposed experimental results.

* Footnote: Oberkampf has now published further reports on this theme: Refs. 105 and 106.

Not surprisingly the values of C_{NP} are over-predicted by the hybrid method since the local spanwise loading was over-predicted in the region of the root. What is surprising is that the results for $\emptyset = 70°$ are not worse. This reflects the overall panel load being a result of opposing positive and negative contributors. Each could be in error and the total could be approximately correct. This does not ensure that the spanwise centre of pressure is correctly predicted. Inspection of Figure 35 will show that although the correct trend of lateral centre of pressure is predicted by the hybrid method for $\emptyset = 70°$, especially the sudden shift for BW_A, the initial values are too far outboard compared with experiment. For $\emptyset = 0°$ and $45°$, as for C_{NP}, the situation is better with lateral centre of pressure position predicted to within 10% of nett wing semi span.

Consider now the poor predictions of the spanwise loading distribution at $\emptyset = 70°$. The main problem is that L (£) and hence, by implication, the local angle of attack distribution, exhibits a shape with too highly pronounced peaks and troughs. The obvious solution is, therefore, to adopt a flow model which smooths out the irregularities of the onset angle of attack distribution. To some extent this is achieved already in the hybrid method by the use of a viscous core and feeding sheet. However, it would appear from these results that even with this model the vorticity is still too concentrated.

With the evidence of the wind tunnel and water tunnel tests in mind some computer simulations have been conducted using the hybrid model as a basis. These have concerned the use of a well dispersed collection of small vortices. This distributed vorticity concept was first prompted by the flow visualisation results which suggested a loss of coherent structure and dispersion of vorticity across a wider area of the flowfield. To a great extent the choice of position and strength of the small vortices used in the dispersed set has been arbitrary with only qualitative flow visualisation evidence available to guide the analysis, whose criterion for success will be the more accurate prediction of the spanwise loading distribution. The adopted procedure has been quite simple. Using distributions of small vortices as shown in Figure 36 the flow conditions have been calculated as an input to the loading estimation method. The same overall strength to the complete vortex system (i.e. all the 21 small vortices) has been used but this has been differently placed within the leeside area. For each small vortex an image is placed at an appropriate point to ensure no flow is predicted through the surface of the body.

Consider the results shown in Figure 37, and compare the predicted spanwise loading distribution with that using the standard hybrid flow model as illustrated in Figure 44 (bottom sketch in this case). The effect of spreading the total vortex strength over a large area of the flowfield can be seen to be the reduction of the large "peak and trough" behaviour in the spanwise load distribution making it more even across the span. The oscillations which are still evident are the result of high induced velocities adjacent to the small vortices which make up the distributed wake (see Figure 36). The model can be "tuned" to yield a smoother spanwise loading distribution by incorporating a larger viscous core around each constituent vortex. It can also be demonstrated that once the concept of a core vortex plus feeding sheet has been departed from, and a distributed pattern adopted, even quite radical changes in this pattern may not have large effects on the predicted spanwise loading distribution.

Computer simulations have, however, shown that the total vortex strength contained within the distributed pattern is much more critical than vortex position in affecting the predicted load distributions. Note how on Figure 38 the use of a lower total vortex strength (dashed line) will yield a better prediction (which in this case uses a relatively large size viscous core around each elementary vortex) than will the vortex strength predicted in Mendenhall and Nielsen. The ratio of strengths is 36%.

It can be thus seen from these results that the dispersion of vortex strength into a larger area of the flow at least holds the promise of improved predicted results for spanwise loadings at high $\emptyset$. However, it must be established that any change to the flow model resulting in an improvement at high $\emptyset$ does not result in a reduction in accuracy at lower values. Figure 39 shows the effect on spanwise loading distribution at $\emptyset = 0°$ and $45°$ of using a distributed vortex pattern. It can be seen how the changes compared to the single core plus feeding sheet representations are not large, and how any change of accuracy is insignificant.

Computer simulations have also been conducted to examine the results on the spanwise loading distributions of assuming that no vortex was present at all. Figure 40 shows results from such calculations. For $\emptyset = 70°$ it will be seen that the resultant "potential - crossflow only" solution does lie in close agreement with the experimental values. However, it is felt that the balance of evidence available from the recent tests indicates that body vortices are indeed present adjacent to wing panels, that their strength is not negligible and their interaction effects must be accounted for. A solution to the problem of correctly predicting the spanwise loading distributions must not, therefore, be sought by simply ignoring the body vortex but rather by optimising the model of its structure and behaviour adjacent to the wing panel.

Although there is enough evidence to suggest that better solutions may be forthcoming by the use of distributed vortices the choice of their position, number and

relative strengths can only be qualitatively guided. A need exists for a systematic and detailed investigation of the flowfield adjacent to wing panels so that these factors may be better predicted.

It is relevant here to consider evidence obtained by other investigators. Grosche (Ref. 28) in a series of tests described in Section 2.2 observed that significant changes to flowfield structure were possible adjacent to, and downstream of, wing panels. Data were included which showed the effect of having an upstream wing in that the vortex structure downsteam of it was much more diffuse than it would have been had the wing not been present. Thus from that source there seems to be evidence that vortex dispersion as suggested here is a possibility but no quantitative evidence is available from Reference 28 to judge exactly where the change of structure occurred.

Other investigators have also suggested that, in terms of adequately predicting the overall characteristics of complete missiles, the body vortex should be assumed to disappear aft of the leading edge of an upstream panel. Thus the version of the NEAP prediction technique reported in Reference 93 had an option for neglecting the body vortices aft of the leading edge of a canard surface since dispersion had been observed over the canard section at quite modest angles of incidence ($\alpha \leqslant 20°$). It should be remarked that the test conditions for the experiments which gave rise to this conclusion were quite different (M0.8 and M1.75) to the recent tests reported here. Personal contact made with NEAR investigators following the publication of Reference 100, indicated that it was their opinion that vortex breakdown adjacent to the upstream panel of their model might have occurred in the same manner as the results shown in the latter reference. This, in turn, could have been responsible for the conclusions drawn concerning the better prediction of loads if the body vortices were simply neglected downstream of the forward wing surfaces.

8. CONCLUDING REMARKS

It has been shown that existing empirical prediction methods for vortex characteristics can yield reasonable estimates of overall circulation contained in the symmetric body vortex wake and that core positions are similarly well predicted. However, it has also been shown that the concept of modelling the vortex wake as a single pair of contra-rotating potential line vortices will not adequately represent the true distributed nature of the vorticity. At the very least a viscous core and feeding sheet should be added to the flow model.

When flow around wing-body combinations is considered the importance of considering the vortices as diffuse rather than concentrated entities is emphasised. Comparison of results for spanwise loading distributions for the predicted and experimental cases shows that, even using a viscous core and feeding sheet model satisfactory results are not likely to be achieved at high angles of incidence with the panel rolled into the leeside.

It is speculated that this follows from the action of the wing panel is dispersing the previously well-defined body vortex core at some point adjacent to the wing panels. Evidence of flow visualisation tests in water and wind tunnels has indicated that significant changes of trajectory and drastic changes of structure are possible in such areas. This phenomenon, subsequently corroborated by other investigators, has been linked to the breakdown of the well-ordered upper-surface flow on the wing panel.

Exploiting evidence from water tunnel and wind tunnel tests, a rough correlation of effects is achieved if the geometric effective angle of attack of the pitched and rolled panel mounted on the body is considered.

Recent flow visualisation tests have also showed that the phenomenon of afterbody vortex generation may not be as prevalent as first thought. The action of the upstream wing panels in reducing the effective angle of attack on the body is shown to be the important factor here.

A complete solution to the understanding of the flowfields will not, however, come until comprehensive flow survey results adjacent to the wing panels are available. This should then enable a more quantitative appreciation to be formed of the flowfield changes and thus enable progress to be made in the further improvement of loading estimation procedures which can only be tentatively modified on the basis of existing results.

This lecture is predominantly based on the author's Ph.D thesis (Ref. 110).

9. REFERENCES

1. BIGNELL, P.R., DEANE, J.R. "Vortex flow fields: A bibliography" BAC (GW) Report ST14446, October 1975
2. DEANE, J.R. "Body vortex effects on the wing panel pressure distributions for a missile configuration" Cranfield Institute of Technology MSc Thesis, September 1976
3. FELLOWS, K.A. "Flow survey above a body of revolution at transonic speeds" ARA MTN 116/1, December 1977

4. GOWEN, F.E., PERKINS, E.W. "A study of the effects of body shape on the vortex wakes of inclined cylinders at a Mach number of 2" NACA RM A53I17, December 1953

5. RANEY, D.J. "Measurement of cross flow around an inclined body at Mach number 1.91" RAE TN Aero 2357, January 1955

6. GAPCYNSKI, J.P. "An experimental investigation of the flow phenomenon over bodies at high angles of attack at a Mach number of 2.01" NACA RM L55H29, October 1955

7. JORGENSEN, L.H., PERKINS, E.W. "Investigation of some wake vortex characteristics of an inclined ogive cylinder body at Mach number 1.98" NACA RM A55E31, August 1955

8. JORGENSEN, L.H., PERKINS, E.W. "Investigation of some wake vortex characteristics of an inclined ogive cylinder body at Mach number 2" NACA Rept. 1371 (Superseded Ref. 7) 1958

9. ALLEN, H.J. "Estimation of the forces and moments acting on inclined bodies of revolution of high fineness ratio" NACA RM A 9 I26, 1949

10. KELLY, H.R. "The estimation of normal force, drag and pitching moment coefficients for blunt-based bodies of revolution at large angles of attack" Jnl. Aero. Sci. Vol 21, No. 8 p549-555, 565, August 1954

11. NIELSEN, J.N., KAATTARI, G.E. "The effects of vortex and shock expansion fields on pitch and yaw instabilities of supersonic airplanes" Inst. Aero. Sci. Preprint 743, 1957

12. SPAHR, J.R. "Theoretical prediction of the effects of vortex flows on the loading, forces and moments of slender aircraft" NASA TR R-101, January 1961

13. ALLEN, H.J., PERKINS, E.W. "A study of the effects of viscosity on flow over slender inclined bodies of revolution" NACA Report 1048, 1951

14. SCHWABE, M. "Pressure distributions in non uniform two dimensional flow" NACA TM 1039, 1943

15. SARPKAYA, T. "Separated flow about lifting bodies and impulsive flow about cylinders" AIAA Jnl. Vol. 4 No. 3 p414-420, March 1966

16. WARDLAW, A.B. "High angle of attack aerodynamics" AGARD LS98 "Missile aero-dynamics", 1979

17. MENDENHALL, M.R., NIELSEN, J.R. "Effect of symmetrical vortex shedding on the longitudinal aerodynamic characteristics of wing-body-tail combinations" NASA CR-2473, January 1975

18. NIELSEN, J.N. "Missile Aerodynamics" McGraw-Hill, 1960

19. MALTBY, R.L., PECKHAM, D.H. "Low speed studies of the vortex patterns above inclined slender bodies using a new smoke technique" RAE TN Aero 2482, November 1956

20. CARROLL, M.E. "A visual investigation of the flow about an inclined body of revolution" Univ. of Notre Dame M.S. Thesis, October 1957

21. MELLO, J.F. "Investigation of normal force distributions and wake vortex characteristics of bodies of revolution at supersonic speeds" Jnl. Aero/Space Sciences Vol 26, No. 3 p155-168, March 1959

22. LANKFORD, J.L. "Preliminary results of flow surveys about an inclined body of revolution at Mach number 3.5 (Phase 1 of aft entry program)" NAVORD Rept. 6708, July 1960

23. TINLING, B.E., ALLEN, C.Q. "An investigation of the normal force and vortex wake characteristics of an ogive cylinder body at subsonic speeds" NASA TN D 1297, 1962

24. LEFF, A.D. "Shadowgraph study of cone-cylinder and cone-cylinder-frustrum-cylinder configurations" LMSC TM54/20-66, December 1965

25. FRIBERG, E.G. "Measurement of vortex separation. Part II. Three dimensional circular and elliptic bodies" MIT Aerophysics Lab TR115, August 1965

26. FIECHTER, M. "On the vortex systems of high fineness ratio bodies of revolution and their influence on the aerodynamic coefficients" (In German) German/French Res. Inst Rept 10/66, 1966

27. CHAMBERLAIN, T.E. "Aerodynamic forces, separation lines and vortex trajectories on slender bodies with several nose shapes" MIT Thesis, June 1966

28. GROSCHE, F.R. "Wind tunnel investigation of the vortex system near an inclined body of revolution with and without wings" AGARD CP 71-71 "Aerodynamic Interference", January, 1971 (See Ref. 62)

29. MORRISON, A.M., INGRAM, C.W. "Experimental investigation of leeside flow from cone cylinder model" AIAA Jnl. Vol 9, No. 7, p1421-1423, July 1971

30. FOLEY, J.E. "Results of a study of Mach number and Reynolds number effects on the leeside vortex flow field characteristics of an ogive-cylinder-frustrum-cylinder at angles of attack to 25 degrees" Chrysler TN AP 72-565, 1975

31. JONES, J.H., O'HARE, J.E. "Flow visualisation photographs of a yawed tangent ogive cylinder at Mach number 2" AEDC TR 73-45, March 1973

32. YANTA, W.J. "Laser Doppler velocimeter measurements of leeward flowfields on slender bodies at large angle of attack" AIAA Paper 77-660, June 1977

33. FIDLER, J.E., SCHWIND, R.G., NIELSEN, J.N. "Investigation of slender body vortices" AIAA Jnl. Vol 15, No. 12, p1736-1741, December 1977

34. OWEN, F.K., JOHNSON, D.A. "Wake vortex measurements of bodies at high angle of attack" AIAA Paper 78-23, January 1978

35. OWEN, F.K., JOHNSON, D.A. "Wake vortex measurements of an ogive cylinder at a = 36 degrees" Jnl. Aircraft Vol 16, No. 9, p577-583, September 1979 (Superseded Ref. 34)

36. SCHWIND, R.G., MULLEN, R. "Laser velocimeter measurements of slender wake vortices" AIAA Paper 79-0302, January 1979

37. DEANE, J.R., TOVEY, M.H. "Vortex dominated flowfields. Analysis of ARA flow survey data" BAe (DG) Bristol Report ST20963, September 1978

38. DEANE, J.R., PONTING, M.H., FELLOWS, K.A. "Symmetric body vortices on slender bodies of revolution at transonic speeds" JSR, Vol 17, No. 3, p282-284, May - June 1980

12-24

39. OBERKAMPF, W.L., BARTEL, T.J., MARTINDALE, W.E. "Supersonic flow measurements in the body vortex wake of an ogive cylinder" AIAA Paper 78-787, April 1978

40. OBERKAMPF, W.L., BARTEL, T.J. "Symmetric body vortex wake characteristics in supersonic flow" AIAA Paper 78-1337, August 1978

41. OBERKAMPF, W.L., BARTEL, T.J. "Symmetric body vortex wake characteristics in supersonic flow" AIAA Jnl. Vol 18, No. 11, p1289-1297, November 1980 (Superseded Ref. 40)

42. OBERKAMPF, W.L., BARTEL, T.J. "Supersonic flow measurements in the body vortex wake of an ogive nose cylinder" AFATL TR 78-127, November 1978

43. HSIEH, T., WANG, K.C. "Concentrated vortex on the nose of an inclined body of revolution" AIAA Jnl. Vol 14, No. 5, p698-700, May 1976

44. HSIEH, T. "An investigation of separated flows about a hemisphere cylinder at incidence in the Mach number range from 0.6 to 1.5" AIAA Paper 77-179, January 1977

45. HSIEH, T. "Low supersonic flow over hemisphere cylinder at incidence" JSR Vol 14, No. 11, p662-668, November 1977

46. WERLÉ, H. "Tourbillons de corps fuseles aux incidence elevees" L'Aeronautique et L'Astronautique 1979-6, 1979

47. RAMASWAMY, M.A., RAJENDRA, G. "Experimental investigation of transonic flow past a blunt cone-cylinder" JSR Vol 15, No. 2, p120-123, March - April 1978

48. BRYSON, A.E. "Symmetric vortex separation on circular cylinders and cones" Jnl. Appl. Mech. Vol 26, p643-648, December, 1959

49. WARDLAW, A.B. "Prediction of normal force, pitching moment and yawing force on bodies of revolution at angles of attack up to 50 degrees using a concentrated vortex flowfield model" NOLTR 73-209, October 1973

50. ANGELUCCI, S.B. "A multivortex method for axisymmetric bodies at angle of attack" Jnl. Aircraft Vol 8, No. 12 p959-966, December 1971

51. MARSHALL, F.J., DEFFENBAUGH, F.D. "Separated flow over bodies of revolution using an unsteady discrete vorticity cross wake. Part I : Theory and applications" NASA CR2414 "Part II : Computer program description" NASA CR2415, June 1974

52. MARSHALL, F.J., DEFFENBAUGH, F.D. "Separated flow over a body of revolution" Jnl. Aircraft Vol 12, No. 2 p78-85 February 1975

53. DEFFENBAUGH, F.D. "Evaluation of the discrete vortex wake crossflow model using vector computers. Part I : Theory and Application" TRW Rept. 30584-6001-RU-00, January 1979

54. DEFFENBAUGH, F.D., VITZ, J.F. "Evaluation of the discrete vortex wake crossflow model using vector computers. Part II : Users manual for DIVORCE" TRW Rept. 30584-6002-RU-00, January 1979

55. MENDENHALL, M.R., SPANGLER, S.B., PERKINS, S.C. "Vortex shedding from circular and non-circular bodies at high angles of attack" AIAA Paper 79-0026, January 1979

56. SHIVANANDA, T.P., OBERKAMPF, W.L. "Prediction of the compressible vortex wake for bodies at high incidence" AIAA Paper 81-0360, January 1981

57. KLOPFER, G.H., NIELSEN, J.N. "Euler solutions of the body vortices of tangent ogive cylinders at high angles of attack and supersonic speeds" AIAA paper 81-0361, January 1981

58. KLOPFER, G.H., NIELSEN, J.N. "Basic studies of wing-body interference at high angles of attack and supersonic speeds" NEAR TR 206/ONR-CR-215-263-1 (AD A087 134), October 1979

59. MENDENHALL, M.R. "Predicted vortex shedding from non-circular bodies in supersonic flow" AIAA Paper 80-1559, August 1980

60. KITSON, S.T. "Vortex dominated flowfields : An investigation into modelling body vortices" BAe (DG) Bristol Rept ST23578, October 1979

61. WEIHS, D. "Approximate calculations of vortex trajectories of slender bodies at incidence" AIAA Jnl. Vol 18, No. 11, p1402-1403, November 1980

62. GROSCHE, F.R. "Windkanaluntersuchung des Wirbelsystems an einem angestellen schlanken Rotationskörper ohne und mit Tragflügel" Z. Flugwiss Bld. 18, Heft 18, 1970

63. DEANE, J.R. "Unpublished results of pressure distribution tests on two cruciform cropped delta wing body models in the Cranfield Institute of Technology 9in. x 9in. supersonic wind tunnel" Unpublished data, 1977

64. MOVASSAGHIE, B. "Experimental study of a wing with strake for a missile configuration in high subsonic and transonic flows" VKI PR 1976-3, 1976

65. ZARGHAMI, A. "Aerodynamic characteristics of a missile configuration featuring a wing with various strakes in subsonic and transonic flows up to high angles of incidence" VKI PR 1977-7, 1977

66. AKCAY, M. "The flowfield over a missile configuration fitted both with and without strake in transonic flow up to high angles of incidence" VKI PR 1978-1, 1978

67. VIGEVANO, L. "Effects of strakes on low aspect ratio trapezoidal wings for missile configurations in compressible flow" VKI PR 1979-5, 1979

68. GREFF, E. "Flow visualisation on missile wing configuration featuring a basic trapezoidal wing and an improved strake wing configuration" U-VKI 1977-24, 1977

69. DEMURIE, F., MUYLAERT, J., WENDT, J.F. "Investigation on the interaction between body vortices and the strake wing panels of a missile configuration" VKI IN 63, 1980

70. DEMURIE, F. "Investigation of the interference effects in the flowfield around a body-strake-wing missile configuration" VKI PR 1980-23, 1980

71. ALLEN, J.M., DILLENIUS, M.F.E. "Vortex development on slender missiles at supersonic speeds" AIAA Paper 79-0360, January 1979

72. DILLENIUS, M.F.E., NIELSEN, J.N. "Computer program for calculating pressure distributions including vortex effects on supersonic monoplane or cruciform wing-body-tail combinations with round or elliptical bodies" NEAR TR 54, August 1978 (Also NASA CR 3122 - April 1979)

73. SMITH, C.A., NIELSEN, J.N. "Prediction of aerodynamic characteristics of cruci-form missiles of high angle of attack utilising a distributed vortex wake" NEAR TR 208, January 1981

74. ERLICH, E. "Some effects of vortices upon the aerodynamic characteristics of missiles" Israel Jnl. Technology Vol 4, No. 1, p17'-185, 1966

75. SMITH, W.G., LAZZERONI, F.A. "Experimental and theoretical study of a rectangular wing in a vortical wake at low speed" NASA TN D 339, 1960

76. PATEL, M.H., HANCOCK, G.J. "Some experimental results of the effect of a stream-wise vortex on a two dimensional wing" Aero. Jnl. p151-155, April 1974

77. HANCOCK, G.J. "Aerodynamic loading induced on a two dimensional wing by a free vortex in incompressible flow" Aero. Jnl. Vol 75, p143-416, June 1971

78. GILLERLAIN, J.D., YANTA, W.J. "Vortex impingement on a control fin" AIAA Paper 82-0171, January 1982

79. BELL, C. "Body vortex flow phenomenon Part 4. Wind tunnel tests of body, wing plus body and wing alone configurations in the presence of a vortex" BAe (AG) Warton Rept. AXR66/2, 1979

80. JEPPS, S.A. "Body vortex flow phenomena Part 4. A comparison of theory and experiment for the flow past a body, a wing and a wing-body combination" BAe (AG) Warton Rept. Ae/A/592, July 1979

81. STONE, R.W., POLHAMUS, E.C. "Some effects of shed vortices on the flowfields around stabilising tail surfaces" AGARD Rept. 108, April – May 1957

82. MORIKAWA, G. "Supersonic wing-body-tail interference" Jnl. Aeronautical Sciences Vol 19, No. 5, p333-345, May 1952

83. SACKS, A.H. "Vortex interference on slender airplanes" NACA TN 3525, 1955

84. SACKS, A.H. "Aerodynamic interference of slender wing tail combinations" NACA TN 3725, 1956

85. SPREITER, J.R., SACKS, A.H. "A theoretical study of the aerodynamics of slender cruciform-wing arrangements and their wakes" NACA TN 3528, March 1956 (Also NACA Rept. 1296)

86. SACKS, A.H. "Vortex interference effects on the aerodynamics of slender airplanes and missiles" Jnl. Aeronautical Sciences Vol 24, No. 6, p393-402, 412, June 1957

87. PITTS, W.C., NIELSEN, J.N., KAATTARI, G.E. "Lift and centre of pressure of wing-body-tail combinations at subsonic, transonic and supersonic speeds" NACA Report 1307, 1957

88. ALDEN, H.L., SCHINDEL, L.H. "The lift, rolling moment and pitching moment on wings, in non-uniform supersonic flow" Jnl. Aeronautical Sciences Vol 19, No. 1, p7-14, January 1952

89. OBERKAMPF, W.L., NICOLAIDES, J.D. "Aerodynamics of finned missiles at high angle of attack" AIAA Jnl. Vol 9, No. 12, p2378-2384, December 1971

90. OBERKAMPF, W.L. "Prediction of roll moments on finned bodies in supersonic flow" JSR Vol 12, No. 1, p17-21, January 1975

91. OBERKAMPF, W.L. "Prediction of forces and moments on finned missiles in subsonic flow" AIAA Paper 79-0365, January 1979

92. SMITH, C.A., NIELSEN, J.N., HEMSCH, M.J. "Prediction of aerodynamic character-istics of cruciform missiles to high angles of attack" AIAA Paper 79-0024, January 1979

93. HEMSCH, M.J., SMITH, C.A., NIELSEN, J.N., PERKINS, S.C. "Calculation of component forces and moments of arbitrarily banked cruciform missiles with control deflections" ONR CR 215-226-3, 1976

94. HEMSCH, M.J., NIELSEN, J.N., SMITH, C.A., PERKINS, S.C. "Component aerodynamic characteristics of banked cruciform missiles with arbitrary control deflections" AIAA Paper 77-1153, 1977

95. NIELSEN, J.N., HEMSCH, M.J., SMITH, C.A. "A preliminary method for calculating the aerodynamic characteristcs of cruciform missiles to high angles of attack including effects of roll angle and control deflections" ONR CR 215-226-4F, 1977

96. RHODES, G.M. "An investigation into the low speed aerodynamic characteristics of multi-diameter bodies of revolution at incidence angles up to 28°" Cranfield Institute of Technology MSc Thesis, November 1980

97. "Notes on the calibration of 8 ft x 6ft wind tunnel balance" Cranfield Institute of Technology Memorandum, September 1962

98. DEANE, J.R. "Visualisation of the vortex dominated flow around a missile type wing-body combination using a water tunnel : Preliminary Report" BAe (DG) Bristol Rept. ST21299, December 1978

99. DEANE, J.R. "Wind and water tunnel investigation of the interaction cf body vortices and the wing panels of a missile configuration" AGARD CP247 "High angle of attack aerodynamics", October 1978

100. DEANE, J.R. "Experimental investigations into interaction between body vortices and wing panels on a missile configuration at low speed" AIAA Paper 80-0032, January 1980

101. HEMSCH, M.J., NIELSEN, J.N., DILLENIUS, M.F.E. "Method of calculating induced rolling moments for cruciform canard missiles at angles of attack up to 20 degrees" NWC TP 5761 (NEAR TR 85), May 1975 (ADB 004751)

102. POPE, A., HARPER, J.J. "Low-speed wind tunnel testing" Wiley, 1966

103. SWABY, H.P. "Visualisation of the vortex dominated flow around a delta wing-body combination using a water tunnel" BAe (DG) Bristol Note 821/RES/6631, October 1980

104. ERICKSON, G.E. "Water tunnel flow visualisation : Insight into complex three dimensional flowfields" AIAA Paper 79-1530, July 1979

105. OBERKAMPF, W.L. "Prediction of forces and moments on finned bodies at high angle of attack in transonic flow" SAND 80-2380, April 1981

106. As 105 but AFATL TR 80-107

107. U.S.A.F. Aircraft Stability + Control Data Compendium

12-26

108. LAMAR, J.E. "Comment on 'Water tunnel flow visualisation : Insight into complex three dimensional flowfields' " Jnl. Aircraft Vol 18, August 1981

109. ERICKSON, G.E. "Reply by author to J.E. Lamar" Jnl. Aircraft Vol 18, August 1981

110. DEANE, J.R. "A study of body vortices and their interaction with cruciform lifting surfaces" Cranfield Institute of Technology Ph.D. Thesis, April 1981
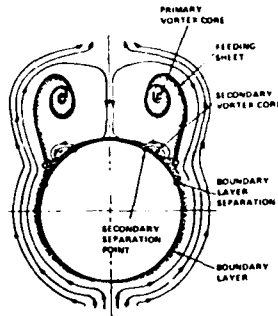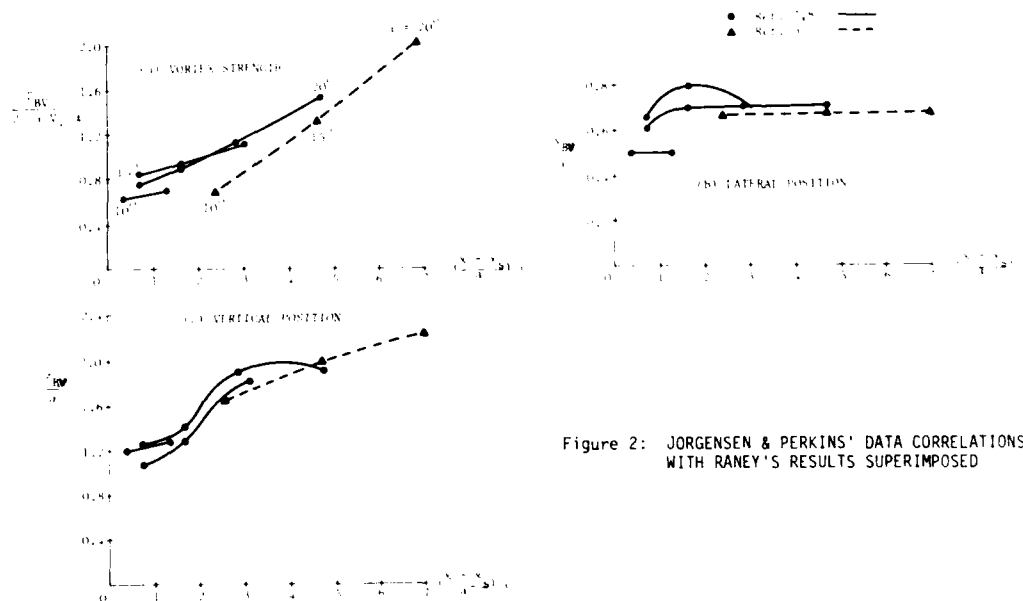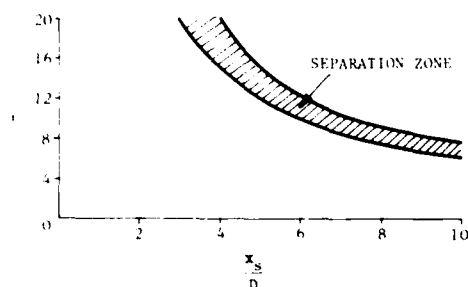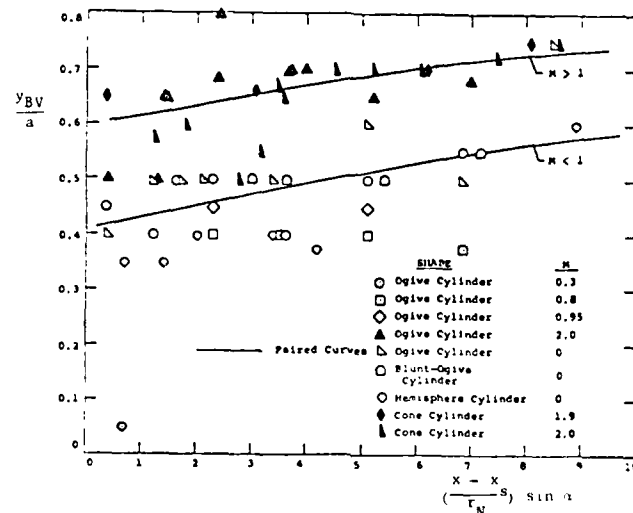
Figure 1: DIAGRAMMATIC REPRESENTATION OF CROSSFLOW

Figure 2: JORGENSEN & PERKINS' DATA CORRELATIONS WITH RANEY'S RESULTS SUPERIMPOSED

Data obtained for a tangent ogive nose (l_N= 3D)/ cylindrical afterbody (l_a= 3D) at supersonic speeds (M = 2.8)

Figure 3: SEPARATION OR VORTEX STARTING POINT DATA PRESENTED BY JORGENSEN & PERKINS (Ref. 7,8)

(a) LATERAL VORTEX POSITION

$\dfrac{y_{BV}}{a}$

$(\dfrac{x - x_s}{r_N}) \sin \alpha$

SHAPE	M
Ogive Cylinder	0.3
Ogive Cylinder	0.8
Ogive Cylinder	0.95
Ogive Cylinder	2.0
Ogive Cylinder	0
Blunt-Ogive Cylinder	0
Hemisphere Cylinder	0
Cone Cylinder	1.9
Cone Cylinder	2.0

Paired Curves

$M > 1$

$M < 1$

(b) VERTICAL VORTEX POSITION

$\dfrac{z_{BV}}{a}$

$(\dfrac{x - x_s}{r_N}) \sin \alpha$

Paired Curve

SHAPE	M
Ogive Cylinder	0.3
Ogive Cylinder	0.8
Ogive Cylinder	0.95
Ogive Cylinder	2.0
Ogive Cylinder	0
Blunt-Ogive Cylinder	0
Hemisphere Cylinder	0
Cone Cylinder	1.9
Cone Cylinder	2.0

(c) NON-DIMENSIONALISED VORTEX STRENGTH
(From Ref 17)

$\dfrac{\Gamma_{BV}}{2\pi a\, V_\infty \sin \alpha}$

$(\dfrac{x - x_s}{r_N}) \sin \alpha$

SHAPE	M
Ogive Cylinder	2.0
Ogive Cylinder	0.3
Ogive Cylinder	0.8
Ogive Cylinder	0.95
Cone Cylinder	1.9
Cone Cylinder	2.0

$M > 1$

$M < 1$

Figure 4: MENDENHALL & NIELSEN'S EMPIRICAL DATA CORRELATIONS
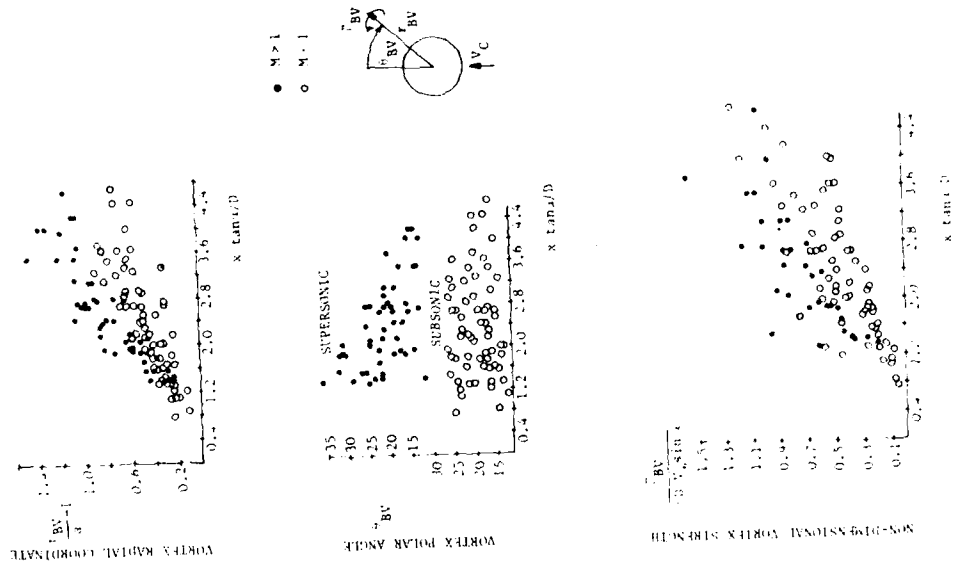
Figure 6. WARDLAW'S CORRELATIONS OF DATA ON SYMMETRIC BODY VORTICES
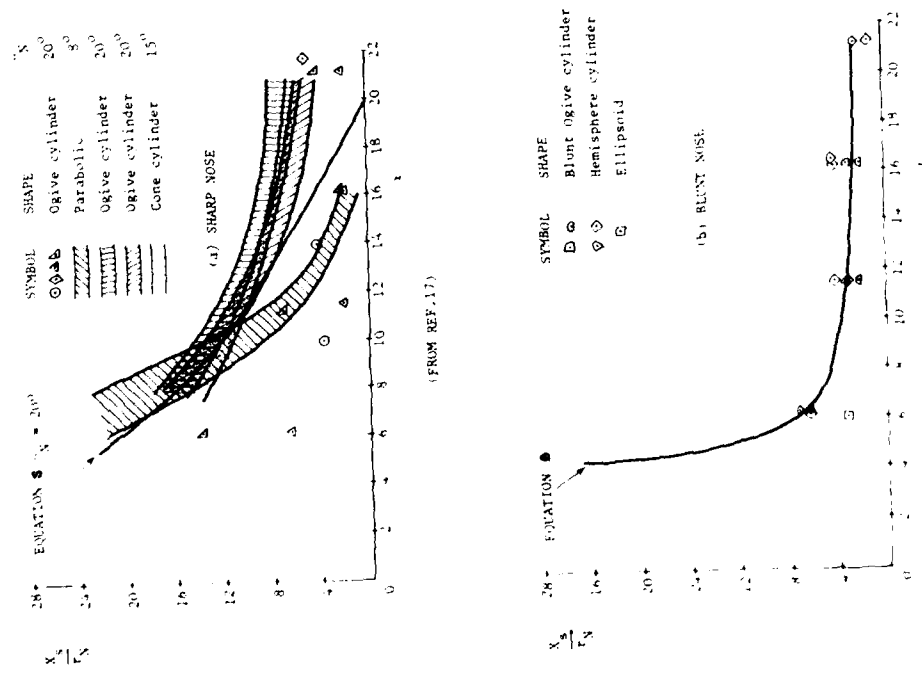
Figure 5. MENDENHALL & NIELSEN'S CORRELATED DATA FOR VORTEX STARTING POINT
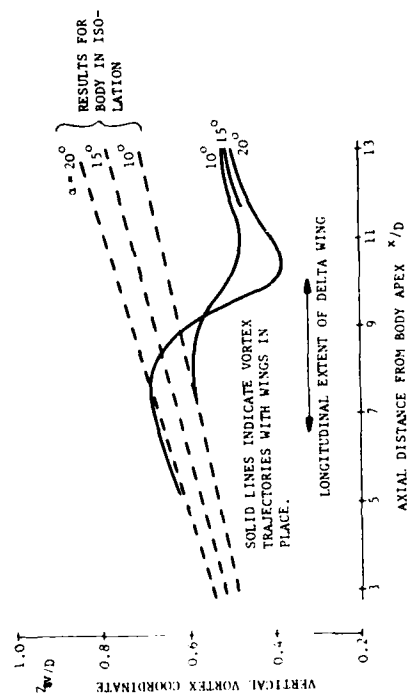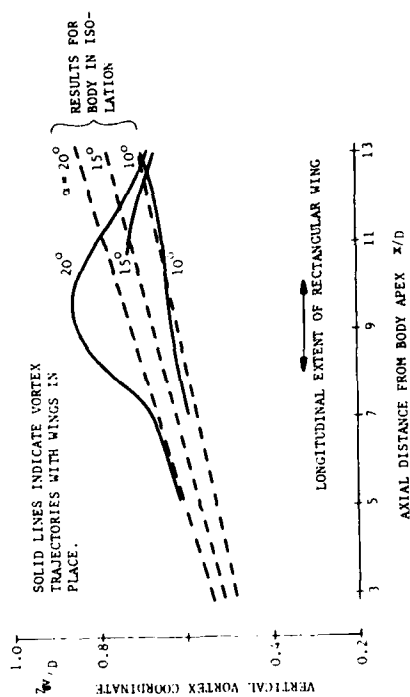
Figure . GROSCHE'S RESULTS FOR VORTEX TRAJECTORIES
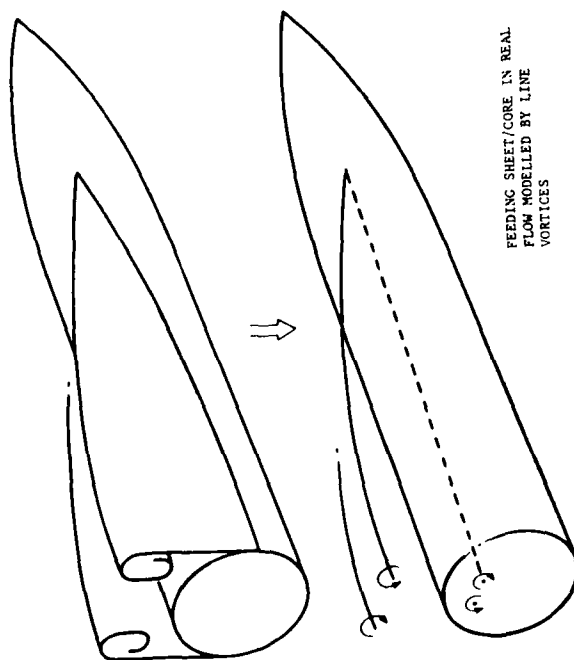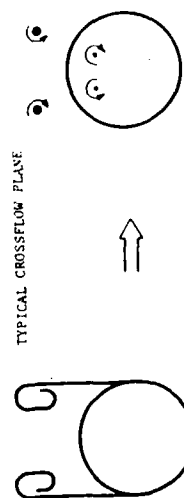
Figure 7: SIMPLIFIED VORTEX MODEL FOR INCLINED SLENDER BODY

Figure 11: RESULTS FROM BODY VORTEX INTERACTION STUDY OF REFERENCE 2
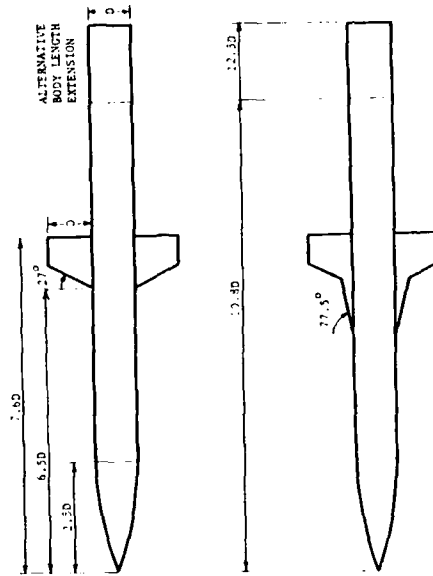
Figure 12: MONOPLANE BODY-WING AND BODY-STRAKE-WING MODELS USED IN VKI TESTS

Figure 9: GROSCHE'S FLOW FIELD MODEL USED TO EXPLAIN CHANGES OF VORTEX TRAJECTORY

Figure 10: MODEL GEOMETRY FOR SUPERSONIC WIND TUNNEL TESTS OF REFERENCE 2

x = EXPERIMENT
— OBERKAMPF METHOD
REF 9)

PANEL NORMAL FORCE COEFFICIENT

C_{N_p}

CROSSFLOW

CROPPED DELTA FIN ON A BODY $\alpha = 20°$ $M_\infty = 2.8$
(ONE FIN OF A CRUCIFORM SET)

PREDICTED SPANWISE DISTRIBUTIONS OF
LOAD FOR CONFIGURATION AS ABOVE

$\alpha = 10°$ $\alpha = 20°$ $M_\infty = 0.8$

Figure 15 : OBERKAMPF'S METHOD APPLIED TO A CROPPED DELTA WING -
BODY COMBINATION

Figure reproduced from Ref.12 : Contours of Interference Factor refer to the effects
of a single vortex on the right hand panel.

Contours of Interference Factor 'i'

← Vortex Lateral Co-ordinate Relative to Body Centreline Y_{BV}/s_p

Vortex Vertical Co-ordinate Relative
to Body Centreline $|Z_{BV}/s_p|$

VORTEX INTERFERENCE FACTORS; ($^a/s_p = 0.2$, TRAPEZOIDAL LOADING)

Figure 13 : TYPICAL VORTEX INTERFERENCE FACTOR CHART FROM SPAHR REFERENCE 12

MAIN VORTEX

FEEDING SHEET MODELLED BY
LARGE NUMBER OF SMALL
VORTICES

IMAGE VORTICES INSIDE CIRCLE
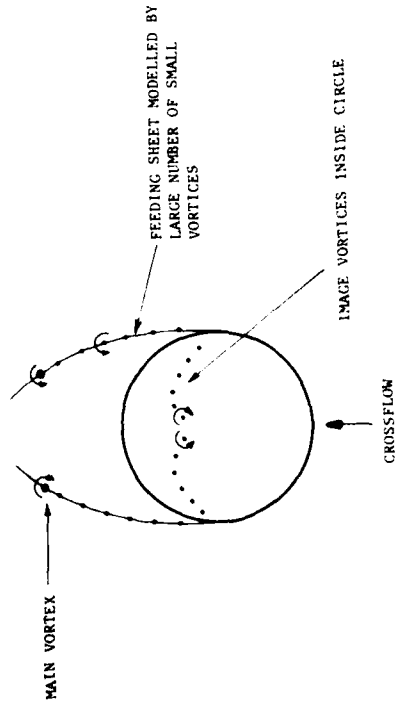
CROSSFLOW

Figure 14 : OBERKAMPF'S CROSSFLOW VORTEX MODEL

Figure 16: WIND TUNNEL MODEL GENERAL ASSEMBLY
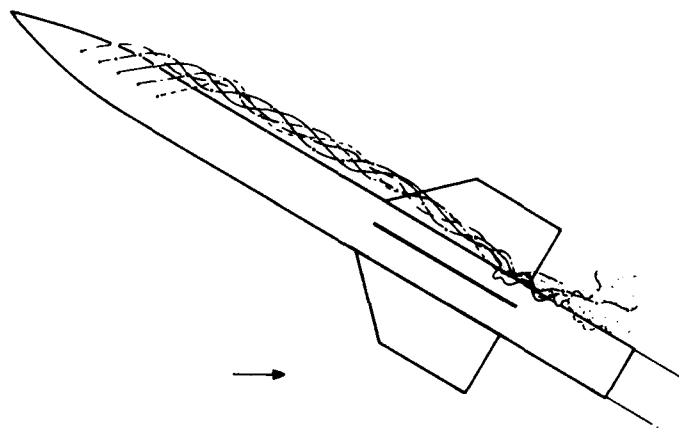
Fig.17: TRACING OF DYE LINE PATTERNS FOR BW_A $\phi = 0$, $\alpha = 30^o$

Fig. 20: TYPICAL CIRCUMFERENTIAL PRESSURE DISTRIBUTIONS FROM LOW SPEED WIND TUNNEL TESTS BW_A $\phi = 70$, $\alpha = 30^0$
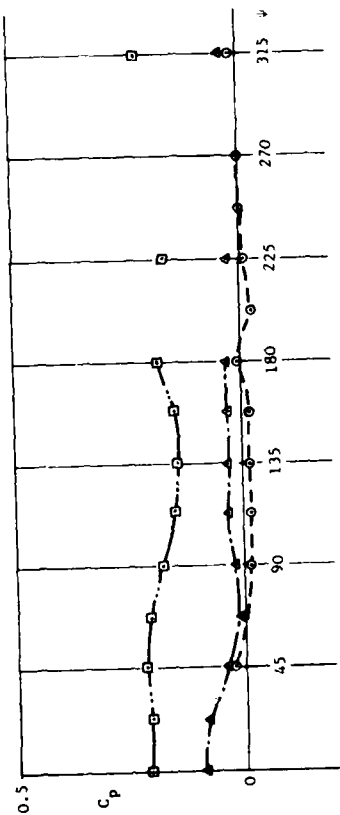
Fig. 21. TYPICAL CIRCUMFERENTIAL PRESSURE DISTRIBUTIONS FROM LOW SPEED WIND TUNNEL TESTS BW_F $\phi = 0$, $\alpha = 15^0$
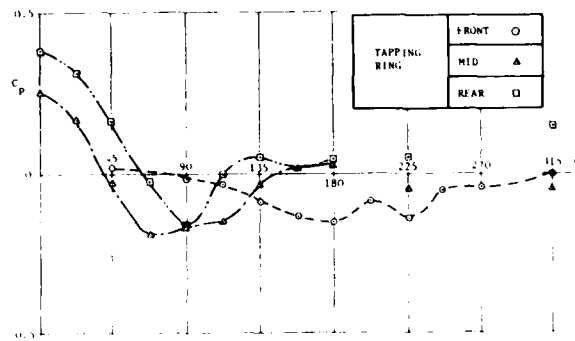
Figure 18: BOUNDARY OF BREAKDOWN AND NO-BREAKDOWN REGIMES FOR VORTICES ABOVE SLENDER WING PANELS ATTACHED TO BODIES

Fig. 19: TYPICAL CIRCUMFERENTIAL PRESSURE DISTRIBUTIONS FROM LOW SPEED WIND TUNNEL TESTS BW_A $\phi = 0$, $\alpha = 30^0$

Fig ... TYPICAL CIRCUMFERENTIAL PRESSURE DISTRIBUTIONS FROM
LOW SPEED WIND TUNNEL TESTS BW$_F$ $\alpha = 0$, $\gamma = 30^\circ$
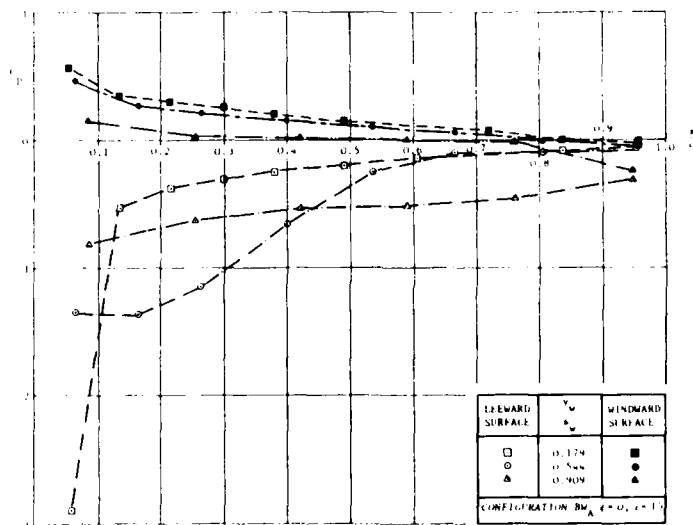
Fig ... TYPICAL CHORDWISE PRESSURE DISTRIBUTIONS FROM
LOW SPEED WIND TUNNEL TESTS
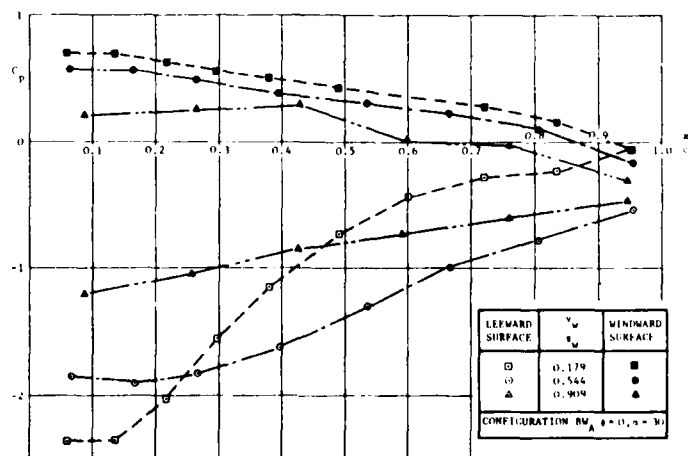
Fig 4: TYPICAL CHORDWISE PRESSURE DISTRIBUTIONS FROM
LOW SPEED WIND TUNNEL TESTS
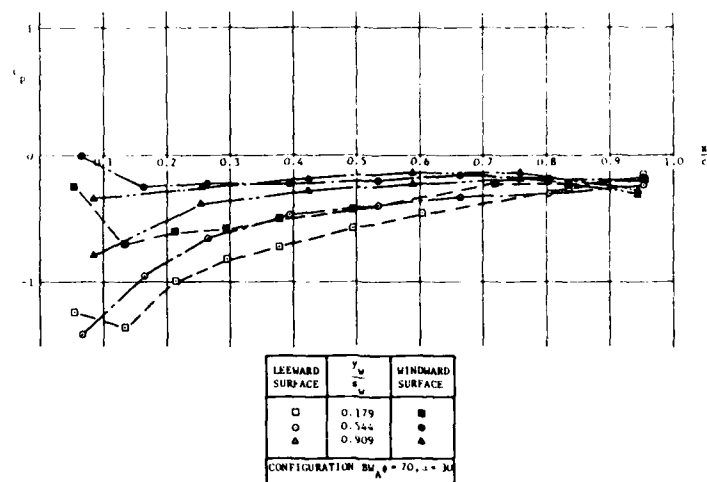
Fig. 25: TYPICAL CHORDWISE PRESSURE DISTRIBUTIONS FROM
LOW SPEED WIND TUNNEL TESTS
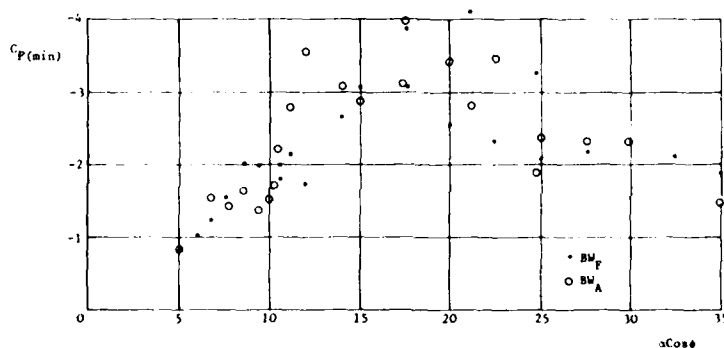
Figure 26: CORRELATION OF LEEWARD SURFACE MINIMUM PRESSURE COEFFICIENT WITH
EFFECTIVE PANEL INCIDENCE ANGLE FOR BOTH WING-BODY CONFIGURATIONS
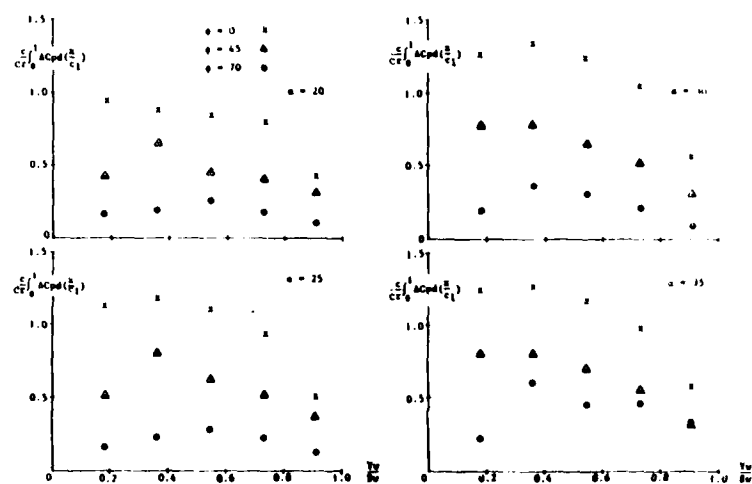
Figure 27: SPANWISE LOADING DISTRIBUTIONS FOR CONFIGURATION BW_A

7.597 D

5.146 D

1.215 D

0.114 D

D = 120.7 mm

TANGENT OGIVE

2:1 ELLIPSOIDAL NOSE

FORWARD FLOW SURVEY STATION

4FT FLOW SURVEY STATION

A | B

A | B
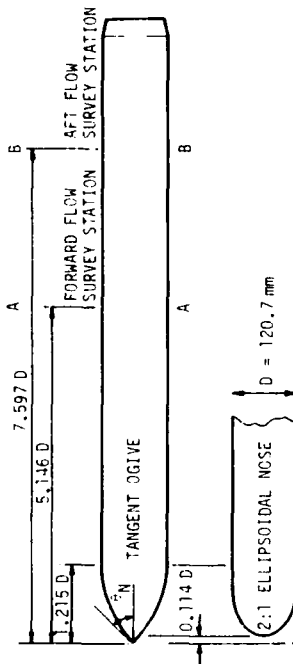
Figure ?: MODELS USED IN ARA FLOW SURVEY TESTS

VALUES SHOWN HERE ARE:

$$\frac{\Gamma_{SEGMENT}}{2\pi a \, V_\infty \sin\alpha}$$

+ ve ANTICLOCKWISE

0.000	0.000	0.004	0.007	0.008	0.003
-0.007	-0.003	-0.004	-0.007	-0.012	0.010
0.002	0.003	0.002	0.006	0.008	0.010
0.008	0.037	-0.005	-0.007	-0.006	-0.007
0.020	0.101	0.045	-0.005	-0.009	0.009
0.035	0.111	0.034	0.039	0.014	-0.003
0.021	0.026	0.000	-0.001	0.048	0.024

0.018

0.016

-0.010

CROSS LINED AREAS INDICATE HIGH ?SEGMENT
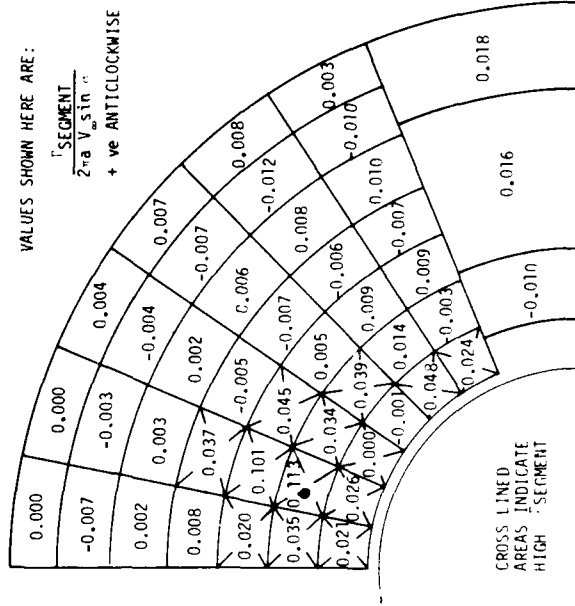
FIG. 4: DISTRIBUTION OF CIRCULATION IN THE LEESIDE QUADRANT FROM A.R.A. FLOW SURVEY TESTS

SIDE VIEW AS IN WIND TUNNEL

Figure 11: PREDICTED AND EXPERIMENTAL SPANWISE LOADING DISTRIBUTIONS - HYBRID FLOW MODEL

Figure 12: PREDICTED LOCAL ANGLE OF ATTACK DISTRIBUTIONS USING HYBRID FLOW MODEL

MENDENHALL & NIELSEN METHOD USED FOR PREDICTION WITH Xs CALCULATED AS FOR A BLUNT BODY
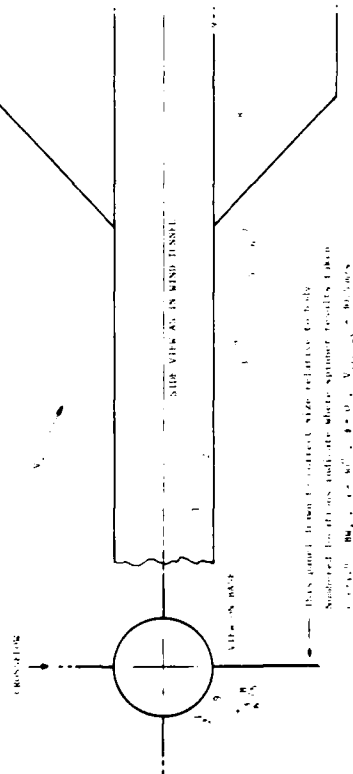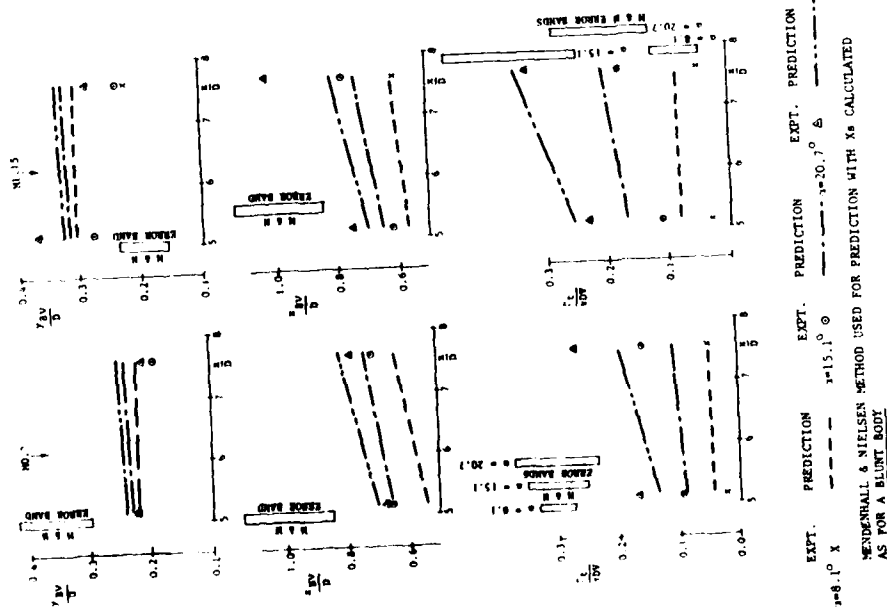
Figure 31: COMPARISON OF EXPERIMENTAL AND PREDICTED BODY VORTEX CHARACTERISTICS FOR A.R.A. SHARP OGIVE-NOSED MODEL

CONFIGURATION BW_F

CONFIGURATION BW_A

PANEL SPANWISE C.P., $\frac{Y_A}{Y_B}$

PANEL SPANWISE C.P., $\frac{Y_A}{Y_B}$
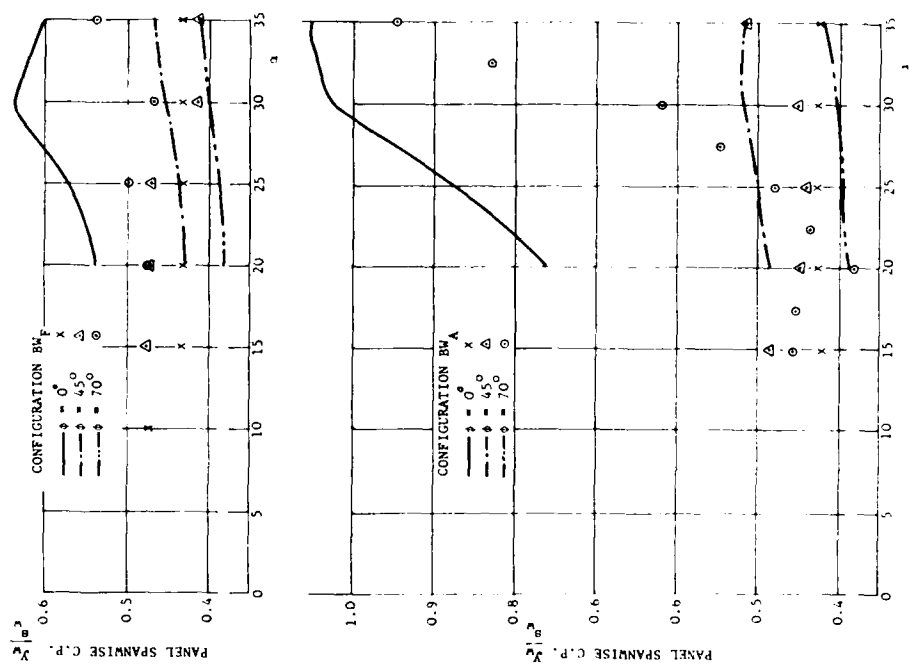
Figure : PANEL SPANWISE CENTRE OF PRESSURE FOR CONFIGURATIONS BW_A, BW_F PREDICTED BY HYBRID METHOD

CONFIGURATION BW_A

HYBRID METHOD   EXPT.   BAe METHOD
$\phi = 0$ ×
$\phi = 45$ ◁
$\phi = 70$ ⊙

C_{NP} PANEL NORMAL FORCE COEFFICIENT (BASED ON BODY AREA)
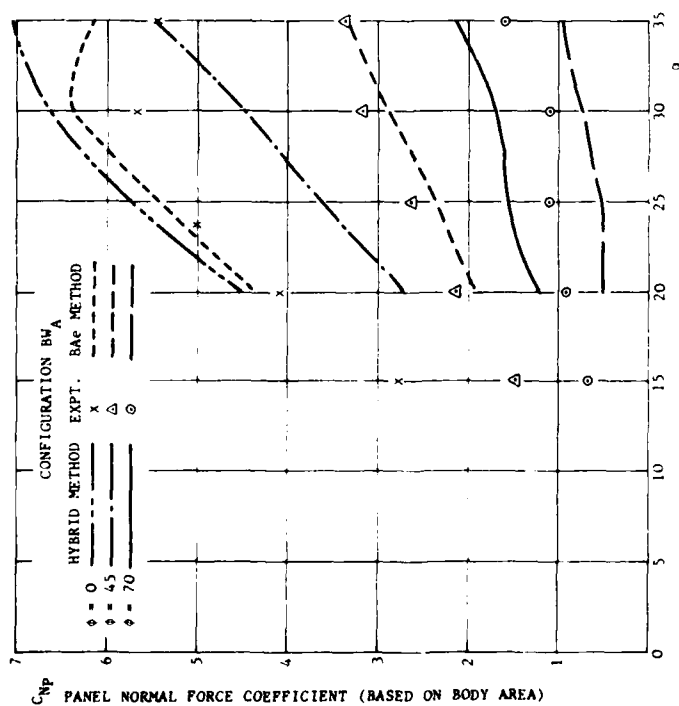
Figure : PREDICTED AND EXPERIMENTAL PANEL LOAD RESULTS - CONFIGURATION BW_A

$\alpha = 20^\circ$

CONFIGURATION BW$_A$
$\phi = 70^\circ$
—— ALTERNATIVE PATTERNS
- - - EXPERIMENT
⊙ EXPERIMENT

L(ξ)

0.5

0

0.5

1.0

ξ

Figure 37 : EFFECT OF DISTRIBUTED VORTEX POSITIONS ON PREDICTED SPANWISE LOADING DISTRIBUTION

$\alpha = 20^\circ$

CONFIGURATION BW$_A$
$\phi = 70^\circ$
—— VORTEX STRENGTH 100%
- - - VORTEX STRENGTH 36%
● EXPERIMENT

L(ξ)

0.4

0.2

0

-0.2

0.5

1.0

Figure 38 : EFFECT OF VORTEX STRENGTH IN THE LEESIDE WAKE ON PREDICTED SPANWISE LOADING DISTRIBUTIONS USING DISTRIBUTED VORTEX PATTERN

TYPICAL OBERKAMPF FEEDING SHEET MODEL AS INCLUDED IN HYBRID METHOD

DISTRIBUTED VORTEX PATTERN 1

$\phi = 70^\circ$

$\phi = 45^\circ$

$\phi = 0^\circ$
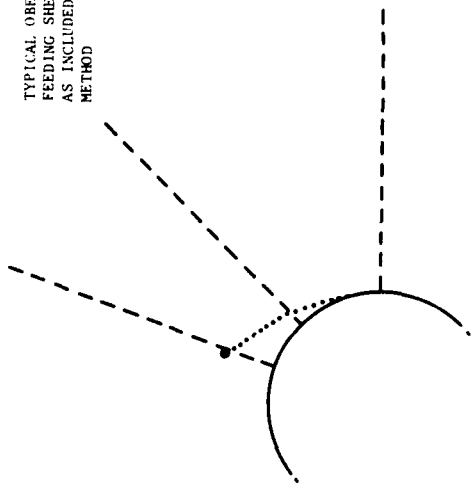
Figure 36 : COMPARISON OF CORE + FEEDING SHEET AND DISTRIBUTED VORTEX MODELS

Figure 4.: PREDICTED AND EXPERIMENTAL SPANWISE LOADING DISTRIBUTIONS - POTENTIAL CROSSFLOW ONLY - NO VORTICES
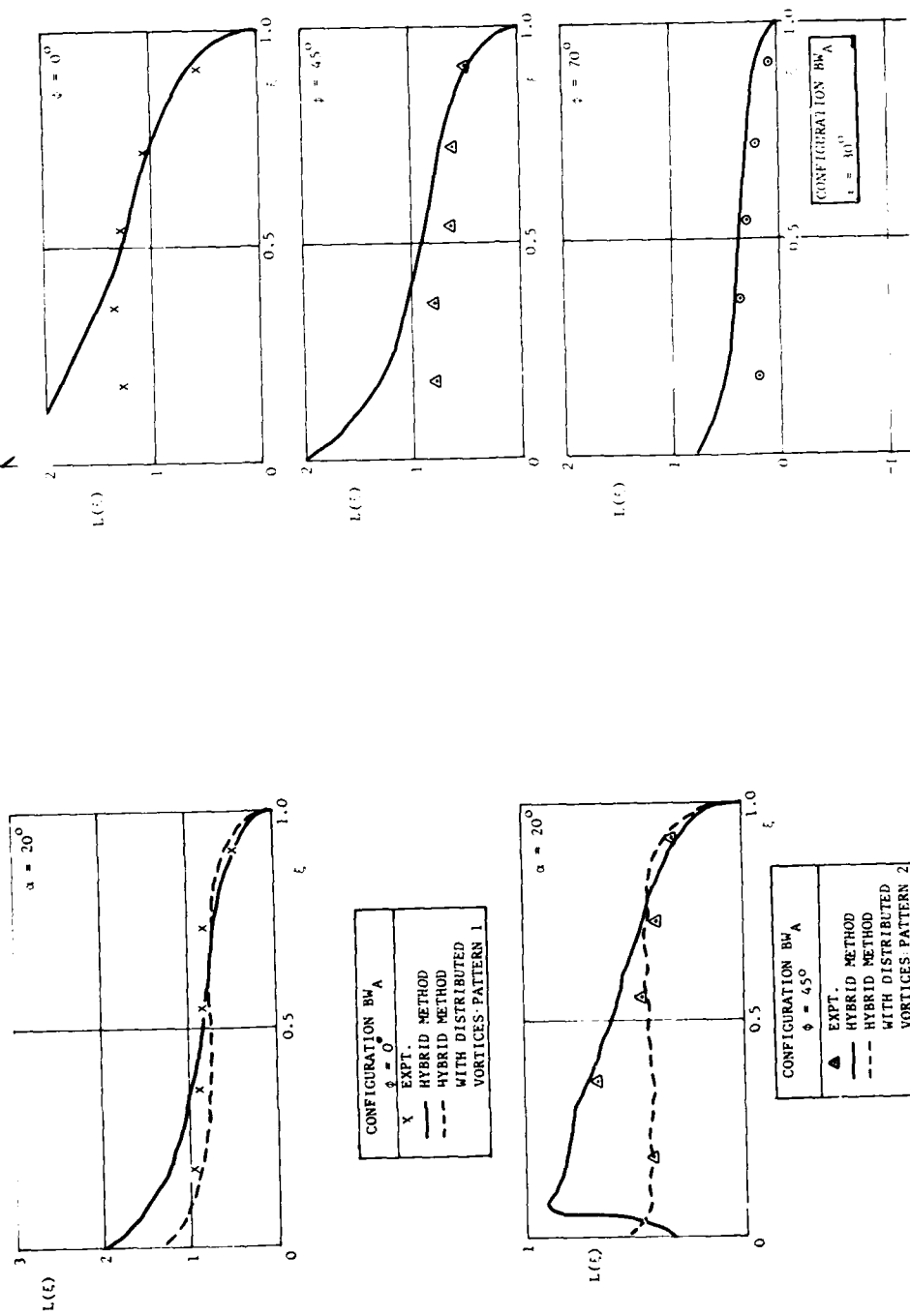
Figure 5.: RESULTS OF USING DISTRIBUTED VORTEX PATTERNS IN HYBRID FLOW MODEL

STRAKE-WING-BODY COMBINATIONS

L. Vigevano
von Karman Institute for Fluid Dynamics
Chaussée de Waterloo, 72
B - 1640 Rhode Saint Genèse, Belgium

SUMMARY

The complex flow fields occurring around a typical strake-wing-body missile configuration at high angle of attack are considered at subsonic and transonic speeds. Force and surface pressure measurements, together with water tunnel visualizations up to 33° incidence were carried out on flat plate trapezoidal wings and strake-wing combinations as well as complete missile configurations to provide a detailed description of the relative flow fields. Emphasis is placed on the improvement in the normal force characteristics due to the addition of the strake, and on the body-wing and wing-body interference mechanism. Compressibility effects are considered.

NOTATION

AR	aspect ratio = $\dfrac{4s^2}{S_w}$
B	body alone configuration
BW	body-wing configuration
BWS	body-wing-strake configuration
c	wing chord
$\bar{c}$	mean wing chord
c_S	strake chord
C_M	pitching moment coefficient : $C_M \dfrac{M}{q_\infty . S_w . \bar{c}}$ or $C_M = \dfrac{M}{q_\infty . S_b . D}$
C_N	normal force coefficient : $C_N = \dfrac{N}{q_\infty . S_w}$ or $C_N = \dfrac{N}{q_\infty . S_b}$
C_p	pressure coefficient = $\dfrac{p-p_\infty}{q}$
D	body diameter
L	total length of the body
M	pitching moment (positive nose-up)
M_∞	free stream Mach number
N	normal force
p	static pressure
P_∞	free stream static pressure
q_∞	free stream dynamic pressure = $\dfrac{1}{2}\rho_\infty U_\infty^2$
R	body radius
Re_c	Reynolds number = $\dfrac{U_\infty \bar{c}}{\nu_\infty}$
Re_D	Reynolds number = $\dfrac{U_\infty D}{\nu_\infty}$
s	wing semi-span
S_b	maximum cross sectional area of the body
S_W	planform area of the trapezoidal wing
S_{WS}	planform area of the wing-strake combination
U_∞	free stream velocity
W	wing alone configuration
WS	wing-strake configuration
X	longitudinal body coordinate, or chordwise wing coordinate
X_S	longitudinal body coordinate, at which the first separation occurs or longitudinal strake coordinate
Y	spanwise wing coordinate
Y_b	lateral coordinate of the body-vortex position
Z_b	vertical coordinate of the body-vortex position
α	angle of incidence
ν_∞	free stream kinematic viscosity
ρ_∞	free stream density

1. INTRODUCTION

The incorporation of the strake-wing concept in modern combat aircraft design has been successful in improving the aerodynamic characteristics of high angle-of-attack aircraft, as shown by several practical examples, such as the General Dynamics F-16. In its basic form, a strake consists of a small slender delta wing fitted ahead of the inner part of the main wing leading edge, having a surface of the order of 10% of the wing surface.

The vortex flow generated from the leading edge of the strake influences to a great extent the flow over the main wing by promoting an induced sidewash that effectively increases the real sweep angle of the wing (Fig. 1), and thus stabilizing the separated flow appearing at high incidence (Fig. 2). A stable separation generates large lift increments, while an unstable separation, which would occur on the wing without strake, leads to lift decay and force fluctuations.

Attempts to model theoretically such a flow field have been successful in predicting these features for aircraft configurations at low speed (Refs. 1,2). They make use of classical vortex theories for slender delta wings (Refs. 3,4) to model the flow over the strake, together with a vortex lattice method or a panel method representing an attached flow over the main wing. Other approaches utilize the concept of the suction analogy and employ an "augmented" term to predict the favourable interference effects observed experimentally (Ref. 5).

For the case of missile configurations there is still a lack of comparable theoretical models because of the larger body-wing interference, although vortex lattice/free vortex methods have been employed (Refs. 6,7). Missile wings are often small aspect ratio flat plates with sharp leading and side edges. Generally their half-span is of the same order as the body radius and they operate in the presence of a long forebody. Separation occurs over the wing already at angles-of-attack of the order of 10°, the wing operates to an important degree within the body boundary layer, and body-wing interference effects are large.

Following the demonstration that strakes added considerable lift to a typical missile configuration (Ref. 8), a research program was initiated with the objective of understanding the physical mechanism which produces this favourable effect. The program plan involved the study of the flow around the individual components of a body-wing-strake configuration as well as selected combinations of those components in such a way as to elucidate the interference effects. The results are presented in a series of VKI reports (Refs. 8-14); a summary of part of the work appears in reference 15. This report collects together all the results presented prior to and following reference 15 and thus serves as a final report on the VKI research dealing with the use of strake on missile configurations.

2. DESCRIPTION OF THE MODELS AND MEASUREMENT TECHNIQUES

The basic missile configuration consists of a ogive-cylinder body of $L/D = 12$ fitted with two main trapezoidal wings of 27° sweepback angle and AR = 2.0 and two triangular strakes of 77°5 sweepback angle and AR = 0.9; it is shown in figure 3 together with the individual elements. The total AR of the strake-wing combination is 1.77. The presence of the body brings the AR for the body-wing configuration to 2.27 and for the body-strake-wing configuration to 1.60. The increment in planform area due to the addition of the strake is 12%.

Separate models were constructed for wind and water tunnel tests. The wings were thin plates with flat leeward surface and sharp leading and side edges. The bevel angle of the edges varied according to the model size; for the models utilized for force measurements and water tunnel flow visualizations it was of 10°, while for the pressure measurements models it was of 15° (wing alone and wing-strake combination) or 30° (complete missile configurations). For pressure measurements the wing and strake leeward surfaces and the missile body were instrumented with pressure taps located along the wing span at five chordwise stations, as shown in figure 4. For the strake-wing model only, an additional station was placed at 90% chord of the strake. In the water tunnel models, the location of the dye injection holes was selected to visualize the body and strake vortices and the flow close to the leading edge of the main wing.

Force and pressure measurements were carried out in the VKI continuous wind tunnel S-1. The test section is 36 cm × 40 cm and includes longitudinal slotted top and bottom walls for transonic operation. Normal force and pitching moment were measured with a two component internal strain gauge balance. Visualization tests were carried out in the VKI water tunnel WT-1. It has a test section of 15 cm × 15 cm and can be run on continuous or blowdown mode. The latter was chosen because it exhibited more stable and uniform flow conditions. Tests were recorded by means of colour photographs and video tapes. The use of water tunnel visualization for comparative purposes with the results obtained in transonic wind tunnel tests might sound illogical; however, it has been established that for flows dominated by large and controlled separation, reasonable similarity does exist (Ref. 16-20). The qualitative information obtained in this way is of great help in understanding the complex flow fields encountered in the high incidence range. A detailed description of the different models and measurement techniques employed can be found in references 8-14.

2.1 Presentation of basic results

The test series carried out for the different configurations are summarized in Table 1, together with information on incidence range, Mach number and Reynolds number. In the following, we will make use of abbreviations to indicate the different configurations:

B : body alone
W : trapezoidal wing alone
WS : trapezoidal wing with strake
BW : complete missile configuration (body with wing) without strakes
BWS : complete missile configuration with strakes.

Force measurements are presented as non dimensional coefficients, C_N and C_M. Total wing area and mean chord length are taken as reference quantities when a wing model is tested, while the body cross sectional area and the body diameter are used for the complete missile configurations. The moment reference point is taken at 1/3 of the basic trapezoidal wing

chord as indicated in figure 3. Pressure measurements are presented in the form of span-
wise C_p distributions on the leeward side of the models, at the chordwise stations
described in figure 4.

3. DESCRIPTION OF THE FLOW FIELD OVER THE SINGLE ELEMENTS

In this section the results of the water tunnel visualizations and the measured pres-
sure distributions are used to provide a description of the flow field around the configu-
rations B, W and WS with angles of attack up to 30°.

3.1 Body alone (B)

The flow field over a long ogive cylinder body is well known and does not need to
be described in detail here. The typical non linear dependence of C_N on α, due to the
pair of well organized vortices lying above the body, was recorded in the wind tunnel
tests. Two points are worth mentioning : (a) for the various models tested, the range of
incidence was within the range of symmetrical steady vortex shedding (Ref. 21); (b)
measurements of the vertical and lateral position of the vortex core obtained from the
water tunnel visualizations and shown in figures 5 and 6, together with low speed wind
tunnel data (Ref. 22) and with a correlation formula (Ref. 23), show that the expected
influence of Reynolds number of these quantities is small enough to validate the qualita-
tive information obtained from these tests.

3.2 Wing alone (W)

The flow over flat-plate trapezoidal wings with small sweepback angle is characterized
already at $3° \div 4°$ incidence by a three dimensional bubble-type separation at the leading
edge. The separated streamlines are able to reattach only near the wing centerline, as
can be inferred from the pressure distribution of figure 7. The decrease in suction at
the 50% chord station is localized only over the inner 30% of the span. Water tunnel
visualizations show the presence of an induced sidewash in the bubble and small tip vor-
tices (not detectable from pressure results because taps could not be placed close to the
side edge). With increasing incidence, the bubble reattachment line travels smoothly but
rapidly towards the wing trailing edge (Fig. 8) and finally bursts at only $10° \div 15°$ inci-
dence. From C_N-α curve of figure 10 we can see how during the extension of the bubble the
rate of increase of normal force becomes negative to reach then a relative maximum at the
bursting point.
At angle of attack above 15° the pressure distribution over the entire suction side
of the wing is nearly uniform indicating a fully separated flow (Fig. 8). With increas-
ing incidence there is a decrease of suction level up to 24° and then a small increase
with α to 33° as shown in figure 9 where only the spanwise distributions at 18% chord are
plotted for clarity. The effect of increasing M_∞ is to decrease the incidence at which a
fully separated flow occurs. This is clearly seen on the C_N-α curve of figure 10 and is
also confirmed by pressure measurements. The bubble bursting appears at a smaller inci-
dence for $M_\infty = 0.83$ than for $M_\infty = 0.42$ and is associated with a smaller suction level and
normal force. The behaviour of the pitching moment is different : in looking at the curve
C_M-α of figure 11 no obvious effect of compressibility is present and the smooth character
of the transition between bubble and fully separated flow is evidenced.

3.3 Strake-trapezoidal wing (WS)

The flow field over a strake-wing configuration is much more complex than the wing
alone case. The flow over the strake itself presents all the characteristics of the flow
over a delta wing of small aspect ratio (well organized leading edge vortices, large and
highly localized suction peaks) for all the incidences tested. However, the strake-vortex
and the flow occurring on the main wing offer features which depend in an important way on
the incidence.
At incidence of $3° \div 4°$, a weak strake-vortex is evident (Fig. 12). When it reaches
the junction between the strake and wing leading edges, instead of following a raywise
direction, it is partially entrained along the leading edge of the main wing. At the tip
of the wing these streamlines are swept back towards the free stream direction by the tip
vortices. The clear regions at the wing tips in figure 12 provide an indication of the
size of the tip vortices. In the incidence range $7 \div 15°$ the sidewash induced by the
increasing strength of the strake-vortex (Fig. 13) triggers another well organized vortex
generated at the leading-edge kink. This kink-vortex has the same sense of rotation as
the strake-vortex and goes between the latter and the wing leading edge. The pressure
distribution of figure 15 shows clearly the presence of two large suction peaks at the 18%
chord station. Eventually the two vortices merge, as for $\alpha = 15°$ in figure 16, where it
is also possible to observe the triangular region of reattached flow close to the wing
centerline and lying between the two strake-vortices. The strength of the kink-vortex
appears to be larger than that of the strake-vortex itself. Water tunnel visualizations
(Fig. 14) confirm these observations and show how the kink-vortex bursts very soon, in
the picture approximately above the injection hole. As discussed in references 1 and 24,
the sidewash induced by the strake-vortex at the leading edge kink has the effect of in-
creasing the effective sweepback angle of the main wing, and the presence of a secondary
vortex has been demonstrated by several authors (Refs. 24-26) on strake-wing combinations
for aircraft configurations with AR = 3 and 32° sweepback angle. It is shown here that
the same phenomenon occurs also when the strake is coupled with an AR = 2 trapezoidal
wing with 27° sweepback angle. Increasing the angle of attack above 15°, the effects of
the kink-vortex on the pressure distribution at 18% chord suddenly disappear; evidently
the bursting point of this vortex has reached the kink. The resulting change in pressure

distribution is seen in figure 16. There seems to be a switch from a strong local effect to a more general one of the strake vortex on the whole span of the wing. This is related to the fact that the strake vortex starts bursting at the wing trailing edge (Fig. 17) and its influence spreads over the entire span. From the C_N-λ curve of figure 25 it is not possible to conclude that the breakdown point jumps forward, as in the case of a delta wing in compressible flow (Ref. 27). In the water tunnel the breakdown point is observed to travel gradually upstream of the trailing edge (Figs. 18-20), a general feature of vortex bursting in incompressible flow (Refs. 28-30). The asymmetrical outboard spreading of the breakdown pocket is essentially due to the adverse pressure gradient encountered in the spanwise direction towards the wing centerline.

At incidences above $25° \div 27°$, when the breakdown pocket approaches the wing leading edge, another change in pressure distribution shape occurs at the forward part of the wing (18% chord station), as seen in figure 21. The local effect of the strake-vortex as shown by the inboard suction peak, is more pronounced. At the same incidence in the water tunnel visualizations the flow over the main wing exhibits a strong sidewash parallel to the wing leading edge. This is not very clearly seen in the photographs of figures 19 and 20, but it becomes evident when observed on video tapes which were systematically employed. Such a flow appears to be qualitatively unchanged both in the water tunnel and wind tunnel experiments when increasing incidence up to the maximum angle considered, i.e., $33°$.

An increase of M_∞ acts to decrease, for a fixed incidence, the strength of the strake-vortex, a consistent result for a slender delta wing (Fig. 22). Compressibility effects on the overall flow field are less easy to assess, e.g., comparing figure 23 with figure 24, in which the spanwise pressure distributions at 18% chord are plotted at different angles of attack, a change in M_∞ corresponds to a change in the value of incidence at which the different types of flow fields are present, so that a direct comparison at a fixed incidence is not necessarily meaningful. The overall normal force increases with increasing M_∞ (Fig. 25), at least up to $18°$ incidence. The kink-vortex appeas to be stronger at low incidence, i.e., $7°$ (Fig. 26) for the higher M_∞, and bursts at lower λ. From the pressure plots of figures 27 and 28, it is possible to see how an incremant in M_∞ decreases the suction level in the forward part of the wing and makes the pressure distribution more uniform chordwise.

3.7 Comparison between W and WS configurations - Effect of the strake -

From the force and pressure measurements it is possible to make an estimation of the effects of fitting a flat plate trapezoidal wing with a strake. At low-to-moderate incidences the presence of the strake induces very high local suction peaks on the forward part of the main wing but does not improve the overall aerodynamic characteristics (Fig. 29). The explanation is that at these small angles of attack the wing alone exhibits a rather organized leading edge separation, and the presence of the strake-vortices, while inducing a beneficial effect on the forward part of the wing, induces a zone of relatively low suction in the main and aft part. That the center of pressure moves forward is confirmed by the observed change in the moment charactertistics (Fig. 30). At higher incidences, while the flow on the wing alone begins to be fully separated, on the strake-wing combination the flow is stabilized by the presence of the strake-vortex which induces a high gain of Suction near the leading edge. Thus the WS configuration begins to exhibit higher values of C_N than W, and this at different values of α for different M_∞, according to the compressibility effect previously discussed. As a result the strake is effective at lower incidence for a higher M_∞ (Fig. 29). Increasing further the incidence, the positive influence of the strake-vortex is spread over the entire wing, and the suction level for the WS configuration is everywhere higher than for W alone. The addition of the strake is thus effective in improving C_N at high angles of attack at the expense of shifting forward the center of pressure.

4. DESCRIPTION OF THE FLOW FIELD OVER COMPLETE MISSILE CONFIGURATIONS - INTERFERENCE EFFECTS

In this section the description of the flow field for the two complete configuration, BW and BWS, is made on the basis of the previous description of the single elements. No quantitative comparison of aerodynamic characteristics between complete configurations and single elements is possible due to the model geometries. Nevertheless, a qualitative analysis of the wing-body and body-wing interference effects, based on pressure measurements and flow visualization, is attempted. Finally, direct comparison between BW and BWS configurations will show the effect of adding the strake to the complete missile configuration.

4.1 Body-wing configuration (BW)

Two observations of a general nature can be made :
- the crossflow induced by the long forebody increases the actual angle of incidence as seen by the wing, as indicated by the fact that already at $11°$ incidence the flow over the wing is fully separated (flat and uniform pressure distribution of Fig. 31);
- the presence of the lifting panels induces an upstream upwash and a downstream down-wash that greatly influence the suction level on the body at the locations corresponding to the wing root.

The first effect has, at moderate angle of attack, a negative influence on the suction exerted on the wing : the three dimensional, relatively well organized separation that was present for the W alone does not exist for BW configuration resulting in a lower overall suction (Fig. 31). Another detrimental effect for the configuration is given by the upwash induced by the wing which lowers the suction on the part of the body located just in front of the wind leading edge (see sections E and F in figure 31). As the

visualization of the body boundary-layer shows (Fig. 34), the streamlines are first swept inboard, and then, passing the wing leading edge, are sucked strongly outboard into the wing. The latter is found to be a favourable wing-body interference effect : the body boundary layer is sucked towards the wing where it finds the higher suction level of the separated flow. This in turn increases the suction level on the body bringing it locally to the wing value (see sections G, H and I in Fig. 31). The body vortices in this inci-dence range (11°-15°), as noted by direct observation, are not very much influenced by the presence of the wing, undergoing only a slight upwash and inboard sidewash in front of the wing, and a downwash and outboard sidewash having passed the wing-leading-edge, confirming the general picture of this flow field.

At high incidence the interference mechanism slightly changes, still retaining the strong local effect on the body pressure distribution close to the wing root. The body vortices begin to become unstable and then to burst. The bursting point moves upstream towards the wing trailing edge with increasing incidence. This negative effect, however, is compensated by the increase in suction featured by the fully separated flow over the wing (Figs. 32 and 33). For $\alpha > 20°$ the suction on the wing for BW becomes larger than for W alone. In addition, a higher suction level on the wing enhances the mechanism of suction of the body boundary layer.

Compressibility affects the complete configuration through the behaviour of the lifting panels : the inflection in the C_N-α curve of figure 36 representing the onset of fully separated flow on the wing occurs at a lower α for the higher M_α considered.

4.2 Body-strake-wing configuration (BWS)

The flow field over the body-strake-wing configuration retains the same two basic characteristics already evidenced for the BW configuration : an increase of the actual incidence as seen by the wing due to the crossflow, and the upwash-downwash caused by the lifting panels. However, this last effect is now altered. It can be seen in figure 35 that the streamlines on the body are sucked strongly by the strake-vortex onto the strake surface and, passing below the vortex itself, pass outwards to the wing tip. The detri-mental effect of the upwash is reduced and a high local suction is generated on that part of the body corresponding to the strake and the forward part of the wing (see sections F and G in Fig. 31). As observed for the WS case on the aft part of the wing (50% and 80% chord), there is a region of lower suction, located inboard of the strake vortex. This region influences the body boundary layer reducing the entrainment mechanism and hence the favourable interference (section I in Fig. 31). The influence of the lifting panels on the body vortices is again similar to that of the previous configuration : for low and moderate incidences the body vortices exhibit an upwash-inboard sidewash ahead of the strake and then a downwash-outboard sidewash having passed the 50% chord line (Fig. 37). At incidences greater than 15° the body vortices become stronger and are less affected when passing close to the wing root, but start to become unstable and finally burst (Fig. 38). The bursting point as observed in the water tunnel travels gradually upstream (Fig. 39) with increasing incidence without reaching the wing trailing edge. On the lifting panels it was not possible to detect the presence of the kink-vortex. In the water tunnel tests the difficulty was due to the small model size, while pressure measure-ments at incidences lower than 11° were not available and, due to the increase in angle of attack caused by the crossflow, the incidence range for which the kink-vortex should exist is certainly lower than 11°. The bursting point of the strake-vortex reaches the wing trailing edge at 9°-10°. Up to that angle the strake-vortex pattern remains closer to the body than it was for the WS case. When the breakdown point moves forward for increasing incidences, the breakdown pocket spreads over the entire wing span (Fig. 37), and the region between the pocket and the wing leading edge decreases gradually, which results finally in a strong sidewash along the wing leading-edge as seen in figure 39. This sidewash induced by the strake-vortex is more effective in the BWS case than in the WS case because the body-vortex and the strake-vortex act together and the strake-vortex is stronger in the BWS configuration due to the increased effective α. This results in a flow close to the wing leading edge that is fed by the body boundary layer and then more organized and more uniform. Confirmation is obtained by the analysis of the pressure measurements plotted in figures 32 and 33. A large zone of high suction, the value of which is comparable to that due to the strake-vortex, is spread along the entire span of the wing at 18% chord, and its value appears to be considerably larger than for the single WS element.

Compressibility effects appear not to be significant for the BWS configuration : in both C_N-α and C_M-α plots of figures 40 and 41 it is not possible to detect a marked M_α influence. Only in the incidence range $0 \div 20°$, the normal force seems to be slightly larger with increasing M_∞, as it was for the WS combination.

4.3 Comparison between BW and BWS configurations - Effect of the strake -

The improvement in normal force characteristics obtained by adding the small strake is confirmed by direct measurements (Fig. 42) and by the analysis of the pressure distri-butions plotted in figures 31-33. The strake appears to be effective at a lower incidence when increasing M_∞. The improvement is summarized in figure 43 which plots the fractional increase in normal force coefficient with respect to the basic configuration versus incidence. The fractional gain due to the strake can be as high as 30%, and again the M_α effect is noticed. This high gain is explained not only by the re-energization of the fully separated flow on the wing by the strong and well organized strake-vortex, but also, keeping mind the interference mechanism described in the previous sections, by a syner-getic effect between the body-wing interference and the strake-vortex on the main wing flow. As a result, the addition of a small strake is more effective for the complete missile configuration than for the wing alone. The strake has the effect of shifting forward the center of pressure, as shown by figure 44, but this negative effect does not

harm significantly the pitching moment characteristics of the complete configuration
which are determined essentially by the missile body.

5. CONCLUSIONS

The improvement of the aerodynamic characteristics of a typical missile configura-
tion at subsonic and transonic speeds by the addition of a small triangular strake has
been explained as a result of the detailed description of the flow fields over different
single wing elements and complete configurations and by the analysis of the interference
effects. The understanding of the properties of such flow dominated by large separated
regions does not present an immediate quantitative aspect but does provide useful infor-
mation for practical designs, taking into account the difficulties encountered in trying
to provide them by means of theoretical or numerical approaches. In conclusion, the
following observations can be made :
- The interaction between the strake vortex and the separated flow on the main wing
depends on the incidence range and on the strake vortex strength. With increasing inci-
dence, a strong local effect coupled with the induction of a secondary vortex is followed
by a larger scale and more effective diffuse interaciton.
- The breakdown of the strake-vortex on a strake-wing combination does not have the
negative effect generally associated with conventional delta wings; instead it enhances
the mixing with the circulating flow over the wing and re-energizes it.
- The interference between body and wing panels has a strong local effect on the body
boundary layer in the region of the wing root, while the body vortices become affected
by the panel wakes at incidences larger than 20°, when bursting begins to occur.
- The presence of the strake modifies the local wing-body interference mechanism. The
negative effect on the body pressure distribution due to the upwash induced by the wing
is reduced and compensated by the lateral suction of the body boundary layer produced by
the strake-vortex.
- The body-wing interference effects and the strake-vortex effects on the fully separated
flow combine in a synergetic way through the suction of the body boundary-layer and the
vortex induced sidewash over the wing.
- The presence of a body of large diameter compared to the wing span stabilizes the flow
field over the lifting panels in such a way as it does not change qualitatively witn
incidence.
- The most relevant compressibility effect influencing both complete missile configura-
tions and wing elements is that an increase of M_∞ shifts towards lower α the improvement
in C_N characteristics due to the addition of the strake. No other effect can be seen on
the complete configurations, while on the single elements (wing alone and strake-wing
combination) compressibility acts in a qualitative way changing the incidence values at
which different types of flow field are present : the general trend is again a shift
towards a lower α when M_∞ increases.

REFERENCES

1 FIDDES, S.P. & SMITH, J.H.B.: Strake induced separation from the leading edges of
wings of moderate sweep. "High Angle of Attack Aerodynamics", AGARD CP 247, 1978,
pp 7-1/7-12.
2 CHAKRABARTTY, S.K. & BASU, B.C.: Approximate analysis of strake wings at low speeds.
AIAA J., Vol. 17, No. 4, April 1979, pp 432-434.
3 BROWN, C.E. & MICHAEL, W.H.: On slender delta wings with leading edge separation.
J. Aero. Sci., Vol. 21, No. 10, 1954, pp 690-694 and 706; also NACA TN 3430, 1955.
4 SMITH, J.H.B.: Improved calculations of leading edge separation from slender delta
wings. RAE TR 66070, 1966.
5 LAMAR, J.E. & LUCKRING, J.M.: Recent theoretical developments and experimental
studies pertinent to vortex flow aerodynamics - with a view towards design. "High Angle
of Attack Aerodynamics", AGARD CP 247, 1978, pp 24-1/24-31.
6 NIKOLITSCH, D.: Calculation of pressure distributions, forces and moments on cruci-
form wing body combination up to high angles of attack. AIAA P 81-0397, Jan. 1981.
7 DINI, D.; PSARUDAKIS, P.; VAGNARELLI, F.: Influenza della fusoliera su ali a carat-
teristiche aerodinamiche non lineari in missili su'sonici (Influence of the body over
wing featuring non-linear aerodynamic characteristics for subsonic missiles). Paper
presented at V° Congresso Nazionale della Associazione Italiana di Aeronautica e Astro-
nautica, Milano, 22-26 Ottobre 1979.
8 MOVASSAGHIE, B.: Experimental study of a wing with strake for a missile configura-
tion in high subsonic and transonic flows. VKI PR 1976-03, 1976.
9 ZARGHAMI, A.: Aerodynamic characteristics of a missile configuration featuring a
wing with various strakes in subsonic and transonic flows up to high angles of incidence.
VKI PR 1977-07, 1977.
10 AKCAY, M.: The flow field over a missile configuration fitted both with and without
strakes in transonic flow up to high angles of incidence. VKI PR 1978-01, 1978.
11 VIGEVANO, L.: Effects of strakes on low aspect ratio trapezoidal wings for missile
configuration in compressible flow. VKI PR 1979-05, 1979.
12 DEMURIE, F.: Investigation of the interference effects in the flow field around a
body-strake-wing missile configuration. VKI PR 1980-23, 1980.
13 DEMURIE, F.; MUYLAERT, J.M.; WENDT, J.F.: Investigation on the interaction between
body vortices and the strake wing panels of a missile configuration. VKI IN 63, 1980.
14 GREFF, E.: Flow visualization on missile configuration featuring a basic trapezoidal
wing and an improved strake wing configuration. U-VKI 1977-24, 1977.
15 ACKAY, M.; RICHARDS, B.E.; STAHL, W.; ZARGHAMI, A.: Aerodynamic characteristics of a
missile featuring wing with strakes at high angles of attack. "High Angle of Attack
Aerodynamics", AGARD CP 247, 1978, pp 20-1/20-7.
16 WERLE, H.: Le tunnel hydrodynamique au service de la recherche aérospatiale.
ONERA Publication 156, 1974.

17 WERLE, H.: Application of hydrodynamic visualization to the study of low speed flow around a delta wing aircraft. ONERA TP 1977-81, 1977.
18 WERLE, H.: Hydrodynamic visualization on streamlines bodies of vortex flows particular to high angles of attack. ONERA TP 1980-106, 1980.
19 ERIKSON, G.E.: Water tunnel flow visualization : insight into complex three dimensional flow fields. J. of Aircraft, Vol. 17, No. 9, September 1980, pp 656-662.
20 LAMAR, J.E.: Comment on 'Water tunnel flow visualizations : insight into complex three dimensional flow fields'. J. of Aircraft, Vol. 18, No. 8, August 1981, p 704.
21 WARDLAW, A.9.: High angle of attack missile aerodynamics. "Missile Aerodynamics", AGARD LS 98, 1979, pp 5-1/5-53.
22 GROSCHE, F.-R.: Windkanaluntersuchung des Wirbelsystems an einem angestellten schlanken Rotationskörper ohne und mit Tragflügel. Z. Flugwiss., Bd 18, Heft 6, 1970, pp 208-217.
23 MENDENHALL, M. & NIELSEN, J.: Effect of symmetrical vortex shedding on the longitudinal aerodynamic characteristics of wing body tail combinations. NASA CR 2473, 1975.
24 WEDEMEYER, E.H.: Stable and unstable vortex separation. "High Angle of Attack Aerodynamics", AGARD CP 247, pp 13-1/13-10.
25 WHITE, R.P.: Wing vortex lift at high angles of attack. "Prediction of Aerodynamic Loading", AGARD CP 204, 1978, pp 9-1/9-12.
26 LIN, M.J.: LÜ, Z.Y.; QIU, C.H.; SU, W.H.; GAO, W.H.; DENG, X.Y.; XIONG, S.W.: Flow patterns and aerodynamic characteristics of a wing strake configuration. J. of Aircraft, Vol. 17, No. 5, 1980, pp 332-338
27 MUYLAERT, J.M.: Effect of compressibility on vortex bursting on slender delta wings. VKI PR 1980-20, 1980.
28 WERLE, H.: Sur l'éclatement des tourbillons. ONERA NT 175, 1971.
29 WENTZ, W.H. & KOHLMAN, D.L.: Vortex breakdown on slender sharp edged wings. J. of Aircraft, Vol. 8, No. 3, March 1971, pp 156-161.
30 EARNSHAW, P.B.: Measurements of the vortex breakdown position at low speed on a series of sharp edged symmetric models. RAE TR 64047, 1964.
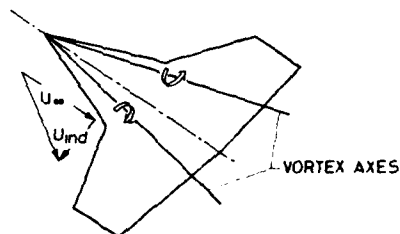
Fig.1   Sidewash velocity component on the main wing induced by the strake

Fig.2   Influence of the strake vortex on the separated flow over the main wing
$M_\infty = 0.8, \alpha = 24°$ (Ref.11)
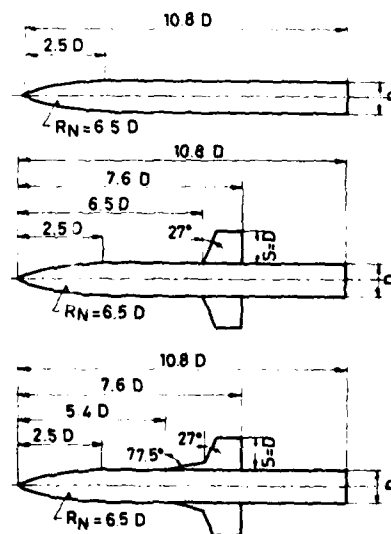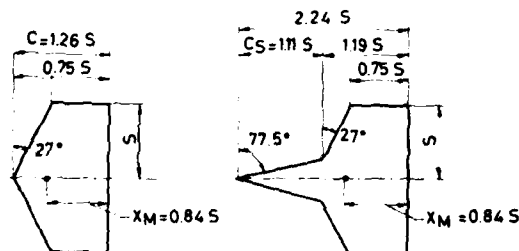
Fig.3   Schematic of the different configurations tested
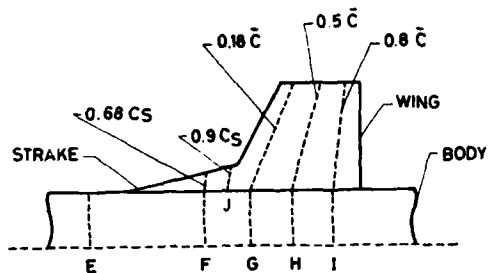
Fig.4   Schematic of the central part of the
model illustrating the position of the rows
of pressure holes
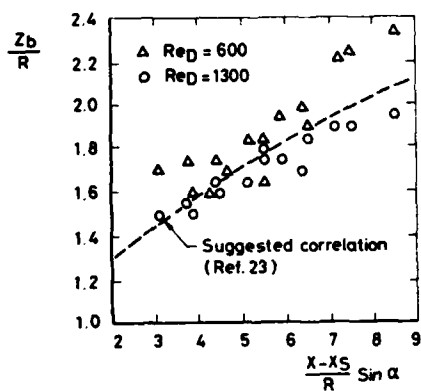
Fig.5   Body vortex vertical position (Ref.13)
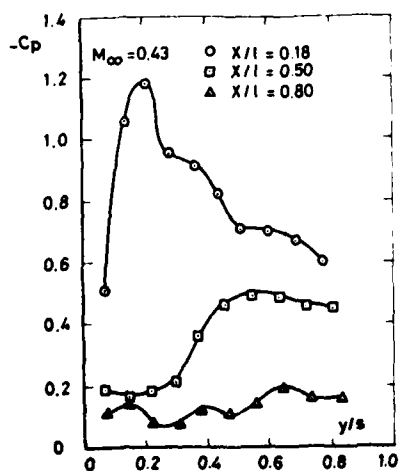
WATER TUNNEL DATA
(ref.13)

$Re_D = 600$ $\varphi_2 = 17.5°$
$Re_D = 1300$ $\varphi_3 = 18.8°$

	α	φ	Re_D
△	20°	15.3°	600
○	25°	17.8°	600
□	30°	16.4°	600
▲	20°	18.0°	1300
●	25°	19.0°	1300
◖	30°	19.0°	1300

WIND TUNNEL DATA
(ref.22)

$Re_D = 5 \times 10^5$
$\varphi_1 = 16°$

	α	φ
◆	-20°	15.5°
▽	-15°	16.5°
▷	-10°	15.5°
×	-7°	13.5°
◆	-20°	
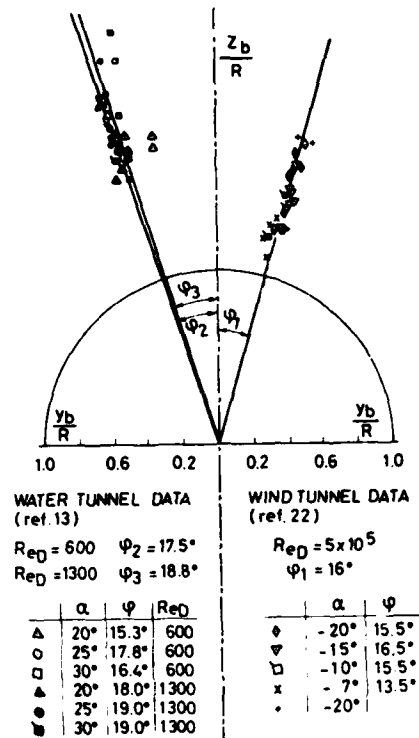
Fig.6   Effect of Reynolds number on the
vortex center position (Ref.12)

Fig.7   Spanwise pressure distributions on the
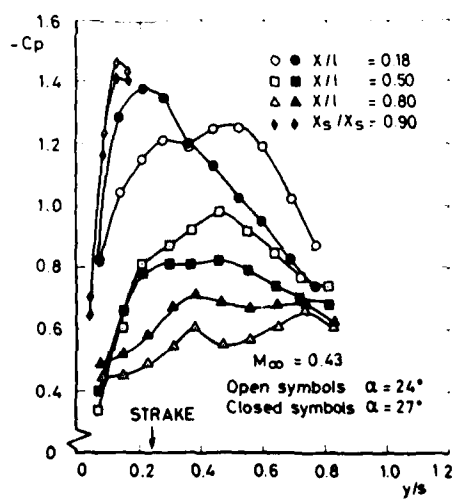wing alone configuration $M_\infty = 0.43, \alpha = 7°$ (Ref.11)
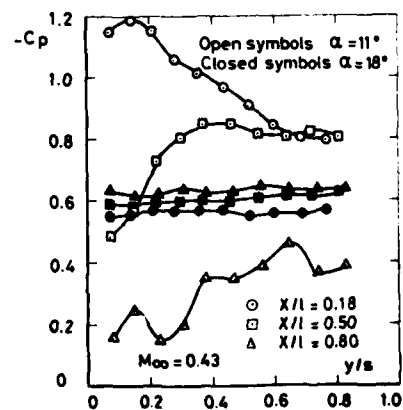
Fig.8   Spanwise pressure distributions
on the wing alone configuration
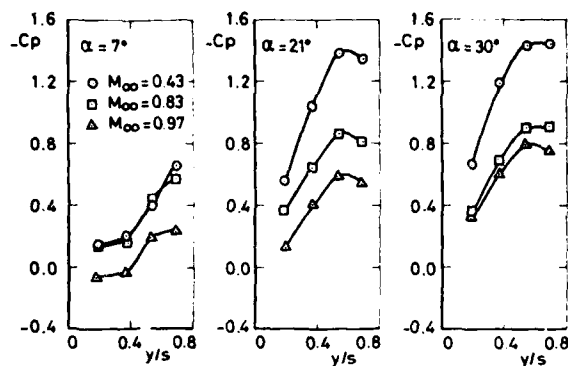$M_\infty = 0.43, \alpha = 11°$ and $\alpha = 18°$ (Ref.11)
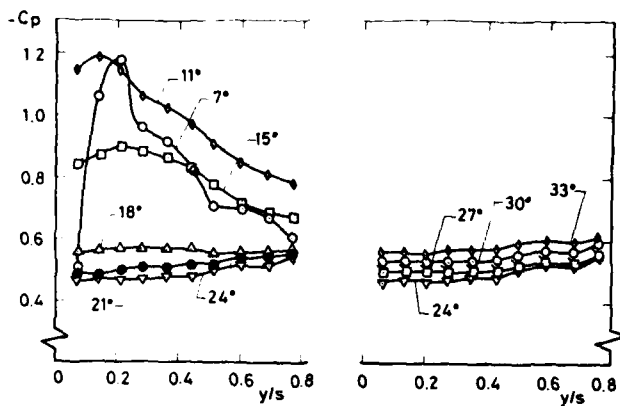
Fig.9   Variation with incidence
of the spanwise pressure
distribution at $\frac{x}{c} = 0.18$ on the
wing alone configuration
$M_\infty = 0.43$ (Ref.11)
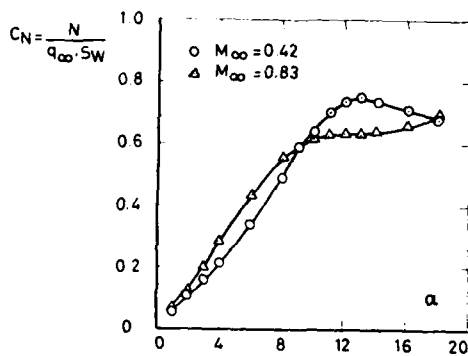
$C_N = \dfrac{N}{q_\infty \cdot S_W}$

○ $M_\infty = 0.42$
△ $M_\infty = 0.83$

$C_M = \dfrac{M}{q_\infty S_W \bar{c}}$

○ $M_\infty = 0.42$
△ $M_\infty = 0.83$

Fig.11   Pitching moment coefficients for the
wing alone configuration as a function of
incidence (Ref.8)
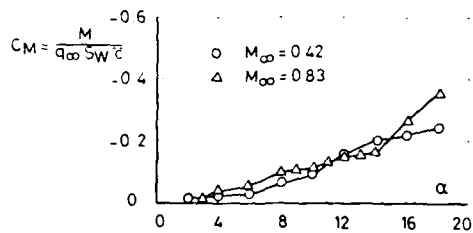
Fig.10   Normal force coefficients for the wing
alone configuration as a function of incidence
(Ref.8)

Fig.12   Water tunnel visualization of the flow
over the wing strake configuration
$Re_{\bar{c}} = 2600, \alpha = 3°$ (Ref.12)

Fig.13   Water tunnel visualization of the flow
over the wing strake configuration
$Re_{\bar{c}} = 2600, \alpha = 7°$ (Ref.12)

Fig.14 Water tunnel visualization of the kink vortex on the wing strake
configuration -- $Re_{\bar{c}} = 10^4$, $\alpha = 7°$ (Ref.12)
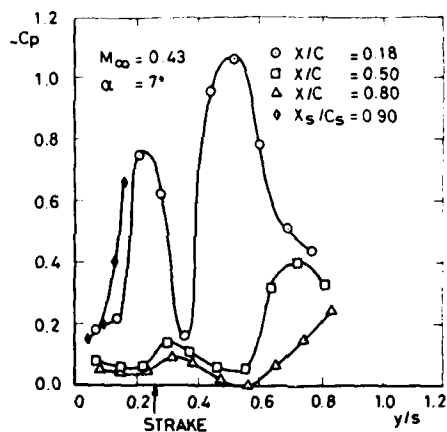
Fig.15 Spanwise pressure distributions on
the wing strake configuration
$M_\infty = 0.43$, $\alpha = 7°$ (Ref.11)
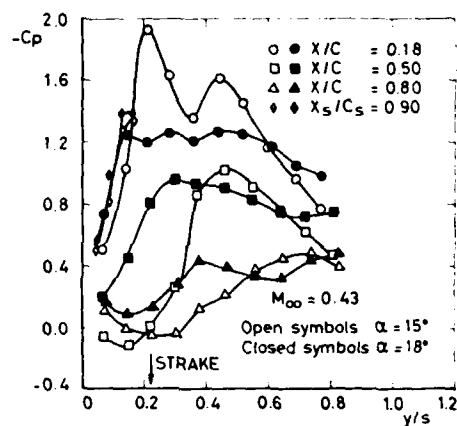
Fig.16 Spanwise pressure distributions on
the wing strake configuration
$M_\infty = 0.43$, $\alpha = 15°$ and $\alpha = 18°$ (Ref.11)
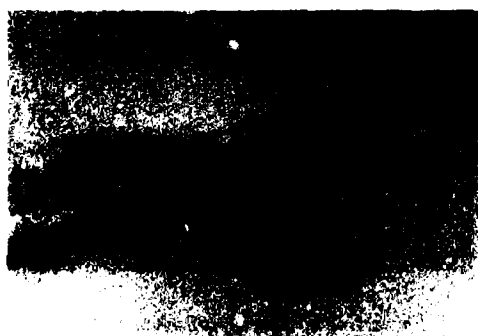
Side view

Top view

Fig.17 Water tunnel visualization of the flow over the wing strake
configuration -- $Re_{\bar{c}} = 2600$, $\alpha = 15°$ (Ref.12)

Fig.18 Water tunnel visualization of the flow
over the wing strake configuration
Re$_c$ = 2600, α = 20° (Ref.12)

Fig.19 Water tunnel visualization of the flow
over the wing strake configuration
Re$_c$ = 2600, α = 25° (Ref.12)

Side view
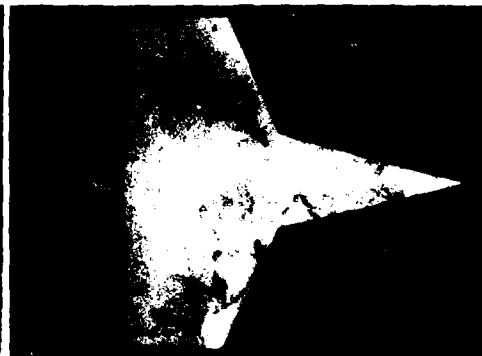
Top view

Fig.20 Water tunnel visualization of the flow over the wing strake configuration
Re$_c$ = 2600, α = 30° (Ref.12)

		X/l = 0.18
O	●	X/l = 0.50
□	■	X/l = 0.80
△	▲	Xs/Xs = 0.90

M_∞ = 0.43
Open symbols α = 24°
Closed symbols α = 27°

STRAKE

Fig.21 Spanwise pressure distributions
on the wing strake configuration
M_∞ = 0.43, α = 24° and α = 27° (Ref.11)

Fig.22 Spanwise pressure distributions on the strake at x_s c_s = 0.90 for different incidences and different Mach numbers (Ref.11)

Fig.23 Variation with incidence of the spanwise pressure distribution at $\frac{x}{c}$ = 0.18 on the wing strake configuration M_∞ = 0.43 (Ref.11)
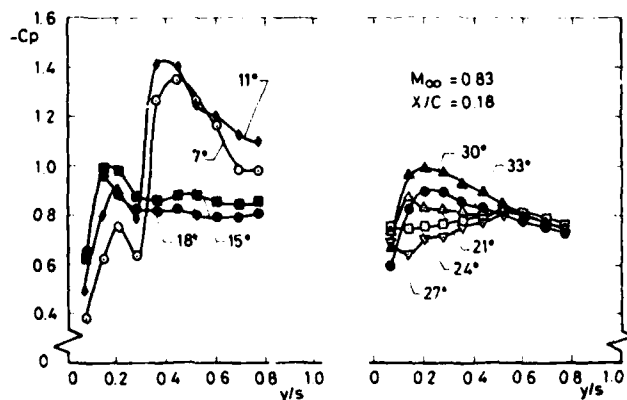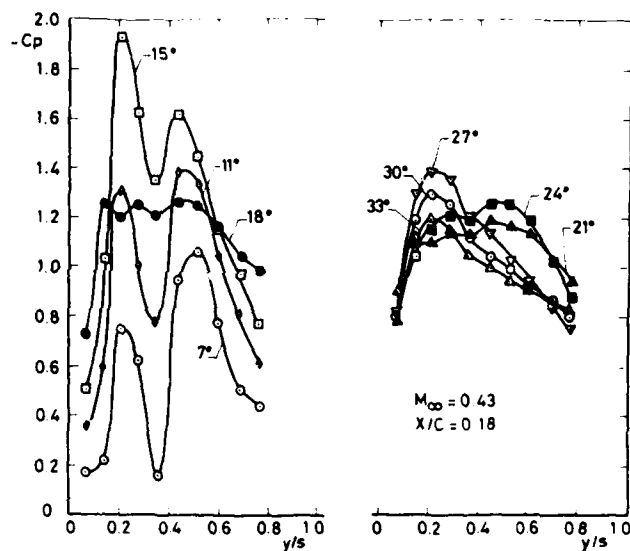
Fig.24 Variation with incidence of the spanwise pressure distribution at $\frac{x}{c}$ = 0.18 on the wing strake configuration M_∞ = 0.83 (Ref.11)
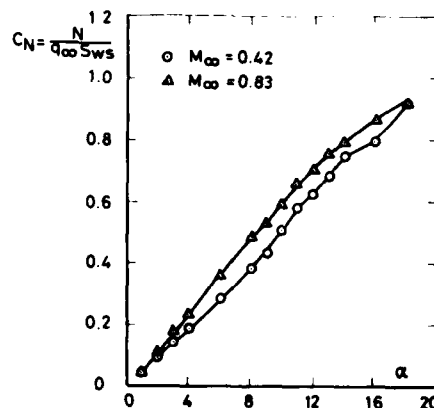
Fig.25 Normal force coefficients for the wing strake configuration
as a function of incidence (Ref.8)
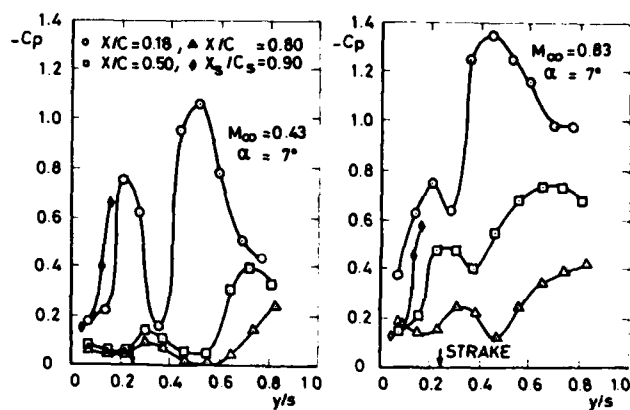
Fig.26 The effect of compressibility on the spanwise pressure distributions
over the wing strake configuration $\alpha = 7°$ (Ref.11)
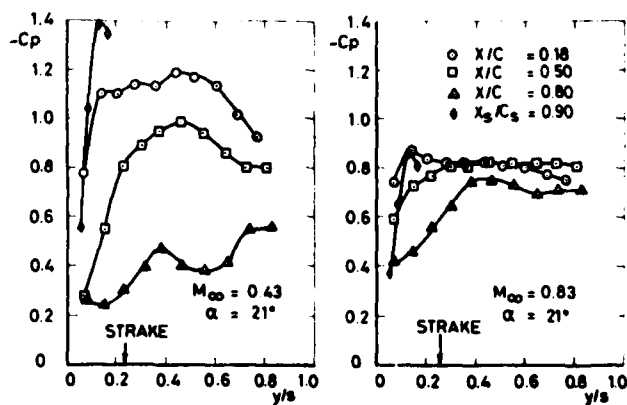
Fig.27 The effect of compressibility on the pressure distributions over
the wing strake configuration $\alpha = 21°$ (Ref.11)
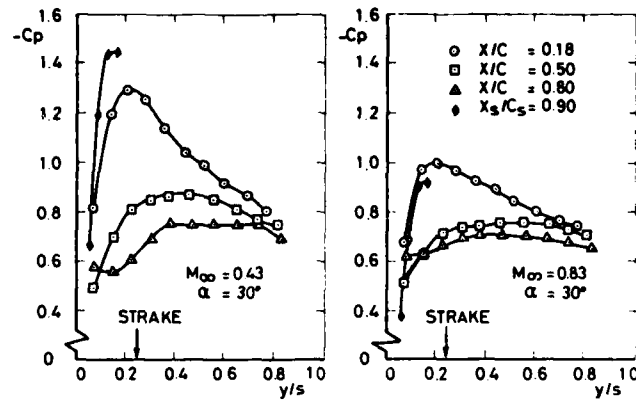
Fig.28 The effect of compressibility on the pressure distributions over
the wing strake configuration – α = 30° (Ref.11)

$$C_N = \frac{N}{q_\infty S_W}$$

$$C_N = \frac{N}{q_\infty S_W}$$
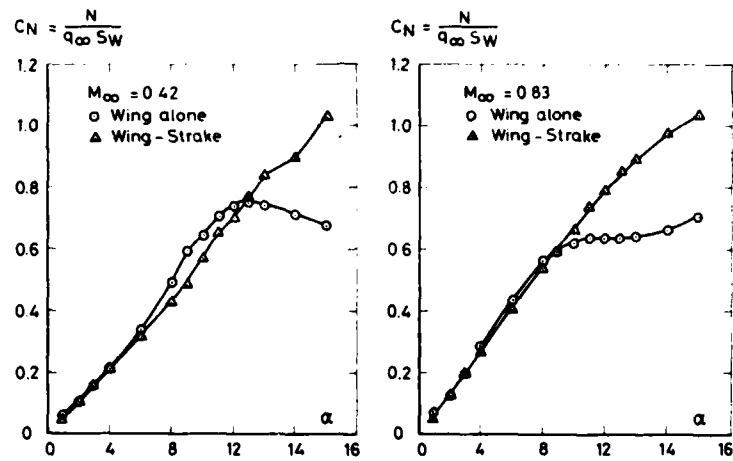
Fig.29 Comparison between wing alone and wing strake normal force coefficients
as a function of incidence (Ref.8)

$$C_M = \frac{M}{q_\infty S_W c}$$
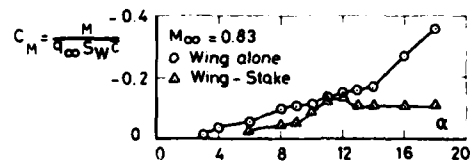
Fig.30 Comparison between wing alone and wing strake pitching moment
coefficients as a function of incidence (Ref.8)
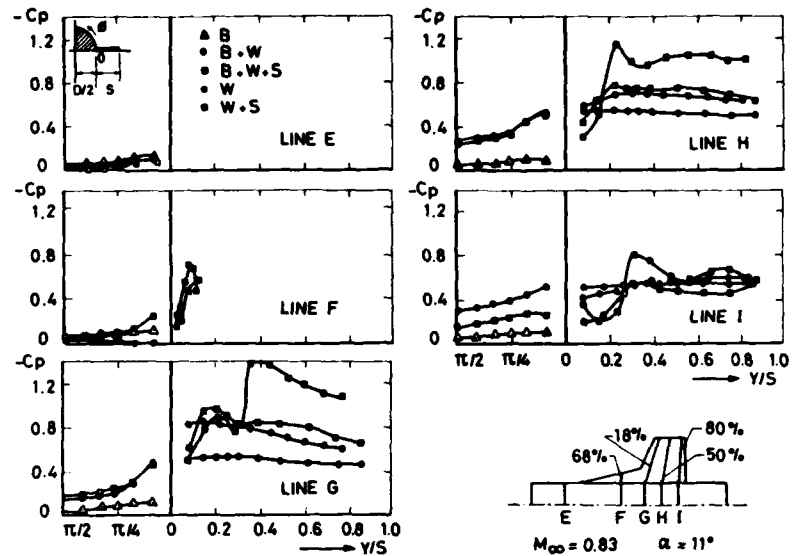
Fig.31 Comparison between the spanwise pressure distributions on all the different configurations
$M_\infty = 0.83, \alpha = 11°$ (Refs. 11, 15)
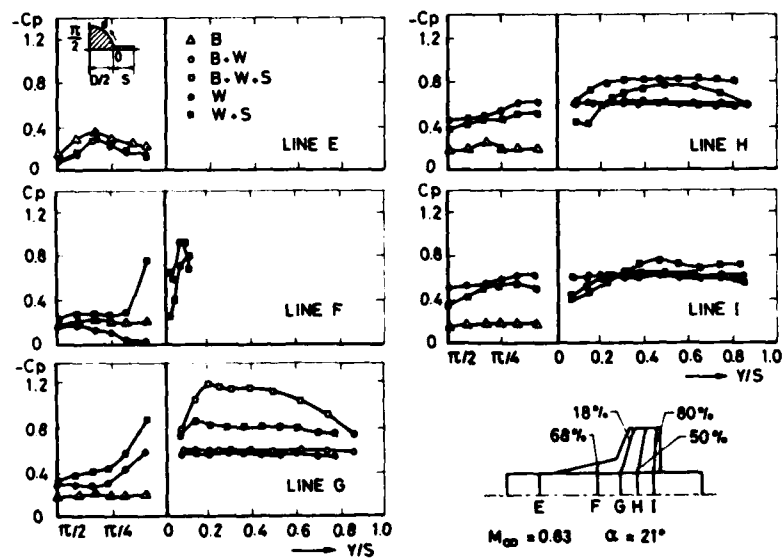
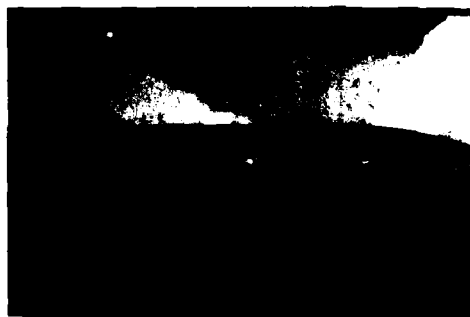Fig.32 Comparison between the spanwise pressure distributions on all the different configurations
$M_\infty = 0.83, \alpha = 21°$ (Refs. 11, 15)
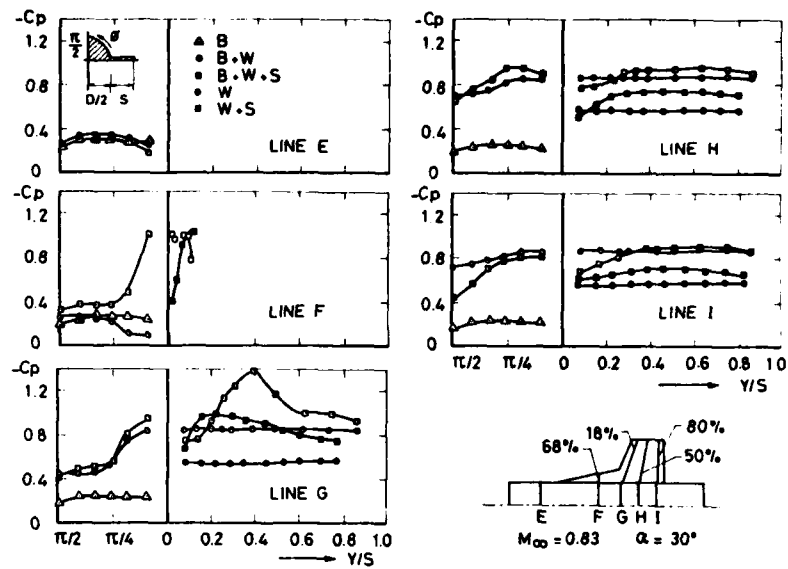
Fig.33   Comparison between the spanwise pressure distributions on all the different configurations
$M_\infty = 0.83, \alpha = 30°$ (Refs. 11, 15)

Fig.34   Water tunnel visualization of the flow
over the body wing configuration
$Re_D = 4200, \alpha = 15°$ (Ref.10)
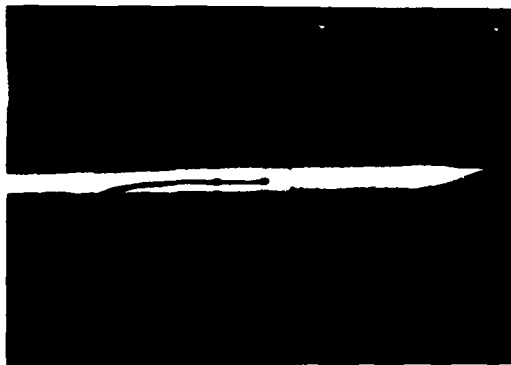
Fig.35   Water tunnel visualization of the flow
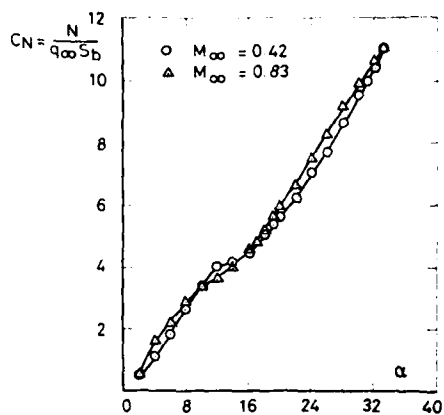over the body wing strake configuration
$Re_D = 4200, \alpha = 15°$ (Ref.10)

Fig.36 Normal force coefficient for the body wing
configuration as a function of incidence (Ref.9)

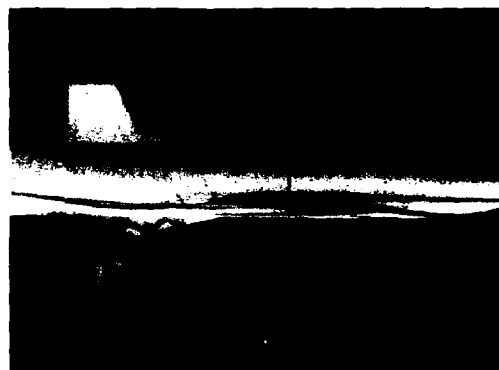

Fig.37 Water tunnel visualization of the flow
over the body wing strake configuration
$Re_D = 1300, \alpha = 12.5°$ (Ref.12)

Fig.38 Water tunnel visualization of the flow
over the body wing strake configuration
$Re_D = 1300, \alpha = 20°$ (Ref.12)

Fig.39 Water tunnel visualization of the flow
over the body wing strake configuration
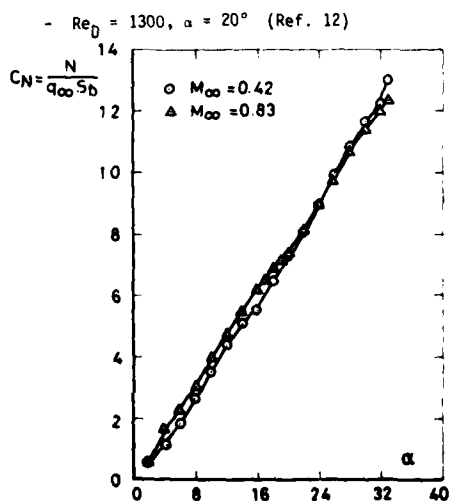$Re_D = 1300, \alpha = 25°$ (Ref.12)

Fig.40 Normal force coefficients for the body
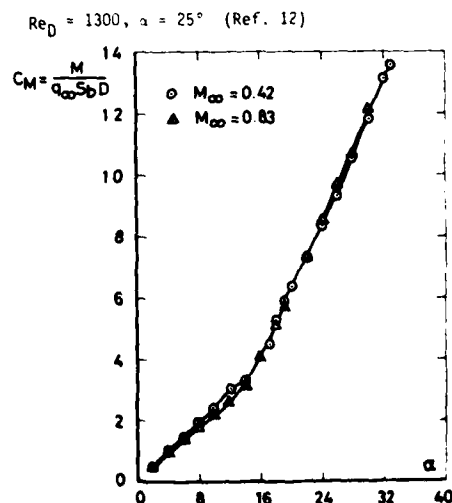strake wing configuration as a function of
incidence (Ref.9)

Fig.41 Pitching moment coefficients for the body
wing strake configuration as a function of
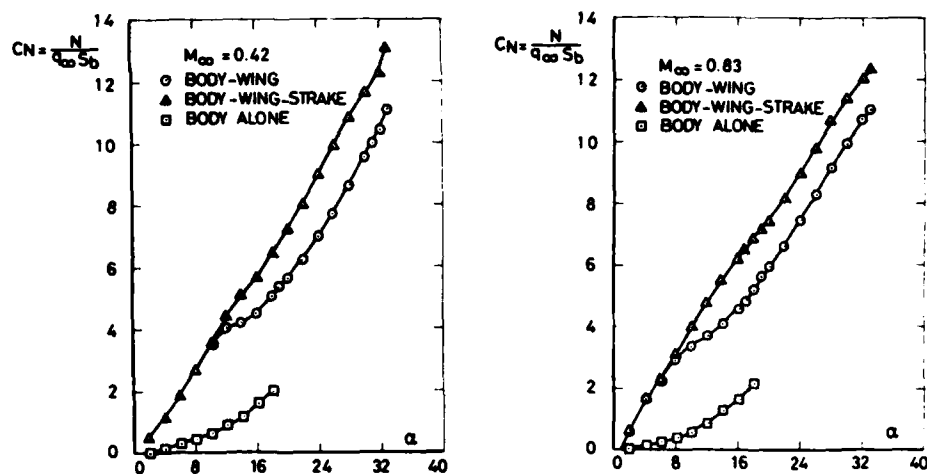incidence (Ref.9)

$$CN = \frac{N}{q_\infty S_b}$$

$M_\infty = 0.42$
⊙ BODY-WING
▲ BODY-WING-STRAKE
□ BODY ALONE

$$CN = \frac{N}{q_\infty S_b}$$

$M_\infty = 0.83$
⊙ BODY-WING
▲ BODY-WING-STRAKE
□ BODY ALONE

Fig.42   Comparisons of normal force coefficients versus α for the
missile configurations with and without strakes at different M_∞ (Ref.9)

$$\frac{\Delta C_N}{C_{N(BW)}}$$
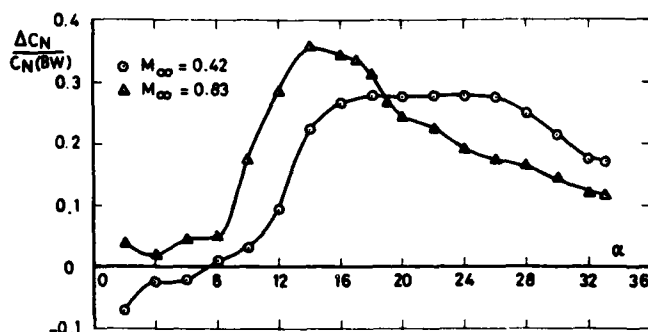
⊙ $M_\infty = 0.42$
▲ $M_\infty = 0.83$

Fig.43   Fractional increase in normal force coefficient due to the addition
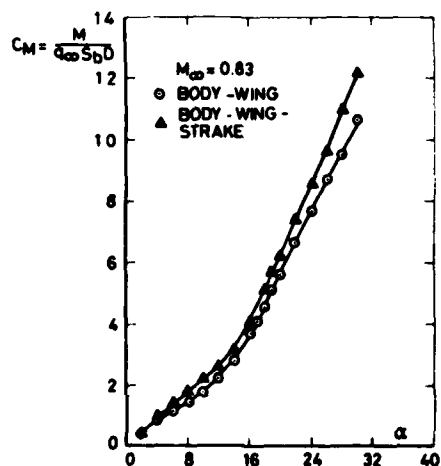of the strake versus incidence at different Mach numbers (Refs. 9, 15)

$$C_M = \frac{M}{q_\infty S_b D}$$

$M_\infty = 0.83$
⊙ BODY-WING
▲ BODY-WING-STRAKE

Fig.44   Comparison of pitching moment coefficients
versus α for the missile configurations
with and without strakes (Ref.9)

CONFIGURATION TESTED	INCIDENCE RANGE	MACH NUMBER	REYNOLDS NUMBER (Re_c or Re_D)	NORMAL FORCE & PITCHING MOMENT	SURFACE PRESSURE	WATER TUNNEL VISUALIZATION	REFERENCE
TRAPEZOIDAL WING ALONE	0°;18°	0.42	1.0×10^5	x			8
		0.83	1.5×10^5	x			
	7°;33°	0.43	1.3×10^5		x		11
		0.83	2.8×10^5		x		
		0.97	3.0×10^5		x		
	0°;24°	-	500:2000			x	14
STRAKE WING COMBINATION	0°;18°	0.42	1.0×10^5	x			8
		0.83	1.5×10^5	x			
	7°;33°	0.43	1.8×10^5		x		11
		0.83	2.8×10^5		x		
		0.97	3.0×10^5		x		
	0°;24°	-	500:2000			x	14
	0°;35°	-	600:1300			x	12
BODY ALONE	0°;18°	0.42	0.95×10^5	x			9
		0.83	1.4×10^5	x			
	11°;33°	0.83	1.4×10^5		x		10
	0°;30°	-	600:1300			x	13
WING BODY	0°;33°	0.42	0.95×10^5	x			9
		0.83	1.4×10^5	x			
	11°;33°	0.83	1.4×10^5		x		10
	0°;25°	-	4200			x	10
	0°;30°	-	600:1300			x	13
STRAKE WING BODY	0°;33°	0.42	0.95×10^5	x			9
		0.83	1.4×10^5	x			
	11°;33°	0.83	1.4×10^5		x		10
	0°;25°	-	4200			x	10
	0°;35°	-	600:1300			x	12,13

TABLE I

BIBLIOGRAPHY

HIGH ANGLE OF ATTACK AERODYNAMICS
Advisory Group for Aerospace Research and Development, Neuilly-sur-Seine, France
AGARD Conf. Proc. CP-247, Papers presented and discussed at the Fluid Dynamics Panel Symp., Sandfjord, Norway,
Oct. 4–6 1978. Publ 1979.

This Conference Proceedings contains thirty eight papers, all concerned with the flight of aircraft and missiles at high
angles of attack. They are in four groups, namely, studies of configurations of practical application; mathematical
modeling and supporting investigations; design methods; and air intakes.

TECHNICAL EVALUATION REPORT ON THE FLUID DYNAMICS PANEL SYMPOSIUM ON HIGH ANGLE OF ATTACK AERODYNAMICS
(AGARD Advisory Report AR-145, 1979) (See previous entry.) In English.
ADVISORY GROUP FOR AEROSPACE RESEARCH AND DEVELOPMENT, NEUILLY-SUR-SEINE, FRANCE.

SYNTHESE DE 32 COMMUNICATIONS SUR LES ASPECTS DE MECANIQUE DES FLUIDES DU VOL A GRANDE
INCIDENCE ET SUR LA CONCEPTION AERODYNAMIQUE DES VEHICULES AEROSPATIAUX. PRINCIPALES
SESSIONS: ETUDE DES CONFIGURATIONS D'APPLICATION PRATIQUE; MODELISATION MATHEMATIQUE;
METHOD DE CONCEPTION; PRISES D'AIR.

WIND TUNNEL CORRECTIONS FOR HIGH ANGLE OF ATTACK MODELS
ADVISORY GROUP FOR AEROSPACE RESEARCH AND DEVELOPMENT/NEUILLY-SUR-SEINE/FRANCE
Ed: NEUILLY-SUR-SEINE: AGARD; Date: 1981; AGARD-R-692; Langue: Anglais

REVUE DE DIFFERENTES METHODES DE CORRECTION POUR ESSAIS AVEC DE GRANDS ANGLES
D'ATTAQUE EN SOUFFLERIES FERMEES, OUVERTES ET VENTILEES. LES NOMBRES DE MACH VONT
JUSQU'AU SUBSONIQUE ELEVE ET CERTAINES METHODES SONT VALABLES POUR LES ECOULEMENT
INCOMPRESSIBLES.

TECHNICAL EVALUATION REPORT ON THE FLUID DYNAMICS PANEL SYMPOSIUM ON PREDICTION OF AERODYNAMIC LOADING
NASA AMES RESEARCH CENTER, 27–29 SEPTEMBER 1976.
ADVISORY GROUP FOR AEROSPACE RESEARCH AND DEVELOPMENT, NEUILLY-SUR-SEINE, FRANCE
AGARD; Date: 1978; Langue: Anglais

PRESENTATION DES PROBLEMES DE MECANIQUE DES FLUIDES LIES AUX PERFORMANCES DES AVIONS:
ILS CONCERNENT LES ANGLES D'ATTAQUE ELEVES ET LES FORTES TRAINEES ET PORTANCES. LES
INTERACTIONS VISQUEUSE/NON-VISQUEUSE DANS LES ECOULEMENTS TRANSSONIQUES. LES FORCES
AERODYNAMIQUES INSTATIONNAIRES DANS LES ECOULEMENTS SUPERSONIQUES ET LES
DECOLLEMENTS.

A METHOD FOR CALCULATING LONGITUDINAL CHARACTERISTICS OF WINGS AND MULTIPLE LIFTING SURFACES IN SUBSONIC FLOW, AND AT HIGH ANGLES OF ATTACK
ALMOSNINO (D.); ZOREA (C.); ROM (J.)
TECHNION-ISRAEL INST. TECHNOL., HAIFA, ISRAEL
ISRAEL J. TECHNOL.; ISR; DATE: 1978; Vol: 16; No; 3; p.: 132-141; Langue: Anglais

CALCUL DES CARACTERISTIQUES AERODYNAMIQUES LONGITUDINALES NON LINEAIRES AVEC LA
METHOD DU RESEAU DE TOURBILLONS ET EN TENANT COMPTE DU DETACHEMENT ET DU SILLAGE.
APPLICATION A DES AILES DE FARINES VARIEES.

SUPPORT INTERFERENCE ON AN OGIVE-CYLINDER MODEL AT HIGH ANGLE OF ATTACK IN TRANSONIC FLOW
Final Report, 1 Jul. 1976 – 30 Sep. 1977
ALTSTATT, M.C.; DIETZ, W.E.

SUPERSONIC FLAT PLATE AT HIGH INCIDENCE
Archer, R.D.; Napier, J.; Betteridge, D.S.
University of NSW, Australia. Australian Conference on Hydraulic and Fluid Mech., 5th. Proc., Univ. of Canterbury,
Christchurch, NZ, Dec. 9–13 1974, V.1, p.507–513.

The numerical method of integral relations in both the one and two strip modes has been used to calculate the inviscid
perfect gas flow field between a plane flat plate and its detached shock wave. Corresponding wind tunnel experiments
are described and results compared with the theory.

AIRCRAFT LONGITUDINAL MOTION AT HIGH INCIDENCE
Babister, A.W.
Aeronautical Journal, Vol.83, June 1979, p.230-232. AA (Glasgow, University, Glasgow. Scotland) 3 p.

The paper studies longitudinal symmetric motion of constant speed and height and determines simple control laws for an autopilot which would prevent a superstall occurring. An equation is presented for pitching motion and analysis with fixed elevator and T-tailed aircraft is made. Finally, the prevention of superstalled flight is discussed and it is concluded that a simple linear feedback control can be used to prevent superstalled flight. M.E.P.

AIRCRAFT STABILITY AT HIGH INCIDENCE
BABISTER, A.W.
Aeronautical Journal, Vol.84, Feb. 1980, p.73-75. AA (Glasgow, University, Glasgow, Scotland) 3 p.

The Kalviste method of analysis of aerodynamic coupling between longitudinal and lateral motion at high incidence, in which aircraft rotary motion alone is considered, is modified. The new method includes certain non-linear aerodynamic effects, and is especially useful in showing some unstable modes that become apparent only on introducing the non-linear terms. O.C.

ETUDE DE L'ECOULEMENT SUPERSONIQUE AUTOUR DES CONES CIRCULAIRES AUX GRANDES INCIDENCES (In Russian)
BACHMANOVA (N.S.); LAPYGIN (V.I.); LIPNITSKIJ (YU.M.)
AFF: MOSKVA. IZVEST. AKAD. NAUK S.S.S.R., MEKH. ZHIDKOSTI GAZA; S.S.S.R.; Date: 1973; No: 6, p.79-84

DETERMINATION DE LA POSITION DU POINT DE FERRI, DE LA FORME DES ZONES SUPERSONIQUES LOCALES ET DE L'ONDE DE CHOC INTERNE, AINSI QUE DE LA VARIATION DE LA PENTE DE L'ONDE DE CHOC EN FONCTION DE L'ANGLE D'INCIDENCE POUR DIFFERENTS REGIMES D'ECOULEMENT

AERODYNAMIC COEFFICIENT PREDICTION TECHNIQUE FOR FINNED MISSILES AT HIGH INCIDENCE
Baker, William B., Jr
ARO, Inc., Arnold Air Force Stn., Tenn., USA. J Spacecr Rockets, Vol.15, No.6, Nov-Dec 1978, p.328-333.

An aerodynamic coefficient prediction technique, based on a high angle-of-attack data base, is presented for the calculation of normal-force and pitching-moment coefficients for slender bodies with low-aspect-ratio fins at angles of attack up to 180 deg. Comparisons are made between predicted coefficients and data from the high angle-to-attack data base. Also, comparisons are made between predicted coefficients and independent data. Tables and graphs are available to allow hand calculation of coefficients for other configurations at selected Mach numbers and angles of attack.

SEPARATED FLOW PAST A SLENDER DELTA WING AT INCIDENCE
BARSBY (J.E.)
UNIV. EAST ANGLIA, NORWICH
AERONAUT. QUART.; G.B.; Date: 1973; Vol: 24; No: 2; p.120-128; Langue: Anglais

AMELIORATION DE LA METHODE AUX DIFFERENCES FINIES DE SMITH PAR L'INTRODUCTION D'UNE METHODE DE NEWTON POUR LA RESOLUTION PAR ITERATION DES EQUATIONS NON LINEAIRES SIMULTANEES. CETTE AMELIORATION PERMET D'ETENDRE LES CALCULS DES ECOULEMENTS DECOLLES SUR DES AILES DELTA AUX INCIDENCES ELEVEES ET PERMET DE TROUVER DE NOUVELLES SOLUTIONS POUR LE TOURBILLON DE BORD DE FUITE.

SURVEY OF RECENT HIGH ANGLE OF ATTACK WIND TUNNEL TESTING AT AERITALIA
Bucciantini, G.; De Silvestro, R.; Fornasier, L.
AERITALIA, Torino, Italy
AGARD Conf. Proc. No.247; High Angle of Attack Aerodyn. Paper presented and discussions from the Fluid Dyn. Panel Symp., Sandfjord, Norway, Oct. 4—6 1978. Publ. 1979. Available from NTIS, Springfield, Va., p.0D8.

The paper illustrates the present status of investigation at Aeritalia regarding wind tunnel testing techniques at high angles of attack and on stall/post stall characteristics of configurations typical of modern combat aircraft.

OCCURRENCE AND INHIBITION OF LARGE YAWING MOMENTS DURING HIGH-INCIDENCE FLIGHT OF SLENDER MISSILE CONFIGURATIONS
Clark, W.H.; Peoples, J.R.; Briggs, M.M.
Naval Weapons Cent, China Lake, Calif. J Spacecr Rockets, V.10, No.8, Aug. 1973, p.510-519.

Study of the occurrence of asymmetric wake configurations, and associated side forces and yawing moments, during high-incidence flight of slender, axisymmetric missile configurations. The relevant phenomena are characterized experimentally, and the root causes of wake asymmetries and means of inhibiting their occurrence are explored. It is concluded that certain flowfield disturbance devices may be effective in significantly reducing the maximum values of yawing moments induced by asymmetric disposition of wake vortices.

SUBSONIC HIGH-ANGLE-OF-ATTACK FLOW INVESTIGATION AT SEVERAL REYNOLDS NUMBERS
Clarkson, Mark H.; Malcolm, Gerald N.; Chapman, Gary T.
Univ. of Fla, Gainesville. AIAA J., Vol.16, No.1, Jan. 1978, p.53-60.

Wind tunnel tests conducted on a rotating research body at angles of attack of 45-90 deg yielded results that were inconsistent with simple crossflow theory. Consequently, force and pressure distribution tests, along with oil and sublimation flow visualization studies, were conducted in the same tunnel on a nonrotating model in an attempt to explain the behavior observed in the rotary tests. These studies indicate that, at appropriate conditions of Reynolds number and angle of attack, inflexional instabilities occur in the boundary layer which materially affects separation and, hence, the aerodynamic forces. Calculations of crossflow Reynolds numbers are made and compared with other works on inflexional instability.

STATIONARY VORTICES BEHIND A FLAT PLATE NORMAL TO THE FREESTREAM IN INCOMPRESSIBLE FLOW
COE (P.L.)
AFF: HOFSTRA UNIV., HEMPSTEAD, N.Y. AIAA J., NEW YORK, USA; Date: 1972; Vol: 10; No: 12; p.1701; Langue: Anglais

DISCUSSION DES CONDITIONS AUX LIMITES AU NIVEAU DES BORDS DE PLAQUE DE L'ECOULEMENT SUBSONIQUE NORMAL A UNE PLAQUE PLANE ET COMPORTANT DEUX TOURBILLONS STATIONNAIRES EN AVAL DE CETTE PLAQUE

SYNTHESIS OF TEST RESULTS ON THE CONCORDE AT HIGH ANGLE OF ATTACK
SYNTHESE DE RESULTATS D'ESSAIS DU CONCORDE A GRANDES INCIDENCES
COLLARD, D.
AAF PAPER NT 80 26 Association Aéronautique et Astronautique de France. Colloque d'Aérodynamique Appliques. 16th, Lille, France, Nov. 13–15, 1979, 13 p. In French. AA (Société Nationale Industrielle Aérospatiale, Direction des Etudes de Toulouse, Toulouse, France) 13 p.

BEHAVIOR OF A TRANSPORT AIRCRAFT WITH AN AIRFOIL HAVING A HIGH SLENDERNESS RATIO AT A HIGH ANGLE OF ATTACK
COMPORTEMENT A HAUTE INCIDENCE D'UN AVION DE TRANSPORT A AILE A GRAND ELANCEMENT
Collard, D.
Aérospatiale, Toulouse, France. AGARD Conf. Proc. CP-247: High Angle of Attack Aerodyn. Paper and discussions from the Fluid Dyn Panel Symp, Sandefjord, Norway, Oct. 4–6 1978. Publ. 1979.

In the supersonic transport aircraft Concorde, the lift component continuously increases almost uniformly up to 35 degrees. However, at an angle of attack of approx. $\alpha = 22$ degrees, a change in the shape of the flow occurs on the wing cell. The effects of this change are discussed, and results of wind tunnel experiments carried out on aircraft production models are presented. (In French)

APPLICATION OF SPANWISE BLOWING FOR HIGH ANGLE OF ATTACK SPIN RECOVERY
Cornish, J.J., III; Jenkins, M.W.M.
Lockheed-Ga Co. AGARD Conf. Proc. CP-247: High Angle of Attack Aerodynamics. Paper presented and discussed at the fluid Dynamics Panel Symp., Sandefjord, Norway, Oct. 4–6 1978. Publ. 1979.

A unique autorotation tunnel test has been performed on a 1/30th scaled model of an F-4 fighter configuration. During this test, air was blown spanwise over the wing from various nozzle locations and the influence of this blowing on the spinning mode was recorded. Over 50 test conditions were evaluated for both flat ($\alpha = 45$ degree) and steep ($\alpha = 80$ degree) spin modes. The wind blowing was very effective in arresting the spin for the steep spin mode and not very effective in stopping the flat spin. Nose blowing was also evaluated with only marginal success. By using 2.25 turns to stop as a criterion, an optimum wing nozzle location and blowing level was identified. These data, when scaled to full-scale values, showed that the required nozzle diameter was 1.92", located close to the wing root one quarter-chord point, and 18 lb/sec. of air was required to effect recovery.

OBSERVATIONS ON LOW-ASPECT-RATIO WINGS AT HIGH INCIDENCE. (LOW-ASPECT-RATIO WINGS AT HIGH INCIDENCE IN WIND TUNNEL STUDY OF SURFACE PRESSURE AND VORTEX FLOW)
DAVIS, H.R.; PARKINS, G.V.; SUN, Y.C.
CANADIAN AERONAUTICS AND SPACE JOURNAL, VOL.13, MAR. 1967, p.111-116.

ASYMMETRIC WAKE DEVELOPMENT AND ASSOCIATED SIDE FORCE ON MISSILES AT HIGH ANGLES OF ATTACK
DEFFENBAUGH (F.D.); KOERNER (W.G.)
TRW DEF. SPACE SYST. GROUP, REDONDO BEACH, CALIF. FLUID PLASMA DYN. CONF. 9; SAN DIEGO, CALIF.; NEW YORK; Ed: AM. INST. AERONAUT. ASTRONAUT.; Date: 1976; Vol: 364; p.1-11; Langue: Anglais

PRESENTATION D'UNE ANALYSE DES DONNEES D'ESSAIS EN SOUFFLERIE, QUI PERMET DE DECRIRE LES INFLUENCES DES NOMBRES DE MACH ET DE REYNOLDS ET DE LA GEOMETRIE DU CORPS SUR LE DEVELOPPEMENT DU TOURBILLON ET SUR LES FORCES ASSOCIEES SUR DES MISSILES, EN ECOULEMENT SUBSONIQUE OU FAIBLEMENT SUPERSONIQUE.

ANALYSIS OF TOTAL AND STATIC PRESSURE FLUCTUATIONS IN AN AIR INTAKE AT HIGH INCIDENCE
ANALYSE DES FLUCTUATIONS DE PRESSION TOTALE ET STATIQUE DANS UNE ENTREE D'AIR A GRANDE INCIDENCE
DELVILLE, J.; BOURIOT, M.
AAAF PAPER NT 80- 61 Association Aéronautique et Astronautique de France. Colloque d'Acoustique Aéronautique, 7th Lyons, France, Nov. 4, 5, 1980, 36p. In French. Direction des Recherches, Etudes et Techniques AB (Poitiers. Universite, Poitiers, France) 36 p.

The paper presents studies of pressure fluctuations in turbulent flow at low speed gathered by microphones placed in the flow at incidence angles of 20, 30, and 40 deg. Results are given for the 30 deg readings and dynamic pressure fluctuation measurements are compared with those taken by hot wire techniques. Graphs of the rms fluctuations are given for dynamic and static pressure and the probability density functions of the dynamic pressure are compared with the probabilities of velocity fluctuations. It was found that the zone of maximum fluctuation is characterized by intermittent forces translated by a flatness coefficient of 18, and near the end of the test channel the PDF approached a normal distribution. D.H.K.

PRESSURES ON A SLENDER, AXISYMMETRIC BODY AT HIGH ANGLE OF ATTACK IN A VERY LOW TURBULENCE LEVEL AIR STREAM
Annual Report, May 1979 – June 1980.
DEXTER, P.C.; FLOWER, J.W.
AD-A092533; PCD/8001 801000 DA-ERO 77-G-073 Dept. of Aeronautical Engineering.

EXPERIMENTAL INVESTIGATION OF SUPPORT INTERFERENCE ON AN OGIVE CYLINDER AT HIGH INCIDENCE
Dietz, W.E., Jr; Altstatt, M.C.
ARO Inc., Arnold Air Force Station, TN, USA. J. Spacecr & Rockets (USA), Vol.16, No.2, p.67-8. March April 1979

Describes a wind-tunnel test conducted to determine the support interference on an ogive-cylinder model at high angles of attack in transonic flow. The model is supported by either a base-mounted sting or a strut attached to the leeside of the model. The strut support acts as a splitter plate and generally reduced the normal-force coefficient, while the sting support increased the normal-force coefficient slightly. The support interference diminishes with increasing Mach number. A simple algebraic method of estimating support interference is used. Two semi-empirical methods for calculation of aerodynamic coefficients are compared with test results.

DEVELOPMENT OF FLOW SEPARATIONS RELATED TO INCIDENCE OF WINGS WITH SHARP LEADING EDGES – THREE-DIMENSIONAL BOUNDARY LAYER ANALYSIS
EICHELBRENNER, E.A.
ADVISORY GROUP FOR AERONAUTICAL RESEARCH AND DEVELOPMENT, PARIS, FRANCE. (AD429671)
AGARD R-275

INTERACTION DES DECOLLEMENTS AU BORD DE FUITE ET DE BORD D'ATTAQUE EN ECOULEMENT TRI-DIMENSIONNEL (THE INTERACTIONS OF FLOW/DETACHMENTS AT THE TRAILING EDGE AND THE ATTACK EDGE IN THREE DIMENSIONAL FLOW)E.A.EICHELBRENNER. APRIL 1960. 18p 7 REFS (IN FRENCH)

WIND-TUNNEL INVESTIGATION OF DIFFERENT MISSILE CONFIGURATIONS AT ANGLES OF ATTACK UP TO 30 DEGREES AND MACH NUMBERS 0.6 to 3.5
ENDMANN (P.)
AFF: MESSERSCHMITT BOELKOW BLOHM, MUNICH, FRG. AMERICAN INSTITUTE OF AERONAUTICS AND ASTRONAUTICS AEROSPACE SCIENCES MEETING. 16/1978/HUNTSVILLE, AL; USA; Ed NEW YORK AIAA. Date: 1978

A SUMMARY OF AGARD FDP MEETING ON DYNAMIC STABILITY PARAMETERS – ADVANCED AIRCRAFT PERFORMANCE AT HIGH ANGLE OF ATTACK
ERICSSON, L.F.
In AGARD Stability and Control. (see N79-30218-21-08) 23p.

EFFECT OF ANGLE OF ATTACK AND MACH NUMBER ON SLENDER-WING UNSTEADY AERODYNAMICS
ERICSSON (L.E.); REDING (P.)
AFF: LOCKHEED MISSILES & SPACE COMPANY INC., Sunnyvale Ca, USA. J.AIRCR., USA. Date 1978; Vol.15, No.6; p.358-365; Langue: Anglais

IDENTIFICATION OF NONLINEAR AERODYNAMIC STABILITY AND CONTROL PARAMETERS AT HIGH ANGLE OF ATTACK
Eulrich, B.J.; Rynaski, E.G.
Calspan Corp., Buffalo, NY, USA. AGARD Conference Proceedings No.172 on Methods for Aircraft State and Parameter Identification. Hampton, Va., USA 5-8 Nov. 1974, p.2/1-15, 1975. AGARD, Neuilly sur Seine, France

The procedure is based on a nonlinear, iterated Kalman filter fixed-point smoother identification algorithm and a least squares equation error method. Key ingredients for successful identification are the mathematical model, instrumentation system, control inputs and the identification algorithm. The major emphasis here is placed on the use of the identification procedure in analyzing high angle of attack flight data.

EXPERIMENTS ON AN AIRFOIL AT HIGH INCIDENCE IN PLUNGING MOTION
FAVIER, D.; REBONT, J.; MARESCA, C.
Centre National de la Recherche Scientifique, Marseilles (France). (CL588493). Inst. de Mécanique des Fluides de Marseille. In FRENCH; ENGLISH summary presented at 16th Colloq. d'Aérodyn. Appl., Lille. 13 - 15 Nov., 1979. 52p. Paris Association Aéronautique et Astronautique de France

Dynamic stall, usually studied in the case of the pitching motion, is investigated by means of plunging motion, where the airfoil is forced to oscillate in translation normal to the uniform airstream. Unsteady effects are made clear by a combination of flow visualization, measurements of aerodynamic components, static pressure, and skin friction distributions along the airfoil chord. The results are compared to those already obtained, on pitching airfoils. The effects involved by the two oscillating modes are shown to be quite similar for frequency parameters from 0.10 to 0.15, amplitudes of fluctuating incidence varying from 5 deg to 15 deg, around mean incidences varying from 0 deg to 20 deg. Author (ESA)

AERODYNAMIC METHODS FOR HIGH INCIDENCE MISSILE DESIGN
Fidler, John E.; Bateman, Michael C.
Martin Marietta Aerosp. Orlando, Fla., USA. J Spacecr Rockets. Vol.12. No.3, Mar 1975, p.162-168

The generation of empirical aerodynamic methods for high incidence missile design is described. A unique feature of the approach is the provision of a comprehensive data base for correlation into methods. This base is acquired through wind tunnel testing of large, specially built, extensively instrumented research models. Tests are carried out over wide, systematically varied ranges of relevant aerodynamic and geometric parameters. The works has produced methods for calculating the aerodynamic characteristics of: low aspect ratio fins, in the Mach number range 0.8 - 2.2; slender missile bodies at angles of attack to 90 degree at transonic speeds and including the effects of crossflow Mach and Reynolds numbers; and body plus tail configurations, including tail deflection effects, at angles to 60 - 90 degrees at transonic speeds.

EXPERIMENTAL AND ANALYTICAL INVESTIGATIONS OF HIGH ANGLE OF ATTACK MISSILE AERODYNAMICS
FLAHERTY, J.I.
AIAA 77-1156. In: Atmospheric Flight Mechanics Conference, Hollywood, Fla., August 8 - 10, 1977. Technical Papers. (A77-43151 20-08) New York, American Institute of Aeronautics and Astronautics, Inc., 1977, p.311-317. AA (USAF, Flight Dynamics Laboratory, Wright-Patterson AFB, Ohio), 7p.

AN ANALYSIS OF HIGH ANGLE OF ATTACK MISSILE AERODYNAMICS AT SUBSONIC FLOW MACH NUMBERS
FLAHERTY, J.I.
AIAA 79-1648. In: Atmospheric Flight Mechanics Conference for Future Space Systems, Boulder, Colo., August 6 - 8, 1978. Collection of Technical Papers. (A79-45302 19-01) New York, American Institute of Aeronautics and Astronautics, Inc., 1979, p.184-193. AA (USAF, Flight Dynamics Laboratory, Wright-Patterson AFB, Ohio) 13 p. Refs. 9.

AERODYNAMIC FORCES AND MOMENTS ON A SLENDER WITH A JET PLUME FOR ANGLES OF ATTACK UP TO 180 DEGREES
FLEEMAN (E.L.); NELSON (R.C.)
AFF: Air Force Flight Dyn. Lab., Wright-Patterson Air Force Base, Ohio. In: Am. Inst. Aeronaut. Astronaut. 12th Aerosp. Sci. Meet.; Washington; 1974; New York; Ed: AIAA; Date: 1974; Vol.110; p.1-15; Langue: Anglais

ETUDE EXPERIMENTALE EN SOUFFLERIE DES EFFETS D'INTERFERENCE DU SILLAGE D'ECHAPPEMENT D'UNE FUSEE SUR LES COEFFICIENTS AERODYNAMIQUES. ON MONTRE L'IMPORTANCE DE CES EFFETS AUX INCIDENCES SUPERIEURES A 40**(O) EN REGIME SUBSONIQUE ET AUX INCIDENCES SUPERIEURES A 90**(O) EN REGIME SUPERSONIQUE. DES DONNEES MONTRENT L'INFLUENCE DU NOMBRE DE MACH ET DU NOMBRE DE REYNOLDS SUR LES FORCES INDUITES PAR LES TOURBILLONS.

THREE-DIMENSIONAL LAMINAR BOUNDARY LAYER OVER A BODY OF REVOLUTION AT INCIDENCE AND WITH SEPARATION
Geissler (W.)
AFF: DEUTSCH FORSCHUNGS- UND VERSUCHSANSTALT FUER LUFT- UND RAUMFAHRT E.V. AERO-DYNAMISCHE VERSUCHSANSTALT GOETTINGEN, F.R. GER. AIAA J., NEW YORK; USA; Date: 1974; Vol.12; No.2; p.1741-1745; Langue: Anglais

RESOLUTION NUMERIQUE DES EQUATIONS COMPLETES DE COUCHE-LIMITE LAMINAIRE TRI-DIMENSIONNELLE, SANS SIMPLIFICATIONS, PAR UNE TECHNIQUE AUX DIFFERENCES FINIES IMPLICITE, ET PAR UTILISATION DE COORDONNEES PARTICULIERES (LIGNES DE COURANT ET DE POTENTIEL). DETERMINATION DE LA POSITION DU DECOLLEMENT EN UTILISANT LE CRITERE DE CONDITION DE STABILITE NUMERIQUE.

VISCOUS FLOWS OVER SLENDER SPHERICALLY BLUNTED CONES AT LARGE ANGLES OF ATTACK
INCLUDING MASS-TRANSFER AND LOW REYNOLD NUMBER EFFECTS
GOGINENI (P.R.); MURRAY (A.L.); LEWIS (C.H.)
VIRGINIA POLYTECH. INST. STATE UNIV. AEROSPACE OCEAN ENG. DEP., BLACKSBURG VA 24061, USA.
AMERICAN INSTITUTE OF AERONAUTICS AND ASTRONAUTICS FLUID AND PLASMA DYNAMICS
CONFERENCE. 11/1978/SEATTLE WA, USA; Ed.: NEW YORK: AIAA; Date: 1978; 78-1188; 12 P.h.t.; 9 REF.;
Cote: YM3800; Langue: Anglais Type: TC, LA. CC: 130.G.04.F

DS: FLUIDE VISQUEUX/CORPS IMMERGE/SPHERE/ANGLE ATTAQUE/NOMBRE REYNOLDS/TRANSFERT
MASSE/COUCHE CHOC/ECOULEMENT TRIDIMENSIONNEL/AERODYNAMIQUE/CONE/CALCUL NUMERIQUE/
CORPS EMOUSSE

COMPUTER PROGRAM FOR ESTIMATING COEFFICIENTS OF AXISYMMETRIC BODIES AT EXTREMELY HIGH
ANGLE OF ATTACK
EIN RECHENPROGRAMM ZUR ABSCHAETZUNG VON BEIWERTENROTATIONSSYMMETRISCHER RUEMPFE
BEI EXTREM HOHERANSTELLUNG
GREGORIOU, G.
Sponsored by Bundesmin. fuer Verteidigung, in German; ENGLISH summary, 42 p., Bonn DOKZENTBW

NONLINEAR ROLLING MOTION OF A CANARD-CONTROLLED MISSILE CONFIGURATION AT ANGLES OF
ATTACK FROM 0 to 30 DEGREES IN INCOMPRESSIBLE FLOW
HARDY (S.R.)
DAHLGREN LAB., DAHLGREN VA, USA. AMERICAN INSTITUTE OF AERONAUTICS AND ASTRONAUTICS
AEROSPACE SCIENCES MEETING. 16/1978/HUNTSVILLE, AL, USA; Ed: NEW YORK: AIAA; Date: 1978; 78-61;
10 P.h.t.; 7 P.

UEBER DEN EINFLUSS DER REYNOLDSZAHL AUF DIE NORMALKRAEFTE SLANKER
FLUGKOERPERRUEMPFE
INFLUENCE DU NOMBRE DE REYNOLDS SUR LES FORCES NORMALES SUR DES CORPS DE REVOLUTION
MINCES
HARMANN (K.)
DFVLR-AVA, 3400 GOETTINGEN. Z. FLUGWISSENSCH. WELTR.-FORSCH.; DTSCH.; Date: 1978, Vol.2, No.1,
p.22-35; Résumé: ANGL.; 25 REF.; Langue: Allemand

ETUDE DES ECOULEMENTS AVEC DES ANGLES D'ATTAQUE ELEVES, CE QUI AUGMENTE L'INFLUENCE DU
DETACHEMENT TOURBILLONNAIRE.

ANALYSIS OF WIND TUNNEL DATA PERTAINING TO HIGH ANGLE OF ATTACH AERODYNAMICS.
VOLUME 1: TECHNICAL DISCUSSION AND ANALYSIS OF RESULTS
Progress Report, June 1977 – April 1978
HEADLEY, J.W.
AFFDL-TR-78-94, VOL-1, AF PROJ. 2404, Aircraft Group, 180 p.

ANALYSIS OF WIND TUNNEL DATA PERTAINING TO HIGH ANGLE OF ATTACK AERODYNAMICS.
VOLUME 2: DATA BASE
Progress Report, June 1977 – April 1978
HEADLEY, J.W.
AFFDL-TR-78-94 VOL-2, AF PROJ. 2404 Aircraft Group, 571 p.

COMPUTATION OF VORTEX MODELS FOR WINGS AT HIGH ANGLE OF ATTACK IN INCOMPRESSIBLE FLOW
Hedman, S.G. (23p.)

VISCOUS FLOW OVER ARBITRARY GEOMETRIES AT HIGH ANGLE OF ATTACK
HELLIWELL (W.S.); DICKINSON (P.P.); LUBARD (C.)
AFF: ARETE ASSOCIATES/SANTA MONICA CA/USA. AIAA J.; 0001-1452; USA; Date: 1981; Vol.19, No.2,
p.191-197. Langue: Anglais

LA METHODE NUMERIQUE POUR LE CALCUL DE L'ECOULEMENT SUPERSONIQUE LAMINAIRE AUTOUR DE
GEOMETRIES ARBITRAIRES SANS DECOLLEMENTS AXIAUX AUX INCIDENCES ELEVEES CONSISTE A
RESOUDRE LES EQUATIONS DE NAVIER-STOKES PARABOLISEES INSTATIONNAIRES A 3 DIMENSIONS
ECRITES EN COORDONNEES "ORIENTEES SUIVANTS LE CHOC" "ORIENTEES SUIVANT LE CORPS".
SYSTEME DE COORDONNES CURVILIGNES NON ORTHOGONALES POUR LES GEOMETRIES DE VEHICULF
DE RENTREE COMPLEXES. CALCULS POUR UN BICONE EMOUSSE AVEC DES DECOUPES AU VENT ET SOUS
LE VENT. A MACH 10 ET JUSQU'A 10 DEGRES D'INCIDENCE. BON ACCORD AVEC LES DONNEES.

STUDY OF LOW-ASPECT RATIO SWEPT AND OBLIQUE WINGS
HOPKINS (E.J.); LEVIN (A.D.)
NASA AMES RES. CENT., MOFFET FIELD, CALIF. J. AIRCR.; USA; Date: 1975; Vol.12, No.8, p.648-652. Langue: Anglais

ON COMPARE LES FORCES ET LES MOMENTS DE DEUX CONFIGURATIONS AILE-FUSELAGE POUR UNE AILE OBLIQUE ET UNE AILE EN FLECHE. ON FAIT VARIER LE NOMBRE DE MACH ET L'ANGLE D'ATTAQUE, ET ON ETUDIE LA PORTANCE, LA TRAINEE, LES MOMENTS DE TANGAGE ET DE ROULIS

EXPERIMENTAL INVESTIGATION OF THE LEEWARD FLOW FIELD OF A CONE AT HIGH INCIDENCE IN SUPERSONIC FLOW
HOUWINK, R.; NEBBELING, C.
000975 Delft Progress Report, Series C - Mechanical and Aeronautical Engineering and Shipbuilding, Vol.1, Sept. 1975, p.69-79. AB (Delft, Technische Hogeschool, Delft, Netherlands)

SUPERSONIC/HYPERSONIC FLOW PAST AN OSCILLATING FLAT PLATE AT HIGH ANGLES OF ATTACK
HUI, (W.H.)
UNIV. WATERLOO DEP. APPLIED MATH, WATERLOO, ONT., CANADA. Z.ANGEW. MATH. PHYS.; CHE; Date: 1978; Vol.29, No.3, p.414-427; Résumé FRE; Langue: Anglais

ETUDE DE L'ECOULEMENT SUPERSONIQUE/HYPERSONIQUE NON VISQUEUX SUR UNE PLAQUE OSCILLANTE INCIDENTE OU POUR DE FAIBLES VALEURS DE L'AMPLITUDE ET POUR UNE FREQUENCE REDUITE, L'ECOULEMENT INSTATIONNAIRE EST CONSIDERE COMME UNE PETIT PERTURBATION DE L'ECOULEMENT STATIONNAIRE DE PRANDTL-MEYER. RESOLUTION DU PROBLEME DE PERTURBATION POUR DES CONDITIONS AUX LIMITES NON APPROPRIEES. APPLICATION A L'ETUDE DE LA STABILITE AERODYNAMIQUE D'UNE PLAQUE PLANE

PRESSURES ON A SLENDER BODY AT HIGH ANGLE OF ATTACK IN A VERY LOW TURBULENCE LEVEL AIR STREAM
Hunt, B.L.; Dexter, P.C.
Dept. of Aeronautical Engng., Univ. of Bristol, Bristol, England. AGARD Conference Proceedings No.247. High Angle of Attack Aerodynamics, Sandefjord, Norway, 4-6 Oct. 1978, p.17/1-14, 23 Refs. 1979. AGARD, Neuilly-sur-Seine, France. p.vii + 550

Reports experimentally measured transient pressures at low speeds on a model consisting of a circular cylinder with a tangent ogive nose in the angle of attack range from 30 to 90 deg. Great care was taken to eliminate extraneous disturbances: a wind tunnel with an extremely low level of free stream turbulence (approximately 0.01%) was used, the model was rigidly mounted and efforts were made to ensure laminar separation without turbulent re-attachment. By comparing the results with those obtained previously on the same model in similar tests at a higher level of free stream turbulence (approximately 0.7%) it is shown that there is a dramatic reduction in unsteadiness in the low turbulence level air stream and switching of the flow pattern is virtually eliminated. However, it is also found that the mean unswitched level is dependent on the roll angle of the model and hence that strict control of the free stream conditions is not sufficient to guarantee results which are independent of the experimental equipment. Some details of the inherent unsteadiness present in the flow pattern are presented.

SEMI-EMPIRICAL THEORY TO ESTIMATE THE AIRFORCES ACTING ON THE HARMONICALLY OSCILLATING TWO-DIMENSIONAL WING AT HIGH ANGLE OF ATTACK WHERE SEPARATION CAN OCCUR (SEMI-EMPIRICAL THEORY FOR ESTIMATING AERODYNAMIC FORCES ACTING ON HARMONICALLY OSCILLATING TWO-DIMENSIONAL WING AT HIGH ANGLE OF ATTACK WHERE FLOW SEPARATION OCCURS)
ISOGAI, K.
DEC. 1968, IN JAPANESE, ENGLISH SUMMARY.

INTERNAL COWL-SEPARATION AT HIGH INCIDENCE ANGLES
JAKUBOWSKI, A.K.; LUIDENS, R.W.
AIAA PAPERS 75-64 000175 American Institute of Aeronautics and Astronautics, Aerospace Sciences Meeting, 13th, Pasadena, Calif., Jan. 20-22, 1975, 15 p. AA (Virgina Polytechnic Institute and State University, Blacksburg, Va.) AB (NASA, Lewis Research Center, V/STOL and Noise Div., Cleveland, Ohio)

HIGH ANGLE OF ATTACK CHARACTERISTICS OF DIFFERENT FIGHTER CONFIGURATIONS
John, H.; Kraus, W.
Messerschmitt-Boelkow-Blohm, Munich, FRG. AGARD Conf. Proc. CP-247; High Angle of Attack Aerodyn. Paper presented and discussions from the Fluid Dyn Panel Symp, Sandefjord, Norway, Oct. 4-6 1978. Publ. 1979.

The paper reviews basic aerodynamic characteristics of different fighter configurations under conditions of separated flow beyond maximum lift where the resultant derivatives are completely different from those associated with the attached flow. The change under trim conditions is primarily dependent on the wind planform and overall aircraft configuration. Results are presented concerning the aerodynamic development of the aircraft configuration which meet these requirements and, at the same time, minimize the resulting drag penalties in the conventional angle-of-attack regime.

TRANSONIC FLOW PAST A SYMMETRICAL AIRFOIL AT HIGH ANGLE OF ATTACK
Johnson, D.A.; Bachalo, W.D.; Owen, F.K.
NASA, Ames Res. Cent., Moffett Field, Calif., USA. J. Aircr v 18 n 1 Jan 1981, p.7-14.

The results of an experimental investigation of shock-induced stall and leading-edge stall on a 64A010 airfoil section are presented. Advanced nonintrusive techniques — laser velocimetry and holographic interferometry — were used in characterizing the inviscid and viscous flow regions. The measurements include Mach contours of the inviscid flow regions, and mean velocity, flow direction, and Reynolds shear stress profiles in the separated regions. The experimental observations of this study are relevant to efforts to improve surface-pressure prediction methods for airfoils at or near stall.

FULL-SCALE WIND TUNNEL INVESTIGATION OF THE EFFECTS OF WING LEADING-EDGE MODIFICATIONS ON THE HIGH ANGLE-OF-ATTACK AERODYNAMIC CHARACTERISTICS OF A LOW-WING GENERAL AVIATION AIRPLANE
JOHNSON, J.L., JR; NEWSOM, W.A.; SATRAN, D.R.
AIAA PAPER 80-1844 800800 American Institute of Aeronautics and Astronautics, Aircraft Systems Meeting, Anaheim, Calif., Aug. 4-6, 1980, 17 p. AC (NASA, Langley Research Center, Hampton, Va.) 17 p. Refs.16.

EXPLORATORY INVESTIGATION OF THE EFFECTS OF VORTEX BURSTING ON THE HIGH ANGLE-OF-ATTACK LATERAL-DIRECTIONAL STABILITY CHARACTERISTICS OF HIGHLY-SWEPT WINGS
Johnson, Joseph L., Jr; Grafton, Sue B.; Yip, Long P.
NASA, Langley Res. Cent., Hampton, Va., USA. AIAA Pap Collect of Tech Pap — AIAA Aerodyn Test Conf, 11th, Colorado Springs, Colo, Mar 18-20, 1980. Publ. by AIAA (CP-801), New York, NY, 1980, p.282-297

A recent low-speed wind-tunnel investigation of highly-swept wings has shown that vortex breakdown at high angles of attack can cause large destabilizing effects on static lateral-directional stability characteristics, and that the destabilizing effects of vortex breakdown can be greatly aggravated by model support strut interference effects. The present paper discusses these effects based on the results of static force tests of several highly-swept setup arrangements.

THE EFFECT OF NON-SYMMETRIC FLIGHT ON AIRCRAFT HIGH ANGLE OF ATTACK HANDLING QUALITIES AND DEPARTURE CHARACTERISTICS
JOHNSTON, D.F.; HOGGE, J.R.
AIAA PAPER 74-792 000874 F33615 73-C-3101 American Institute of Aeronautics and Astronautics, Mechanics and Control of Flight Conference, Anaheim, Calif., Aug. 5-9, 1974, 10p. AB/Systems Technology, Inc., Hawthorne, Calif.)

IDENTIFICATION OF KEY MANEUVER-LIMITING FACTORS IN HIGH-ANGLE-OF-ATTACK FLIGHT
JOHNSON, D.E.
In AGARD Dyn. Stability Parameters, 12p.

NONLINEAR PREDICTION OF THE AERODYNAMIC LOADS ON LIFTING SURFACES
KANDIL (O.A.); MOOK (D.T.); NAYFEH (A.H.)
VIRGINIA POLYTECH. INST., STATE UNIV., BLACKSBURG, VA. IN: AM. INST. AERONAUT. ASTRONAUT. 7TH FLUID PLASMA DYN. CONF.; PALO ALTO, CALIF.; 1974; NEW YORK; Ed: AIAA; Date: 1974; Vol.503, p.1-14; 1 P.; Langue: Anglais

METHODE NUMERIQUE POUR LE CALCUL DES CARACTERISTIQUES AERODYNAMIQUES SUBSONIQUES NON LINEAIRES DES SURFACES PORTANTES DE FAIBLE ALLONGEMENT, AUX INCIDENCES ELEVEES. UTILISATION DE LA METHODE DES RESEAUX DE TOURBILLONS ET PRISE EN COMPTE DU DECOLLEMENT AUX EXTREMITES ET AUX BORDS D'ATTAQUE AIGUS. CALCUL DE LA FORME DE SILLAGES. EXEMPLES NUMERIQUES POUR LES AILES DELTA

STATE-OF-ART OF NONLINEAR, DISCRETE-VORTEX METHODS FOR STEADY AND UNSTEADY HIGH ANGLE OF ATTACK AERODYNAMICS
Kandil, Osama A.
Old Dom Univ., Norfolk, Va, USA. AGARD Conf. Proc. CP-247: High Angle of Attack Aerodyn. Paper presented and discussions from the Fluid Dyn. Panel Symp., Sandefjord, Norway, Oct. 4-6 1978. Publ. 1979.

The current status of development of inviscid models for predicting the aerodynamic characteristics of wings exhibiting leading-edge and/or wing-tip separations is reviewed. Numerical examples are presented.

STRUCTURES TOURBILLONNAIRES DES AILES MINCES DANS LE CAS D'ECOULEMENT DECOLLE
KARASK (A.A.); NISHT (M.I.)
DOKL. AKAD. NAUK S.S.S.R.; SUN; Date: 1979; Vol.246, No.6, p.1317-1320; Langue: Russe

ETUDE EXPERIMENTALE DES PARTICULARITES DE LA FORMATION DES STRUCTURES TOURBILLON-NAIRES DES AILES MINCES ET DETERMINATION DES VALEURS DES ANGLES D'ATTAQUE ET DE GLISSE-MENT POUR LES QUELLES LA RUPTURE A LIEU.

ECOULEMENT AUTOUR DES CONES EMOUSSES ET DE CORPS EN FORME DE CALOTTE SPHERIQUE
KARYAGIN (V.P.); LOSHAKOV (A.B.); SHVETS (A.I.)
P.M.T.F.; SUN; Date: 1978; No.5, p.98-102; Langue: Russe

A PARTIR DES DONNEES EXPERIMENTALES, ON ANALYSE LES CARACTERISTIQUES AERODYNAMIQUES
DE DIVERSES MODIFICATIONS DE CORPS EMOUSSES A FAIBLE ALLONGEMENT. DONNEES SUR LA
RESISTANCE, LA FORCE PORTANTE ET LE MOMENT DE TANGAGE POUR DES NOMBRES DE MACH DE
0.4 A 3.0 AVEC DES ANGLES D'ATTAQUE JUSQU'A 15 DEG.

SIMILARITY IN VORTEX ASYMMETRIES OVER SLENDER BODIES AND WINGS
Keener, E.R.; Chapman, G.T.
NASA Ames Res. Center, Moffett Field, CA, USA. AIAA J. (USA), Vol.15, No.9, p.1370-2, 7 Refs, Sept. 1977.

The similarities between asymmetric flow about bodies and wings at high angles of attack and with zero side-slip are
dealt with. The analysis of the experimental results of a previous wind-tunnel test program yielded some evidence that
the vortex asymmetry was the result of a hydrodynamic instability. In an effort to understand the cause of the
asymmetry examples of asymmetric flow were sought. Highly swept delta wings were one obvious possibility.

DELTA CANARD CONFIGURATION AT HIGH ANGLE OF ATTACK
KRAUS, W.
International Council of the Aeronautical Sciences, Congress, 12th, München, West Germany, Oct. 12-17, 1980. Paper
34 p. AA (Messerschmitt-Boelkow-Blohm, GmbH, Ottobrunn, West Germany).

STRAKE-WING ANALYSIS AND DESIGN
LAMAR (J.E.)
NASA LANGLEY RES. CENT. HAMPTON, VA 23665, USA. AMERICAN INSTITUTE OF AERONAUTICS AND
ASTRONAUTICS FLUID AND PLASMA DYNAMICS CONFERENCE. 11/1978/SEATTLE WA, USA; Ed: NEW YORK:
AIAA; Date: 1978; Langue: Anglais

YF-16 HIGH ANGLE OF ATTACK TEST EXPERIENCE
LAMERS, J.P.
In AGARD Stall/Spin Probl. of Mil. Aircraft, 14 p. (see N76-29245 20-08)

ASSESSMENT OF EXISTING ANALYTIC METHODS FOR PREDICTION OF HIGH ANGLE-OF-ATTACK LOADS ON DELTA WINGS AT SUPERSONIC SPEEDS
Landrum, Emma Jean; Townsend, James C.
NASA Langley Res. Cent., Hampton, Va, USA. AGARD Conf. Proc. CP-204: Predict of Aerodyn. Loading, from the
Fluid Dyn. Panel Symp., NASA Ames Res. Cent., Moffett Field, Calif, Sep. 27-29, 1975. Publ. by AGARD, Neuilly-sur-
Seine, Fr, Feb 1977, p.14

An assessment is made of the applicability of four loading prediction methods to high angle-of-attack conditions for
simplified wing-body configurations, namely, the tangent wedge approximation, the linear theory methods of Middleton
and Woodward, and a shock-fitting finite-difference technique. Estimates obtained by these methods were compared
with experimental pressure data on delta wings to examine the effects of Mach number, camber, sweep angle, and angle
of attack. Results indicate that all of the methods provided reasonable estimates at moderate angles of attack. At these
moderate angles of attack, the methods of Middleton and Woodward provided good estimtes at Mach numbers higher
than those usually associated with linear theory. Only the finite-difference method provided reasonable load estimates
at high angles of attack, where the other methods were unable to predict lower surface pressures.

A NUMERICAL STUDY OF LAMINAR FLOW SEPARATION ON BLUNT FLARED CONES AT ANGLE OF ATTACK
LI (C.P.)
LOCKHEED ELECTRONICS CO. INC., HOUSTON, TEX., USA. IN: AM. INST. AERONAUT. ASTRONAUT. 7TH
FLUID PLASMA DYN. CONF.; PALO ALTO, CALIF.; 1974; NEW YORK; Ed: AIAA; Date: 1974; Vol.585, p.1-10;
Langue: Anglais

ETUDE NUMERIQUE DES ECOULEMENTS SUPERSONIQUES LAMINAIRES AUTOUR DE CONES EMOUSSES
AVEC DES DECOLLEMENTS INDUITS PAR LES ECOULEMENTS TRANSVERSAUX ET LES ARRONDIS. LES
CHAMPS D'ECOULEMENT DECOLLE COMPLETS SONT CALCULES DIRECTEMENT A PARTIR DES EQUATIONS
DE NAVIER STOKES INSTATIONNAIRES. EN PARTANT DE LA CONDITION AURONT POUR LAQUELLE LES
VARIABLES DE L'ECOULEMENT SONT CALCULEES DANS LA REGION VISQUEUSE DU NEZ ET EN
ETENDANT LE CALCUL A UNE SURFACE EN AVAL DU POINT D'ATTACHEMENT DE L'ECOULEMENT A LA
PAROI.

A NEW VISCOUS-INVISCID FLOW INTERACTION METHOD
Losito, V.; de Nicola, C.
Inst. of Aerodynamics, Univ. of Naples, Naples, Italy. Numerical methods in laminar and turbulent flow. Swansea,
Wales, 17-21 July, 1978, p.433-40, 9 Refs, 1978. Pentech Press, London, England. 1006
Taylor, C.; Morgan, K.; Brebbia, C.A.

The numerical simulation of viscous flows at high Reynolds numbers is considered. An alternative to the integration of boundary layer equations is presented in the form of a viscous-inviscid interaction blowing or suction flow method. It is derived from the definition of displacement thickness and the continuity equation and applied to steady and unsteady flows, and laminar and turbulent boundary layers. It is shown that the influence of the boundary layer on the inviscid flow solutions can be represented as a basic nonuniform onset flow around the given geometry of the body. Computing time is reduced to 1/4 of the time required using the modified body technique. Strong viscous-inviscid interactions are examined for aerofoil stalling. Extension to separated flow yields accurate results for high incidence aerofoil lifting.

CALCULATION OF THE FLOW ON A CONE AT HIGH ANGLE OF ATTACK
LUBARD (S.C.); HELLIWELL (W.S.)
R & D ASSOC., SANTA MONICA, CALIF., USA. AIAA J., NEW YORK, USA; Date: 1974; Vol.12, No.7; p.965-974; 25 REF.; Langue: Anglais. CC:130.F.02

DS: ECOULEMENT SUPERSONIQUE/ECOULEMENT LAMINAIRE/CONE/CHAMP ECOULEMENT/METHODE CALCUL/METHODE ITERATIVE/ECOULEMENT HYPERSONIQUE/DECOLLEMENT/EQUATION PARABOLIQUE/ CALCUL NUMERIQUE/METHODE NUMERIQUE/CALCUL DIFFERENCES/SCHEMA IMPLICITE/INCIDENCE ELEVEE
METHODE DE CALCUL DU CHAMP D'ECOULEMENT SUR DES CONES A FORTE INCIDENCE EN REGIME LAMINAIRE SUPERSONIQUE; CETTE METHODE EST FONDEE SUR L'HYPOTHESE QUE LES DERIVEES LONGITUDINALES SONT PETITES PAR RAPPORT AUX DERIVEES NORMALES ET CIRCONFERENTIELLES. LES EQUATIONS OBTENUES SONT VALABLES DANS LES REGIONS VISQUEUSES ET NON VISQUEUSES, Y COMPRIS LA ZONE DE DECOLLEMENT PERIPHERIQUE QUI SE DEVELOPPE DU COTE AU VENT AUX INCIDENCES ELEVEES. RESOLUTION NUMERIQUE DES EQUATIONS PARABOLIQUES OBTENUES A L'AIDE D'UNE TECHNIQUE NOUVELLE DE DIFFERENTIATION IMPLICITE AVEC ITERATION. COMPARAISON DES RESULTATS AINSI OBTENUS AVEC DES DONNEES EXPERIMENTALES CONCERNANT UN CONE DE 10 DEG. DE DEMI-ANGLE A 12 DEG. D'INCIDENCE A MACH 8 ET UN CONE DE 5.6 DEG. DE DEMI-ANGLE.

THEORETICAL AND EXPERIMENTAL AERODYNAMICS OF STRAKE-WING INTERACTIONS UP TO HIGH ANGLES-OF-ATTACK
LUCKRING (J.M.)
NASA LANGLEY RES. INST., HAMPTON, VA 23665, USA. AMERICAN INSTITUTE OF AERONAUTICS AND ASTRONAUTICS FLUID AND PLASMA DYNAMICS CONFERENCE. 11/1978/SEATTLE, WA, USA; Ed: NEW YORK: AIAA; Date: 1978; 17 REF.; Langue: Anglais

NUMERICAL SIMULATION OF SUPERSONIC CONE FLOW AT HIGH ANGLE OF ATTACK
McRae, David S.; Hussaini, M.Y.
NASA, Ames Res. Cent., Moffett Field, Calif., USA. AGARD Conf. Proc. CP-247: High Angle of Attack Aerodyn. Paper presented and discussions from the Fluid Dyn. Panel Symp., Sandefjord, Norway, Oct. 4-6, 1978. Publ. 1979.

A conical symmetry assumption is applied to the full Navier-Stokes equations resulting in an equation set containing time and two coordinate directions as independent variables. The set is integrated by use of MacCormack's finite difference technique for the particular case of sharp cones at incidence. Solutions are obtained and compared with experiment for auxiliary conditions corresponding to both laminar and turbulent flow. Closure for the turbulent flow case is provided by use of a scalor eddy viscosity model based on the mixing length hypothesis. Modifications to the eddy viscosity model were found which led to excellent surface pressure and surface flow direction agreement for turbulent flow at low supersonic Mach numbers.

A COMPUTATIONAL AND EXPERIMENTAL STUDY OF HIGH REYNOLDS NUMBER VISCOUS/INVISCID INTER-ACTION ABOUT A CONE AT HIGH ANGLE OF ATTACK
MCRAE, D.S.; FISHER, D.F.; PEAKE, D.J.
AIAA PAPER 80-1422 800700 NAS2 10578 American Institute of Aeronautics and Astronautics, Fluid and Plasma Dynamics Conference, 13th, Snowmass, Colo., July 14-18, 1980. 14 p. AA (NASA Ames Research Center, Moffett Field, Calif., USAF, Flight Dynamics Laboratory, Wright-Patterson AFB, Ohio) AB (NASA, Ames Research Center, Moffett Field; NASA, Flight Research Center, Edwards, Calif.) 14 p.

BIFURCATION ANALYSIS OF AIRCRAFT HIGH ANGLE-OF-ATTACK FLIGHT DYNAMICS
Mehra, Raman K.; Carroll, James V.
Sci. Syst. Inc., Cambridge, Mass., USA. AIAA Pap Collect of Tech. Pap – AIAA Atmos. Flight Mech. Conf., Danvers, Mass, Aug. 11-13, 1980. Publ. by AIAA (CP-806), New York, NY, 1980, Pap 80-1599, p.358-371.

A new approach is presented for analyzing nonlinear and high-alpha dynamic behavior and stability of aircraft. This approach involves the application of bifurcation analysis and catastrophe theory methodology (BACTM) to specific phenomena such as stall, departure, spin entry, flat and steep spin, nose slice, and wing rock. Quantitative results of a global nature are presented, using numerical techniques based on parametric continuation. It is shown how BACTM provides a complete representation of the aircraft equilibrium and bifurcation surfaces in the state-control space, using a rigid body model and aerosurface controls.

AERODYNAMIC PROBLEMS WITH A MISSILE AT HIGH ANGLE OF ATTACK TO AN INCOMPRESSIBLE FLOW, AS ENCOUNTERED IN A WIND TUNNEL STUDY
PROBLEMES AERODYNAMIQUES D'UN MISSILE A GRANDE INCIDENCE EN INCOMPRESSIBLE
MESNIERE, M.; LACAU. G.
Div. des Engins Tactiques. In French; English summary. Presented at 16th Colloq. d'Aerodyn. Appl., Lille, 13–15 Nov., 1979, 24 p. Association Aeronautique et Astronautique de France.

VORTEX PATTERN DEVELOPING ON THE UPPER SURFACE OF A SWEPT WING AT A HIGH ANGLE OF ATTACK
SYSTEM TOURBILLONNAIRE PRESENT A L'EXTRADOS D'UNE AILE EN FLECHE A GRAND INCIDENCE
Mirande, Jean; Schmitt. Volker; Werle, Henri
Off. Natl. d'Etude et de Aerosp., Châtillon, France. AGARD Conf. Proc. CP-247: High Angle of Attack Aerodyn. Paper presented and discussions from the Fluid Dyn. Panel Symp., Sandefjord, Norway, Oct. 4–6, 1978. Publ. 1979.

An experimental study, based on a swept wing, has been undertaken in a water tunnel and a wind tunnel at low speeds ($V//0 < = 90$ m/s) with a view to improve the understanding of the intervening phenomena and to make easier their modeling. The vortex flow effects on this wing are illustrated. The domain of vortex flow appearance is deduced as a function of the sweep angle and the angle of attack. Based on a phenomenological study in the water tunnel, an attempt is then made to describe the physical pattern of the vortex flow from its formation near the apex to its breakdown at the trailing edge. Finally, the flow field over the wing is determined using a directional probe. 12 refs. In French.

MOVING SURFACE BOUNDARY LAYER CONTROL FOR AIRCRAFT OPERATION AT HIGH INCIDENCE
Modi, V.J.; Sun, J.L.C.; Akutsu, T.; Lake, P.; McMillan, K.; Swinton, P.G.; Mullins, D.
Univ. of BC, Vancouver. AIAA Pap Collect to Tech Pap – AIAA Atmos Flight Mech Conf., Danvers, Mass, Aug. 11–13, 1980. Publ. by AIAA (CP806), New York, NY, 1980 Pap 80-1621, p.515-522.

The paper studies effectiveness of the moving surface boundary layer control on a NACA 63-218 (modified) two-dimensional wing used in the Canadair CL-84, a twin propeller V/STOL design. The results suggest that the concept of moving surface can serve quite effectively as a boundary layer control. It can provide a significant increase in the maximum lift coefficient and stall angle. It appears that a rotating cylinder at the leading edge of an airfoil is likely to provide the maximum benefit. The concept presents several possible applications including a mechanism for delaying vortex-induced resonance of bluff bodies.

US NAVY FLIGHT TEST EVALUATION AND OPERATIONAL EXPERIENCE AT HIGH ANGLE OF ATTACK
MONEY, A.F.; HOUSE, D.E.
In AGARD Stall/Spin Probl. of Mil. Aircraft, 10 p. (see N76-29245 20-28) AB (Naval Air Test Center)

HIGH INCIDENCE AERODYNAMICS
MOORE, T.W.F.
British Aircraft Corp., Filton (England). (BX322534) 740400 Guided Weapons Div. In Von Kármán Inst. for Fluid Dyn. Missile Aerodyn., Vol.1, 27 p. (SEE N79-27201 18-15) 27 p. Jpn. 2374 HC A14/MF A01

High incidence flow aspects of aerodynamics are discussed. The method used for predicting forces in the incidence plane is outlined. Some results of the wind tunnel tests on the basis of which the technique was compiled are shown. J.M.S.

EFFECTS OF FOREBODY, WING AND WING-BODY-LEX FLOWFIELDS ON HIGH ANGLE OF ATTACK AERO-DYNAMICS
Moore, William A.; Erickson, Gary E.; Lorincz, Dale J.; Skow, Andrew M.
Northrop Corp., USA. SAE Prepr No. 791082 for Meeting Dec. 3–6, 1979, 25-p.

Vortex flows emanating from the forebody and from hybrid wings can have a strong influence on the high angle-of-attack handling qualities and the departure and spin resistance of fighter aircraft. Depending on the strengths, orientation, and breakdown characteristics of these vortices, an aircarft may be departure prone or departure resistant. Northrop has conducted in-depth studies to determine the effect of these shed vortices. Arising from these studies general guidelines have been developed for the design of forebody shapes and hybrid-wing planform such that aircraft stability will be enhanced.

THE INFLUENCE OF AERODYNAMIC INTERFERENCE ON HIGH ANGLE OF ATTACK WIND TUNNE TESTING
MOUCH, T.N.; NELSON, R.C.
AIAA 78 827 780000 AF-AFOSR-77-3299. In: Aerodynamic Testing Conference, 10th, San Diego, Calif., April 19–21, 1978, Technical Papers. (A78-32326 12-09) New York, American Institute of Aeronautics and Astronautics, Inc., 1978, p.426-432. AB (Notre Dame, University, Notre Dame, Ind.) 7 p.

EXPERIMENTAL INVESTIGATION OF THE SUPERSONIC FLOW PAST A SLENDER CONE AT HIGH INCIDENCE
NEBBELING, C.; BANNINK, W.J.
780815 Journal of Fluid Mechanics, Vol.87, Aug. 15, 1978, p.475-496. AB (Delft Technische Hogeschool, Delft, Netherlands) 25 p.

The supersonic flow field past a circular cone of semi-apex angle 7.5 deg at incidences up to 26 deg has been investigated experimentally at a freestream Mach number of 2.94. Since the flow past the cone was found to be conical, the flow phenomena may be described in a plane perpendicular to the cone axis. This paper gives the direction of the conical streamlines, the conical sonic line and the conical Mach number in such a plane. At incidences exceeding twice the cone semi-apex angle a separated flow regime was observed which consisted of two main vortices on either side of the leeward plane of symmetry, and probably also two secondary vortices close to the cone surface. From incidences of 17 deg on-wards, an embedded region of conical supersonic flow terminated by a shock wave was revealed. At 22 deg, approxi-mately, a second embedded shock wave was measured close to the cone surface and extended slightly across the leeward plane of symmetry. This shock wave may have been generated by the vortex system, which induced supersonic cross-flow components towards the cone. (Author)

HIGH ANGLE-OF-ATTACK AERODYNAMICS ON A SLENDER BODY WITH A JET PLUME
Nelson, R.C.; Fleeman, E.L.
Air Force Flight Dynamics Lab., Wright-Patterson Air Force Base, Ohio, USA. J. Spacecr. & Rockets (USA), Vol.12, No.1, p.12-16, 8 Refs, Jan. 1975.

Presents an aerodynamic analysis of data obtained from recent wind-tunnel tests on a slender body configuration. Force and moment coefficients are presented for angles of attack up to 180°, Mach numbers up to 2.2, and Reynolds numbers (based on diameter) up to 106. The rocket exhaust plume was simulated by exhausting cold air (ambient total temperature) through the nozzle of the model. This permitted study of the plume interference effects on the aero-dynamic coefficients. The jet effects on normal force were found to be important when the angle of attack exceeded 40° in subsonic flow and 90° in supersonic flow. Deflecting the nozzle at high angles of attack also caused large excursions in the centre-of-pressure location. Another problem associated with high angle-of-attack flight is the appearance of large side forces in yawing moments for a symmetric flight condition. These are due to steady asymmetric shedding of the body vortices. Data are presented which illustrate the influence of Mach number and Reynolds number on the out-of-plane forces.

THE INFLUENCE OF AERODYNAMIC INTERFERENCE ON HIGH ANGLE OF ATTACK WIND TUNNEL TESTING
Final Report, 1 April, 1977 – 31 March 1978
NELSON, R.C.; MOUCH, T.N.
AD-A056045; AFOSR-78-1079TR 780600 AF-AFOSR-3299-77; AF PROJ. 2307 Dept. Aerospace and Mechanical Engineering, 38 p.

NORMAL-FORCE AND PITCHING-MOMENT COEFFICIENTS OF WING-BODY COMBINATIONS AT VERY HIGH ANGLES OF ATTACK
NIKOLITSCH (D.)
AFF: MESSERSCHMITT-BOELKOW-BLOHM GMBH, MUNICH, DEU. AMERICAN INSTITUTE OF AERONAUTICS AND ASTRONAUTICS AEROSPACE SCIENCES MEETING. 16/1978/HUNTSVILLE, AL., USA; Ed: NEW YORK: AIAA; Date: 1978; 78-63; 9 P.H.T.; 19 REF; Langue: Anglais

PREDICTION OF FORCES AND MOMENTS ON FINNED BODIES AT HIGH ANGLE OF ATTACK AT TRANSONIC FLOW
OBERKAMPF, W.L.
SAND-80-2380 Aeroballistics Division, 65 p.

AERODYNAMICS OF FINNED MISSILES AT HIGH ANGLE OF ATTACK
Oberkampf, W.L.; Nicolaides, J.D.
Univ. Texas, Austin, USA. AIAA 9th Aerospace Sciences Meeting (Programme). New York, USA, 25–27 Jan. 1971, p.17, 1971.. American Inst. Aeronautics and Astronautics. New York, USA.

A theoretical and experimental investigation of the aerodynamics of finned missiles at high angle of attack is presented. Of primary concern is the interaction of the body vortex wake region at high angle of attack with the missile fins and the resulting effect on the forces and moments produced by the fins. An aerodynamic flow model is derived and is used in conjunction with a semi-empirical lifting theory to predict the forces and moments produced by the fins. Generally good agreement is obtained between theory and experiment. Results given particular attention are nonlinear rolling phenomena, induced side force, and fin Magnus.

PREDICTION OF ROLL MOMENTS ON FINNED BODIES IN SUPERSONIC FLOW
OBERKAMPF (W.L.)
AFF: UNIV. TEXAS, AUSTIN, TEX., USA. J. SPACECR. ROCK.; USA; Date 1975; Vol.12, No.1, p.17-21; 13 REF.; Langue: Anglais; TYPE CC: 130.F.02

METHODE POUR LE CALCUL DES MOMENTS DE ROULIS PROVOQUES PAR LES NERVURES SUR DES CORPS D'ENGINS SPATIAUX AUX INCIDENCES ELEVEES EN ECOULEMENT SUPERSONIQUE. ON SUPPOSE QUE LES CONFIGURATIONS DE FUSEE ONT DES NEZ POINTUS ET DES CORPS CYLINDRIQUES CIRCULAIRES. ON ETUDIE L'EFFET L'ECOULEMENT INDUIT PAR LE CORPS SUR LES MOMENTS DE ROULIS PRODUITS PAR LES NERVURES. ON EXAMINE NOTAMMENT LES TOURBILLONS DE FUSELAGE ET L'ECOULEMENT

DECOLLE SUR LE COTE AU VENT DE L'ENGIN. ANALYSE D'UNE CONFIGURATION CRUCIFORME AVEC DES NERVURES AYANT UNE FORME EN PLAN RECTANGULAIRE. RESULTATS CONCERNANT L'INCLINAISON DES NERVURES, LE ROULIS INDUIT ET LES MOMENTS D'AMORTISSEMENT DU ROULIS.

WAKE VORTEX MEASUREMENTS OF BODIES AT HIGH ANGLE OF ATTACK
OWEN (F.K.); JOHNSON (D.A.)
AFF: OWEN INTERNATIONAL INC., PALO ALTO. CA, USA. AMERICAN INSTITUTE OF AERONAUTICS AND ASTRONAUTICS AEROSPACE SCIENCES MEETING. 16/1978/HUNTSVILLE, AL, USA; Ed: NEW YORK: AIAA: Date: 1978; 78-23; 9 P.h.t.; 7 REF.; Langue: Anglais

NONLINEAR OSCILLATIONS AT HIGH INCIDENCE
PADFIELD, G.D.
Royal Aircraft Establishment, Bedford (England). (R2487540) 781100 Structures Dept. In AGARD Dyn. Stability Parameters 16 p (SEE N79-15061 06-08) 16 p.

Approximations were developed for free aircraft motion when nonlinear effects are present and when the aircraft is flying close to a stability boundary. The analysis is based on the behavior of the isolated critical mode. The method of multiple scales is used to predict the transient oscillatory growth to a limit cycle condition. Results for the lateral motion of slender aircraft with nonlinear aerodynamic moments have revealed that limit cycles are possible above and below the critical incidence. Aircraft motions can be stable when the linear theory predicts instability and unstable when stability is predicted. Within the framework of the perturbation analysis it is shown how damping moments may be synthesized from response measurements. S.E.S.

METHODE APPROCHEE POUR LE CALCUL DES CARACTERISTIQUES AERODYNAMIQUES DES AILES SEMI-ANNULAIRES A FLECHE CONSTANTE LE LONG DE L'ENVERGURE
(In Russian)
PASTUKHOV (A.I.); KUDRYAVTSEV (G.S.)
IZVEST. VYSSH. UCHEBN. ZAVED., AVIAC. TEKH.; S.S.S.R.; Date: 1975: Vol.18, No.2, p.106-111.

ETUDE DE SURFACES PORTANTES AUXQUELLES SE RAPPORTENT DES AILES MINCES CYLINDRIQUES BICOUPOLES (SEMI-ANNULAIRE) D'UNE FORME RECTANGULAIRE, TRIANGULAIRE, TRAPEZOIDALE OU EN DELTA DANS LE PLAN. ON PROPOSE UNE METHODE APPROCHEE PERMETTANT DE CALCULER LES CARACTERISTIQUES AERODYNAMIQUES DE TELLES AILES DANS UN FLUX INCOMPRESSIBLE POUR UNE LARGE GAMME DES ANGLES D'ATTAQUE ET DES ALLONGEMENTS RELATIFS.

AERODYNAMICS OF SLENDER BODIES AT HIGH ANGLES OF ATTACK
PRZIREMBEL (C.E.G.); SHEREDA (D.E.)
AFF: RUTGERS-STATE UNIV., PISCATAWAY, NJ, USA. J. SPACECR. ROCK.; USA; Date: 1979; Vol.16, No.1, p.10-14; Langue: Anglais

ETUDE EXPERIMENTALE EN SOUFFLERIE AVEC DES NOMBRES DE REYNOLDS ELEVES. ON SOULIGNE L'IMPORTANCE DE L'ANGLE DE ROULIS SUR LA MESURE DE LA FORCE LATERALE

WIND TUNNEL TESTING OF MISSILES AT HIGH ANGLE OF ATTACK – INFLUENCE OF THE TEST APPARATUS AT TRANSONIC SPEEDS
ESSAI EN SOUFFLERIE DE MISSILE A GRANDE INCIDENCE – INFLUENCE DU DISPOSITIF D'ESSAI EN SUBSONIQUE ELEVE
REGARD, D.
ONERA, TP No. 1980-16 800000, Israel Annual Conference on Aviation and Astronautics, 2nd, Haifa, Israel, March 12, 13, 1980. ONERA, TP No. 1980-16, 1980. 9 p. In French. Research supported by the Direction des Recherches, Etude et Techniques. AA (ONERA, Châtillon-sous-Bagneux, Hauts-de-Seine, France) 9 p. Refs.5.

A COMPREHENSIVE INVESTIGATION INTO THE SUPERSONIC VISCOUS FLOW ABOUT A SLENDER CONE AT HIGH ANGLE OF ATTACK: EXPERIMENTAL AND THEORETICAL RESULTS
Ph.D. Thesis
RICE. T.S.

INVESTIGATION OF NON-LINEAR AERODYNAMIC CHARACTERISTICS OF SLENDER BODIES AT HIGH INCIDENCE, IN SUBSONIC AND TRANSONIC SPEEDS
Final Technical Report
ROM, J.; ALMOSNINO, D.
Technion – Israel Inst. of Tech., Haifa. (TG136290) AD-A101415 801200 DA-ERO-78-G-119 Dept. of Aeronautics Engineering. 82 p.

This report presents the results of the experimental investigation of the effect of small, symmetric jet injection from the nose of a slender body on the lateral forces and moments at high incidence. The investigation includes the effects of Mach and Reynolds numbers rate of injection and the position of injection. It is demonstrated that at low speeds of jet

blowing even small rates are a very useful means of side-force and yawing moment alleviation and even control, influencing both separation and structure of the vortex field. Such effects are also obtained at high subsonic and even transonic Mach numbers but require much higher injection rates. The results of some visualization tests are also included for better understanding and interpretation of the flow phenomena involved. The report includes also presentation of some preliminary results of a method for the calculation of the longitudinal aerodynamic characteristics of bodies at incidence including the separation of symmetric vortices, in subsonic flow. Preliminary results of the prediction method which consists of a combined source/vortex lattice model, are presented. This method is being further developed for calculations of the aerodynamic characteristics of more complex wing-body configurations of high angles of attack. Author (GRA)

MATHEMATICAL MODELING OF THE AERODYNAMICS OF HIGH-ANGLE-OF-ATTACK MANEUVERS

Schiff, Lewis B.; Tobak, Murray; Malcolm, Gerald, N.
NASA, Ames Res. Cent., Moffett Field, Calif., USA. AIAA Pap Collect of Tech Pap – AIAA Atmos. Flight Mech. Conf., Danvers, Mass, Aug. 11–13, 1980. Publ. by AIAA (CP806), New York, NY, 1980, Paper 80-1583, p.222-235.

A review is presented of the current state of aerodynamic mathematical modeling for aircraft motions at high angles of attack. The mathematical model serves to define a set of characteristic motions from whose known aerodynamic responses the aerodynamic response to an arbitrary high angle-of-attack flight maneuver can be predicted. Means are explored of obtaining stability parameter information in terms of the characteristic motions, whether by wind-tunnel experiments, computational methods, or by parameter-identification methods applied to flight-test data. A rationale is presented for selecting and verifying the aerodynamic mathematical model at the lowest necessary level of complexity.

INCOMPRESSIBLE TURBULENT FLOW IN 2-D AIR INTAKE AT HIGH INCIDENCE BY FINITE ELEMENT METHOD

SEROU, P.; TSEN, L.F.
780000 DRME-76/1178. In: Numerical methods in laminar and turbulent flow; Proceedings of the First International Conference, Swansea, Wales, July 17–21, 1978. (A79-29801 11-34) London, Pentech Press, 1978, p.709-715. Direction des Recherches et Moyens d'Essais AB (Poitiers, Universite, Poitiers, France) 7 p.

The aim of the present study was to predict numerically the steady two-dimensional inc··mpressible turbulent flow field in an air intake. In order to cope with any geometrical configuration, use is made of the finite element method. A simple eddy viscosity model is chosen for the turbulent closure problem. This eddy viscosity, with or without relaxation effects, is taken as a function of the mean flow. In order to arrive at the finite element approximation, Galerkin's method of weighted residuals is applied to the Reynolds equations governing the flow problem. V.P.

PREDICTION OF THE COMPRESSIBLE VORTEX WAKE FOR BODIES AT HIGH INCIDENCE

SHIVANANDA, T.P.; OBERKAMPF, W.L.
AIAA PAPER 81-0360 810100 F08635-77-C-0049 American Institute of Aeronautics and Astronautics, Aerospace Sciences Meeting, 19th, St. Louis, Mo., Jan. 12–15, 1981, 16 p. AB (Texas, University, Austin, Tex.) 16 p. Refs. 22.

This paper is concerned with the theoretical prediction of the symmetric and asymmetric body vortex wake and the resulting forces and moments on the body for compressible cross-flow. The present analysis uses the impulsive flow analogy in conjunction with the discrete vortex method and extends to compressible flow in the cross flow plane by using the Rayleigh-Janzen method. The perturbation velocity potentials of the Rayleigh-Janzen method are numerically determined by means of a finite difference solution of Poisson equations. With the compressible velocity potential known at steps along the body, the axial distribution of normal force and side force is calculated. Results are presented for symmetric and asymmetric wake flow fields and body forces and moments. These results are compared to experimental measurements for both subsonic and supersonic freestream flow. (Author)

AN ASSESSMENT OF THE MARTIN-MARIETTA HIGH ANGLE OF ATTACK AERODYNAMIC METHODOLOGY FOR BODY TAIL MISSILES

SPRING, D.J.; DERRICK, J.N.; WINN, G.C.
AD-A028053; RD-76-33 760628 DA PROJ. 1M3-62303-A-214 127 p.

REYNOLDS NUMBER EFFECTS ON AERODYNAMIC CHARACTERISTICS AT LARGE ANGLES OF ATTACK

STALLINGS (R.L., JR)
AFF: NASA, LANGLEY RES. CENT., HAMPTON, VA, USA. J. SPACECR. ROCK.; USA; Date: 1980; Vol.17, No.2, p.129-133; 5 REF.; LangueAnglais

ETUDE EXPERIMENTALE DE L'EFFET DU NOMBRE DE REYNOLDS SUR LES CARACTERISTIQUES AERO-DYNAMIQUES D'UN CORPS A AILES CRUCIFORMES A GRAND ANGLE D'ATTAQUE. DETERMINATION DES DISTRIBUTIONS DE PRESSION, DES FORCES ET MOMENTS POUR DES NOMBRES DE MACH DE 1, 6 ET 2, 7, DES NOMBRES DE REYNOLDS DE 2 X $10^{**}(5)$ A 28 X $10^{**}(5)$ ET DES ANGLES D'ATTAQUE DE 0 A $50^{**}(0)$.

EXPERIMENTAL AND NUMERICAL STUDY OF THE FLOW IN AN AIR INTAKE AT HIGH INCIDENCE
ETUDE EXPERIMENTALE ET NUMERIQUE DE L'ECOULEMENT DANS UNE PRISE D'AIR A GRANDE INCIDENCE
STANISLAS, M.
AAAF PAPER NT 80-19 791100 Association Aéronautique et Astronautique de France. Colloque d'Aérodynamique Appliquée. 16th, Lille, France, Nov. 13–15, 1979, 52 p. In French. AA (Lille 1, Université, Villeneuve-d'Ascq, Nord, France) 52 p. Refs.21.

Recent studies of fighter aircraft have tried to extend the flight range through high incidence, improving thus the combat performance at high altitude. However, this creates aerodynamic problems, especially for the air intake of the jet engine, and the paper discusses the possibilities to remedy these problems. A two-dimensional model with rectilinear walls is used in two aspects: experiments at low speeds with the help of the double exposure holography method, obtaining the three vectors of the instantaneous velocity, and a numerical study computing the integral turbulent flow based on the velocity profile at the inlet of the air intake. N.D.

HIGH ANGLE-OF-ATTACK STABILITY AND CONTROL ANALYSIS
STENGEL, R.F.
760000 NAS1-13618; N00014-75 0-0432 In N/SA. Langley Res. Center Advan. in Eng. Sci., Vol.4, p.1753-1766 (see N77-10345 01-31), 14 p.

ON THE LEE-SIDE FLOW OVER DELTA WINGS AT HIGH ANGLE OF ATTACK
Szodruch, Joachim; Ganzer, Uwe
Tech. Univ. Berlin, FRG. AGARD Conf. Proc. CP-247; High Angle of Attack Aerodyn. Paper presented and discussions from the Fluid Dyn. Panel Symp., Sandefjord, Norway, Oct. 4-6, 1978. Publ. 1979. Available from NTIS, Springfield, Va, p.21. 1-21.

A classification of various types of lee-side flow for slender delta wings is presented for a range of supersonic Mach numbers and angles of attack. Two particular types of flow which occur at high angles of attack are discussed in more detail. One type exists when the leading edges are subsonic or just sonic. It is distinguished by a shock wave between the strong counterrotating leading edge vortices. The other type of flow occurs for supersonic leading edges, in which case a pair of separation bubbles occurs with embedded shock waves on the top. In this case, strong nonconical effects have been observed.

NONLINEAR AERODYNAMICS OF AIRCRAFT IN HIGH-ANGLE-OF-ATTACK MANEUVERS
TOBAK (M.); Schiff (L.B.)
AFF: AMES RES. CENT., NASA, MOFFETT FIELD, CALIF. 94035. IN: AM. INST. AERONAUT. ASTRONAUT. 12TH AEROSP. SCI. MEET.; WASHINGTON; 1974; NEW YORK; Ed: AIAA; Date: 1974; Vol.85, p.1 10; 12 REF. Langue: Anglais

FORMULATION D'UN SYSTEME DE MOMENTS AERODYNAMIQUES NON LINEAIRES POUR LES MOUVEMENTS ARBITRAIRES D'UN AVION AUX INCIDENCES ELEVEES. ON MONTRE QUE LE MOMENT TOTAL EST LA SOMME DES CONTRIBUTIONS DE TROIS MOUVEMENTS SIMPLES: UN MOUVEMENT DE BASE CONIQUE ET DES PERTURBATIONS OSCILLATOIRES DE CE MOUVEMENT DE BASE. RECOMMANDATIONS RELATIVES AUX TYPES D'ESSAIS EN SOUFFLERIE LES PLUS APPROPRIES POUVANT ETRE REALISES EN SUIVANT LES CONDITIONS DE CETTE FORMULATION.

EXPECTED IMPROVEMENTS FROM WIND TUNNEL MODEL TESTING AT HIGH ANGLE OF ATTACK
AMELIORATIONS ENVISAGEES POUR RESOUDRE LES PROBLEMES RENCOUNTRES AU COURS D'ESSAIS A GRAND INCIDENCE DE MAQUETTES EN SOUFFLERIE
VAUCHERET, X.
ONERA, TP No.1980-36 800000 (NATO, AGARD, Symposium on Subsonic/Transonic Configuration Aerodynamics, Munich, West Germany, May 5-7, 1980.) ONERA, TP No.1980-36, 1980. 23 p. In French. AA (ONERA, Châtillon-sous-Bagneux, Hauts-de-Seine, France) 23 p.

THE IMF LILLE ROTATION BALANCE AND ASSOCIATED EXPERIMENTAL TECHNIQUES – FOR WIND TUNNEL CONTROL LOSS SIMULATION DURING HIGH ANGLE OF ATTACK FLIGHT
BALANCE ROTATIVE DE L'I.M.F. LILLE ET TECHNIQUES EXPERIMENTALES ASSOCIEES
VEPBRUGGE, R.
AAAF PAPER NT 80-13 791100 Association Aéronautique et Astronautique de France, Colloque d'Aérodynamique Appliquée, 16th, Lille, France, Nov. 13–15, 1979, 50 p. In French. AA (Lille D, Université, Villeneuve-d'Ascq, Nord, France)

RECENT RESULTS IN PARAMETER IDENTIFICATION FOR HIGH ANGLE-OF-ATTACK STALL REGIMES
VINCENT, J.H.; GUPTA, N.K.; HALL, W.E., JR
AIAA PAPER 79-1640 790800 N00014-72 C 0328; N00014-78-C-0641 American Institute of Aeronautics and Astronautics, Atmospheric Flight Mechanics Conference, Boulder, Colo., Aug. 6-8, 1979, 16 p. AC (Systems Control, Inc. /VT/, Palo Alto, Calif.) 16 p. Refs. 7 Jpn. 4281.

ANALYSIS OF T-2C HIGH ANGLE OF ATTACK FLIGHT TEST DATA WITH NONLINEAR SYSTEM IDENTIFICA-
TION METHODOLOGY
Final Report, 3 April, 1972 – 31 May, 1978
VINCENT, J.H.; HALL, W.E., JR; BOHN, J.G.
AD-A086327; ONR-CR-212-259-1F 800300 N00014 72-C-0328 90 p.

HIGH ANGLE OF ATTACK FLIGHT TESTS OF THE F-15
WALKER, D.N.
750000 In: Toward more effective testing; Proceedings of the Sixth Annual Symposium, St. Louis, Mo., August 13–16,
1975. (A76-34233 16-35) Lancaster, Calif., Society of Flight Test Engineers. 1975, p.227-245. AA (McDonnell Aircraft
Co., St. Louis, Mo.) 19 p.

BOUNDARY LAYER OVER A BLUNT BODY AT HIGH INCIDENCE WITH AN OPEN-TYPE OF SEPARATION
WANG, K.C.
030974 F44620-70-C-0085 Royal Society (London), Proceedings, Series A, Vol.340, No.1620, Sept. 3, 1974, p.33-35.
AA (Martin Marietta Laboratories, Baltimore, Md.)

LAMINAR BOUNDARY LAYER OVER A BODY OF REVOLUTION AT EXTREMELY HIGH INCIDENCE
Wang, K.C.
Martin Marietta Labs., Baltimore, Md., USA. Phys. Fluids (USA), Vol.17, No.7, p.1381-5, 8 Refs, July 1974.

Results of an exact solution to three-dimensional problem of boundary layer flow at extremely high incidence over an
oblate spheroid are given. High incidence flow over such a body is marked by an increase of circumferential flow and a
decrease in meridional flow. At the same time the separation pattern which had been open at lower incidences, closes up
again. The calculation is carried out for $b/a = 1/4$ and an angle of incidence of 45.

HIGH-ANGLE-OF-ATTACK MISSILE AERODYNAMICS
Wardlaw, Andrew B., Jr
Nav. Surf. Weapons Cent., White Oak Lab., Silver Spring, Md, USA. AGARD Lecture Series LS-98, Missile Aerodyn.: for
Meet. Ankara, Turkey, March 5–6, 1978; Rome, Italy, March 8–9, 1978; Rhode-Saint-Gènese, Belgium, March 12–16,
1978. Publ. 1979.

The paper reviews experimental data on and predictive methods for bodies, fins, and complete missile configurations. An
outline and description is provided of the various vortex regimes that exist on a missile and its components at high angles
of attack. Data is examined to determine quantitative trends in surface pressure distributions and loads. Available
analytic, semi-empirical, and empirical predictive methods are reviewed.

PREDICTION OF YAWING FORCE AT HIGH ANGLE OF ATTACK
WARDLAW (A.B., JR)
AFF: NAV. ORDNANCE LAB., SILVER SPRING, MD, USA. AIAA J., NEW YORK; USA; Date: 1974; Vol.12, No.8,
p.1142-1144; Langue: Anglais

DESCRIPTION APPROCHEE DU CHAMP D'ECOULEMENT ASYMETRIQUE DU COTE AU VENT D'UN CORPS DE
REVOLUTION A GRANDE INCIDENCE, PERMETTANT LA PREVISION DE LA FORCE ET DU MOMENT DE
LACET CREES, AINSI QUE DES FORCES NORMALES

HIGH ANGLE-OF-ATTACK AERODYNAMICS
WARDLAW, A.B., JR
EXPERIMENTAL AERODYNAMICS BRANCH. In Von Kármán Inst. for Fluid Dynamics. Missile Aerodyn., Vol.2.
144 p. (See N79-18927-10-02) 144 p.

EXPERIMENTAL STUDY OF FORCES AND MOMENTS ON CIRCULAR BODIES AT HIGH ANGLE OF ATTACK
WARDLAW, A.B., JR

INDUCED SIDE FORCES ON BODIES OF REVOLUTION AT HIGH ANGLE OF ATTACK
WARDLAW, A.B.; MORRISON, A.M.

PREDICTION OF YAWING FORCE AT HIGH ANGLE OF ATTACK
Wardlaw, Andrew B., Jr
Nav. Ordnance Lab., Silver Spring, Md, USA. AIAA J., Vol.12, No.8, Aug. 1974, p.1142-1144.

An approximate flowfield description is developed which is an extension of a previously proposed model. The current
formulation is applicable to bodies of revolution and models the flow using the impulsive flow analogy with viscous
effects being simulated using point vortices. The symmetric wake assumption present in preceding studies is relaxed and
growing vortices near the missile as well as those shed into the wake, are taken into the account.

USER'S MANUAL FOR THE MARTIN-MARIETTA HIGH ANGLE OF ATTACK AERODYNAMIC METHODOLOGY FOR BODY TAIL MISSILES
WINN, G.C.
AD-A057138; DRDMI-T-78-63 780600 Technology Lab., 85 p.

STALL/SPIN SEVENTY YEARS LATER – AIRCRAFT PERFORMANCE AT HIGH ANGLE OF ATTACK
WOODCOCK, R.J.; CORD, T.J.
000674 Air University Review, Vol.25, May June 1974, p.25-36. AB (USAF, Flight Dynamics Laboratory, Wright-Patterson AFB, Ohio)

ESTIMATION OF TRANSONIC AIRCRAFT AERODYNAMICS TO HIGH ANGLES OF ATTACK
XELSON (J.A.)
AFF: AMES RES. CENT., NASA, MOFFETT FIELD, CALIF. 94035, USA. IN: AM. INST. AERONAUT. ASTRONAUT. AIRCR. SYST. TECHNOL. MEET ; LOS ANGELES: 1975: NEW YORK; Ed: AIAA; Date: 1975; Vol.996. p.1-9; Langue: Anglais

DESCRIPTION D'UNE NOUVELLE METHODE D'ETUDE ET D'OPTIMISATION DES VOLS TRANSSONIQUES. ON DONNE DES EQUATIONS NON LINEAIRES POUR LES VOLS A DIFFERENTES VITESSES, ET DE NOUVEAUX ALGORITHMES POUR TENIR COMPTE DES EFFETS DE COMPRESSIBILITE ET POUR ANALYSER LES PROBLEMES D'ONDE DE CHOC.

WING ROCK AS A LATERAL-DIRECTIONAL AIRCRAFT LIMIT CYCLE OSCILLATION INDUCED BY NON-LINEAR AERODYNAMICS OCCURRING AT HIGH ANGLE OF ATTACK
M.S. Thesis
YOUNG, P.D.

MULTI-STABLE VORTEX PATTERNS ON SLENDER, CIRCULAR BODIES AT HIGH INCIDENCE
YANTA, W.J.; WARDLAW, A.B., JR
AIAA PAPER 81-0006 810100 American Institute of Aeronautics and Astronautics. Aerospace Sciences Meeting. 19th. St. Louis, Mo., Jan. 12 -15, 1981, 13 p. AB (US Navy, Naval Surface Weapons Center, Silver Spring, Md.)

A rigidly supported tangent ogive model has been tested in low turbulent, incompressible flow at incidences of 35, 45 and 55 deg. A constant streamwise Reynolds number of 1.5 was maintained which produced laminar boundary layer separation. Both unsteady pressures and flow field velocities were measured, the latter with a three component laser Doppler velocimeter. Analysis of the results indicates that the vortex pattern may be unsteady at times, but that the flow field can be idealized as steady and that variations in the measured side force are principally a result of changes in the mean vortex pattern. Large side forces are shown to be induced by flow fields that shed a major part of the first vortex. A relationship is established between side force magnitude and surface pressure fluctuations. The repeatability of side force measurements is examined and tests featuring high side force levels are found to be the most reproducible. Tests on a blunted model produced a decrease in side force and body vortices located a greater distance from the model surface. (Author)

REPORT DOCUMENTATION PAGE

1. Recipient's Reference	2. Originator's Reference	3. Further Reference	4. Security Classification of Document
	AGARD-LS-121	ISBN 92-835-0322-8	UNCLASSIFIED

5. Originator   Advisory Group for Aerospace Research and Development
North Atlantic Treaty Organization
7 rue Ancelle, 92200 Neuilly sur Seine, France

6. Title

HIGH ANGLE-OF-ATTACK AERODYNAMICS

7. Presented at

8. Author(s)/Editor(s)	9. Date
Various	December 1982

10. Author's/Editor's Address	11. Pages
Various	416

12. Distribution Statement   This document is distributed in accordance with AGARD
policies and regulations, which are outlined on the
Outside Back Covers of all AGARD publications.

13. Keywords/Descriptors

Aerodynamics	Missiles
Angle of attack	Fighter aircraft
Three dimensional flow	Computation
Boundary layer separation	Unsteady flow
Flow visualization	

14. Abstract

The purpose of this Lecture Series is to review:

> three-dimensional flows with separation and re-attachment including compressibility
> effects
> the impact of visualization techniques on understanding complex flows
> the aerodynamic design of modern missiles and fighter aircraft for high angle-of-attack
> operation
> the status of computational fluid dynamics in the case of large-scale separated three-
> dimensional flows
> unsteady aerodynamics and dynamic stability considerations.

The material in this publication was assembled to support a Lecture Series under the sponsor-
ship of the Fluid Dynamics Panel and the Consultant and Exchange Programme of AGARD
presented on 10–11 March 1982 at the NASA Langley Research Center, USA, and on 22–23
March 1982 at DFVLR, Göttingen, Germany. The publication also includes the additional
papers of the expanded version of the series sponsored by AGARD and the von Kármán
Institute for Fluid Dynamics which was presented at the VKI, Rhode-Saint-Genèse, Belgium
on 15–19 March 1982.